Physicochemical Problems of Mineral Processing

Volume 50, Issue 2

June 1, 2014

Physicochemical Problems of Mineral Processing

Volume 50, Issue 2, June 1, 2014

The papers published in the Physicochemical Problems of Mineral Processing journal are abstracted
in BazTech, Chemical Abstracts, Coal Abstracts, EBSCO, Google Scholar, Scopus, Thomson Reuters
(Science Citation Index Expanded, Materials Science Citation Index, Journal Citation Reports)
and other sources

CONTENTS

INVESTIGATION OF ADSORPTION BEHAVIOR OF PHOSPHONIUM SALTS ONTO Na-MONTMORILLONITE

Kenan CINKU, Burak BAYSAL

Istanbul University, Engineering Faculty, Mining Engineering Department, 34320, Avcilar, Istanbul, Turkey.
kenan@istanbul.edu.tr

Abstract. Montmorillonite is an important clay mineral due to its cation exchange capacity and technological properties such as swelling and gelling. It has been widely used in many scientific applications like organoclay. Adsorption studies, involving montmorillonite in the presence of variety of organic compounds, like ammonium and phosphonium salts, are very important because of their application in organoclay and polymer nanocomposites. These materials have a high thermal resistivity. Different types of phosphonium salts, including hexadecyl triphenyl phosphonium bromide (HTPB), hexadecyl tributyl phosphonium bromide (HTBPB), and tetraphenyl phosphonium bromide (TPB), were used to investigate their adsorption on Na-montmorillonite. They have different structures and TPB contains only one aromatic part without any organic chain, HTBPB possess an organic chain with three branches while HTPB has an organic chain and an aromatic part. The adsorption of the surfactants was supplemented with other properties such as zeta potential, surface tension, and ability to flocculation. The results indicated that the adsorption behavior of these surfactants depended on their structure.

Keywords: Na-montmorillonite, phosphonium salts, adsorption

Introduction

Montmorillonite is a widely used clay mineral in scientific studies such as adsorption, preparation of organoclay and nanocomposites of high exchange capacity, and other physicochemical properties due to the sandwich-type 2:1 crystal lattice structure. The layers of montmorillonite are connecting each other due to weak van der Waals forces, water molecules as well as cations presence between them (Bergaya et al. 2006; Grim 1968; Lagaly 1993; Mittal 2009; Van Olphen 1977). Since the net surface charge of montmorillonite is always negative (Sondi et al. 1997), it can be modified with cationic surface active agents via ion exchange mechanism. Modification processes, based on cation exchange and properties of organoclay and nanocomposite, have been performed for a long time in literature.

In the current of era of nanotechnology, new types of materials have been discovered, which have brought a significant technological progress. Production of nanoclays and organoclays (organically modified layered silicates) has been a turning point for nanotechnology. The use of nanoclays in polymer matrix as a strengthen phase, as a rheological agent, and as a water treatment reagent (Patel 2006) accelerated this process. Application of nanocomposites has become very popular and many studies, particularly about layered silicate composites, hybrid or nanocomposites, were started by the Toyota research group in the 1980's (Okada and Usuki 2006) and has been continued until now.

The studies started with improvement of mechanical and thermal stability of the organoclays and have been continued with application of barriers (LeBaron et al. 1999; Usiki et al. 1992; Ray and Okamoto 2003). Academic and patent based studies with nanocomposites produced with clay minerals are quickly used in industrial applications such as thermoplastics. For example, organophilic montmorillonites are used as filler for nanocomposites because of their low prices and useful properties. Montmorillonite, which is hydrophilic, can be converted to hydrophobic using quaternary ammonium salts (Lagaly 1986; Hartwig et al. 2003), silane compounds (Silva et al. 2011), phosphonium salts (Hartwig et al. 2003), imidazolium (Abate et al. 2008), and pyridinium reagents by cationic exchange to form organomontmorillonite which is compatible with polymers. With addition of organoclay into polymer, nanocomposite structure being filled with clay is formed due to exfoliation and intercalation of clays in the matrix. Initially, the studies were done for improvement of mechanical and barrier properties of the organoclays (Messermith and Giannelis, 1995; Osman et al 2007) and later changed to investigation of thermal properties (Abdallah and Yilmazer 2012; Calderon 2008; Gilman et al. 2000; Xie et al. 2001 and 2002). The studies showed that while ammonium and silane compounds improved mechanical properties, phosphonium, imidazolium and pyridinium compounds improved thermal properties of organoclays or nanocomposites (Awad et al. 2004; Byrne and McNally 2007; Hartwig 2003; Patro et al. 2009).

Phosphonium, imidazolium and pyridinium cations have higher strength, when compared with ammonium ions, in terms of the thermal properties (Mittal 2012). Phosphonium salts, which have high thermal stability, are very important compounds, which become popular because of their usages in organoclay and polymer nanocomposites. Besides, there have been many studies about the use of phosphonium compounds for ionic liquids (Byrne and McNally 2007), eutectic solvents (Kareem et al. 2012), humidity sensor (Son and Gong 2002), and antibacterial applications (Wu et al 2011).

In this study, adsorption characteristics of phosphonium salts, due to their thermal resistance in comparison to other organics, on montmorillonite, was investigated in detail. It is suggested that the reason for thermal stability of organoclays prepared by using phosphonium salts depends on their aromatic structure (Abdallah and Yilmazer 2013). In this study, three different phosphonium surfactants were used. The first one

was composed of one aromatic head without any organic chain, another one had an organic chain with three branches, and the last one had an organic chain and aromatic head. Therefore, the effect of surfactants structure on adsorption on montmorillonite was also studied.

Materials and methods

Materials

The sodium-montmorillonite (Na-MMT) sample used in this study was obtained from Resadiye, Tokat region in northeast Turkey. Hexadecyl triphenyl phosphonium bromide (HTPB), hexadecyl tributyl phosphonium bromide (HTBPB), and tetraphenyl phosphonium bromide (TPB) were provided by Welink International Enterprise Limited, China. The chemical compositions of these surfactants are shown in Table 1. Millipore Milli-Q Synthesis ultrapure water (18.2 mΩ) was used for all experiments, except during physical purification process of the sample carried out by means of a Falcon concentrator.

Table 1. Specifications of the surfactants used in this study

Surfactant	Molecular formula	Molecular weight, g/mol	Structure
Hexadecyl Triphenyl Phosphonium Bromide (HTPB)	$C_{34}H_{48}BrP$	567.62	
Hexadecyl Tributyl Phosphonium Bromide (HTBPB)	$C_{28}H_{60}BrP$	507.65	
Tetraphenyl Phosphonium Bromide (TPB)	$C_{24}H_{20}BrP$	419.30	
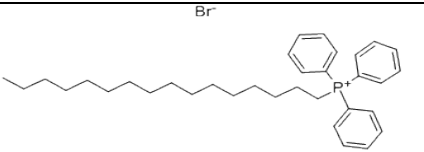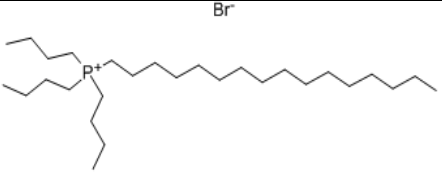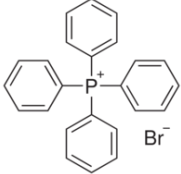
Methods

Sample characterization
The sample was purified in order to increase its adsorption capacity. The purification of montmorillonite was carried out by using a laboratory type Falcon Z40 model concentrator with a centrifuge force of 300 G, which is suitable for an effective

beneficiation in a short time compared to a number of physical methods such as sedimentation, decantation, centrifuge, and hydrocyclone. The raw and purified samples were characterized using several methods. For example, mineralogical compositions of the samples were determined by the X-Ray diffraction (XRD) technique with Shimadzu XRD 6000 (Cu(K$_\alpha$) radiation). Major elemental analyses of the samples were performed by the Rigaku Rix-3000 instrument. Technological properties of the raw and purified samples were obtained with cation exchange capacity (CEC), swelling and gelling index, and water adsorption capacity tests.

The CEC's of the raw and purified Na-montmorillonite were determined by using the methylene blue test based on the ASTM standard (ASTM C 837, 2003). The swelling index tests were performed in several graduated cylinders. For this purpose 2-g samples of ground (-38 μm) and dried (at 105 ^{o}C) montmorillonite were slowly added into 100 cm^3 of ultrapure water for 1 h to avoid aggregation of the samples. The suspension was left undisturbed for 24 h while the volume of the sediment was continuously recorded as swelling index.

The gelling index of the samples was also determined by using graduated cylinders. A certain amount of the samples (from 0.5 to 1.3 g) was added into 10 cm^3 of water, and shaken for 5 min. The samples were left for a day to allow the suspension to gel. After 24 h, the cylinders were bent 45° to let the suspensions to flow out. The amount of samples in the suspensions, which allows the flow more than a minute was determined and the ratio of 10 (cm^3)/sample amount (g) was defined as the gelling index.

In the case of the water adsorption tests, 20 g dried (at 105 ^{o}C), crushed, and screened montmorillonite granules (–4+1 mm) was added into 1000 cm^3 water. The Na-montmorillonite samples were steeped into water for 20 min by putting them into reservoir which was cylindrical in the cross-section and a 1 mm open sieve space. The sample was kept in a hanger for 20 min to remove the excessive water from the clay surfaces, then the sample was weighed, and the adsorbed water was determined.

Adsorption experiments

The adsorption experiments were conducted in 100 cm^3 glass bottles. The purified Na-montmorillonite suspension at the solid ratio of 1% was stirred using a magnetic stirrer for 30 min at 500 rpm. A desired amount of surfactant solution was added into the suspension and the experiments were carried out for 1 h. After the adsorption, the suspension was transferred into a 50 cm^3 test tube, and subjected to centrifuge at 5000 rpm in order to obtain a clear solution of surfactants. The solution was filtered through a 0.23 μm filter. The final concentration of the surfactant solution was measured by a UV/visible spectrometer (PG Instrument Ltd, London, UK, Model T80) at wavelengths of 199, 197, and 192 nm for HTPB, TTPB, and TPB, respectively. A calibration curve for each surfactant was obtained as seen Figs. 1, 2, and 3.
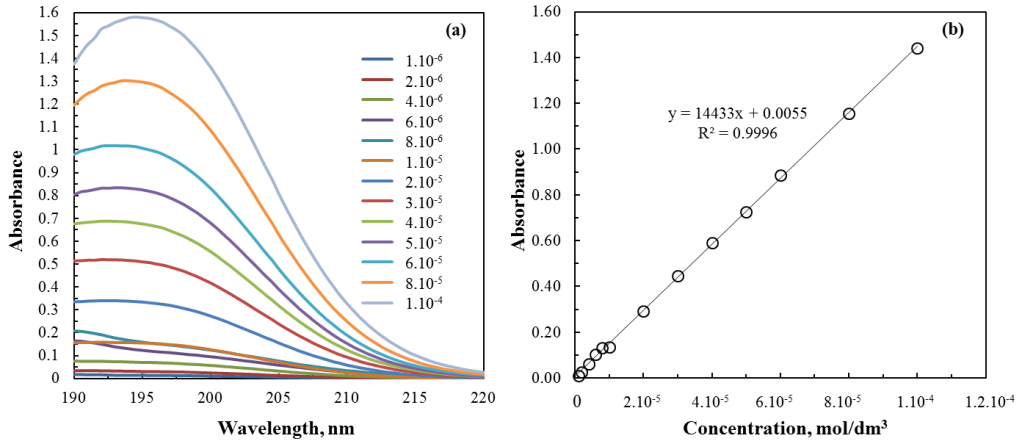
Fig. 1. (a) UV spectra for HTPB at different concentrations
(b) Calibration curve (absorbance values at 199 nm)
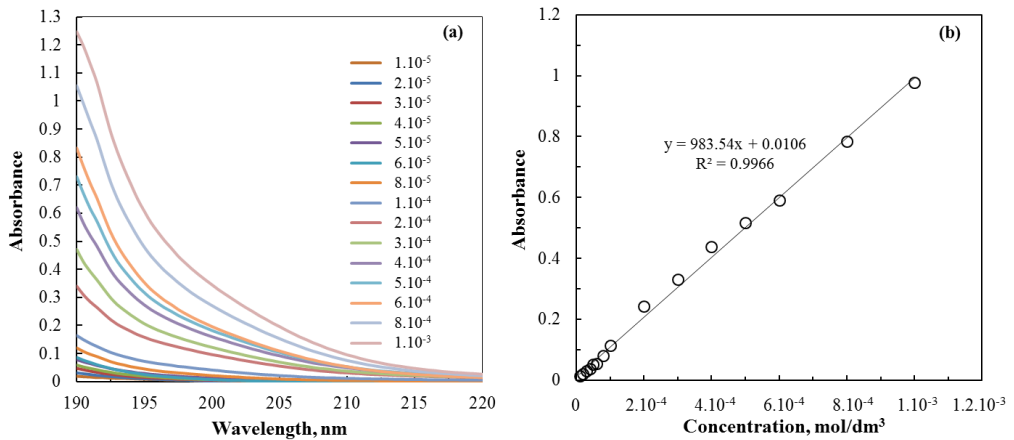
Fig. 2. (a) UV spectra for HTBPB at different concentrations
(b) Calibration curve (absorbance values at 192 nm)

Additionally, the equations obtained from these calibration curves were used to calculate the residual concentration of the surfactants.

The adsorption density was calculated by means of the following formula:

$$\Gamma = \frac{(C_i - C_e)V}{m} \tag{1}$$

where C_i is the initial concentration (mol/dm^3), C_e equilibrium concentration (mol/dm^3), V solution volume (dm^3), m solid amount (g), and Γ adsorption density (mol/g).
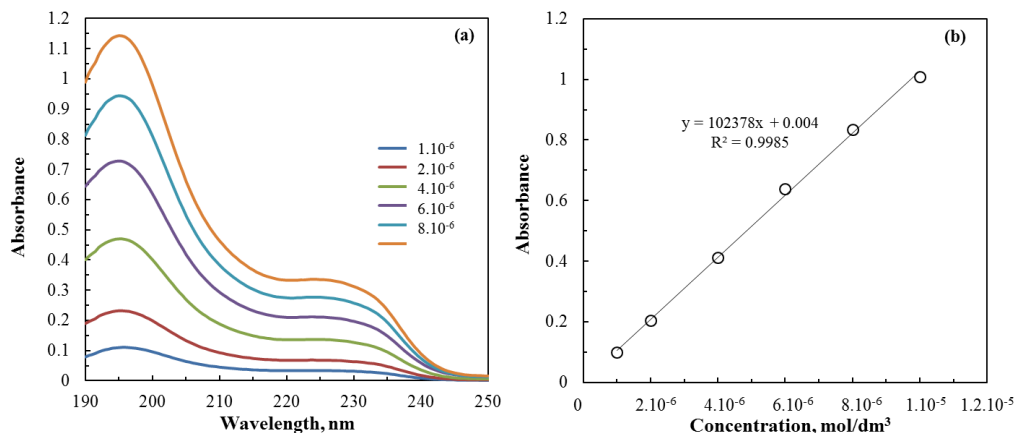
Fig. 3. (a) UV spectra for TPB at different concentrations
(b) Calibration curve (absorbance values at 197 nm)

Zeta potential measurements

The zeta potentials of the samples in the presence of the phosphonium salts were determined using a ZetaPlus instrument (Brookhaven Instruments, Holtsville, NY). First, the sample was added into the surfactant solution at the desired concentration (solid ratio of 0.1 %), and stirred using a magnetic stirrer at 500 rpm for 30 min. Next, the suspension was centrifuged for 5 min at 5000 rpm in order to make solid-liquid separation. Then, a 5 cm^3 of clear solution was taken from the top of the suspension, and mixed with a small amount of solid taken from the bottom of the tube, and this suspension was shaken for 10 times by hand. Finally, the suspension was transferred to the measurement cell, and ten measurements at each surfactant concentration were performed. An average value of these measurements was used further on and the average error was about 3%. The experiments were carried out at room 23 °C.

Surface tension measurements

The surface tension measurements were carried out by using an optical tensiometer with a fully computer-controlled apparatus (Theta Lite, Attension, Finland). In this method, a drop hanging down was generated, the drop profile was captured, digitized and the image data processed. The digitized drop profiles were fitted numerically with the solution of the Young–Laplace equation to obtain the surface tension value. In addition, the critical micelle concentration (CMC) of each surfactant was also determined from the surface tension measurements.

Flocculation experiments

The flocculation experiments were carried out with the suspensions in the presence of HTPB, HTBPB and TPB solutions ranging from 10^{-6} mol/dm^3 to 10^{-2} mol/dm^3 to

determine the critical phosphonium salt concentration. The experiments were carried out at a solid ratio of 0.1 %. The suspensions were first homogenized in an ultrasonic bath for 3 min, and left for 24 h overnight. Finally, the critical flocculation concentration for each surfactant was determined based on the level of maximum settling.

Results and discussions

Results

Sample characterization

The mineralogical analysis of the raw and purified samples indicated that the samples contain smectite (S) (Na-montmorillonite having basal spacing for raw and purified clay of 12.45 Å and 11.62 Å, respectively) as the main mineral with impurities such as quartz (Q), feldspar (F), calcite (C) and opal-CT (O) (Fig. 4).
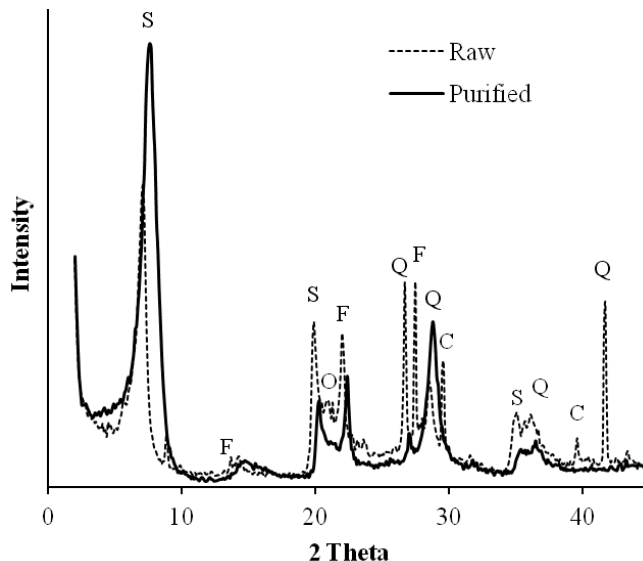
Fig. 4. XRD patterns of raw and purified Resadiye Na-montmorillonite

After the purification, significant amounts of feldspar was removed as seen from the chemical analysis and the XRD patterns of the samples presented in Table 2 and Fig. 4. A decrease in the CaO content of the sample is clearly seen in Table 2.

The results of the characterization test for the samples are shown in Table 3. The results indicated that the purification of the raw sample using a Falcon separator significantly increased cation exchange capacity (CEC), swelling, gelling index, and water adsorption capacity of Na-MMT (Table 3).

Table 2. Chemical composition of the raw and purified Na-MMT

Component	Raw Na-MMT Mass, %	Purified Na-MMT Mass, %
SiO_2	64.1	65.9
Al_2O_3	15.6	16.9
Fe_2O_3	3.6	4.8
MgO	1.8	2.0
CaO	3.1	0.7
Na_2O	2.5	2.7
K_2O	1.1	0.4
TiO_2	0.2	0.2
P_2O_5	0.1	0.1
MnO	0.1	0.1
LOI	7.6	5.8
Total	99.8	99.6

Table 3. Technological properties of the raw and purified Na-MMT

Sample	CEC (meq/g)	Swelling (cm^3)	Gelling index	Water adsorption capacity (%)
Raw	0.78	23.0	11.8	240.8
Purified	0.98	40.0	20.0	543.6

Adsorption experiments

A series of adsorption experiments was carried out to determine the adsorption isotherms of Na-montmorillonite/phosphonium salts (Fig. 5).

As seen from Fig. 5, the adsorption isotherms for surfactants exhibit three regions: a low adsorption region, linear increase region, and finally plateau region. When the results are analyzed carefully, it can be seen that the HTPB adsorption capacity of Resadiye Na-montmorillonite $1.8 \cdot 10^{-3}$ mol/g (1.8 meq/g). Higher adsorption capacities than these values showed the effect of ion exchange reactions as well as ion adsorption by considering that the cation exchange capacity of the same product is 0.98 meq/g. The HTBPB adsorption capacity was calculated as $1 \cdot 10^{-3}$ mol/g (1 meq/g). The adsorption capacity of HTPB and HTBPB showed both ion exchange capacity and ion adsorption reaction if considered that the cation exchange capacity as 0.98 meq/g. Besides, their adsorption capacities, when close to the CEC value, cause a bilateral (double) layer formation. The TPB adsorption capacity of Na-montmorillonite was identified as $1.2 \cdot 10^{-3}$ mol/g by analyzing the adsorption isotherm. The ion exchange and ion adsorption reactions are effective as the adsorption capacity is higher than the CEC

values (0.98 meq/g). However, the aromatic structured TPB was absorbed mainly on the surface due to the low equilibrium concentration in the solution.
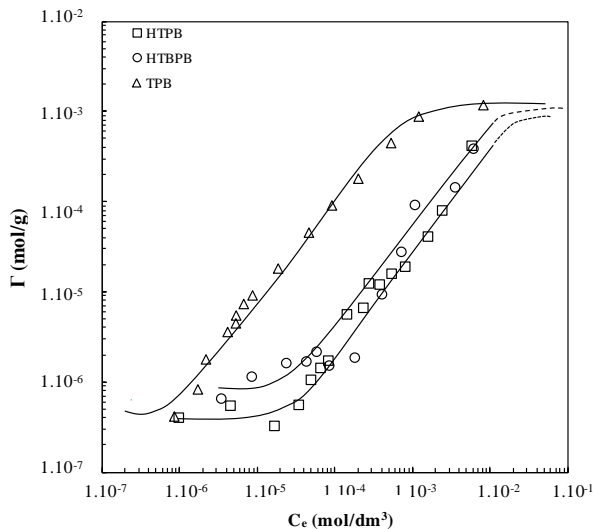
Fig. 5. Adsorption isotherms for phosphonium salts on Na-montmorillonite

According to the adsorption isotherms of HTPB and HTBPB on Na-montmorillonite the cation exchange as well as ion adsorption reactions are present. In addition, the adsorption capacities, which are nearly equal to the CEC values, showed the existence of a monolayer and a bilayer due to a function of its concentration between layers. This is also consistent with the study of Patel (2007). The adsorption value of TPB, which showed a much higher value than the CEC of 0.98 meq/g of the Resadiye Na-montmorillonite, indicates that the ion adsorptions as well as ion exchange reactions are apparent. However, the low equilibrium concentration of the TPB implies that the aromatic surfactant adsorbed only on the surfaces by building monolayers between the Na-MMT sheets.

The adsorption density values of HTBPB and HTPB are nearly equal and the shape of the isotherms shows similarities by considering the adsption isotherm curves. In the case of HTBPB and HTPB, this could be explained by the chemical composition of both of the surfactants and their molecular surface area.

The study of adsorption isotherms shows that the ion exchange, which is pointed by the initial portion of the curve, takes a long time to complete the process. The isotherm of the TPB is rather different than other phosphonium salts as a result of its tendency to adsorption acceleration. However, this depends on its moleculer area which is different for other surfactant and also on its aromatic structure that includes one head group.

In conclusion the TPB adsorption capacity of Resadiye Na-montmorillonite is greater than that of HTPB and HTBPB. This depends on the chemical structures of the surface active agents. It is well known that TPB has a rounded shape whereas HTPB and HTBPB have a long chained form (Table 1). A similar trend is shown in Fig. 5 for

HTPB and HTBPB in contrast to the ion exchange duration for TPB, which is completed much earlier. In addition, when considering TPB, it can be seen that the ion exchange capacity is accomplished soon, and the surfactants adsorb by moving quickly onto the surface.

The results obtained from the adsorption experiments with the phosphonium salts were considered in the accordance with the models of Langmuir and Freundlich adsorpsion isotherms (Freundlich 1926; Langmuir 1926). The plots of the Langmuir and Freundlich isotherms are illustrated in Table 4 and Fig. 6. The parameters such as K_L and a_L for the Langmuir equation (Eq. 2) and K_f and $1/n$ for the Freundlich equation (Eq.3), were calculated and listed in Table 4. The results indicated that adsorption of phosphonium salts on Na- montmorillonite shows a better distribution according to the Freundlich model where a standard deviation is close to 1. On the other hand, only adsorption of TPB on montmorillonite is consistent with the Langmuir model when compared to others (Table 4). This can be attributed to its structure because it is composed of only one aromatic head rather than chain structure

$$q_e = \frac{K_L a_L C_e}{1} + a_L C_e \qquad (2)$$

$$q_e = K_f C_e^{\frac{1}{n}} \qquad (3)$$

where K_L – Langmuir isotherm constant, $dm^3\ g^{-1}$, a_L – Langmuir isotherm constant, $dm^3\ mol^{-1}$, K_f – Freundlich isotherm constant, $dm^3\ g^{-1}$, n – Freundlich isotherm constant, $dm^3\ mol^{-1}$.

Table 4. Langmuir and Freundlich adsorpsion model parameters

	Langmuir				Freundlich		
	K_L	a_L	$q_m = K_L/a_L$	R^2	K_f	$1/n$	R^2
HTPB	0.028	–90.279	–0.0003	0.3413	0.99	0.0693	0.9372
HTBPB	0.019	–138.314	–0.0001	0.2936	0.99	0.0599	0.9501
TPB	1.078	338.675	0.0032	0.9383	1.0	0.7907	0.9958

The zeta potential measurements of Na-montmorillonite as a function of the equilibrium concentration of phosphonium salts are shown in Fig. 7. The zeta potential of purified Na-montmorillonite was measured as -50 mV at natural pH. After the modification of the sample at low concentrations of the surfactants, this value increased to -60 mV. With increasing surfactant concentration, the zeta potential value started to decrease and reached zero point of charge at $3\cdot10^{-3}$ mol/dm^3, $4\cdot10^{-3}$ mol/dm^3, and $1\cdot10^{-3}$ mol/dm^3 for HTBPB, HTPB, and TPB, respectively. Finally, above these concentrations, the zeta potential of the clay reached +60 mV.
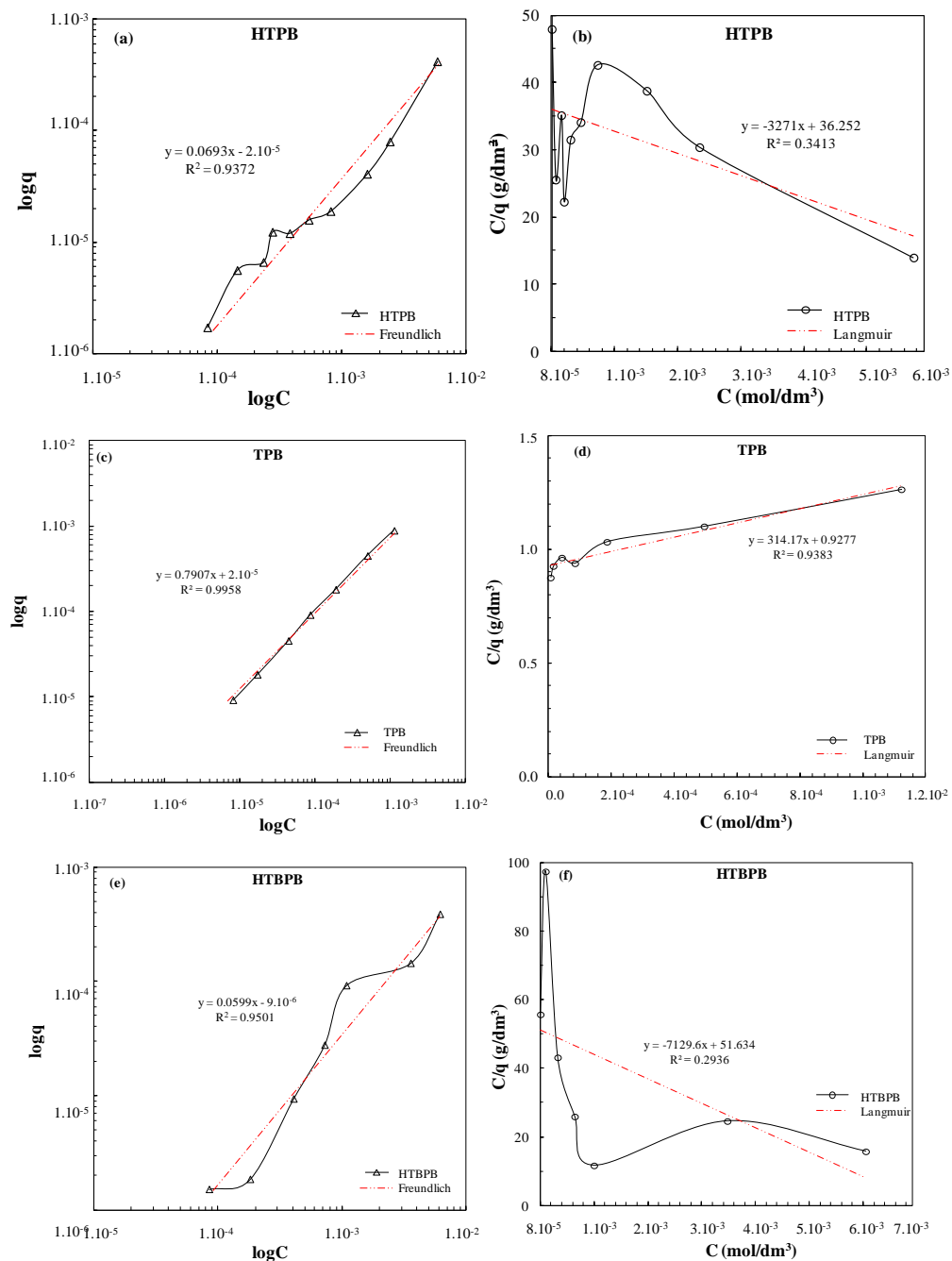
Fig. 6. Freundlich (a)(c)(e) and Langmuir (b)(d)(f) plots for phosphonium salts

According to the zeta potential and the adsorption isotherm profiles for the modified Na-montmorillonite, it can be seen that the adsorption reached plateau at concentrations where the zeta potential reached positive values (Figs 5 and 7). The parallel increase of the charge with the surfactant concentration confirmed adsorption of the phosphonium salts on montmorillonite.
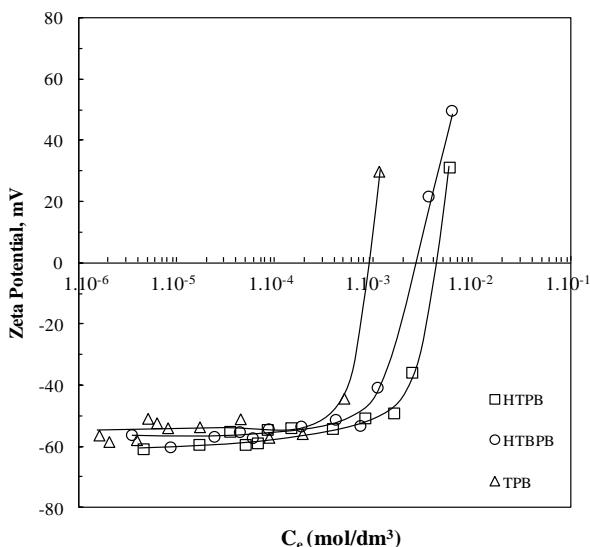
Fig. 7. Effect of surfactant concnetration on zeta potential of Na-montmorillonite

The surface tension of aqueous solutions of HTPB and HTBPB at different concentrations was measured and the results are presented in Fig. 8. As can be seen in Fig. 8, the surface tension decreases with an increase in the surfactant concentrations, and finally reaches the equilibrium point at a specific surfactant concentration. This concentration is known as the critical micelle concentration (CMC). The CMC for HTPB was found to be $2–3 \cdot 10^{-3}$ mol/dm^3, which is consistent with the results of Verma and Ghosh (2010), whereas it is $2 \cdot 10^{-3}$ mol/dm^3 for HTBPB (Fig. 8). On the other hand, the CMC for TPB could not be measured because of its chemical composition showing no hydrocarbon tail and a high Kraft point and it crystallizes at room temperature in a short period time. However, it gives rise to flocculation when subjected to interaction with clay in water. For this reason, an empirical approach is developed for determining the surface tension based upon the critical coagulation concentration conception (Lagaly and Ziesmer 2003).
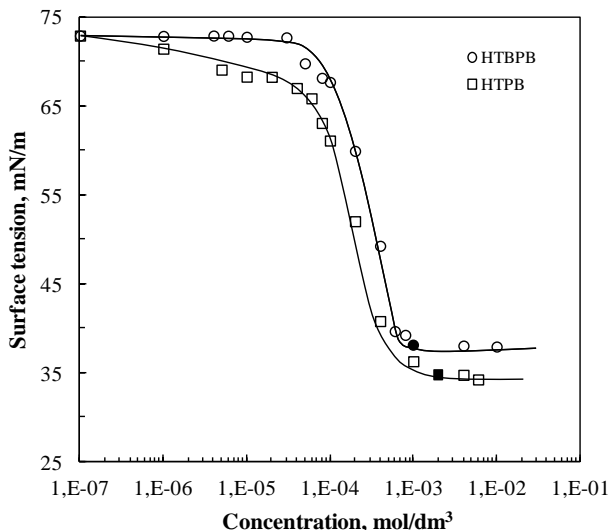
Fig. 8. Surface tension of HTPB and HTBPB solutions at room temperature

The critical flocculation concentration (CFC) test showed that the CFC values were found to be 2–$3 \cdot 10^{-4}$ mol/dm^3, $2 \cdot 10^{-4}$ mol/dm^3, and approximately $2 \cdot 10^{-4}$ mol/dm^3 for HTPB, TPB, HTBPB, respectively. It is also interesting to note that there is an approximately ten-fold difference between the CFC and CMC values for HTPB and HTBPB. Additionally, as already mentioned, it was not possible to measure the surface tension of TPB due to its high Kraft point, which causes its crystallization even at room temperature because of lack of the tail part. From this point of view, the CMC value for TPB can be accepted as $2 \cdot 10^{-3}$ mol/dm^3 by applying the CFC test.

It can be concluded that the results obtained from this study showed a great consistency when considering adsorption isotherms, zeta potential measurements, and the CMC test curves (Figs 5, 7 and 8) along with the CFC test results.

Conclusions

In this study, the adsorption of selected phosphonium salts (HTPB, HTBPB, and TPB) on Resadiye sodium montmorillonite (Na-MMT) which was purified with a Falcon concentrator was investigated in detail. The characterization tests for the raw and pure samples showed that the clay mineral used in this study is a good quality sodium montmorillonite due to its swelling volume of 23–39 cm^3, a high gelling index of 11.8–20, and a characterisitic (d_{001}) smectite peak of 11 Å and 12 Å.

The adsorption experiments with HTPB, HTBPB, and TPB showed that the maximum adsorption densities for HTPB, HTBPB and TPB on Na-MMT were found to be $1.8 \cdot 10^{-3}$, $1 \cdot 10^{-3}$ and $1.2 \cdot 10^{-3}$ mol/g, respectively. These results were also supported

with zeta potential, surface tension and critical flocculation concentration (CFC) measurements. The difference in the adsorption capacity among the surfactants was attributed to their structures, especially the variations in their polar parts. The chain lenghts of the surfactants were 16 C, except TBP, and the the adsorption capacity widely depended on the difference of the surface area of the head that forms the polar part.

It is concluded that the technological properties of Na-montmorillonite can be improved using mineral processing equipment such as a Falcon concentrator. Additionally, the adsorption properties of the phosphonium salts on the purified Na-montmorillonite obtained from this study will be fundamental in the case of production of organoclay/nanocomposites modified with these surfactants which has a higher thermal stability.

Acknowledgements

References

ABATE L., BLANCO I., BOTTINO F.A., DI PASQUALE G., FABBRI E., ORESTANO A., POLLICINO A., 2008, *Kinetic study of the thermal degregation of PS/MMT nanocomposites prepared with imidazolium surfactants*, Journal of Thermal Analysis and Calorimetry, 91(3), 681–686.

ABDALLAH W., YILMAZER U., 2013, *Preparation and characterization of thermally stable phosphonium organoclays and their use in poly(ethylene terephthalate) nanocomposites*, Journal of Applied Polymer Science, DOI: 10.1002/APP.38651.

ASTM C 837, 2003, *Standart test method for methylene blue index of clay,* ASTM International, 2, USA.

AWAD W.H., GILMAN J.W., NYDENA M., HARRIS R.H., SUTTO JR. T.E., CALLAHAN J., TRULOVE P.C., DELONGC H., C., FOX D.M., 2004, *Thermal degradation studies of alkyl-imidazolium salts and their application in nanocomposites*, Thermochimica Acta, 409, 3–11.

BERGAYA F., THENG B.K.G., LAGALY G. (Eds.), 2006, *Handbook of Clay Science*, Elsevier, Amsterdam.

BYRNE C., MCNALLY T., 2007, *Ionic liquid modification of layered silicates for enhanced thermal stability*, Macromolecular Rapid Communications, 28, 780–784.

CALDERON J.U., LENNOX B., KAMAL M.R., 2008, *Thermally stable phosphonium-montmorillonite organoclays*, Applied Clay Science, 40, 90–98.

FREUNDLICH H., 1926, *Colloid and Capillary Chemistry*, Methuen, London.

GILMAN J.W., JACKSON C.L., MORGAN A.B., HARRIS JR. R. H., 2000, *Flammability properties of polymer-layered-silicate nanocomposites, polypropylene and polystyrene nanocomposites*, Chemistry of Materials, 12, 1866–1873.

GRIM R. E., 1968, *Clay Mineralogy*, Mc Graw Hill Company, New York, USA.

HARTWIG A., PUTZ D., SCHARTEL B., BARTHOLMAI M., WENDSCHUH-JOSTIES M., 2003, *Combustion behaviour of epoxide based nanocomposites with ammonium and phosphonium bentonites*, Macromolecular Chemistry and Physics, 204(18), 2247–2257.

KAREEM M.A., MJALLI F.S., HASHIM M.A., ALNASHEF I.M., 2012, *Liquid–liquid equilibria for the ternary system (phosphonium based deep eutectic solvent–benzene–hexane) at different temperatures: a new solvent introduced*, Fluid Phase Equilibria, 314, 52–59.

LAGALY 1986, *Interaction of alkylamines with different types of layered compounds*, Solid State Ionics, 22, 43–51.

LAGALY G., 1993, *Praktische verwendung und einsatzmöglichkeiten von tonen. In tonminerale und tone: struktur, eigenschaften, anwendung und einsatz in industrie und umwelt (ed. K. JASMUND and G. LAGALY)*, 89–167, 358–427, Steinkopff Verlag.

LAGALY G., ZIESMER, 2003, *Colloid chemistry of clay minerals: the coagulation of montmorillonite dispersions*, Advances in Colloid and Interface Science, vol. 100–102, 105–128.

LANGMUIR I., 1916, *The constitution and fundemental properties of solids and liquids*, Journal of American Chemistry Society, 38, 2221–2232.

LEBARON P.C., WANG Z., PINNAVAIA T.J., 1999, *Polymer-layered silicate nanocomposites: an overview*, Applied Clay Science, 15, 11–29.

MESSERSMITH P.B., GIANNELIS E.P., 1995, *Synthesis and barrier properties of poly(e-capro1actone)-layered silicate nanocomposites*, Journal of Polymer Science: Part A: Polymer Chemistry, 33, 1047–1057.

MITTAL V., 2009, *Polymer Layered Silicate Nanocomposites: A Review*. Materials, 2, 992–1057.

MITTAL V., 2012. *Modification of montmorillonites with thermally stable phosphonium cations and comparison with alkylammonium montmorillonites*, Applied Clay Science, 56, 103–109.

OKADA A., USUKI A., 2006. *Twenty years of polymer-clay nanocomposites*, Macromolecular Materials and Engineering, 291, 1449–1476,

OSMAN, M.A. MITTAL, V., SUTER, U.W., 2007, *Poly(propylene)-layered silicate nanocomposites: gas permeation properties and clay exfoliation*, Macromolecular Chemistry and Physics, 208, 68–75.

PATEL SOMANI R.S., BAJAJ H.C., JASRA R.V., 2006, *Nanoclays for polymer nanocomposites, paints, inks, greases and cosmetics formulations, drug delivery vehicle and waste water treatment*, Bulletin of Materials Science, 29(2), 133–145.

PATEL H.A., SOMANI R.S., BAJAJ H.C., JASRA R.V., 2007, *Preparation and characterization of phosphonium montmorillonite with enhanced thermal stability*, Applied Clay Science, 35, 194–200.

PATRO T.U., KHAKHAR D.V., MISRA A., 2009, *Phosphonium-based layered silicate-poly(ethylene terephthalate) nanocomposites: stability, thermal and mechanical properties*, Journal of Applied Polymer Science, 113, 1720–1732.

RAY S.S., OKAMOTO R., 2003, *Polymer/layered silicate nanocomposites; a review from preparation to processing*, Prog. Polym. Sci. 28, 1539–1641.

SILVA A.A., DAHMOUCHE K., SOARES B.G., 2011, *Nanostructure and dynamic mechanical properties of silane-functionalized montmorillonite/epoxy nanocomposites*, Applied Clay Science, 54, 151–158.

SON S.Y., GONG M.S., 2002, *Polymeric humidity sensor using phosphonium salt-containing polymers*, Sensors and Actuators B, 86, 168–173.

SONDI I., MILAT O., PRAVDIC V., 1997, J. Colloid Interface Sci. 189, 66.

USUKI A., KOJIMA Y., KAWASUMI M., OKADA A., FUKUSHIMA Y., KURAUCHI T., KAMIGAITO O., 1993, *Synthesis of nylon 6-clay hybrid*, J. Mater. Res., 8(5), 1179–1184.

WU T., XIE A.-G., TAN S.-Z., CAI X., 2011, *Antimicrobial effects of quaternary phosphonium salt intercalated clay minerals on Escherichia coli and Staphylococci aureus*, Colloids and Surfaces B: Biointerfaces, 86, 232–236.

VAN OLPHEN H., 1977, *An introduction to clay colloid chemistry,* 2nd ed., Interscience, NY, 318.

VERMA S.K, GHOSH K.K., 2011, *Micellar and Surface Properties of Some Monomeric Surfactants and a Gemini Cationic Surfactant*, Journal of Surfactants and Detergents, 14(3), 347–352.

XIE W., GAO Z., LIU K., PAN W.-P., VAIA R., HUNTER D., SINGH A., 2001, *Thermal characterization of organically modied montmorillonite,* Thermochimica Acta, 367–368, 339–350.

XIE W., XIE R., PAN W.-P., HUNTER D., KOENE B., TAN L.-S., VAIA R., 2002, *Thermal stability of quaternary phosphonium modified montmorillonites*, Chemical Materials, 14, 4837–4845.

COMPARATIVE ANALYSIS OF PROCESS PARAMETERS OF TALC MECHANICAL ACTIVATION IN CENTRIFUGAL AND ATTRITION MILL

Ljubisa ANDRIC[*], Anja TERZIC[**], Zagorka ACIMOVIC-PAVLOVIC[***], Ljubica PAVLOVIC[*], Milan PETROV[*]

[*] Institute for Technology of Nuclear and Other Mineral Raw Materials, Franchet d'Esperey 86, Belgrade, Serbia

[**] Institute for Materials Testing, Vojvode Misica Blv. 43, Belgrade, Serbia, anja.terzic@institutims.rs

[***] University of Belgrade, Faculty of Technology and Metallurgy, Karnegy st. 4, Belgrade, Serbia

Abstract: The efficiency of talc mechanical activation by means of two different mechano-activators - centrifugal and attrition mill is investigated in this study and the comparative analysis of the characteristics of obtained talc powders is presented. A new approach for obtaining high-grade talc concentrate with low Fe_2O_3 content is achieved through effect of mechanical activation of talc accompanied by hydrometallurgical process. The applied mechanical activation process conditions of ultra-centrifugal mill were defined by number of rotor revolutions, sieve mesh size, and current intensity. These operating parameters of the ultra-centrifugal mill were variable. Ultra fine grinding of talc in attrition mill (attritor) was carried out in various time intervals - from 5 to 15 min. The following technological parameters of the mechanical activation were monitored: time of mechanical activation, circumferential rotor speed, capacity of ultra-centrifugal mill, and specific energy consumption. The investigation was based on a kinetic model. The structure and behavior of activated samples were characterized by scanning electron microscopy (SEM), X-ray diffraction (XRD) analysis, and differential thermal analysis (DTA).

Introduction

Talc belongs to the advanced materials which are setting new limits for the industrial standards since their particle size is becoming extremely fine. It is difficult to produce extremely fine particles through plain mechanical milling and furthermore, due to low capacity and high energy consumption the milling is an expensive process (Cho et al., 2006). Talc as a non-metallic raw material is irreplaceable in a large number of industrial applications: ceramics manufacturing (synthesis of the cordierite and

steatite), cast products, paints, rubber, cables, paper, lead, pharmaceutical products, insecticides and herbicides, civil engineering, military industry, etc. The standard way of the talc processing can satisfy only a limited number of the applications. Introduction of the mechanical activation procedure carried out by means of the different types of mechano-activators (centrifugal mill, stirred media mill/attrition mill, jet mill, planetary mill, vibratory mill, mortar mill) can help in overcoming of this problem (Sanchez-Soto et al., 1997, Inoue et al., 1996, Inoue et al., 1999, Lee et al., 2010, Mahmoodian et al., 2013, Neesse et al., 2004, Shinohara et al., 1999, and Perez-Maqueda et al., 2006.).

Centrifugal mill is a variation of the planetary mill in which the mill tube operates in a force field generated by the gyration of the tubes around the common axis. Furthermore, centrifugal mills differ from planetary mills with regard to the ratio of the gyration diameter to the mill tube diameter (G/D), which is less than 1 for centrifugal mills. When G/D becomes very small, i.e. when the mill tube is placed near the center of the rotation, the centrifugal mill begins to resemble a vibration mill. In this sense, the centrifugal mill is a type of vibration mill with increased amplitude of circular vibration (Cho et al., 1999).

Attrition mill (attritor) is applied in the production of fine particles in chemical, pharmaceutical and mineral processing industry, and also, in the process of intensifying of the mineral waste and providing cleaning efficiencies (Schaaff et al. 1999). Attrition mill (stirred-ball mill) enables the production of the submicron particles. In this case, the breakage mechanism can be explained by impact of the operating parameters of attritor mill, such as initial size of particles, ball loading, slurry mass fraction, diameter of grinding media, pin tip velocity and ratio of Young's modulus can influence the Rosin-Rammler equation parameter (Shinohara et al., 1999, and Shrivastava et al., 2011). Particle surfaces are abraded by intense shear and friction stresses between the agitated grinding elements. Attrition grinding can be used as pre-concentration method in talc mineral processing industry. Further removal of carbonates and the separation of talc from chlorite can be obtained by flotation process (Piga et al., 1992). Elongation and smoothness of talc mineral directly influence the increasing of the hydrophobicity or floatability (Yekeler et al., 2004; Yang et al., 2006, and Mahadi et al., 2010).

Mechano-chemical treatment applied on dolomitic talc results in production of ultra fine particles. However, the mechano-chemical treatment might also promote amorphization of talc (Balaz, 2003, Haug et al., 2010, and Tavangarian et al., 2011). Thus, the process of mechanical activation might be considered as pre-treatment to the subsequent hydrometallurgical leaching in order to obtained high-grade talc concentrate with low Fe_2O_3 (Tavangarian et al., 2010 and Zhang et al., 2010).

Material and Methods

Applied material

The sample of the raw talc from "Bela Stena" mine (Serbia) was used in this study. Comminution of raw talc ore was performed by crushing and grinding up to the particle size that could be used as input for the mechanical activation. Particle size distribution, and the results of the chemical and mineralogical analyses performed on talc sample are shown in Table 1.

Table 1. Particle size distribution, chemical and mineralogical composition of raw talc

Class of coarseness (mm)	Mass portion (%)	Undersize (%)	Oversize (%)
-0.589+0.417	6.67	6.67	100.00
-0.417+0.295	13.89	20.57	93.33
-0.295+0.208	19.18	39.74	79.43
-0.208+0.147	16.60	56.35	60.26
-0.147+0.104	15.47	71.82	43.65
-0.104+0.074	10.40	82.22	28.18
-0.074+0.063	3.33	85.55	17.78
-0.063+0.053	3.74	89.28	14.45
-0.053+0.040	3.13	92.41	10.72
-0.040+0.030	2.80	95.21	7.59
-0.030+0.020	2.22	97.43	4.79
-0.020+0.000	2.57	100.00	2.57
Oxides	Content (%)	Talc minerals	Content (%)
SiO_2	37.18		
TiO_2	<0.01	Talc	54.1
Al_2O_3	0.68	Chlorite	8.30
Fe_2O_3	2.6	Quartz	2.20
FeO	3.49	Magnetite	3.40
CaO	3.87	Hematite	0.70
MgO	28.88	Carbonate	29.20
MnO	0.42	Calcite	1.00
Na_2O	0.02	Limonite	0.50
K_2O	0.01	Other	0.60
LoI	22.94		

The basic physico-chemical and mineralogical characteristics of talc were also determined and they are as follows: density $\tau = 2.70$ g/cm^3; humidity $W_1 = 6.00$ %, $W_2 = 0.50$% (after drying); volume density $\Delta = 1.50$ g/cm^3.

Primary crushing of the raw talc sample was conducted by means of a jaw crusher (output opening sizing 10 mm) working in a closed circle with screen. Afterwards, primary crushed sample was subjected to crushing in the roll crusher (output opening sizing 5 mm). Grinding of the secondary crushed sample was performed in the ceramic-lined ball mill. Ceramic balls were used as grinding media. Ceramic-lined ball mill is working in closed circle with air classifier, which enabled liberation of the minerals presented in Table 1. Afterwards, raw talc ore was subjected to dry micronization in ultra-centrifugal mill and attrition mill (stirring ball mill). The micronization caused partial releasing of the iron mineral, while other minerals (chlorite, quartz, and calcite) were still retained in the sample. The mechanical activation of the talc was conducted by ultra-centrifugal mill and attrition mill.

The activated talc sample was subjected to quantitative characterization. Physical characterization of the ground talc was determined by Coulter Electronics – Coulter Multisizer. The mineralogical composition and microstructural characteristics were determined using X-ray (Philips PW 1710) and scanning electron microscopy (SEM) (Jeol JSM T20) analyses, respectively.

Ultra-centrifugal mill with a peripheral comminution path

The ultra-centrifugal mill with a peripheral comminution path "Retsch ZM-1" was used in this investigation (Gemini BV, Netherlands). The ultra-centrifugal mill "Retsch ZM-1" is supplied with rotor made of high alloyed steel. A number of rotor revolutions can be adjusted (10.000 or 20.000 rpm). Diameter of the rotor (D) was 100 mm. The ring sieve of variable mesh size is static element of the ultra-centrifugal mill also made of high alloyed steel. The two elements together make a reacting system for transfer of energy from a device to a dispersive phase-mechanical activated product.

Ultra-centrifugal mill with a vibrating adder can operate discontinuously or continuously. Mechanical reduction of coarse particles was performed by means of a dynamic counter-balancing of material between working element (rotor) and ring sieve. Rotor cogs are shaped as three-sided prisms placed on a basis, while one its side is turned towards the sieve. This shape of cogs enables streaming of air and fluidized dispersed material.

The tolerance between rotor cogs and ring sieve is 1 mm. It creates a ring volume of $V = 4.74$ cm^3 during the mechanical activation. Due to a high rotor speed and strong centrifugal force, this space is permeable in one direction only - towards the sieve. A principle of dynamic counterbalancing is particle movement from rotor to the sieve and vice versa in the ring zone. Finally, material leaves this zone only when the particle size becomes smaller from the mesh size. Dry mechanical activation of talc in four series of experiments was carried out. The experiments were based on a grinding

kinetic model. It means that achieved results can be described by the Rosin-Ramler-Sperling graph-exponential function and equation as well.

Mathematical interpretation

By applying the Rosin-Ramler-Sperling graph, average particle size (d') dependency on circumferential rotor speed (v) of ultra-centrifugal mill with a peripheral comminution path may be formed. The layout of this dependency is presented in Fig. 1 (Senna, 2010).
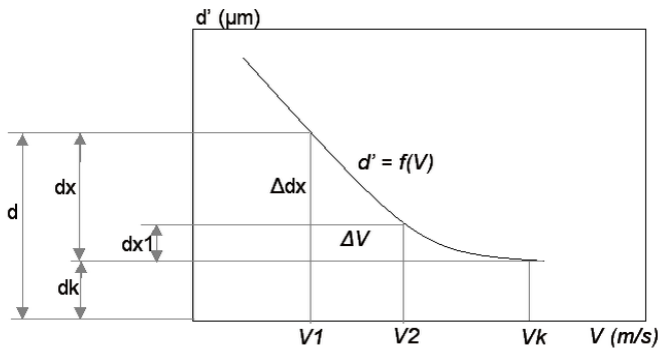
Fig. 1. Average grain size (d') vs. circumferential rotor speed (v)

The slope or position of the curves could be changed. Their changes depend on operational conditions of ultra-centrifugal mill. The experimental results may be described by functional dependence of average grain size (d') vs. circumferential rotor speed (v).

With the increase of circumferential rotor speed (v) the average grain size (d') abruptly decreases. At the same time, this tendency is slowing down towards the final value ($d' > 0$), and vice versa. This is the common characteristic for all curves $d_i' = f_i(v)$ (Ocepek, 1976, Heinicke, 1984, Yvon et al., 2005, and Andric et al., 2005).

According to what was said this phenomenon may be expressed by an exponential equation:

$$y = y_0 \cdot \exp^{-kt} \tag{1}$$

where: k – constant which depends on the experimental conditions; and y_0 – starting value of (y) that is analogue to the equation $R = R_0 \exp^{-kt}$.

The characteristic phenomenon could be significant for the curve $d' = f(v)$. It could be increased when the value of parameter d' inclines toward definite value d_k'. In this case, the value d_k' is equivalent with the value v_k'. According to this, the value

of d' is split into two portions: a constant portion d_k' and variable portion d_x'. It can be seen on Fig.1.

Based on the analysis of the diagram given in Fig. 1. the following equation can be deducted:

$$d' = d_x' + d_k' . \tag{2}$$

The dependence between the influential parameter v could be determined. Namely, if the circumferential speed of rotor v is increased up to the value v_1, for a slight value change Δv, it means the value d_x' will automatically be decreased to the d_{x1}' value, also for a slight value change of $\Delta d_x'$.

This must be proportionally equivalent to the exponential equation (Eq. 1). By analogy to the equation $R = R_0 \exp^{-kt}$ the next relation $\Delta d_k'/\Delta v$ is equivalent to d_x'. The following equation is including the factor of proportionality k:

$$\frac{dd_k'}{\Delta v} = -kd' . \tag{3}$$

Solving differential equation (Eq. 3), the next equation is obtained:

$$\frac{dd_k'}{dv} dv = -kd_k' \Rightarrow \frac{dd_k'}{d_k'} = -kdv . \tag{4}$$

Further integrating,

$$\int dd_k'/d_k' = \int -kdv \Rightarrow \ln d_k' - \ln d_0 = -kv + kv_k \Rightarrow \ln d_k'/d_0' = -k(v - v_k), \tag{5}$$

the equation in the following form is obtained:

$$d_x' = d_0' \exp^{-k(v-v_k)} . \tag{6}$$

Using equations (2) and (6) the next equation is obtained:

$$d' = d_x' + d_k' = d_k' + d_0' e^{-k(v-v_k)} . \tag{7}$$

In all series of mechanical activation experiments, the following operational parameters of ultra-centrifugal mill were variable: number of rotor revolutions (rpm), screen mesh size (μm) and current intensity (A). Also, dry mechanical activation experiments were preformed under the following conditions: time of mechanical activation, t (min); circumferential rotor speed, v (m/s); capacity of ultra-centrifugal mill, Q (kg/h) and specific energy consumption, W_e (kWh/t).

Achieved experimental results of mechanical activation were observed trough the following parameters: d_1 and d_2 – the mesh sizes of the used screens, μm; R_1 and R_2 –

cumulative oversize, %; d' – parameter which depends on particle size distribution of the sample. It characterizes sample coarseness at the same time represents the measure of the mesh size for oversize cumulative $R = 36.79\%$; n – parameter which depends on particle size distribution of the sample; d_{95} – sieve mesh size that is appropriate to 95% cumulative undersize of the micronized product, μm; S_t – calculated-theoretical specific surface, (m^2/kg); and S_r – real specific surface, m^2/kg.

Attrition mill (Attritor)

In this investigation attrition mill type RSG.INC-ufg-10 (RSG Inc, located in Sylacauga, Alabama USA) was used (www.airclassify.com). High-energy attrition mill ("attritor" or "stirred ball mill") is one of the most efficient devices for fine and ultrafine dry micronization of material. The key of its efficiency is in possibility to input material directly into dry micronization section where no rotation or vibration of the working elements exists. The grinding media is formed of small balls made of stainless chromium-nickel steel, glass, or various ceramic materials of high purity. In this study, chromium-nickel steel balls in diameter range of 0.5–5 mm were used. The attrition mill contains internally agitated media. The attritor can be used for dry grinding and for wet grinding, but in this laboratory testing the attritor for dry grinding was used. The power input is directly used for driving of agitating media which is the key of grinding efficiency and the great advantage compared to other mechano-activators.

The operation of attritor is simple and effective. The material is placed in the stationary grinding chamber of attritor with the grinding media. The material and media are agitated by a rotating central shaft with arms. Particle size reductions and homogeneous particle dispersion with very little wear on the chamber walls were performing by impact and shearing action. The configuration of the attritor arms enables a constant motion of the material and grinding media around the grinding chamber. The area of the greatest media agitation is located approximately on two-thirds of the radius from the center shaft. In machine production, the movement is augmented by adding a pumping, circulation system. Grinding does not take place against the tank walls. This is great advantage, because it enables little wear on the walls, at the same time, leading to longer service life of the vessel. For this reason, the vessel walls can be made thinner and by providing enhanced head transfer and greater temperature control.

The following equation can be used to relate grinding time to media diameter and agitator speed:

$$t = KD^2 \big/ \sqrt{N} \tag{8}$$

where t is grinding time for achieving a certain median particle size; K – constant, depends on processed material, type of media and the model of used attritor; D – grinding media diameter; N – number of shaft revolution, rpm.

From Eq. 8 can be seen that the total grinding time is directly proportional to the media, or square of ball diameter, at the same time, inversely proportional to the square root of the number of shaft revolution. From Eq. 8 it can be concluded that by increasing media size, the grinding time will be increased and vice versa.

Hydrometallurgical leaching

Mechanically activated talc, from both devices, was subjected to leaching by hydrochloric acid (15% wt). Leaching was performed at a constant temperature ($T = 80 °C$), in three-neck bottle for time period of 3.5 hours. During the process, calcite (green) was separated in bottom layer, at the same time talc concentrate (white) was separated in upper layer. Carbon dioxide (CO_2) was produced during the leaching process, carrying the fine talc particles to concentrate while lighter than chlorite particles remained at the bottom. In addition talc concentrate in warm condition was rinsed by water, then filtered and dried. The same process was applied to chlorite and intermediate product (talc-chlorite) and a final tailing were produced.

Results and Discussion

Results of mechanical activation of talc by means of ultra-centrifugal mill

Comprehensive experimental results of mechanical activation kinetics are shown in Tables 2 and 3.

The results for all sieve mash sizes (80, 120, 200, 500 μm) at nominal number of rotor revolution transition $n_0 = 20000$ rpm and/or $n_0 = 10000$ rpm were presented. It can be seen that with increasing of the mechano-activator load, the current intensity was increased from 1.20 A to 4.00 A. The following experimental results were found: technological parameters of mechanical activation were changing with the increasing of the mechano-activator load; The reduction of mechanical activation time t directly effected increasing of the mechanoactivator capacity Q; The values of parameter d_{95}, which defines a fineness of mechanical activation, were increased.

The increased values of parameter d_{95} indicated that the increasing of coarseness of the talc sample. It means that the value of parameter d' was increasing, while the value of parameter v was decreasing. The reduction of parameters S_t, S_r and W_e were observed as well. Specific surface and specific energy consumption were decreased.

Table 2. Parameters of mechano-activator and of mechanical activation procedure

Series number	Experim. Seq. no.	Parameters of ultra-centrifugal mechano-activator				Technological parameters of mechanical activation			
		RPM	Actual number of RPM	Sieve size (μm)	Current intensity (A)	Duration (min)	Speed (m/s)	Mechanical capacity (kg/h)	Energy consumption (kWh/t)
I	1		14.62		1.40	15	75.36	0.10	290.96
	2	10000	10.72	80	2.30	7	55.26	0.22	220.22
	3		9.46		3.00	5	48.78	0.31	165.2
	4		8.22		3.75	3	42.37	0.52	106.25
	5		23.89		2.10	13	123.11	0.12	235.94
	6	20000	22.65	80	2.30	6	116.74	0.26	220.22
	7		21.02		2.80	4	108.33	0.39	180.92
	8		17.25		3.50	2	88.88	0.78	125.9
II	1		14.62		1.40	8	75.36	0.19	290.96
	2	10000	13.65	120	1.60	5	70.34	0.31	275.24
	3		10.01		2.70	2	51.58	0.78	188.78
	4		8.36		3.50	1	43.09	1.55	125.9
	5		22.65		2.20	6	116.74	0.26	228.08
	6	20000	20.02	120	2.50	3	103.17	0.52	204.5
	7		18.54		3.00	1.5	95.55	1.03	165.2
	8		15.98		4.00	0.8	82.35	1.94	86.6
III	1		14.62		1.40	4	75.36	0.39	290.96
	2	10000	11.94	200	1.90	1	61.55	1.55	251.66
	3		9.84		2.80	0.5	50.7	3.10	180.92
	4		8.09		3.80	0.2	41.67	7.75	102.32
	5		23.33		2.20	3	120.26	0.52	228.08
	6	20000	21.02	200	2.60	0,6	108.33	2.58	196.64
	7		18.93		3.00	0.1	97.57	15.50	165.2
	8		16.37		4.00	0.08	84.37	19.38	86.6
IV	1		14.62		1.20	3	75.36	0.52	306.68
	2	10000	11.94	500	2.00	0.5	61.55	3.10	243.8
	3		10.01		2.80	0.1	51.58	15.50	180.92
	4		9.46		3.20	0.06	48.78	25.83	149.48
	5		22.65		2.20	2	116.74	0.78	228.08
	6	20000	21,02	500	2.40	0.7	108.33	2.21	212.36
	7		20.02		2.80	0.06	103.17	25.83	180.92
	8		18.54		3.20	0.02	95.55	77.50	149.48

Table 3. Mechanical activation product parameters

Series number	Exper. sequence number	RPM	d_1 (μm)	d_2 (μm)	R_1 (%)	R_2 (%)	d' (μm)	n	d_{95} (μm)	S_t (m²/kg)	S_r (m²/kg)
I	1		1	8	73	6	2.96	1.05	8.10	3839.45	4607.34
	2	10000	1	8	78	4	3.1	1.89	7.30	2405.46	2886.56
	3		1	8	80	5	3.3	1.25	7.70	2170.52	2604.62
	4		1	8	86	4	3.4	1.47	7.40	1445.63	1734.76
	5		1	8	77	10	3.6	1.05	9.80	3261.76	3914.12
	6	20000	1	8	82	8	3.8	1.22	8.90	2019.20	2423.04
	7		1	8	85	7	3.9	1.34	8.40	1595.13	1914.16
	8		1	8	88	7	4.13	1.46	8.40	1294.90	1553.88
II	1		1	8	85	5	3.7	1.40	7.70	1556.81	1868.17
	2	10000	1	8	87	7	4	1.42	8.40	1387.53	1665.04
	3		1	8	80	14	4.2	1.05	11.40	2804.05	3364.86
	4		1	8	91	16	5.2	1.43	10.90	1053.44	1264.13
	5		3	10	73	11	6.1	1.62	11.70	739.16	886.99
	6	20000	3	10	79	16	7	1.70	13.00	604.61	725.54
	7		3	10	84	16	7.3	1.95	12.60	497.97	597.57
	8		3	10	85	17	7.5	1.98	12.70	480.35	576.42
III	1		1	8	88	16	5	1.28	11.30	1368.19	1641.83
	2	10000	1	10	89	18	6.3	1.17	15.50	1350.86	1621.04
	3		1	10	94	26	8	1.34	17.60	777.36	932.83
	4		1	15	93	21	10.1	1.13	25.60	912.33	1094.79
	5		1	8	89	11	4.6	1.41	9.60	1224.65	1469.58
	6	20000	1	10	88	10	5.1	1.26	11.90	1384.73	1661.68
	7		1	10	89	16	6	1.20	14.50	1326.33	1591.59
	8		1	15	90	16	8.4	1.05	22.90	1356.94	1628.32
IV	1		1	10	85	19	6	1.01	17.10	2196.60	2635.92
	2	10000	2	10	80	22	7.1	1.19	17.10	1149.66	1379.59
	3		2	12	92	17	8.6	1.71	15.90	492.89	591.46
	4		1	15	92	17	9	1.13	22.90	1033.73	1240.48
	5		2	13	92	28	11	1.46	22.70	483.11	579.74
	6	20000	2	15	92	27	12.3	1.37	26.60	484.46	581.35
	7		5	17	89	28	15	1.95	25.70	243.11	291.73
	8		5	19	91	29	17	1.93	29.30	217.41	260.89

Mathematical interpretation of talc mechanical activation by mean of ultra-centrifugal mill

The experimental results of mechanical activation of mica could be explained by parameter d'. Parameter d' provides the best approximations of experimental measurements and is presented by the equation

$$d' = d'_k + d'_0 \cdot \exp^{-k \cdot (v - v_k)}. \tag{9}$$

Inserting the experimental values from Tables 2 and 3 in (Eq. 9), the charts of average grain size vs. circumferential rotary speed $d' = f(v)$ for all sieves mesh sizes were obtained. The charts of dependency of average grain size d' on circumferential rotary speed are presented in Figs. 3-6, respectively.
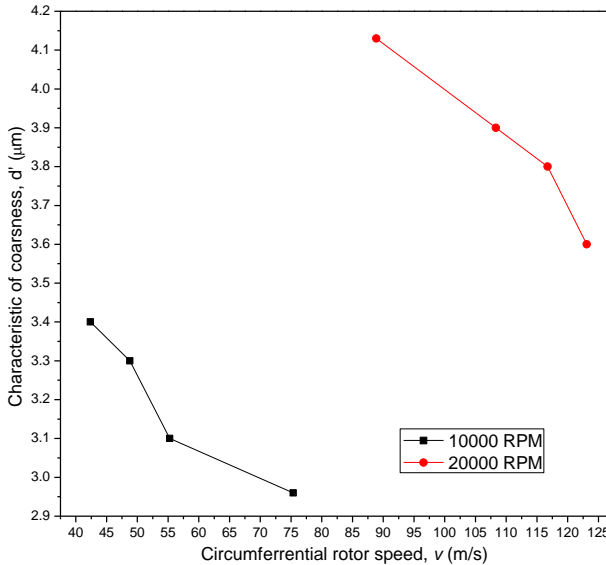
Fig. 2. Average grain size d' of mechanically activated talc vs. circumferential rotor speed v of ultra-centrifugal mill for sieve mesh size 80 μm

Experimental investigation of mechanical activation of talc in the ultra-centrifugal mill showed that this method did not provide good quality talc with a low iron content ($Fe_2O_3 = 1.00–1.50\%$).
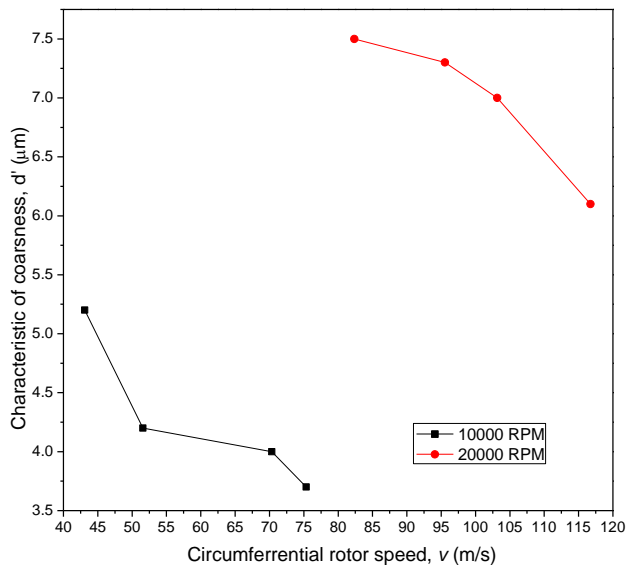
Fig. 3. Average grain size d' of mechanically activated talc vs. circumferential rotor speed v of ultra-centrifugal mill for sieve mesh size 120 μm
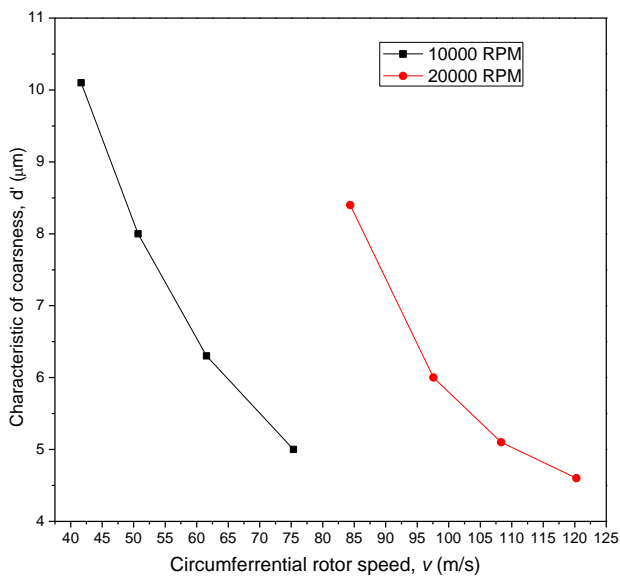
Fig. 4. Average grain size d' of mechanically activated talc vs. circumferential rotor speed v of ultra-centrifugal mill for sieve mesh size 200 μm
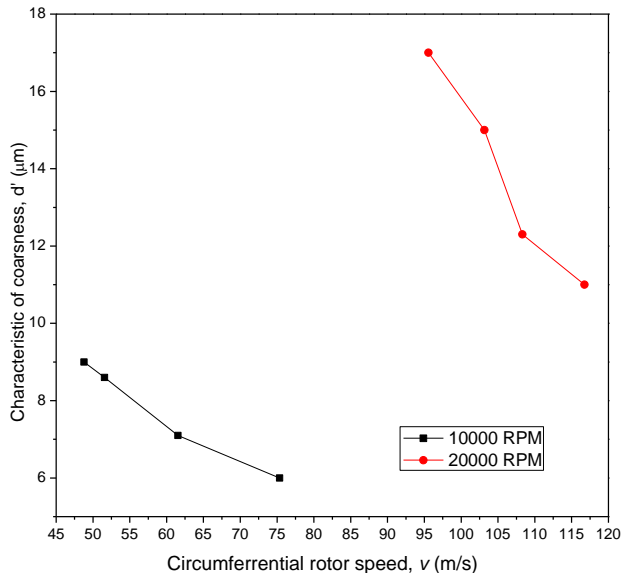
Fig. 5. Average grain size d' of mechanically activated talc vs. circumferential rotor speed v of ultra-centrifugal mill for sieve mesh size 500 μm

Achieved results of mechanical activation of talc by means of attrition mill

Fine and ultra fine milling of talc in attrition mill (attritor) were carried out at various time periods from 5 to 15 min. At the same time, the data of talc grinding in vibratory and conventional ball mill for milling time periods from 8 to 40 min were used for comparison and detailed assessments. Experimental data are listed in Table 4.

Operating the attrition mill is simple. Its efficiency is based on ceramic materials milling in the submicron zone, while other mills (conventional and some types of vibratory mills) cannot efficiently operate in this zone to produce sub micro particles. Table 4 shows that for specific energy consumption of 150 kWh/megagram, the average size of particles obtained by attrition mill is decreasing, i.e. the particles are finer. For specific energy consumption above 200 kWh/t, attrition mill continues ultrafine grinding in sub micro zone. Other mills have either longer grinding time or higher (or equal) specific energy consumption. However, they produce particles with higher average size than attrition mill. This points out to the fact that attritor has shorter milling time, it produces material with lower average particle size, and thus, it is more efficient than other mills used in comparative analysis.

Figure 6 shows the relative ultra fine grinding effectiveness of talc by attrition, vibratory and conventional ball mills. It can be seen that the curve for the vibratory ball mill is on the top, two middle curves are describing ultra fine talc grinding effectiveness in conventional ball mill, and the bottom curve is describing ultra fine talc grinding effectiveness in attritor.

L. Andric, A. Terzic, Z. Acimovic-Pavlovic, L. Pavlovic, M. Petrov

Table 4. Milling efficiency of attritional mill (Attritor-stirred ball mill)

Type of mill	Milling time - t, min	Specific energy consumption - W_e, kWh/Mg	Average particle Size - d, µm
Conventional ball mill (wet milling)	27.50	361.54	2.30
	25.00	176.92	3.60
	17.00	92.33	4.80
	11.00	61.54	5.80
Conventional ball mill (dry milling)	15.00	423.09	1.80
	10.00	211.62	2.20
	8.00	130.76	3.00
Vibratory mill with balls	40.00	361.54	3.80
	23.00	176.92	4.50
	20.00	50.00	8.00
Attritional mill	15.00	423.09	1.00
	13.00	284.74	1.30
	10.00	176.92	1.60
	8.00	146.29	2.00
	6.00	61.54	2.80
	5.00	30.76	3.00
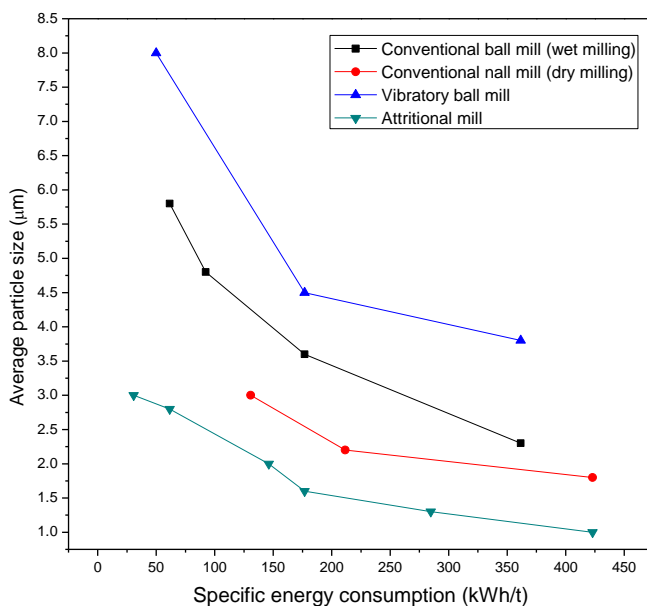
Fig. 6. The mean particle size vs. specific energy input in various mills

For a specific energy input of approximately 100 kWh/Mg the mean particle diameter produced by the attritor is approximately 50% smaller than the mean particle diameter obtained with the conventional ball mill. At the same time, the mean particle diameter obtained by attritor is about 33% lesser than mean particle diameter obtained by vibratory ball mill. At a specific energy input above 200 kWh/Mg, the attritor continued to grind to the submicron range, while other machines could not longer efficiently produce small submicron particles. Therefore, the time required for grinding of submicron particles is much shorter for the attritor.

During dry milling of talc in attritor, iron minerals have been released, while other minerals such as chlorite, quartz and calcite were still retained in the talc sample. It was confirmed by microscopic examination. It indicated that this method is not enable to provide good quality talc with low iron content ($Fe_2O_3 = 1.00–1.50\%$).

Achieved results of mechanical activation of talc in ultra- centrifugal and attrition mill did not provide good quality talc with low iron content ($Fe_2O_3 = 1.00–1.50\%$). For this reason hydrometallurgical method was applied.

Hydrometallurgical leaching of mechanically activated talc

Mechanically activated talc, from both devices, was subjected to leaching by hydrochloric acid (15% wt). Results of dry mechanically activated talc which underwent hydrometallurgical leaching were confirmed by physico-chemical, mineralogical, X-ray and DTA data, which are presented in Tables 5 and 6 and Figs. 7–10.

Table 5. Particle size distribution of talc ($n = 1.34$; $d' = 3.9$; $d_{95} = 8.4$; $St = 1595.13$ m^2/kg)

Class of coarseness (µm)	Mass portion (%)	Undersize (%)	Oversize (%)
-10+9	3	3	100.00
-9+8	4	7	97
-8+5	15	22	93
-5+3	34	56	78
-3+2	14	70	44
-2+1	15	85	30
-1+0	15	100.00	15
Total	100.00		

Table 6. Chemical composition of talc concentrate, intermediate product and tailing

Product	Component and content				
	Mass portion (%)	MgO (%)	Fe$_2$O$_3$ (%)	LoI (%)	Mineral
Talc concentrate	75.90	28.30	1.15	5.00	pure talc
Intermediate product	15.77	12.94	5.83	6.90	talc chlorite
Tailing	8.33	14.57	10.00	9.75	chlorite
Total	100.00	24.22	2.80	5.84	-

In order to explain the influence of mechano-activation on the structure and characteristics of talc and to confirm results obtained during mechanical activation, specific analyses were performed before and after activation procedure including differential thermal analysis (DTA); X-ray powder diffraction analysis (XRD) and scanning electron microscopy (SEM).

The DTA curve for talc is presented in Fig. 7. The peaks appearing at 390 °C and 850 °C are exothermic. Talc is relatively thermally stable up to 850 °C after which the endothermic effect was noticed. The endothermic effect reached its peak at 967 °C. This effect could be explained by the loss of structural water by recrystallization into enstatite ($MgSiO_3$) (Andric et al., 2005). Melting of the talc samples is not recorded. There were not significant changes of the DTA curve of the mechanically activated talc sample in comparison with the DTA curve recorded before activation treatment. Namely, mechanical activation procedure does not influence shifting of the endothermic and exothermic peaks on talc DTA curve. Also it does not initiate decreasing of the melting point for talc.
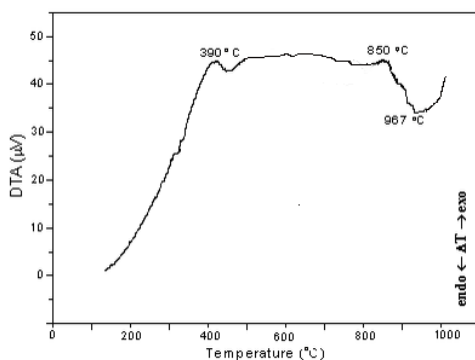
Fig. 7. DTA diagram of mechanically activated talc

Mineralogical phase changes as well as variations in crystallinity occurring in the talc samples were monitored by means of the XRD analysis. In Figs 8 and 9 the diffractograms of talc sample before and after mechanical activation are given. It was noticed that changes in the crystal structure of talc appeared within 30 minutes of the mechanical activation process. Mechanical reduction of the original particles of investigated mineral appears to have reached a limit at 30 minutes grinding time and longer grinding times might produce opposite effect, that is an increase in the particle size.

It can be concluded that mechanical activation influences the crystal structure of talc, i.e. level of crystallinity is decreasing with the increasing mechano-activation time. The mechanical activation makes the structure disordered and generates crystal lattice defects or other meta-stable forms. The mechano-activation treatment can promote the amorphization of treated material, noticeable change of the micro-structure, size and shape of particles etc.
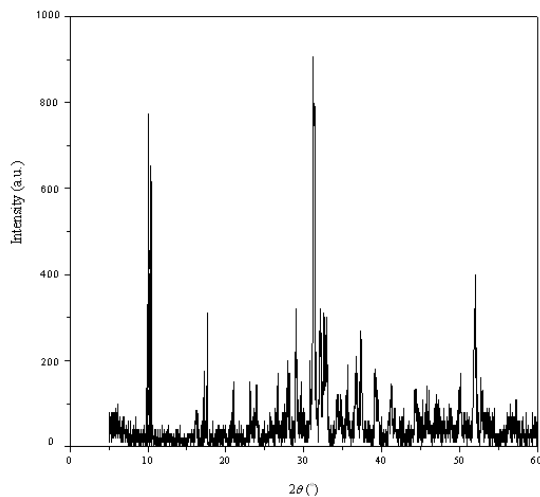
Fig. 8. Diffraction peak values and intensities of original talc sample (before activation)
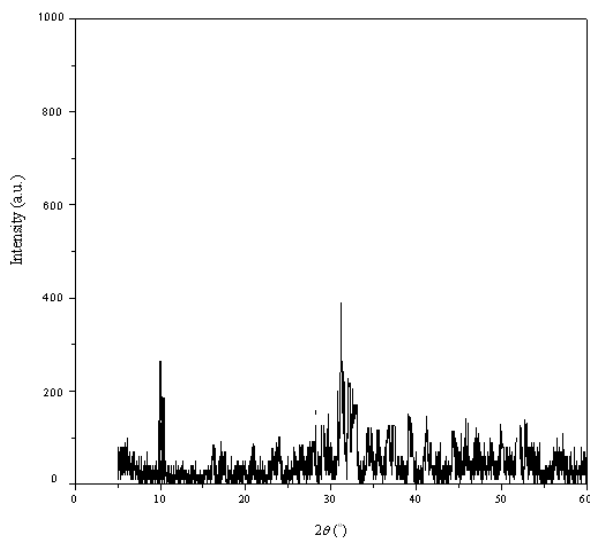
Fig. 9. Diffraction peak values and intensities of talc sample after mechanical activation

The original talc particles are rounded, slightly elongated and the dimensions of the original talc particles vary significantly. The SEM microphotograph of talc sample after mechanical-activation, which is given in Fig. 10., shows that the talc particles gained rather angular shape. The talc particles possess a semi-layered structure while their size is reduced and rather uniform.
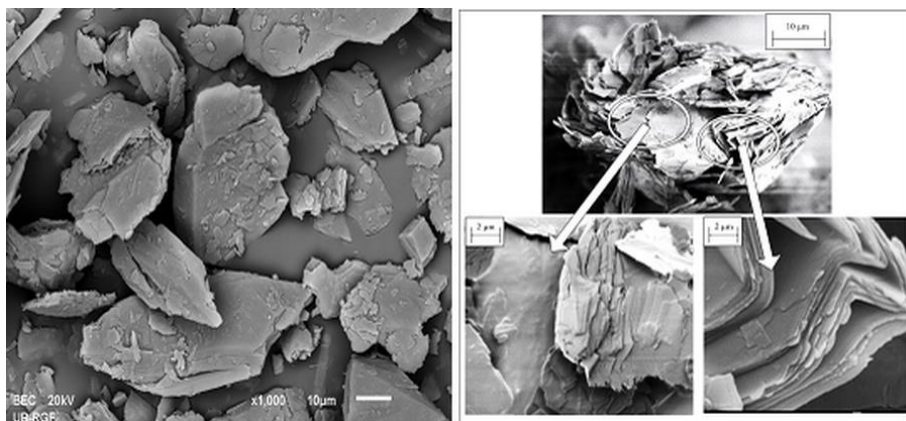
Fig.10. SEM microphotograph of talc after mechanical activation

Conclusion

Good liberation of raw talc ore was achieved by means of mechano-activation performed by means of ultra-centrifugal and attrition mills. The obtained talc concentrate had homogenous particle size distribution, low content of Fe_2O_3, and 5% loss on ignition. The X-ray analysis showed presence of 98% of pure talc accompanied only by negligible amounts of chlorite and quartz. However, the hydrometallurgical leaching is adequate additional procedure which could successfully elevate the iron content and improve the overall quality of the activated talc product.

Investigation of talc mechanical activation in both ultra-centrifugal and attrition mills, pointed out to the fact that the characteristics of the dry activated product directly depend on the values of technical-technological parameters of the activation procedure. The rate of the mechanical activation in the ultra-centrifugal mill was increasing with the increase of the amplification of mill load and of rotor revolutions. The rate of the mechanical activation reached the highest level at the nominal load of ultra-centrifugal mill, i.e. the best performance was achieved for a full ultra-centrifugal mill. It was concluded that the attrition mill was suitable for specific energy consumptions above 200 kWh/Mg, because the attritional mill continued ultra fine grinding in the submicron zone. This, furthermore, points out to a relatively short milling time which is a huge advantage of attrition mill in comparison to other grinding devices.

The DTA analysis showed that activation did not cause shifting of the melting point of the activated talc in comparison with non-activated product, meaning that the activated talc would not melt when applied in a high temperature material. The X-ray analysis of the non-activated and activated talc samples confirmed that mechanical activation contributes to the decreasing of its crystallinity and transformation in the amorphous state. Additionally, the SEM analysis showed that the activated talc particles were reduced in size and became more uniform, which facilitate better

packing of the filler particles in a material. A better 'packing' of the components in the material structure influences the increase of the material strength.

Acknowledgements

References

ANDRIC, LJ, MILOŠEVIC, V., PETROV, M., MIHAJLOVIC, S., 2005, *Operating Technique of Mills in the process of Micronization Milling of Alumina*, J. Mining and Metallurgy 41A, 27–43.

BALAZ P. 2003, *Mechanical activation in hydrometallurgy*, Int. J. Miner. Process. 72, 341–354.

CHO H., LEE H., LEE Y., 2006, *Some breakage characteristics of ultra-fine wet grinding with a centrifugal mill*, Inter. J. of Min. Process. 78, 250–261.

HAUG T.A., KLEIV R.A., MUNZ I.A., 2010, *Investigating dissolution of mechanically activated olivine for carbonation purposes,* Applied Geochem. 25, 1547–1563.

HEINICKE G., 1984, *Tribochemistry*, first ed., Academie-Verlag, Berlin.

INOUE T., OKAYA K., 1996, *Grinding mechanism of centrifugal mills – a simulation study based on the discrete element method*, Int. J. Miner. Process. 44–45, 425–435.

INOUE T., OKAYA K., OWADA S., HOMMA T, 2010, *Development of a centrifugal mill a chain of simulation, equipment design and model validation*, Powder Technology. 105, 342–350

LEE H., CHO H., KWON J., 2010, *Using the discrete element method to analyze the breakage rate in a centrifugal/vibration mill,* Powder Technology 198, 364–372

MAHADI M.I., PALANIANDY S., 2010, *Mechanochemical effect of dolomitic talc during fine grinding process in mortar grinder,* Int. J. Miner. Process. 94,172–179.

MAHMOODIAN, R., HASSAN, M.A., RAHBARI, R.G., YAHYA, R., HAMDI, M., 2013, *A novel fabrication method for TiC–Al2O3–Fe functional material under centrifugal acceleration,* Composites: Part B 50,187–192.

NEESSE TH., SCHAAFF F., TIEFEL H., 2004, *High performance attrition in stirred mills*, Minerals Engineering 17, 1163–1167.

OCEPEK D., 1976, *Mehanska procesna tehnika*, first ed. D.D.U., Ljubljana (in Serbian).

PEREZ-MAQUEDA L.A., DURAN A., PEREZ-RODRIGUEZ J.L, 2006, *Preparation of submicron talc particles by sonication*, Appl. Clay Sci. 28, 245–255.

PIGA L., MARRUZZO G., 1992, *Preconcentration of Italian talc by magnetic separation and attrition*, Int. J. of Min. Process. 35, 291–297.

SANCHEZ-SOTO P.J., WIEWIORA A., AVILES M.A., JUSTO A., PEREZ-MAQUEDA L.A., PEREZ-RODRIGUEZ J.L., BYLINA P., 1997, *Talc from Puebla de Lillo, Spain. II. Effect of dry grinding on particle size and shape*, App. Clay Sci. 12, 297–312.

SCHAAFF F, SCHNEIDER M., NEEGE TH., 1999, *Intensifying the attrition of mineral waste in stirrer mills*, Int. J. Miner. Process. 74S, S291–S298.

SENNA M., 2010, *Finest grinding and mechanical activation for advanced materials*, 7th European Symposium on Comminution, Ljubljana, 21–37.

SHINOHARA K., GOLMAN B., UCHIYAMA T., OTANI M., 1999, *Fine-grinding characteristics of hard materials by attrition mill,* Powder Technology 103, 292–296.

SHRIVASTAVA A., SAKTHIVEL S., PITCHUMANI B., RATHORE A.S., 2011, *A statistical approach for estimation of significant variables in wet attrition milling*, Powder Tech. 211, 46–53.

TAVANGARIAN F., EMADI R., SHAFYEI A., 2010, *Influence of mechanical activation and thermal treatment time on nanoparticle forsterite formation mechanism*, Powder Techn. 198, 412–416.

TAVANGARIAN F., EMADI R., 2011, *Effects of mechanical activation and chlorine ion on nanoparticle forsterite formation,* Materials Letters 65,126–129.

www.geminibv.nl/labware/retsch-zm1-grinder, Gemini BV, Netherlands

www.airclassify.com/

YANG H., DU C., HU Y., JIN S., YANG W., TANG A., AVVAKUMOV E.G., 2006, *Preparation of porous material from talc by mechanochemical treatment and subsequent leaching*, App. Clay Sci. 31 (2006) 290–297.

YEKELER M., ULUSOY U., HICYILMAZ C., 2004, *Effect of particle shape and roughness of talc mineral ground by different mills on the wettability and floatability*, Powder Tech. 140, 68–78.

YVON J., VILLIERAS F., MICHOT L., 2005, *Effect of Different Dry Grinding Procedures on the Immersion Heat of Talc and Chlorite*, J. Mining and Metallurgy 41A, 1–9.

ZHANG Y, LI X., PAN L., WEI Y, LIANG X, 2010, *Effect of mechanical activation on the kinetics of extracting indium from indium-bearing zinc ferrite*, Hydrometallurgy 102, 95–100.

EFFECT OF CALCINATED MAGNESITE ON RHEOLOGY OF BENTONITE SUSPENSIONS. MAGNESIA-BENTONITE INTERACTION

Kenan CINKU[*], Fırat KARAKAS[**], Feridun BOYLU[**]

[*] University of Istanbul, Engineering Faculty, Mining Engineering Department, Avcilar, Istanbul, Turkey
[**] Istanbul Technical University, Faculty of Mines, Mineral Processing Engineering Department, 34469, Maslak, Istanbul, Turkey, boylu@itu.edu.tr

Abstract: In this study, the effect of calcination temperature and time on the structure of calcinated magnesite was investigated. In addition, the effect of calcinated magnesite on rheology when added into bentonite suspension was also examined. Electrokinetic, rheological and stabilization studies including coagulation and gelation tests were performed to explain the mechanism of viscosity increase in bentonite suspension upon addition of the calcinated products. FTIR, SEM, BET analyses and rheological data were used to determine the transition degree of $MgCO_3$ to MgO, and evaluate the structure of MgO and bentonite suspensions. The results from this study showed that specific surface area (SSA) and mean pore radius (MPR) values for the calcinated products were directly affected by the calcination temperature and time. According to the ignition loss and transition ratio from $MgCO_3$ to MgO of the calcinated samples, it was found that the calcination was completed above 800 $^{\circ}$C. In order to obtain a bentonite suspension with higher viscosity, interaction of the sufficient amount of MgO particles with bentonite particles were necessary. Based on these results, the formation of gelation and heterocoagulation between MgO and bentonite particles were found to be responsible for these effects.

Keywords: $MgCO_3$, MgO, activation, bentonite, interaction, viscosity

Introduction

Typical production process of MgO is thermal treatment of naturally occurring minerals such as magnesium hydroxide and carbonate that occurs abundantly in nature (Aramend et al., 2003). Hydromagnesite and magnesite are distributed locally in Russia (22%), North Korea (24%) and China (27%). Dolomite ($CaMg(CO_3)_2$) is more widely distributed in the world and provides cost benefits (Sasaki et al., 2013). Magnesium oxide is manufactured in various kinds of kilns by one of the following reactions as shown in Eq.1. and Eq. 2. using calcination process where $MgCO_3$

thermally decomposes to produce MgO and CO_2, when it is heated from 700 to 1000 °C

$$MgCO_3 + \text{heat} \rightarrow CO_2 + MgO, \qquad\qquad (1)$$

$$CaCO_3 \cdot MgCO_3 + \text{heat} \rightarrow 2CO_2 + CaO \cdot MgO \text{ (dolomitic magnesia).} \qquad (2)$$

The calcination process directly affects the reactivity of the magnesium oxide, therefore it is the most important step to determine how the final product will be used (Aphane et al., 2007).

MgO can be obtained in various reactivity grades based on the temperature and duration at which it is heat treated. Medium reactive magnesia, called as light burnt or caustic magnesia, is produced by calcinations of magnesium carbonate in the temperature range between 700–1000 °C while hard burnt magnesia with an average surface area of 0.1-1.0 m^2/g is produced in the temperature range between 1100–1650 °C. Due to its narrow range of reactivity, this grade is typically used in applications where slow degradation or chemical reactivity is required such as with animal feeds and fertilizers. Dead burnt magnesia or refractory grade magnesia is produced by calcination between 1450–2200 °C and its average surface area is <0.1 m^2/g.

Among magnesia forms, caustic ones have the largest specific surface areas ranged from 1.0 m^2/g to 250 m^2/g. Fused magnesia is normally produced by melting caustic magnesia.

Due to the material's wide reactivity range, industrial applications are quite varied and include plastics, rubber, paper and pulp processing, steel boiler additives, adhesives, and acid neutralization. In bentonite industry, it is also an interesting additive for producing gel like materials (Aphane et al., 2007)

Gel like materials like clays can be used in a number of applications such as paints, adhesives, and drilling muds etc. Some inorganic materials can be used to improve the gelation property of clay. For example, Na-bentonite (Wyoming) and MgO mixture was evaluated as an additive in water-borne paints (Karakas et al., 2011). According to this study, flowability and stability of Na-bentonite was improved by the addition of MgO, and the optimum MgO dosage was found as 1.5 wt.% of Na-bentonite (Karakas et al., 2011). Karaguzel et al. (2010) also reported the thickened bentonite suspension with MgO for preparing of drilling mud. However, it is worth to mention that the addition of MgO into the suspension significantly increases the viscosity of bentonite suspensions, whereas in the case of calcium and mixed bentonite activation with MgO, initial soda activation is required as shown in our previous study (Karaguzel et al., 2010). In addition, it was reported that among magnesium based additives only MgO with the very low dissolution rates regulates the viscosity behaviors of clay suspensions (Alther, 1986) and others such as $MgCO_3$, $Mg(OH)_2$, $MgCl_2$ do not work well (Abut and Girgin, 2005; Cinku, 2008). This is an interesting point that the positive effect of Mg ions in bentonite suspensions was announced in literature, however, without emphasizing the effect of MgO particles in suspensions. Since MgO

does not dissolve well in bentonite suspensions, the effect of dissolved Mg ions on suspension viscosity can be eliminated. Therefore, the positive effect of MgO addition on increased suspension viscosity appears by the other factors which were aimed to be clarified in this study.

In this study, the interaction mechanism of the bentonite suspension with magnesium was investigated in detail. The electrokinetics, rheology, coagulation, and gelation experiments were also performed to understand the interaction mechanism between MgO and bentonite particles.

Material and methods

Centrifugally concentrated Na-bentonite sample was used in this study. The detailed method to prepare this sample was explained elsewhere (Boylu et al., 2010; Boylu et al., 2012). The raw Na-bentonite sample (ROM) used in this study was obtained from Tokat-Resadiye (Turkey) with the sample which is mainly dacitic tuffs (Akbulut, 1996), and having CEC value of 78 meq/100 g, swelling index of 21 $cm^3/2$ g and FANN viscosity values of 20 and 35 mPa·s (at 300 and 600 rpm) at 6% solids. Following the pretreatment, the purification resulted in the production of concentrated Na-bentonite with CEC of approximately 103 meq/100 g, swelling index of 45 and FANN viscosity values of 32 and 56 mPa·s (at 300 and 600 rpm) at 6% solids. Further experiments were performed with the concentrated Na-bentonite sample. The increase on CEC value of pretreated bentonites points out its high purity. The raw magnesite sample (ROM) was hand collected from Kutahya Region (Turkey) with quartz content less than 1.5%, which can be attributed to a quite pure $MgCO_3$. Prior to the final use in the experiments, the ROM magnesite was purified through high intensity dry magnetic separation to remove the colorful impurities such as magnetite, hematite etc. Further calcination tests were also performed to produce MgO at different calcination degrees.

The zeta potential measurements for the bentonite suspensions were conducted using Zeta-Meter System 3.0 at 0.1% wt following the previous reports (Sabah et al., 2007). The rheological measurements were carried out with the hydrocyclone products of 4.75% (w/w). The bentonite slurries were blended at 1200 rpm for 5 min using an Arcelik brand blender and kept in stretched film covered beakers to prevent vaporization of the water during 24 h. Following a day period, the suspensions were re-agitated at low mixing rates (1200 rpm) for 5 min before the viscosity measurements. A Brookfield RVD [++] viscometer and small sample adapter with the spindles of SC 21 and 28 # were utilized for data acquisition. Viscosities of the suspensions were measured with the spindle speeds ranging from 0.5 to 100 rpm at 100 rpm (93 s^{-1} shear rate) where the viscosities versus spindle rate remain constant were considered.

The gelling index of the hydrocyclone products were determined by using graduated cylinders containing 10 cm^3 water with various amounts of solids ranging from 0.5 to 1.3 g. Following shaking of the cylinders, the samples were left for a day

to allow gel development. After a day, the cylinders were bent in 45° to allow the suspensions flow out. The amount of samples in the suspensions, which allow the flow to last for more than a minute was determined and the ratio of 10 (cm^3)/sample amount (g), was defined as the gelling index.

All measurements were reproducible. Zeta potential measurements of bentonite particles in the absence and presence of calcinated $MgCO_3$ were performed on at least 20 individual particles and the final results were recorded based on the average values. Only repeated viscosity measurements exhibiting small changes in the range of 5–10% were used and this is a well-known and tolerated behaviour.

It is known that one of the production methods of MgO is calcination of $MgCO_3$. In this process CO_2 is separated from the structure and pure MgO is produced by the influence of heat above 1400 °C. Stoichiometrically, 52.3% of weight loss occurs upon the exact transition from $MgCO_3$ to MgO. Transition ratios of $MgCO_3$/MgO were calculated based on dividing 52.3% by the weight losses found in experiments conducted with different calcination temperatures.

Results and discussion

Characterization of Calcinated Products

Figure 1 shows transition ratio changes depending on the calcination temperature and time. As seen from Fig. 1, calcination starts at 600 °C for 30 min and for the same calcination time a 90% of transition was achieved at 800 °C while calcination was completed at 1000 °C. The increase on calcination time resulted in a complete calcination at relatively lower temperatures. Viscosity tests were performed with MgO products in different calcination degree (calcination time was selected as 30 min).

The FTIR analyses for the calcinated samples at different temperatures are shown in Fig. 2. As can be seen from Fig. 2 that carbonate peaks at 1420 °C and HCO_3^- peaks (also indicates the dehydration) at 850 °C for the calcinated samples disappeared, hence the calcination process completed above 800 °C.

The changes in the specific surface areas (SSA) and mean pore radius (MPR) of the calcination products are shown in Fig 3. Interestingly, the sample calcinated at 800 °C has the biggest SSA with 76m^2/g, whereas the sample calcinated at 600 °C has the biggest MPR with 26.0 nm. These results were also in agreement with the literature (Liu et al., 2007).

It is apparent from the results that the increasing trend in SSA and MPR at relatively lower calcination temperatures changed with the increasing calcination temperature because of sintering process which caused melting of surfaces by covering the porous structure at above 1200°C.

In another study, the optimum calcination temperature was found to be at around 600 °C. This is possible because of the changes in the heating rate and particle size
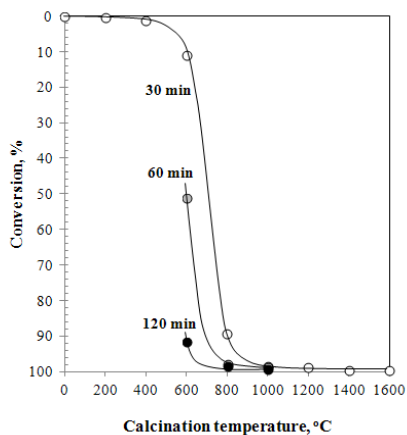
Fig. 1. Conversion degrees of MgCO$_3$/MgO at different calcination temperatures and durations
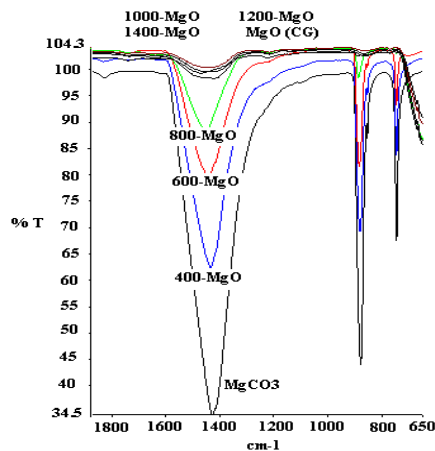
Fig. 2. FTIR patterns of the ROM and calcinated MgCO$_3$ at different calcination temperatures for 30 min calcination time
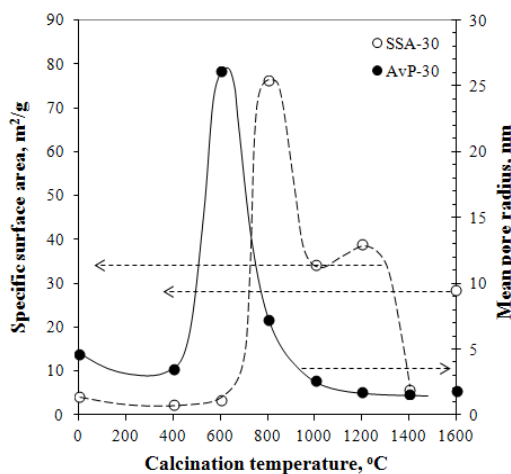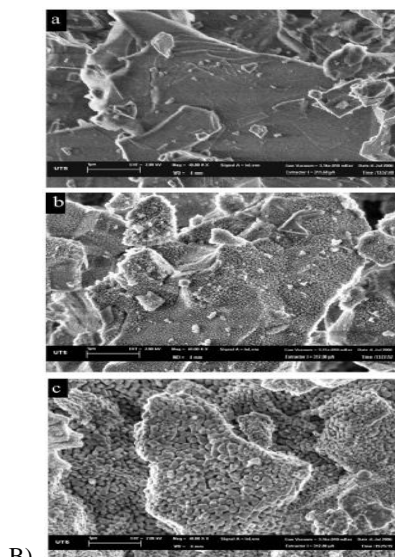
Fig. 3. A) SSA, MPR values of calcinated MgCO$_3$ as a function of calcination temperature, B) SEM analyses (40000 x of MgCO$_3$ (a), calcinated MgCO$_3$ at 600 °C (b) and 1000 °C (c) (from Liu et al., 2007 with the permission of the publisher)

which affect the calcination degree. The SEM pictures of MgCO$_3$ (a) and samples calcinated at 600 °C (b) as well as at 1000 °C (c) in Fig. 3b from the study of Liu et al. (2007) showed porous structure, supporting the changes in SSA and MPR values as

explained in the previous section (Liu et al., 2007). In agreement with Liu's study, the calcination tests in this study revealed that the largest SSA (76 m^2/g) was obtained at around the optimum calcination temperature of 800 °C. When the SSA of calcinated samples compared to ones from Liu's study, a porous system as in Fig 3b (b) can be expected with our calcinated product at temperature of 800°C. SSA and MPR values of samples obtained at 1000°C, which is the completion temperature of calcination process, are 35–40 m^2/g and 2.5–3.0 nm, respectively.

When the SSA and MPR values of the samples obtained at different calcination temperatures are compared to those of the chemical grade MgO, it will be seen that the samples calcinated at 1000-1200 ^{o}C have similar properties with the chemical grade MgO.

Rheology of the bentonite-Calcinated Magnesite suspensions

The rheological measurements were carried out for the bentonite suspensions (4.75 % solid by weight) with the addition of $MgCO_3$/MgO obtained at various calcination temperatures. The results are shown in Figs 4-6. The amount of $MgCO_3$/MgO added into the bentonite suspensions was kept constant (2% wt.).
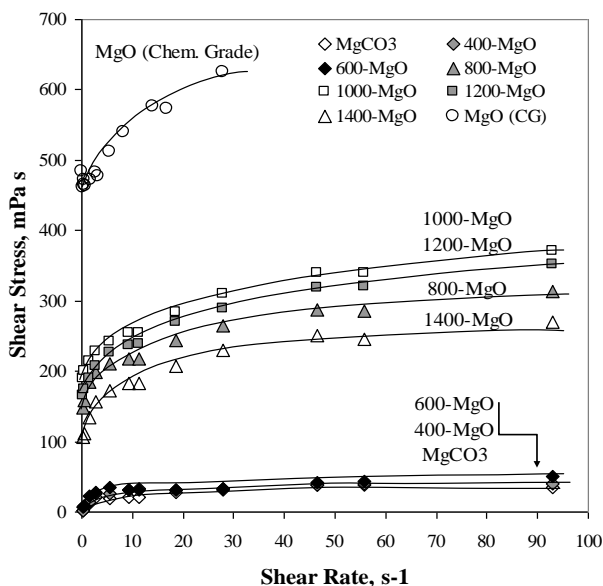
Fig. 4. Rheology of bentonite suspensions with calcinated $MgCO_3$ (2%) depending on the calcination temperature

It was found that all the suspensions have pseudoplastic flow and their rheological behaviors are compatible with the Hersell Bulkley model $\tau = \tau_c + \kappa\gamma^n$, where τ_c is the yield stress (Pa), κ consistency index, and n is the flow index, as shown in Fig. 4. The

rheological behavior of the bentonite suspension prepared with the chemical grade of MgO is also presented. In Figs 4–6, the chemical grade of MgO yields the thickest suspensions characterized by its highest viscosity and yield stress values because of its purity. For the evaluation of calcinated products, the bentonite suspensions, including MgO obtained by calcination at 1000–1200 °C, gave the highest viscosity. The calcination process conducted above 1200 °C deteriorated the positive effect of MgO addition on the viscosity of the bentonite suspensions.

When the SSA and MPR of calcinated samples are evaluated in terms of calcination temperature, it is seen that SSA increases up to 800 °C and it decreases above this temperature, while the MPR value is maximum at 600 °C and it again decreases above this temperature. Using of MgO with SSA of 35–40 m^2/g and MPR of 2.0–2.5 nm have definitely an advantage considering viscosity increase of bentonite suspensions. Therefore, there is no considerable effect of SSA and MPR values difference on viscosity increase of bentonite suspensions.
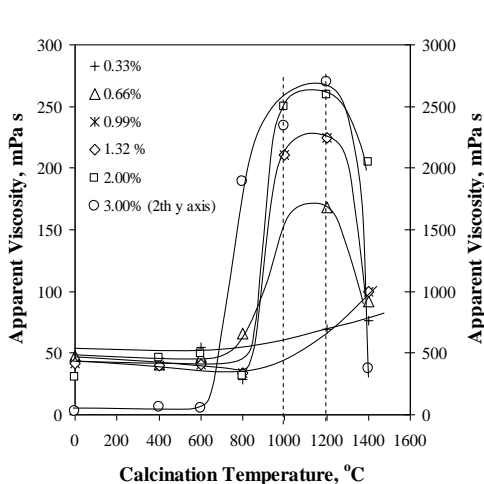
Fig. 5. Apparent viscosities of bentonite suspensions (solid ratio is 4.75 %) with calcinated MgO_3 depending on the MgO addition (at legend) and calcination temperature at shear rate of 93 s^{-1}
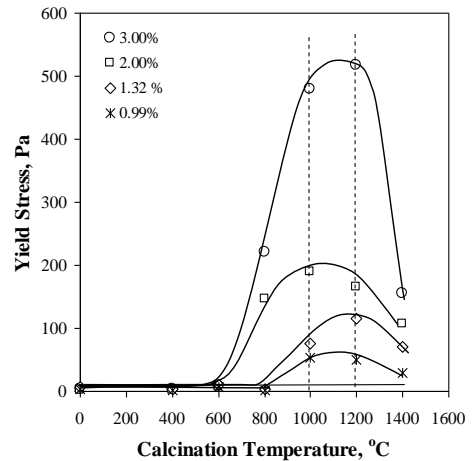
Fig. 6. Yield stress of bentonite suspensions with calcinated $MgCO_3$ depending on the MgO addition (at legend) and calcination temperature at shear rate of 93 s^{-1}

The similar trend in shear stress/shear rate was also observed for apparent viscosity and yield stress as presented in Figs 5 and 6. When the shear stress/shear rate lines are examined in detail, it is realized that the apparent viscosity changes (Fig. 5) are due to yield stress changes shown in Fig. 6. When the formula proposed by the Hersell Bulkley model is used, it can be seen that one of the biggest parameters which causes the viscosity increase of a system is yield stress designated as τ_o, in the equation. An increase in τ_o value indicates an increase in apparent viscosity of a system. Even if shear stress τ, flow index n, and consistency k do not change, an increase in τ_o value directly makes an increase in the viscosity. Therefore, the increase in the apparent

viscosity of bentonite suspensions can be directly related to the properties of $MgCO_3/MgO$ which change the yield stress. Changing of the yield stresses is a result of medium pH and particle-particle interaction. For this reason, electrokinetics, coagulation and gelation properties of different calcinated samples resulted in the increase in viscosity and yield stresses of the bentonite suspensions. Lagaly and Ziesmer (2003) stated that coagulation conditions can also be indicated by viscosity and starting point of a dramatic increase in viscosity and can be defined as critical coagulation point.

Dissolution properties of calcinated $MgCO_3$ products and resultant pH of the system

It is well known from literature that MgO has the lowest solubility in comparison to other magnesium compounds (6 mg/100 cm^3 of water). However, when it is added to bentonite suspension at pH 10, which is the natural pH of the bentonite suspension, some $Mg(OH)_2$ are formed through hydrolysis. $Mg(OH)_2$ is a very strong hydrogel, and hinders the penetration of water molecules into the MgO particles, making a film on the surface.

The concentration of total dissolved ions (TDS) versus accompanying pH for the calcinated samples at different temperatures is shown in Fig 7. Similar properties were also observed for both pure $MgCO_3$ and $MgCO_3$ calcinated at 400 °C with the medium pH values varying from 7.8 to 10.2, and TDS values from 25 ppm/50 cm^3 water to 30 ppm/50 cm^3 water. The samples calcinated at 600 °C changed the pH and TDS values from 9.8 to 11 and from 45 to 50 ppm/50 cm^3 water, respectively.
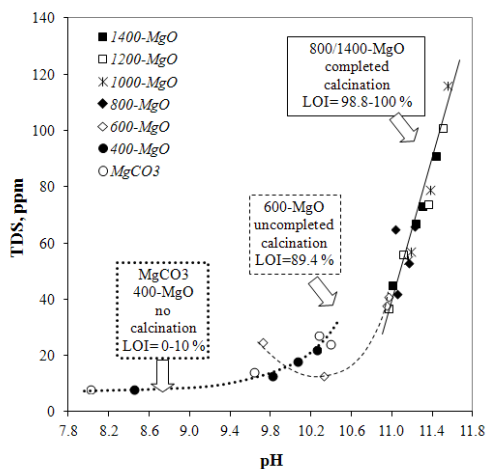
Fig. 7. Total dissolved solids concentrations and pHs of $MgCO_3$ calcinated at various temperatures
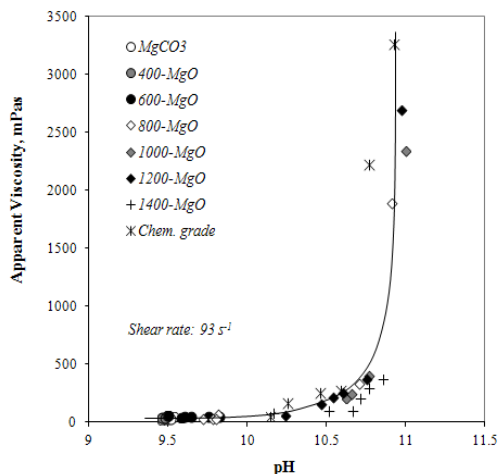
Fig. 8. Apparent viscosities of bentonite suspensions with the addition of 3 % $MgCO_3$ calcinated at various temperatures

Both pH and TDS values for the calcinated $MgCO_3$ suspensions produced at starting and completion temperature of calcination and even at the temperature necessary for forming sinter magnesite were dramatically increased and their TDS values were measured as 120 ppm/50 cm^3 water. Interestingly, a greater transition from $MgCO_3$ to MgO resulted in more soluble calcinated products. This can be attributed to transition of magnesite with relatively higher solubility to $Mg(OH)_2$, which has very low solubility due to hydrolysis of magnesite in water

$$MgCO_3 + H_2O \leftrightharpoons Mg(OH)_2 + CO_2. \tag{3}$$

On the other hand, these products increased the pH of distilled water to 11.8. According to Fig. 8, which shows the relationship between the apparent viscosity and pH, the viscosity of bentonite suspensions increased with the increase of pH of these suspensions. It is known that apparent viscosity of bentonite suspensions increased at higher pHs from neutral pH value (van Olphen, 1963; van Olphen, 1977; Tombacz and Szekeres, 2004). At this point, beside the particle-particle interaction, which was the proposed mechanism by us for viscosity increase of bentonite suspensions, dissolved Mg ions and increased pH of media might be responsible for increase of the viscosity.

The additional rheological tests were performed to investigate whether the increase in pH and dissolved Mg ions caused an increase on viscosity of bentonite suspensions or not. For the tests of the MgO samples obtained by calcinations at 1000 and 1400 °C were dissolved in distilled water for a day with the amount equal to 3% of bentonite addition. After a day, sample was centrifuged and supernatant were added into the bentonite suspensions. With this supernatant addition, the same dissolved ion concentration and medium pH were achieved with the solid MgO addition into bentonite suspensions for comparison. Next, the rheological measurements were conducted with bentonite suspensions including the supernatants. The relative rheological behavior and apparent viscosity values of bentonite suspensions with and without solid MgO particles were presented in Figs 9 and 10. As shown in Fig 9, the bentonite suspension with supernatant of MgO suspension shows similar properties to the original bentonite suspensions. It can be concluded from this that there is a need to add solid MgO particles to the bentonite suspensions in order to obtain highly viscous bentonite suspensions. The reason for this is particle-particle interaction and heterocoagulation. It is thought that pH of the aqueous solution and dissolved Mg ions show no significant effect on the viscosity.

The electrokinetic studies, including zeta potential and iep determination, of bentonite and MgO samples obtained by calcination of $MgCO_3$ at different temperatures were performed to evaluate the particle-particle interaction and show its effect on viscosity in detail. The zeta potential measurements were carried out at different pH values in distilled water and neutral pH of supernatant obtained from the bentonite suspension. The results from the measurements are given in Fig 11. It was found that the iep values for pure $MgCO_3$ and $MgCO_3$ calcinated at 400 °C are close to

7 while the iep values for $MgCO_3$ samples calcinated at 600 °C or higher are at around 11–12.
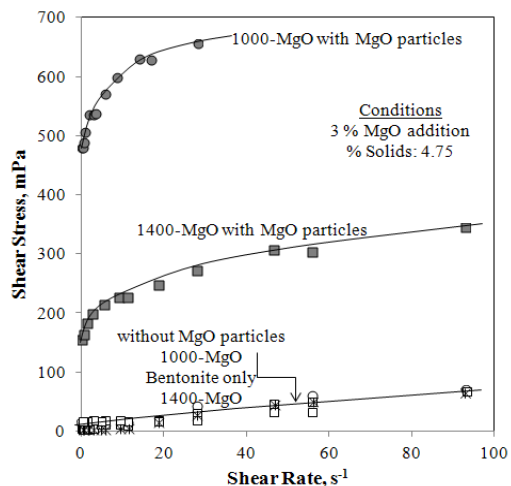
Fig. 9. Rheological behavior of bentonite suspensions in the presence of $MgCO_3$ calcinated at various temperatures
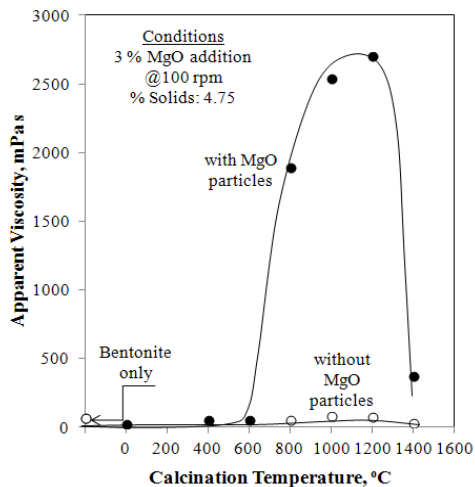
Fig. 10. Apparent viscosities of bentonite suspensions in the presence of $MgCO_3$ calcinated at various temperatures
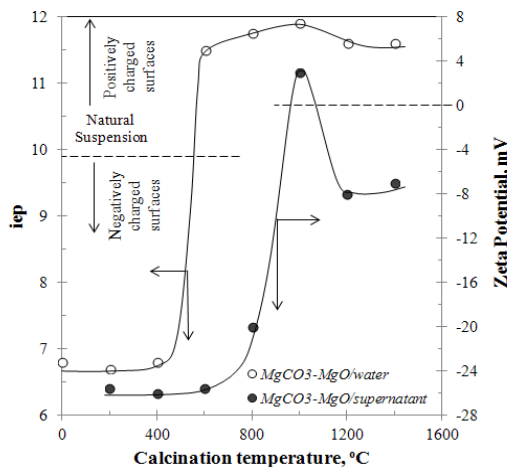
Fig. 11. Electrokinetics of $MgCO_3$ particles in water and supernatant
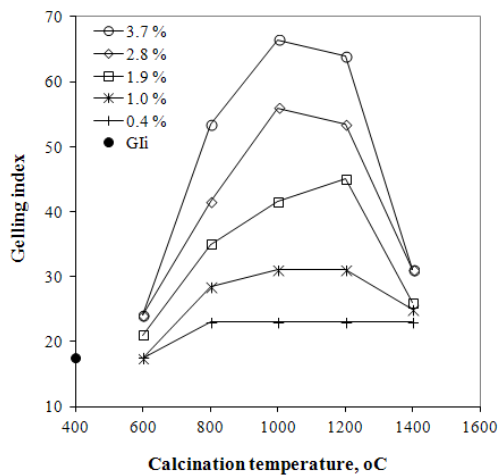
Fig. 12. Gelation characteristics of bentonite suspensions with $MgCO_3$ calcinated at various temperatures

These results agree with literature data because Gence et al. (2006) found the iep value of $MgCO_3$ as 6.8. Moreover, Rynkowski and Dobrosz-Gomez (2009) and Tari et al. (1997) declared the iep value of calcinated MgO as 12.0 and 10.8 (not confirmed

by our study), respectively, while it is around 11–12.4 for sinter magnesite found by Flatt et al. (1997) (Rynkowski and Dobrosz-Gomez, 2009; Tari et al., 1997; Flat et al., 1997). The probable reason for small differences between our and their results is purity of the $MgCO_3$ samples used in the studies.

Bentonite surface at natural pH 9 has a negative charge in a broad range of pH. Meanwhile, while pure $MgCO_3$ particle is negatively charged, the calcinated and sinter magnesite particles are positively charged. Therefore, it is clear that the calcinated and sinter magnesite particles have an attraction interaction with bentonite particles due to electrostatic forces while pure magnesite has repulsion. It was found by zeta potential measurements conducted on supernatant obtained from bentonite suspensions that the surface potential is positive only for $MgCO_3$ particles calcinated at 1000 °C while it is negative for $MgCO_3$ particles calcinated at 600, 800, 1200 and 1400 ^{o}C.

The surface charge and structure of $MgCO_3$ particles change when calcination is performed above 1200 °C. Material calcinated above 1200 °C loses its porosity, hydrogel form and surface charge avoiding the particle-particle interactions (heterocoagulation) and gelling ability. These findings support obtaining the highest viscosity of the bentonite suspensions with $MgCO_3$ calcinated at 1000°C. A similar heterocoagulation behavior for MgO with alumina was reported in literature (Tari et al., 1997; Rao, 1987; Rao, 1988a; Rao, 1988b).

Since original bentonite and the calcinated magnesite particles have different surface charges, it is expected that heterocoagulation can occur between bentonite and magnesite particles. For this reason, the coagulation tests were performed to explain the mechanism between these particles. The results indicated that there is no coagulation process occurring up to a month of waiting period despite the addition of 30% MgO.

The gelation tests were also performed as a next step, because gelation is the other form of particle–particle interaction and MgO is in a hydrogel form. The tests were carried out with original bentonite suspensions and bentonite suspension including different concentrations of $MgCO_3$ calcinated at different temperatures. The results are shown in Fig 12. The calcinated magnesite produced at 1000 and 1200 °C showed the highest gelation index. Moreover, gelation index values increased with increasing the amount of $MgCO_3$/MgO addition for all the calcinated samples and the gelation index of bentonite suspensions increased from 17.8 to 68 with the addition of $MgCO_3$ calcinated at 1000–1200 °C.

In the previous studies, one of the main effects to obtain a bentonite suspension with a high viscosity was a sufficient amount of Na ions increasing delamination in the suspension (Abend and Lagaly, 2000). It was also indicated that some Mg ions are also useful and the highest viscosity will be obtained with Na:Ca:Mg ratio of 60:20:20, respectively (Abend and Lagaly, 2000; Erdogan and Demirci, 1996). However, the results of this study showed that MgO is superior among the magnesium compounds in order to increase the viscosity of bentonite suspensions. MgO has the lowest solubility among the rest of the magnesium compounds. Although past studies

indicated the importance of Mg ions, in this study the effect of MgO particles, not Mg ions was emphasized. The effect of MgO addition was explained by particle-particle interaction, heterocoagulation mechanisms and gelation effect of the remaining, non-dissolved, MgO particles.

Conclusions

In this study, the interaction mechanism of MgO with bentonite suspensions was studied in detail, and several possible mechanisms of the process were evaluated. When the specific surface area (SSA) and mean pore radius (MPR) values of the sample are considered, it was observed that the $MgCO_3$ calcinated at 800 °C gave the largest SSA of 76 m^2/g, even though more viscous bentonite suspensions were obtained with $MgCO_3$ calcinated at 1000 °C which had the SSA of 35–36 m^2/g. This result is similar to that with chemical grade MgO, which gave the most viscous bentonite suspensions. It was also found that the optimal MPR values should be around 30–40 nm.

The degree of the calcination also affected the concentration of total dissolved solids (TDS) of the suspension due to hydration of the calcinated products to $Mg(OH)_2$, and this increased the pH of the magnesia solutions. The increase in pH also improved the rheology of the bentonite suspension. Additionally, the high degree calcination products increased the pH of the solution and apparent viscosity of the suspensions as well. However, further experiments showed that a sufficient amount of MgO particles and interaction of these particles with bentonite particles are necessary to get the bentonite suspension having greater viscosity even if pH and the total amount of dissolved ions of the suspension slightly change.

In contrast to the solubility and pH of the suspension, there was no relationship between the SSA and MPR values and apparent viscosity of the suspension. It is believed that coagulation is mostly dominated by the particle-particle interaction mechanism. Hence it causes an increase in the viscosity of the suspension.

The electrokinetic studies showed that the zeta potential of the calcination products changed from negative to positive values with increasing degree of calcination. Moreover, the iep values of $MgCO_3$, calcinated magnesite, and sintered magnesite were obtained as 6.8, 12.0, and 11.0, respectively. While the zeta potential of $MgCO_3$ particles in the presence of the bentonite suspensions at neutral pH (~9) was negative, the zeta potential of calcinated and sintered magnesite was positive, or very close to neutral. Therefore, an electrostatic interaction takes place between negatively charged bentonite and either calcinated or sintered magnesite. However, the coagulation tests showed that no coagulation occurred even with the addition of MgO in the amount of 30% of bentonite.

Finally, the gelation tests showed that the gelation capabilities of the magnesite calcinated products increase with the calcination degree. Consequently, the gelation

was caused by the increase of the viscosity of the bentonite suspension upon the addition of MgO.

References

ABEND S., LAGALY G., 2000, *Sol-gel transitions of sodium montmorillonite dispersions*, Appl. Clay Sci. 16: 201.

AKBULUT A., 1996, *Bentonite*. MTA Publications 32 Ankara (in Turkish).

ALTHER G.R., 1986, *The effect of the exchangeable cations on the physico-chemical properties of Wyoming bentonites*. Appl. Clay Sci., 1:273.

APHANE M.E., 2007, *The hydration of magnesium oxide with different reactivities by water and magnesium acetate*, *MSc Thesis*, University of South Africa.

ARAMEND M.A., BORAU V., JIMENEZ C., MARINAS J.M., RUIZ J.R., URBANO F.J., 2003, *Influence of the preparation method on the structural and surface properties of various magnesium oxides and their catalytic activity in the Meerwein–Ponndorf–Verley reaction*, *Appl Catalysis A: General*, 244, 207–215

BOYLU F., CINKU K., ESENLI F., CELIK M.S., 2010, *The separation efficiency of Na-bentonite by hydrocyclone and characterization of hydrocyclone products*, Int. J. Miner Process 94(3–4): 196.

BOYLU F., HOJIYEV R., ERSEVER G., ULCAY Y., CELIK M.S., 2012, *Production of ultrapure bentonite clays through centrifugation techniques*, Sep. Sci. Technol. 47: 842.

CINKU K., 2008, *Investigation of Production of water based thickeners from activated bentonite suspensions*, PhD thesis, University of Istanbul, Istanbul, 296 (in Turkish).

ERDOGAN B., DEMIRCI Ş., 1996, *Activation of some Turkish bentonites to improve their drilling fluid Properties,* Appl. Clay Sci. 10: 401.

FLATT R.J., HOUST Y.F., BOWEN P., HOFMANN H., WIDMER J., SULSER V., MAEDER U., BÜRGE T.A., SIKA A.G., 1997, *Adsorption of Superplasticizers on Model Powders: Temperature Dependence, Effect On Zeta Potential And Role Of Chemical Structure*, Proceedings of the 10th International Congress on the Chemistry of Cement, 3 (editor: H.J. Justness) paper 3iii002.

GENCE N., OZBAY N., YEREL S., 2006, *Statistical relationship between electrokinetic potential and pH of magnesite and dolomite minerals*, Science and Eng. J of Fırat Univ., 3: 397.

KARAGUZEL C., CETINEL T., BOYLU F., CINKU K., CELIK M.S., 2010, *Activation of (Na, Ca)-bentonites with soda and MgO and their utilization as drilling mud*, Appl. Clay Sci. 48: 398.

KARAKAS F., PYRGIOTAKIS G., CELIK M.S., MOUDGIL, BRIJ M., 2011, *Na-bentonite and MgO Mixture as a Thickening Agent for Water-Based Paints,* Kona Powder and Particle Journal 29

LAGALY G., ZIESMER S., 2003, *Colloid chemistry of clay minerals: the coagulation of montmorillonite dispersions*, Adv. in Coll. and Interf. Sci., 100-102: 105.

LIU B., THOMAS P.S, RAY A.S., GUERBOIS J.P., 2007, *A TG analysis of the effect of calcination conditions on the properties of reactive magnesia*, J. Therm. Anal Calorim. 88: 145.

OBUT A., GIRGIN I., 2005, *The effect of Mg, Pb and Mn ions on gelling properties of bentonite suspensions*, *Madencilik,* 44 (2): 17 (in Turkish).

RAO A.S., 1987, *Effect of pH on the suspension stability of alumina, titania and their mixtures,* Ceram. Int. 13: 233.

RAO A.S., 1988a, *Electrophoretic mobility of alumina, titania and their mixutures in aqueous dispersions,* Ceram. Int. 14: 71.

RAO A.S., 1988b, *Effects of surface active agents on the electrokinetic and rheological behavior mobility of alumina and titania slips*, Ceram. Int. 14: 141.

RYNKOWSKI J.M., DOBROSZ-GOMEZ I., 2009, *Ceria-Zirconia Supported Gold Catalysts*, Annales Univesitatis Maria Curie-Sklodowska Lublin-Polonia, 14 AA: 197.

SABAH E., MART U., CINAR M., CELIK M.S., 2007, Zeta potentials of sepiolite suspensions in concentrated monovalent electrolytes, *Sep. Sci. Technol*. 42 (10): 227.

SASAKI K., QIU X., HOSOMOMI Y., MORIYAMA S., HIRAJIMA T., 2013, *Effect of natural dolomite calcination temperature on sorption of borate onto calcinated products*, *Microporous and Mesoporous Materials* 171, 1–8.

TARI G., FERREIRA J.M.F., LYCKFELDT O., 1997, *Influence of magnesia on colloidal processing of Alumina*, Journal of European Ceramic Society 17: 1341.

TOMBACZ E., SZEKERES M., 2004, *Colloidal behavior of aqueous montmorillonite suspensions: the specific role of pH in the presence of indifferent electrolytes*, Appl. Clay Sci. 27: 75.

VAN OLPHEN H., 1963, *An introduction to Clay Colloid Chemistry*, Interscience, New York.

VAN OLPHEN H., 1977, *An Introduction to Clay Colloid Chemistry*, John Wiley and Sons, New York.

USE OF PUMICE AND SCORIA AGGREGATES FOR CONTROLLING ALKALI SILICA REACTION

Mucip TAPAN

Natural Resources of Van Lake Basin Research and Application Center, Yuzuncu Yil University, Zeve Campus, 65080 Van, Turkey, muciptapan@gmail.com

Abstract: Turkey has important potential pumices reserves (68% of the reserve of the world) and 56 % of pumice reserve of Turkey is in the East Anatolia Region. It is important to assess huge pumice reserves in Eastern Turkey for its use in the cement and concrete industry. Use of acidic pumice and basic pumice (scoria) as cement additive or aggregate are gaining popularity because of their proven structural/durability properties. This paper presents the results of an investigation to assess the effectiveness of pumice and scoria aggregates in controlling alkali silica reaction (ASR) of alkali silica reactive aggregate using the following test methods: the accelerated mortar bar test (ASTM C 1260) and the scanning electron microscopy technique (SEM). The morphologies, structures and properties of the samples were determined by XRD, ICP-MS, XRF and thin section study. Mortar cubes were specially prepared according to ASTM standards using 10, 20 and 30% pumice or scoria aggregate as alkali silica reactive aggregate replacement. The results are compared with ASTM requirements to assess the suitability of pumice or scoria for preventing alkali silica reactivity. According to the results of these methods, pumice aggregates control the alkali silica reaction whereas scoria aggregates decrease expansion but is not as effective as pumice in preventing ASR. The results of SEM analysis showed alkali silica gel formation and serious decomposition of aggregate texture due to ASR in scoria added mortar bars.

Keywords: alkali silica reaction, aggregate, pumice, scoria, SEM

Introduction

The most important factors that affect the durability of reinforced concrete structures are physical, mechanical, and chemical properties of the materials used for concrete production. Concrete durability may decrease due to internal and external effects (i.e. environmental conditions etc.) and physical/chemical reactions. The most important chemical reaction that affects concrete durability is alkali silica reactivity (ASR) which is a chemical reaction between alkalis (sodium oxide, Na_2O) and potassium oxide (K_2O) found in cement paste and the reactive silica contained in the aggregates.

This process creates an alkali-silicate gel that absorbs water and increases in volume (Stanton, 1940; Taylor, 1991). The reaction in concrete can develop fast or slow depending on the characteristics of reactive aggregates and water in the pores. There are many minerals that affect alkali silica reactivity. According to earlier studies that have been made on the effect of the ASR, the most active minerals in terms of ASR are found to be volcanic glass, quartz, opal, tridymite, chalcedony, and cristobalite (Ineson, 1990).

Natural materials that are extensively used as mineral admixture in concrete industry found to be effective in decreasing ASR due to aggregate used in concrete (Saglik, 2009; Davraz and Gunduz, 2013). The highly porous structure of natural materials (i.e. perlite, pumice, scoria etc.) were considered to work as an air entrainment agent that holds expanded alkali-silica gels in its structural pores and consequently prevent ASR in concrete (Saglik, 2009).

This study is organized to find the effectiveness of pumice and scoria used as fine aggregate in preventing the ASR in concrete. For this purpose, alkali silica reactive aggregate named ETRA is replaced with 10, 20 and 30% pumice or scoria aggregate and the effect of pumice and scoria in controlling alkali silica reaction is investigated. The accelerated mortar bar test method (ASTM C 1260) which is among widely used tests for evaluating the potential alkali reactivity of aggregates for concrete is used for evaluating ASR of the mixtures. Alkali silica gel formation in each mixture was observed using the SEM analysis.

Materials and methods

Aggregate and cement

Pumice aggregate (PA) and scoria aggregate (SA) were obtained from a quarry in Ercis (Van) and Patnos (Agri). Alkali silica reactive aggregate (ETRA) was collected from Etrusk Volcano located in Ercis, Van, Eastern Turkey. More than 50 kg of pumice and scoria samples were collected from each location. In order to reduce the amount of sample, sampling was done using cone and quartering method and riffles, since sampling must represent the mineralogical, physical and chemical homogeneity. The samples were crushed and ground using laboratory dodge jaw crusher, rod mill and ball mill to reduce their size to -200 mesh (74 µm) for mineralolological and chemical analyses. Three hand samples which were chosen from each location were prepared for thin section studies. Cutting, polishing and thinning processes were performed using an oil system. Glue that hardened under UV light was used.

Table 1. Chemical composition of the cement using experimental study

Component (%)	SiO_2	Al_2O_3	Fe_2O_3	CaO	MgO	SO_3	LOI	Total alkali
Cement	20.03	4.53	3.50	64.13	1.14	2.65	2.50	0.65

The cement used in the Accelerated Mortar Bar test was an ordinary portland cement – CEM I 42.5 R (Table 1) according to EN 197-1 (equivalent to ASTM C150 Type I).

Characterization

To investigate the petrographical characteristics of aggregates, thin sections of three aggregate samples were prepared and determined by using LEICA Polorizan Microscope. Major oxide element analyses of the ETRA, PA and SA samples were obtained at the ACME Analytical Laboratories in Vancouver, Canada, using ICP-MS. Compositions of the pumice samples were checked by X-ray Powder Diffraction. By comparing the positions of the diffraction peaks against that of the ICDD cards, the target material could be identified. The XRD data were collected using Rigaku X-ray Diffractometer (Model, RadB-DMAX II) with Cu K_α (30 kV, 15 mA, λ = 15.4051 nm) radiation at room temperature. In addition, to confirm the occurrence of alkali–silica gel in mortar bars, LeO EVO 40 scanning electron microscope was used.

Experimental study

A number of tests are available for evaluation of the potential alkali silica reactivity of aggregates. The accelerated mortar bar test (ASTM C 1260) which is one of the widely used tests for evaluating the potential alkali reactivity of aggregates for concrete is used to determine effectiveness of pumice and scoria in controlling ASR. The alkali content of the cement does not affect the expansion in this test method because the specimens are stored in a NaOH solution at 80 ^{o}C. Alkali amount of CEM I 42.5R cement that is used in accelerated mortar bar test is 0.65%. Water/cement ratio of the mortar bars is 0.47 and aggregate grain size is between 4.75 mm and 150 μm as specified in ASTM C 1260. Length changes of samples (original and pumice and scoria added) in the solution are measured on the third, seventh and fourteenth days according to ASTM C 1260 and effectiveness of pumice and scoria aggregate in controlling ASR is determined.

Results and discussion

Characterization of Aggregates

The thin sections, which were randomly selected from the images, are given in Figure 1. PA consists of plagioclase, sanidine, volcanic glass and microphenocrystals of the some mafic minerals such as amphibole and pyroxene. Plagioclase, pyroxene, rare amphibole and volcanic glass form mineralogical assemblage of SA sample. Plagioclase, sanidine, ortho-clinopyroxene, and rare olivine phenocrystals constitute the mineralogical assemblages of the ETRA aggregate. ETRA sample which have intersertale groundmass contains microcrystals of the same mineral assemblage and volcanic glass. Sanidine and plagioclase phenocrystals are partly absorbed,

magmatically corroded, displaying sieve texture and they display alteration to clay minerals and serisite (Oyan, 2011; Oyan et al. 2011).
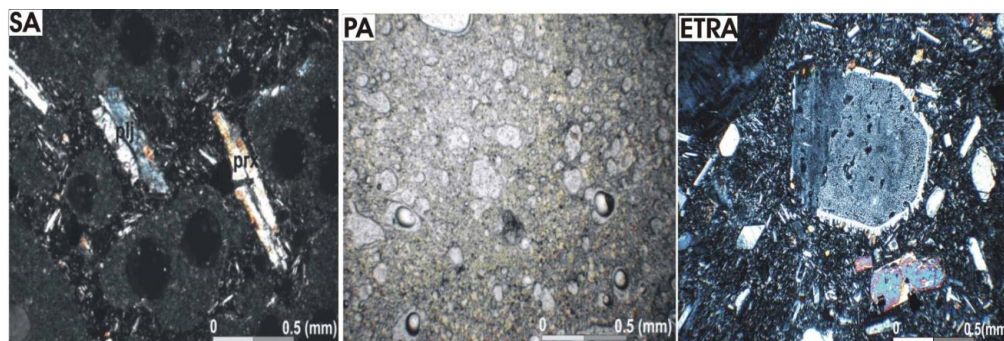
Fig. 1. Thin sections of the aggregates

Major oxide element analyses of the ETRA, PA and SA samples were obtained at the ACME Analytical Laboratories in Vancouver, Canada, using ICP-MS. The major element contents of the samples are given in Table 2. The chemical analysis indicates that SiO_2, Al_2O_3 and Fe_2O_3 constitute major contents of the samples. Pumice aggregates are named pumice and scoria depending on the SiO_2 content. According to chemical analysis, PA and SA can be classified as acidic pumice and basic pumice, respectively. In addition, chemical analysis results show that SiO_2, Al_2O_3 and Fe_2O_3 content is greater than 50%, and CaO content is less than 10%. According to ASTM C 618-08a (2008), the samples having this chemical composition possesses pozzolanic and cementitious properties, which can be used in the concrete industry.

Table 2 . Results of chemical analyses of the ETRA, pumice and scoria samples

Samples	SiO_2	Al_2O_3	Fe_2O_3	MgO	CaO	Na_2O	K_2O	TiO_2	P_2O_5	MnO	LOI	Sum
ETRA	59.21	16.53	6.01	2.57	4.99	4.37	3.06	1.02	0.38	0.11	1.45	99.7
PA	71.29	12.67	1.50	0.09	0.52	3.66	4.60	0.09	0.02	0.07	5.4	99.93
SA	48.58	16.19	14.10	4.41	7.21	3.64	1.10	2.40	0.66	0.22	1.2	99.70

The XRD patterns of the samples are given in Figure 2. PA is an amorphous volcanic rock. X-ray diffraction data indicates that PA has not a crystalline structure and very broad reflection (peak) between 20° and 30° (2θ) confirming the presence of amorphous quartz as the characteristic properties of the acidic pumice. The XRD patterns of others show little crystalline mineral phases. Anorthite (JCPDS Card File No. 73-1435), hornblend (JCPDS Card File No. 71-1062) and crystalline quartz (JCPDS Card File No. 76-0823) are also observed in the XRD pattern.
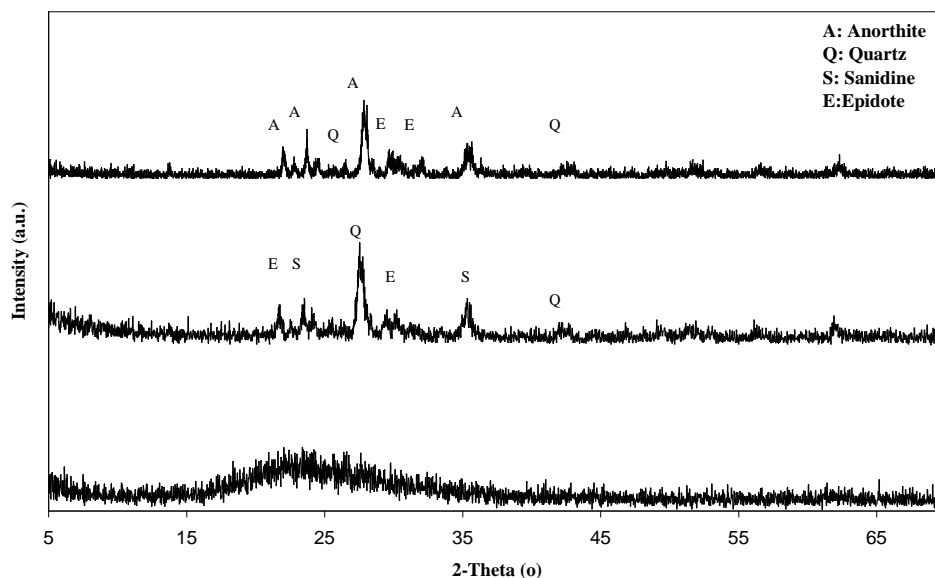
Fig. 2. XRD patterns of the samples

Accelerated mortar-bar test and determination of alkali–silica gel

Mortar bars were prepared using the ETRA aggregate and pumice and scoria added (10, 20 and 30% pumice or scoria replacement) ETRA aggregate. All samples were tested according to the ASTM C1260 Standard "Test method for Potential Reactivity of Aggregates (Mortar-Bar- Test)" and the results are given in Table 3.

Table 3. Average values of mortar-bar of ETRA and pumice and scoria added
(30% pumice or scoria replacement) ETRA. P-pumice, S-scoria

Sample	3 day	7 day	14 day	ASTM C 1260	
ETRA	0.070	0.165	0.407	$0.407 > 0.2$	Deleterious
ETRA+%10 P	0.040	0.046	0.052	$0.05 < 0.1$	Innocuous
ETRA+%20 P	0.032	0.036	0.042	$0.04 < 0.1$	Innocuous
ETRA+%30 P	0.024	0.028	0.03	$0.03 < 0.1$	Innocuous
ETRA+%10 S	0.028	0.03	0.291	$0.291 > 0.2$	Deleterious
ETRA+%20 S	0.02	0.02	0.224	$0.22 > 0.2$	Deleterious
ETRA+%30 S	0.013	0.013	0.118	$0.10 < 0.118 < 0.2$	Potentially Deleterious

According to the results of accelerated mortar bar method test, expansions of the ETRA sample were found to be higher than 0.20 % as shown in Table 3. The 14-day expansions were respectively decreased to 0.05, 0.04 and 0.03% for 10, 20 and 30% pumice replacement. Ten and 20% replacement of scoria aggregate decreased the alkali silica gel formation but the aggregate mixture still found to be deleterious. Use

of 30% scoria aggregate decreased the 14-day expansion to 0.118%. These results show that pumice used as fine aggregate substantially decreases ASR of deleterious aggregates whereas scoria used as fine aggregate prevent ASR of deleterious aggregate but is not as effective as pumice (Fig. 3).
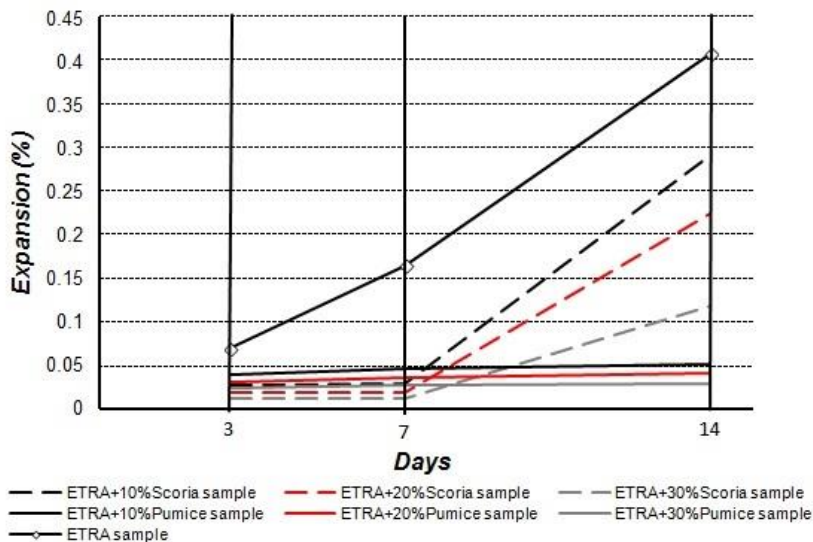
Fig. 3. Mortar-Bar test results showing the effect of percentage of pumice
and scoria aggregate on expansion and time

The SEM observations of mortar bars tested according to ASTM C 1260 confirm the occurrence of alkali–silica gel in the samples in Figure 4 and Figure 5. Figure 4 (a) shows ASR gel formation in ETRA sample displaying the characteristic expansion cracks in the concrete. ASR gel formation are rarely observed in tested mortar bars produced with pumice added ETRA aggregate (Figs 4b and 5b). The 10% pumice aggregate replacement prevented ASR gel formation but could not prevent expansion cracks. 20% replacement was as effective as 30% pumice replacement in decreasing ASR gel formation. In contrary, the SEM observations of tested mortar bars prepared using scoria and ETRA aggregates confirm the occurrence of alkali–silica gel. Figures 4c, 4d, 5c, and 5d show alkali silica gel formation in ETRA+Scoria samples exhibiting the characteristic expansion cracks on the aggregate surface inside the mortar bars. 10 and 20% scoria added aggregates were found to be deleterious in terms of the 14-day expansion percentages whereas 30% scoria added aggregate was found to be potentially deleterious.
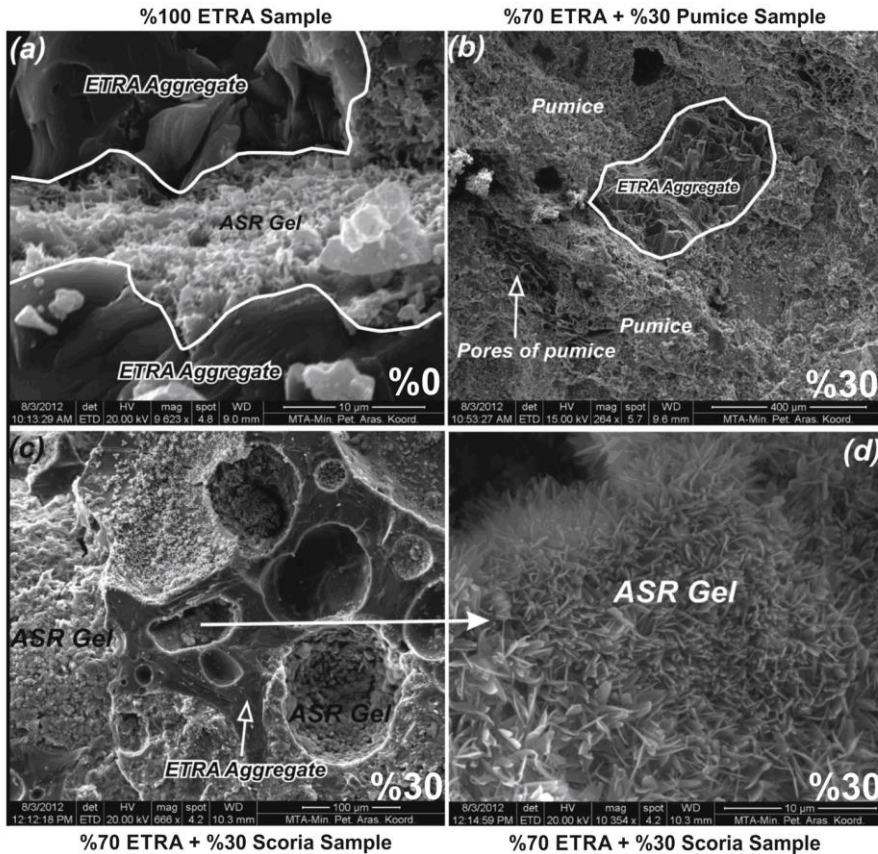
Fig. 4. SEM photomicrographs of the original and 30% pumice and scoria added samples

Conclusion

This study is organized to find the effectiveness of pumice and scoria used as fine aggregate in preventing the ASR in concrete. According to the results of this study, pumice used as fine aggregate substantially decreases ASR of deleterious aggregate. 10% pumice aggregate replacement prevented ASR gel formation but could not prevent expansion cracks. 20% replacement was as effective as 30% pumice replacement in decreasing ASR gel formation. It was also found that scoria used as fine aggregate prevent ASR of deleterious aggregate but is not as effective as pumice in preventing ASR. 10 and 20% scoria added aggregates were found to be deleterious in terms of the 14-day expansion percentages whereas 30% scoria added aggregate was found to be potentially deleterious. Future studies should be organized to find the effect of chemical composition of pumice and scoria aggregate in controlling ASR. Such studies are important for sustainable construction.
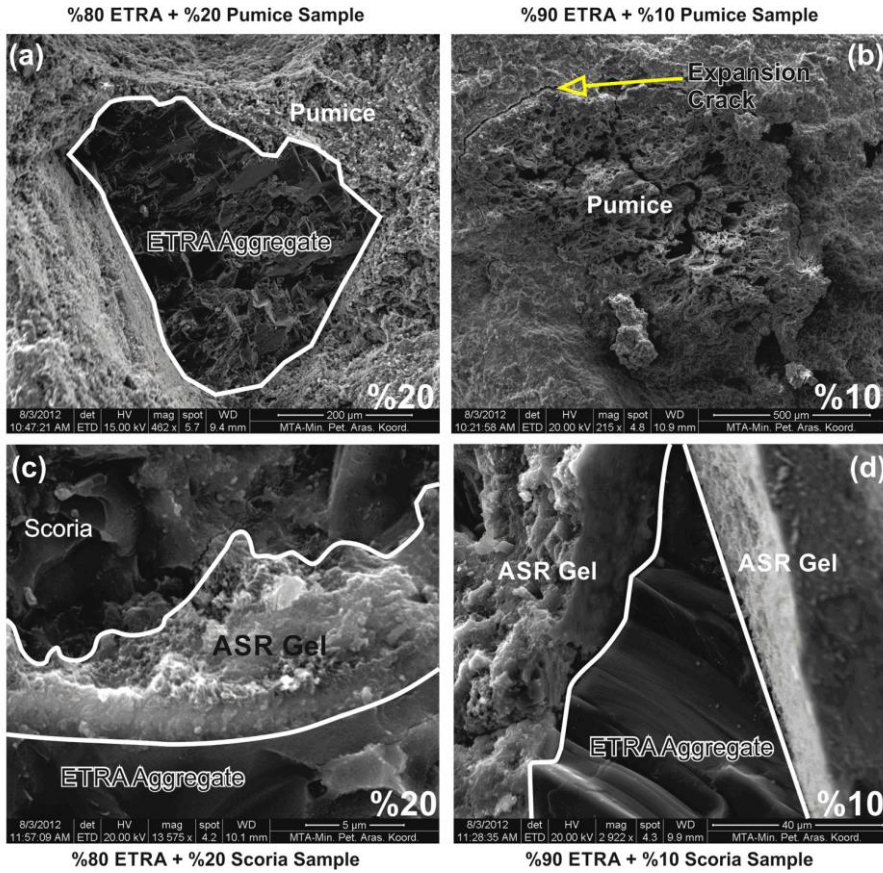
Fig. 5. SEM photomicrographs of the 10 and 20% pumice and scoria added samples

Acknowledgements

References

ASTM C-1260-94. Standard Test Method for Potential Alkali Reactivity of Aggregates (Mortar-Bar Method), Concrete and Mineral Aggregates, American Society for Testing and Materials, USA, 1994; 4(2): 650-653.

ASTM C 618–08a. Standard specification for coal fly ash and raw or calcined natural pozzolan for use in concrete. ASTM. 2008.

ASTM C150-02. Standard specification for Portland cement. Annual book of ASTM standards, West Conshohocken, PA: ASTM, 2002; vol. 04.02.

Cement and Concrete Association of New Zealand, Technical Report 3, Alkali Silica Reaction, Minimising the Risk of Damage to Concrete Guidance Notes and Recommended Practice (Second Edition), ISBN: 0908956185.

DAVRAZ M., GUNDUZ L., *Reduction of alkali silica reaction risk in concrete by natural (micronised) amorphous silica*. Construction and Building Materials. 2008; 22: 1093-1099.

INESON P.R., *Siliceous components in aggregates*. Cement and Concrete Composites 1990; 12(3): 185-190.

LE BAS M.J., LE MAITRE R.W., STRECKEISEN A, ZANETTIN B., *A chemical classification of volcanic rocks based on the total alkali–silica diagram*. Journal of Petrology. 1986; 27: 745–750.

OYAN V, KESKIN M, LEBEDEV AV, SHARKOV E, CHUGAEV A.., *Importance of Assimilation Combined With Fractional Crystallization (AFC) and Magma Mixing Processes in The Magmatic Evolution of The Pliocene Etrusk Volcano, Northeast of Lake Van, E Turkey*. 64th Geological Congress of Turkey, Ankara, 2011;162-164.

OYAN V., *Etrüsk Volkanı ve Çevresinin (Van Gölü Kuzeyi) Volkanostratigraifisi, Petrolojisi ve Magmatik Evrimi*. PHD, Yuzuncu Yil University, Van, 2011, p.352.

RHOADES R., *Discussion of a paper by Stanton, Porter, Meder and Nicol, California experience with the expansion of concrete through reaction between cement and aggregate*. J. Am. Concrete Inst. Proc. 1942, 38: 7–11.

SAGLIK A., 2009. *Alkali-Silica Reactivity and Activation of ground Perlite-Containing Cementitious Mixtures*, MSc, Graduate School of Natural and Applied Sciences of METU.

TAYLOR G.D., *Construction Materials*. London: Longman Scientific & Technical Publications; 1991.

INVESTIGATION OF EFFECTIVE PARAMETERS FOR MOLYBDENITE RECOVERY FROM PORPHYRY COPPER ORES IN INDUSTRIAL FLOTATION CIRCUIT

Fardis NAKHAEI, Mehdi IRANNAJAD

Department of Mining & Metallurgical Engineering, Amirkabir University of Technology, Tehran, Iran, iranajad@aut.ac.ir

Abstract. The Sarcheshmeh copper mine is a significant copper and molybdenum producer. Sampling of the Sarcheshmeh flotation circuit (in a six-month period) showed that a large share of waste of molybdenite took place in rougher cells. Since the rougher cells tailing is transferred to tailing thickener, the main focus of this paper was on this section. In the current study, the factors which influence the recovery of molybdenite and copper were investigated. Molybdenite recovery in the bulk flotation circuit was consistently lower than that of the copper sulphides as well as being far more variable. This paper describes the methodically use of size by size recovery data, quantitative mineralogy, and liberation degree analysis to identify the factors contributing to molybdenite recovery relative to copper in industrial rougher circuit. The results showed that the size by size recovery for both metals in the ultrafine and coarse fractions recovery was reduced. On the other hand, the highest recovery occurred in the intermediate sizes from 27 μm to 55 μm. Molybdenum recovery in the fine and ultrafine and coarse fractions drops off to a greater extent than the recovery of copper. The investigations of degree liberation showed that the recovery of copper sulphides is more dependent on the liberation state of valuable minerals while for molybdenite some other factor splay a significant role.

Keywords: Flotation, copper, molybdenum, recovery

Introduction

About 50% of the world's molybdenite (MoS_2) concentrate is evolved from its primary ores and the rest as a low-grade concentrate by-product of copper, uranium and tungsten mining. Molybdenite reserves of the world are distributed in eight countries such as China, USA, Chile, Canada, Russia, Armenia, Peru, Iran and Kazakhstan.

Recently, molybdenum has been regarded as an almost insignificant by-product of copper production. In 2004, molybdenum underwent some changes when the price of the metal increased as a result of high demand from Chinese steel makers. Rising the

price of molybdenum has led to the expansion of the metal production, including efforts for optimizing control.

According to the literature, in the various sources the molybdenum recoveries are lower than the copper recoveries. Much research has been done in an attempt to connect the flotation response of molybdenite to the mineral crystal structure, textural features, and lithology. One of the factors that have influenced molybdenite flotation is the degree of crystallisation (Podobnik and Shirley 1982).

According to Triffett and Bradshaw (2008), molybdenite particles with high aspect ratio (major axis over minor axis) are more likely to transfer to the concentrate, and the coarse particles with high perimeter to area ratio tend to enter the tailings.

In another study by Ametov et al. (2008) a series of surveys at different porphyry copper flotation plants was examined. According to the operations, the recovery of molybdenite in the rougher/scavengers of the bulk Cu/Mo flotation circuit was consistently lower than that of copper sulphide. Moreover, reducing the flotation feed solids percent led to an increase in molybdenite recovery whereas copper flotation was relatively unaffected.

Little study has been carried out to identify losing of molybdenite and copper in industrial scale and the influence of particle size, liberation degree on the flotation of porphyry copper ores although extensive studies have been done with regard to be the influence of crystal structure on molybdenite flotation.

The Sarcheshmeh copper ore body which may rank as the third or fourth largest in the world comprises 1 billion tones (1 petagram) averaging 0.90% copper and 0.03% molybdenum. Geologically, it is separated into three zones: oxide, supergene, and hypogene (Nakhaei and Irannajad 2013).

The goal of this paper is to determine some of the factors that give a contribution to the molybdenum recovery being lower than copper in the bulk flotation circuit at the Sarcheshmeh copper complex. Total sampling of the Sarcheshmeh flotation circuit showed that large share of waste of molybenite took place in rougher cells. Therefore, the several factors were investigated including morphology of molybdenite and how this manifests itself in the flotation feed, the size by size recovery and liberation characteristics of the copper and molybdenite.

This paper is organized as follows. Section 1 describes theoretical considerations of copper–molybdenum flotation, and reviews most of the published applications. Section 2 gives a description of the industrial plant briefly. The materials and methods are introduced in Section 3. Finally, Section 4 analyzes the effect of some of the factors on the flotation of molybdenum and copper.

Flotation of porphyry copper–molybdenum ores (theoretical considerations)

Molybdenite-bearing copper sulphide ores are typically beneficiated by froth flotation techniques in two stages. The first stage, commonly known as the copper circuit, produces a bulk copper sulphide molybdenum sulphide concentrate. The second stage

subjects the bulk copper-molybdenum sulphide concentrate to a selective flotation technique to separate molybdenite from copper sulphide.

Reagents

Reagent programs applied for the treatment of porphyry copper and copper-molybdenite ores are relatively simple, and usually include lime as a modifier, xanthate as the primary collector and a secondary collector. The secondary collector type varies from condition to condition, and is selected from a variety of collectors including dithiophosphates, mercaptans, thionocarbamates, and xanthogen formates etc.

The choice of secondary collector is related to a relatively great number of factors, some of which consist of (1) kind of copper - molybdenite minerals present in the ore, (2) composition of gangue minerals in the ore, (3) the presence and type of clay minerals and (4) type of frother used (Srdjan, 2007).

Oily collector is typically added in molybdenite flotation to enhance the mineral's hydrophobicity. The presence of exposed hydrophilic edges on the bent and distorted particles may also prevent spreading of oil droplets on hydrophobic surfaces, thus reducing the effect of the collector (Zanin et al. 2009).

Physicochemical investigations concerning the role of collectors and depressants in molybdenite flotation were carried out by Wie and Fuerstenau (1974). Dextrin and dyes have found widespread use as a molybdenite depressant. The interaction of dextrin with molybdenite has been examined in detail. They obtained evidence for the adsorption of dextrin to take place via hydrophobic bonding. Moreover, they worked on the interaction of collectors with molybdenite. They conducted a detailed investigation of the adsorption of potassium diethyldithiophosphate on molybdenite and suggested an electrochemical mechanism to account for the observed features.

Selection of the type of frother is based on a wide variation, and in many operating plants and integration of two or more frothers are used. The main reason behind this is interference from clay minerals, which causes a dry froth and hence difficult to remove. A combination of frothers may solve this problem.

In many plants, lime is employed as a pH modifier as well as for the depression of pyrite during the cleaning operation. The flotation pH in most of the plants is above 10 and most often over 11. The relatively high pH used in the operating plants is not designed to depress pyrite, but rather as a frother modifier. In reality, the higher pH produces a stable froth with better carrying power than at a lower pH for the majority of porphyry copper- molybdenite ores. These findings were obtained with xanthate dithiophosphate collectors (Srdjan 2007). Experimental test work carried out at a number of plant laboratories has mentioned two major factors that dictate the amount of lime used.

1. Flotation of copper at different pH is associated with the type of frother used. With certain frothers, copper recovery can be significantly increased at a lower pH range while some frothers need a higher pH to keep a more lasting frothing power.

2. Flotation of middling particles (i.e. higher than 200 μm) improves with increased
    pH.

This is true in the case when chalcocite is the major copper mineral. In the case of
chalcopyrite ore, a lower pH is more desirable (i.e. 8.5–9.5) because at a higher pH,
the flotation of chalcopyrite is decreased, especially for the coarser particles.

Depression of pyrite in the case of porphyry ores containing chalcocite takes place
at an almost high pH (i.e. higher than 11.5) while in the case of chalcopyrite, the pH is
kept at about 10.5 -11 (Srdjan 2007).

One of the most difficult functions is the selection of a proper frother. Its
significance has not always been recognized despite the fact that many operating
plants treating porphyry copper ores apply two or more frothers. Frequently, a frother
does not have enough power to recover coarse and middlings or is not selective
enough to float fine copper. In the literature (Bulatovic 1992), seven basic
requirements for a good flotation frother have been listed, which also include low
sensitivity to changes in pH and dissolved salt content. However, the frothing in
porphyry copper flotation is generally controlled by pH. The presence of clay in the
ore is the main reason for unstable froths and lowered frothing power.

It has been shown that destabilization of frother takes place in the presence of
ultrafine particles (Srdjan 2007). It is a common practice that during flotation of
porphyry copper ores containing clay minerals, the copper froth becomes highly
flocculated after xanthate collector additions which result in a dry froth which is
difficult to remove. In order to prevent froth dryness, a collector with frothing
properties in combination with two or more frothers is used.

According to recent studies (Srdjan 2007), the stability of the froth may be more
effectively controlled by modifying or preventing flocculation of hydrophobic
particles. The reagents that control frothing properties at the lower pH region are
certain amine oxides, which if added to an alcohol or alkoxy paraffin frother, are able
to reduce the detrimental effect of ultra-fine clay minerals on froth stability. Studies
have shown that the use of these frother mixtures can result in a significant
improvement in the rate of copper molybdenum flotation.

Interactions with gangue minerals

Flotation schemes for the separation of molybdenite from ores are based on the
inherent natural flotation of molybdenite. Chander and Fuerstenau (1972) undertook a
detailed investigation to elucidate the factors that affect the surface properties of MoS_2
which in turn govern the natural flotation of molybdenite. They found that the
flotation was strongly affected by surface oxidation, primarily because of the effect of
the oxidation products on electrical and hydration phenomena. The relative flotation of
MoS_2 was found to be a maximum at the pH range 5.5-6.5. Calcium ions were found
to exhibit a strong affinity to adsorb onto molybdenite surface, and were able to
reverse its zeta potential. The investigations of the electrokinetic characteristics of

MoS_2 were reported by Arbiter et al. (1974), and Chander and Fuerstenau (1974). These studies indicated that molybdenite is negatively charged at the pH range 3-10.

The problems associated with the recovery of molybdenite from porphyry copper ores were summed up by Hernlund (1961). He expressed that the mineralogy of the deposit and the slime coating of molybdenite to be particularly detrimental to the molybdenite recovery. Cuthbertson (1961) also showed that clay minerals, particularly bentonitic type, seriously impaired the flotation of molybdenite. A great compilation of the molybdenum recovery techniques in plants treating porphyry copper ores were done by Sutulov (1971). As mentioned in this study, there are at least three types of molybdenite in copper porphyries. These are: (1) coarse, clean molybdenite with perfect basal cleavage which occurs in quartz veins; (2) fine-grained scaly molybdenite which appears as fine coatings along the joints and fractures of breccia; and (3) amorphous and dull variety which often exhibits a lower flotation than quartz. The problems in the primary flotation of molybdenite arose mainly from the amorphous and finely disseminated molybdenite. These investigations have revealed that molybdenite and quartz particles are negatively charged at the pH commonly used for bulk sulphide flotation, namely 11. While the adsorption of calcium ions reduces the magnitude of negative charge on molybdenite, the adsorption can reverse the surface charge on quartz particles when the calcium concentration in solution exceeds 10^{-3} M (Raghavan and Hsu 1984). The maximum effect of the calcium ions on the zeta potential is within pH range of 11-12 due to the specific adsorption of the hydroxo-complex ions of calcium, $CaOH^+$, into the calcium molybdenite formed in the edges of the molybdenite particles.

Compared to sodium butyl xanthate, a selective collector N-propyl-N-ethoxycarbonyl thiourea (PECTU) decreased 2/3 lime consumption in the flotation separation of Cu/Fe sulphide minerals in the Dexing copper mine, and increased the Mo grade and recovery in the copper cleaner concentrate (Liu et al. 2011).

Surface chemistry

As mentioned before, lack of hydrophobicity may be related to mineral slimes adsorbing onto the surface, surface oxidation, and scale precipitation from process water. The possibility that surface oxidation and scale precipitation are occurring is examined using surface analysis. The methodology being used is Time of Flight Laser Ionization Mass Spectrometry (TOFLIMS). There is a trend of decreasing sulphide sulphur with the slower floating molybdenite. The fastest floating material has the highest surface sulphide sulphur analysis. It means that surface sulphur is responsible for the natural hydrophobicity of the molybdenite. Tail particles have a lower concentration of sulphide sulphur than concentrate particles. It is also revealed that decreasing in sulphide sulphur occurs simultaneously with increasing in the oxidation product, MoO_3 as well as calcium. This is consistent with slower floating molybdenite.

Surface analysis of molybdenite particles by TOFLIMS was demonstrated that surface sulphide sulphur is totally removed on slower floating particles whereas surface oxidation and calcium coating increased (Triffett and Bradshaw 2008).

Industrial plant

Process description

The Sarcheshmeh concentrator plant consists of grinding circuits (SAG milling followed by ball milling) and flotation circuit where copper/molybdenum concentrate is produced. This bulk concentrate is then processed through a separate molybdenum flotation plant where the copper is depressed and a high grade molybdenum concentrate is produced. Figure 1 shows the Sarcheshmeh flotation circuit.

The flotation circuit comprises the rougher, cleaning, and column flotation stages. The rougher flotation bank consists of eight cells (130 m^3) and the regrind mill is a 3.962 m by 5.791 m ball mill. The cleaner, scavenger banks each has three (50 m^3), five (50 m^3) cells, respectively. The single stage column flotation operation is composed of a Metso Minerals CISA column with 4 m internal diameter, 12 m height, and associated instruments. The target d_{80} of the flotation feed was 75 μm, and the pH in the rougher/scavengers was controlled between 11.8 and 12. A bulk concentrate assaying about 28–30% Cu and 0.6–0.7% Mo was produced depending on the ore blend processed (Nakhaei and Iranajad 2013). Since most of the molybdenite and copper losses occurred in the rougher cells, this part of the circuit became the focus of investigations.
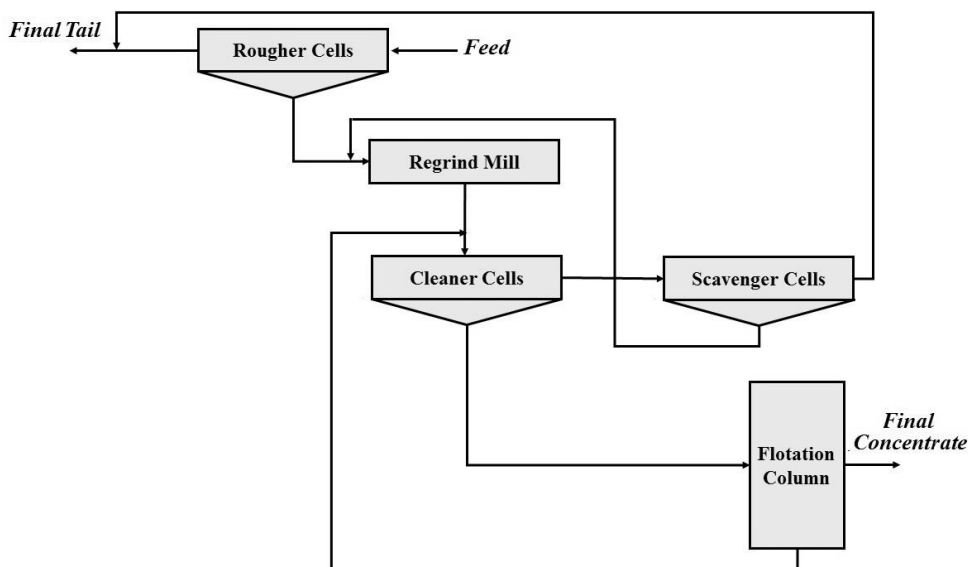
Fig. 1. The flow sheet of flotation circuit of the Sarcheshmeh industrial plant

Statement of the problem

Characteristically, in porphyry copper flotation plants, molybdenum shows lower recovery than copper despite the apparent natural hydrophobicity of molybdenite (Kelebek 1988). In the studied plant, the average of copper recovery is usually 86%, and the average of molybdenum recovery changes between 45% and 55%. Of the copper sulphide minerals, chalcopyrite usually has higher flotation rate and recovery, but also chalcocite, bornite and covellite can be recovered at values higher than 80% if the suitable electrochemical conditions are kept in the slurry to minimise surface oxidation (Orwe et al. 1998). On the contrary, molybdenite recovery, which may fluctuate significantly from operation to operation, is also within different ore bodies in the same operation. Copper and molybdenum recovery data for a six month of the Sarcheshmeh copper flotation plant (between 2011 and 2012) are reported in Fig. 2. The results revealed higher variability of molybdenum recovery than copper as a function of time. The daily molybdenum recovery has varied from 20% up to the maximum of approximately 75% whereas the copper recovery is concentrated into a narrower range from 80% to 92%. In general, bulk flotation recoveries of molybdenum are consistently lower than that of copper as well as being far more variable.
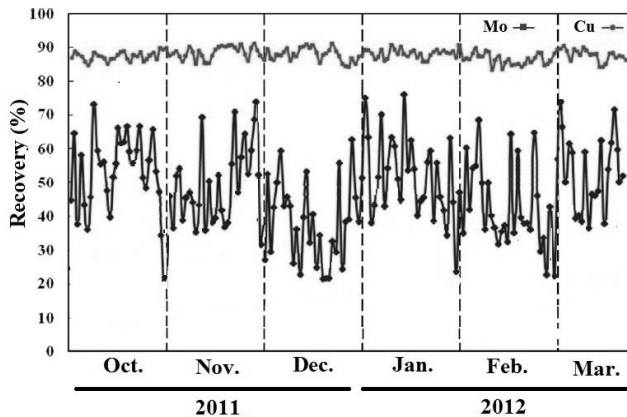
Fig. 2. History of recovery data for the Sarcheshmeh copper plant

Materials and methods

Since the recovery at the rougher stage has a significant effect on the overall copper and molybdenite recoveries, this paper investigates the possible problems of the operation procedure for rougher flotation circuit. In the Sarcheshmeh copper plant, much level of Cu and Mo are wasted in the rougher tail. Therefore, in the current study, the factors which influence the recovery of molybdenite and copper were investigated.

Two one-week samplings were taken during the period of two months when the plant condition was completely stable (seven continual days per month). In this paper, the average of the obtained data from the first week and the second week were called Sample 1 and Sample 2, respectively.

In the plant, the samples of the feed, concentrate, and tailings of rougher cells were taken for 2 h every day. The sampling period was chosen as 12 min (in each survey, ten sampling rounds were performed) in which multiple samples were collected to reduce fluctuation error. Before the sampling procedure, the plant stability was ensured from the control room, and plant data (throughput, feed solids per cent, air flows, and froth levels) were recorded. The samples from selected surveys were sized by wet/dry sieving and assayed on a size-by-size basis.

The size analysis of the samples showed that the rougher feed has a top size of 250 μm and 80% finer than 115 μm. The head grade of rougher feed was on average 0.85% Cu while the Mo grade of the rougher feed was 0.03%. Figure 3 shows a typical size distribution of feed used in the test work.
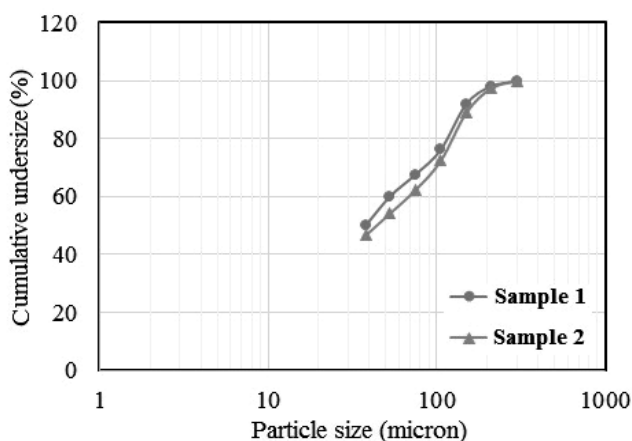
Fig. 3. Rougher feed size distribution

The reagents used in this study, in the plant, was oily collector for molybdenite (7 g/Mg diesel oil was used), Z_{11}, sodium isopropyl xanthate, dithiophosphate and mercaptobenzthiazole, Nascol 451 for copper minerals, at a typical addition rate of 27 g/Mg, MIBC, polypropylene glycol, Dowfroth 250 or Aerofroth 65 as frother (30 g/Mg). The reagents' type and dosage were kept constant for all the samplings. The chemical reagents were added into the ball mill, rougher cells (numbers 3 and 5), regrind mill, and scavenger cell (number 1), simultaneously. Therefore, the effect of adding chemical reagents in the rougher cells as a control variable was removed. The pH was adjusted to 11.8 using lime. The per cent solids, which were under standard operating conditions, were adjusted by varying the water flow rate and summarized in Table 1.

Table 1. The percent solids in flotation circuit

Stream	% solid
Rougher feed	28
Rougher concentrate	19.3
Ball mill discharge	60
Scavenger concentrate	10
Cyclone. overflow	16
Cleaner concentrate	17.5

The factors that may have an effect on the flotation of molybdenite and copper from porphyry ores include mineralogy of ore, grinding, and liberation. These factors will be discussed in more details in the next section.

Results and discussions

As mentioned before, in the flotation circuits in which the rougher tailing is the major tailing stream, and the overall recovery of the plant is mainly dependent on the rougher tailing grade. Therefore, preventing losses of values through this stream is crucial to keep the grade of the tailings as low as possible. This action is not possible without recognizing influential factors in recovery.

Flotation kinetic of molybdenum and copper in rougher cells

In this section, the rougher circuit flotation kinetics of the proposed scheme were investigated in details during two days following the conditions described above. The samples of each cell (concentrates and tailings of rougher cells (1, 2,…, 8) were then filtered, dried, weighed, and analysed for copper and molybdenum. The results are presented in Fig. 4. The results showed that Cu and Mo recoveries almost reached 93% and 67%, respectively.
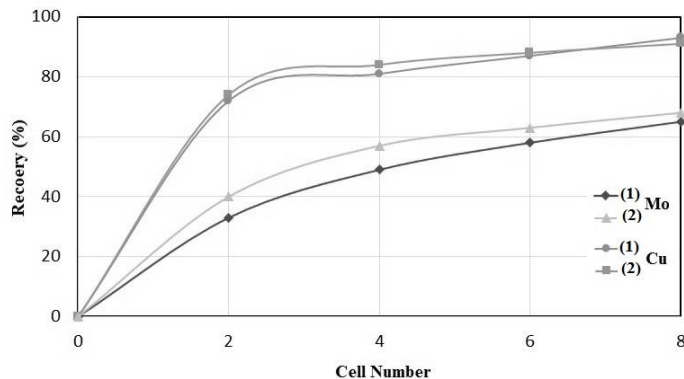
Fig. 4. Copper and molybdenite flotation kinetic curves in rougher cells

The rougher concentrate grade relationship for copper, molybdenum, and silica (SiO_2) for the two sampling periods are reported in Fig. 5. The approach was to reference the average of the daily analysis for the period of two weeks. Cu and Mo grades dramatically reduced with increasing the cell numbers therefore this reduction rate for Cu was from 28–30% to 2–7% and for Mo was from 0.27–0.3% to 0.08%. On the contrary, SiO_2 grade increased from 10 to 51%.
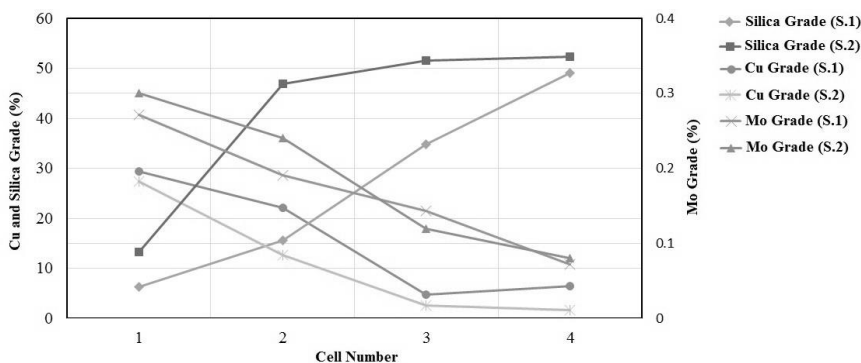
Fig. 5. Relationship between molybdenite, copper and SiO_2 grades in rougher concentrate

Liberation degree

The liberation degrees of chalcopyrite, chalcocite, covellite, and molybdenite in the feed and rougher tail are shown in Fig. 6.
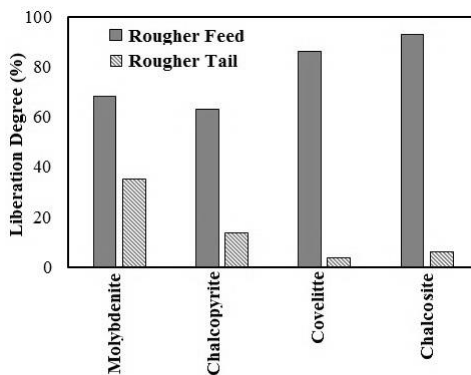
Fig. 6. The liberation degrees of Cu and Mo minerals in the rougher circuit

A comparison of the liberation degrees of Cu and Mo minerals showed that Mo liberation degree of rougher tail is higher than chalcopyrite (the main ore mineral of copper in Sarcheshmeh is chalcopyrite $CuFeS_2$). The liberated particles contain greater than 80% by area of the mineral which are being discussed. Based on the molybdenite data, on most days at least 37% of the molybdenite lost to tailings is liberated, and on

a significant number of days it is greater than 40%. By contrast, the copper sulphide losses are less liberated than the molybdenite (less than 10%). In conclusion, the recovery of copper sulphides is more dependent on the liberation state of these minerals while for molybdenite some other factor plays a significant role.

Size by size analysis

Separation of minerals by froth flotation is highly dependent on the particle size distribution. According to the literature on metallic ores, particles respond well to flotation up to 100 μm, but with increasing particle size the recovery rate declines considerably (Trahar 1981). The reasons for poor flotation of coarse particles have existed for a long time, and include detachment from bubbles because of the centrifugal forces which arise from the rotational motion of bubble-particle aggregate in the turbulent field and the limitation due to the buoyancy force of the bubbles. It has been claimed that coarse particles are powerless to detachment at the pulp-froth interface during their transfer from the pulp zone to the froth layer (Ata 2012).

Figures 7 and 8 display the average size by size copper and molybdenum recovery for two different weeks. These curves were calculated based on the analysis of daily composites of feed and tails. In Figs. 7 and 8, the number of size fractions has been reduced to assist in the presentation of these data. According to the results, the recovery for both the molybdenum and copper is highest in the 9–38 μm range. In the case of molybdenum, the fine -5 μm fraction recovery 12% lower than the optimum size range while for copper, this offset is closer to 5%. Figure 8 reflects the quicker drop off in recovery for molybdenum in the very fine size ranges. For both metals the coarse fractions +75 μm and +106 μm recover at a far lower rate and the slope of the line is steeper implicating that overall recovery is more driven by changes in coarse particle recovery than fines. Comparing molybdenum to copper the finer size fractions have almost similar slopes while the coarse fractions are somewhat steeper which in the case of molybdenum, indicating an even greater dependence on coarse particle recovery for it.
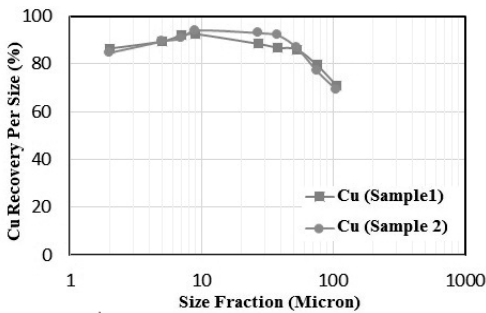
Fig. 7. Average size by size of copper recovery for 2 weeks
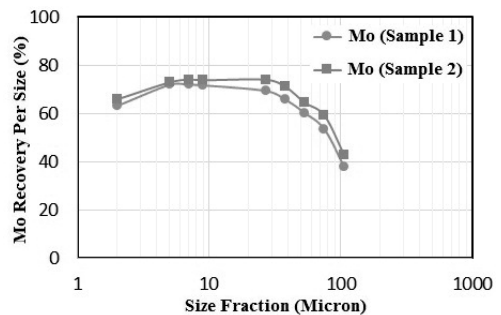
Fig. 8. Average size by size molybdenum recovery for 2 weeks

The recovery of molybdenum reaches a peak in the 7–27 µm size range while the copper recovery is high across a wider range of sizes from 7 to 53 µm. The recovery of molybdenum also descends to a greater extent than the copper in the coarse and fine sizes. In Figs. 9 and 10 bar charts reporting the average distribution of copper and molybdenum in the feed.
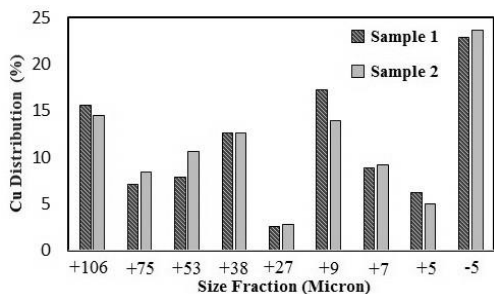
Fig. 9. The content percent of Cu
in rougher feed
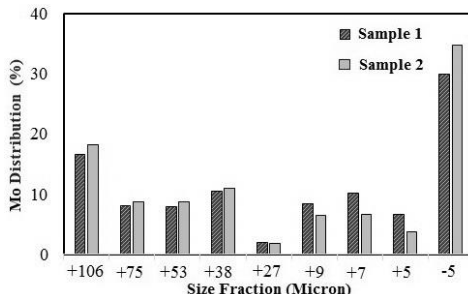
Fig. 10. The content percent of Mo
in rougher feed

About 1/4 of the mass and about 22% and 32% of the total copper and molybdenite content are in the ultra fines fractions respectively. Particles less than 5 µm were considered as ultra fines in this work.

The distribution of Cu and Mo losses in different size fraction in the rougher tailings is illustrated in Figs. 11 and 12. It is shown that about 42% of copper particles were lost from the rougher bank in +75 and +106 µm size fractions and 25% of copper particles were lost from the rougher bank in -5 µm size fraction. It is also shown that about 35% of molybdenite particles were lost from the rougher bank in +75 and +106 µm size fractions, and 30% of molybdenite particles were lost from the rougher bank in -5 µm size fraction. As can be seen from Figs. 11 and 12 that molybdenum was lost mainly from rougher bank cells. Therefore, optimum interval to obtain the highest recovery is in the size fraction of 27 to 55 µm.
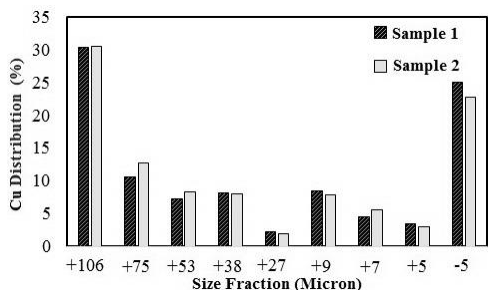
Fig. 11. The content per cent of Cu losses from
rougher tailing
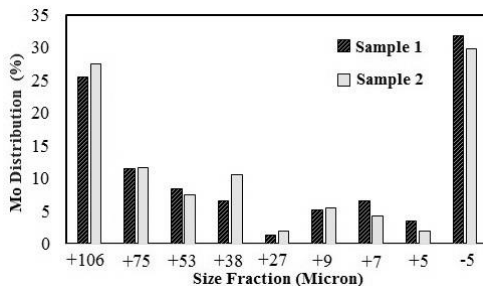
Fig. 12. The content per cent of Mo losses from
rougher tailing

The main reason behind this is the lack of Mo and Cu in the rougher circuit was the existence of coarse and ultrafine particle size. In general, the metallurgy (grade and recovery) of the rougher stage depended greatly on the primary grind. In this study, it has been proven that a grind of a d_{80} of 70 μm was more beneficial for Cu and Mo than 110 μm. Moreover, there is need to study the mineralogy and its effect on metallurgy.

Molybdenite structure and morphology

The low and highly variable flotation recovery of molybdenum may be result of several factors which are related to the properties of the molybdenite mineral. Molybdenite crystal structure comprises hexagonal layers of molybdenum atoms between two layers of sulphur atoms. The crystalline structure of MoS_2 is presented in Fig. 13. The interaction between S-Mo-S is a strong covalent bond while that between S-S is weak van der Waals force. It is far easier to break S-S band than S-Mo bond which gives rise to characteristic cleavage along the [001] plane. Therefore, the ground molybdenite particles illustrate two kinds of surfaces entitled face and edge. The former is hydrophobic due to the weak unsaturated band while the latter is hydrophilic because of the strong band. At large particle size, molybdenite is viewed as a naturally hydrophobic mineral, and is generally concentrated by froth flotation. Along with the size reduction, the face/edge ratio reduced and thus the hydrophobicity of the molybdenite surfaces decreased, resulting in the marked drop in flotation efficiency (Chander and Fuerstenau 1972). On the other hand, froth flotation does not respond well for fine mineral particles due to the small mass of the particles. Therefore, low probability of collision and adhesion of particles to air bubble leads to a low flotation rate (Zanin et al. 2009). Ultimately, during grinding, platelet shaped fragments, exfoliating from larger particles, are generally produced. Furthermore, the particles formed are characterised by strongly hydrophobic and inert faces and hydrophilic and reactive edges, generated by the breakage of the covalent bonds. Accordingly, it is difficult for froth flotation to beneficiate molybdenite fines from ores.
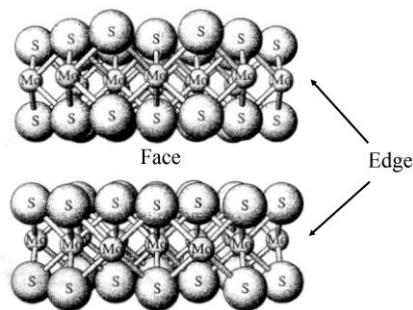
Fig. 13. Crystalline structure of molybdenite
(hydrophobic faces and hydrophilic edges)

Conclusions

The goal of this work was to determine the factors that contribute to the molybdenum and copper recovery in the rougher flotation circuit at the Sarcheshmeh Copper plant. The factors investigated include the morphology and how this manifests itself in the flotation feed, the size by size recovery and liberation characteristics. The size by size recovery and liberation analysis of both molybdenite and copper sulphide minerals has been implemented to examine the processing characteristics of the molybdenum relative to copper.

The size by size recovery of both metals showed that the flotation recovery reduced for the ultrafine and coarse fractions. On the other hand, the highest recovery occurred for the intermediate sizes from 27 μm to 55 μm. The molybdenum recovery in the fine and ultrafine and coarse fractions drops off to a greater extent than the copper.

The variations in the overall recovery of copper and molybdenum is driven to a larger extent by coarse particle recovery than fines with molybdenum being influenced more than copper. The liberation degree results showed that the recovery of copper sulphides is more dependent on the liberation state of valuable minerals while some other factor plays a significant role for molybdenite. Overall, further work is required to determine if mineralogical characteristics have different behaviours in the grinding and flotation circuits.

Acknowledgments

References

AMETOV I., GRANO S.R., ZANIN M., GREDELJ S., MAGNUSON R., BOLLES T., TRIFFETT B., 2008, *Copper and Molybdenite Recovery in Plant and Batch Laboratory Cells in Porphyry Copper Rougher Flotation*, Proceedings of XXIV International Mineral Processing Congress, Beijing, China 24–28 September 2008, Volume 1, 1129–1137.

ARBITER N., FUJII Y., HANSEN B., RAJA A., 1975, *Surface Properties of Hydrophobic Solids*, AICHE Symp. Ser. 71, 176–182.

ATA S., JAMESON, G. J., 2013, *Recovery of Coarse Pparticles in the Froth Phase – A Case Study*, Minerals Engineering 45, 121–127.

BULATOVIC S.M., 1992, *Evaluation of Different Amines in Flotation of Nickel Ores*, Report of Investigation, LR029.

CHANDER S., FUERSTENAU D.W., 1972, *On the Natural Flotation of Molybdenite,* Trans. Amer. Inst. Min. Metall. Engrs. 252, 62–69.

CHANDER S., FUERSTENAU D.W., 1974, *The Effect of Potassium Diethyldithiophoshate on the Interfacial Properties of Molybdenite*, Trans. Inst. Min. Met. 83, 180–185.

CUTHBERTSON R.E., 1961, *New Facets in Flotation at Climax*. Colo., Sch. Mines Q. 56, 199–214.

HERNLUND R.W., 1961, *Extraction of Molybdenite From Copper Flotation Products*, Colo. Sch. Mines Q. 56(3), 179–196.

KELEBEK S., 1988, *Critical Surface Tension of Wetting and of Flotation of Molybdenite and Sulphur*, J. Colloid Interface Sci. 124, 504–514.

LIU, G.Y., ZHONG, H., XIA, L.Y., WANG, S., XU, Z.H., 2011, *Improving Copper Flotation Recovery From a Refractory Copper Porphyry Ore by Using Ethoxycarbonyl Thiourea as a Collector*, Miner. Eng. 24, 817–824.

NAKHAEI F., IRANNAJAD M., 2013, *Comparison Between Neural Networks and Multiple Regression Methods in Metallurgical Performance Modeling of Flotation Column*, Physicochem.Probl. Miner. Process. 49(1), 255–266.

NAKHAEI F., IRANNAJAD M., 2013, *Prediction of On-Line Froth Depth Measurement Errors in Industrial Flotation Columns: A Promising Tool for Automatic Control*, Physicochem. Probl. Miner. Process. 49(2), 757–768.

ORWE D., GRANO S.R., LAUDER D.W., 1998, *Increasing Fine Copper Recovery at the Ok Tedi Concentrator,* Papua New Guinea. Miner. Eng. 11, 171–187.

PODOBNIK D.M., SHIRLEY J.F., 1982, *Molybdenite Recovery at Cuajone*, Min. Eng. 1473–1477.

RAGHAVAN S., HSU L.L., 1984, *Factors Affecting the Flotation Recovery of Molybdenite From Porphyry Copper Ores*, Inter. J. Min. Proc. 12, 145–162.

SRDJAN M.B., 2007, *Handbook of Flotation Reagents Chemistry, Theory and Practice: Flotation of Sulfide Ores*, Publisher: Elsevier Science & Technology Books.

SUTULOV, A., 1971, *Recovery of Molybdenum and Rhenium from Porphyry Copper Ores*, University of Concepcion, Chile.

TRAHAR W.J., 1981, *A Rational Interpretation of the Role of Particle Size in Flotation*, Int. J. Min. Proc. 8, 289–327.

TRIFFETT B., BRADSHAW D., 2008, *The Role of Morphology and Host Rock Lithology on the flotation behaviour of molybdenite at Kennecott Utah Copper*, AusIMM Publication Series, 9th International Congress for Applied Mineralogy, ICAM 2008 – Proceedings, 465–473.

WIE J.M., FUERSTENAU D.W., 1974, *The Effect of Dextrin on Surface Properties and the Flotation of Molybdenite*, Int. J. Miner. Process. 1, 17–32.

ZANIN M., AMETOV I., GRANO S., ZHOU L., SKINNER W., 2009, *A Study of Mechanisms Affecting Molybdenite Recovery in a Bulk Copper/Molybdenum Flotation Circuit*, Int. J. Miner. Process. 93, 256–266.

EFFECT OF OXIDATION ROASTING ON ILMENITE FLOTATION

Akbar MEHDILO, Mehdi IRANNAJAD, Bahram REZAI

Department of Mining and Metallurgical Eng., Amirkabir University of Technology, Tehran, Iran.
iranajad@aut.ac.ir

Abstract: In this study, the oxidation roasting was used to modify the ilmenite chemistry to improve the collector adsorption and ilmenite flotation behavior. The results indicated that the increase of the roasting temperature up to 600 ºC increased the ilmenite flotation recovery. The maximum collector adsorption density occurred on ilmenite roasted at 600 °C which resulted in the increase of ilmenite flotation recovery from 73.5% to 91% at pH 6.3. This improvement was attributed to a greater conversion of Fe^{2+} to Fe^{3+} ions and significant decrease in the zeta potential of ilmenite. At the roasting temperatures of 750 °C and 950 °C, ilmenite was converted to rutile and some trivalent iron containing phases such as hematite and pseudobrookite. Under these conditions, the collector adsorption and hence ilmenite flotation improved, however the flotation recovery decreased after the roasting at 950 °C.

Introduction

With the consumption of rutile resources, ilmenite plays an increasingly important role in the titanium industry (Zhong and Cui 1987). Ilmenite as a titanate of ferrous iron mineral ($Fe^{2+}Ti^{4+}O_3$) is one of the major TiO_2 containing minerals from which titanium dioxide and titanium metal is produced (Song and Tsai 1989). Ilmenite structure is somewhat similar to that of hematite but with some distortion in the oxygen layers. Along the direction of the triad axis, pairs of Ti^{4+} ions alternate with pairs of Fe^{2+} ions; thus each cation layer is a mixture of Fe^{2+} and Ti^{4+} as shown in Fig. 1 (Zhong and Cui 1987; Deer et al. 1991; Fan et al. 2009).

The conventional methods used in the processing of ilmenite ores are gravity separation, high-intensity magnetic separation (HIMS), electrostatic separation or a combination of them. In some ores, ilmenite is freely disseminated in the gangue, and is not effectively separated from the associated gangue minerals using these separation methods. Froth flotation as a physico-chemical separation process is an effective tool

for separating fine disseminated particles (Song and Tsai 1989; Fan et al. 2009; Pownceby et al. 2008; Fan and Rowson 2000a; Fan and Rowson 2000b). However, ilmenite displays poor flotation under conventional flotation conditions in comparison with other oxide minerals such as magnetite and rutile. The poor flotation of ilmenite requires a large dosage of flotation reagents to promote ilmenite surface hydrophobicity and attachment to air bubbles. Even a large dosage of collectors gave flotation recovery of less than 80% for ilmenite (Zhong and Cui 1987; Pownceby et al. 2008; Fan and Rowson 2000a; Fan and Rowson 2000b).
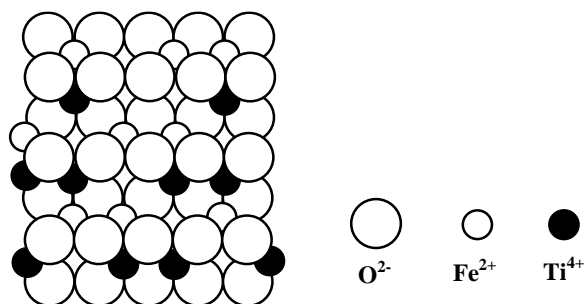
Fig. 1. The arrangement of ions in ilmenite structure on the plane (2110)

Liimatainen and Techn (1977) reported the increase of ilmenite flotation recovery with raising pulp temperatures. Runolinna and Rinne (1960) suggested agglomeration flotation for improvement of fine ilmenite recovery. Gutierrez (1976) offered aeration into ilmenite pulp as an effective method to improve ilmenite flotation recovery. Reverse flotation methods were applied for upgrading of massive ilmenite ore by Behera and Mohanty (1986). Fan and Rowson used the pre-treatment by microwave radiation to modify ilmenite surface properties prior to flotation and to improve ilmenite recovery (Fan et al. 2009, 2000; Fan and Rowson 2000a, 2002). The modification of ilmenite surface properties and improvement of its flotation using lead ions (lead nitrate) were also investigated by Fan and Rowson (2000b). The acid surface dissolution is another method which was used for improvement of ilmenite flotation behavior (Zhu et al. 2011; Bulatovic and Wyslouzil 1999). After the microwave radiation treatment and surface dissolution, Fe^{2+} ions on ilmenite surfaces are converted into Fe^{3+} ions. This conversion reduces the zeta potential of ilmenite and increases the chemical adsorption of oleate ions significantly (in the presence of sodium oleate as collector) (Fan et al. 2009, 2000; Fan and Rowson 2000a, 2002; Liimatainen and Techn 1977; Zhu et al. 2011).

In this paper, the pre-treatment by oxidation roasting was used to modify ilmenite surface properties prior to flotation and to improve ilmenite recovery. For this purpose, the physical and chemical properties of ilmenite surfaces were investigated before and after the roasting at different temperatures.

Materials and methods

Materials

The samples were taken from the Qara-aghaj hard rock deposit located at north-west of Iran. The samples were first crushed and ground under 150 μm, and determined as ilmenite liberation degree. The sample was prepared using sieving and several stages of tabling, and low and high intensity magnetic separation methods. The pure ilmenite sample was washed several times with distilled water, and dried at room temperature. The examination under Scanning Electron Microscopy (SEM) showed ilmenite grains with clean surface and almost free from gangue minerals. The chemical analysis of purified ilmenite is presented in Table 1. The XRD pattern suggests that the purified sample was essentially composed by ilmenite.

Sodium oleate (with 95% purity), and the analytical grade H_2SO_4 (97%) and NaOH (98%) were used as a collector and pH adjustment chemicals, respectively. Additionally, double distilled water was used throughout this study.

Table 1. Chemical composition (wt %) of studied ilmenite samples

composition	TiO_2	Fe_2O_3	MnO	V_2O_5	P_2O_5	CaO	MgO	SiO_2	Al_2O_3	Na_2O	K_2O	L.O.I	Total
(Wt %)	46.2	48.6	1.04	0.29	0.24	0.38	2.53	0.19	0.44	0	0.006	0	99.92

Methods

Materials characterization

The chemical composition of the samples was determined using X-ray fluorescence (XRF, Philips X Unique2). The phase composition was analyzed with XPERT MPD diffractometer employing Cu Ka radiation. The microscopic studies for evaluation of textural and morphological features were performed using Philips XL30 model Scanning Electron Microscopy (SEM). The electron microprobe (EMP) analysis was carried out using Cameca SX 100 equipped with five wavelength dispersive (WD) spectrometers. Accelerating voltage of 15 kV and 100 s counting time were used to perform analysis in 25 μm^2 areas. The SEM images were taken under accelerating voltage of 25 kV.

Roasting

The oxidation roasting was performed in a laboratory muffle furnace at 250, 500, 600, 750, and 950 °C for 45 min. The furnace was heated to a predetermined temperature before the sample was introduced. For each temperature, 30 g of ilmenite sample was placed in a ceramic crucible. The oxidation roasting was conducted in the crucible open to air. At the end of the roasting process, the crucible was removed from the furnace, and cooled slowly in air at room temperature.

Flotation experiments

The flotation tests in this study were carried out in a 300 cm^3 Hallimond tube. A 2 g of material (unroasted or roasted ilmenite) with a size of 45–150 µm was used for each test. The sample was added to double distilled water and conditioned for 5 min. After this period, the collector was added to the suspension, and the pH was adjusted to the desired value, and a second conditioning stage of 8 min was given to the suspension. The prepared pulp was then transferred to the Hallimond tube where flotation was carried out for 4 min. After the flotation tests, the concentrate and tailing were filtered, dried, and weighed.

Zeta potential measurements

The zeta potential of minerals was measured using a Malvern instrument (UK). First, the samples were ground under 15 µm. Then, the suspension was prepared by adding 50 mg of mineral sample to 100 cm^3 of double distilled water containing $2 \cdot 10^{-3}$ M KCl as a supporting electrolyte. In order to determine the zeta potential of the sample after the collector interaction, $3.65 \cdot 10^{-4}$ M sodium oleate was used in the presence of $2 \cdot 10^{-3}$ M KCl as an indifferent electrolyte. The resultant suspension was conditioned for 15 min during pH was measured. The pH was adjusted using either NaOH or H_2SO_4 over the pH range of 2–11. The repeating tests showed that a measurement error was about ±2 mV.

Results and discussion

Results

Flotation experiments

The flotation recovery of untreated ilmenite and roasted ilmenite under different temperatures as a function of pH values is presented in Fig. 2. Two recovery peaks appeared on the flotation recovery curve of untreated ilmenite which is in a good agreement with other results reported in the literature (Fan et al. 2009; Fan and Rowson 2000a). The first peak is located at a pH 6.3 where the flotation recovery is 73.5%. The second peak is at about pH 2.5–3.5, which is similar to the flotation behavior of rutile (Bulatovic and Wyslouzil 1999) and the flotation recovery is 42.5 %. This indicates that the titanium ions are mainly active sites for reaction with sodium oleate collector at this pH rang. When the pH values were over 8 or less than 2.5, the flotation recoveries decreased rapidly. The reason is for that is due to the strong competition between the oleate ions from the collector and OH$^-$ ions present in the pulp on the ilmenite surface in the alkaline aqueous solution. Additionally, most of the active sites on the ilmenite surface should be occupied by OH$^-$ ions with the increase of alkalinity. In strong acidic solution, the metallic ions dissolved from ilmenite surfaces, and there were no active sites in which oleate ions adsorb (Fan et al.

2009; Fan and Rowson 2000a). The optimum pH for the flotation was located between 6 and 7.

The results indicated that after the oxidation roasting up to 600 °C, the flotation behavior of ilmenite was greatly improved across a wide pH range. The maximum increase in ilmenite flotation recovery was about 50% at pH values ranging from 4.0 to 4.5. After the roasting of ilmenite at 600 °C, ilmenite was floated with a recovery of 91% at pH 6.3. The maximum improvement of recovery at this pH was about 17.5%. In alkaline aqueous solutions, ilmenite flotation recovery was improved slightly. The flotation behavior of ilmenite roasted at 750 °C is very similar to that of unroasted ilmenite. After the oxidation roasting at 950 °C, ilmenite floatability was improved slightly at pH values below 5 but it dropped significantly above this pH value.
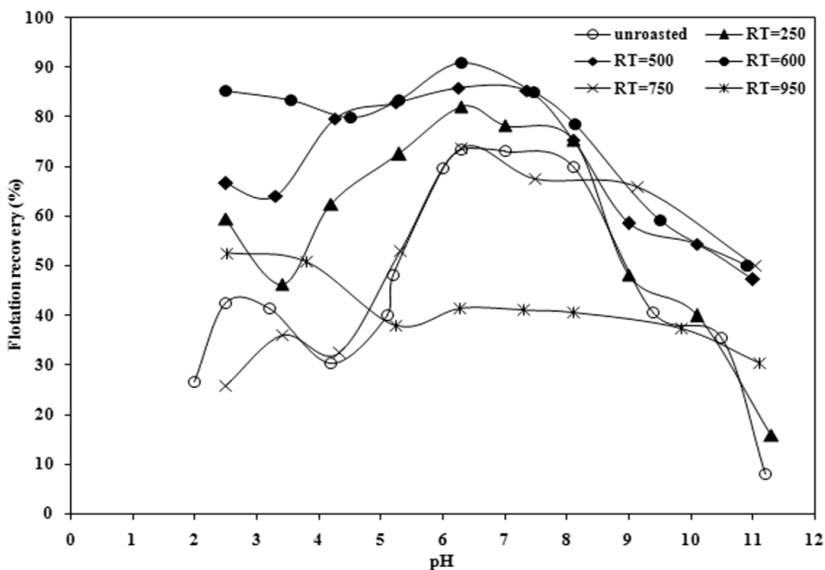
Fig. 2. The flotation behavior of unroasted and roasted ilmenite
as a function of pH (sodium oleate concentration $3.65 \cdot 10^{-4}$ M)

Figure 3 shows the effect of sodium oleate concentration on the flotation of untreated and treated ilmenite at pH 6.3. As seen from Fig. 3, the increase of oleate concentration clearly promotes flotation recoveries. The maximum recovery of untreated ilmenite (73.5%) was obtained at $3.65 \cdot 10^{-4}$ M of sodium oleate. When the collector dosage was $3.65 \cdot 10^{-4}$ M, the maximum flotation recoveries of roasted ilmenite at temperatures 250 °C, 500 °C, and 600 °C reached to 82%, 85.9%, and 91%, respectively. After the heat treatment, the ilmenite flotation recovery increased dramatically with a little increase as a function of the collector concentration. Almost 83.3% and 85% of ilmenite floated in the presence of only $1.83 \cdot 10^{-4}$ M of sodium oleate after the pretreatment at 500 °C and 600 °C, respectively. These recoveries were not achieved for untreated ilmenite even at higher dosages of the collector.
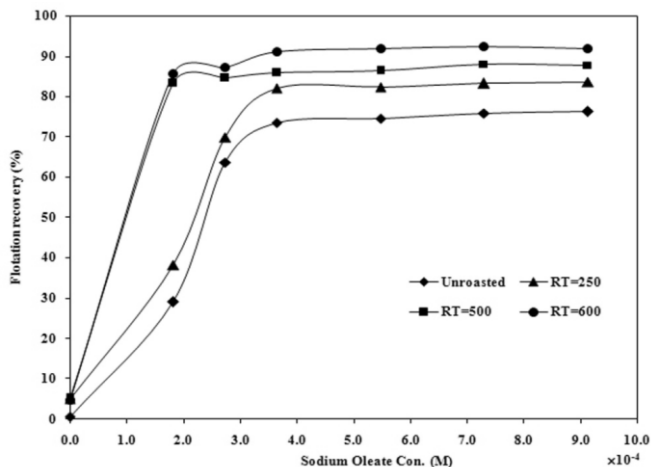
Fig. 3. Effect of sodium oleate concentration on flotation behavior
of unroasted and roasted ilmenite (pH=6.3)

Zeta potential

The zeta potentials of roasted and unroasted ilmenite, measured as a function of pH in the presence of $2 \cdot 10^{-3}$ M KCl as a background solution, are shown in Fig. 4. For the unroasted ilmenite, the point of zero charge (pzc) was found to be pH 5.4. The heat treatment process caused to a decrease of ilmenite zeta potential over pH range from 2.5 to 7.5. The pzc of ilmenite shifted to about pH 4.6, 3.9, 2.9, and 3 for treated ilmenite at temperatures 500 °C, 600 °C, 750 °C, and 950 °C, respectively.

Figure 5a shows the zeta potential of different ilmenites in the presence of sodium oleate solution. Using sodium oleate of $3.65 \cdot 10^{-4}$ M, the zeta potential of ilmenite displayed a negative value over a wide pH range from 3 to 11. The pzc of ilmenite shifted to between 2.6 to 3.2. The zeta potential values for raw ilmenite, roasted ilmenite at 600 °C, and roasted ilmenite at 950 °C at pH 6.3 were measured as −66.3 mV, −73.1 mV and −55.9 mV, respectively.

The zeta potential-pH profile of raw ilmenite and ilmenite roasted at 600 °C and 950 °C in the absence and presence of sodium oleate is shown in Figs 5b-d. In all experiments, in order to maintain the ionic strength, hence the double layer thickness at constant level, the concentration of KCl was fixed at $2 \cdot 10^{-3}$ M. The zeta potential measurements in the presence and absence of the collector showed that the collector adsorption resulted in a significant change in the zeta potential. When the oleate was present between about pH 3 and pH 11, the zeta potential of raw ilmenite and roasted ilmenite at 600 °C was considerably more negative than when KCl was present only. This phenomenon took place for ilmenite roasted at 950 °C at above pH 3.2. More negative surface zeta potential is a clear indication of strong adsorption of oleate ions derived from sodium oleate as an anionic collector. The adsorption of the collector in Stern plane causes the pzc (point of zero charge) of ilmenites to shift to pzr (point of zeta potential reversal) at pH 2.5–3.5.
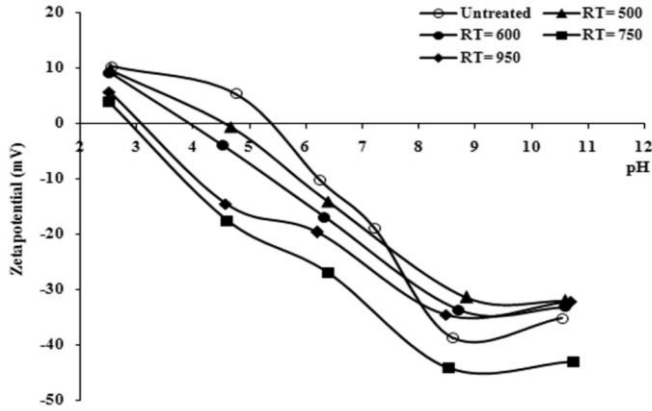
Fig. 4. Zeta potential of unroasted and roasted ilmenite as a function of pH
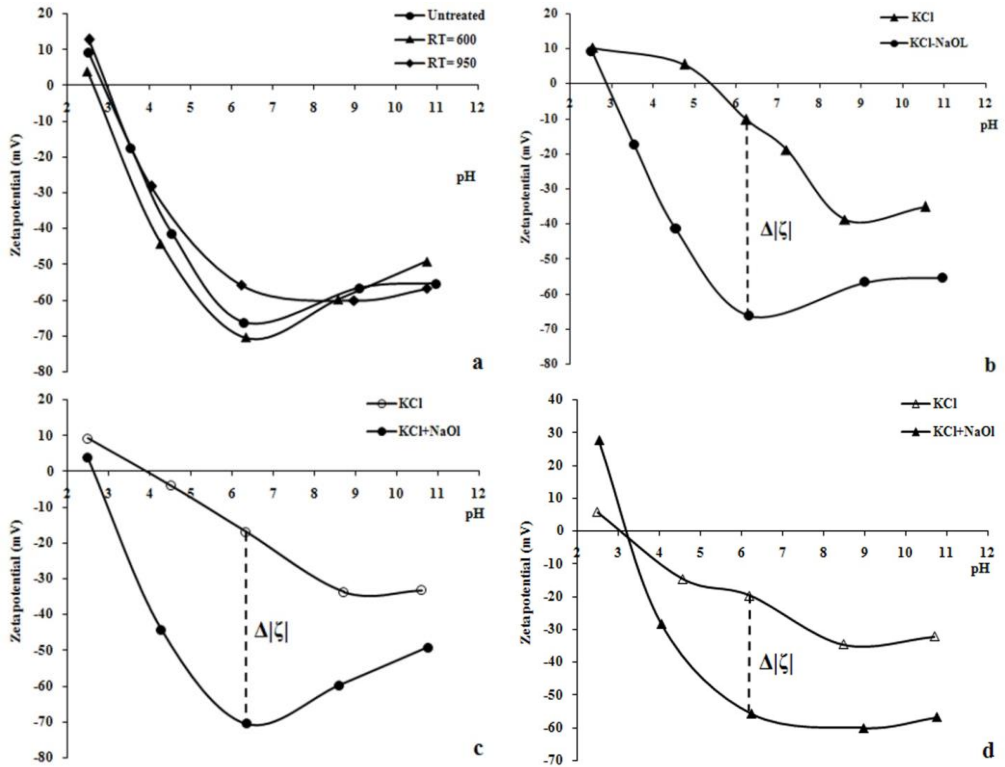
Fig. 5 Zeta potential of different ilmenites as a function of pH in the presence of KCl (2×10^{-3} M) and KCl + NaOl (3.65×10^{-4} M sodium oleate and 2×10^{-3} M KCl). (a) Different ilmenites in the presence of KCl + NaOl. (b) Unroasted ilmenite. (c) Roasted ilmenite at 600 °C. (d) Roasted ilmenite at 950 °C

X-Ray diffraction

The XRD patterns of ilmenite before and after the roasting at different temperatures are shown in Fig. 6. The main phase present in the sample heated up to 600 °C was ilmenite and hematite formation was not observed. It was found that some of ilmenite phase began to change into hematite and rutile via the oxidation roasting process above 600 °C. When the temperature increased the formation of hematite and rutile became more obvious. After the roasting at 750 °C, the ilmenite phase was almost completely converted into hematite and rutile. This means that the main reactions were the oxidation of ilmenite to the intermediate phase Fe_2O_3–$2TiO_2$ and decomposition to hematite and rutile at temperatures up to 750 °C. With the increasing of the temperature up to 950 °C, the most dominant phase was ferric pseudobrookite (Fe_2TiO_5) which was formed by combining of hematite and rutile. As seen from Fig. 5, most of the hematite and rutile peaks disappeared. The other weak peaks observed at this temperature are attributed to the negligible amount of metallic iron which is probably due to the local melting phenomena in the ilmenite surface.
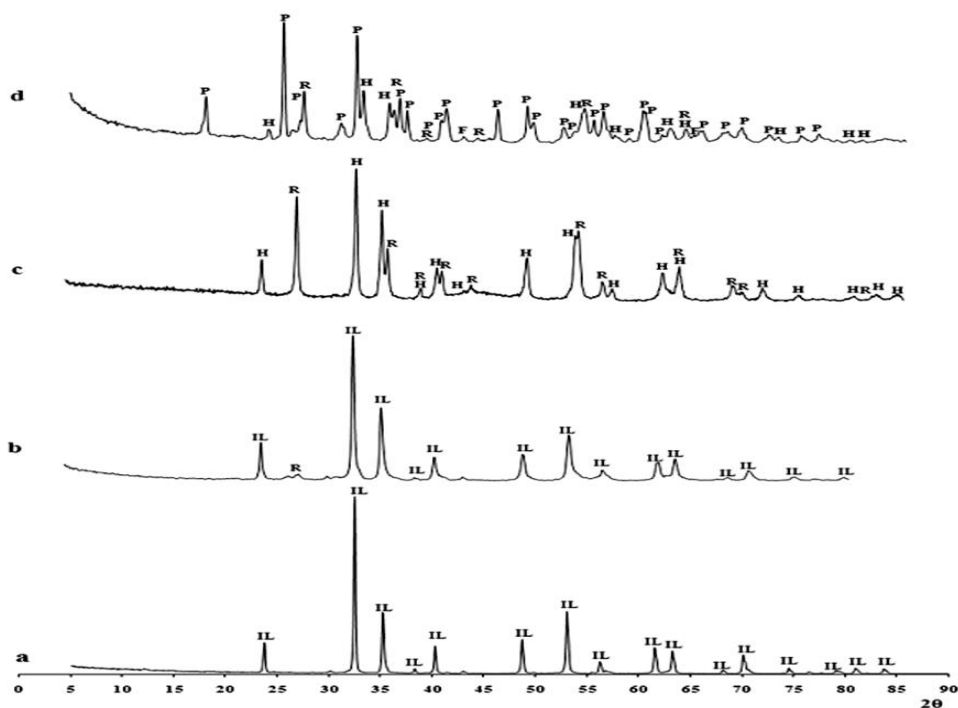
Fig. 6. XRD patterns of unroasted ilmenite and roasted ilmenite at different temperatures (a) Unroasted ilmenite (b) roasted ilmenite at 600 °C (c) roasted ilmenite at 750 °C and (d) roasted ilmenite at 950 °C. (IL: ilmenite, H: hematite, R: rutile, P: pseudobrookite, F: Fe (metallic iron))

Reactions during the oxidation of ilmenite

Oxidation of iron(III) into iron(II) occurs mainly in the surface of ilmenite. Formation of an intermediate $Fe_2O_3 \cdot 2TiO_2$ phase and its decomposition with the formation of hematite and rutile at 600–750 °C is given by:

$$2FeTiO_3 + 1/2O_2 \rightarrow Fe_2O_3\text{-}2TiO_2 \tag{1}$$

$$Fe_2O_3 \cdot 2TiO_2 \rightarrow Fe_2O_3 + 2TiO_2 \tag{2}$$
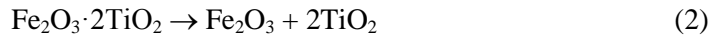
while formation of ferric pseudobrookite (Fe_2TiO_5) from the combination of hematite with rutile at 750–950 °C by:

$$Fe_2O_3 + TiO_2 \rightarrow Fe_2TiO_5. \tag{3}$$

Scanning Electron Microscopy (SEM)

The morphology of ilmenite before and after the roasting at different temperatures studied by SEM is shown in Fig. 7. The particles of raw ilmenite are composed of clusters of fine grains which accounts for the high porosity of ilmenite. When the roasting temperature was increased, the conversion of Fe^{2+} ions to Fe^{3+} ones in the ilmenite surface increased. This conversion leads to non-uniformity in the composition and different surface appearance across the ilmenite particles. The oxidation of Fe^{2+} ions to Fe^{3+} appeared as a formation of light particles in the surface. The chemical composition of these particles analyzed by microprobe is presented in Table 2. These results indicated that these particles are mainly composed of Fe^{3+} as active sites in flotation, and the formation of these particles increased with the increasing of the temperature. At the roasting temperature of 600 °C, these particles covered almost the all surface of the grains. At temperatures of 750 °C and 950 °C where ilmenite was decomposed to hematite, rutile and pseudobrookite, the iron content decreased in the surface.

Discussion

The ilmenite surface chemistry is strongly dependent on the solution pH. At pH values less than 3 which most of Fe(II) ions are dissolved from ilmenite surface, titanium ions are the most dominant cations appearing as $Ti(OH)^{3+}$ and $Ti(OH)^{2+}$ species (Fan et al. 2009; Fan and Rowson 2000a). The recovery peak at about pH 2.5 in Fig. 2 is attributed to these titanium hydroxyl complexes as active sites on which oleate ions are adsorbed. In weakly acidic or weakly alkaline solutions titanium ions mainly existed in the more stable form ($Ti(OH)_4$) while ferrous ions existed in the forms of Fe^{2+} and $FeOH^+$ are active sites for adsorption of oleate ions (Fan et al. 2009). Because of the solubility product of iron(II) oleate $K_{spFeOl_2} = 10^{-15.5}$ and that of iron(II) oleate $K_{spFeOl_3} = 10^{-29.7}$, $FeOl_3$ is much more difficult to dissolve than $FeOl_2$. The

oxidation of Fe^{2+} ions on the surface of ilmenite into Fe^{3+} ions facilitates the action on oleate and consequently the increase of its floatability (Zhong and Cui 1987).
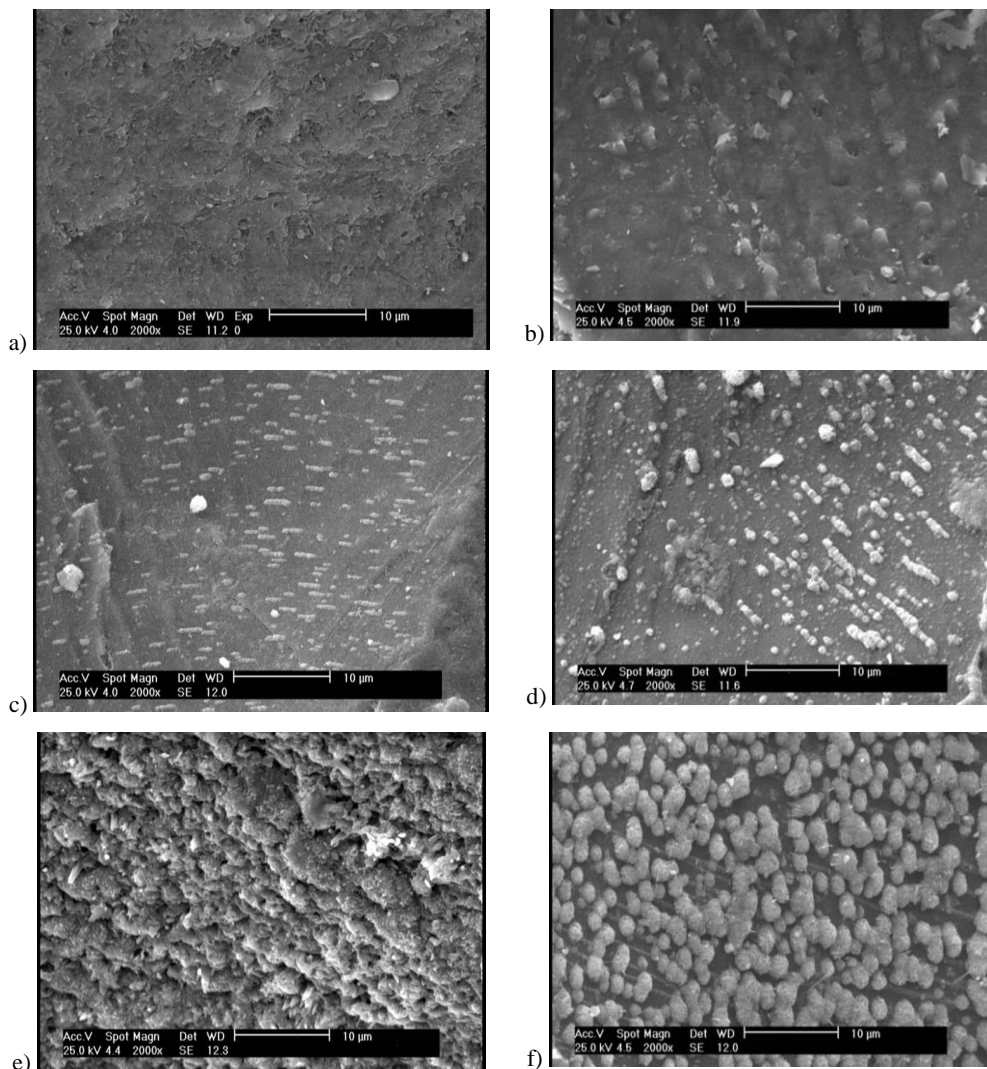
Fig. 7. SEM images of unroasted and oxidation roasted ilmenite. (a) Unroasted ilmenite
(b) roasted ilmenite at 250 °C (c) roasted ilmenite at 500 °C (d) roasted ilmenite at 600 °C
(e) roasted ilmenite at 750 °C and (f) roasted ilmenite at 950 °C

Table 2. Microprobe analysis of light particles appeared in the surface of ilmenite

Composition (%)	Fe_2O_3	TiO_2	MnO	V_2O_5	P_2O_5	CaO	MgO	SiO_2	Al_2O_3	Cr_2O_3	SO_2	Total
$T = 250$ °C	49.34	44.79	1.59	0.19	0.1	0.21	1.51	0.25	0.78	0.29	0.89	99.94
$T = 500$ °C	87.13	6.45	1.75	0.58	0.08	0.23	1.42	0.25	0.64	0.36	0.96	99.85
$T = 600$ °C	89.09	4.28	1.37	0.23	0.11	0.2	1.62	0.26	1.1	0.11	1.44	99.81

With the increasing conversion of Fe^{2+} into Fe^{3+} ions due to the raising roasting temperature, pzc of ilmenite decreased and consequently its floatability improved significantly. These changes in ilmenite surface properties are in a good agreement with literature (Zhong and Cui 1987; Fan et al. 2009; Fan and Rowson 2000a; Mehdilo et al. 2013). At the roasting temperature of 600 °C, where it has not been taken place any significant phase decomposition in ilmenite structure (Fig. 6b); iron(III) oxide fine particles cover almost all surface of ilmenite and the capability to chemically bind with oleate ions is significantly increased. This is clearly seen from Fig. 5c, in which the zeta potential of ilmenite after the oleate ions adsorption reaches to its highest negative value. At temperatures higher than 600 °C, despite the formation of different phases containing trivalent iron and reduction of zeta potential, the collector adsorption and flotation recovery considerably decreased. This can be due to the changes in ilmenite structure and disruption of cations arrangement on the surface of particles. The decrease of flotation recovery after the roasting at 950 °C in comparing with that roasted at 750 °C can be related to increase of zeta potential (Fig. 4).

The relative adsorption densities of collector in Stern plane can be estimated with the Stern–Grahame equation (Fuerstenau and Shibata 1999). This simplified equation (5) for the case when the collector concentration is constant and the pH or zeta potential is variable (the zeta potential is varied by pH variation, Fig. 5b, c and d) is

$$\Gamma_s = (\text{Constant})C \exp\left(-\frac{zF\Delta|\zeta|}{RT}\right) \tag{4}$$

$$\Gamma_s = (\text{Constant})C' \exp(\Delta|\zeta|) \tag{5}$$

where C is the bulk concentration, R the gas constant, T the absolute temperature, z is the valence of the adsorbing ion, F is the Faraday constant, C' is constant and $\Delta|\zeta| = \zeta_2 - \zeta_1$; ζ_1 and ζ_2 are the measured zeta potential before and after anionic collector adsorption, respectively. The difference in the two values of the zeta potential ($\Delta|\zeta|$) results from the strong adsorption of the collector in Stern plane is a necessary condition for good flotation.

Using Eq. 5 and the results presented in Fig. 5, the relative adsorption densities of oleate (Γ_s) are estimated for unroasted ilmenite and roasted ilmenite at 600 °C and 950 °C at pH 6.3 according Table 3. As seen from Fig. 5 and Table 3 that the relative adsorption densities of oleate at a wide pH range are in good agreement with flotation recoveries shown in Fig. 2.

Table 3. Zeta potential, adsorption densities of oleate and the standard free energy of adsorption at pH 6.3 for unroasted and roasted ilmenite samples

Sample	PZC	PZR	ζ_2	ζ_1	$\Delta|\zeta|$	Γ_s
Unroasted ilmenite	5.4	2.83	−66.3	−10.3	56.0	C′×exp (56.0)
roasted ilmenite at 600°C	3.85	2.6	−73.1	−16.9	57.2	C′×exp (57.2)
roasted ilmenite at 950°C	3.05	3.2	−55.9	−19.7	36.2	C′×exp (36.2)

Conclusions

The oxidation roasting converts the Fe^{2+} to Fe^{3+} ions on ilmenite surfaces, and enhances the adsorption of oleate, and consequently improving flotation. This conversion also reduced the collector dosage. The maximum collector adsorption density and flotation recovery were achieved after the roasting of ilmenite at 600 °C where the highest conversion of Fe^{2+} to Fe^{3+} ions took place. There was no improvement in the ilmenite flotation at the roasting temperatures above 600 °C. This is probably due to the occurrence of phase decomposition and disruption of the arrangement of metallic cations in the particle surface.

References

BEHERA R.C., MOHANTY A.K., 1986, *Beneficiation of massive ilmenite by froth flotation*, International Journal of Mineral Processing, 17, 131–142.

BULATOVIC S., WYSLOUZIL D.M., 1999, *Process development for treatment of complex perovskite, ilmenite and rutile ores*, Minerals Engineering, 12, 1407–1417.

DEER W.A., HOWIE R.A., ZUSSMAN J., 1991, *An Introduction to the Rock-Forming Minerals*, Longman Scientific & Technical, 412–414.

FAN X., ROWSON N.A., 2000a, *Fundamental investigation of microwave pretreatment on the flotation of massive ilmenite ores*, Developments in Chemical Engineering and Mineral Processing, 8, 167–182.

FAN X., ROWSON N.A., 2000b, *The effect of Pb(NO₃)₂ on ilmenite flotation*, Minerals Engineering, 13, 205–215.

FAN X., KELLY R.M., ROWSON N.A., 2000, *Effect of microwave radiation on ilmenite flotation*, Canadian Metallurgical Quarterly, 39, 247–254.

FAN X., ROWSON N.A., 2002, *Surface modification and column flotation of a massive Ilmenite ore*, Canadian Metallurgical Quarterly, 41, 133-142.

FAN X., WATERS K.E., ROWSON N.A., PARKER D.J., 2009, *Modification of ilmenite surface chemistry for enhancing surfactants adsorption and bubble attachment*, Journal of Colloid Interface Science, 329, 167–172.

FUERSTENAU D.W., SHIBATA J., 1999, *On using electrokinetics to interpret the flotation and interfacial behavior of manganese dioxide*, International Journal of Mineral Processing, 57, 205–217.

GUTIERREZ C., 1976, *Influence of previous aeration in water or heating in air of ilmenite on its flotation with oleic acid*, International Journal of Mineral Processing, 3, 247–256.

LIIMATAINEN V., TECHN L., 1977, *Conditioning and flotation of ilmenite at various pulp temperatures*, Trans. Znst. Min. Metall. (Sect. C. Mineral Process.), 4, 160–161.

MEHDILO A., IRANNAJAD M., REZAI B., 2013, *Effect of chemical composition and crystal chemistry on the zeta potential of ilmenite*, Colloids and Surfaces A: Physicochemical and Engineering Aspects, 428, 111–119.

POWNCEBY M.I., SPARROW G. J., FISHER-WHITE M.J., 2008, *Mineralogical characterization of Eucla Basin ilmenite concentrates–First results from a new global resource*, Minerals Engineering, 21, 587–597.

RUNOLINNA U., RINNE R., 1960, *Agglomeration flotation of ilmenite ore at Otanmaki*, Int. Miner. Process. Cong., 447–475.

SONG Q., TSAI S.C.,1989, *Flotation of ilmenite using benzyl arsonic acid and acidified sodium silicate*, International Journal of Mineral Processing, 26, 111–121.

ZHONG Kang-nian, CUI Lin, 1987, *Influence of Fe^{2+} ions of ilmenite on its flotability*, International Journal of Mineral Processing, 20, 253–265.

ZHU Yang-ge, ZHANG Guo-fan, FENG Qi-ming, YAN Dai-cui, WANG Wei-qing, 2011, *Effect of surface dissolution on flotation separation of fine ilmenite from titanaugite*, Trans. Nonferrous Met. Soc. China, 21, 1149–1154.

INFLUENCE OF LEAD NITRATE ON CYANIDE LEACHING OF GOLD AND SILVER FROM TURKISH GOLD ORES

Baris SAYINER

Kozagold Corp. Kaymaz Gold Mine, P.O. Box 26640, Eskisehir, Turkey, baris.sayiner@gmail.com

Abstract: Effect of lead nitrate addition on cyanidation of Havran, Ovacik, Mastra LCu (low copper) and Mastra HCu (high copper) gold ores was investigated by laboratory tests at the Ovacik Gold Mine Metallurgy Laboratory. Leach tests were performed at optimum NaCN additions and pH values while different lead nitrate additions were applied. Ovacik cyanidation plant leaching time, 24 hours for the constant 100 Mg/h ore feed rate was applied as optimal for all lead nitrate tests. Results showed the increase in gold and silver recoveries between 0.4-1.2% for gold and 3.9-11.6% for silver at the end of 24 hours leaching by the addition of lead nitrate as 0.1-0.5 kg/Mg. NaCN consumption decreased or did not change except for the Ovacik ore. In the case of the Ovacik ore it slightly increased.

Keywords: lead nitrate, gold, silver, cyanide leaching

Introduction

Extraction of gold from its ores by cyanide leaching has been the preferred method for more than a century because of its simplicity, cost efficiency and high stability of cyanide. Dissolution of gold and silver in alkaline cyanide solutions can be represented by the half-cell oxidation reactions (Cerovic et al., 2005):

$$Au + 2CN^- \rightarrow Au(CN)^-_2 + e^- \tag{1}$$

$$Ag + 2CN^- \rightarrow Ag(CN)^-_2 + e^- \tag{2}$$
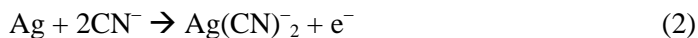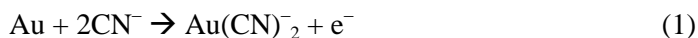
The cathode reaction of dissolved oxygen may be shown as a four-electron transfer reaction (Cerovic et al., 2005):

$$O_2 + 2H_2O + 4e^- \rightarrow 4OH^-. \tag{3}$$

The anodic dissolution of gold in the aqueous cyanide solution is a complicated process and can be retarded by the formation of intermediate species such as insoluble polymeric Au(CN) film, Au(OH)(CN) and AuS_x on the surface of gold. These species form a passivation layer and may inhibit diffusion of oxygen and cyanide to the gold surface, causing inhibition of gold dissolution. The polymerization of the $AuCN_{ads}$ to form …-Au-CN-Au-CN-…. chain may be the self-poisoning reaction, which blocks the gold surface preventing its dissolution (Cerovic et al., 2005; Sandenbergh and Miller, 2001).

It is well known that the presence of heavy metal ions such as lead, bismuth, thallium and mercury exerts the catalytic effect both on gold cyanidation as well as oxygen reduction (Cerovic et al., 2005; Dai and Breuer, 2013; Dai and Jeffrey, 2006; Deschenes et al., 2009; Senanayake, 2008)

The catalytic activity of lead on anodic dissolution of gold consists of the formation of gold-lead alloys such as $AuPb_2$, $AuPb_3$ and metallic lead on the surface of gold. These alloys occupy some of the surface sites on gold and prevents the formation of polymerized Au(CN) film and some other passivation species. However, excessive lead retards the anodic dissolution of gold by formation of $Pb(OH)_2$ passive layer on the gold surface (Deschenes et al., 2000; Sandenbergh and Miller, 2001; Tan et al., 2005).

According to Sandenbergh and Miller (2001) and Cerovic et al. (2005) small amounts of lead nitrate supplying lead up to 2 mg/dm^3 increase the anodic dissolution rates of both gold and gold-10% silver alloy. However, dissolution rate started to decrease at lead concentrations above 2 mg/dm^3. Besides, it is shown that oxygen reduction rate on the surface of gold increased and was continuing to increase even above 2 mg/dm^3 of lead, up to at least 10 mg/ dm^3 lead concentration. Thus, it is stated that maximum dissolution rate is not determined by anodic dissolution reaction, but by the rate of oxygen mass transfer to the metal surface and the catalytic activity of lead in the oxygen reduction reaction. In other words, the dissolution rate of gold was controlled by the mass transfer of oxygen to the gold surface.

A study by Arslan et al. (2003) on a gold-silver ore resulted in Ag recovery increase from 45.0% to 48.9% as well as Au recovery increase, after 24 hours of cyanide leaching, by addition of 300 g/Mg lead nitrate to the leach slurry.

Furthermore, numerous studies have shown that lead nitrate addition reduces the detrimental effect of metallic sulfides, increases gold leaching recovery and/or inhibits the dissolution of metallic sulfides, thus reduces cyanide consumption (Deschenes et al., 2003).

Metallic sulfides such as pyrite, chalcopyrite and pyrrhotite show different reaction mechanisms with lead nitrate. Lead nitrate passivizes pyrite by forming a hydroxide ($Pb(OH)_2$) layer on pyrite surface reducing the dissolution of pyrite. Dissolution of pyrite forms a sulfur layer on gold causing inhibition of gold dissolution. Thus, in presence of lead this layer is less important. Pyrrhotite shows a similar effect

inhibiting partially the formation of sulfur layer. However, in the case of chalcopyrite this mechanism is not observed (Deschenes et al., 2000).

On the other hand, in the presence of pyrite and pyrrhotite, formation of lead or lead alloys is not observed on the gold surface, but very thin layer forms in the presence of chalcopyrite. Thus, it is proposed that lead does not deposit on gold because of its high affinity to sulfide minerals. It means that lead nitrate addition should be a function of mineralogical composition of the ore (Deschenes et al., 2000; Deschenes and Prud'homme, 1997).

In this paper, the effect of lead nitrate addition to the cyanidation of the Ovacik, Havran, Mastra Low Copper and Mastra High Copper gold ores was investigated and discussed. The Ovacik and Havran ores are processed in the Ovacik Gold CIP Plant in Izmir in Turkey, while Mastra is planned to be processed at a CIP plant which will be built in Gumushane in Turkey. The ores are owned by Kozagold Corporation.

Materials and methods

Mineralogy and metal contents

The Ovacik gold ore consists mainly of quartz (about 90%) with small amount of pyrite and arsenopyrite, which are partially oxidized to limonite and to other iron oxides. It is indicated that most of the gold would be free-milling. The small amount contained within pyrite could probably also be liberated fairly readily.

The Havran gold ore consists mainly of silicified and carbonate minerals with free gold, pyrite, hematite, magnetite, quartz and calcite. Pyrite is mostly converted to hematite (Guney and Gurkan, 2008).

In the Mastra low copper ore the major component is disseminated pyrite while gangue is mainly quartz and fine muscovite while coarse pyrite is present in small quantities veined by galena or rimmed by chalcopyrite. The main gold occurrences were associated with pyrite, chalcopyrite, silica and gold telluride. The gold occurred within the silica and around the sulfide and telluride grains, with grain sizes varying between 1and 40 micrometers (Lycopodium, 1996).

The Mastra high copper ore contains mainly pyrite, chalcopyrite, sphalerite and galena. Gangue is mainly quartz and fine muscovite. Three occurrences of gold were detected optically, which is associated with fine and coarse sulfide mineralization and within gangue minerals (Lycopodium, 1996).

Table 1. Chemical analysis of the ores

Ore	Au, ppm	Ag, ppm	Cu, ppm	Zn, ppm	Pb, ppm	Fe, %	S, %
Ovacik	9.17	15.06	38	42	34	1.69	0.07
Havran	5.19	17.31	65	405	282	0.71	0.02
HCu	14.8	11.56	3192	585	963	1.70	3.15
LCu	17.8	3.11	1686	774	1988	1.55	3.00

Table 1 shows the metal content of the the Ovacik, Havran, Mastra High Copper (HCu) and Mastra Low Copper (LCu) ores.

Equipment and experimental procedure

All experimental works were conducted at the Metallurgy Laboratory of Ovacik Gold Mine. The Havran and Ovacik ore samples were taken from the Fine Ore Bin of the Ovacik cyanide leaching plant, while the Mastra ore was supplied from Gumushane region of Turkey. All samples were dried, crushed by a lab type jaw crusher and divided to about 1 kg samples. The samples were then dry ground to p80: – 59 μm for Ovacik, – 52 μm for Havran, –73 μm for Mastra High Copper (HCu) and –63 μm for Mastra Low Copper (LCu) by lab type disc mill.

Leaching tests were conducted in two-liter glass beakers and mechanical agitators by sparkling oxygen through the pulp to maintain the 40 ppm dissolved oxygen level which is controlled by dissolved oxygen meter. pH of the slurry was adjusted by lime to be between 10.5 and 11. Solid/pulp ratio was 43%. Leaching time was 24 hours as at the Ovacik CIP plant while pulp temperature was maintained at 20 ^{0}C by air conditioning the lab area. NaCN and $Pb(NO_3)_2$ were added to the pulp as solids at the beginning of the leaching.

After leaching, the final pulp was filtered by pressure filter separating the residual solid and the solution. All samples were analyzed for Au and Ag to determine the metal extraction recovery. Solutions were also analyzed for final NaCN concentrations by silver nitrate titration with rhodamine indicator.

Results and discussion

The cyanide leach tests were applied to the Ovacık, Havran, Mastra Low Copper (LCu) and Mastra High Copper (HCu) ores with different concentrations of lead nitrate additions.

Ovacik ore test results

Three 24 h leaching tests were conducted with 0.4 kg/Mg initial NaCN addition as in the Ovacik plant. The first leaching test was performed without $Pb(NO_3)_2$, second with 100 g/Mg and third with 300 g/Mg lead nitrate addition. After head and residual solid-solution analysis it is indicated that the Ovacik ore showed an increase from 96.72% to 97.35% gold and 73.70% to 77.59% silver leaching efficiency with 0.4 kg/Mg NaCN and 0.1 kg/Mg of lead nitrate. A further increase of lead nitrate to 0.3 kg/Mg resulted in the decrease of Au and Ag leach recovery by comparing with the test of 0.2 kg/Mg lead nitrate, indicating the formation of $Pb(OH)_2$ passive layer on gold. Besides, NaCN consumption increased from 0.24 kg/Mg without lead nitrate to 0.27 kg/Mg with 0.1 kg/Mg lead nitrate addition. This indicates the precipitation of insoluble lead cyanide. Results are shown in Table 2.

Table 2. Ovacik ore leach results

Initial NaCN addition, kg/Mg ore	Lead Nitrate addition, kg/Mg ore	Au Leach Recovery %	Ag Leach Recovery %	NaCN consumption kg/Mg ore	Initial NaCN in solution, ppm	Final NaCN in solution, ppm
0.4	0.0	96.72	73.70	0.24	302	120
0.4	0.1	97.35	77.59	0.27	302	100
0.4	0.3	97.05	76.11	0.28	302	90

Havran ore test results

Havran ore was investigated in four 24 h leach tests, first without lead nitrate and the others with 0.1, 0.2 and 0.3 kg/Mg lead nitrate. All of the tests were conducted with initial 0.5 kg/Mg NaCN addition corresponding to the plant NaCN consumption for this ore. According to the leach results Au recovery increased from 94.32% to 95.41% with 0.3 kg/Mg lead nitrate while Ag recovery increased from 69.14 % to 74.28%. NaCN consumption decreased up to 0.2 kg/Mg lead nitrate while further increase of lead nitrate to 0.3 kg/Mg resulted in the increased consumption of NaCN. The cause of this phenomenon may be the passivation of the cyanide consuming sulfides by lead nitrate addition up to 0.2 kg/Mg. By further increase of lead nitrate to 0.3 kg/Mg, excessive lead nitrate consumes the NaCN by formation of insoluble lead cyanide. Results are shown in Table 3.

Table 3. Havran ore leach results

Initial NaCN addition, kg/Mg ore	Lead Nitrate addition, kg/Mg ore	Au Leach recovery %	Ag Leach recovery %	NaCN consumption kg/Mg ore	Initial NaCN in solution, ppm	Final NaCN in solution, ppm
0.5	0.0	94.32	69.14	0.27	378	170
0.5	0.1	95.22	74.01	0.25	378	190
0.5	0.2	95.10	74.36	0.23	378	200
0.5	0.3	95.41	74.28	0.30	378	150

Mastra ore test results

The Mastra low and high copper ores were tested by four leaches: one with no lead nitrate and others with 0.1, 0.3, 0.5 kg/Mg lead nitrate all of which were with 0.5 kg/Mg NaCN, to obtain 378 ppm initially as it was found as optimum parameter by the previous tests. The results are shown on Tables 4 and 5.

The low Cu ore with 0.3 kg/Mg lead nitrate Au extraction recovery increased from 92.81% to 94.04% while NaCN consumption decreased from 0.30 to 0.20 kg/Mg. Besides, Cu in solution decreased with increased dose of lead nitrate showing that lead nitrate partially passivizes the chalcopyrite surface as well as pyrite surface. Thus, the decrease in NaCN consumption can depend on passivation of chalcopyrite preventing

copper from reacting with cyanide (Deschenes et al., 2000). However, increasing the lead nitrate up to 0.5 kg/Mg resulted in a slight increase of the consumption of NaCN. Ag recovery increased from 58.19% to 65.58% by 0.3 kg/Mg lead nitrate addition as well. A further increase in lead nitrate up to 0.5 kg/Mg decreased the Au and Ag leach indicating the formation of $Pb(OH)_2$ passive layer on Au and Ag surface (Deschenes et al., 2000; Sandenbergh and Miller, 2001; Tan et al., 2005).

Table 4. Mastra low copper ore (LCu) leach results

Initial NaCN addition, kg/Mg ore	Lead Nitrate addition, kg/Mg ore	Au Leach Recovery %	Ag Leach Recovery %	NaCN consumption kg/Mg ore	Final NaCN in solution, ppm	Cu in solution, ppm
0.5	0.0	92.81	58.19	0.30	150	30.52
0.5	0.1	93.52	59.15	0.29	160	23.06
0.5	0.3	94.04	65.58	0.20	230	14.45
0.5	0.5	93.26	59.84	0.23	200	10.03

Table 5. Mastra high copper ore (HCu) leach results

Initial NaCN addition, kg/Mg ore	Lead Nitrate addition, kg/Mg ore	Au Leach Recovery %	Ag Leach Recovery %	NaCN consumption kg/Mg ore	Final NaCN in solution, ppm	Cu in solution, ppm
0.5	0.0	96.77	38.08	0.41	70	34.84
0.5	0.1	97.14	36.45	0.38	90	31.40
0.5	0.3	96.77	36.25	0.35	110	25.23
0.5	0.5	97.16	49.69	0.34	120	26.78

For the high copper ore Au the leaching recovery slightly increased from 96.77% to 97.16% while NaCN consumption decreased from 0.41 to 0.34 kg/Mg with 0.5 kg/Mg lead nitrate addition. The aqueous solution analysis indicated that Cu dissolution was prevented with increasing lead nitrate addition. Thus, the reduction of NaCN consumption, proportional to the increasing lead nitrate addition can be related to the increased passivation of chalcopyrite by lead nitrate (Deschenes et al., 2000). Besides, Ag leach recovery increased from 38.08% to 49.69% confirming the references indicating the increase of Ag as well as Au recovery (Arslan et al., 2003).

Conclusions

The effect of lead nitrate addition in cyanide leaching of four different gold ores was investigated. All of the ores showed increases in gold and silver leaching recoveries with lead nitrate addition. In the case of the Ovacik ore leach, the recovery increased from 96.72% to 97.35% in gold and from 73.70% to 77.59% in silver with 0.1 kg/Mg lead nitrate; in the case of the Havran ore was from 94.32% to 95.41% in gold and

69.14% to 74.28 in silver with 0.3 kg/Mg lead nitrate. In the case of the Mastra LCu ore from 92.81% to 94.04% in gold and 58.19% to 65.58% silver with 0.3 kg/Mg lead nitrate; in the case of the Mastra HCu ore from 96.77% to 97.16% in gold and from 38.08% to 49.69% in silver by 0.5 kg/Mg lead nitrate. NaCN consumption, in general, decreased down to certain lead nitrate concentrations, except the Ovacik ore. In the case of the Ovacik ore it increased proportionally to increasing lead nitrate addition.

In the case of lead nitrate addition to cyanide leaching of these Turkish ores, an increase in the production of gold and silver is predicted to be 2704 troy oz Au and 26362 troy oz Ag per year, when the plant ore feed tonnage is estimated as 100 Mg/h with 24 h leaching time and when the average recovery increases are calculated as 0.8% for gold and 7.8% for silver with average contents of 12 ppm gold and 12 ppm silver. Thus, the annual increase of revenue has been expected as $4.3 million for gold and $0.8 million for silver when metal prices are predicted as $1600/troy oz for gold and $30/troy oz for silver.

References

ARSLAN F., OZDAMAR D.Y., MUDUROGLU M., 2003, *Cyanidation of Turkish gold-silver ore and the use of hydrogen peroxide,* The European Journal of Mineral Processing and Environmental Protection, vol 3,No 3, 309–315.

CEROVIC K., HUTCHISON H., SANDENBERGH R.F., 2005, *Kinetics of gold and a gold – 10% silver alloy dissolution in aqueous cyanide in the presence of lead*, Minerals Engineering 18, 585–590.

DAI X., BREUER P.L. 2013, *Leaching and electrochemistry of gold, silver and gold–silver alloys in cyanide solutions: Effect of oxidant and lead(II) ions*, Hydrometallurgy, Vol. 133, 139–148.

DAI X., JEFFREY M.I. 2006 *The effect of sulfide minerals on the leaching of gold in aerated cyanide solutions*, Hydrometallurgy, Vol. 82, Iss. 3–4, 118–125.

DESCHENES, G., LACASSE, S., FULTON, M., 2003, *Improvement of cyanidation practice at Goldcorp Red Lake Mine,* Minerals Engineering 16, 503–509.

DESCHENES G., LASTRA R., BROWN J.R., JIN S., MAY O., GHALI E., 2000, *Effect of lead nitrate on cyanidation of gold ores: Progress on the study of the mechanisms,* Minerals Engineering, 13, 1263-1279.

DESCHENES G., PRUD'HOMME P.J.H., 1997, *Cyanidation of a copper-gold ore,* Int. J. Mineral Processing, 50, 127–141.

DESCHENES G., XIA C., FULTON M., CABRI LOUIS J., PRICE J. 2009, *Evaluation of leaching parameters for a refractory gold ore containing aurostibite and antimony minerals: Part I – Central zone*, Minerals Engineering, Vol. 22, Iss. 9–10, 799–808.

GUNEY A., GURKAN V., 2008, *Cesitli Kayac Orneklerinin Mineral Ozellikleri ve Altin Faz boyutlarinin Belirlenmesi,* ITU Maden Fakultesi Vakfı Iktisadi Isletmeleri, Technical Report.

LYCOPODIUM PTY. LTD., 1996, *Prefeasibility study*, volume 3 (1996).

SANDENBERGH R.F., MILLER J.D., 2001, Catalysis of the leaching of gold in cyanide solutions by lead, Bismuth and Thallium, Minerals Engineering 14, 1379–1386.

SENANAYAKE G., 2008 *A review of effects of silver, lead, sulfide and carbonaceous matter on gold cyanidation and mechanistic interpretation*, Hydrometallurgy, Vol. 90, Iss. 1, 46–73.

TAN H., FENG D., LUKEY G.C., VAN DEVENTER J.S.J., 2005, *Effect of carbon coatings on gold dissolution in the presence of sulfide and lead*, Minerals Engineering 18, 1361–1372.

Pr-DOPED TIO₂. THE EFFECT OF METAL CONTENT ON PHOTOCATALYTIC ACTIVITY

Joanna RESZCZYNSKA[*]**, Daniel ARENAS ESTEBAN**[**,**]**, Maria GAZDA**[***]**, Adriana ZALESKA**[*]

[*] Department of Chemical Technology, Faculty of Chemistry, Gdansk University of Technology, Gdansk, Poland, e-mail: adriana.zaleska@pg.gda.pl
[**] Faculty of Chemical Sciences, Complutense University of Madrid, Madrid, Spain
[***] Department of Solid State Physics, Faculty of Applied Physics and Mathematics, Gdansk University of Technology, 80-952 Gdansk, Poland

Abstract: Pr-TiO₂ nanoparticles were prepared by using a sol-gel method. As-prepared samples were characterized by BET measurements, X-ray powder diffraction analysis (XRD) and UV-Vis spectra. Visible and ultraviolet light photocatalytic activity of the sample was studied by photodegradation of phenol, while considering the influence of the dopant concentration. TiO₂ doped with 0.25 mol% of praseodymium showed the highest photocatalytic activity under visible light irradiation. Pr-TiO₂ had anatase structure. The surface area was higher for powders with higher content of rare earth metal ion, and ranged from 121 to 150 m²/g. Red shifts of absorption edge toward the visible region were observed for the doped samples compared to pure TiO₂.

Keywords: photocatalysis, rare earth metal, praseodymium, modified TiO₂, phenol

Introduction

Phenols are generally considered to be one of important organic pollutants discharged into the environment causing unpleasant taste and odor of drinking water (Grabowska et al., 2012a). Phenol is toxic even at low concentrations, and also its presence in natural waters can lead further to formation of substituted compounds during the disinfection and oxidation processes (Busca et al., 2008). In response, it has become a challenge to achieve an effective removal of persistent organic pollutants from wastewater effluent to minimize the risk of pollution problems from such toxic chemicals and to enable its reuse. TiO₂ is a commonly used photocatalyst in water purification, wastewater and gas streams treatment (Gorska et al., 2008; Zielinska-Jurek et al., 2010; Grabowska et al., 2012b; Nischk et al., 2013). However, utilization

of pure TiO_2 is significantly constrained because of its wide band gap, low efficiency of sunlight utilization, low quantum efficiency, and high recombination rate of electrons-holes. Therefore, it is of great interest to improve the photocatalytic activity of TiO_2 in order to enlarge practical applications of TiO_2-based photocatalysts (Shi et al., 2012). Rare-earth ion doped materials have played an important role in the development of optical communication technology during the past few decades (Shang et al., 2008). Lanthanide ions are known for their ability to form complexes with various Lewis bases (e.g., acids, amines, aldehydes, alcohols, thiols, etc.) in interaction of these functional groups with the f-orbitals of lanthanides (Ranjit et al., 2001). Titania doping with lanthanides is a method to shift the maximum of absorption as well as enhance the photocatalytic activity (Hassan et al., 2012). Rare earth metals could be introduced to the surface of TiO_2 by various methods such as: sol-gel (Sheng et al., 2011; Tang et al., 2012), hydrothermal (Pedroni et al., 2012; Li et al., 2013), electrospinning (Cacciotti et al., 2011; Hassan et al., 2012) and surface impregnation (Parida and Sahu, 2008).

In our previous paper (Reszczynska et al., 2012) the sol-gel method to synthesize Er and Yb modified TiO_2 nanoparticles was presented. It was observed that the dopant amount affected photocatalytic activity of semiconductor. The presence of erbium was found more beneficial for visible light activation of TiO_2 doped photocatalysts than ytterbium.

In this work, a series of Pr-doped TiO_2 nanoparticles were synthesized using the sol–gel technique with various Pr concentrations. The photocatalytic activity of as-prepared Pr-doped TiO_2 was evaluated using degradation of phenol in aqueous solutions under UV and Vis irradiation. The BET surface area, X-ray powder diffraction analysis (XRD) and UV-Vis spectra were evaluated.

Experimental

Materials and instruments

Titanium(IV) isopropoxide (97%) was purchased from Sigma-Aldrich Co. and used as titanium source for the preparation of TiO_2 nanoparticles. $Pr(NO_3)_3 \cdot 5H_2O$ (99.99%), from Sigma– Aldrich Co. was used as rare earth metal source in the preparation procedure. Acetic acid and ethanol (POCH S.A. Poland) were used without further purification. Deionized water was used for all reactions and treatment processes. A commercial form of TiO_2 (P25, crystalline composition: 80% anatase, 20% rutile) from Evonik, Germany was used for the comparison of the photocatalytic activity.

The nitrogen adsorption–desorption isotherms were recorded at liquid nitrogen temperature (77 K) on a Micromeritics Gemini V (model 2365) and the specific surface areas were determined by the Brunauer–Emmett–Teller (BET) method in a relative pressure (p/p_0) range of 0.05–0.3 Pa. All the samples were degassed at 200 °C prior to nitrogen adsorption measurement.

DRS UV–Vis spectra of synthesized materials were recorded in a scan range 350–700 nm using a UV–Vis spectrophotometer (UV-Vis Thermo model: Nicolet Evolution 220 with ISA-220 integrating sphere) equipped with an integrating sphere and BaSO$_4$ was used as the reference. X-ray diffraction patterns (XRD) were recorded on a X-ray diffractometer (Xpert PRO-MPD, Philips) with Cu target K$_\alpha$-ray (λ=0.15404 nm) in the range 2θ=20-68°. The patterns were analyzed by the Rietveld refinement method using LHPM program (Hill and Howard, 1986). The crystallite size was estimated by Scherrer equation. The accuracy of the grain size analysis was estimated to be about 20%.

PREPARATION OF Pr DOPED TiO$_2$ PHOTOCATALYSTS

For the preparation of photocatalyst the sol-gel method was used. TiO$_2$-based photocatalysts were obtained according to the procedures presented by a simplified block diagram in Fig. 1. The sample of 15 cm^3 titanium isopropoxide was added to the mixture of 3.0 cm^3 acetic acid and 60 cm^3 ethanol. The sol was stirred for 1 h, then 20 cm^3 of Pr(NO$_3$)$_3$ water solution, with pH adjusted to 3.5 (with 65 % HNO$_3$), was added dropwise. The obtained solution was stirred for 2.5 h. The prepared gel was filtered and washed four times with water using a centrifugal and dried at 80 ˚C. The heat-treatment of 400 ˚C for 2.5 h in the air was applied to the sample (heating rate of 5 ˚C/min). The concentration of metal precursors, which varied from 0 to 1.5 mol%, was related to the concentration of TIP in the sol-gel system.

MEASUREMENTS OF PHOTOCATALYTIC ACTIVITY

The photocatalytic activity of Pr-TiO$_2$ powders in the visible and ultraviolet lights were estimated by measuring the decomposition rate of phenol in an aqueous solution. A 25 cm^3 of photocatalyst suspension (125 mg) in 0.21 mM phenol aqueous solution was placed in a quartz photoreactor. After 30 min aeration (5 dm^3/h) the suspension was irradiated with a Xenon 1000 W lamp. The optical path included water filter to cut off IR irradiation. For the test of visible-light-induced activity the light beam was passed through a GG420 filter to cut-off wavelengths shorter than 420 nm. One milliliter aliquots of aqueous suspension were collected at regular time periods during irradiation and filtered through the syringe filters (Ø = 0.2 mm) to remove the photocatalyst particles. The temperature of suspension was maintained at 10 ˚C using a thermostatically controlled water bath. Phenol concentration was estimated by the colorimetric method (λ = 480 nm) after derivatisation with diazo-pnitroaniline using the UV-Vis spectrophotometer (DU-520, Beckman).

Results and discussion

The sample labels, BET surface areas, crystal size and photoactivity for praseodymium-doped TiO$_2$ photocatalysts were listed in Table 1. For all the doped samples prepared by the sol-gel method, the BET surface area was higher than for the

commercially available P25 (50 m^2/g). The surface area was higher for powders with higher content of rare earth metal ion, and ranged from 121 to 150 m^2/g. The Pr-doped sample has larger BET surface area than the undoped sample, indicating that the Pr-doping increases the thermal stability of mesoporous framework. Based on the literature data, it is likely that lanthanides ions are not incorporated into the matrix of TiO$_2$ but rather form rare-earth oxides, RE$_2$O$_3$ (Yang et al., 2011).
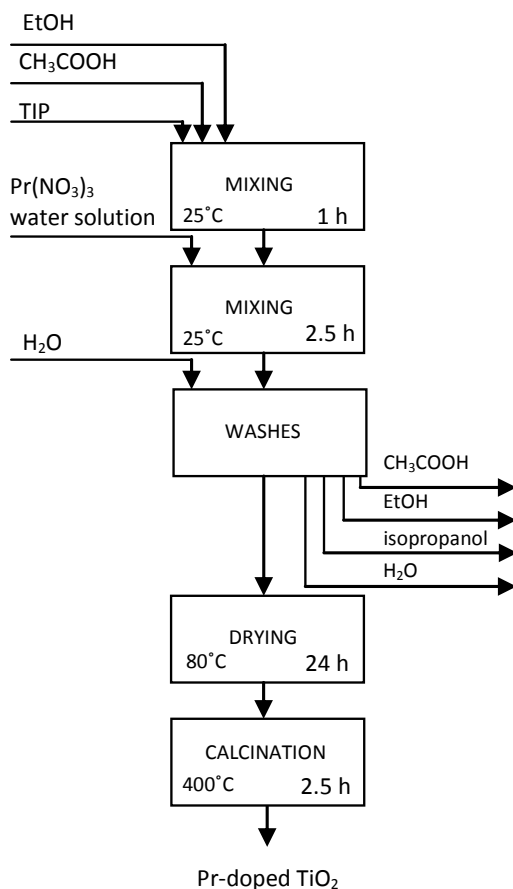
Fig. 1. Block diagram of Pr-doped TiO$_2$ prepared by the sol-gel method

The melting point of Pr$_2$O$_3$ is 2138 °C is higher than that of TiO$_2$. The surface coverage of metal oxide with higher melting point probably hampers the adjustment of matrix particles and rearrangement of crystal. Consequently, the Pr-doping improves the microstructural properties of TiO$_2$. Similar observation was made for Yb/N-TiO$_2$ photocatalysts (Yan et al., 2013). Rare earth ions doping can reduce the crystallite size but increase the surface area of TiO$_2$, which also contribute to the enhancement of

adsorption capacity of TiO_2 for organic pollutants (Liang et al., 2006; 2009).The exceeded surface area for lanthanoid doped TiO_2, in comparison with the pure one, was also reported by Bingham and Daoud (2011).

Table 1. Surface characteristics and photocatalytic activity of Pr-TiO₂ photocatalysts

Photocatalysts type	Amount of metal precursor (mol%)	S_{BET} (m^2/g)	Average crystallite size (nm)	Phenol degradation rate under Vis irradiation ($\lambda > 420$ nm) ($\mu mol/dm^3 \cdot min$)	Phenol degradation rate under UV-Vis irradiation ($\mu mol/dm^3 \cdot min$)
TiO2_Pure	none	130	11.1	0.42	2.80
TiO2_Pr(0.1)	0.1	121	11.2	0.69	2.77
TiO2_Pr(0.25)	0.25	146	11.0	1.01	2.55
TiO2_Pr(0.5)	0.5	135	10.0	0.77	2.84
TiO2_Pr(0.7)	0.7	139	9.6	0.56	3.17
TiO2_Pr(1.0)	1.0	148	9.7	0.54	1.48
TiO2_Pr(1.5)	1.5	150	9.6	0.75	3.12
P25	none	50	not measured	0.34	3.19

To study the optical absorption properties of as-prepared samples, the UV-Vis absorption spectra in the range 350–700 nm were investigated, and the results are shown in Fig. 2. It can be seen that modification of titania with praseodymium significantly affected the light absorption property of photocatalysts. Red shifts of
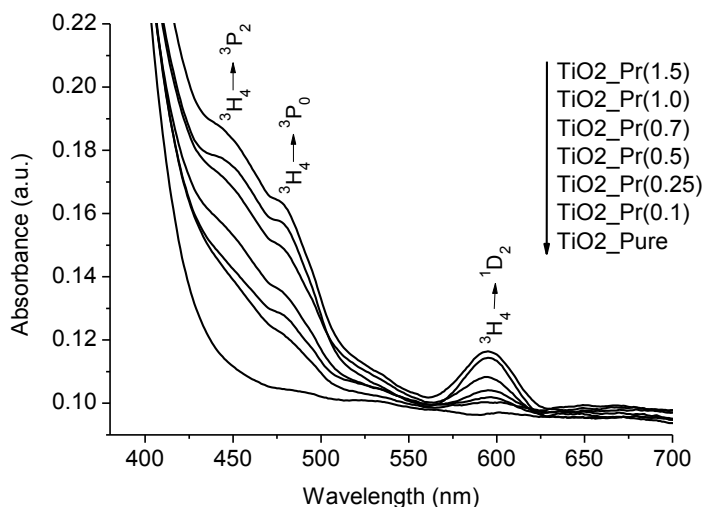
Fig. 2. Absorption properties of Pr-TiO₂ prepared by the sol-gel method

absorption edge toward the visible region were observed for the doped samples compared to pure TiO_2. The correlation between the amount of rare earth metal and the absorption edge shift to a longer wavelength was observed. Furthermore, it can be seen that there are three typical for praseodymium absorption peaks located at 446, 480 and 595 nm and they are attributed to transitions of $^3H_4$ to $^3P_2$, $^3P_0$ and $^1D_2$ (Su et al., 2008; Yang et al., 2011). The intensity of rare earth ion absorption bands was found to increase with increasing in the rare earth ion content.

The X-ray diffraction analysis (XRD) was used to verify the crystalline phase of synthesized doped TiO_2 and to estimate the crystallite size. The XRD patterns of examined samples are shown in Fig. 3. In all prepared photocatalysts, Fig. 3 presents a group of lines at 2θ values of 25.3°, 37.8°, 48.0°, 53.9°and 55.1°,which are attributed to anatase phase (El-bahy et al., 2009). However, no peaks related to the presence of praseodymium or praseodymium oxides were detected for Pr-TiO_2 photocatalysts. Thus, it indicates that the dopant nanoparticles at the TiO_2 surface are very small and highly dispersed (Zhou and He, 2012) or the concentration of rare earth metal was too low for the XRD to reveal (Wu et al., 2011). In our data the average particle size, determined on the base of Scherrer equations, ranged from 9.6 to 11.2 nm for TiO2_Pr(1.5) and TiO2_Pr(0.1), respectively. For undoped TiO_2 the particle size was 11.2 nm (Table 1). The particle size was found to decrease with increase in metal ion dopant concentration in TiO_2.
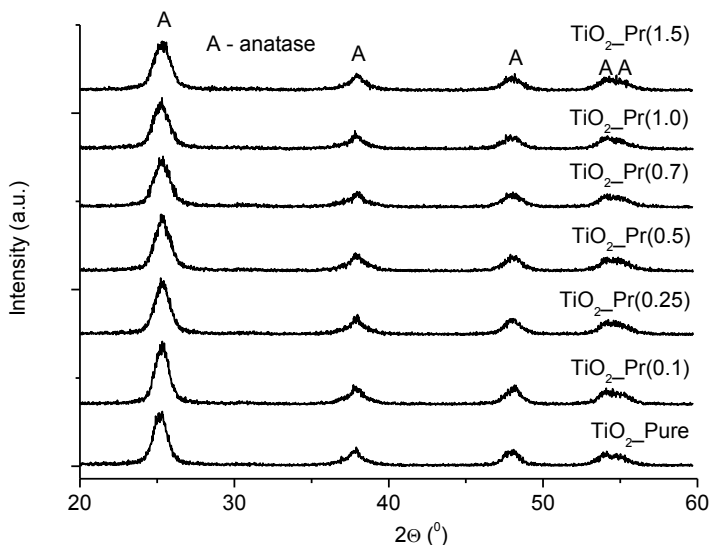
Fig. 3. XRD pattern of Pr-TiO_2 photocatalysts prepared by sol-gel method

The photocatalytic activity of obtained TiO_2 powders was estimated by measuring the decomposition rate of phenol in the aqueous solution in the presence of UV-Vis or

visible light irradiation ($\lambda > 420$ nm). No degradation of phenol was observed in the absence of photocatalysts or illumination. The pure TiO$_2$ synthesized by the sol-gel method without any dopant and P25 were used as the reference system. Kinetics of phenol photodegradation in aqueous solution under Vis/UV-Vis light irradiation in the presence of Pr-doped TiO$_2$ nanoparticles is shown in Figs. 4a,b, respectively. The observed rate constants are listed in Table 1.

a)   b)

| —■— P25 | —▲— TiO2_Pr(0.1) | —◇— TiO2_Pr(0.5) | —▷— TiO2_Pr(1.0) |
| —●— TiO2_Pure | —▼— TiO2_Pr(0.25) | —◁— TiO2_Pr(0.7) | —⊕— TiO2_Pr(1.5) |
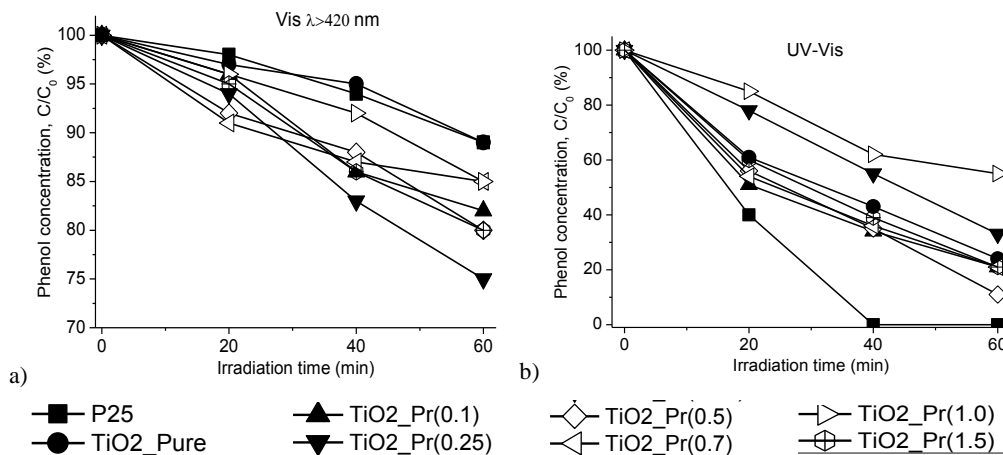
Fig. 4. Efficiency of phenol photodegradation in the presence of Pr-doped TiO$_2$ during irradiation light: a) Vis ($\lambda > 420$ nm), b) UV/Vis

Phenol degradation under visible light irradiation with the participation of praseodymium doped TiO$_2$ is presented in Fig. 4a. The highest photoactivity was observed for the sample prepared with 0.25 mol% Pr. After 60 min irradiation of aqueous suspension initially containing 20 mg/dm^3 of phenol, 25 % of those was degraded. All rare earth metal-doped photocatalysts had better photocatalytic activity than the undoped ones and P25 under visible light irradiation. The phenol degradation rate under UV-Vis irradiation increased from 2.55 to 3.17 μmol/dm^3·min for 0.25 to 0.7 mol% praseodymium-doped TiO$_2$, respectively. Praseodymium and nitrogen co-doped titania (Pr/N-TiO$_2$) photocatalysts, which could degrade Bisphenol A (BPA) under visible light irradiation, were prepared by the modified sol–gel process by Yang et al. (2011). It was found that Pr doping inhibited the growth of crystalline size and transformation from anatase to rutile. For the best photocatalytic activity, the optimal dopant amount of Pr was 1.2 mol% and the calcination temperature was 500 °C. Pr doping could slow the radiative recombination of photogenerated electrons and holes in TiO$_2$. The improvement of photocatalytic activity was ascribed to the synergistic effects of nitrogen and Pr co-doping.

Chiou and Juang (2007) prepared the Pr-doped TiO$_2$ nanoparticles with a composition of Ti$_{1-x}$Pr$_x$O$_2$(x= 0.018–0.22) using the acid-peptized sol–gel method. The Pr-doped TiO$_2$ showed high activity for photocatalytic degradation of phenol.

Light absorption reached the maximum for the particles with 0.072 mol% Pr, which was consistent with the trends of phenol photodegradation efficiency.

It is presumed that rare earth doping can lead to defects in the TiO_2 lattice and these defects act as electron traps. The doping may also favor separation of charge carriers efficiently and enhance the photocatalytic activity. It is suggested that rare earth oxides are located on the surface of titania, but more detailed studies about the mechanism of its photoexcitation is required (Wang et al., 2010).

Conclusion

In summary, the Pr-TiO_2 nanoparticles were prepared by the sol-gel method and had the anatase structure. Photocatalysts based on TiO_2 and doped with praseodymium caused an increase of photocatalytic activity under visible light irradiation. It was observed that the dopant affects the surface area and crystal size of TiO_2 powder samples. The photocatalytic activity depends on rare earth ion precursor concentration used during preparation. TiO_2 doped with 0.25 mol% of praseodymium showed the highest photocatalytic activity under visible light. After 60 min of irradiation, 25 % of phenol was degraded. The absorption spectra of Pr-TiO_2 samples show stronger absorption in the UV–Vis region than pure TiO_2.

Acknowledgements

References

BINGHAM S., DAOUD W., 2011, *Recent advances in making nano-sized TiO_2 visible-light active through rare-earth metal doping*, J. Mater. Chem. 21, 2041–2050.

BUSCA G., BERARDINELLI S., RESINI C., ARRIGH, L., 2008, *Technologies for the removal of phenol from fluid streams: A short review of recent developments*, J. Hazard. Mater. 160, 265–288.

CACCIOTTI I., BIANCO A., PEZZOTTI G., GUSMANO G., 2011, *Terbium and ytterbium-doped titania luminescent nanofibers by means of electrospinning technique*, Mater. Chem. Phys. 126, 532–541.

CHIOU C.-H., JUANG R.-S., 2007, *Photocatalytic degradation of phenol in aqueous solutionsby Pr-doped TiO_2 nanoparticles*, J. Hazard. Mater. 149, 1–7.

GORSKA P., ZALESKA A., KOWALSKA E., KLIMCZUK T., SOBCZAK J. W., SKWAREK E., JANUSZ, W., HUPKA, J., 2008, *TiO_2 photoactivity in Vis and UV light: the influence of calcination temperature and surface properties*, Appl. Catal., B 84, 440–447.

GRABOWSKA E., RESZCZYNSKA J., ZALESKA A., 2012a, *Mechanism of phenol photodegradation in the presence of pure and modified-TiO_2: A review*, Water Res. 46(17), 5453–5471.

GRABOWSKA E., SOBCZAK J., GAZDA M., ZALESKA A., 2012b, *Surface properties and visible light activity of W-TiO_2 photocatalysts prepared by surface impregnation and sol-gel method*, Appl. Catal., B 117–118, 351–359.

HASSAN M. S., AMNA T., YANG O.-B., KIM H.-C., KHIL M.-S., 2012, *TiO_2 nanofibers doped with rare earth elements and their photocatalytic activity*, Ceram. Int. 38, 5925–5930.

HILL R. J., HOWARD C. J., 1986, *The High Score plus Rietveld alghoritm is based on the source codes of the program LHPM*, A computer program for Rietveld analysis of fixed wavelength X-ray and neutron diffraction patterns, Australian Atomic Energy Commission Research Report M112.

LI H., ZHENG K., SHENG Y., SONG Y., ZHANG H., HUANG J., HUO Q., ZOU H., 2013, *Facile synthesis and luminescence properties of TiO₂:Eu³⁺ nanobelts*, Opt. Laser Technol. 49, 33–37.

LIANG C.-H., HOU M.-F., ZHOU S.-G., LI F.-B., LIU C.-S., LIU T.-X., GAO Y.-X., WANG X.-G., LÜ, J.-L., 2006, *The effect of erbium on the adsorption and photodegradation of orange I in aqueous Er³⁺-TiO₂ suspension.*, J. Hazard. Mater. 138, 471478.

LIANG C.-H., LIU C.-S., LI F.-B., WU F., 2009, *The effect of praseodymium on the adsorption and photocatalytic degradation of azo dye in aqueous Pr³⁺-TiO₂ suspension*, Chem. Eng. J. 147, 219–225.

NISCHK M., MAZIERSKI P., GAZDA M., ZALESKA A., 2013, *Ordered TiO₂ nanotubes: The effect of preparation parameters on the photocatalytic activity in air purification process*, Appl. Catal., B 144, 674–685.

PARIDA K. M., SAHU N., 2008, *Visible light induced photocatalytic activity of rare earth titania nanocomposites*, J. Mol. Catal. A: Chem. 287, 151-158.

PEDRONI M., PICCINELLI F., POLIZZI S., SPEGHINI A., BETTINELLI M., HARO-GONZÁLEZ P., 2012, *Upconverting Ho-Yb doped titanate nanotubes*, Mater. Lett. 80, 81-83.

RANJIT K. T., WILLNER I., BOSSMANN S. H., BRAUN A. M., 2001, *Lanthanide oxide-doped titanium dioxide photocatalysts: Novel photocatalysts for the enhanced degradation of p-chlorophenoxyacetic acid*, Environ. Sci. Technol. 35, 1544-1549.

RESZCZYNSKA J., IWULSKA A., ŚLIWINSKI G., ZALESKA A., 2012, *Characterization and photocatalytic activity of rare earth metal-doped titanium dioxide* Physicochem. Probl. Miner. Process. 48(1), 201-208.

SHANG Q., YU H., KONG X., WANG H., WANG X., SUN Y., ZHANG Y., ZENG Q., 2008, *Green and red up-conversion emissions of Er³⁺-Yb³⁺ co-doped TiO₂ nanocrystals prepared by sol-gel method*, J. Lumin. 128, 1211-1216.

SHENG Y., ZHANG L., LI H., XUE J., ZHENG K., GUO N., HUO Q., ZOU H., 2011, *Photoluminescence of TiO₂ films co-doped with Tb³⁺/Gd³⁺and energy transfer from TiO₂/Gd³⁺ to Tb³⁺ ions*, Thin Solid Films 519, 7966-7970.

SHI H., ZHANG T., AN T., LI B., WANG X., 2012, *Enhancement of photocatalytic activity of nano-scale TiO₂ particles co-doped by rare earth elements and heteropolyacids*, J. Colloid Interface Sci. 380, 121-127.

SU W., CHEN J., WU L., WANG X., WANG X., FU X., 2008, *Visible light photocatalysis on praseodymium(III)-nitrate-modified TiO₂ prepared by an ultrasound method*, Appl. Catal., B 77, 264-271.

TANG J., CHEN X., LIU Y., GONG W., PENG Z., CAI T., JIN L., DENG Q., 2012, *Europium-doped mesoporous anatase with enhanced photocatalytic activity toward elimination of gaseous methanol*, J. Phys. Chem. Solids 73, 198-203.

WANG C., YANHUI A., WANG P., HOU J., QIAN J., 2010, *Preparation, characterization and photocatalytic activity of the neodymium-doped TiO₂ hollow spheres*, Appl. Surf. Sci. 254, 227-231.

WU J., LIU Q., GAO P., ZHU Z., 2011, *Influence of praseodymium and nitrogen co-doping on the photocatalytic activity of TiO₂*, Mater. Res. Bull. 46, 1997-2003.

YAN P., JIANG H., ZANG S., LI J., WANG Q., WANG Q., 2013, *Sol-solvothermal preparation and characterization of (Yb, N)-codoped anatase-TiO₂ nano-photocatalyst with high visible light activity*, Mater. Chem. Phys. 139, 1014-1022.

YANG J., DAI J., LI J., 2011, *Synthesis, characterization and degradation of Bisphenol A using Pr, N co-doped TiO₂ with highly visible light activity*, Appl. Surf. Sci. 257, 8965–8973.

ZHOU W., HE Y., 2012, *Ho/TiO₂ nanowires heterogeneous catalust with enhanced photocatalytic properties by hydrothermal synthesis method*, Chem. Eng. J. 179, 412–416.

ZIELINSKA-JUREK A., WALICKA M., TADAJEWSKA A., LACKA I., GAZDA M., ZALESKA A., 2010, *Preparation of Ag/Cu-doped titanium (IV) oxide nanoparticles in w/o microemulsion*, Physicochem. Probl. Miner. Process. 45, 113–126.

APPLICATION OF ULTRASONIC VELOCITY MEASUREMENT AND THERMAL ANALYSIS FOR DETERMINATION OF LIMESTONE QUALITY

Ozen KILIC

Department of Mining Engineering, Faculty of Engineering-Architecture, University of Cukurova, Balcali-Adana, 01330, Turkey, zenkilic@cu.edu.tr

Abstract: Limestone is an important industrial raw material. It is consumed by chemical and other industries (84%), used as refractory and road construction material (12%) and applied in civil engineering and agricultural applications (4%). Substantial amounts of limestone are also used as lime in the iron and steel industry. The aim of this study was to determine the properties of limestones. The chemical, physical and thermal properties of limestones were determined by standard methods while the P-wave velocities of limestones were measured with an ultrasonic non-destructive tester and relationships between limestone properties were estimated. It was found that there is a statistical correlation between physical properties and the P-wave velocity of limestones. The P-wave velocity is a very good characteristic parameter for the study and estimation of the limestone quality.

Introduction

In broadest definition, limestone is any rock rich in $CaCO_3$. Limestone can be obtained from a variety of sources and various limestones differ considerably in their chemical compositions and physical structure. The chemical and physical properties of carbonate rocks are interdependent. Physical characteristics of limestone play an important role in evaluation of a deposit. Certain physical characteristics of limestones may indicate the general susceptibility to decrepitation during calcination. However, not all stones with these characteristics will decrepitate. Limestones that display the following attributes or conditions, alone or in combination, are prone to decrepitation; coarse crystallinity, friability, foliation, excessive calcite veining, microfracturing, highly porous and thin-bedded structure. The chemical reactivity of different limestones shows a large variation due to their differences in crystalline structure and the nature of impurities such as silica, iron, magnesium, manganese, sodium, and

potassium. Magnesium and ferrous iron cations occurring in limestone may change the carbonate mineralogy of limestone as well as its physical characteristics such as color, brightness, specific gravity, hardness, tenacity and decomposition properties (Boynton, 1980; Krukowski, 2006).

The main chemical property of limestone is its susceptibility to thermal decomposition, known as calcination, during which lime (CaO) and carbon dioxide are produced (Eq. 1) (Boynton, 1980; Oates, 1998).

The calcination reaction is endothermic

$$CaCO_3 \rightarrow CaO + CO_2 \quad \Delta H = 182.1 \text{ kJ mol}^{-1} \tag{1}$$
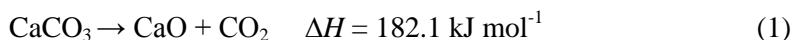
which means that the forward reaction is favored by higher temperatures. The reaction will proceed only if the partial pressure of CO_2 in the gas above the solid surface is less than the decomposition pressure of the $CaCO_3$. The latter pressure is determined by equilibrium thermodynamic considerations (Coats and Redfern, 1964).

The reaction (Eq.1) begins only when the temperature is above the dissociation temperature of the carbonates in the limestone. According to Boynton (1980), the $CaCO_3$ decomposition temperature determined by several researchers at the beginning of the 20th century is generally still accepted as 898 ºC at 1 atm in a 100% CO_2 environment. However, according to some studies, this temperature is 902.5 °C (Turkdogan et al., 1973; Thompson, 1979; Borgwardt, 1985). Kilic (2005) reported that the weight loss above 600 °C, measured by DTA-TG in nitrogen atmosphere is attributed to CO_2 from the decomposition of calcium carbonate that is initiated at 682-691°C and completed at 944-961 °C.

The internal structure of a rock having open and closed pores in its texture affects the heat transfer. The specimen comprises a dense carbonate core surrounded by porous oxide layer. The changes in pore structure also play a significant role in the calcination/heat treatment mechanism and the reactivity of a calcined limestone strongly depends on its chemical, physical and structural properties, which in turn are highly dependent on heat treatment conditions (Rubiera et al., 1991; Khinast et al., 1996). In the good calcination process, limestone should consist approximately 97% of $CaCO_3$ and contain little impurities. Impurities such as iron, magnesium and aluminum oxides lead to lower surface areas in both the limestones and their calcines (Trikkel and Kuusik, 2003).

Ultrasonic techniques have been used for many years in geotechnical practice and mining science. They are employed in the field of geophysical investigations and in the laboratory for the determination of the dynamic properties of rocks. Since these techniques are non destructive and easy to apply, they have increasingly been used. Most researchers (Timur 1977; Parasnis, 1997; Vajdova et al., 1999; Kilic, 2006) studied the relations between rock properties and sound velocity and found that it is closely related with the rock properties. P-wave velocity is a very good index for the quality of rocks and other materials (e.g., mortars, lime quality).

The current demand of limestone worldwide has necessitated investigation of the limestone quality regarding the limestone chemical composition, physical properties and thermal properties. The aim of this study is to examine the properties of the limestone by standard test methods and to estimate these properties using the Pundit instrument, i.e. by an indirect method. The determination methods of chemical and physical and thermal properties of limestones are highly time-consuming and costly methods.

Materials and methods

The limestones were taken from different large commercial deposits: Karaisali region (L_k) and Yilankale region (L_y) in Adana, Turkey. During sampling, rock types having no bedding planes were selected to eliminate any anisotropic effects in the measurements of the samples. Limestones present macroscopically different characteristics. L_k is a 'dirty white' and light coloured grey limestone comprising discrete and tiny crystals. L_y is light-coloured 'dirty white' without any distinguished crystals. Microcracks were not present throughout the mass of L_k limestones, but microcracks, dense vein system and schistosity were observed throughout the mass of L_y limestones.

Analytical methods and techniques

Analyses were performed on limestone samples by using the following analytical procedures.

- XRF (Siemens SRS 300 X-ray Fluorescence Spectrometer) was used to determine the chemical compositions of limestone samples.
- X-ray diffraction (XRD) analyses of finely pulverized limestone samples for the identification of the presented crystalline compounds were performed with a Rigaku Minflex 2. The diffraction angle (2θ) interval was 20°–60° with a step of 0.02°.
- Physical properties (the bulk density, effective porosity, water absorption rate) of the limestones were determined using saturation and buoyancy techniques, as recommended by ISRM and TSE (TS EN 1097-2, 2010).
- P-wave velocities were measured by the Pundit instrument (CNS Farnel Pundit Plus C-Portable Ultrasonic Non-Destructive Indicator Tester), which has two transducers (a transmitter and a receiver) having a frequency of 54 kHz.
- Differential thermal and thermogravimetric analyses (simultaneous TG/DTA, Setaram 92 16 DTA-TG) were carried out to determine quantitatively and qualitatively the various compounds presented in samples. Analyses were performed in samples of limestone in nitrogen atmosphere in the temperature range of 25–1000 °C and gradient of 10 °C/min.

Results and discussion

The chemical analyses results of limestone samples are presented in Table 1. It was found that the studied limestones are very pure with an average $CaCO_3$ content higher than 97%. The impurities concentrations (MgO, Fe_2O_3, Al_2O_3 and SiO_2) are very low. Since the $MgCO_3/CaCO_3$ ratio varies with the type of limestone, the decomposition temperature does not remain constant and therefore must be determined for every type of limestone.

The mineralogical analysis of the limestones (L_y and L_k) was done by XRD analysis technique. It was found that they were very pure and calcite was the main component in both samples, with little quartz.

Table 1. Chemical compositions of limestone (%)

Sample	CaO	MgO	SiO$_2$	Fe$_2$O$_3$	Al$_2$O$_3$	Loss on Ignition
L_k	55.13±0.14	0.44±0.04	0.34±0.22	0.08±0.04	0.07±0.03	43.95±0.15
L_y	54.90±0.35	0.74±0.58	0.55±0.31	0.10±0.05	0.08±0.06	43.63±0.53

The physical properties results of limestones are presented in Table 2. All limestone samples indicated low values of porosity and water absorption rate (lower than 1%). The value of apparent density (>2.55 g/cm^3) was found to be characteristic for a limestone (Stanmore and Gilot, 2005). Comparing the limestones, L_y demonstrated higher values in porosity.

The physical properties depend not only on the properties of the individual minerals, but also upon the way in which the minerals are assembled, porosity, vein system and micro-cracks. The relevant information is given by P-wave velocities, which includes the pores and cracks. Information on the porous nature of rock materials is frequently omitted from physical descriptions, but is required if these descriptions are to be used as a guide to mechanical performance (Smorodinov et al., 1970). Bulk density is relevant to chemical composition of the limestone. Bulk density increases with the increase in $MgCO_3$ content.

The P wave velocity was used to determine the changes in the physical properties of the limestone samples. P-wave velocity measurements may be performed by the direct method at room conditions through ultrasonic pulse transmission technique by the Pundit instrument (Fig. 1). Velocity measurements were carried out on the cubic specimens. The test was repeated three times in three perpendicular directions and the mean values were recorded as the P-wave velocity.

The P-wave velocity in the limestones ranges between 3.500 and 6.500 km/s (Parasnis, 1997) while, for a calcite crystal, the P-wave velocity is 6.490 km/s (Vajdova et al., 1999). In the tests, the P-wave velocity in L_k and L_y was measured as 5.701±0.044 and 5.635±0.051 km/s, respectively (Table 2). The P-wave velocity measurement values have showed that all specimens have minor cracks and porosity.

Fig. 1. The method of measuring P-wave velocity

Table 2. Physical properties of the limestones

Sample	Bulk density (g/cm^3)	Water absorption rate (weight) (%)	Porosity (%)	P-wave velocities (km/s)
L_k	2.65±0.08	0.62±0.12	0.75±0.08	5.701±0.044
L_y	2.66±0.14	0.79±0.19	0.85±0.16	5.635±0.051

The P-wave velocity, as a natural characteristic of rocks and different materials, depends on their micro- and macro-structure, the existence of minor cracks and porosity and the characteristics of their mineralogical components, such as elastic parameters, density and micro-porosity (Vajdova et al., 1999). Increased velocity with an increase in the dry apparent weight and vice versa is reported by Babuska (1968) and Kopf et al. (1985).

According to Toksoz et al. (1976), an important factor affecting the decrease of P-wave velocity, apart from the dry apparent weight, is the creation of micro-cracks. These micro-cracks are created due to anisotropic thermal expansion of the material inside the cracks, in relation to the matrix, when a rock contains secondary veins.

The graphs (Figs. 2–4) of the P-wave velocity versus bulk density and porosity have been presented for L_k and L_y. Among the relations, bulk density (Fig. 2), water absorption rate (Fig. 3) and porosity (Fig. 4) against P-wave velocity have a correlation $R^2 = 0.9862$, $R^2 = 0.9812$ and 0.9875, respectively. Strong statistical correlations between physical properties and P wave velocity were found.

$$y = -12.78x^2 + 68.785x - 86.843$$
$$R^2 = 0.9862$$
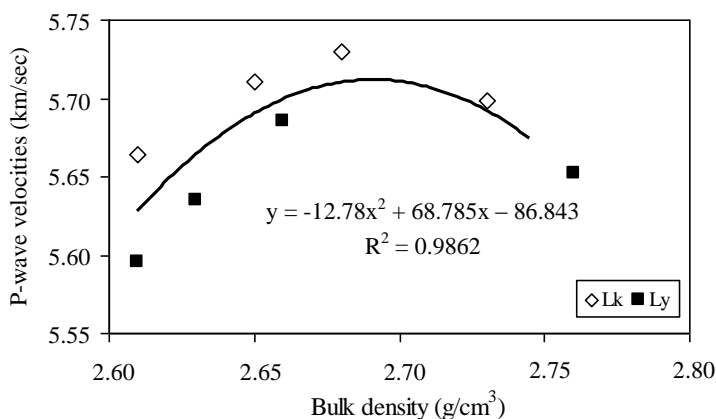
Fig. 2. Correlation of P-wave velocity vs. bulk density
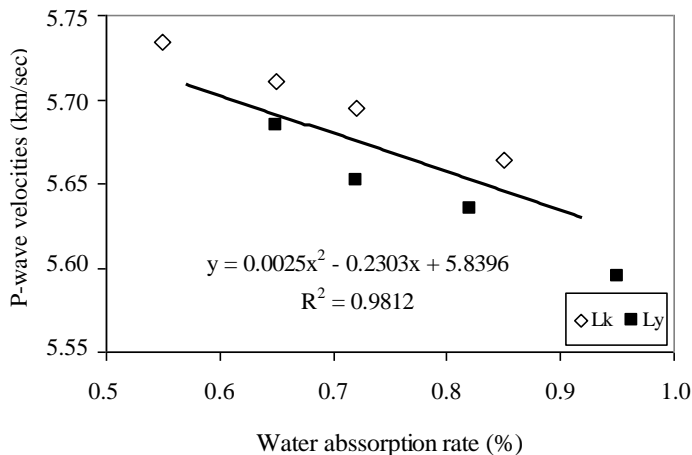
Fig. 3. Correlation of P-wave velocity vs. water absorption rate
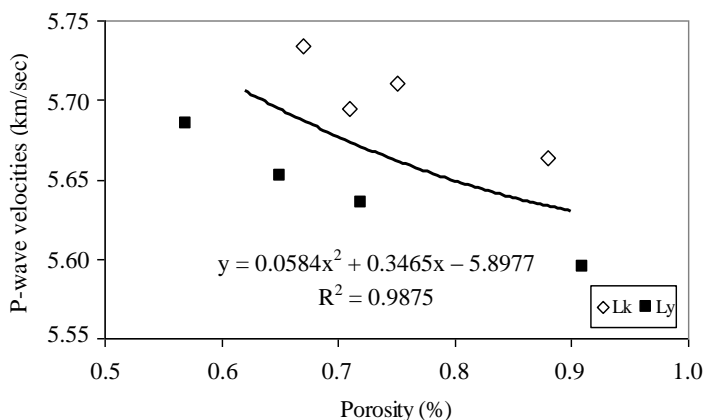
Fig. 4. Correlation of P-wave velocity vs. porosity

The differential thermal analysis technique has been used for the quantitative determination of the heats of decomposition of carbonate materials. It is observed that the carbonates; i.e. limestone, dolomite, have lower heats of decomposition and higher energies of activation in a carbon dioxide atmosphere compared to values obtained in air.

The thermal analysis was performed simultaneously by means of TG–DTA. TG and DTA curves (Figs. 5–6) for the limestones L_k and L_y were obtained by continuous heating from room temperature to 1000 °C at a heating rate of 10 ºC/min. The observed changes are attributed to CO_2 from the decomposition of calcium carbonate.
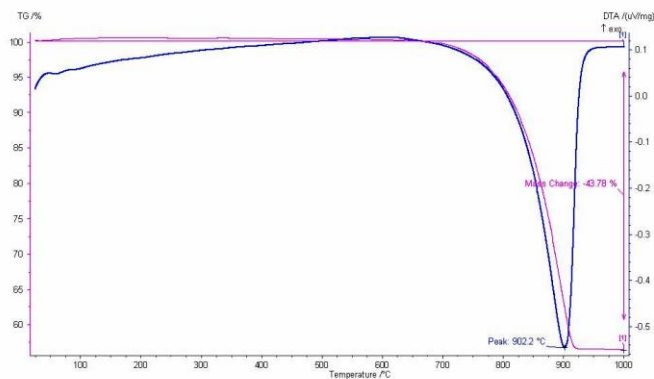
Fig. 5. The TG-DTA curve for L_k decomposition
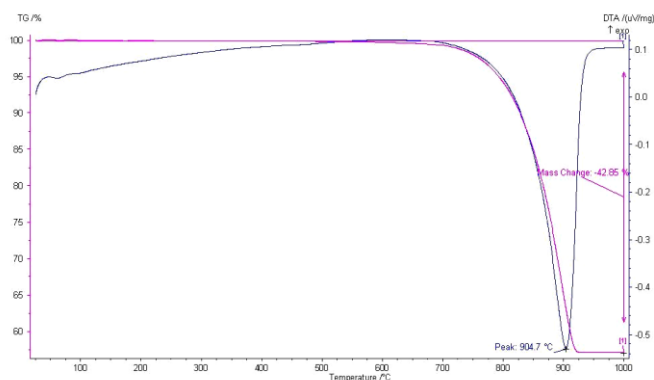
Fig. 6. The TG-DTA curve for L_y decomposition

The figures showed that the weight loss is initiated at 625 and 675 ^{o}C and full decomposition ended approximately at 925 and 935 ^{o}C for L_y and L_k, respectively. Comparing the percentage values of CO_2 measured by DTA/TG, it is evident that the values are very high and similar to each other. Thus, the limestones could be characterized as high calcium ones. Furthermore, it is observed that the percentage of CO_2 for limestones is higher than the theoretical one.

In the evaluation of the thermal decomposition of limestone is complicated by the CO_2 presence, which inhibits the reaction; particle size, which may introduce both thermal and mass transfer limitations, and catalysis/inhibition by impurities. When calcination takes place (Eq.1), the obtained calcium oxide weighs only 56% of the parent carbonate. It was understood that limestones are very pure and main mineral is calcite in both samples because no other endothermic peaks (Figs. 5–6) are observed.

This study also showed that depending on the chemical, petrographic and mechanical features of limestone, before it undergoes calcination it is possible to give

an estimation of the quality the produced lime, basing on the conditions and temperature of calcination. Using the measurement of P-wave velocity it is possible to give the estimation of the quality of the limestone without analyses which are costly and takes much time.

Conclusions

The studies aiming to determine the properties of the limestones by standard test methods and estimate them by means of P-wave velocity using the Pundit instruments by indirect method are presented. The relation between limestone properties and the results of P-wave velocity measurements were established.

The analysis showed that L_k and L_y contain sufficiently high percentages of calcium oxide and calcite mineral was the main component of both samples. Since the $MgCO_3/CaCO_3$ ratio varies with the type of limestone, the decomposition temperature does not remain constant and therefore must be determined for every type of limestone.

It was found in this study that the density of limestone is larger than 2.55 g/cm^3 and the samples showed low porosity and low water absorption rate (<%1). These findings show the fact that these limestones have compact texture and this type of stones could be preferred as quality limestone.

The thermal decomposition of limestone depends on chemical composition, physical properties and decomposition temperature of calcium carbonate. The reaction temperature has a direct effect on the conductivity of limestone depending on their impurities, porosity and micro-cracks, and hence on the rate of reaction. The reaction rate can be enhanced through improved heat transfer systems.

Samples with higher $CaCO_3$ content and P-wave velocity and lower bulk density and porosity show relatively higher activation energy and rate of lime crystallite growth. This is due to the original grain channel pores and the formation of triple junction fractures during decomposition process, which facilitate transfer of hot gases and diffusivity of the evolved CO_2. It is finally concluded that decomposition process of limestone is a temperature, chemical and physical properties dependent process.

These results of the experiments show that limestones (L_k and L_y) have compact texture, low porosity, high CaO and low impurity and good thermal conductivity. This type of stones are preferred in industries such as road construction and production of lime.

References

BABUSKA V., 1968. *Elastic Anisotropy of Igneous and Metamorphic Rocks*. Stud. Geph. Geod. 12:291–303.

BORGWARDT RH., 1985. *Calcination Kinetics and Surface Area of Dispersed Limestone Particles.* AIChE J.; 31(1):103–111.

BOYNTON RS., 1980. *Chemistry and Technology of Lime and Limestone*. 2nd Edition. John Wiley and Sons, Inc., New York.

COATS AW. REDFERN J P., 1964. *Kinetic Parameters from Thermogravimetric Data*, Nature 201, 68-69.

KHINAST JG, KRAMMER G, BRUNNER C, STAUDINGER G., 1996. *Decomposition of limestone: The influence of CO_2, and particle size on the reaction rate*. Chem. Eng. Sci.; 51(4):623–634.

KILIC, O., 2005. *Comparison of Calcination Parameters of Classic (Eberhart) and Parallel Flow Regenerative Kiln (Maerz) and Applications on Çukurova Region Limestones*, PhD Thesis, Department of Mining Engineering, Institute of Natural and Applied Sciences, University of Çukurova, Adana, p. 171.

KILIC O., 2006. *The Influence of High Temperatures on Limestone P-wave Velocity and Schmidt Hammer Strength*, Technical note, International Journal of Rock Mechanics & Mining Sciences, 43, 980–986.

KOPF M., MULER H.J., GOTTESMANN B., 1985. *Correlation Between Pyroxene Content and Vp and Vs Under High Pressure*. In: KAPICKA A., KROPACEK V., PROS Z., editors. Physical Properties of the Mineral System of the Earth's Interior. Prague: Union of Czechoslovak Mathematical Physics.

KRUKOWSKI ST., 2006. *Lime*, Industrial Minerals&Rocks 7th edition, Society for Mining Metallurgy and Exploration Inc (SME), USA.

OATES JAH., 1998. *Lime and Limestone Chemistry and Technology Production and Uses*. Wiley-VCH Verlag GmbH, Germany, 169.

PARASNIS SD., 1997. *Principles of Applied Geophysics*. London: Chapman&Hall; 429.

RUBIERA F., FAURTES B.A., PIS J.J., ARTOS V., MARBAN G., 1991. *Changes in Textural Properties of Limestone and Dolomite During Calcination*. Thermochim. Acta; 179: 125–134.

SMORODINOV MI, MOTOVILOV EA, VOLKOV VA., 1970. *Determinations of Correlation Relationships Between Strength and Some Physical Characteristics of Rocks*. Proceedings of the Second Congress of the International Society of Rock Mechanics, Belgrade, 2:35–37.

STANMORE BR, GILOT P, 2005. *Review-Calcination and Carbonation of Limestone During Thermal Cycling for CO_2 Sequestration*, Fuel Processing Technology (86)16, 1707–1743.

THOMPSON L.J., 1979. *Predicting Lime Burning Rate Via New Dynamic Calcination Theory. Solid State Diffusion Controls Reaction Speed in Kiln. Pit Quarry*, 5:80–83.

TIMUR A., 1977. *Temperature dependence of compressional and shear wave velocities in rocks*. Geophysics, 42:950–956.

TOKSOZ MN, CHENG CH, TIMUR A., 1976. *Velocities of Seismic Waves in Porous Rocks*. Geophysics, 41:621–645.

TRIKKEL A., KUUSIK R., 2003. *Modeling of Decomposition and Sulphation of Oil Shale Carbonates on the Basis of Natural Limestone*, Oil Shale, (20)4, 491–500.

TS EN 1097-2, 2010. *Tests for Mechanical and Physical Properties of Aggregates - Part 2: Methods for the Determination of Resistance to Fragmentation*.

TURKDOGAN TE., OLSSON GR, WRIEDT AH, DARKEN SL., 1973. *Calcination of limestone*. Trans. Soc. Min. Eng.-AIME, 254:9–21.

VAJDOVA V, PRSLASH IKRYL R, PROS Z, KLIMA K, 1999. *The Effect of Rock Fabric on P-Waves Velocity Distribution in Amphibolites*. Phys Earth Planet In, 114:39–47.

INVESTIGATION ON DIFFERENT BEHAVIOR AND MECHANISM OF Ca(II) AND Fe(III) ADSORPTION ON SPODUMENE SURFACE

Fushun YU, Yuhua WANG, Jinming WANG, Zhenfu XIE

School of Minerals Processing and Bioengineering, Central South University, Changsha 410083, China, csuwangyh@163.com

Abstract: Behavior and mechanism of Ca^{2+} and Fe^{3+} adsorption on spodumene surface were investigated by micro flotation tests, zeta potential measurements, and density functional theory (DFT) calculation methods. The micro flotation tests showed that Ca^{2+} and Fe^{3+} activated the flotation of spodumene remarkably. However, the effect of Fe^{3+} was more significant than that of Ca^{2+}. Additionally, Fe^{3+} significantly changed the zeta potential of spodumene while Ca^{2+} showed a little change. Meanwhile, the calculated adsorption energy of Fe^{3+} on spodumene surface was much greater than that of Ca^{2+} indicating that Fe^{3+} is more apt to be adsorbed on spodumene surface than Ca^{2+}. The value of bond population in Ca-O illustrated that the bond of Ca-O consists of partial covalent proportion and some ionic component. On the contrary, the bond of Fe-O showed a relatively strong covalent property. The partial density of states (PDOS) of free Ca/Fe and the reacted O atom on spodumene (110) surface before and after the adsorption showed that Fe 3d orbital and O 2p orbital formed hybridization. The density of states (DOS) near the Fermi level of spodumene surface after adsorption with Fe^{3+} was much stronger than that with Ca^{2+}.

Keywords: spodumene surface, calcium ions, iron ions, adsorption mechanism, DFT calculation

Introduction

Spodumene $(LiAl(SiO_3)_2)$ is a typical pyroxene mineral consisting of lithium aluminium chain silicate containing approximately 8% Li_2O. It is the richest lithium bearing minerals in nature. In the past time, the major consumer of spodumene was the aluminum and ceramics industry (Wendt 1971; Nicholson 1978). However, a great number of applications of spodumene and lithium compounds are being developed rapidly in the battery and fuel cell industry (Landgrebe and Nelson 1976; Cooper and Borg 1976; Burns and Nelson 1978).

In the crystal model of spodumene, silicates tetrahedron $[SiO_3]^{2-}$ are represented by the chains of tetrahedron which are bound together laterally through the ionic bonding

with Li and Al in octahedral coordination. The irregular six coordination of Li^+ and Al^{3+} with oxygen are indicated by the octahedral linking the silicate tetrahedral chains (Bragg and Claringbull 1965). Aluminum is in octahedral coordination with six oxygen including two non-bridging basal oxygen and four apical oxygen. Lithium in spodumene coordinates with six oxygen which consist of two non-bridging basal oxygen, two bridging basal oxygen, and two apical oxygen (Zachariasen 1963; Bloss 1971; Kwang and Douglas 2003). Spodumene has a very pronounced cleavage plane (110), which results in typically lath-shaped particles on breaking (Krause 1968). The Si-O bond in spodumene crystallographic structure mainly possesses covalent component, the average length of which is 0.158 nm while the bond of Li-O and Al-O has obvious ionic features. The average bond length of Li-O is 0.221 nm, and for Al-O the value is 0.192 nm. The calculated ionic component of Li-O bond is 79.81%, the ionic component of Al-O bond is 64.30 %, according to the Pauling empirical formula (Chuanyao and Wanzhong 2001). Therefore, the bond strength of Li-O is relatively weak and disaggregation of spodumene would occur mainly alone the broken directions of Li-O bond. The exposed ions on the disaggregated surface of spodumene will be Li, a bit of Si and Al, which has been verified by the investigation results of X-ray photoelectron spectroscopy (XPS) (Chuanyao and Wanzhong 2001). The occurrence of ion exchange makes H^+ in the liquid replace the Li^+ on the mineral surface. H^+ ions are adsorbed on the oxygen districts of the mineral surface while the Si and Al districts adsorb OH^-. Consequently, a large quantity of hydroxyl are bonded on the surface of spodumene, which leads to the negative charge of spodumene surface on a wide range of pH value, in other words, the point of zero charge of spodumene is very low. This explains the reason of the floatability of spodumene is bad by using anionic collectors, e.g., sodium oleate, and turns good with cationic collectors, e.g. lauryl amine.

In the flotation practice of industry, spodumene is activated by the presence of Ca^{2+} and Fe^{3+} which derives from operating water and iron balls in the mill. Floatability of the activated spodumene enhances greatly as anionic collectors are adopted. In this paper, effects of Ca^{2+} and Fe^{3+} ions on the flotation behavior of spodumene were investigated by pure minerals micro-flotation tests. The zeta potential measurements were carried out to reveal the charge changing on the mineral surface. The adsorption of Ca^{2+} and Fe^{3+} ions on spodumene (110) surface was simulated by the density functional theory (DFT), which was an attempt to display the mechanisms of the interaction of Ca/ Fe and spodumene surface by means of microscopic quantum chemical calculations.

Materials and methods

Materials

A pegmatic spodumene ore was obtained from the Keketuohai Rare Metal Mine located in the Xinjiang Altay district. The hand-picked high-grade spodumene sample

was first crushed with hammer, then ground in a porcelain mill with agate balls in it, and finally screened with stainless steel screens. The sample was immersed in HCl of 3% concentration for 30 min to eliminate the impurities on the mineral surface. The processed sample was washed repeatedly using distilled water until the pH of the supernatant reached natural level. Subsequently, the -0.105+0.038 mm and -0.038 mm samples were filtered, vacuum-dried, and stored in glass bottles for the flotation tests and measurements.

Spodumene sample used in this study was a fairly pure crystal with a bit of Fe, Na, K, Ca, etc. as impurities as presented in Table 1.

Table 1. Chemical compositions of spodumene sample (%)

Li_2O	Al_2O_3	SiO_2	Fe_2O_3	Na_2O	K_2O	CaO	MnO	P_2O_5	BeO	Ta_2O_5	Nb_2O_5
7.81	25.99	62.74	0.54	0.312	0.156	0.36	0.127	0.16	0.028	0.019	0.028

The infrared spectrum of spodumene sample is shown in Fig. 1. The characteristic marked peaks in Fig. 1 meet well with the standard peaks of spodumene (Wenshi Peng and Gaokui Liu 1982), which also indicates that spodumene sample possesses a high purity.
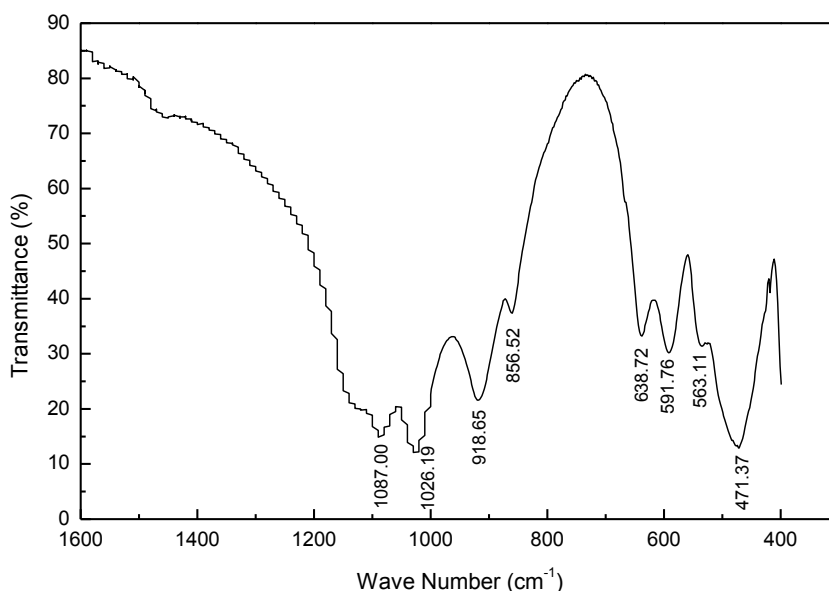
Fig. 1. Infrared spectra of spodumene sample

Sodium oleate of analytical quality was used as a collector for the micro-flotation tests while $FeCl_3 \cdot 6H_2O$ and $CaCl_2$ of analytical quality were used as activators. The solutions of HCl and NaOH were used to adjust the pH of the system.

Methods

Micro flotation tests

The micro flotation tests were performed in a laboratory flotation apparatus using -0.105+0.038 mm spodumene sample as a feed. At each test, 5 g of sample was placed in a plexiglass cell (40 cm^3), which was then filled with distilled water. The pH was adjusted to the target value before adding the individual flotation reagents. The sample was conditioned for 2 min after the reagent adding each, and the flotation time was kept as 5 min. All flotation tests were carried out at room temperature around 25 ^{o}C. The concentrate and tailings were filtered, dried, and weighed to calculate the flotation recovery of spodumene under various flotation conditions.

Zeta potential measurements

The zeta potentials of the sample were measured using a Brookhaven Zeta plus zeta meter (USA). The sample was ground to 0～5 μm in an agate mortar by hand. A 0.05 g of sample was placed in a 100 cm^3 breaker, stirred for 15 min with 80 cm^3 distilled water and reagents. Next, the pH was adjusted and measured. The results presented in this paper are the average of three independent measurements with a typical variation of ±2 mV. Repeated tests showed that the conditioning procedure was reasonable and credible.

Computational methods

The geometry optimizations were performed using Cambridge Serial Total Energy Package (CASTEP), developed by Payne et al. (1992), which is a first-principle pseudopotential method based on Density-Functional Theory (DFT). The DFT calculations employing plane wave (PW) basis sets and ultrasoft pseudopotentials were performed (Perdew and Wang 1992; Vanderbilt 1990). The exchange correlation functional used was the generalized gradient approximation (GGA) developed by Perdew, Burke and Ernzerhof (PBE) (Perdew and Burke 1996). The interactions between valence electrons and the ionic core were represented by ultrasoft pseudopotentials. The computations were based on spodumene structure where space group is $C2/c$ (15). The valence electron configurations considered in the study included Ca 3p6 4s2, Fe 3p6d6 4s2, O 2s2p4, Li 2s1, Al 3s2 p1, Si3s2 p2. The kinetic energy cut-off of 260 eV for the plane wave basis was used throughout the study, and the Brillouin zone was sampled using Monkhorst and Pack special k-points of a 1×2×3 grid for surface calculation (Monkhorst and Pack 1976), which shows that the cut-off energy and the k-point meshes are sufficient for the system. For self-consistent

electronic minimization, the Pulay Density Mixing method was employed with a convergence tolerance of $2.0 \cdot 10^{-6}$ eV/atom. The convergence criteria for structure optimization and energy calculation met the conditions of (a) an energy tolerance of $2 \cdot 10^{-5}$ eV/atom; (b) maximum force tolerance of 0.05 eV/Å; and (c) maximum displacement tolerance of 0.002 Å.

After testing the slab thickness and vacuum slab thickness, a $2 \times 2 \times 1$ perfect spodumene (110) surface using super-cell geometries with 3 atomic layers and 10 Å vacuum slab was modeled. The outermost atomic layer of the substrate was allowed to relax while the two bottommost atomic layers of the substrate were fixed to the bulk coordinates in the adsorption calculations. The optimizations of Ca and Fe atoms were calculated in a $10 \times 10 \times 10$ Å cubic cell and the optimizations were performed at the gamma point in the Brillouin zone. The optimized lattice parameters of perfect spodumene are $a=9.486$ Å, $b=8.237$ Å, $c=5.152$ Å, $\beta=110.74$ °, which are very close to the experimental values (Joan et al. 1969) of $a=9.449$ Å, $b=8.386$ Å, $c=5.213$ Å, $\beta=110.10°$. These values indicate that the calculated results agree well with experimental data.

Results and discussion

Results

Micro-flotation of spodumene

The micro-flotation tests were conducted to show flotation behavior of spodumene and the activation of Ca^{2+} and Fe^{3+} as a function of solution pH. Sodium oleate was used as a collector in these tests at the concentration of $7 \cdot 10^{-4}$ M. Calcium chloride and ferric chloride were used as an activator at the concentration of $1.2 \cdot 10^{-3}$ M and $1.5 \cdot 10^{-4}$ M, respectively. As seen from Fig. 2, the natural floatability of spodumene was poor, and the highest recovery was under 10% at the whole pH range. Ca^{2+} and Fe^{3+} activated the flotation of spodumene. In addition, the recovery reached to over 70% in a strong alkaline pH range when the mineral was activated with Ca^{2+}. On the contrary, the highest recovery of spodumene reached as high as 95% in the pH range of 7-9 after the activation with Fe^{3+}. It is interesting to note that the flotation recovery of spodumene activated by Fe^{3+} decreased largely in alkaline pH range of exceeding 9. The rational explanation is that the adsorption of Fe^{3+} ions on the surface of spodumene made negative ions easier to interact with the mineral surfaces. A competitive adsorption occurred between the anionic collectors and OH^- ions in the solution. At acidic and neutral pH values, the anionic collectors preferentially adsorbed on the activated mineral surface while in strong alkaline pH range the activity of OH^- ions was more than that of anionic collector. The OH^- ions prior adsorbed on the mineral surface caused a decrease in the flotation recovery in alkaline pH range. It is also noteworthy that the effective dosages of Ca^{2+} and Fe^{3+} are fairly different because the effective concentration of Fe^{3+} is nearly one-tenth of Ca^{2+}, which

implies the adsorption of Fe^{3+} on spodumene surface was more efficient than that of Ca^{2+}. Figures 3 and 4 illustrate this further.
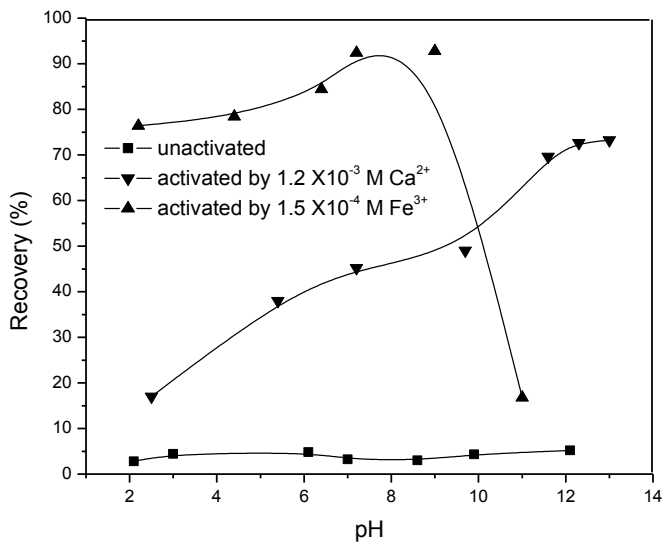
Fig. 2. Flotation recovery of spodumene as a function of pH
in $7 \cdot 10^{-4}$ M sodium oleate solution
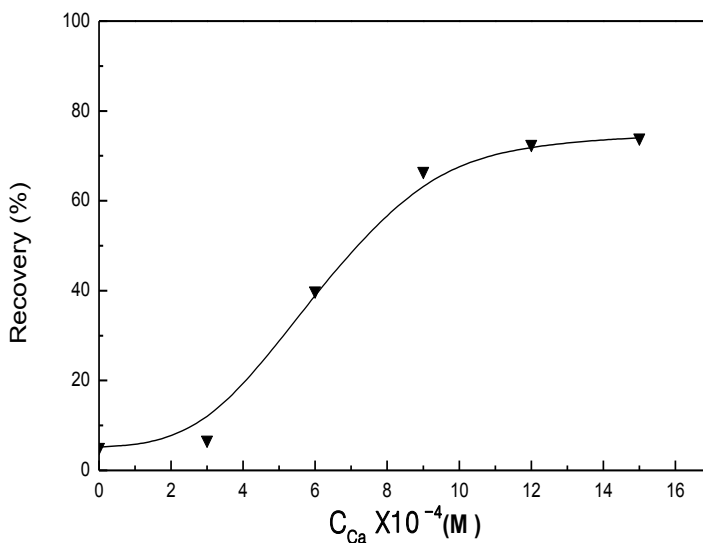
Fig. 3. Flotation recovery of spodumene as a function of Ca^{2+} dosage
in $7 \cdot 10^{-4}$ M sodium oleate solution at pH 12.3±0.15
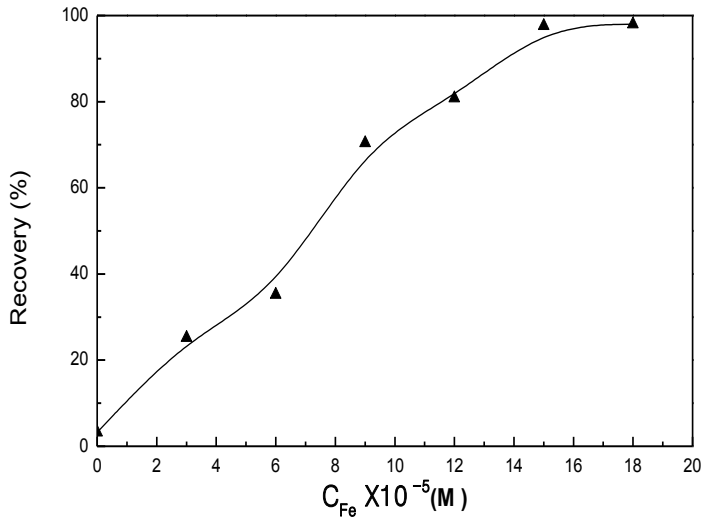
Fig. 4. Flotation recovery of spodumene as a function of Fe^{3+} dosage in $7 \cdot 10^{-4}$ M sodium oleate solution at pH7.5±0.15
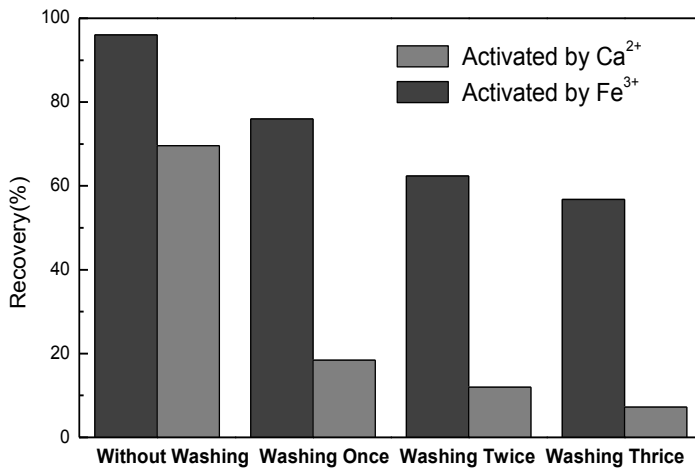
Fig. 5. Effect of washing on the flotation of spodumene activated by Ca^{2+}, Fe^{3+}

The washing tests were also carried out to investigate the effect of Ca^{2+} and Fe^{3+} adsorption on spodumene surface. In this test work, spodumene sample was first activated by Ca^{2+} or Fe^{3+}, then the pulp was precipitated for 1 min, and the upper liquid was decanted, then distilled water was added into the pulp, and agitated for 1 min. The pulp was also precipitated for 1 min, and the upper liquid was decanted again. This procedure is called 'washing once'. Repeating this procedure one gets 'washing twice', 'washing thrice', and so on. In the activation tests, calcium chloride

was used at a dosage of $1.2 \cdot 10^{-3}$ M at a pH of 12.3±0.15, and ferric chloride was used at a dosage of $1.5 \cdot 10^{-4}$ M at a pH of 7.5±0.15. After the washing process, the flotation was carried out using sodium oleate as collector at a dosage of $7 \cdot 10^{-4}$ M. The results are shown in Fig. 5.

It can be seen from Fig. 5 that flotation of spodumene decreased rapidly after the washing when it was activated by Ca^{2+}, the flotation recovery declined to a non-activated level after the washing thrice. In contrast, the influence of the washing on the floatability of spodumene was not so notable when the mineral was activated by Fe^{3+}. These results showed that the adsorption of Fe^{3+} on spodumene was more firm than that of Ca^{2+}.

Zeta potential measurement

The electrophoretic mobility of spodumene in absence and in the presence of Ca^{2+}/Fe^{3+} was measured, and the results are shown in Fig. 6. The zeta potential of spodumene follows the general trend of other silicate minerals. The point of zero charge (PZC) of spodumene was found to be pH of about 2.68. The surface charge of spodumene was negative at pH range of 3 to 12. This result is agreed with the results by other researchers (Fuerstenau and Pradip 2005). Figure 6 also shows the effect of Ca^{2+}/Fe^{3+} on the zeta potential of spodumene. The zeta potentials of spodumene slightly shifted towards positive values in the presence of Ca^{2+} and the pzc of spodumene shifted slightly to the alkaline pH value of about 3.3 as well. This indicates that the adsorbed Ca^{2+} ions
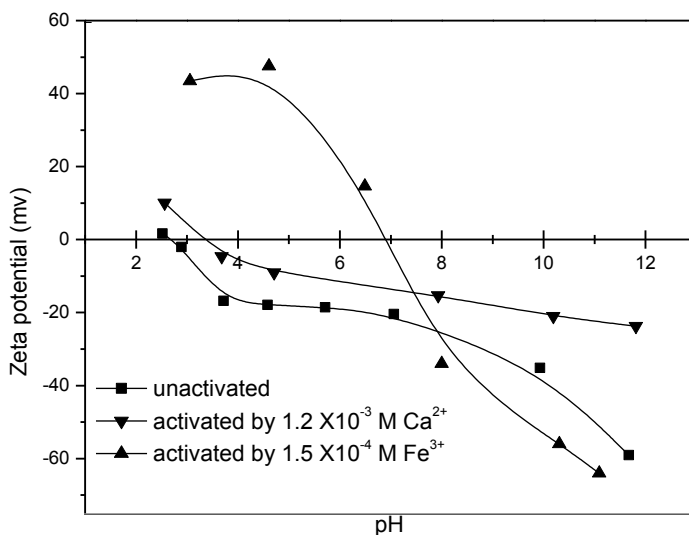
Fig. 6. Zeta potential of spodumene vs. pH in absence and in the presence of Ca^{2+}/Fe^{3+}

may lie closer to the outer stern planes of the electrical double layer of the mineral. It can be said that this adsorption is mainly by electrostatic attraction. However, the zeta potentials of spodumene showed a pronounced shift to positive values in presence of Fe^{3+}, the PZC of the sample shifted largely to alkaline pH value of about 6.9. It can be deduced that the adsorbed Fe^{3+} ions may lie on the inner stern planes of the electrical double layer. The adsorption can be attributed to chemical adsorption or specific adsorption. It is also worth noting that the zeta potentials of spodumene turn greatly to much negative values in alkaline pH range in the presence of Fe^{3+}. This phenomenon may be caused by the liable adsorption of OH^- ions on the surface of the mineral via the already adsorbed Fe^{3+} ions in alkaline pH values.

DFT calculation results

The electronic structure and properties of spodumene (110) surfaces and the super-cell model of spodumene (110) surface is shown in Fig. 7.
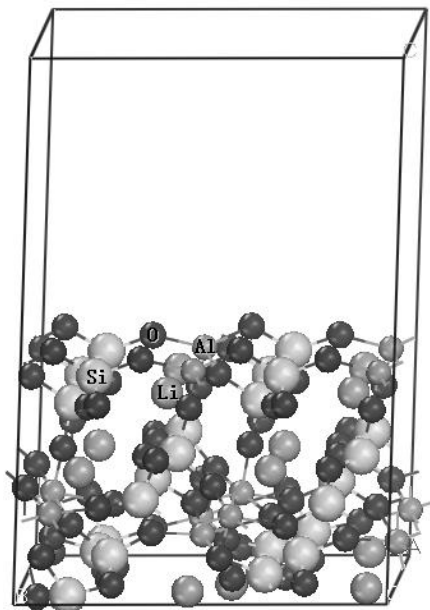
Fig. 7. The slab models of spodumene (110) surface

The analysis of density of states (DOS) could give an insight into the surface properties of the mineral at an electronic level. The partial DOS of the perfect spodumene (110) surface was calculated by the CASTEP module and the Fermi energy was set at 0 eV ($E_f = 0$) in the DOS curve is shown in Fig. 8. As seen in Fig. 8, there are mainly two kinds of oxygen: non-bridging basal oxygen and bridging basal oxygen, which were marked as O1 and O2 respectively. The valence bands of spodumene (110) surface are extended down to approximately -22 eV below the Fermi

level (E_f). The whole valence bands could be divided into two parts: the upper valence band between -10 eV and 0 eV and the deep level of valence band between -22 eV and -15.5 eV. The conduction band consists of the Al 3s and Al 3p orbital, together with the Li 2s orbital. It is known that electrons near the Fermi level have a strong activity and physical or chemical reactions usually occur around Fermi level. The reactivity of a certain atom can be judged from the composition of the DOS around the Fermi level. It can be seen that Li and Al has little contribution to the DOS around the Fermi level, which indicates the activity of Li and Al are weak, and it is hard to act as active sites for the absorption of anionic collectors, e.g., sodium oleate on spodumene surface. This conclusion is consistent with the previous flotation test results.
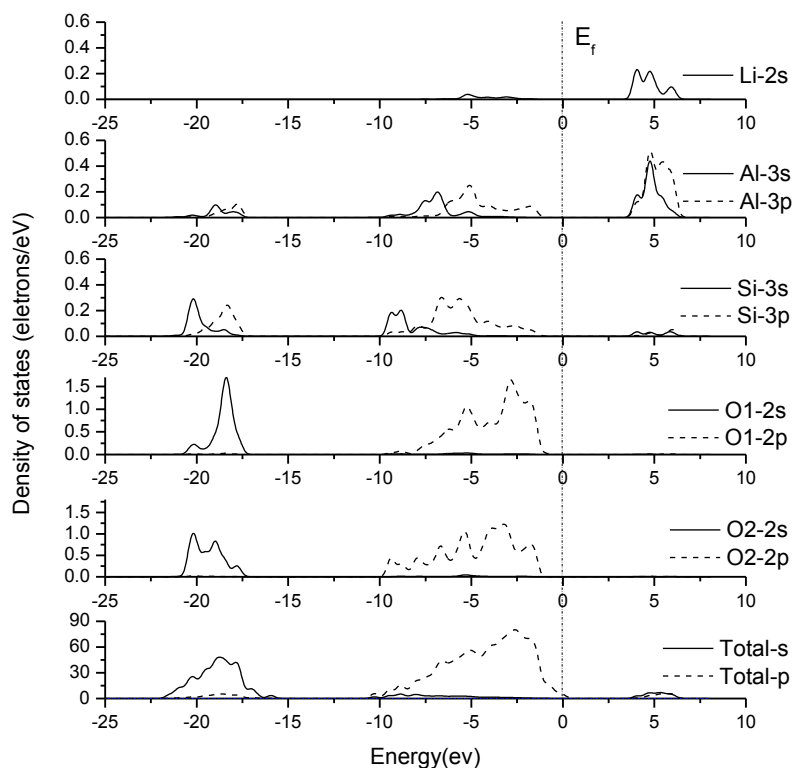
Fig. 8. PDOS of Li, Al, Si, O atoms on spodumene (110) surface

Adsorption of Ca/Fe on spodumene (110) surface

After the geometry optimization, Ca/Fe was positioned on spodumene (110) surface at various possible adsorption sites. For the feasibility and validity of calculation by CASTEP, Ca/Fe was set as uncharged. Particularly, Ca, Fe atoms were substituted for Ca^{2+}, Fe^{3+} respectively in the simulate adsorption calculation.

The adsorption energy of Ca or Fe atoms on different adsorption sites can be expressed by Eq. 1 (Kazume et al. 2008; Reuter and Scheffler 2001):

$$\Delta E = E_{\text{slab+adsorbate}} - E_{\text{slab}} - E_{\text{adsorbate}} \tag{1}$$

where $E_{\text{slab+adsorbate}}$ E_{slab} represent the total energies of spodumene model before and after Ca^{2+}/Fe^{3+} adsorption, respectively. $E_{\text{adsorbate}}$ represents the calculated energy of Ca/Fe atom and ΔE represents the adsorption energy of Ca/Fe atom. More negative value of ΔE indicates that the adsorption reaction of Ca^{2+}/Fe^{3+} occurs more readily.

Using a perfect spodumene (110) surface, various initial structures were generated for the adsorption of Ca/Fe atom on the O atoms. It was found that Ca/Fe atom was voluntarily close to the bridge site between two non-bridging basal O atoms after geometry optimization. This observation indicates that the bridge site between two non-bridging basal O atoms on spodumene (110) surface is the most stable position for the adsorption of Ca/Fe atom. The optimized configurations of the adsorption of Ca/Fe atom on spodumene surface are shown in Fig. 9.
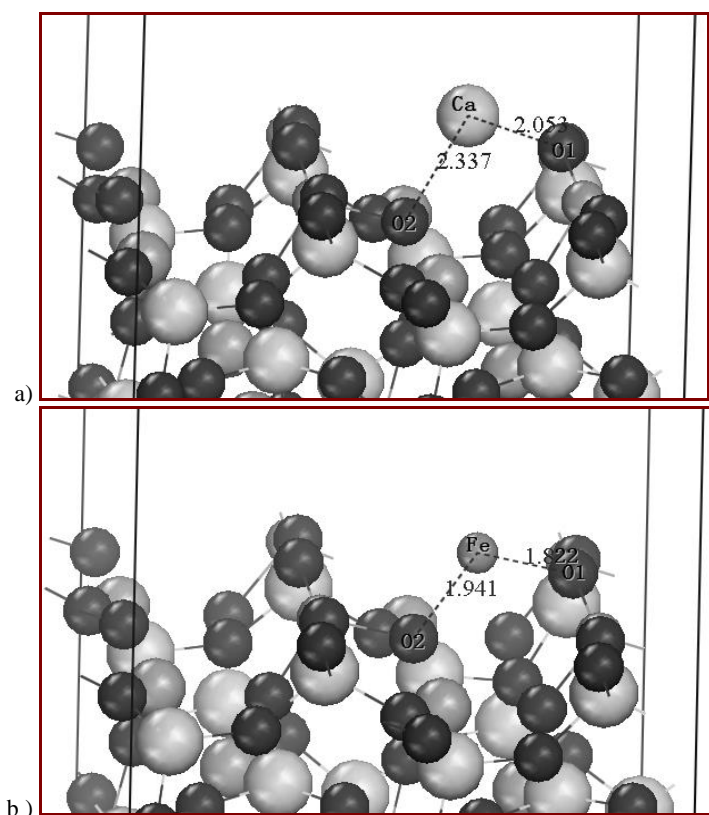
Fig. 9 (a) Adsorption of Ca atom on spodumene (110) surface
(b) Adsorption of Fe atom on spodumene (110) surface

As shown in Fig. 9, the bond lengths of Ca-O1 and Ca-O2 are 0.2053 nm (2.053 Å) and 0.2337 nm (2.337 Å), respectively. These values are bigger than that of Fe-O where 1.822 Å and 1.941 Å values were obtained for Fe-O1 and Fe-O2. Additionally, the adsorption energy of Fe on spodumene surface was calculated as -369.00 kJ/mol which is much greater than that of Ca as -187.14 kJ/mol. This illustrates further that Fe is more apt to be adsorbed on spodumene surface and the combination is more firm than Ca.

Bond population analysis schemes implemented in CASTEP were used to determine the strength of the bonds in the observed multi atomic complexes. Its values, on a scale from -1 to 1, represent a bonding state when the overlap population values are positive and anti-bonding state when the values are negative. The values with zero overlap indicate no significant interaction occurred between two atoms (Segall et al. 1996). Besides bonding states, covalence of the bond can also be determined since it is proportional to the overlap population. Therefore, the closer the bond population to 1, the more covalent the bond is between the atoms. Relative overlap population between two atoms would indicate the degree of covalence of the bond. Furthermore, iconicity of the bond can be indicated from the effective mulliken charges on the participating atoms. A Mulliken population analysis, while not giving realistic charges at individual lattice atom sites, is a valuable tool for comparing changes in charge between one lattice atom and another (Von et al. 2007). The calculated atomic populations in Ca, Fe and O, and the bond population in Ca-O and Fe-O bonds are presented in Table 2.

Table 2. Mulliken atomic population and charge on Ca, Fe, O and Mulliken bond population analysis

Mulliken Atom Population						Bond Population Analysis		
Atom	s	p	d	Total	Charge(e)	Bond	Bond population	Bond length(Å)
Ca	2.68	5.99	0.57	9.24	0.76	Ca-O1	0.09	2.053
Fe	0.46	0.05	7.12	7.63	0.37	Ca-O2	0.02	2.337
O1 (absorbed with Ca)	1.87	5.19	0	7.06	−1.06	Fe-O1	0.25	1.822
O2 (absorbed with Ca)	1.86	5.32	0	7.18	-1.18	Fe-O2	0.17	1.941
O1 (absorbed with Fe)	1.87	5.11	0	6.98	-0.98			
O2 (absorbed with Fe)	1.85	5.24	0	7.09	-1.09			

As seen in Table 2 that the bond populations in Ca-O1 and Ca-O2 are 0.09 and 0.02, respectively, indicating the covalent proportion in the bond of Ca-O1 and Ca-O2 are very weak. Moreover, the effective charge on Ca (+0.76 e) and O (-1.06/-1.18 e) shows the existence of ionic bonds between Ca atom and O atoms. On the contrary,

the bond populations in Fe-O1 and Fe-O2 are 0.25 and 0.17, respectively, indicating that a steady covalent bond of Fe-O is formed after the Fe atom adsorption on spodumene surface.

The analysis of density of states

The PDOS of free Ca/Fe and the reacted O atom on spodumene (110) surface before and after the adsorption are shown in Figs.10 and 11.
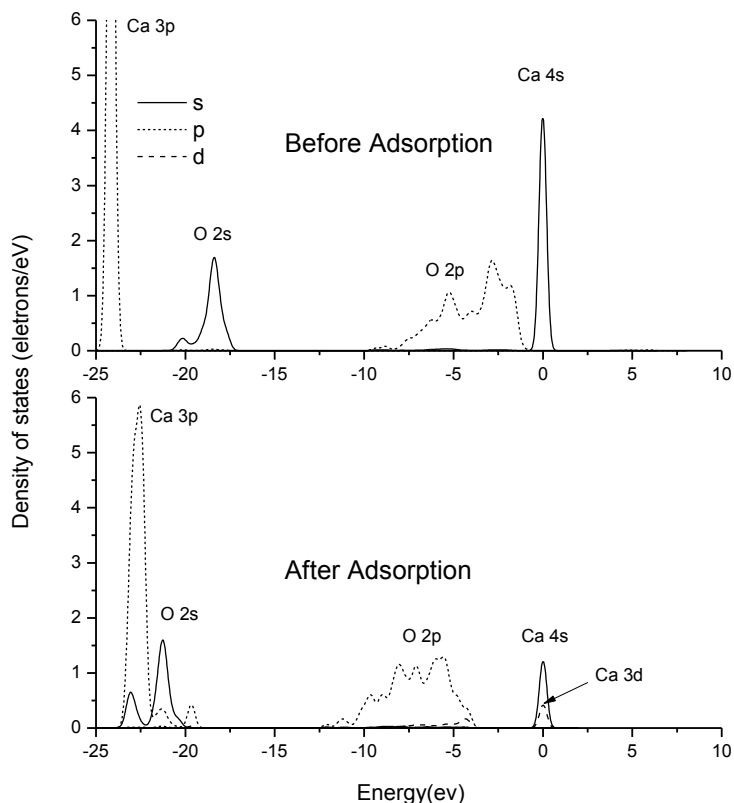
Fig. 10. PDOS of Ca and O on spodumene (110) surface
before and after the adsorption between them

For free Ca^{2+} before adsorption, the state of Ca 3p orbital is located at -23 eV to -25 eV; and the state of Ca 4s orbital lies at the Fermi level ($E_f = 0$), indicating a certain activity of the free Ca^{2+}. After the adsorption on spodumene surface, the state peak of Ca 4s orbital reduced largely, and the peak value of 3p state moved to the higher energy level. For the O atom on spodumene surface, which reacts with the Ca atom, the PDOS of the O 2s and O 2p shift to the lower energy level after the adsorption.
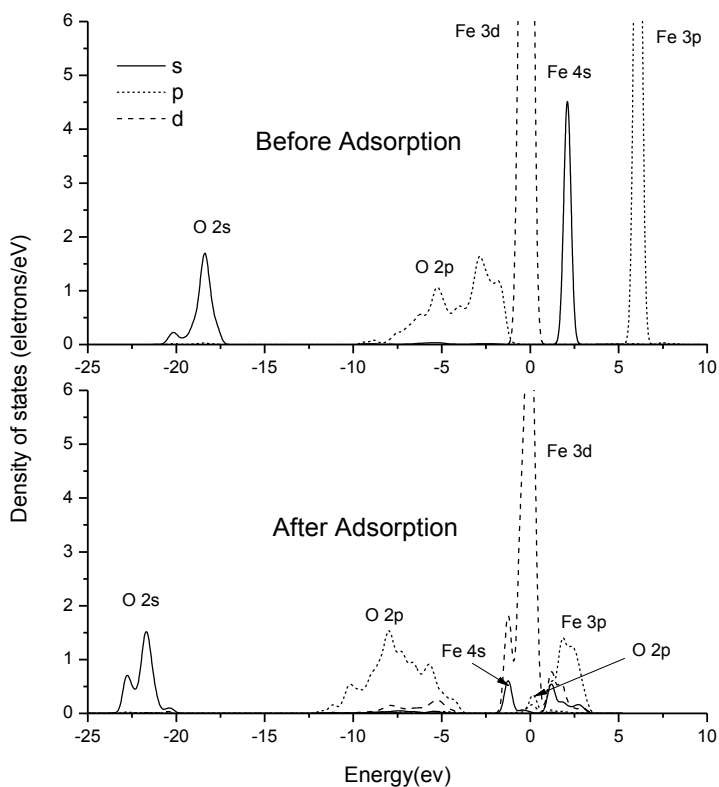
Fig. 11. PDOS of Fe and O on spodumene (110) surface
before and after the adsorption between them

The PDOS of free Fe atom consists of Fe 3d orbital at the Fermi level, Fe 4s and Fe 3p orbital at the conduction band. After adsorption on spodumene surface, the PDOS of Fe changes apparently. The state peak of Fe 3d orbital reduces. Meanwhile, the Fe 4s state moves to the valence band, and the peak of which deceases; the peak value of Fe 3p shifts from -6 eV to -2 eV. In addition, the peaks of Fe 3d orbital and O 2p orbital are overlapped at the Fermi level ($E_f = 0$), implying a strong hybridization between them has formed. In other words, the adsorption of Fe^{3+} on spodumene surface is a steady chemical adsorption, as confirmed from the analysis of Table 2.

It is worthy to note that the DOS near the Fermi level of spodumene surface after adsorption with Fe^{3+} is much stronger than that with Ca^{2+}, which implies that the activity of the adsorbed Fe^{3+} on the mineral surface is greater than that of Ca^{2+}. This conclusion is also verified by the previous flotation tests.

Conclusions

The micro flotation tests showed that the natural flotation of spodumene is poor in the presence of anionic collectors. The results showed that Ca^{2+} and Fe^{3+} can remarkably activate the flotation, among which, Fe^{3+} displayed a more superior performance compared to Ca^{2+}. The analysis of the PDOS of spodumene (110) surface indicated that the activities of Li and Al on spodumene surface were too weak to act as active sites for the absorption of anionic collectors. The adsorption energy of Fe^{3+} on spodumene surface was calculated as -369.00 kJ/mol which is much greater than that of Ca^{2+}, i.e. -187.14 kJ /mol. This showed that Fe^{3+} is more apt to be adsorbed on spodumene surface than Ca^{2+} is.

The bond population in Ca-O was very low which indicated that the covalent proportion of the bond was very weak and ionic component existed in Ca-O bond. The bond population in Fe-O was high, illustrating that a covalent bond of Fe-O is formed. The PDOS of free Ca/Fe and the reacted O atom on spodumene (110) surface before and after the adsorption showed that the peaks of Fe 3d orbital and O 2p orbital overlapped at the Fermi level ($E_f = 0$) after the adsorption, implying a strong hybridization between them is formed. The DOS near the Fermi level of spodumene surface implied that the activity of the adsorbed Fe^{3+} on the mineral surface was greater than that of Ca^{2+}.

Acknowledgements

References

BLOSS F.D., 1971, *Crystallography and Crystal Chemistry*, Holt, Rinehart and Winston, New York.

BRAGG L., CLARINGBULL G.F., 1965, *Crystal Structures of Minerals*, G. Bell and Sons, London.

BURNS L., NELSON P.A., 1978, *Advanced batteries for vehicle propulsion*, Technical Paper Series, vol. 780458, Society of Automative Engineers, Warrendale.

COOPER J.F., BORG I.Y., O'CONNEL, L.G., BEHRIN E., RUBIN B., WIESNER H.J., 1976, *Lithium requirements for electric vehicles using lithium–water–air batteries.* In: Vine, J.D. (Eds.), Lithium Resources and Requirements by the Year 2000, Geological Survey Professional Paper, vol. 1005, U.S. Government Printing Office, Washington, 9-12.

FUERSTENAU D W, PRADIP, 2005, *Zeta potentials in the flotation of oxide and silicate minerals*, Advances in Colloid and Interface Science, 114–115, 9-26.

JOAN R., CLARK, ET AL., 1969, Crystal-chemical characterization of clinopyroxenes based on eight new structure refinements, Mineral. Soc. Amer. Spec. Pap., 2, 31-50.

KAZUME N., MASAHITO Y., MASAYUKI H., Energetics of Mg and B adsorption on polar zinc oxide surfaces from first principles, Phys. Rev. B, 2008, 77, 35330-35336.

KRAUSE J. T., 1968, *Internal Friction of Twinned Spodumene*, J. Appl. Phys., 39, 44-72.

KWANG SOON MOON, DOUGLAS W. FUERSTENAU, 2003, Surface crystal chemistry in selective flotation of spodumene (LiAl[SiO3]2) from other aluminosilicates, Int. J. Miner. Process., 72, 11-24.

LANDGREBE A.A., NELSON P.A., 1976, *Battery research sponsored by the U.S. energy research and development administration*, In: Vine, J.D. (Eds.), Lithium Resources and Requirements by the Year 2000, Geological Survey Professional Paper, vol. 1005, U.S. Government Printing Office, Washington, 2-5.

MONKHORST H.J., PACK J.D., 1976, *Special points for Brillouin-zone integrations*, Physical Review B, 13, 5188-5192.

NICHOLSON P., 1978, *Past and future development of the market for lithium in the world aluminum industry*, The International Journal of Energy, 3, 235-413.

PAYNE M.C., TETER M.P., ALLAN D.C., ARIAS T.A., JOANNOPOULOS J.D., 1992, *Iterative minimization techniques for ab initio total energy calculation: molecular dynamics and conjugate gradients*. Reviews of Modern Physics, 64, 1045-1097.

PENG WENSHI, LIU GAOKUI, 1982, *Atlas of mineral infrared spectroscopy*, Science Press, Beijing.

PERDEW J.P., BURKE K., ERNZERHOF M., 1996, *Generalized gradient approximation made simple*, Physical Review Letter, 77, 3865-3868.

PERDEW J.P., WANG Y., 1992, *Accurate and simple analytic representation of the electron-gas correlation energy*, Physical Review B, 45, 13244-13249.

REUTER K., SCHEFFLER M., *Composition, structure, and stability of RuO2(110) as a function of oxygen pressure*, Phys. Rev. B, 2001, 65, 035406-035417.

SEGALL M D, SHAH R, PICKARD C J, PAYNE M C, 1996, *Population analysis in plane wave electronic structure calculations*, Molecular Physics, 89, 571-577.

SUN CHUANYAO, YIN WANZHONG, 2001, *Difference in Floatability of Spodumene and Aegirine from the Same Ore Body*, Journal of China University of Mining & Technology, Vol. 30, 531-536.

VANDERBILT D., 1990, *Soft self-consistent pseudopotentials in a generalized eigenvalue formalism*, Physical Review B, 41, 7892-7895.

VON OERTZEN G.U., SKINNER W.M., NESBITT H.W., PRATT A.R., BUCKLEY A.N., 2007, *Cu adsorption on pyrite (100): ab initio and spectroscopic studies*, Surface Science, 601, 5794-5799.

WENDT G., 1971, *Operating experiences with electrolytes containing lithium fluoride, Metallurgical Transactions*, 2, 155-161.

ZACHARIASEN W.H., 1963, *The crystal structure of monoclinic metaboric acid*, Acta Crystallographica, 16, 385-392.

Au-RE-TiO$_2$ NANOCOMPOSITES. SURFACE CHARACTERISTICS AND PHOTOACTIVITY

Anna KRUKOWSKA[*,**], Joanna RESZCZYNSKA[*], Adriana ZALESKA[*,**]

[*] Department of Chemical Technology, Gdansk University of Technology, 80-233 Gdansk, Poland
[**] Department of Environmental Engineering, University of Gdansk, 80-952 Gdansk, Poland,
adriana.zaleska@pg.gda.pl

Abstract: Photocatalysts based on TiO$_2$ co-doped with rare earth metal (RE) and gold nanoparticles have been prepared using a sol-gel method and followed by gold reduction. Specific surface areas of the modified photocatalysts were calculated by the Brunauer-Emmett-Teller method (BET). Diffuse reflectance spectra of the obtained photocatalysts were recorded with a UV-Vis spectrophotometer (DRS UV-Vis). The influence of the type of rare earth metal on photoactivity of Au-RE-TiO$_2$ nanocomposites in model reaction manifested by toluene photodegradation in a gas phase was investigated. The obtained results showed that photodegradation of toluene in the gas phase is possible over Au-RE-TiO$_2$ irradiated by UV or Vis light. The Au-RE-TiO$_2$ photocatalysts relative to undoped TiO$_2$, did not caused an increase of toluene degradation in the air under visible light. The samples doped with Er^{3+} or Pr^{3+} presented the highest activity in solar light among of Au-RE-TiO$_2$. It was observed that both metal dopants affected the surface area of TiO$_2$. The Au-RE-TiO$_2$ photocatalysts relative to undoped TiO$_2$ exhibited the absorption properties under Vis light.

Keywords: photocatalysis, modified TiO$_2$, rare earth metal, Au nanoparticles, toluene degradation

Introduction

Advanced oxidation with the aid of sunlight sensitive photocatalysts may prove to be a solution to environment pollution (Fujishima et al., 2000). Photochemical reactions catalyzed by TiO$_2$ were investigated in the degradation of dyes, hazardous substances in contaminated air and wastewater streams (Ibhadon and Fitzpatrick, 2013). Titanium dioxide is one of the most promising materials in heterogeneous photocatalytic oxidation due to its effectiveness, chemical stability, cheapness and availability. It also exhibits strong purifying power (Zaleska et al., 2007). Although TiO$_2$ has a large band gap of 3.3 eV in anatase crystalline phase, it can be activated only by UV light and from 3% to 5% of Vis light, limiting utilization of sunlight as the source in

photocatalytic reactions. The development of modified TiO_2 photocatalysts should exhibit high reactivity under Vis light in the main part of the solar spectrum (Parida et al., 2008). Modified TiO_2 photocatalysts with enhanced activity under sunlight can be prepared by doping metal elements such as rare earth metal (Parida and Sahu, 2008) or noble metal (Boyd et al., 2005; Zielinska-Jurek et al., 2011).

If a metal or non-metal is used as a doping agent for TiO_2, these energy levels can be incorporated into the band gap of TiO_2. A new energy levels can either accept electrons from the valence band or donate electrons to the conduction band. Owing to less energy separation between the new energy levels and the valence band or conduction band, visible light becomes energetic enough to facilitate the above mentioned electron transitions (Bingham and Daoud, 2010). Reducing the size of the band gap by introducing energy levels between the conduction band and valence band allowed TiO_2 to be active under visible light. This is the main idea of metal and non-metal doping.

Doping can be achieved through the sol-gel process, hydrothermal synthesis, electrospinning and magnetron sputtering (Diamandesceu et al., 2008; Yang et al., 2011). The sol-gel is one of the wet chemistry method used in non-metal or metal doping TiO_2. The wet chemistry methods usually involve hydrolysis of titanium precursor in a mixture of water and other reagents followed by heating (Chen and Mao, 2007). The benefits of sol-gel method are compositional control, homogeneity on the molecular level due to mixing liquid precursors and low preparation temperature. However, the influence of organic traces on the optical quality of the material might be noticeable. Furthermore, the traditional sol-gel techniques might not be applicable to complex-shaped surfaces (Kanarjov et al., 2008). It can be inferred that the sol-gel method conditions can allow for either lanthanide ions to form oxides dispersed on the exterior of the semiconductor or incorporation in the titania matrix (Su et al., 2004).

Noble metal nanoparticles (gold, silver, platinum, et cetera) were used to enhance photocatalytic activity of TiO_2 (Chuang and Chen, 2009). Gold nanoparticles possess ability to absorb visible light, due to a localized surface plasmon resonance (LSPR). The samples of Au-TiO_2 nanoparticles showed plasmon absorption bands at about 550 nm. The activity of Au-TiO_2 photocatalysis depends on the preparation method and on the size and shape of gold nanoparticles (Kowalska et al., 2010). The gold nanoparticles less than 5 nm in size are the most active catalysts (Haruta et al., 1993).

A rare earth metal (RE) was doped TiO_2 in an attempt to achieve visible light photocatalysis. The rare earth metal established complexation with RE-O-Ti bond on the inner sphere surface, which inhibited the transformation from anatase to rutile (Liu et al., 2012). The best photocatalytic properties in visible light were the TiO_2 doped with Nd^{3+} (Stengl et al, 2009), and Gd^{3+} (Xu et al., 2002) due to their the lowest band gap, particle size, highest surface area and pore volume. The RE-doped TiO_2 nanomaterials usually showed large surface area and high porosity. A larger surface area provided more surface active sites for the adsorption of reactants molecules,

which make the photocatalytic process more efficient (Hassan et al., 2012). Co-doping TiO$_2$ with different elements showed different absorption and photocatalytic properties to those doped individually (He et al., 2008).

In this paper, we present a novel approach for obtaining RE-doped TiO$_2$ loaded with Au nanoparticles. The influence of rare metal type (Ho, Nd, Er, Eu and Pr) on Au-TiO$_2$ surface properties and photoactivity in the gas phase reaction was investigated.

Experimental

Materials and instruments

Titanium isopropoxide (97%, Sigma Aldrich) with acetic acid (99 %, POCH S.A.) and ethanol (96 %, POCH S.A.) were used for the preparation of TiO$_2$ nanoparticles. The precursors of rare earth metal as salts: Ho(NO$_3$)$_3$·5H$_2$O, Nd(NO$_3$)$_3$·6H$_2$O, Er(NO$_3$)$_3$·5H$_2$O, Eu(NO$_3$)$_3$·5H$_2$O and Pr(NO$_3$)$_3$·6H$_2$O were provided from Sigma Aldrich. Hydrogen tetrachloroaurate (III) (99%, Sigma Aldrich) was used as the precursor for preparation gold nanoparticles. Ammonium hydroxide (25%, Sigma Aldrich) was exploited to adjust the pH above 8.5 of the solution. Sodium borohydride (99%, Sigma Aldrich) was used to reduce the gold nanoparticles. Deionized water was exploited for all the reactions and treatment processes.

Specific surface areas of the modified photocatalysts were determined by the Brunauer-Emmett-Teller method (BET). Nitrogen adsorption-desorption isotherms were measured at liquid nitrogen temperature (77 K) on a Micromeritics Gemini V, model 2365 PC. Prior to analysis, the samples were degassed at 200 ºC for 2 h.

Diffuse reflectance spectra (DRS) of the obtained photocatalysts were characterized using a UV-Vis spectrophotometer Thermo Evolution Nicolet, model 220 equipped with ISA 220 integrating sphere accessory. The UV-Vis DRS spectra were recorded in the range of 300–900 nm using sulfate barium as the reference standard.

Prepartion of Au-RE-TiO₂ photocatalysts

The preparation of Au-RE-TiO$_2$ photocatalysts is presented in a block diagram in Fig. 1. In the first step RE-modified TiO$_2$ was prepared using the sol-gel method. The sample of 15 cm^3 titanium isopropoxide was added to the mixture of 3 cm^3 acetic acid and 60 cm^3 ethanol. The sol was stirred for 10 min. Then rare earth nitrate was dissolved in 2 cm^3 water, added dropwise to the solution, and stirred for 2 h. The gel was dried at 80 ºC for 24 h to remove the solvents and then calcined in air at 400 ºC for 4 h at the heating rate of 2 ºC/min in an oven. Calcination is used to transform TiO$_2$ amorphous form to anatase or rutile crystal structure. Enhancing the photocatalytic activity of TiO$_2$ can be achieved by calcination at temperature of 400 °C allowing TiO$_2$ to receive anatase crystal structure. The temperature of anatase

TIP

CH$_3$COOH

C$_2$H$_5$OH

| MIXING |
| 25°C |

WATER SOLUTION RE(NO$_3$)$_3$

| MIXING |
| 25°C |

| DRYING |
| 80°C |

→ WATER, SOLVENT

| CALCINATION |
| 400°C |

→ WATER, SOLVENT, POLLUTION

HAuCl$_4$

| MIXING |
| 25°C |

NH$_4$OH

| ADJUSTMENT OF pH |

NaBH$_4$

| REDUCTION OF GOLD |

H$_2$O

| WASH IT OUT |

→ WASHINGS

| DRYING |
| 80°C |

Au-RE-TiO$_2$ PHOTOCATALYSTS
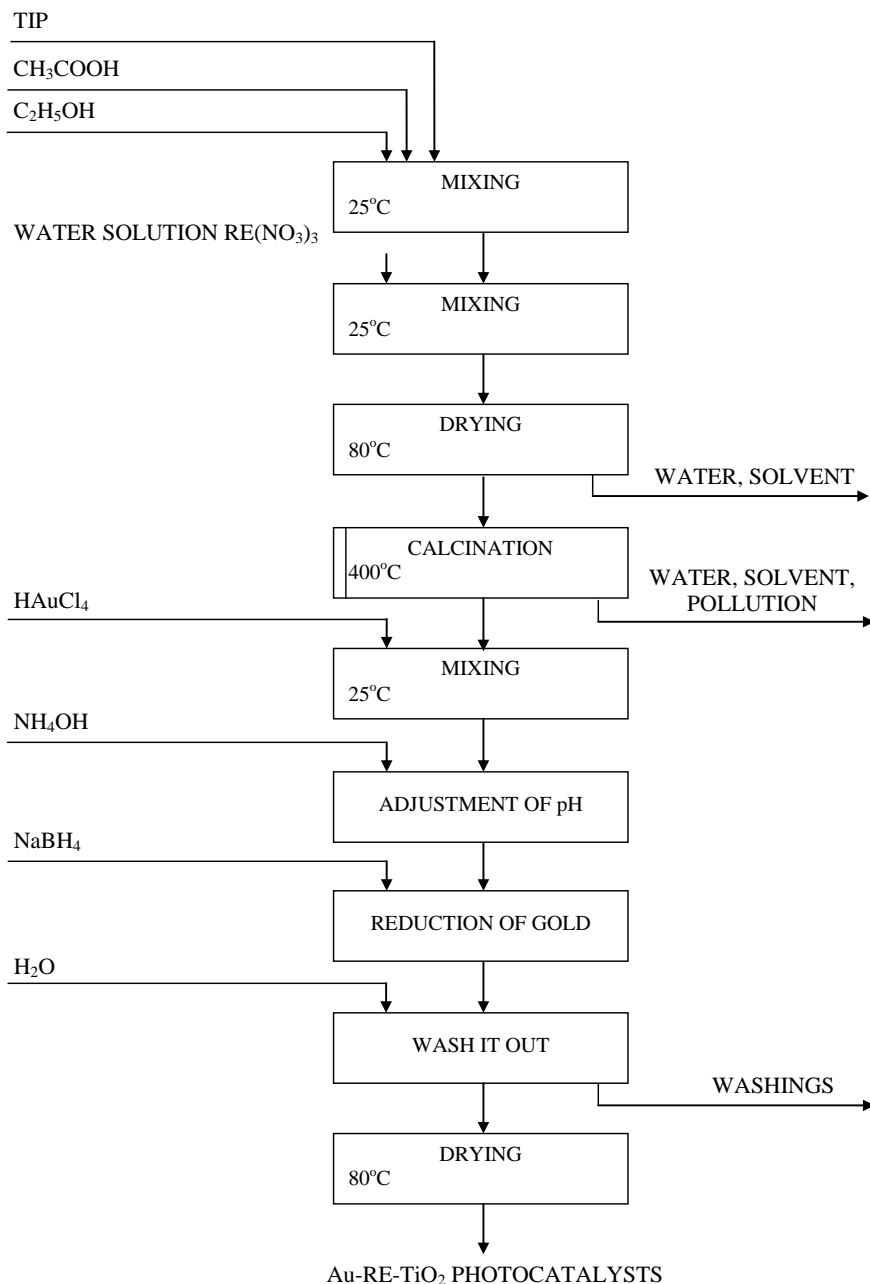
Fig. 1. Block diagram of preparation of Au-RE-TiO$_2$ photocatalysts

to rutile transformation is estimated to be over 500 ºC (Chen and Mao, 2007). The obtained sample was milled into powder. In the second step Au-modified RE-TiO$_2$

was prepared by the reduction method. Hydrogen tetrachloroaurate (III) as the gold precursor was added to water suspension of RE-TiO$_2$ powder. The pH 8.5 of dispersion was adjusted with 25% ammonium hydroxide. The gold nanoparticles were reduced by sodium borohydride. The solution turned from transparent to violet color due to reduction of Au ions. The gel was dried again at 80 ºC for 12 h. In modified TiO$_2$ the concentration of rare earth metal was permanently 0.5 mol.% and the concentration of gold nanoparticles were 1 or 2 mol % related to the concentration of TIP. Pure TiO$_2$ and Au-TiO$_2$ were prepared in the same way.

Measurements of photocatalytic activity

The photocatalytic activity of Au-RE-TiO$_2$ powders in visible light was estimated by a model photodegradation toluene in the air. Photochemical reactions were carried out in a custom-made photoreactor with replacements, two sets of 25 LED lamps in range UV light (wavelength 375 nm) or Vis light (wavelength 415 nm). Gases from the reactor were analyzed using an on-line gas chromatography, PerkinElmer, model Clarsus 500 (Nischk et al., 2014).

Results and discussion

Table 1 summarizes the measured BET surface area, total pore volume, pore diameter and photocatalytic activity results for TiO$_2$ co-doped with selected rare earth metal (holmium, neodymium, erbium, europium or praseodymium) and gold nanoparticles. The TiO$_2$ as a reference material has the lowest BET surface area and pore volume of about 115 m^2/g and 0.1 cm^3/g. The 2 % Au-0.5 % Pr-TiO$_2$ and 2 % Au-0.5 % Eu-TiO$_2$ have the highest surface area equal to about 139 m^2/g. For other Au-RE-TiO$_2$ samples containing from 1 to 2 mol % of gold and 0.5% rare earth metal the surface areas varied from 134 to 139 m^2/g. The 2% Au-0.5% Nd-TiO$_2$ had the lowest pore diameter of about 1.91 nm. The pure TiO$_2$ showed well-crystallized anatase structure. Despite having a higher BET surface area, Au-RE-TiO$_2$ have not caused an increase photocatalytic activity relative to undoped TiO$_2$. It could be considered that pore accessibility of TiO$_2$ is constrained by rare earth metals. On the other hand it might be a consequence of remaining carbon deposits on the nanocomposites, which came from titanium isopropoxide. Xu et al. (2002) reported that the rare earth metal salts can be changed into rare earth oxides during the calcinations process. Therefore, it can be inferred that the rare earth ions were dispersed on the surface of TiO$_2$ in the form of small clusters, which inhibit TiO$_2$ amorphous structure transform to the anatase crystal structure.

The light absorption properties of prepared Au-RE-TiO$_2$ photocatalysts, DRS UV-Vis absorption spectra in the range of 300-900 nm were investigated and the results are shown in Fig. 2. The spectrum of DRS UV-Vis showed that the undoped TiO$_2$ decreased by light reflection at a wavelength of about 380 nm, what proved that it

Table 1 Surface properties and photocatalytic activity of Au-RE-TiO$_2$ samples

Photocatalysts type	S$_{BET}$ (m^2/g)	Pore volume (cm^3/g)	Pore diameter (4V/S$_{BET}$) (nm)	Photocatalytic activity (%)	
				UV light	Vis light
2 % Au-0.5 % Ho-TiO$_2$	135	0.1	1.92	31	46
2 % Au-0.5 % Nd-TiO$_2$	137	0.1	1.91	38	47
2 % Au-0.5 % Er-TiO$_2$	137	0.1	1.95	63	99
2 % Au-0.5 % Eu-TiO$_2$	139	0.1	1.95	52	76
2 % Au-0.5 % Pr-TiO$_2$	139	0.1	1.95	44	99
1 % Au-0.5 % Pr-TiO$_2$	134	0.1	1.93	38	88
2 % Au-TiO$_2$	122	0.1	1.95	39	97
TiO$_2$	115	0.1	1.95	100	100

absorbs only UV light. Other photocatalysts Au-RE-TiO$_2$ had the highest absorption properties under Vis light in typical absorption peaks located at about 550 nm, which is characteristic for gold plasmon. The maximum absorbance under Vis light exhibited 2% Au-0.5% Pr-TiO$_2$. It proved that a redshift in the band gap transition of TiO$_2$ is due to the presence of the rare earth metal and gold. It could be achieved by a charge transfer transition between the lanthanide f electrons and the conduction or valence band of the TiO$_2$ (Hassan et al., 2012).
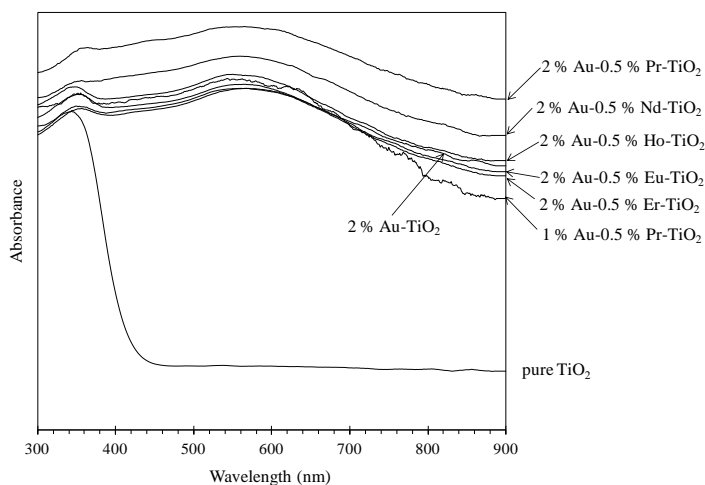
Fig. 2. Diffuse reflectance spectroscopy spectra of Au-RE-TiO$_2$ photocatalysts

The photocatalytic activity of Au-RE-TiO$_2$ photocatalysts was checked by measuring the decomposition of toluene in the air under UV or Vis light. The efficiency of toluene photodegradation after 30 min of exposure to visible light in the presence of Au-RE-TiO$_2$ photocatalysts is reported in Table 1 (efficiency of photodegradation toluene in one cycle of photocatalytic reaction) and Figs. 3 and 4

(efficiency of toluene photodegradation under UV or Vis light in four subsequent cycles). All photocatalysts based on TiO$_2$ co-doped with the rare earth metal and gold nanoparticles showed lower photocatalytic activity than pure TiO$_2$. The highest activity in solar light from among Au-RE-TiO$_2$ presented the sample doped with Er^{3+} or Pr^{3+} as the rare earth metal, which received about 50% efficiency degradation of toluene. It indicates that the presence of 2% Au-0.5% Er-TiO$_2$ and 2% Au-0.5% Pr-
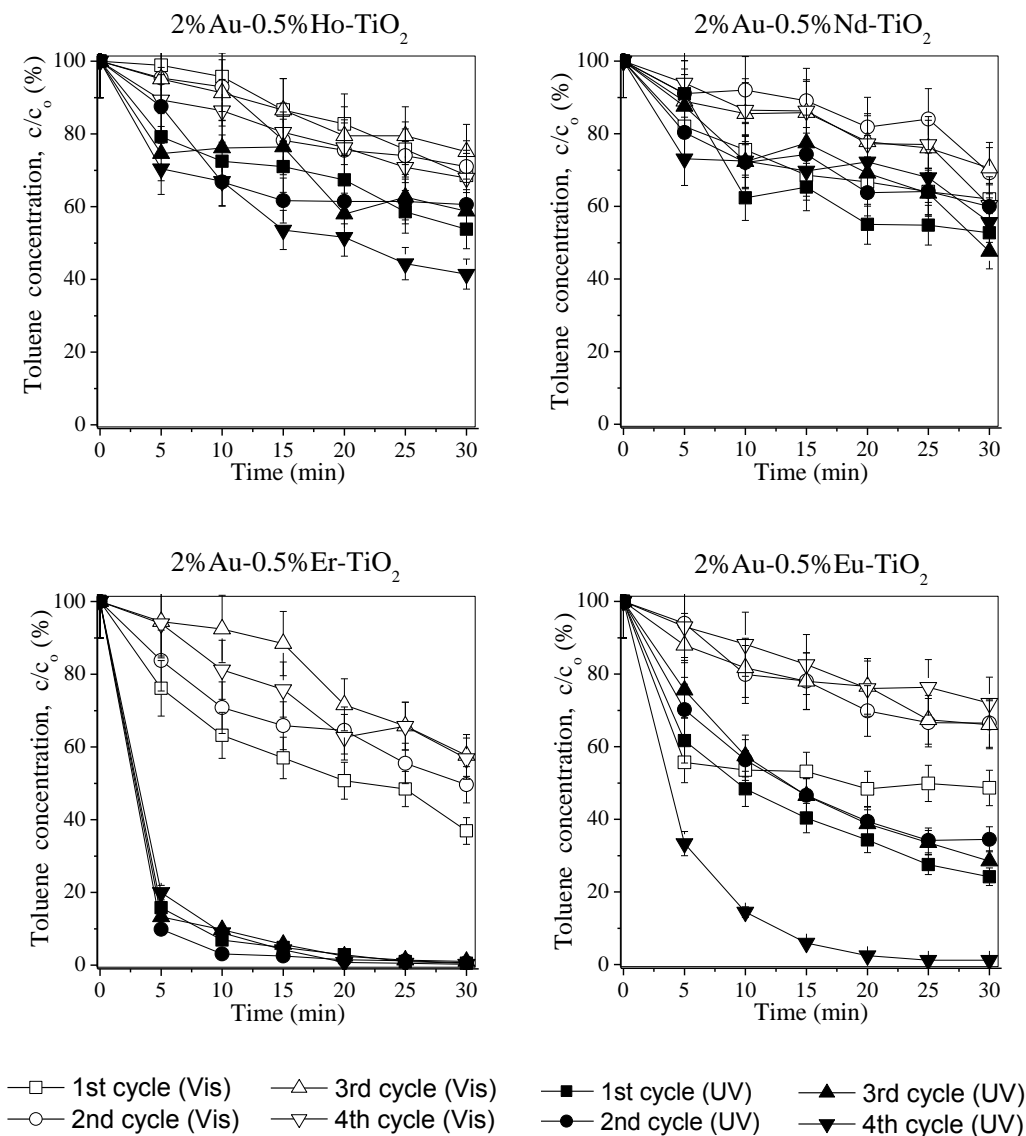
Fig. 3. Efficiency of toluene removal from gas phase in four subsequent cycles in the presence of Au-RE-TiO$_2$ under UV or Vis irradiation
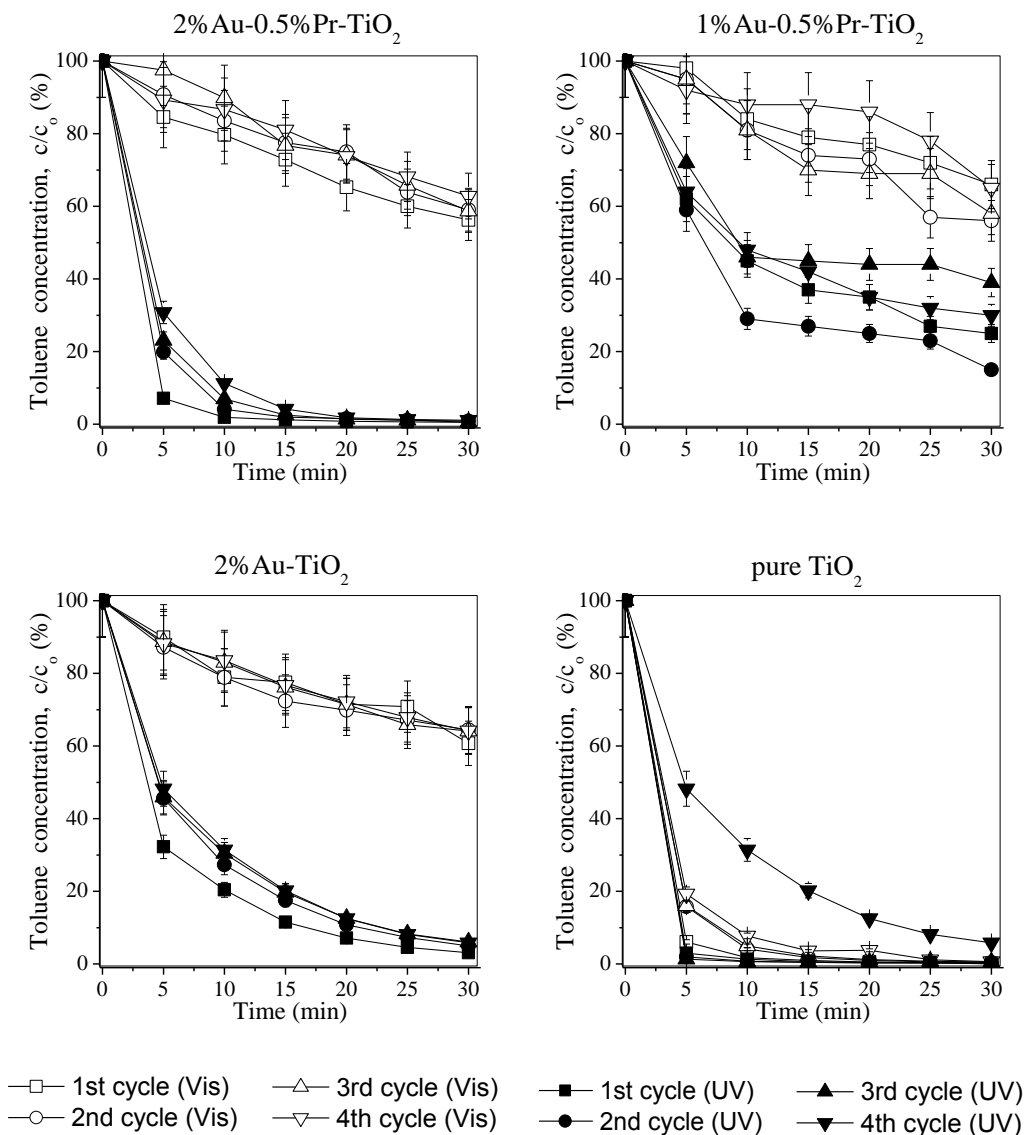
Fig. 4. Efficiency of toluene removal from gas phase in four subsequent cycles
in the presence of Au-Pr-TiO$_2$, Au-TiO$_2$ and pure TiO$_2$ under UV or Vis irradiation

TiO$_2$ were close for UV light activation to undoped TiO$_2$, where the maximum efficiency of toluene degradation was almost 100%. Other photocatalysts Au-RE-TiO$_2$ based on TiO$_2$ co-doped with Ho^{3+}, Ne^{3+} or Eu^{3+} and gold nanoparticles showed lower activity in UV and Vis light compared to unmodified TiO$_2$. As can be seen in the investigations that toluene photodegradation efficiency did not decrease in fourth

cycles photocatalytic reactions. The photocatalytic activity of Au-RE-TiO$_2$ under UV light is always higher than under Vis light due to physico-chemical properties of TiO$_2$ and energy of light. The curtailment amount of gold from 2% to 1% wt % in the photocatalysts Au-Pr-TiO$_2$ under UV light causes reduction in toluene photodegradation activity. To the best of our knowledge no one has previously reported photocatalyst activity of Au-RE-TiO$_2$ powders and it cannot be compared to results from literature data. Xu at el. (2002) reported that results of photodegradation conversion of nitrite over RE-doped TiO$_2$ (RE: Er^{3+}, Pr^{3+}, La^{3+}, Nd^{3+}, Ga^{3+}) and UV-Vis light show higher photoreactivity than pure TiO$_2$. Zielinska-Jurek et al. (2011) investigated impacts in decomposition of aqueous phenol solution by Au-TiO$_2$ and Au/Ag-TiO$_2$ powders under Vis light. The Au/Ag-TiO$_2$ samples show higher photocatalytic activity than Au-TiO$_2$.

Conclusion

Our preliminary results showed that photodegradation of toluene in the air over Au-RE-TiO$_2$ using light emitting diodes is possible. However, it was found that co-doping of TiO$_2$ with the rare earth metal and gold nanoparticles inhibited photoactivity both under UV and Vis irradiation compared to pure TiO$_2$. The highest activity under visible light from among Au-RE-TiO$_2$ was observed for the sample doped with Er^{3+} or Pr^{3+}. Reducing the concentration of gold precursor from 2 to 1 mol.% during synthesis, resulted in decrease of photocatalytic activity. It was observed that TiO$_2$ surface modification with the rare earth metal and gold nanoparticles caused decrease of the surface area of modified TiO$_2$ powders. Since plasmon band near 550 nm typical for gold nanoparticles was observed, the sol-gel preparation method followed by chemical reduction of gold ions did not enhance photoactivity under visible light. On the basis of the analysis, it is suggested that more detailed studies into the mechanism of Au-RE-TiO$_2$ photoexcitation is required.

References

BINGHAM S., DAOUD W.A., 2011*, Recent advances in making nano-sized TiO$_2$ visible-light active through rare-earth metal doping,* J. Mater. Chem. 21, 2041–2050.

BOYD, D., GOLUNSKI, S., HEARNE, G.R., MAGADZU, T., MALLICK, K., RAPHULU, M.C., VENUGOPAL, A., SCURRELL, M.S., *Reductive routes to stabilized nanogold and relation to catalysis by supported gold,* Appl. Catal. A 292, 76–81.

CHEN X., MAO S.S., 2007, *Titanium dioxide nanomaterials: Synthesis, properties, modifications and applications,* Chem. Rev. 107, 2891–2959.

CHUANG H.,CHEN D., 2009, *Fabrication and photocatalytic activities in visible and UV light regions of Ag-TiO₂ and NiAg-TiO₂ nanoparticles*, Nanotechnology 20, 105704.

DIAMANDESCU L., VASILIU F., TARABASANU-MIHAILA D., FEDER M., VLAICU A.M., TEODORESCU C.M., MACOVEI D., ENCULESCU I., PARVULESCU V., VASILE E., 2008, *Structural and photocatalytic properties of iron- and europium-doped TiO₂ nanoparticles obtained under hydrothermal conditions,* Mater. Chem. Phys. 112, 146–152.

FUJISHIMA A., RAO T.N., TRYK D.A., 2000, *Titanium dioxide photocatalysis*, J. Photochem. Photobiol., C: Photochem. Rev. 1, 1–21.

HARUTA M., TSUBOTA S., KOBAYASHI T., KAGEYAMA H., GENET M.J., DELMON B., *Low-temperature oxidation of CO over gold supported on TiO₂, α-Fe₂O₃, and Co₃O₄,* 1993, J. Catal. 144, 175–192.

HASSAN M.S., AMNA T., YANG O.-B., KIM H.-C., KHIL M.-S., 2012, *TiO₂ nanofibers doped with rare earth elements and their photocatalytic activity,* Ceram. Int. 38, 5925–5930.

HE Y.Q., XU X., SONG S., XIE L., TU J.J., CHEN J.M., YAN B., 2008, *A visible light-driven titanium dioxide photocatalyst codoped with lanthanum and iodine: an application in the degradation of oxalic acid*, J. Phys. Chem. C 112, 16431–16437.

IBHADON A.O., FITZPATRICK P., 2013, *Heterogeneous photocatalysis: recent advances and applications*, Catalysts 3, 189–218.

KANARJOV P., REEDO V., OJA ACIK I., MATISEN L., VOROBJOV A., KIISK V., KRUNKS M., SILDOS I., 2008, *Luminescent materials based on thin metal oxide films doped with rare earth ions,* Phys. Solid State 50, 1727–1730.

KOWALSKA E., MAHANEY O.O., ABE R., OHTANI B., 2010, *Visible-light-induced photocatalysis through surface plasmon excitation of gold on titania surfaces* Phys. Chem. Chem. Phys. 12, 2344–2355.

LIU H., YU L., CHEN W., LI Y., 2012, *The progress of TiO₂ nanocrystals doped with rare earth ions* J. Nano Mat. 2012, art. no. 235879.

NISCHK M., MAZIERSKI P., GAZDA M., ZALESKA A., 2014, *Ordered TiO₂ nanotubes: The effect of preparation parameters on the photocatalytic activity in air purification process*, App. Catal. B-Environ. 144, 674–685.

PARIDA K.M., MOHAPATRA P., MOMA J., JORDAAN W.A., SCURRELL M.S., 2008, *Effects of preparation methods on gold/titania catalysts for CO oxidation*, J. Mol. Catal. A: Chem. 288, 125–130.

PARIDA K.M., SAHU N., 2008, *Visible light induced photocatalytic activity of rare earth titania nanocomposites*, Appl. Catal. A 287, 151–158.

SU C., HONG B.Y., TSENG C.M., 2004, *Sol-gel preparation and photocatalysis of titanium dioxide,* Catal. Today 96, 119–126.

STENGL V., BAKARDJIEVA S., MURAFA N., 2009, *Preparation and photocatalytic activity of rare earth doped TiO₂ nanoparticles*, Mater. Chem. Phys. 114, 217–226.

XU A.W., GAO Y., LIU H.Q., 2002, *The preparation, characterization, and their photocatalytic activities of rare-earth-doped TiO₂ nanoparticles,* J. Catal. 207, 151–157.

YANG Z., ZHU K., SONG Z., ZHOU D., YIN Z., QIU J., 2011, *Preparation and upconversion emission properties of TiO₂: Yb, Er inverse opals,* Sol. Stat. Comm. 151, 364–367.

ZALESKA A., SOBCZAK J.W., GRABOWSKA E., HUPKA J., 2007*, Preparation and photocatalytic activity of boron-modified TiO₂ under UV and visible light*, Appl. Catal. B 78, 92–100.

ZIELINSKA-JUREK A., KOWALSKA E., SOBCZAK J., LISOWSKI W., OHATANI B., ZALESKA A., 2011, *Preparation and characterization of monometallic (Au) and bimetallic (Ag/Au) modified-titania photocatalysts activated by visible light*, Appl. Catal. B 101, 504–514.

APPLICATION OF DATABASE TECHNOLOGY TO ANALYSIS OF ROCK STRUCTURE IMAGES

Mariusz MLYNARCZUK, Magdalena LADNIAK, Adam PIORKOWSKI

AGH University of Science and Technology, Faculty of Geology, Geophysics and Environmental Protection, Department of Geoinformatics and Applied Computer Science, al. Mickiewicza 30, 30-059 Cracow, Poland, mlynar@agh.edu.pl

Abstract: The aim of this paper is to present a possibility to use information technology in the form of databases for processing and analyzing large image sets based on methods of image analysis and mathematical morphology. Up to now the use of databases in the image analysis process has been reduced to storing large amounts of data in the form of images. However, all transformations and analyses of such sets are made on user's computers. This requires a large data set (images) to be sent by network each time, and also it may possess the problems resulting from managing such large amounts of analyzed photographs on a computer. The proposed approach completely eliminates these problems by moving all transformations of image analysis to a database platform. For this purpose a set of routines realizing transformations of the image analysis and mathematical morphology was developed. The proposed approach allows the unification of the image processing and analysis area and advanced statistical analyses of obtained parameters describing geometrical sizes of objects on photographs. The proposed methodology was illustrated by practical realization of two measurement types for a simple structure of copper concentrate and more complicated, from the point of view of image analysis, structures such as dolomites from Redziny and Laskowa Gora and sandstones from Tumlin and Wisniowka.

Keywords: image processing, mathematical morphology, quantitative analysis of rocks, databases, user defined functions

Introduction

The idea and application of stereological analysis in mining and geology has been developing in Poland since 1960s. The initial, mainly theoretical ideas, dealt with the determination of estimators of total curvature for diameters of the objects under examination (Bodziony, 1965), determination of numerical and geometric characteristics of rock structures on an example of stereological analysis of selected rock structures. Examples of such studies are the analyses of sandstone from the Rudna mine (Bodziony et al., 1979) and Lower Silesian coals from the Thorez mine

(Kraj and Ratajczak, 1989), measurements of spatial orientation of granite discontinuities (Kraj and Kruszyński, 1981), stereological analysis of traces of intercrystalline and transcrystalline cracks observed on thin sections of various rock types (Bodziony et al, 1993). The beginnings of studies on automation of rock structure measurements by using methods of image analysis go back to the 1990s (Młynarczuk, 1999). The full automation of measurements is an unusually task due to high degree of complication and wide variety of rock structures (Mlynarczuk, 2008). However, the use of image analysis algorithms allows the studies to be quick. An important feature of such methods should be its universality and usability not only to individual photographs but also to large series of images.

In recent years, the development of network services changed the way of data gathering and accessing. They became no longer connected with a computer or data carrier but became the open-access resources stored on network servers as databases. These changes apply also to data in the form of digital images. Such tendency induces a change in approach to the way of analysis and interpretation of data contained in digital images. It seems that the image analysis systems being currently available on the market do not keep a pace with changes mentioned above, and still offer a possibility of the image analysis on a local computer only, while reducing the database support to importing a desired image from a database, performing appropriate operations on a local computer, and (possibly) writing the obtained result to the database. However, it seems that the feature of the automatic image analysis systems relies on integrating them with the database systems and developing such technologies that enable the image processing and analysis to be moved directly into the systems compatible with network servers. The approach consisting in leasing of the virtual disc and computational space for customers who want not only a store but also process large-sized data sets in a distributed and mobile way becomes more and more popular among commercial providers. The question of leasing of a dynamic number of computer resources is known in the literature under the name of cloud computing. In this paper, the results of efforts targeted at creation of a system enabling analysis of digital data in a homogenous database environment are presented. The proposed system allows database technologies and statistic software to be used to do complex analysis based on microscopic rock images. It was shown that such approach enables the determination not only simple parameters but also those requiring advanced and complicated algorithms of mathematical morphology to be programmed.

Experimental studies

The idea of data processing and analysis by using database technologies

Image processing is a well-known dynamically developing discipline. In this paper its basic issues will be omitted, because of available publications of other authors (Gonzalez and Wintz, 1987; Serra, 1982; Tadeusiewicz and Korohoda, 1997).

In computer image analysis the purpose of transformations is most often to gain a properly segmented binary image. To obtain such image a series of transformations of the input image is carried out. As a result a contrast imaging is obtained where objects are clearly distinguishable from the background. This result is a starting point of measurements of stereological analysis for all parameters under examination. A series of transformations of the input image are made, to get this image. These transformations are in most cases defined and programmed in the computer image analysis systems, and the role of the observer is to determine the correct sequence and the correct parameters with which these transformations are called. This approach is widespread to process and analyse the image. Despite its apparent simplicity, it requires a thorough knowledge of the field of image processing and analysis and also high programming skills. The analysis of some of the images is very difficult to implement and sometimes even impossible. In recent years, many works have been reported by stating effective methods of computer image analysis to describe the geometrical structures of rocks (Petruk, 1989; Serra and Mlynarczuk, 2000, Mlynarczuk, 2006; Obara, 2007). Many of the publications on this subject deal with typical problems of mineral processing (Petruk, 1988a; Petruk, 1988b; Petruk et al, 1991 Tasdemir, 2008; Tasdemir et al., 2011) including Mineral Liberation Analysis (MLA) or QEMSCAN® (Miller et al., 1982; Pirrie et al., 2004; Goodalll et al., 2005; Fandrich et al., 2007). The authors of this paper are aware that the proposed method in comparison to MLA can be considered as less effective, but their intention was not to present a substitute for commonly used image analysis softwares, but to present an alternative, easily extensible methodology for image exploration of very large data sets. Literature on this subject is limited to description of the image processing only on the local computers and using images in the computer local memory or imported from databases. The authors of this paper believe that the future of image analysis involves the calculation of the total transfer of database servers. However, the desktop computers (in the form of desktops, laptops, tablets, smartphones etc.) will be used only to manage the calculations and to review the obtained results.

The idea of data processing and analysis by using database technologies

The database in the context of this paper is understood as a data set in the form of digital images gathered according to the rules of a specialized computer program referred to as database management system (DBMS). The database management systems is necessary for any course in the database systems or file organization (Ullman, 1985; Batini et al., 1992; Ramakrishnan and Gehrke, 2000). The detailed description of the structure and performance issues of the proposed system is available in literature (Ladniak et al., 2013a; Ladniak et al., 2013b). As mentioned above, the database environments were used so far mainly as containers of large amounts of data – e.g. images. By moving the problem of image processing and analysis directly to the database servers, that are fully compatible with network servers it will be possible to increase mobility, widen the range of application, make workspace accessible for other

users without intervention in a complicated catalogue structure. The realization of such approaches enable also considerable reduction in the number of necessary programs used for the full analysis of two-dimensional (2D) data.

The use of the mechanism of the user defined functions in the database environment gives the user complete freedom in creating his/her own image processing operations and algorithms, including advanced ones. These algorithms were created by the authors for the purpose of this study. The absolute freedom in designing a database schema should be here emphasized. The stored images can be taken out by DMBS for user's request, processed and the results can be placed into a result table. Any number of operations can be involved each time in processing. This may be either a single operation that builds a complex algorithm or a set of cyclic image processing operations. Any number of input images can be processed. In addition, it is possible to write images being partial solutions in the database. The mechanisms used allows easy reference also to these images what is of the importance to the creation process and verification of proper operation of new image processing algorithms. Information flow and schematic context of analysis for the presented example is given in Fig. 1.
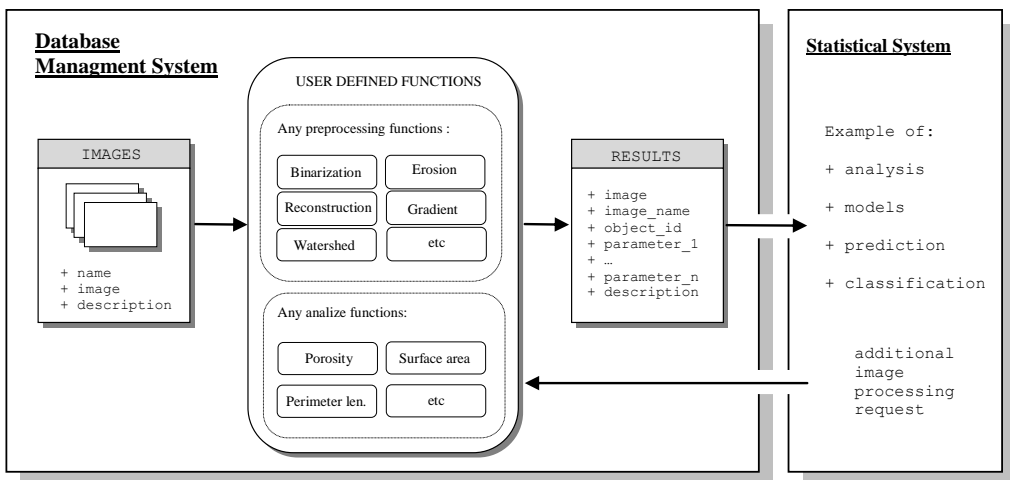
Fig. 1. Proposed schematic process information using database technology and statistical tools

The application of the proposed solution enables construction of knowledge base of very large number of parameters. This can be used in the next step in the statistical data analysis. There are many tools for the whole process of converting data into usable knowledge. In a study described here a Waikato environment for knowledge analysis (Weka) was used. This is an open source software under the general public license (Chuchro and Piorkowski, 2010). The possibility of direct communication with a database system and graphic presentation of data were utilized in this software. Thanks to provided communication with a database user's request for image

processing is sent directly by doing the queries of a structured query language (SQL). In practice, it indicates a capability to run image analysis routines directly from a statistical tool (for instance Statistica software), when the user sees a potential need for an additional analysis.

Realization of simple morphological transformations to retrieve information on grain size in copper concentrate

The described measuring methodology was implemented in detection of well contrasted grains in copper concentrate. The material was taken from the ore enrichment process in dense liquids. The grains obtained in this process were drowned in a glue and photographed by using an optical microscope at magnification 200x (Fig. 2a). In total 150 photographs of this preparation were taken for purposes of this study. For object detection purposes the information on the pixel grey levels for individual RGB colour components was used. The top-hat operation enabling the image background equalization was carried out. In the picture in Fig. 2a there are also pyrite particles (in yellow colors). They were excluded from the calculations. The individual color channels were then binearized. To remove measuring noise the morphological filtering, opening by reconstruction was performed. These operations allow to obtain the correctly segmented binary images (Fig. 2b).

a)   b)
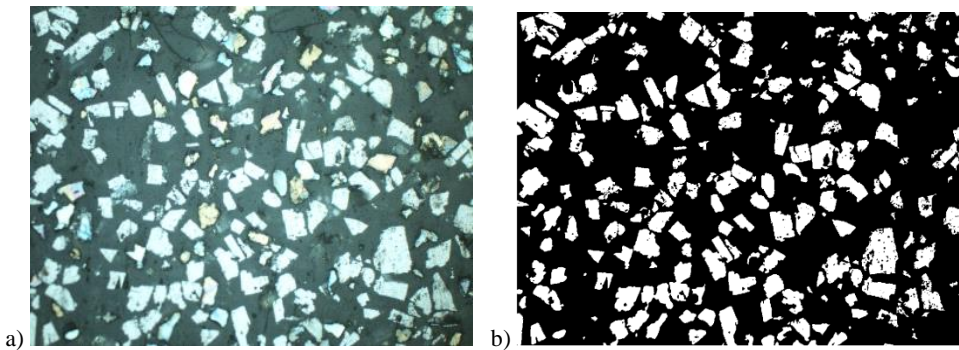
Fig. 2. Sample image of copper concentrate (a) and the result of its binarization (b)

In total 47,267 copper grains were selected in the analysed photographs. The following parameters set were used to describe them.

- Surface area was calculated by summing all pixels within the object and multiplying by the calibration factor (this value depends on the magnification of optical microscope and for copper concentrate photographs is 0.82).
- Average object chord length was calculated using the average length of the intersection between the segmented image and the regular set of horizontal/vertical lines.
- To determine approximate length of object perimeters the eroded object was subtracted from the original one.

- Volume diameter (equivalent) *d*, that is the diameter of a sphere having the same volume as the grain under consideration (Drzymala, 2009) was calculated by using the mathematical formula (for 2D images):

$$d = 2\sqrt{\frac{S}{\pi}}$$

where *S* is the surface area of a grain, π = 3.14.

The results are given in Table 1 and the histograms for chosen parameters are shown in Fig. 3. In fact, it is possible to measure a much larger set of object parameters.

Table 1. Values of basic statistics of copper concentrate parameters

	Surface area μm^2	Chord length μm	Perimeter length μm	Equivalent spherical diameter μm
Mean	482	11.14	130	20.74
Std-Dev	579	7.01	112	13.58
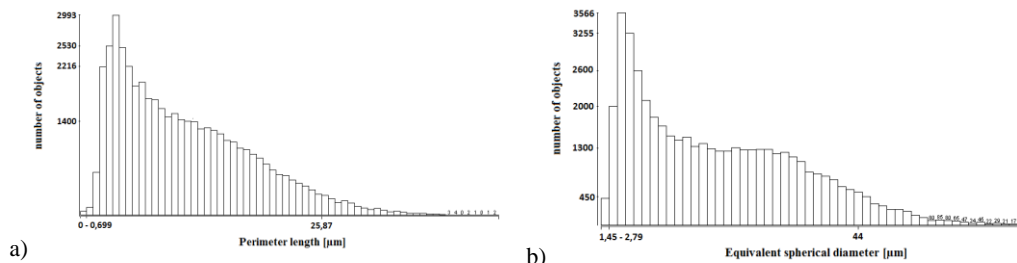
Fig. 3. Histograms of perimeter length (a) and equivalent spherical diameter (b) for copper concentrate – graphical visualization in Weka

Algorithm for grain segmentation in thin sections

At the next stage of this study it was decided to check measuring capabilities of the proposed database system on the significantly more complex structures. There following rocks were selected: dolomite from Redziny (hereinafter referred to as DZR), quartzite from Wisniowka (KZW), dolomite from Laskowa Gora (DZLG) and sandstone from Tumlin (PZT). For each of the rocks the photographs of 150 randomly distributed measuring fields were taken under optical microscope equipped with a specialized CCD camera (Mlynarczuk, 2008) at magnification 100x (see Fig. 4).
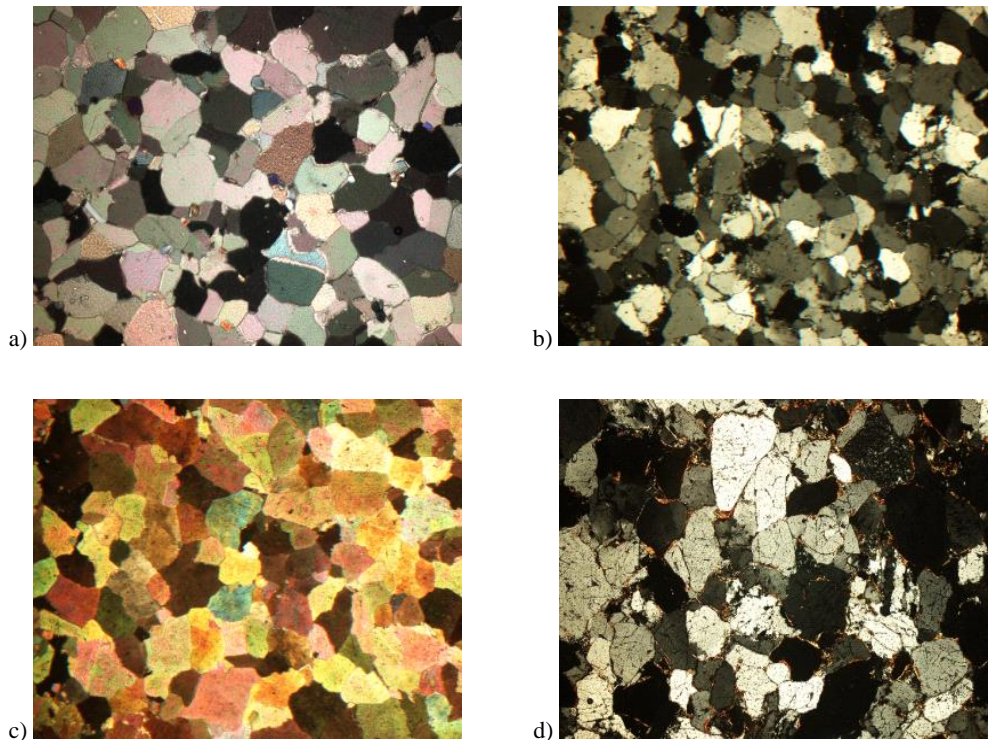
Fig. 4. Sample images of dolomite from Redziny (a), quartzite from Wisniowka (b),
dolomite from Laskowa Gora (c) and sandstone from Tumlin (d)

To analyse grain sizes in rocks under examination, the advanced algorithm described by Mlynarczuk (2008) was employed (Fig. 5). A method of grain size segmentation based on the watershed transformations was proposed in this algorithm. The main idea is to find such input image transformation to obtain two output images: masks (marked MASK in Fig. 5) and marker image (denoted MARKER in Fig. 5). The mask is created as the maximum gradients of the individual RGB channels of an input image under investigation. The marker image (much more difficult to obtain) is determined on the basis of opening by dynamics of grey levels followed by binearization and opening by reconstruction. The dynamics parameters are the variables in this algorithm and are different for each of rocks under examination. The detailed algorithm used in application of the described procedure is presented schematically in Fig. 5. It should be noted that for the PZT additional photographs taken with a polarizer were analyzed and they were used as a basis for getting information on binder location in the examined images. An example of the result of segmentation for the selected DZR photograph is presented in Fig. 6. Such images

were then used for further measurements describing the size of individual minerals forming rock.
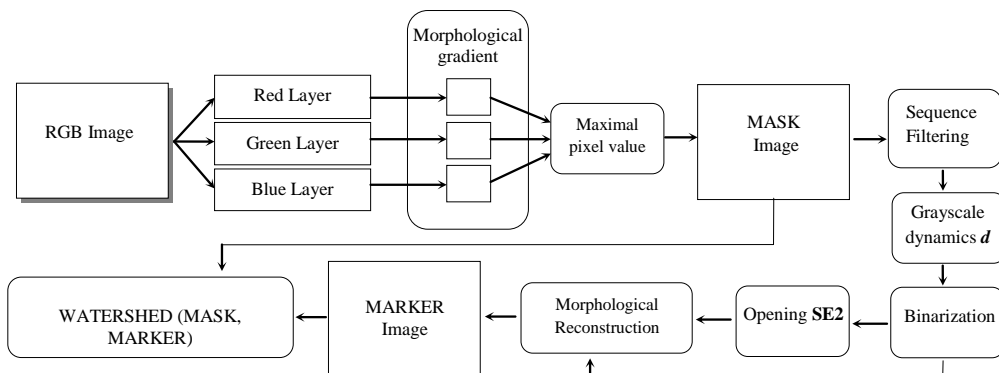
Fig. 5. Diagram of algorithm for grain segmentation
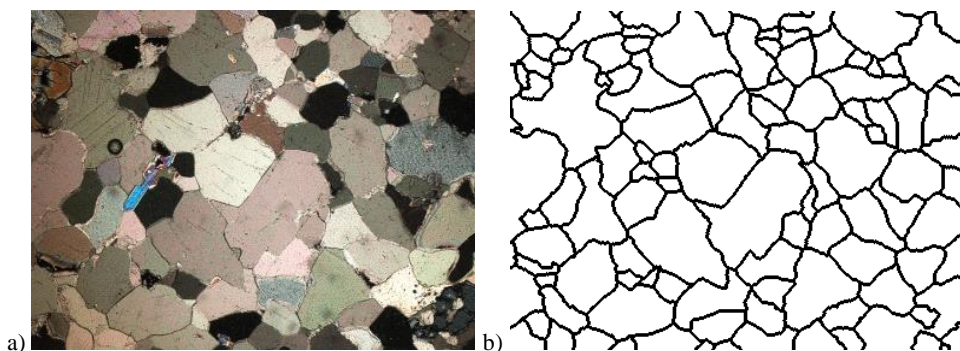
Fig. 6. Image of DZR (a) and the result of its segmentation (b)

Analysis results

The measurements of dynamic parameters of grey levels and size were made for each grain identified with the described algorithm. A set of 600 photographs was used. As a result, a very large knowledge set related to basic graining geometry of rocks under examination is obtained. The following amounts of grains were selected: 14,800 dolomite grains from DZR, 8,795 dolomite grains from DZLG, 18,539 quartzite grains from KZW and 12,588 quartzite grains from PZT. All measurements were made automatically by using the database technologies (Table 2). The user was required only to parameterize a request for type and range of computations to be done. The histograms of individual equivalent spherical parameters and values of basic statistics are shown in Fig. 7.

Table 2. Values of basic statistics of DZR, DZLG, KZW, PZT parameters

	Rock	Surface area μm²	Chord length μm	Perimeter length μm	Equivalent spherical diameter μm
Mean	DZR	40044	126.92	896.36	193.52
	DZLG	67582	178.44	1170.85	265.37
	KZW	31647	123.62	848.06	187.23
	PZT	47470	130.60	934.73	198.71
Std-Dev	DZR	69402	72.53	686.20	116.53
	DZLG	61474	87.67	670.33	125.01
	KZW	30217	46.86	849.06	72.39
	PZT	99538	84.23	922.99	144.77
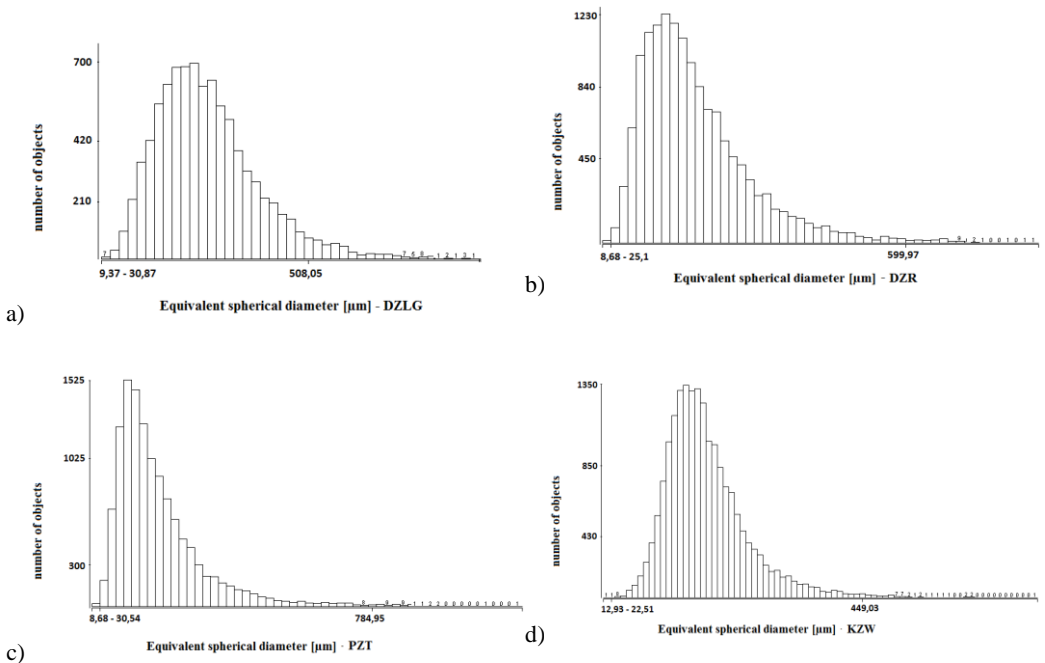
Fig 7. Histograms of individual equivalent spherical diameter for (a) DZLG, (b) DZR, (c) PZT and (d) KZW, graphical visualization in Weka

Conclusions

In this paper, the possibilities of extending database systems using the methods of image analysis and mathematical morphology were presented. Therefore, the authors of this paper proposed a system that offers storage and analysis of raster images on the database side, while providing possibility for easy exploration of such data by using a common statistical software. The Authors' intention was not to present a substitute for the commonly used image analysis software, but to present an alternative

methodology for exploration of very large data sets, and perhaps in the future, construction of fully automatic systems capable to learn and recognize the examined rock structures. The idea of the presented system allows the application of database technologies and statistical software not only for simple strictly defined transformations, but also for highly complicated authorial algorithms retrieving information contained in the microscopic images of rocks. The presented studies demonstrated suitability of the proposed methodology.

Acknowledgement

References

BATINI C., CERI S., NAVATHE S.B., 1992, *Conceptual database design: an Entity-relationship approach,*. Redwood City: Benjamin/Cummings.

BODZIONY J., 1965, *On Certain Indices Characterizing the Geometric Structure of Rocks*, Bulletin de l'Academie Polonaise des Sciences, 8, 9.

BODZIONY J., KRAJ W., PINDEL Z., RATAJCZAK T., WILCZYŃSKI J., 1979, *Analiza stereologiczna zespołu minerałów miedzionośnych białego spągowca*, Archiwum Górnictwa, 24.

BODZIONY J., MŁYNARCZUK M., RATAJCZAK T., 1993, *Identification of trans-and intercrystalline image of the fracture surfaces of rock specimens*, Acta Stereol, 12, 2.

CHUCHRO M., PIÓRKOWSKI A., 2010, *Methods and tools for data mining of intensity variability inlet to municipal wastewater treatment plant, Studia Informatica*, 31, no 2B, 347–358.

DRZYMALA J., 2009, *Podstawy mineralurgii*. Oficyna Wyd. Politechniki Wrocławskiej.

FANDRICH R., et al., 2007, *Modern SEM-based mineral liberation analysis*. International Journal of Mineral Processing, 84, 310–320.

GONZALEZ RC., WINTZ P., 1987, *Digital Image Processing*, Addison Wesley.

GOODALL W. R., SCALES P. J., BUTCHER A. R., 2005, *The use of QEMSCAN and diagnostic leaching in the characterisation of visible gold in complex ores*, Minerals Engineering, 18, 877–886.

KRAJ W., RATAJCZAK T., 1989, *Zastosowanie funkcji kowariancji do scharakteryzowania struktury węgla dolnośląskiego*, Archiwum Górnictwa, 34.

KRAJ W., KRUSZYŃSKI M., 1981, *Wyznaczanie orientacji przestrzennej nieciągłości w skale na przykładzie granitu strzegomskiego*. Archiwum Górnictwa 26(3).

LADNIAK M., PIORKOWSKI A., MŁYNARCZUK M., 2013a, *Structure of systems for data exploration for raster images*, Studia Informatica, vol. 34, no 2B (112), 7–20.

LADNIAK M., PIORKOWSKI A., MŁYNARCZUK M., 2013b, *The Data Exploration System for Image Processing Based on Server-Side Operations,* Lecture Notes in Computer Sciences 8104, 156–164.

MILLER P.R., REID A. F., ZUIDERWYK M. A., 1982, *QEM* SEM image analysis in the determination of modal assays, mineral associations, and mineral liberation*, Proceedings XIV International Mineral Processing Congress, 3.

MLYNARCZUK M., 1999, *Some Remarks on the Application of Image Analysis and Image Processing for the Description of the Geometrical Structures of Rock*, Physicochemical Problems of Mineral Processing, 33, 107–116.

MLYNARCZUK M., 2006, *Możliwości wykorzystania metod analizy obrazu do opisu petrograficznego wybranych skał okruchowych*, Gospodarka Surowcami Mineralnymi, 22, 3, 135–144.

MLYNARCZUK M., 2008, *Zastosowanie metod analizy obrazu i morfologii matematycznej do ilosciowego opisu uksztaltowania powierzchni przelamow skalnych*, Archives of mining Sciences, Monografie.

OBARA B., 2007, *Identification of transcrystalline microcracks observed in microscope images of dolomite structure using image analysis methods based on linear structuring element processing*, Computers & Geosciences 33, 151–158.

PIRRIE D., et al., 2004, *Rapid quantitative mineral and phase analysis using automated scanning electron microscopy (QemSCAN), potential applications in forensic geosciences*, Geological Society, 232, 123-136.

PETRUK W., 1988a. *Automatic image analysis for mineral beneficiation,* Journal of Metals 40 (4), 29–31.

PETRUK W., 1988b. *Automatic image analysis to determine mineral behaviour during mineral beneficiation*, Process Mineralogy VIII. In: Carson, D.J.T., Vassiliou, A.H. (Eds.). The Minerals, Metals & Materials Society, 347–357.

PETRUK W., 1989, Short course on image analysis applied to mineral and earth sciences, Mineralogical Association of Canada, Ottawa.

PETRUK W., WILSON J.M.D., LASTRA R., HEALY R.E., 1991. *An image analysis and materials balancing procedure for evaluating ores and mill products to obtain optimum recoveries*. Proceedings of 23rd Annual Meeting of the Canadian Mineral Processors, 1–16. (Section 19).

RAMAKRISHNAN, R., GEHRKE, J., 2000, *Database management systems,* Osborne/McGraw-Hill.

SERRA, J., 1982, *Image Analysis and Mathematical Morphology*, Academic Press, London.

SERRA J., MŁYNARCZUK M., 2000: *Morphological Merging of Multidimensional Data*, Proceedings of STERMAT.

TADEUSIEWICZ R., KOROHODA P., 1997, *Komputerowa analiza i przetwarzanie obrazów*, Wydawnictwo Fundacji Postępu Telekomunikacji.

TASDEMIR A., 2008, *Evaluation of grain size distribution of unbroken chromites*, Minerals Engineering, 21 (10), 711–719.

TASDEMIR A. OZDAG H. ONAL G., 2011, *Image analysis of narrow size fractions obtained by sieve analysis - an evaluation by log-normal distribution and shape factors*, Physicochem. Probl. Miner. Process. 46 (2011) 95-106

ULLMAN J. D., 1985, *Principles of database systems*, Galgotia Publications.

MULTI-PARAMETER DATA VISUALIZATION BY MEANS OF PRINCIPAL COMPONENT ANALYSIS (PCA) IN QUALITATIVE EVALUATION OF VARIOUS COAL TYPES

Tomasz NIEDOBA

AGH University of Science and Technology, Faculty of Mining and Geoengineering, Department of Environmental Engineering and Mineral Processing, al. Mickiewicza 30, 30-059 Krakow, tniedoba@agh.edu.pl

Abstract: Multi-parameter data visualization methods are a modern tool allowing to classify some analyzed objects. When it comes to grained materials, e.g. coal, many characteristics have an influence on the material quality. Besides the most obvious features like particle size, particle density or ash contents, coal has many other qualities which show significant differences between the studied types of material. The paper presents the possibility of applying visualization techniques for coal type identification and determination of significant differences between various types of coal. The Principal Component Analysis was applied to achieve this purpose. Three types of coal 31, 34.2 and 35 (according to Polish classification of coal types) were investigated, which were initially screened on sieves and subsequently divided into density fractions. Next, each size-density fraction was analyzed chemically to obtain other characteristics. It was pointed out that the applied methodology allowed to identify certain coal types efficiently, which makes it useful as a qualitative criterion for grained materials. However, it was impossible to provide such identification based on contrastive comparisons of all three types of coal. The presented methodology is a new way of analyzing data concerning widely understood mineral processing.

Keywords: Principal Component Analysis, PCA, multi-parameter data visualization, coal, identification of data, covariance matrix, pattern recognition

Introduction

In mineral processing operations particle properties influence processing results (Drzymala, 2009; Kelly and Spottiswood, 1989). In the case of coal the most important parameters are size and density. But it is often not enough to classify coal type properly. In modern statistical research there is often a need of applying multi-parameter (called also as multidimensional) statistical methods. A simple regressive analysis is not enough in more complex cases (Brozek and Surowiak, 2005; 2007, 2010). That is why many new techniques are introduced in scientific works. Of course,

there are many methods connected with regressive equations (Gawenda et al., 2005; Lyman, 1993; Niedoba, 2009; 2011; 2013a; 2013b; Niedoba and Surowiak, 2012; Saramak, 2011; 2013; Snopkowski and Napieraj, 2012; Tumidajski, 1997; Tumidajski and Saramak, 2009) or even fractals (Ahmed and Drzymala, 2005) but many methods of data-mining are also in use. A special type of statistical analysis involves multi-parameter data visualization methods geared towards recognizing differences and similarities between analyzed sets of data. Finding these differences is often a very important issue in mineral processing, where processes depend on many material features.

The qualitative analysis of multi-parameter data (properties of material) obtained from the results of empirical experiments can be carried out by applying the multi-parameter visualization method. The results of analyses can be helpful thanks to the characteristics of materials as well as the development of mineral processing models based on this data. Attempts to depict multi-parameter data have been undertaken on many occasions. Among many methods, the following ones can be selected: grand-tour method (Asimov, 1985, Cook et al., 1995), use of neural networks for data visualization (Aldrich, 1998; Jain and Mao, 1992; Kraaijveld et al., 1995), parallel coordinates method (Chatterjee et al., 1993; Chou et al., 1999; Gennings et al., 1999; Inselberg, 1985), star graph method (Sobol and Klein, 1989), multidimensional scaling (Kim et al., 2000), scatter-plot matrices method (Cleveland, 1984), relevance maps method (Assa et al., 1999). Visualization of multidimensional solids is also possible (Jamroz, 2001; 2009). The observational tunnels method (Jamroz, 2001; 2014) makes it possible to obtain an external view of the observed multi-parameter sets of points using tunnel radius introduced by the present author (Jamroz and Niedoba, 2014; Niedoba and Jamroz, 2013).

The use of methods of multi-parameter data visualization by transformation of multidimensional space into two-dimensional space makes it possible to show multi-parameter data on computer screen. This allows to conduct a qualitative data analysis in the most natural way for human with a sense of sight. One of such methods is the Principal Component Analysis (PCA). It was used in the work to present and analyze a set of seven-parameter data describing samples of three various coal types 31, 34.2 and 35 (according to Polish classification of coals). It was decided to check whether this method allows to state that an amount of information contained in seven coal features is sufficient for the proper classification of coal types. The application of various methods for analyzing possibilities of recognition of various coal properties is becoming an increasingly interesting issue. Earlier, other visualization methods were applied, including the observational tunnels method (Jamroz and Niedoba, 2013; 2014). An application of the PCA method for this purpose is a new way of approaching the subject.

Material characteristics

Three types of coal, types 31 (energetic coal), 34.2 (semi-coking coal) and 35 (coking coal) in the Polish classification were used in the investigation (Olejnik et al., 2010). The classification of coal types can be found in (Drzymala, 2009). The coals originated from three various Polish mines and all of them were initially screened on a set of sieves of the following sizes: −1.00, −3.15, −6.30, −8.00, −10.00, −12,50, −14.00, −16.00 and −20.00 mm. Subsequently, the size fractions were additionally separated into density fractions by separation in dense media using zinc chloride aqueous solution of various densities (1.3, 1.4, 1.5, 1.6, 1.7, 1.8 and 1.9 g/cm^3). The fractions were used as a framework for further consideration and additional coal features were determined by means of chemical analysis. For each density-size fraction the following parameters were determined: combustion heat, ash contents, sulfur contents, volatile parts contents and analytical moisture, making up, together with the mass of these fractions, seven various features for each coal. The examples of such data were presented in Table 1 containing the data for size fractions of 14.00-12.50 mm for each type of coal. The complete data can be found in Niedoba (2013a).

Principal Component Analysis

Method description

The PCA method is one of statistical methods of factor analysis. It consists of perpendicular projection of multi-parameter data on the plane represented by properly selected eigenvectors V_1 and V_2, which are related to the highest eigenvalues of covariance matrix of observational set. The selection of vectors V_1 and V_2 allows to obtain an image on plane representing the greatest number of data changes whose mutual distance is the biggest (Li et al., 2000).

Algorithm

A set of input data consists of parts described by *n* of features. It can be then treated as a set of *n*-dimensional vectors. Let us mark the vector of input data as $x_k=(x_{k,1}, x_{k,2}, \ldots x_{k,n})$. The algorithm performing visualization by means of PCA consists of several steps:

- scaling of initial data. Individual features represented by individual data dimensions are scaled in the way ensuring their compliance with the same selected range. In this paper, the individual coordinates (features) of data set vectors were scaled to the range (0, 1),

T. Niedoba

Table 1. Data for size fractions of 14.00-12.50 mm for all three types of coal

Coal type 31						
Density [Mg/m^3]	Mass [g]	Combustion heat [kJ]	Ash contents [%]	Sulfur contents [%]	Volatile parts contents V^a	Analytical moisture W_a
<1.3	308.6	29.51	6.41	0.72	34.32	3.23
1.3–1.4	292.5	24.53	19.61	0.7	29.22	3.36
1.4–1.5	36.1	12.34	16.55	0.76	28.92	3.87
1.5–1.6	10.7	21.42	26.10	1.55	31.08	3.40
1.6–1.7	25.6	18.70	35.78	2.28	26.71	2.40
1.7–1.8	139	16.41	37.20	1.23	29.24	2.19
1.8–1.9	12.7	12.89	48.20	1.13	24.05	2.23
>1.9	601.2	1.91	86.53	0.40	9.30	0.91
Coal type 34.2						
Density [Mg/m^3]	Mass [g]	Combustion heat [kJ]	Ash contents [%]	Sulfur contents [%]	Volatile parts contents V^a	Analytical moisture W_a
<1.3	360.5	34.44	2	0.32	28.96	1.04
1.3–1.4	57	32.02	7.67	0.71	24.16	1.87
1.4–1.5	25.5	28.89	15.33	0.83	24.58	1.34
1.5–1.6	12.2	24.27	33.73	0.17	27.85	0.95
1.6–1.7	3.2	20.22	34.3	0.34	no data	no data
1.7–1.8	15	17.38	36.15	0.34	27.93	0.37
1.8–1.9	3.6	18.48	27	0.05	31.75	1.01
>1.9	68.9	2.90	79.33	0.91	12.08	0.52
Coal type 35						
Density [Mg/m^3]	Mass [g]	Combustion heat [kJ]	Ash contents [%]	Sulfur contents [%]	Volatile parts contents V^a	Analytical moisture W_a
<1.3	268.7	34.86	2.38	0.28	20.28	1.45
1.3–1.4	89.3	31.86	8.97	0.36	20.10	1.21
1.4–1.5	39.8	27.49	19.61	0.56	18.83	1.28
1.5–1.6	22.0	21.06	35.68	0.39	16.22	1.32
1.6–1.7	25.7	20.88	34.62	1.26	19.42	1.47
1.7–1.8	29.0	19.21	40.60	0.38	18.86	1.61
1.8–1.9	28.1	13.76	52.24	1.14	17.95	1.51
>1.9	589.5	2.94	80.57	0.20	10.84	1.37

- calculation of covariance matrix. The general formula for covariance was used:

$$\mathrm{cov}(X,Y) = E(X \cdot Y) - E(X) \cdot E(Y) \tag{1}$$

where E is the expected value. First, the expected values are calculated:

$$E_i = \frac{\sum_{k=1}^{m} x_{k,i}}{m} \tag{2}$$

and

$$E_{i,j} = \frac{\sum_{k=1}^{m} x_{k,i} x_{k,j}}{m} \tag{3}$$

where, E_i – expected value of ith coordinate of input data, $E_{i,j}$ – expected value of product of ith and j^{th} coordinate of input data, m – number of vectors of input data, $x_{k,i}$ – i^{th} coordinate of kth vector of input data. If the covariance matrix is marked as A, then each element of the matrix a_{ij} is calculated as:

$$a_{ij} = E_{i,j} - E_i E_j . \tag{4}$$

In this way, the symmetrical covariance matrix of input data set is obtained,
- calculation of eigenvalues and eigenvectors of covariance matrix. For numerical calculations the Jacobi method was selected. It draws upon the fact that orthogonal transformation does not change own values and vectors of matrix. Consequently, it is possible to perform a set of orthogonal transformations on matrix A to conduct it to diagonal form D:

$$A = W \cdot D \cdot W^T . \tag{5}$$

In the diagonal matrix the eigenvalues are located on the main diagonal while the related eigenvectors are located in columns of matrix W. Matrices D and W which fulfill Eq. 5 by means of the Jacobi method can be achieved in the following steps:
1. as matrix W the identity matrix of dimension nxn is accepted,
2. as matrix A covariance matrix of dimension nxn is accepted, calculated according to equation (4),
3. the main element is selected apart from the main diagonal of matrix A, which is the element of the highest module value not located on the main diagonal. The location of this element in the matrix is searched, so coordinates p and q must be found fulfilling the condition:

$$\forall i, j = 1,...,n \text{ and } i \neq j \text{ is}: \left|a_{pq}\right| \geq \left|a_{ij}\right|, \tag{6}$$

4. the values c and s are calculated using the following formulas:

$$r = \frac{a_{qq} - a_{pp}}{2a_{pq}} \tag{7}$$

$$t = \frac{\text{sgn}(r)}{\left|r\right| + \sqrt{r^2 + 1}} \tag{8}$$

where: a_{ij} is an element of the matrix from i^{th} line and j^{th} column, $\text{sgn}(r) = 1$ for $r >= 0$ and $\text{sgn}(r) = -1$ for $r < 0$. Next, the calculations are performed according to formulas (9) and (10):

$$c = \frac{1}{\sqrt{t^2 + 1}} \tag{9}$$

and

$$s = tc \tag{10}$$

1. having applied calculated values c and $s,$ matrix B is created ensuring identity matrix of dimension nxn in which four elements are changed: $b_{pp} = c$, $b_{qq} = c$, $b_{pq} = s$ and $b_{qp} = -s$,
2. the new value of matrix A is assigned by application of previous value of matrix A, matrix B created in the previous step and transposition matrix B:

$$A := B^T \cdot A \cdot B, \tag{11}$$

3. the new value of matrix W is assigned by application of previous value of matrix W and matrix B created in step 5.

$$W := W \cdot B, \tag{12}$$

4. it is checked whether the matrix A, obtained as a result of transformations, is a diagonal matrix according to previously accepted preciseness of calculations ε, so:

$$\frac{\max\limits_{i,j=1,...,n \,\wedge\, i \neq j} \left|a_{ij}\right|}{\max\limits_{i=1,...,n} \left|a_{ii}\right|} < \varepsilon. \tag{13}$$

For experiments described in section 3, $\varepsilon = 0.000001$ was accepted. If inequality (13) is not fulfilled, a return to step 3 is required and calculations are continued. In

other case, the obtained matrix *A* is diagonal. The situation described by Eq. 5 is achieved in this way. That means that the eigenvalues of output matrix are located on the main diagonal of obtained matrix *A* and the eigenvectors related to these values occur in columns of obtained matrix *W*,

- the determination of two coordinate axes. Two eigenvectors related to two biggest module eigenvalues of covariance matrix are selected from vectors calculated in stage C. Let us mark them as $V_1 = (v_{1,1}, v_{1,2}, \ldots v_{1,n})$, $V_2 = (v_{2,1}, v_{2,2}, \ldots v_{2,n})$. In this way two coordinates axes are obtained on which all data will be projected,
- drawing the set of points on screen. For each point x_k two coordinates are calculated $(\tilde{x}_{k,1}, \tilde{x}_{k,2})$ preceded by their projection on axes V_1 and V_2, which means:

$$\tilde{x}_{k,1} = \sum_{i=1}^{n} v_{1,i} x_{k,i} \qquad (14)$$

$$\tilde{x}_{k,2} = \sum_{i=1}^{n} v_{2,i} x_{k,i} \ . \qquad (15)$$

As a result, the image of each vector can be presented on computer screen. It is achieved by drawing on the screen a symbol, in place of coordinates $(\tilde{x}_{k,1}, \tilde{x}_{k,2})$, representing fraction to which the related data vector x_k belongs. In this way the image of multidimensional points representing various coal types is created on the computer screen.

Results of experiment

As part of the investigation, for the purpose of visualizing seven-parameter data describing various coal types, a computer program was created based on assumptions presented in the previous chapter. The obtained results were presented in Figs 1-4. The views show a transformation of seven-parameter data by means of PCA into two dimensions. The visualization algorithm in PCA, despite reduction to only two dimensions, has been organized to ensure the view representing the biggest number of data changes whose mutual distance is the biggest. In this way it is possible to see significant features of seven-parameter data on the computer screen.
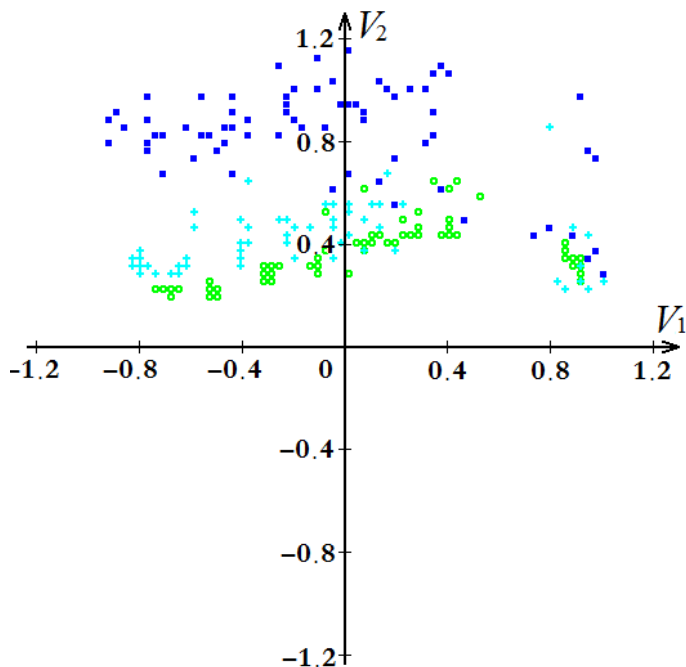
Fig. 1. View of seven-parameter data representing three various types of coal.
Images of points representing coal, type 31 were marked with (■),
(+) – samples of coal type 34.2, (o) – samples of coal type 35.

Figure 1 presents obtained view of points representing seven-parameter data vectors that describe three various coal types: 31, 34.2 and 35. In order to obtain it, the system calculated the covariance matrix:

$$\text{cov} = \begin{bmatrix}
0.0834 & -0.0101 & -0.0773 & 0.0751 & 0.0162 & -0.0419 & -0.0151 \\
-0.0101 & 0.0241 & 0.0057 & -0.0056 & -0.0049 & 0.0049 & 0.0062 \\
-0.0773 & 0.0057 & 0.0810 & -0.0771 & -0.0135 & 0.0418 & 0.0079 \\
0.0751 & -0.0056 & -0.0771 & 0.0770 & 0.0097 & -0.0473 & -0.0148 \\
0.0162 & -0.0049 & -0.0135 & 0.0097 & 0.0438 & 0.0074 & 0.0150 \\
-0.0419 & 0.0049 & 0.0418 & -0.0473 & 0.0074 & 0.0545 & 0.0245 \\
-0.0151 & 0.0062 & 0.0079 & -0.0148 & 0.0150 & 0.0245 & 0.0396
\end{bmatrix}.$$

Furthermore, eigenvectors were calculated:

$$V_1 = (0.5401, -0.0589, -0.5340, 0.5307, 0.0763, -0.3425, -0.1225),$$

$$V_2 = (0.1289, 0.0025, -0.1631, 0.0202, 0.6594, 0.4273, 0.5822).$$

In the above Figure, it is clearly visible that images of data points representing coal samples of a certain type gather in separated subareas and create clusters. It can be noticed that almost on the whole area of the Figure these clusters can be separated. In some parts of the space, however, the images of points representing various coal types overlap. Therefore, according to Figure 1, it is impossible to state that the analyzed data allow to classify coal types properly.
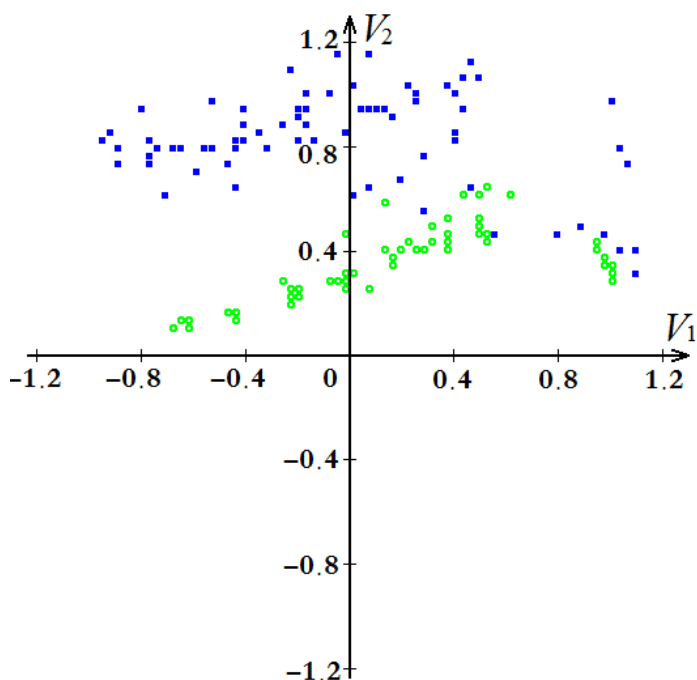
Fig. 2. View of seven-parameter data representing two various types of coal. Images of points representing coal type 31 were marked with (■), (o) – samples of coal type 35.

With a view to achieving clearer results, it was decided to present this data by means of the PCA method in some other way. A decision was made to analyze the data representing various types of coal in pairs. Figure 2 shows the view obtained for data representing coal types 31 and 35. In order to obtain this view, the system calculated the covariance matrix:

$$cov = \begin{bmatrix} 0.1071 & -0.0115 & -0.0827 & 0.0842 & 0.0214 & -0.0466 & -0.0261 \\ -0.0115 & 0.0305 & 0.0053 & -0.0056 & -0.0077 & 0.0068 & 0.0056 \\ -0.0827 & 0.0053 & 0.0731 & -0.0719 & -0.0144 & 0.0351 & 0.0149 \\ 0.0842 & -0.0056 & -0.0719 & 0.0746 & 0.0095 & -0.0445 & -0.0251 \\ 0.0214 & -0.0077 & -0.0144 & 0.0095 & 0.0508 & 0.0159 & 0.0152 \\ -0.0466 & 0.0068 & 0.0351 & -0.0445 & 0.0159 & 0.0564 & 0.0453 \\ -0.0261 & 0.0056 & 0.0149 & -0.0251 & 0.0152 & 0.0453 & 0.0498 \end{bmatrix}.$$

Furthermore, eigenvectors were calculated:

V_1 = (0.5936, -0.0637, -0.4798, 0.5031, 0.0701, -0.3325, -0.2116),

V_2 = (0.1948, -0.0316, -0.1952, 0.0507, 0.6128, 0.4902, 0.5519).

In Figure 2 it is clearly visible that images of points representing samples of coal type 31 gather in clusters, which can be easily separated from clusters of points representing coal type 35. In Figure 3 the view obtained for data representing coal types 34.2 and 35 is presented. Also, in this case it is clearly visible that images of points representing samples of coal type 34.2 gather in clusters, which can be easily separated from clusters of points representing samples of coal type 35. The covariance matrix obtained from the creation of this Figure is as follows:

$$cov = \begin{bmatrix} 0.0840 & -0.0101 & -0.0851 & 0.0811 & 0.0111 & -0.0440 & -0.0021 \\ -0.0101 & 0.0222 & 0.0059 & -0.0046 & -0.0083 & -0.0007 & 0.0007 \\ -0.0851 & 0.0059 & 0.0922 & -0.0886 & -0.0059 & 0.0523 & 0.0028 \\ 0.0811 & -0.0046 & -0.0886 & 0.0868 & 0.0055 & -0.0542 & -0.0005 \\ 0.0111 & -0.0083 & -0.0059 & 0.0055 & 0.0278 & -0.0010 & 0.0015 \\ -0.0440 & -0.0007 & 0.0523 & -0.0542 & -0.0010 & 0.0650 & -0.0143 \\ -0.0021 & 0.0007 & 0.0028 & -0.0005 & 0.0015 & -0.0143 & 0.0374 \end{bmatrix}.$$

Its eigenvectors are as following:

V_1 = (-0.5174, 0.0414, 0.5554, -0.5404, -0.0480, 0.3575, -0.0090),

V_2 = (-0.2219, 0.1868, 0.1310, -0.0412, -0.1434, -0.6099, 0.7102).

Furthermore, Fig. 4 shows the view obtained for data representing coal types 31 and 34.2. It can be easily noticed that images of points representing samples of coal type 31 gather in clusters which can be easily separated from clusters of points representing samples of coal type 34.2. In this case the covariance matrix is as follows:

$$\text{cov} = \begin{bmatrix} 0.0840 & -0.0121 & -0.0763 & 0.0745 & 0.0208 & -0.0494 & -0.0246 \\ -0.0121 & 0.0256 & 0.0080 & -0.0081 & -0.0037 & 0.0080 & 0.0103 \\ -0.0763 & 0.0080 & 0.0805 & -0.0770 & -0.0178 & 0.0518 & 0.0149 \\ 0.0745 & -0.0081 & -0.0770 & 0.0778 & 0.0149 & -0.0551 & -0.0227 \\ 0.0208 & -0.0037 & -0.0178 & 0.0149 & 0.0536 & -0.0020 & 0.0161 \\ -0.0494 & 0.0080 & 0.0518 & -0.0551 & -0.0020 & 0.0513 & 0.0254 \\ -0.0246 & 0.0103 & 0.0149 & -0.0227 & 0.0161 & 0.0254 & 0.0543 \end{bmatrix}.$$

The eigenvectors are:

$$V_1 = (-0.5243, 0.0776, 0.5169, -0.5167, -0.1134, 0.3743, 0.1788),$$

$$V_2 = (0.0762, 0.0760, -0.1317, 0.0184, 0.7040, 0.1959, 0.6608).$$
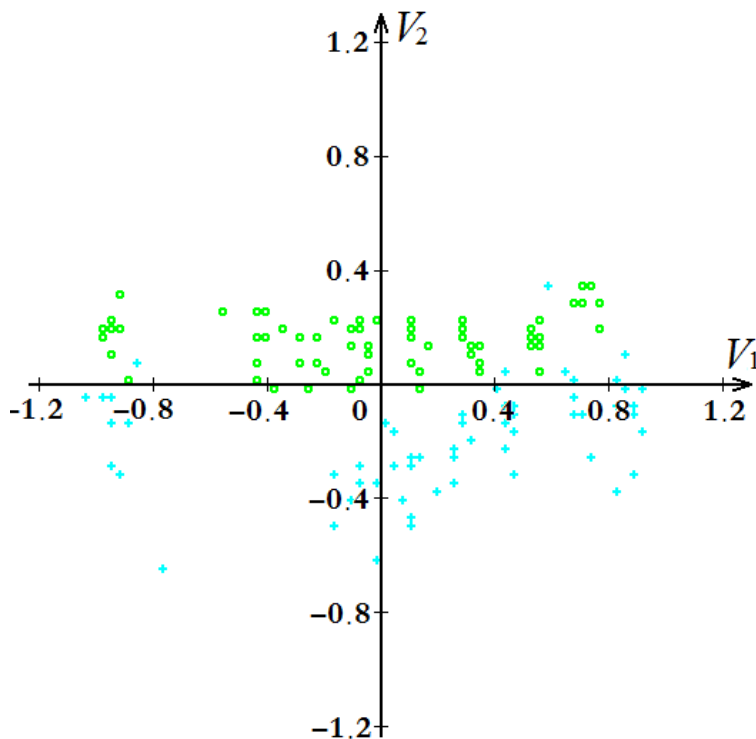
Fig. 3. View of seven-parameter data representing three various types of coal. Images of points representing coal type 34.2 were marked with (+), (o) – samples of coal type 35.

If we can state that the distinction of coal type 31 samples from coal type 35 samples is possible (Fig. 2) and we can state that the distinction of coal type 34.2

samples from coal type 35 samples is possible (Fig. 3), as well the distinction of coal type 31 samples from coal type 34.2 samples is possible (Fig. 4), then the possibility of distinction of samples of each of the three coal types is confirmed. Thanks to the visualization of multi-parameter data by means of PCA, it is possible to state that information covered in seven-parameter data describing samples of three types of coal is sufficient for its proper classification.

It is worth paying attention to the fact that the algorithm of visualization by means of PCA does not use the information of affiliation of points representing data to certain fractions. In this situation grouping of points representing certain fraction depends only on some properties of data noticed by the algorithm.
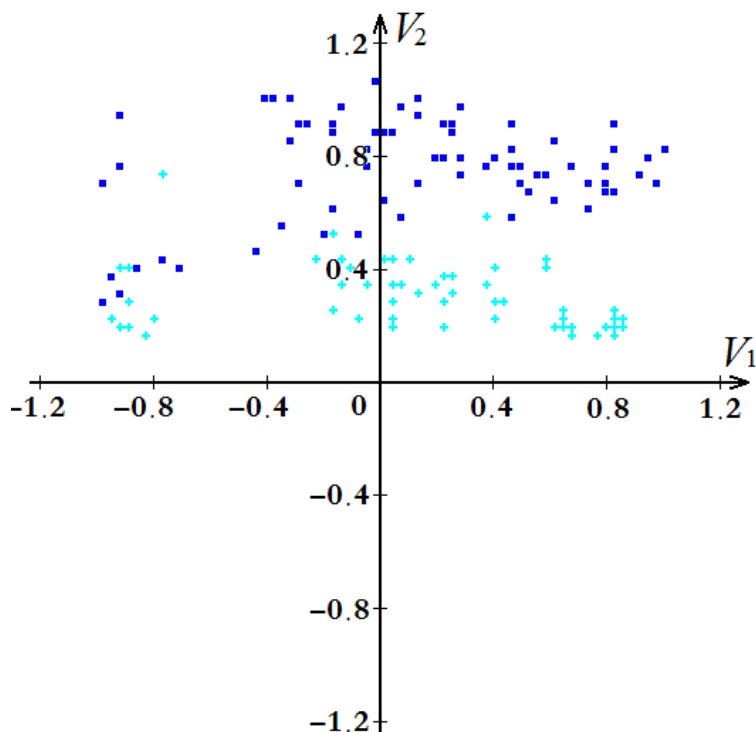
Fig. 4. View of seven-parameter data representing two various types of coal. Images of points representing coal type 31 were marked with (■), (+) – samples of coal type 34.2

Conclusions

The conducted experiments based on visualization of seven-parameter data by means of PCA allowed to arrive at the following conclusions.

1. Multi-parameter visualization by means of the PCA allows to state that information covered in analyzed seven-dimensional data is sufficient for a proper classification of coal types 31, 34.2 and 35.
2. The visualization of data concerning three types of coal within one figure allowed to state that images of data points representing coal samples of certain type gather in clusters which can be separated almost on the whole area of the figure. However, in some areas of the space, the images of points representing various coal types overlap. Therefore, based on such view it was impossible to state whether the analyzed data allows for a proper classification of coal types.
3. Only presentation of data representing three various types of coal in pairs allowed to obtain clear results. They allowed to conclude that images of points representing samples of coal of certain type gather in clusters which can be separated. It means that data contains a sufficient amount of information to classify coal types properly.
4. The advantage of the PCA method is the fact that during visualization it is not necessary to select any parameters in contrast to many other methods of multi-parameter data visualization.

Acknowledgements

References

AHMED H.A.M., DRZYMALA J., *Two-dimensional fractal linearization of distribution curves*, Physicochemical Problems of Mineral Processing, vol. 39, pp. 129-139, 2005.

ALDRICH C., *Visualization of transformed multivariate data sets with autoassociative neural networks*. Pattern Recognition Letters, Volume: 19, Issue: 8, June, 1998, pp. 749-764.

ASIMOV D., *The Grand Tour: A Tool for Viewing Multidimensional Data*, SIAM Journal of Scientific and Statistical Computing, pp. 128-143, vol. 6, No, 1985.

ASSA J., COHEN-OR D., MILO T., *RMAP: a system for visualizing data in multidimensional relevance space*, Visual Computer, vol.15, no.5, pp.217-34. Publisher: Springer-Verlag, Germany, 1999.

BROZEK M., SUROWIAK A., *Argument of Separation at Upgrading in the Jig*, Archives of Mining Sciences, vol. 55, pp. 21-40, 2010.

BROZEK M., SUROWIAK A., *Effect of Particle Shape on Jig Separation Efficiency*, Physicochemical Problems of Mineral Processing, vol. 41, pp. 397-413, 2007.

BROZEK M., SUROWIAK A., *The Dependence of Distribution of Settling Velocity of Spherical Particles on the Distribution of Particle Sizes and Densities*, Physicochemical Problems of Mineral Processing, vol. 39, pp. 199-210, 2005.

CHATTERJEE A., DAS P.P., BHATTACHARYA S., *Visualization in linear programming using parallel coordinates*, Pattern Recognition, vol. 26(11), pp.1725-1736, 1993.

CHOU S.-Y., LIN S.-W., YEH C.-S., *Cluster identification with parallel coordinates*, Pattern Recognition Letters, vol. 20, pp.565-572, 1999.

CLEVELAND W.S., MCGILL R., *The many faces of a scatterplot*, Journal of the American Statistical Association, vol.79, pp.807-822. 1984.

COOK D., BUJA A., CABRERA J., HURLEY C., *Grand Tour and Projection Pursuit*, Journal of Computational and Graphical Statistics, vol. 4, no. 3, pp. 155-172, 1995.

DRZYMALA J.: *Basics of minerallurgy*, Oficyna Wydawnicza Politechniki Wrocławskiej, 2009. [in Polish]

GAWENDA T., SARAMAK D., TUMIDAJSKI T., *Regression models of rock materials crushing in jaw crushers*, Scientific Issues of Civil Engineering and Environmental Engineering Faculty of Koszalin University of Science and Technology, series: Environmental Engineering, no 22, pp. 659-670, 2005. [in Polish]

GENNINGS C., DAWSON K.S., CARTER W.H., JR. MYERS R.H., *Interpreting plots of a multidimensional dose-response surface in a parallel coordinate system*. Biometrics, vol. 46, pp. 719-735, 1990.

INSELBERG A., *The plane with parallel coordinates*. Visual Computer, vol. 1, pp. 69-91, 1985.

JAIN A.K., MAO J., *Artificial neural network for non-linear projection of multivariate data*. In: Proc. IEEE Internat. Joint Conf. On Neural Networks, Baltimore, MD, vol. 3, pp. 335-340, 1992.

JAMROZ D., NIEDOBA T., *Application of Observational Tunnels Method to Select Set of Features Sufficient to Identify a Type of Coal*, Physicochemical Problems of Mineral Processing, vol 50(1), pp. 185-202, 2014.

JAMROZ D., *Visualization of objects in multidimensional spaces*, Doctoral Thesis, AGH, Kraków, 2001. [in Polish]

JAMROZ D., *Application of Multidimensional Data Visualization in Creation of Pattern Recognition Systems*, In: Gruca A., Czachórski T., Kozielski S. (eds.), Man-Machine, Interactions 3, AISC, Heidelberg, Springer-Verlag, vol. 242, pp. 443-450, 2014.

JAMROZ D.: *Multidimensional labyrinth - multidimensional virtual reality*. In: Cyran K., Kozielski S., Peters J., Stanczyk U., Wakulicz-Deja A. (eds.), Man-Machine, Interactions, AISC, Heidelberg, Springer-Verlag, pp. 445–450, 2009.

KELLY E.G., SPOTTISWOOD D.J., *The Theory of Electrostatic Separations, a Review, Part I. Fundamentals, Minerals Engineering*, vol. 2/1, 33-46, 1989.

KIM S.-S., KWON S., COOK D., *Interactive visualization of hierarchical clusters using MDS and MST*. Metrika, vol. 51, Springer-Verlag, pp. 39-51, 2000.

KRAAIJVELD M., MAO J., JAIN A.K., *A nonlinear projection method based on Kohonen's topology preserving maps*. IEEE Trans. Neural Networks, vol. 6(3), pp. 548-559, 1995.

LI W., YUE H. H., VALLE-CERVANTES S., QIN S. J., *Recursive PCA for adaptive process monitoring*. Journal of Process Control, vol. 10, iss.: 5, pp. 471-486, 2000.

LYMAN G. J., *Application of Line-Length Related Interpolation Methods to Problems in Coal Preparation – III: Two dimensional Washability Data Interpolation*, Coal Preparation, vol. 13, pp. 179-195, 1993.

NIEDOBA T., *Multidimensional characteristics of random variables in description of grained materials and their separation processes*, Wydawnictwo Instytutu Gospodarki Surowcami Mineralnymi i Energią PAN, Kraków, 2013a [in Polish].

NIEDOBA T., *Multidimensional distributions of grained materials characteristics by means of non-parametric approximation of marginal statistical density function*, AGH Journal of Mining and Geoengineering, iss. 4, pp. 235-244, 2009 [in Polish].

NIEDOBA T., *Statistical analysis of the relationship between particle size and particle density of raw coal*, Physicochemical Problems of Mineral Processing, vol. 49, iss. 1, pp. 175-188, 2013b.

NIEDOBA T., JAMROZ D.: *Visualization of multidimensional data in purpose of qualitative classification of various types of coal*, Archives of Mining Sciences, vol. 58, iss. 4, pp. 1317-1333, 2013.

NIEDOBA T., SUROWIAK A., *Type of coal and multidimensional description of its composition with density and ash contents taken into consideration*, in Proceedings of the XXVI International Mineral Processing Congress, vol. 1, pp. 3844-3854, 2012.

NIEDOBA T., *Three-dimensional distribution of grained materials characteristics*, in Proceedings of the XIV Balkan Mineral Processing Congress, Tuzla, Bosnia and Herzegovina, vol. 1, pp. 57-59, 2011.

OLEJNIK T., SUROWIAK A., GAWENDA T., NIEDOBA T., TUMIDAJSKI T., *Multidimensional coal characteristics as basis for evaluation and adjustment of its beneficiation technology*, AGH Journal of Mining and Geoengineering, vol. 34, iss. 4/1, pp. 207-216, 2010. [in Polish]

SARAMAK D., *Mathematical models of particle size distribution in simulation analysis of High-pressure grinding rolls operation*, Physicochemical Problems of Mineral Processing, vol. 49(1), pp. 495–512, 2013.

SARAMAK D., *Technological Issues Of High-Pressure Grinding Rolls Operation In Ore Comminution Processes*, Archives of Mining Sciences, vol. 56, no 3, pp. 517-526, 2011.

SNOPKOWSKI R., NAPIERAJ A., *Method Of The Production Cycle Duration Time Modeling Within Hard Coal Longwall Faces*, Archives of Mining Sciences, vol. 57, no. 1, pp. 121-138, 2012.

SOBOL M.G., KLEIN G., *New graphics as computerized displays for human information processing*. IEEE Trans. Systems Man Cybernet., vol. 19 (4), pp. 893-898, 1989.

TUMIDAJSKI T., SARAMAK D., *Methods and models of mathematical statistics in mineral processing*, Wydawnictwo AGH, Kraków, 2009. [in Polish]

TUMIDAJSKI T., *Stochastic analysis of grained materials properties and their separation processes*, Wydawnictwo AGH, Kraków, 1997 [in Polish].

A SURFACE PROBABILITY MODEL FOR ESTIMATION OF SIZE DISTRIBUTION ON A CONVEYOR BELT

Zelin ZHANG, Jianguo YANG, Dongyang Dou

National Engineering Research Center of Coal Preparation and Purification, China University of Mining and Technology, Xuzhou, Jiangsu 221116, China; zhangzelin3180@163.com; scetyjg@126.com.

Abstract: Estimation of size distribution by image analysis is a key issue in mineral engineering. However, only the surface information of ore piles can be captured, which is a problem in this field while only a few researchers pay attention to this problem. A new surface probability model was proposed for estimation of size distribution on a conveyor belt based on the Chavez model in this investigation. This model was tested and verified to have smaller errors in single size fraction but have larger errors in multiple size fractions. Several error trends were found and a correction factor was introduced to correct the higher errors. A series of linear equations were developed to calculate this specific correction factor according to the average particle size and height of pile. Therefore, empirical probability can be estimated by the specific correction factor and calculated probability, and the surface information on ore piles can be converted into global information.

Keywords: size distribution, surface probability model, conveyor belt, particles

Introduction

Image analysis techniques have been used in mineral engineering since 1980. The related fields include the size distribution estimation (Al-Thyabat and Miles, 2006; Al-Thyabat et al., 2007; Casali et al., 2001; Chavez et al., 1996; Ko and Shang, 2011; King, 1982; Kemenny et al., 2001; Guyot et al., 2004; Zhao, 2013;Vallebuona et al., 2003; Zhang et al, 2012; Yang et al, 2013), ores grade estimation (Claudio et al., 2011; Jayson et al., 2007;Chatterjee et al., 2010a; Chatterjee et al., 2010b), ores type prediction (Perez et al., 1999; Singh and Rao, 2006; Tessier et al., 2007; Singh et al., 2010), and other related researches (Petruk, 1988a; Petruk, 1988b; Petruk, 1989; Petruk et al., 1991; Sun and Su, 2013). Among these fields, the estimation of size distribution is mostly studied and widely applied, such as blasting, crusher controlling and mineral processing.

The traditional measure of size distribution of ores is obtained by screening or sieving, which is considered to be accuracy but time-consuming, not suitable for real-time monitoring. Therefore, image analysis techniques have been used to estimate the size distribution. However, this method can only obtain the surface information of ore piles, which is a problem in this field and few researchers pay attention to this problem.

Chavez et al. (1966) proposed a model to estimate the probability of particles appearing on the surface of ores piles (Eq.1). This surface probability model is suitable for particles in a recipient with a constant height. They selected a typical modeling unit, like Fig. 1, and indicated a particle F_i of size D_i appearing on the surface depends on the number of particles within the height H of the unit. They stated that "the probability P_i within a given pile depends on the particle size, and that all particles of size i will have the same probability to appear on the surface". In Eq. (1), given the average fragment size D_M, the expression $(H - D_i)$ is the remaining height of the pile below the surface particle F_i, and $(H - D_i) / D_M$ approximates the average number of particles within the remaining height. Therefore, the expression $1 + (H - D_i) / D_M$ is the number of particles within the height H of unit, and the reciprocal is the probability of particle F_i of size D_i to appear on the surface. In Eq. (2), N_i is the sum of particles of size D_i, therefore E_i is the number of particles of size D_i on the surface.

$$P_i = \frac{1}{1 + \left(H - D_i\right)/D_M} \tag{1}$$

$$E_i = N_i P_i \tag{2}$$
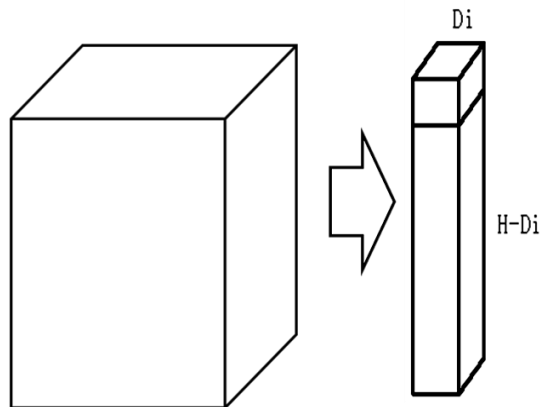
Fig. 1. Recipient with a constant height and the modeling unit

Chavez et al. tested the model using various recipients with different heights, such as 40 mm, 90 mm, 140 mm and 420 mm, and the results indicated the higher the pile height is, the lower the error between empirical probability and calculated probability.

In addition, they indicated smaller block positions may not be modeled by simple geometric stacking, especially when much larger blocks were present within the pile. Although they found several error trends and concluded several reasons, the method of correction was not considered. They even stated the model is suitable for the piles on the truck or some recipients, but it is not suitable for the conveyor belt with non-uniform heights (Chavez et al., 1996).

A new surface probability model was proposed for the estimation of particles size distribution on a conveyor belt based on the Chavez model. Experiments have been carried out to test and verify the surface probability model in this investigation. Several error trends were concluded and a correction method proposed for errors between empirical probability and calculated probability also was introduced for multiple size fractions, which is a key finding for the correction of size distribution estimation on conveyor belt by image analysis techniques.

Surface probability model for conveyor belt

Figure 2(a) is a sketch map of conveyor belt, the maximum height and breadth of which are *H* and *L* respectively, and the length is random. The conveyor belt was divided into two same parts, which have the same surface probability in theory. Therefore, one of the divided parts was considered as the typical model unit of conveyor belt. However, this typical model unit also is a recipient with non-uniform heights. Then it continued to be divided into several sub-units by the interval of D_i, the heights of which can be considered as constant. Now each sub-unit is suitable for the probability model of Chavez, like Fig. 2(c).
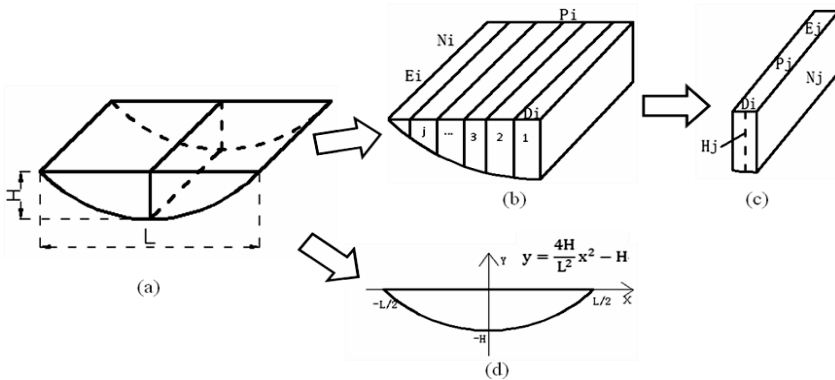
Fig. 2. Sketch map of typical model unit of conveyor belt and the parabola equation

In Fig. 2(b), *i* stands for size fraction; D_i is the mid-value of size fraction *i*; N_i is the sum of particles in size fraction *i*; E_i is the sum of surface particles in size fraction i; P_i is the surface probability of particles in size fraction i; *j* stands for sub-unit.

In Fig. 2(c), P_j is the surface probability of particles appearing on the sub-unit by the Chavez model, like Eq. (3), however, when H_j is less than D_i, the particles in size fraction i were considered as no chance to appear on the sub-unit, so the corresponding P_j is considered as zero. Supposing the particles of each size fraction were the uniform distribution, then N_j can be estimated by Eq. (4), then the surface particles of each sub-unit can be calculated by Eq. (5).

For the height H_j of each sub-unit, the profile of conveyor belt can be considered as a parabola, like Fig. 2(d). The equation of parabola can be developed by H and L. To test and verify the parabola equation, three lengths corresponding to three heights were measured by ruler and calculated by parabola equation, respectively, then the errors between measure and calculation is less than 3mm, so the parabola equation is considered to be able to calculate the height of sub-unit. Therefore, H_j was calculated by Eq. (6), and the horizontal ordinate was the mid-value of each sub-unit.

Finally, E_i is the sum of E_j, therefore P_i can be calculated by Eq. (7), which is the new surface probability model suitable for the conveyor belt and it only related with H_j and P_j at last.

$$P_j = \frac{1}{1+\left(H_j - D_i\right)/D_M}, if\ H_j < D_i, \quad P_j = 0 \tag{3}$$

$$N_j = \frac{H_j N_i}{\sum H_j} \tag{4}$$

$$E_j = N_j P_j \tag{5}$$

$$H_j = \left|\frac{4H}{L^2}x^2 - H\right|, \quad \frac{(2j-1)D_i}{2}\ x = \frac{D_i}{2}, \quad \frac{3D_i}{2} \tag{6}$$

$$P_i = \frac{E_i}{N_i} = \frac{\sum E_j}{N_i} = \frac{\sum N_j P_j}{N_i} = \frac{\sum H_j P_j}{\sum H_j} \tag{7}$$

Model validation and test

Surface probability model for conveyor belt was established and several experiments were carried out to test and validation the model and try to find out several relationships between empirical probability and calculated probability.

Fig. 3(a) and 3(b) are the equipments designed for testing surface probability model. A belt was closed by two organic glasses in two sides, which was convenient to measure the height and breadth of particle pile by tape, like Fig. 3(c). In addition, a mobile dam-board was used to adjust the height of particle pile, like Fig. 3(d).
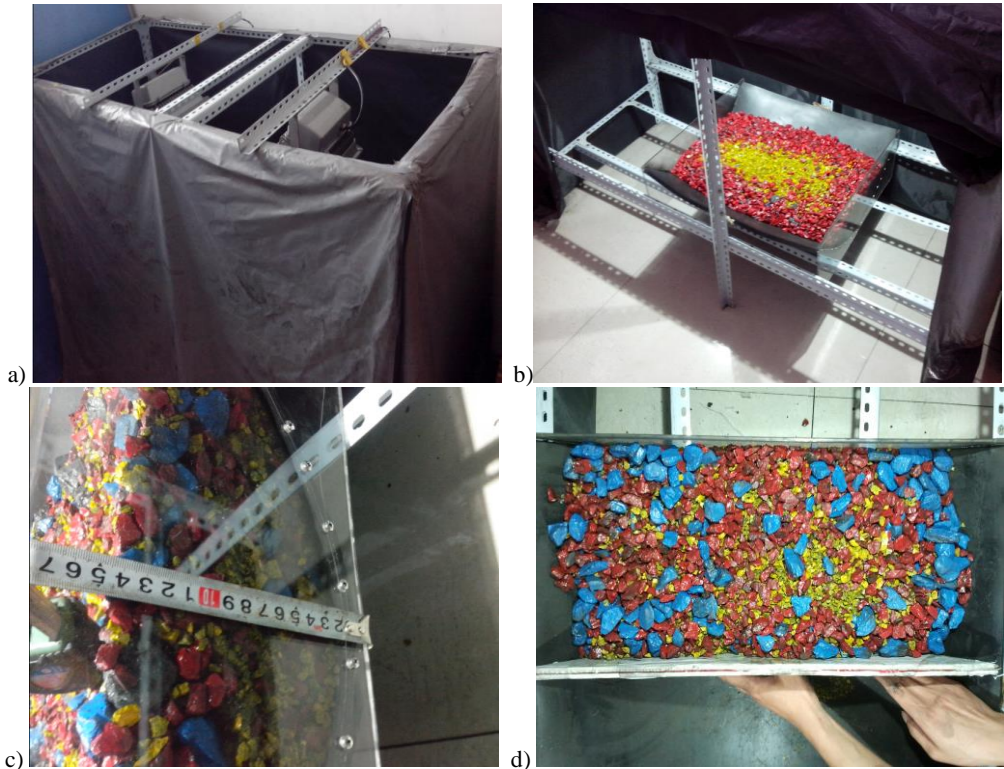
Fig. 3. Equipment for testing the surface probability model

Model validation was carried out in four size fractions, 3–6 mm, 6–13 mm, 13–25 mm and 25-50 mm. The experimental procedures were as follows.

1. Counting the number of particles in each size fraction
2. Mixing particle pile homogeneously on a flat tablet by rolling-over them from one place to another place three times
3. Pouring the homogeneous pile into the belt, and using the mobile dam-board to control the height of pile
4. Flatting the surface of pile and capturing the image of pile surface
5. Counting the number of particles in each size fraction by drawing tool in computer, zoom functions in which was used to recognize the small particles on surface and marker function was used to count with no repetition
6. The number of particles on surface divided by sum of particles in each size fraction was the empirical surface probability
7. Repeating (2) to (6) three times, and considering the mean value of three empirical probabilities as the final empirical probability
8. Calculating the surface probability of each size fraction by Eq. (7), and comparing the empirical probability and calculated probability

Test one: particles in single size fraction were used to test the model in three heights of pile (100 mm, 120 mm and 150 mm).

The reason of selecting these three heights was that the height of conveyor belt on mineral industry was usually about 160 mm, therefore the heights of piles in belt usually were less than 160 mm, but not more. In this test, the sums of each size fraction were 45833 particles in 3–6 mm, 4058 particles in 6–13 mm, 1250 particles in 13–25 mm and 262 particles in 25–5 0mm. The breadths (B) corresponding to heights 100 mm, 120 mm and 150 mm were 434 mm, 476 mm and 532 mm, respectively. The values of D_m of four size fractions were 4.5 mm, 9.5 mm, 19.5 mm and 37.5 mm, respectively. Figure 4(a) is the images of four size fractions captured in the height of 100 mm, and the expression "3–6–100" means the size fraction 3–6 mm in the height of 100 mm. Figures 4(b), 4(c) and 4(d) are the comparisons of empirical probability and calculated probability in three heights of pile. The results indicated the empirical probability and calculated probability of each size fraction were almost equal in three heights, which demonstrated the surface probability model for the conveyor belt is feasible in single size fraction, but the differences between these two probabilities increased with the increase of size fraction, because the range of larger size fraction is bigger and the pile surface of larger size fraction is more rugged. In addition, the probability of every size fraction reduced with the increase of height.
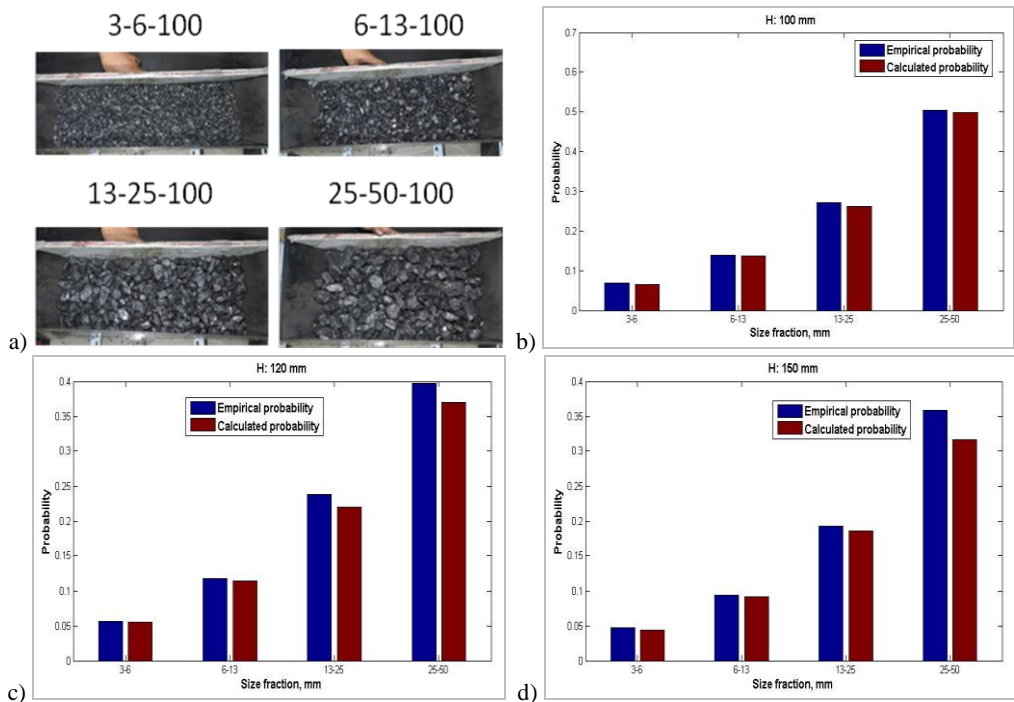
Fig. 4. (a): Images of four size fractions captured in the height of 100mm; (b), (c) and (d): Comparisons of empirical probability and calculated probability in three heights of pile

Test two: multiple size fractions were mixed to test the model in three heights (100 mm, 120 mm and 150 mm).

In order to recognize the size fractions of particles on the surface, particles of different size fractions were painted with different colors. Size fraction 3–6 mm is yellow and has 58500 particles; 6–13 mm is red and has 9600 particles; 13–25 mm is blue and has 620 particles; 25–50 mm is self–colored and has 70 particles. Figure 5(a) shows the number of particles in four size fractions. Multiple size fractions 3–13 mm, 3–25 mm and 3–50 mm were mixed respectively and used to compare the empirical probability and calculated probability of each size fraction in three heights of pile. Figures 5(b), 5(c) and 5(d) show multiple size fractions 3–13 mm, 3–25 mm and 3–50 mm in the height of 100 mm. The breadths (B) corresponding to heights 100 mm, 120 mm and 150 mm also were 434 mm, 476 mm and 532 mm, respectively. Dm of 3–13 mm, 3–25 mm and 3–50 mm were 5.205 mm, 5.334 mm and 5.367 mm, respectively. In each multiple size fraction, empirical probability and calculated probability of every
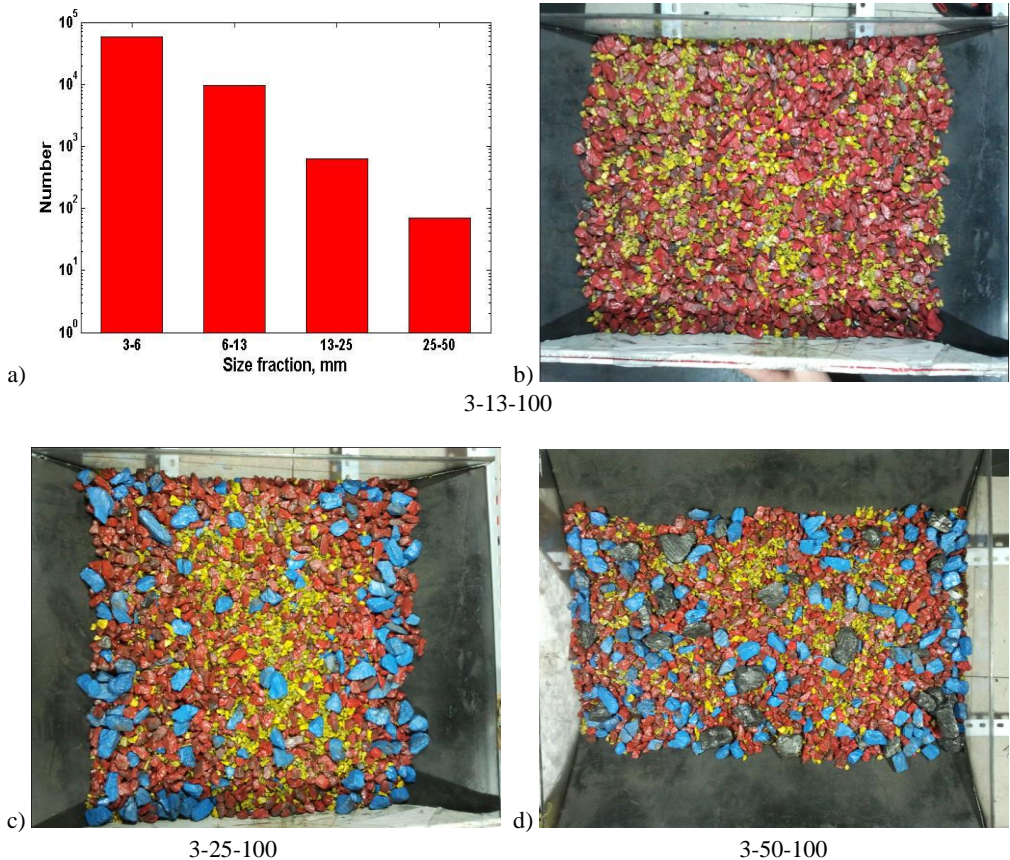
Fig. 5. (a): number of particles in four size fractions; (b), (c) and (d): multiple size

a)

b)
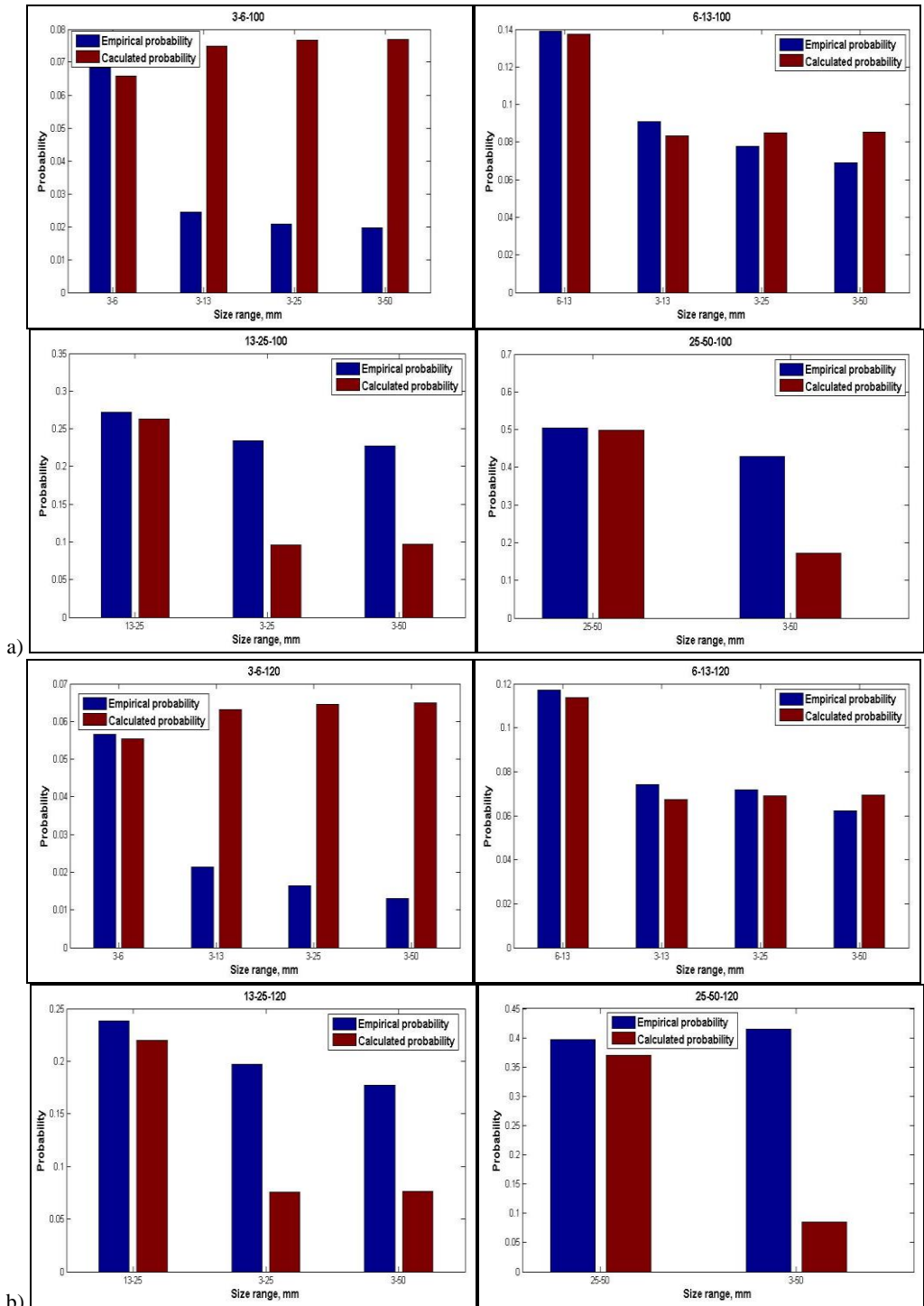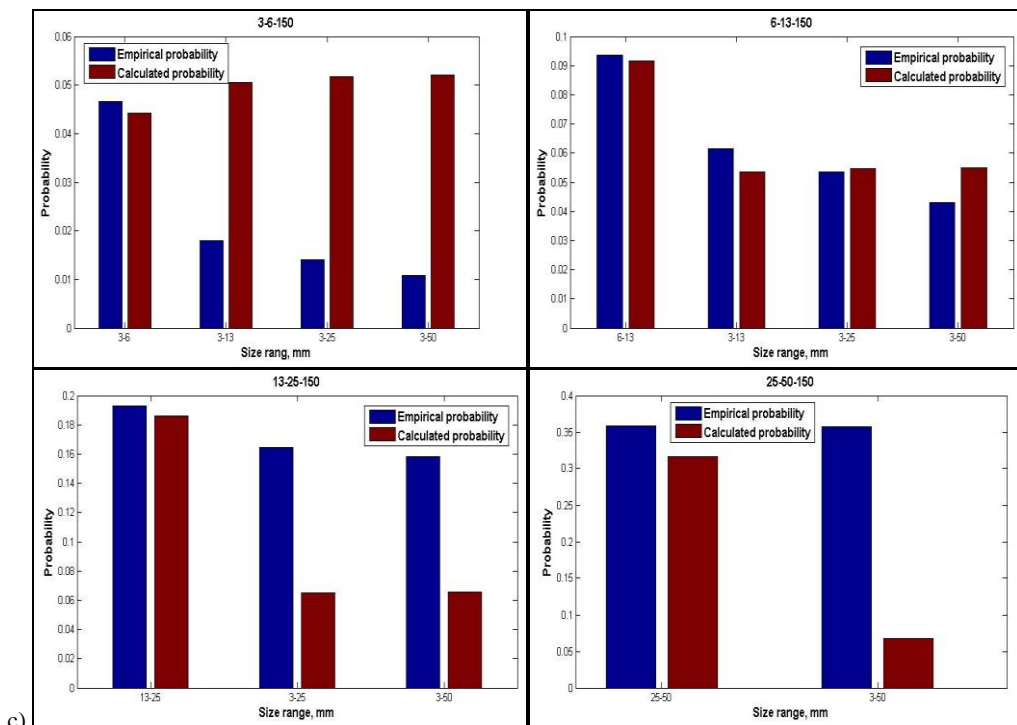
Fig. 6. Comparisons of empirical probability and calculated probability of every size fraction
in multiple size fractions and different heights

size fraction in different heights were obtained and showed in Fig. 6, which combined the results in test one. Results indicated the differences between empirical probability and calculated probability of each size fraction increased with the increase of range of multiple size fractions, the main reason of which is the covering of particles in different size fractions. In addition, empirical probabilities of 3–6 mm was smaller than calculated probabilities all the time. The empirical probabilities of 6–13 mm were sometimes larger and sometimes smaller than calculated probabilities. The empirical probabilities of 13–25 mm and 25–50 mm were larger than the calculated probabilities all the time, which indicated that larger particles should easier appear on the surface than smaller particles in the multiple size fractions. According to the comparisons for different heights, the larger the pile height, the lower is the difference between empirical and calculated probabilities.

Correction method for model error

Tests one and two indicated that the empirical and calculated probabilitiesa of each size fraction were almost equal in single size fraction, but they were very different in multiple size fractions. The main reason is the covering of particles in different size fractions. We considered the empirical surface probability as the "actual surface

probability", therefore, the difference between empirical and calculated probability is the error of surface probability model for the conveyor belt. In engineering applications, piles usually had wide range of multiple size fractions. Therefore, particles of 3-50 mm were used to find the relationship between empirical and calculated probability and try to propose a method to correct the model error.

According to a constant size range of particles, only the size distribution and the height of pile in belt were the variables. D_m can stand for the condition of size distribution of number in a degree. However, different size distributions maybe have the same value of D_m, and the empirical probability of every size fraction maybe change, but the calculated probability is constant in a constant height of pile. Under this condition, a pile with three different size distributions (shown in Fig. 7(a)) but with the same value of D_m (D_m = 7.438) was used to investigate the changes of empirical probability in three heights, the results of which were shown in Fig. 7(b), 7(c) and 7(d). In the expression "100/7.438", "100" means the height of pile and "7.438" means the value of D_m. Results indicated the empirical probabilities of every size fraction in three different size distributions were almost equal in three heights of pile. Therefore, we can consider one D_m corresponds to one empirical probability in a constant height of pile, in spite of the change of size distributions. One D_m also corresponds to one calculated probability in a constant height of pile, therefore, variation tendencies of the empirical and calculated probabilities with D_m can be obtained to find some relationships.

Finally, three heights (100 mm, 120 mm and 150 mm) of piles and five different D_m (5.367 mm, 6.037 mm, 7.438 mm, 8.399 mm and 9.7799 mm) were used to find the relationship between empirical and calculated probability. Figure 8(a) shows the particle numbers of four size fractions corresponding to five different D_m. These four size fractions were the colored particles on test two. Because particles in 3–6 mm were much more than other size fractions, only adjusting the number of particles in 3–6 mm will obtain five different D_m easily. We defined the correction factor (r)

$$r = \frac{\text{Empirical probabilit y}}{\text{Calculated probabilit y}}.$$ (8)

Figure 8(b), 8(c) and 8(d) showed the variation tendencies of empirical probability, calculated probability and the correction factor with D_m in three heights of pile. The Y-axis of every trend image used LOG coordinate for the convenience of data display. Results indicated the variation tendencies of empirical probability and calculated probability with D_m were not the same in four size fractions, but the correction factor of four size fractions reduced with the increase of D_m in three heights. We used linear equation to model the correction factor and Dm by software MATLAB, showing in Fig. 8(a), 8(b) and 8(c). R-square and Root-Mean-Square Error (RMSE) were used to measure the goodness of fitting of linear equations, which indicated these equations were well fitted. Twelve fitting equations were as follows:

3-6-100: $\quad r = -0.035\, Dm + 0.4286$ (9)

3–6–120: $\quad r = -0.02669\, Dm + 0.3354$ (10)

3–6–150: $\quad r = -0.03197\, Dm + 0.3594$ (11)

6–13–100: $\quad r = -0.1037\, Dm + 1.322$ (12)

6–13–120: $\quad r = -0.1156\, Dm + 1.445$ (13)

6–13–150: $\quad r = -0.129\, Dm + 1.494$ (14)

13–25–100: $\quad r = -0.3214\, Dm + 3.989$ (15)

13–25–120: $\quad r = -0.2869\, Dm + 3.782$ (16)

13–25–150: $\quad r = -0.3346\, Dm + 4.07$ (17)

25–50–100: $\quad r = -0.3066\, Dm + 4.019$ (18)

25–50–120: $\quad r = -0.6866\, Dm + 8.147$ (19)

25–50–150: $\quad r = -0.8358\, Dm + 9.546$ (20)
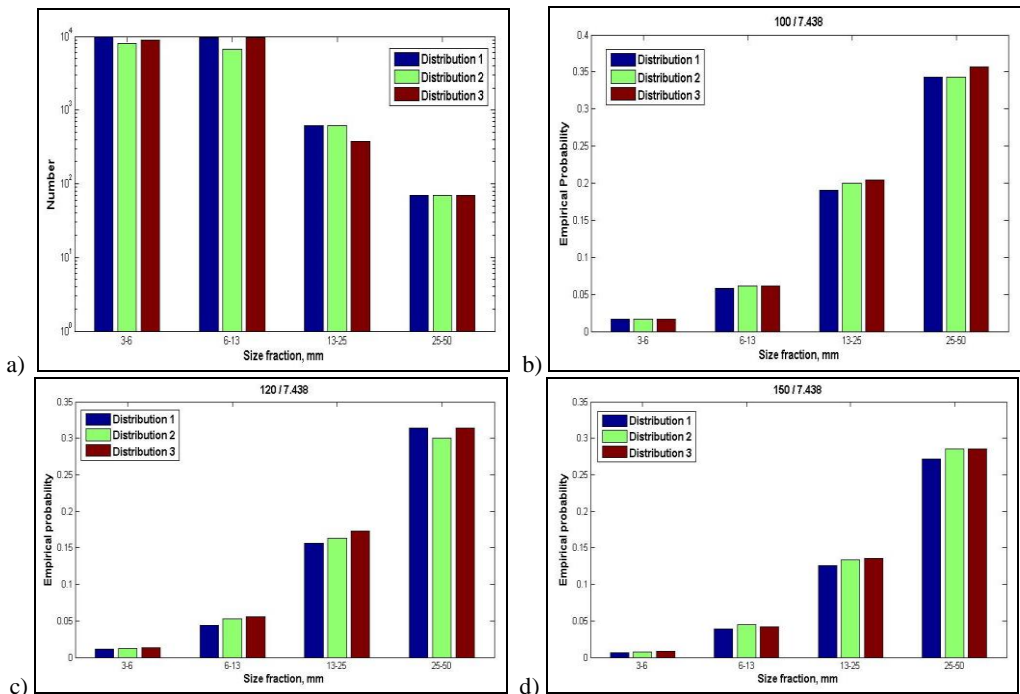
Fig. 7. (a): three different size distributions with the same value of Dm; (b), (c) and (d): comparisons of empirical probabilities of four size fractions in three size distributions and three heights of pile
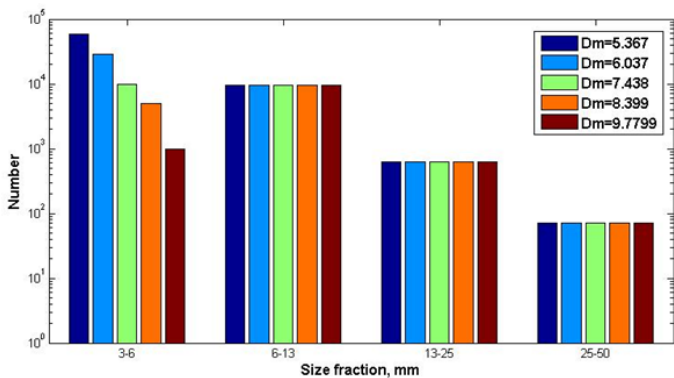
a)
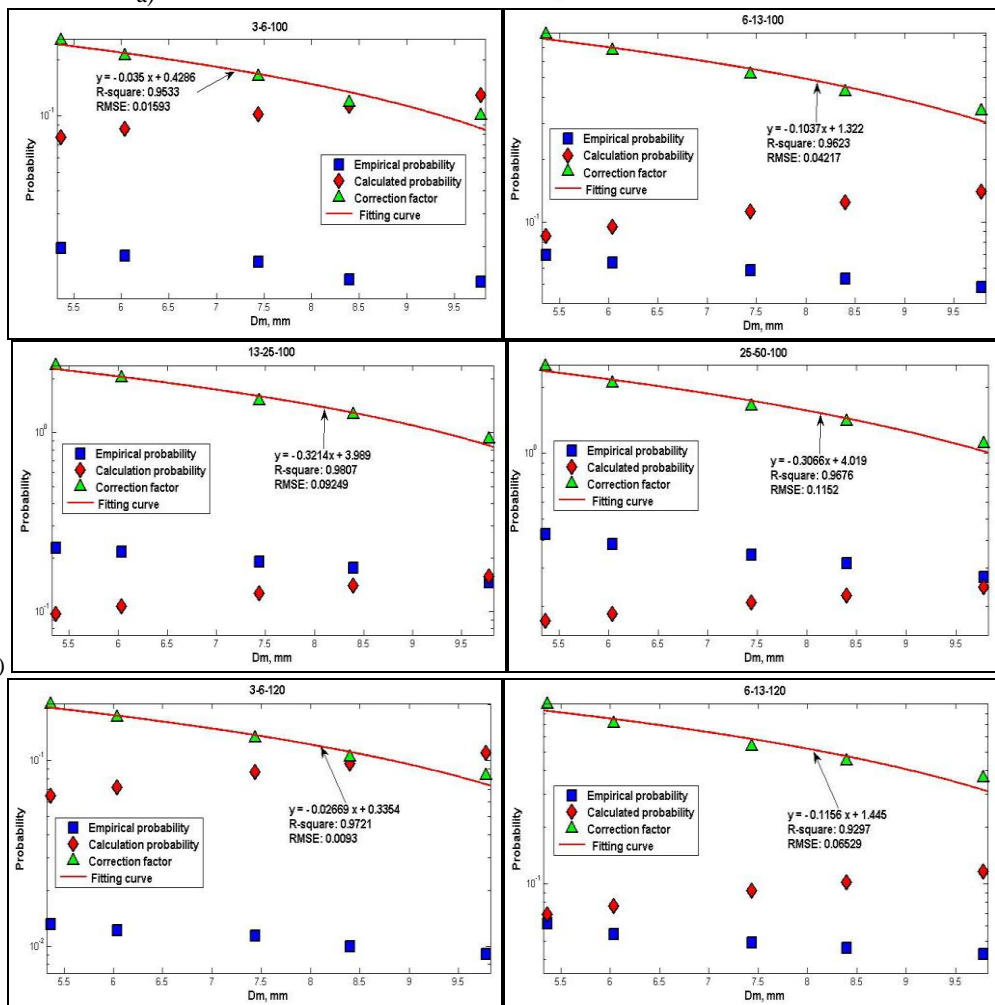
b)
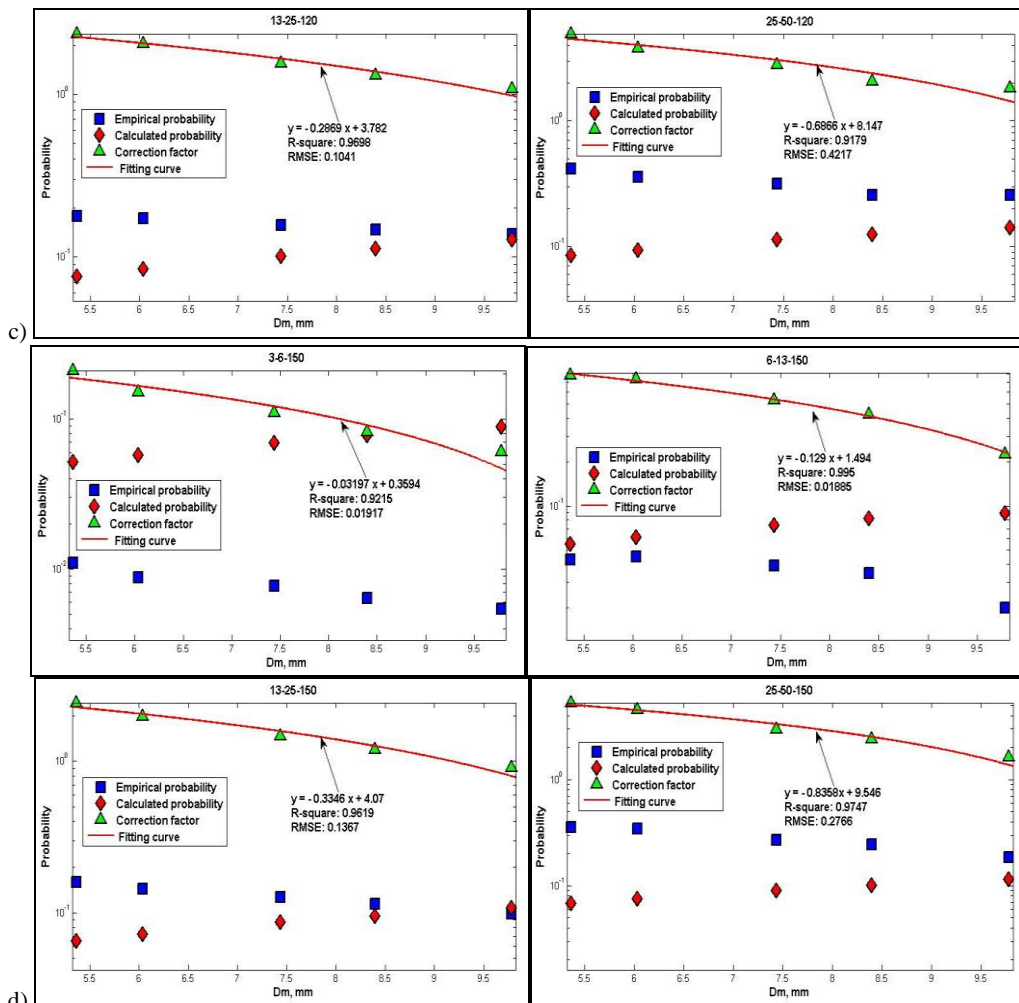
Fig. 8. (a): size distributions corresponding to five different values of Dm; (b), (c) and (d): variation tendencies of empirical probability, calculated probability and the correction factor of four size fractions with Dm in three heights of pile

These linear equations showed different size fractions and heights of pile had different correction model. Therefore, according to *Dm* and the height of particle pile of 3–50 mm, a corresponding correction equation can be selected to calculate the correction factor and correct the error of surface probability model. More correction equations in different conditions needed to be developed in the future.

Conclusions

A new surface probability model for the estimation of particles size distribution on a conveyor belt was developed based on the Chavez model, which can be used to correct the capturing error and improve the estimation accuracy of size distribution by image analysis in mineral engineering. A series of experiments were carried out to test and verify the new model and several conclusions were obtained as follows.

- The empirical probability and calculated probability of each size fraction were almost equal in single size fraction, and the two probabilities of each size fraction reduced with the increase of height of pile.
- Differences between empirical probability and calculated probability of each size fraction increased with the increase of range of multiple size fractions, the main reason of which is the covering of particles in different size fractions. In addition, larger particles should be easier to appear on the surface than smaller particles in multiple size fractions. In addition, the higher the pile height is, the lower the difference between empirical probability and calculated probability is.
- One D_m corresponds to one empirical probability in a constant height of pile, in spite of the change of size distributions.
- The variation tendencies of empirical probability and calculated probability with Dm were not the same in four size fractions, but the correction factor of four size fractions reduced with the increase of D_m in three heights.
- A series of linear equations of correction factor and D_m were developed to correct the errors between empirical probability and calculated probability, and more correction equations in different conditions needed to be developed in the future.

Acknowledgements

References

Al-Thyabat S., Miles N.J., 2006. *An improved estimation of size distribution from particle profile measurements*. Powder Technology 166, 152–160.

Al-Thyabat S., Miles N.J., Koh T.S., 2007. *Estimation of the size distribution of particles moving on a conveyor belt*. Minerals Engineering 20, 72–83.

Casali A., Gonzalez G., Vallebuona G., Perez C., Vargas R., 2001. *Grindability Softsensors based on Lithological Composition and On-Line Measurements*. Minerals Engineering 14, 689–700.

Chavez R., Cheimanoff N., Schleifer J., 1996. *Sampling problems during grain size distribution measurements*. In: Proceedings of the Fifth International Symposium on Rock Fragmentation by Blasting - FRAGBLAST 5. Montreal, Quebec, Canada, 245–252.

Claudio A., Pablo A., Estévez A., 2011. *Ore grade estimation by feature selection and voting using boundary detection in digital image analysis*. International Journal of Mineral Processing 101, 28–36.

Chatterjee S., Bandopadhyay S., Machuca D., 2010a. *Ore Grade Prediction Using a Genetic Algorithm and Clustering based Ensemble Neural Network Model*. Mathematical Geosciences 42, 309–326.

Chatterjee S., Bhattacherjee A., Samanta B., Pal S.K., 2010b. *Image-based Quality Monitoring System of Limestone Ore Grades*. Computers in Industry 16, 391–408.

Guyot O., Monredon T., LaRosa D., Broussaud A., 2004. *VisioRock, an Integrated Vision Technology for Advanced Control of Comminution Circuits*. Minerals Engineering 17, 1227–1235.

Jayson T., Carl D., Gianni B., 2007. *A machine vision approach to on-line estimation of run-of-mine ore composition on conveyor belts*. Minerals Engineering 20, 1129–1144.

Kemeny J., Mofya E., Kaunda R., Lever P., 2001. *Improvements in blast fragmentation models using digital image processing*, in: Explosives in Mining Conference, Explo, 357–363.

King R.P., 1982. *Determination of the distribution of size of irregularly shaped particles from measurements on sections or projected areas*. Powder Technology 32, 87–100.

Ko Y. D., Shang H., 2011. *Time delay neural network modeling for particle size in SAG mills*. Powder Technology 205, 250–262.

Petruk W., 1988a. *Automatic image analysis for mineral beneficiation*. Journal of Metals 40 (4), 29-31.

Petruk W., 1988b. *Automatic image analysis to determine mineral behaviour during mineral beneficiation*, Process Mineralogy VIII. In: Carson, D.J.T., Vassiliou, A.H. (Eds.). The Minerals, Metals & Materials Society, 347–357.

Petruk W., 1989, *Short course on image analysis applied to mineral and earth sciences*, Mineralogical Association of Canada, Ottawa.

Petruk W., Wilson J.M.D., Lastra R., Healy R.E., 1991. *An image analysis and materials balancing procedure for evaluating ores and mill products to obtain optimum recoveries*. In: Proceedings of 23rd Annual Meeting of the Canadian Mineral Processors, 1–16 (Section 19).

Perez C., Casali A., Gonzalez G., Vallebuona G., Vargas R., 1999. *Lithological Composition Sensor based on Digital Image Feature Extraction, Genetic Selection of Features and Neural Classification*. IEEE International Conference on Information Intelligence and Systems, Bethesda, MD, Oct.31-Nov.3, 236–241.

Singh V., Rao S., 2006. *Application of Image Processing in Mineral Industry: a Case Study of Ferruginous Manganese Ores*. Mineral Processing and Extractive Metallurgy 115, 155–160.

Singh N., Singh T. N., Tiwary A., Sarkar K.M., 2010. *Textural identification of basaltic rock mass using image processing and neural network*. Computers & Geosciences 14, 301–310.

Sun J., Su B., 2013. *Coal-rock interface detection on the basis of image texture features*. International Journal of Mining Science and Technology 23, 681–687.

Tessier J., Duchesne C., Bartolacci G., 2007. *A Machine Vision Approach to On-line Estimation of Run-of-mine Ore Composition on Conveyor Belts*. Minerals Engineering 20, 1129–1144.

Vallebuona G., Arburo K., Casali A., 2003. *A procedure to estimate weight particle distributions from area measurements*. Minerals Engineering 16, 323–329.

Yang H., Liu Y., Xie H., Xu Y., Sun Q., Wang, S., 2013. *Integrative method in lithofacies characteristics and 3D velocity volume of the Permian igneous rocks in H area, Tarim Basin*. International Journal of Mining Science and Technology 23, 167–172.

Zhao Y., 2013. *Multi-level denoising and enhancement method based on wavelet transform for mine monitoring*. International Journal of Mining Science and Technology 23, 163–166.

Zhang Z., Yang J., Ding L., Zhao Y.M., 2012. *An improved estimation of coal particle mass using image analysis.* Powder Technology 229, 178–184.

PHASE CHANGE OF CHLORITE IN REDUCING ATMOSPHERE

Xinghua LIU, Yongfu YU, Wen CHEN, Xiaoyin LIU

Changsha Research Institute of Mining and Metallurgy, Changsha 410012, Hunan, China
liu-xinghua0731@163.com

Abstract. Magnetizing roasting is an important pre-treatment technique for beneficiation of hematite and limonite ores. Reduction mechanisms of these iron minerals have been fully studied while the mechanism of reduction of chlorite is not well understood. In this study, a reduction roasting study examining the phase change of chlorite with roasting temperature was undertaken. The major finding from this study was that chlorite partially was reduced to magnetite by carbon at 750 $^{\circ}$C, and the newly formed magnetite was finely disseminated within quartz and olivine. It was demonstrated that these locked magnetite particles would be reported to iron concentrate by low intensity magnetic separation resulting in high impurity content, especially SiO_2 and Al_2O_3 contents in the concentrate.

Keywords: chlorite, phase change, magnetizing, reducing roasting, magnetite

Introduction

Magnetizing roasting is a very effective process in treatment of iron ores, which are poorly responsive to conventional beneficiation techniques. It involves conversion of weakly magnetic iron minerals in the ore to a strongly magnetic form by subjecting the ore to a reducing atmosphere at elevated temperatures. In most magnetizing reduction systems, the ore is reduced at a particular temperature, and then quenched in water (Svoboda 2004). Hematite and limonite are two most common feebly magnetic iron minerals. They have the main chemical composition of Fe_2O_3, and their magnetizing roasting is a process in which Fe_2O_3 is deoxidized by carbon to yield magnetite Fe_3O_4. The reaction formulas are as the following (Zhang 1983):

$$3Fe_2O_3 + C \xrightarrow{570°C} 2Fe_3O_4 + CO \qquad (1)$$

$$3Fe_2O_3 + CO \xrightarrow{570°C} 2Fe_3O_4 + CO_2 \qquad (2)$$
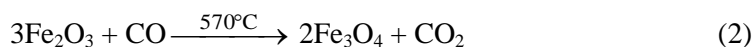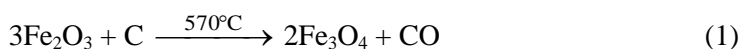
The resulting magnetite is strongly magnetic and can be recovered by low intensity magnetic separation.

Although the reduction mechanisms of hematite and limonite have been fully understood, the reduced simultaneously associated chlorite has not been found in the literature. Chlorite, as an iron-bearing alumino-silicate mineral, is widely distributed in various rocks, especially in about 70–90% sedimentary rocks (Yang and Zhang 1994). Chlorite also occurs in almost all of the Chinese large iron ore deposits (Wang et al. 2008). Chlorite which in fact is a general term for a group of minerals with a general formula $(Mg, Al, Fe)_6[(Si, Al)_4O_{10}](OH)_8$ is 2:1 phyllosilicates with an interlayer sheet. The 2:1 "talc-like" layer has two sheets of SiO_4 tetrahedron separated by an interlayer "brucite-like" sheet containing Mg, Al and Fe octahedrally coordinated (Silvester et al. 2011).

In our previous work, we have found that chlorite is a refractory gangue mineral in hematite ore just using conventional beneficiation techniques (Chen and Liu 2010). Chlorite has a specific susceptibility similar to that of hematite, and will have a high enrichment in concentrate after a high intensity magnetic separation. Structural iron ions on the surface of chlorite crystals also can cause some difficulties in flotation of chlorite from hematite (Liu et al. 2012; Chen and Liu 2012). Not long ago, another similar phenomenon was observed when we adopted reduction roasting- low intensity magnetic separation technique to beneficiate a high chlorite-containing hematite ore. The roasted chlorite was found to be enriched in magnetic concentrate after low intensity magnetic separation, which caused a large amount of SiO_2 and Al_2O_3 in the concentrate. The optimum temperature conditions for reduction roasting tests were determined as 750 ^{o}C, 10% of coal/sample ratio, and 90 min of the roasting time. In this study, we present an investigation on the phase change of the chlorite mineral in the reducing atmosphere by different roasting temperature tests. The aim was to find out the reason why the roasted chlorite minerals are enriched in iron concentrate and caused contamination.

Experimental

Samples

Chlorite with a purity above 90% was prepared for reductive roasting tests. The preparation procedure was as follows. First, high chlorite-containing rocks were selected from a hematite ore, and then crushed, ground, and screened. The undersize of the sample was first subjected to the magnetic separation at 0.4 T for discarding ferromagnetic materials, and second at 0.8 T for rejecting non-magnetic materials, and this separation process was performed repeatedly. Finally, the left material was chlorite concentrate, which was cleaned with distilled water and dried in an oven at 60 ^{o}C for 12 h. The size of the chlorite sample was below 30 μm, and a specific surface area of the sample was found to be as 3.8609 m$^2\cdot$g^{-1}. Its chemical composition and X-ray diffraction pattern are shown in Table 1 and Figure 1, respectively.

Table 1. Chemical composition of the chlorite sample

Component	SiO_2	Al_2O_3	MgO	FeO	Fe_2O_3	CaO	TiO_2	MnO	K_2O	Na_2O
Content (%)	27.24	18.35	7.11	25.36	11.21	0.55	0.50	0.12	0.086	0.025
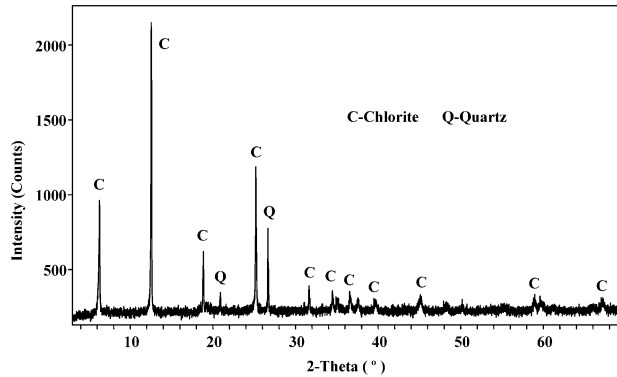
Fig. 1. X-ray diffraction pattern of the chlorite sample

Table 1 shows that the chlorite is a high iron-bearing alumino-silicate, which contains 25.36% FeO, 11.21% Fe_2O_3, 18.35% Al_2O_3, and 27.24% SiO_2. Figure 1 indicates that the chlorite sample was relatively pure, besides a small amount of quartz, and there are no iron mineral peaks.

Methods

The reduction roasting tests were conducted in a SX-8-10 type muffle roaster. Firstly, 10 g of chlorite sample and 1 g coal powder were weighed and blended each time. Secondly, the mixture was packed into a 30 cm^3 ceramic crucible. Thirdly, the crucible was sealed and placed in the heating muffle roaster which had reached a desired temperature. Finally, after a certain time, the roasted crucible was taken out from the roaster and quenched in cool water. In the roasting process, duration time and coal/chlorite sample ratio were held constant at 90 min and 10%, respectively. Meanwhile, the roasting temperatures were examined ranging from 500 °C to 750 °C. The roasted products were analyzed, and identified by X-ray diffraction and an electronic microscope.

Results and discussions

Phase change of chlorite at different roasting temperatures

Figure 2 plots the X-ray diffraction pattern of the roasted product at 500 °C. Compared with Figure 1, the diffraction pattern showed no big difference while the chlorite diffraction peaks are still there, and no other new phase appeared. When the roasting temperature increased to 600 °C, the diffraction peaks of chlorite disappeared and an

intermediate phase appeared as seen in Figure 3. With the roasting temperature continuing to increase up to 750 ^{o}C, the intermediate phase disappeared, while magnetite and olivine were newly formed, and their diffraction peaks are displayed in Figure 4. This clearly indicates that chlorite is partially reduced to magnetite by carbon at 750 ^{o}C, and the rest is turned into olivine which still has a complex chemical composition. According to the electron probe microanalysis (EPMA), olivine has a general formula of $(Fe_{1-a}X_a)_2SiO_4$, where X = Al, Mg and other isomorphous cations, which shows that this newly formed olivine is also, like chlorite, an iron-bearing alumino-silicate mineral.

In the past decades, different investigators have studied the differential thermal analysis (DTA) of chlorite (Martin 1955; Yang 1991; Yang and Zhang 1994), for relatively pure chlorite samples. Variations in chemical composition are reflected in the differential thermal curves, and their thermal behaviors mainly depend on the type of cation in octahedral sites. Chlorites high in ferrous iron lose most of their hydroxyl water at a lower temperature than do the magnesian and aluminous chlorites, which indicates iron atoms produce a marked change in the thermal behavior of chlorite because (a) the Fe-OH bond is weaker than the A1-OH or Mg-OH bond, (b) Fe atoms are larger than Al or Mg atoms, and therefore, do not fit into the structure as well, and (c) ferrous ions are subject to oxidation. From Table 1, the chlorite sample used in this study also contains Fe, A1, and Mg atoms, and among the three atoms, Fe atoms are the majority. According to the DTA results of chlorite, as the roasting temperature increases, Fe-OH bond is easier to be broken and ferrous ions in octahedral sites are also more appropriate to react with atmosphere than that of Al and Mg ions. Therefore, the reduction products of Fe atoms (magnetite) were first produced at 750 ^{o}C, as shown in Figure 4.

Many researches (Caillere and Henin 1951; Phillips 1963; Schneider et al. 2008) also showed that the major endothermic peak is controlled by ferrous iron in chlorite structure depending on iron content. The dehydroxylation and the mineral reactions occur at different temperatures. And chlorites, high in ferrous iron, begin their initial dehydration at appreciably lower temperatures than low-iron chlorites. For chlorites very high in ferrous iron ($\geq 18.7\%$ FeO), oxidation of ferrous to ferric iron occurs during the first dehydration stage at 450 ^{o}C. The second dehydration occurs between 500 ^{o}C and 600 ^{o}C, and the oxidation reaction within chlorite structure may be in accordance with conversion of one OH^- species to O^{2-} for each conversion of Fe^{2+} ion to Fe^{3+}.

With the continuing heating, the recrystallization products are finally formed depending on the type of chlorite. Magnesian chlorite is turned into forsterite and enstatite, aluminous chlorite is converted into mullite, and chlorite high in ferrous iron is oxidized into hematite and hercynite (Yang 1991). These reactions take place in vacuum or in a flow of N_2 or in air, but no references to chlorite reactions in reducing atmosphere have been found in the literature. In fact, the thermal behaviour of a high FeO content chlorite is markedly influenced by the nature of the furnace atmosphere (Martin 1955). Therefore, one possible reduction mechanism is that the high iron

content chlorite is first oxidized into hematite with the increasing temperature, and hematite is next reduced quickly to magnetite by burning carbon or CO. It can also be inferred that the olivine formed at 750 ^{o}C is still an intermediate phase, not the final reduction product. Further work on this will need to be undertaken.
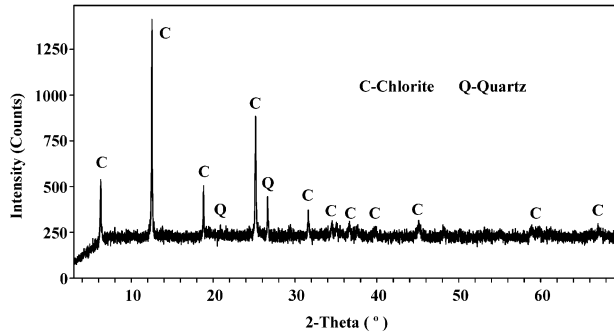
Fig. 2. X-ray diffraction pattern of the roasted product at 500 ^{o}C
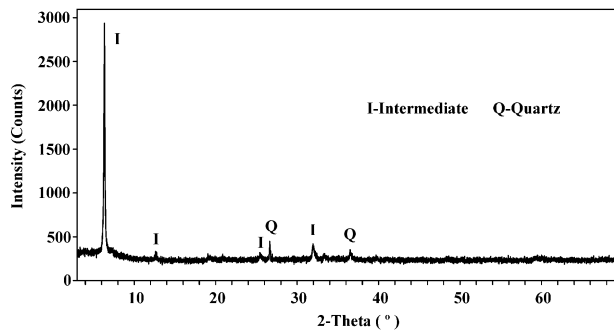
Fig. 3. X-ray diffraction pattern of the roasted product at 600 ^{o}C
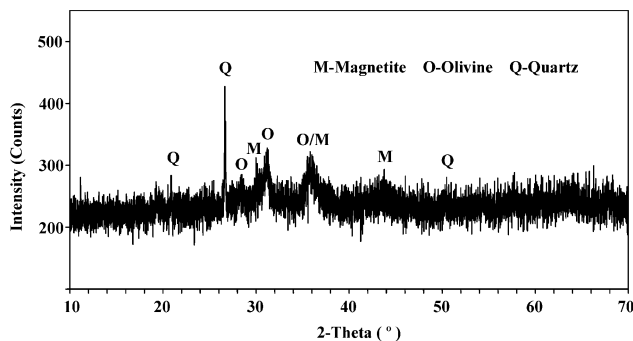
Fig. 4. X-ray diffraction pattern of the roasted product at 750 ^{o}C

Characteristics of the chlorite reduction product

Figure 5 shows the photomicrographs of the chlorite reduction product at 750 ^{o}C. Although the reduction product is no longer for the former chlorite, they still retain in the shape of chlorite crystal structure as seen in Figures 5 a and b. Additionally, Figures 5 c and d indicate that the newly formed magnetite particles are very fine and mostly below 10 µm, which are all locked with gangues (quartz and olivine) closely.

Furthermore, specific susceptibilities of chlorite sample and its reduction product were determined through the Gouy method. The specific magnetic susceptibility of chlorite sample is $41.46 \cdot 10^{-6}$ cm$^{3} \cdot$g^{-1} and its reduction product is $476.45 \cdot 10^{-6}$ cm$^{3} \cdot$g^{-1} which shows that the specific susceptibility increased nine-fold after the reduction roasting. Using a magnet with a field intensity of 0.2T to attract the chlorite reduction product, a small amount of magnetic particles was picked up. It can be inferred from this phenomenon that these intergrown magnetite particles will report to the iron concentrate during the low intensity magnetic separation. As a result, the quality of iron concentrate will be deteriorated.
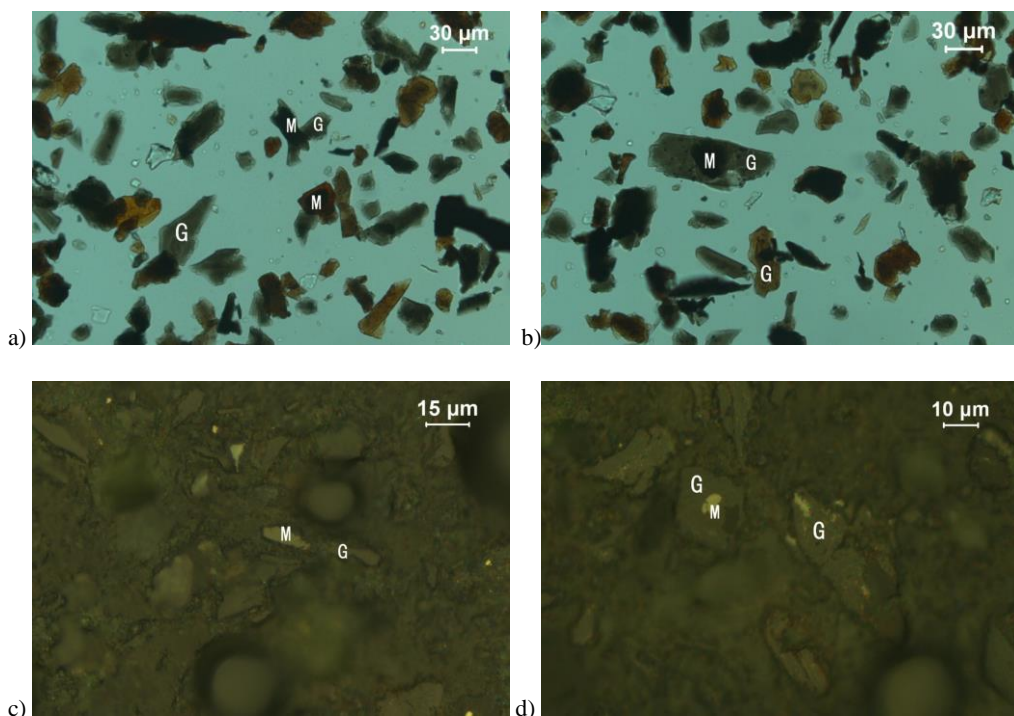
Fig. 5. Photomicrographs of the chlorite reduction product at 750 ^{o}C
(M – magnetite, G – gangue minerals including quartz and olivine)

Conclusions

Above 90% pure chlorite was used for the reduction roasting tests in a muffle roaster. The chlorite sample was a high iron-bearing alumino-silicate mineral which assayed 25.36% FeO, 11.21% Fe_2O_3, 18.35% Al_2O_3, and 27.24% SiO_2. At the coal/chlorite sample ratio of 10% and the roasting time of 90 min, chlorite showed no big phase change at 500 °C, and then the chlorite phase disappeared and an intermediate phase appeared at 600 °C, and then the intermediate phase changed into magnetite and olivine at 750 °C. Obviously chlorite is partially reduced to magnetite by carbon.

The photomicrographs of the chlorite reduction product at 750 °C showed that they still retain the shape of chlorite crystal structure, though the former chlorite no longer exists. All the newly formed magnetite particles were very fine and also associated with gangues (quartz and olivine). These intergrown magnetite particles will report to the iron concentrate during low intensity magnetic separation, which can lead to a high impurity content of SiO_2 and Al_2O_3 in the magnetic concentrate.

Olivine formed at 750 °C is still an intermediate phase, which can be further reduced to magnetite in the reducing atmosphere by extending the roasting time or improving the roasting temperature. More work and further study on detailed reduction mechanism of chlorite need to be carried out in future.

Acknowledgments

References

CAILLERE S., HENIN S., 1951, *Observations on the chlorites of iron ores*, Clay Minerals, 1(5), 134–137.

CHEN W., LIU X.H., 2010, *Experimental investigation of reducing chlorite content in iron concentrates*, 2010 International Symposium on Project Management, New South Wales, Australia, 18–24.

CHEN W., LIU X.H., 2012, *Flotation technology for Yuanjiacun iron ore*, Separation Technologies for Minerals, Coal, and Earth Resources (SME), Colorado, USA, 489–496.

SVOBODA J., 2004, *Magnetic Techniques for the Treatment of Materials*, Kluwer Academic Publishers, Dordrecht.

LIU X.H., YU Y.F., CHEN W., YAN X.H., 2012, *Effect of selective flocculation desliming on flotation of fine grained Yuanjiacun iron ore*, XXVI International Mineral Processing Congress, New Delhi, India, pp. 2980–2992.

MARTIN R.T., 1955, *Reference chlorite characterization for chlorite identification in soil clays*, Clays and Clay Minerals, 3(1), 117–145.

PHILLIPS W.R., 1963, *A differential thermal study of the chlorites*, Mineralogical Magazine, 33(260), 404–414.

SCHNEIDER P., TROPPER P., WERTL W., BERTOLDI C., 2008, *The breakdown behavior of chlorite at high temperatures: a combined high-T XRD and DTA/TG study*, 86th Annual Meeting of the German Mineralogical Society-DMG, Berlin, Germany.

SILVESTER E.J., BRUCKARD W.J., WOODCOCK J.T., 2011, *Surface and chemical properties of chlorite in relation to its flotation and depression*, Mineral Processing and Extractive Metallurgy, 120(2), 65–70.

WANG Y.M., TIAN J.Y., WANG H.J., FENG Q., 2008, *Mineral Processing Practice of Chinese Ferrous Metal Ores*, Science Press, Beijing (in Chinese).

YANG Y.X., 1991, *A study on the thermal behaviour of chlorite-group minerals*, Acta Mineralogica Sinica, 12(1), 36-44 (in Chinese).

YANG Y.X., ZHANG N.X., 1994, *Clay Minerals of China*, Geology Press, Beijing (in Chinese).

ZHANG H.E., 1983, *Mineral Processing of Red Iron Ore*, Metallurgical Industry Press, Beijing (in Chinese).

FIELD MONITORING AND PERFORMANCE EVALUATION OF CRUSHING PLANT OPERATION

Erol YILMAZ

Inmet Mining Corporation, Toronto (Ontario) Canada, yilmazer@cayelibakir.com

Cayeli Bakir Isletmeleri A.S., Madenli Beldesi, P.K. 42, Cayeli (Rize) 53200 Turkey

Abstract. Crushing plants are of great interest in reducing particle size of rocks and ores as milling operations need to consider sustainable development. Since the crushing plants operate under harsh conditions and involve very abrasive material, multiple factors can influence their performance. This paper assesses a number of factors affecting the performance of a crushing plant by addressing the critical design parameters and consideration of ore characteristics, operability and maintainability. Due to the fact that the ore properties should remain the same during milling, its control may become difficult for yield and quality of a product. However, an operation factor can contribute positively to the performance if it is well managed by experienced operators. The present paper also considers the operational, instrumental, mechanical and maintenance aspects of crushing plant, focusing on the capacity and quality.

Introduction

In industries supporting mining and milling operations, crushing plays an important role in reducing particle sizes of rocks and ores. To reach desirable end product size, the feed material endures a few crushing stages that form a circuit. A crushing plant system consists of a combination of unit operations for storing, feeding, crushing, screening, and conveying (Viilo, 2011). The crushing plants are often designed to be able to produce certain throughput on predefined specification and a size distribution while keeping the plant capacity and quality, resulting in a reasonable cost and energy consumption (Beerkircher et al., 2003, Lindqvist, 2008; Asbjornsson et al., 2012). The main challenging of running a crushing plant as competently as possible is to know how each production unit affects efficiency of the whole plant (Svedensten and Evertsson, 2004). Therefore, these units should be built up with technologies and improvements which give savings at great amounts for every ton (megagram, Mg) of

ore crushed, high capacity of use, ability to consume little energy and low repair-service costs (Utley, 2003; Wills and Napier-Munn, 2006, Drzymala, 2007).

The crushing plants like any other production process are greatly affected by changes over time, since it is a continuous process where equipment is subjected to variations. These variations can be caused by unmatched or degrading equipment performance, which can be minimized overall plant capacity and thus a decreased product quality (Major, 2003; Bengtsson et al, 2009; Itavuo, 2009). In order to attain a certain product quality, numerous crusher settings (i.e., closed size setting, speed etc.) can be varied by plant operators on a daily basis. Ore properties play also a vital role in the product quality and plant performance (Schonert, 1996; Guimaraes et al., 2007). Practitioners are striving to build up better and more reliable crushing plants. One of the central functions of well-running and professionally-managed crushing plants is to present several documents for owners, engineers, operators, practitioners, or even visitors (Boyd, 2008). Those documents will allow them to review and better understand recent developments in operating areas.

In this paper, factors that affect the performance of the crushing plant operation are evaluated by focusing several critical design parameters associated with downtimes and production losses. It also provides the operational, instrumental, mechanical and maintenance aspects of crushing plant. Specific objectives are: i) to get detailed knowledge, which can be used for assessing the plant performance and control development, ii) to collect a bunch of system data, which can be used for calculating plant availability and utilization, and finally iii) to better describe the bottlenecks of crushing plant, which can lead to production delays.

Ore crushing plant

The mine studied is located at Rize in eastern Turkey and is the first fully mechanized underground copper and zinc mine operating since 1994. The run-of-mine ore is delivered directly from both underground and over a distance of 1 km from the shaft to the stockpile (having a 24 gigagram (Gg) capacity) by trucks. Based on their types and grades, the ores extracted are then stored in bins. To get optimal metallurgical results, the ore is blended and fed to crusher by loader bucket for size reduction. Crushing is done in three stages with a combination of one jaw and two cone crushers that work in close circuit with a screen (Fig. 1).

A feed hopper which feeds jaw crusher has 50 Mg capacity and it has a 45×45 cm grizzly screen on it. Materials finer than 45 cm pass through a screen. At entry of the jaw crusher, there exists a vibrating feeder equipped with steel chains for homogeneous feeding. A 80% of crusher final product is less than 8–9 mm. A rock breaker is also used to break oversize rocks accumulating over the feed hopper grizzly. The crushing circuit consists mainly of the jaw and cone crushers, double deck vibrating screens, belt conveyors, transfer house, fine ore bin, metal collection systems (magnets and metal detectors) and de-dusting system.
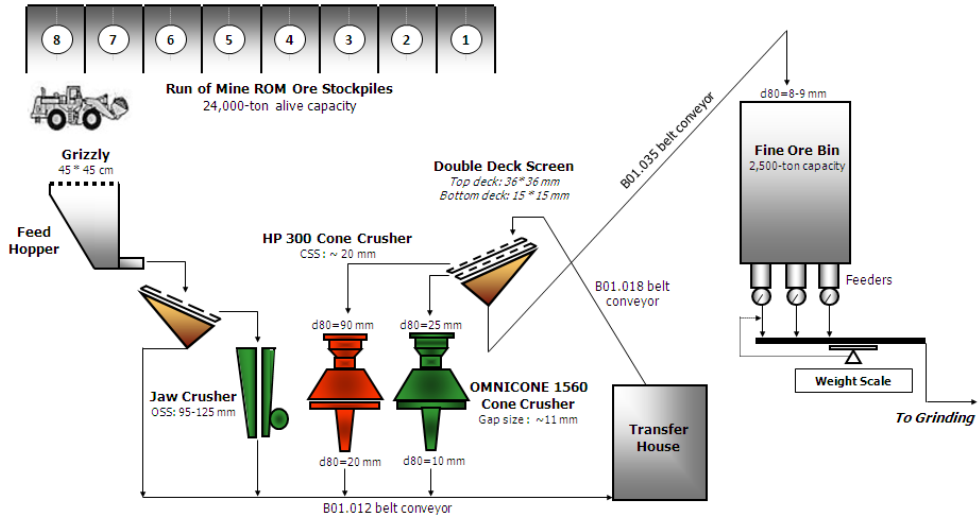
Fig. 1. Typical flowsheet of crushing plant

Factors affecting crusher performance

Figure 2 shows a number of factors that can affect the performance in ore crushing plant. However, these factors can be illustrated by three categories of influence: ore characteristics, equipment factor and operation factor. The following subsection will discuss these factors in details. The aspects, which affect the process are site-specific and subjected to change based on the operation. Identifying problems and debottlenecking in a crushing plant is a challenging task because it requires information and experience of the plant. The bottleneck in an open circuit is often the last production unit, which ensures steady output from plant. In closed circuit, it may however be a bit more complex causing some problems.
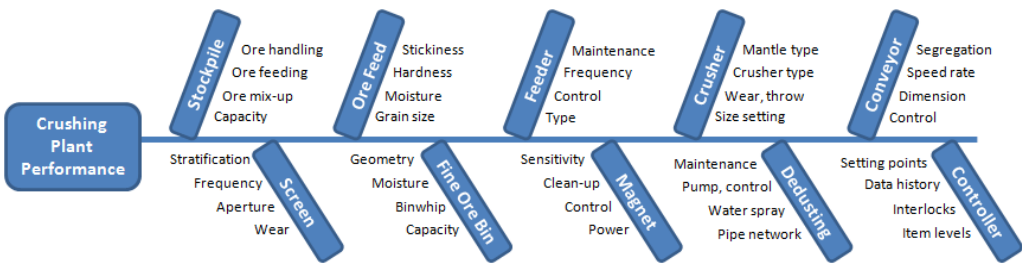
Fig. 2. Cause-and-effect diagram showing factors that can influence plant performance

The main reasons behind the low crusher throughput were identified to originate from the stockpiling run-of-mine ores, which may wet or contain non-ore materials, such as wood, plastic, metal, etc. This issue will be clearly mentioned in the following

subsections. The vibrating feeder under the feed hopper grizzly is another important factor since it provides the ore to the crusher. Sometimes it is not efficiently running due to tacky ore and/or structural mechanical problems, such as easy wear, etc. The ore crushed per hour will remarkably drop, giving rise to a low throughput. In similar way, crushers and their size settings and mantle types will directly play a role on the sum of crushed run-of-mine ore while making an allowance for the dimension and speeds of belt conveyors. Based on a structural formation of the crushed ore, a proper screen, which prevents wear and stratification should be chosen.

The fine ore bin capacity presents a clear flexibility to make maintenance in the crusher in a timely manner, especially when its level is high. Due to a combined problem caused by the bin geometry, some run-of-mine ores remain in the dead zones, which are positioned around three feeders within the fine ore bin. To trim the front surface of ores and hence provide ores to feeders for better operation, the hydraulic powered bin cleaning system was used efficiently. It is also worth to mention that the crusher operation cannot be performed without a metal and dust collection system. Due to the fact that there are metals pieces within ore and dust particles during crushing, it is of great importance to integrate those items to the system from the operational, mechanical and environmental points of view.

Ore characteristics factor

Material characteristics play a major role in the quality of the end product in the crushing plant. The ore entering the crusher will affect the plant performance, based on its change in the mineral content, grain size distribution and moisture. In addition, ores that contain non-ore products, such as sticky, mixed-up, wet, and dry materials, metals, woods and plastics can influence crusher performance resulting in lower production rate. Wet and sticky ores may clog chutes, lessen the live storage capacity of bins or silos. Drier ores are dustier because they are likely to stick together into larger particles. Based on the ores mineralogical composition, copper and zinc grades, there exist six types of run-of-mine ores: yellow YO, black BO, clastic CO, bornite yellow BYO, bornite clastic BCO and low grade LYO. CO contains more than 10% sphalerite clasts in matrix. BO and YO types are based on contained zinc grade and mined singly to allow for the most favourable grade blending from stockpile bins. These two ore types are referred to "Spec Ore". BO is defined as the ore with more than 4.5% Zn and a Cu/Zn ratio of less than 1. YO consists of pyrite and chalcopyrite clasts up to 20 cm in size, in matrix containing less than 10% sphalerite.

Figure 3 shows thin sections of different ore types. Although CO looks like a hard ore in its physical appearance initially, its crushing process is easy due to numerous small scattering grains. These grains are very susceptible to breaking because they are the residues of weathering. One can also say that bornite could exhibit plastic behavior in which crushing may become problematic. However, bornite-free ores such as YO, BO, and LGO act as the massive sulphide blocks, and can be crushed in a hardly

manner. The loose joints and well-developed ores, such as CO, are easily broken in the crushing plant.
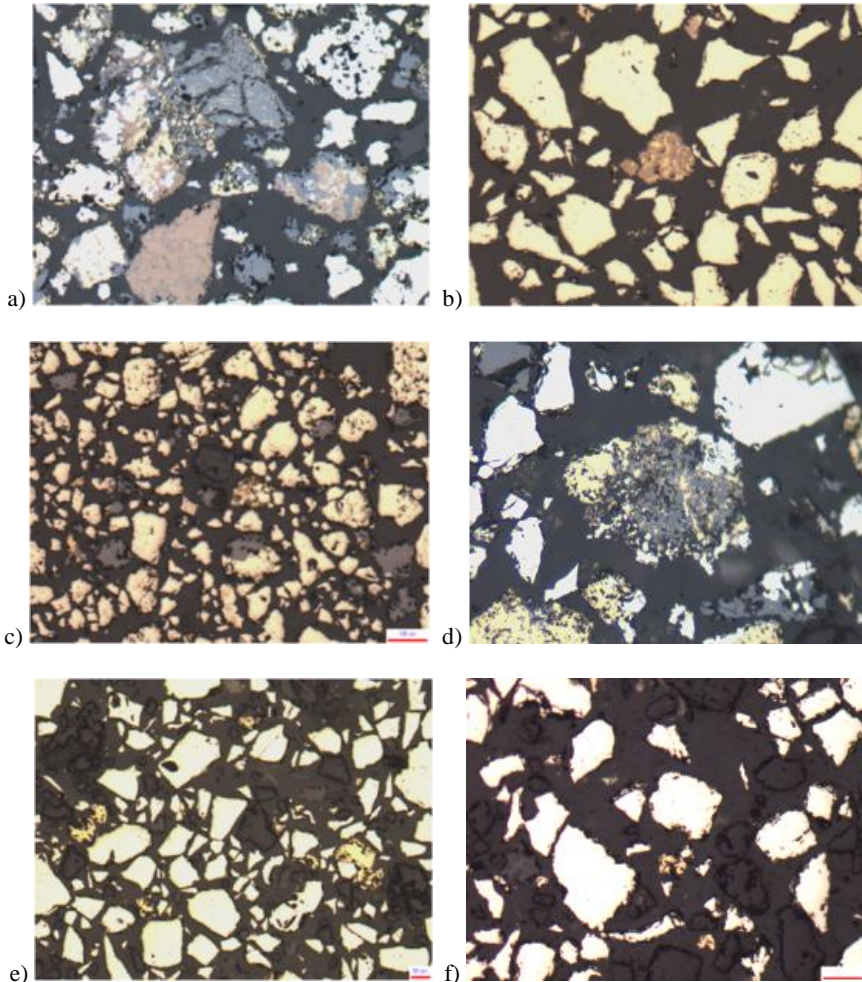
Fig. 3. Thin sections of different ore types: a) BCO, b) BYO, c) BO, d) CO, e) YO, and f) LYO

Figure 4 shows the variation in the total amount of the crushed run-of-mine ore for year 2012. It can be seen that the crusher shows a fairly good performance in 2012, except April, when the production remained behind a threshold value of 100,000 wmt (wet metric tons), resulting in a production rate of 94,610 wmt. The cogent reasons behind this are mechanical, instrumental, maintenance and operational downtimes, causing a drop in production for a time period of 66, 57 and 110 hours, respectively.
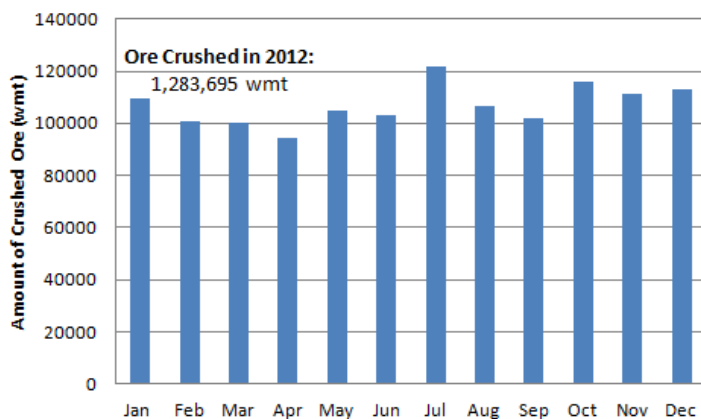
Fig. 4. Variation of ore crushed in 2012 (wmt – wet metric tonne)

The most important factor is that, if the ore is clean, excluding non-ore materials and when its brittleness is high, the ore is being crushed in a quicker and easier way without causing any problem. More fragile particles are easily broken into smaller particles. The harder the ore is, the higher compressive strength is and more effortless to be crushed. The crusher capacity will be drastically low if the ore material contains more chunks, dust, wet and ore fines, which will eventually expand the stickiness of ore and accordingly reduce ore the discharge speed. As discussed earlier, there are six different ore types in order to make four campaigns as follows: Spec, Non-spec CO, BCO and BYO. Table 1 lists the crushed ore according to campaign type and distribution. The use rates of Spec, CO, BYO, and BCO ores are respectively 29%, 42%, 10%, and 19%, taking into consideration the crusher throughput of 1,283,695 wmt. The most problematic ore campaign is BCO since its mineralogy (i.e. bornite) is different. The ores requires steps and different ways of crushing. Some of them will be crushed readily, while others generate difficultness to be crushed efficiently. The degree of difficultness will vary according to the texture of bornite-bearing minerals. Some minerals, like quartz and feldspars, are very brittle, while others, like micas and calcite, are more ductile. This is mainly a result of the chemical bond types that hold them together. Consequently, the mineralogical composition of ore will be a great factor in determining deformational behavior during crushing. Another aspect is the presence or absence of water within the mass. Water appears to weaken the chemical bonds and forms films around mineral grains along which slippage can take place. As a matter of this fact, wet rocks or ores tend to behave in ductile manner, while dry rocks or ores tend to behave in brittle manner. How a material behaves will furthermore rely on the following factors: temperature, confining pressure, and strain rate.

Table 1. Distribution of types of ore crushed

Blend type	Crushed ore (%)	Ore type distribution (%)					
		BO	YO	CO	LGO	BYO	BCO
Spec	29	14	60	13	10	3	0
CO	42	6	1	73	8	1	11
BYO	10	1	5	2	6	83	3
BCO	19	5	0	12	9	6	68

The best crushing performance is respectively obtained for the CO, YO, BYO, and BCO ores. Due to the fact that CO contains groups of broken fragments within the ore mass in micrometer size, its breakable rate is higher when compared with others. In fact, these fragments disperse homogenously in the ore and help to increase its crushing performance. Since CO is of loosen structure and fracture cleavage within the mass, the particle fragility index gets higher, hence offering the higher crusher capacity. Figure 5 shows the variation in crushed run-of-mine ore in a month, taking into consideration six different ore types. Results reveal that the usage percentages of CO, BCO, YO, BYO, BO, LGO are respectively 36, 19, 18, 11, 8 and 8%. The usage amounts of the ores by month are strictly depending on both present ROM ore availability at stockpile area and the campaign switches. Overall, a specific order for ore campaigns is used as following: Spec → BYO → Non-Spec CO → BCO → BYO → Spec. Because of the high availability of clastic ore being extracted from underground, this type of ore is often used in the plant for Spec (with YO) and Non-Spec (with BO) campaigns. LGO are hauled from underground as least as possible since the stockpile copper and zinc grades are decreased appreciably.
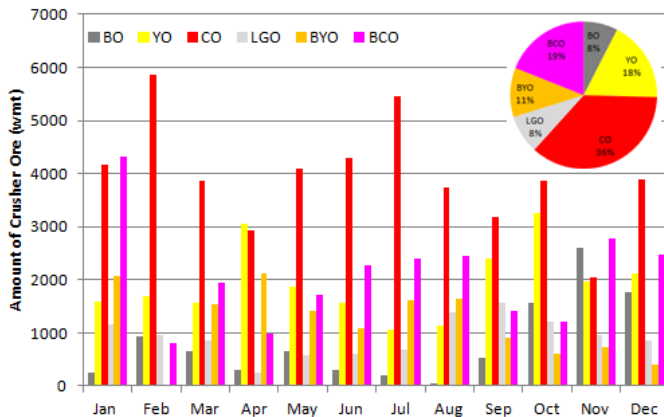
Fig. 5. Distribution of types of ore crushed

It is also good to point out that comminution involves a sequence of crushing and grinding processes. Grinding consumes large amount of energy, therefore effective

carrying out of the process is very important. Excessive grinding may give rise to high costs, while fine grinding usually makes further difficult with upgrading. The Bond grindability test is widely used for predictions of ball and ball mill energy requirements and for selection of the plant scale comminution equipment. This work provides the Bond ball mill work index, which expresses the resistance of material to ball milling. Table 2 lists a number of physico-mechanical properties of ores used in the facility. For each ore type, the standard Bond work index tests (unconfined compression) and moisture content tests were carried out individually on the representative ore samples. The results indicate that there is no significant change in the Bond work index values of samples. The highest work index (10.1 kWh/Mg) was achieved with the bornite yellow ore. The unconfined compression test confirms that CO has the maximum compressive strength of 27.5 MPa. The unconfined compressive strengths of YO, BYO and BCO are respectively 19.2, 18.8, and 17.8 MPa. The samples moisture remains in the range of 3.3-3.8%.

Table 2. Physicomechanical properties of ore campaigns

Blend type	Bond work index (kWh/Mg)	Compressive strength (MPa)	Moisture content (%)
Spec	9.9	19.2	3.5
CO	9.3	27.5	3.8
BYO	10.1	18.8	3.3
BCO	9.7	17.8	3.6

Equipment factor

To control the quality of ore produced from the crushing plant, the appropriate equipments should be selected for the sustainable operation. The choice of crusher equipment depends on the type and amount of material to be crushed. The equipment parameters, such as speed, model and less maintenance need are more closely related to the success of a confident level of the product quality. Higher rotate speed can increase crusher productivity, but it consumes more energy and may lead to blockages. Due to the fact that changing the equipment parameters affects the product quality, they are more susceptible to changes at any time based on the crusher production requirements. Figure 6 indicates the usage hours of three loaders (17-655, 17-662, and 17-663) and rock breaker (17-666), which are the key items to feed the ore stockpiling to the crusher and to control the grain size of ore on the surface stockpile area.

It is clear that the usage of 17-662 loader is reduced, while there is an incread usage of both 17-655 and 17-663 loaders over time (Fig. 6). Note that 17-663 loader is used as a spare one when others are out of service. The rock breaker shows a stable usage over years, since it is most often used for crushing the coarse-size ores on the feed hopper grizzly in the beginning and end of the shifts. It is noteworthy to mention that
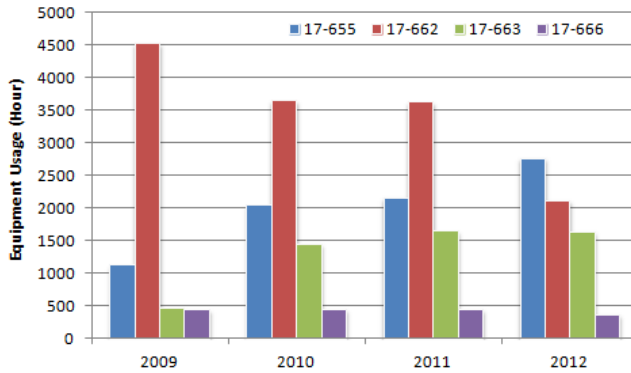
Fig. 6. Usage hours of three loaders and rock breaker used in crushing operations
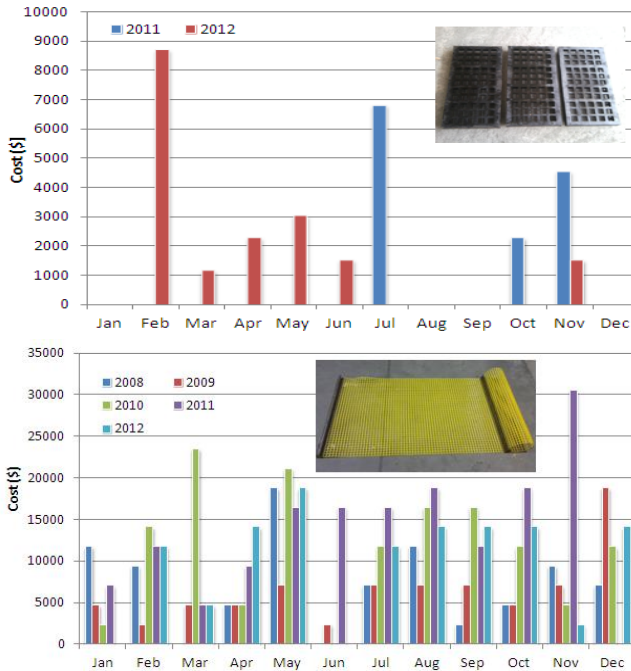
Fig. 7. The cost change in bottom (left) and top (right) deck screens as a function of time

loaders are crucial to the crushing and milling operations, since the blending and concentrate loading are made through these items. Figure 7 shows the change of frequency and connected costs of bottom deck vibroflex, polyurethane screens (800×1850 mm) and top rubber-clad screens (600×300 mm). The bottom deck screens (equipped with an aperture size of 15×15 mm) are constantly subjected to abrasive wear due to the ore relative motion. To prevent overloading in the circuit and thus to reduce the wear rate of screen, vibroflex screens, which are anti-static and

hydrophobic are preferred. The screen apertures were initially often plugged. Operators tried to open them by using air pressure, which is time-consuming and costly. Lately, the change rate of bottom decks was increased substantially from a time period of 30 to 45 days, based on a well collaboration between the mechanical and operational teams.
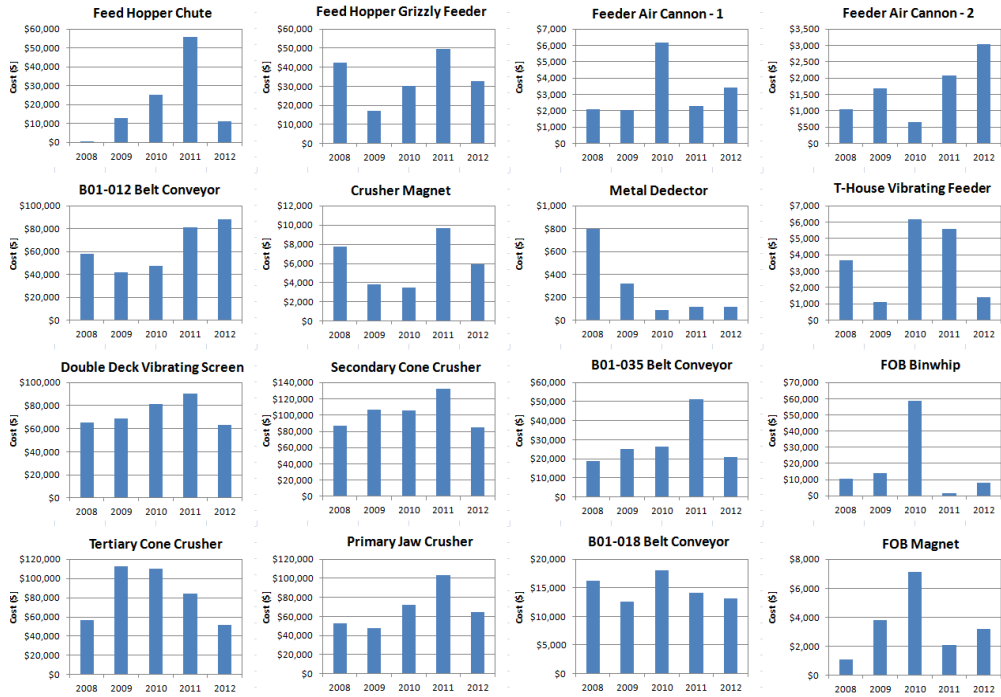
Fig. 8. The cost change in the major equipment of crushing plant

Figure 8 shows the change frequency and connected costs of the major equipment used in the crushing plant, which include the crusher, feeder, screen, conveyor, air cannon, magnet and metal detector. The cost change is expressed as a function of time. The crushing performance is directly based on operating time of the equipment without being out of service. Change in performance due to wear differs acutely depending on the feed material and equipment. The wear plates are of great importance for the lifetime of liners and crushers and therefore, high manganese plates are utilised by increasing the capacity and obliging less mechanical repair. On the whole, the maintenance costs of both jaw and cone crushers are decreased palpably. The key reason behind this reduction may be well explained by the oil and lubrication systems and by the reduced crusher wear parts. Serious improvement in the feeder, chutes, and conveyor were realized by keeping the particle size distribution of the crushed material constant. However, the cost of the B01.012 belt conveyor seems to be increased in 2012. This is mainly due to a number of sharp metals or objects, which

are dropped on the conveyor for different reasons and causing damages. To prevent this to happen again, a rip detection system was installed in this belt conveyor.

In addition, the double deck screen costs are significantly reduced by implementing a new strategy during and after its placement. The strategy relies on more maintenance and care for a couple of days just after panel replacement, and also the clean-up process of non-ore materials (i.e. plastics and woods) on screens at shift breaks on a daily basis. Due to a more efficient blend preparation, the magnet and metal detectors costs are lowered to a great extent, while the air costs have dimly increased in 2012. This increase is due to the wet, sticky ores, which may clog the surfaces, and therefore it deteriorates their proper functions. This situation is observed especially in the winter season.

One can conclude that, although crushers, chutes and belts are all a subject to extensive wear, and wear of parts and places can be heavy, the crushing performance is getting better. This is perceptibly a result of talented, experienced operators, well-organized teams and a well-developed collaboration between the mill and maintenance departments.

Operation factor

An efficient operation of the rock crusher plays an important role in crushing productivity. Not only design and layout of equipment, but also the cost of running should be considered in order to reach the best performance of the plant. This process is succeeded by experienced operators and their practical appliances during shifts. To meet the production goals for a given budget, the equipment used for crushing should have high operating availability, which is reached by keeping maintenance requirements to the minimum level as much as possible. Figure 9 illustrates the change in crusher performance in terms of both availability and utilization percents. The average availability and utilization rates were respectively 89% and 78%, thus corresponding to an overall asset utilization of 69%. Note that February 2012 conferred the best performance.
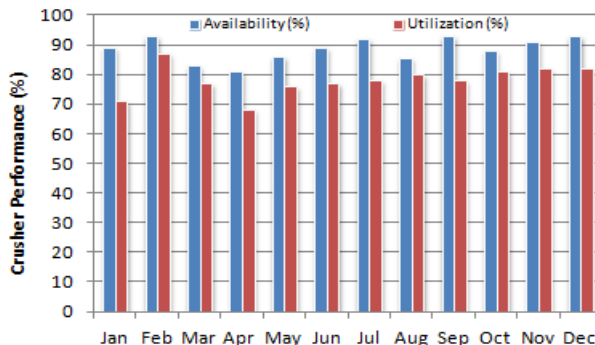
Fig. 9. Change in crusher performance in terms of availability and utilization

There are also production losses in the crushing plant, which can cause a disruption in normal operations leading to inefficiency, and thereby increase the costs. Figure 10 shows the change in production losses, which are mainly categorized as the ore, selection of non-ore material retained over the conveyor, rock breaker and fullness induced by wet, sticky ores. One can conclude that during the winter season, the ore may become problematic due to raining and inadequate ore production. This causes to fullness of the cone crushers, secreens and t-house. Producton loss induced by ROM ore, selection, rock breaker and fullness were respectively 259, 887, 273 and 611 minutes. To boost the crushing plant performance, a project relating to non-ore material sorting from ROM ores stockpiled just before letting them introduce to the crushing plant is now in progress. Details will be given later.
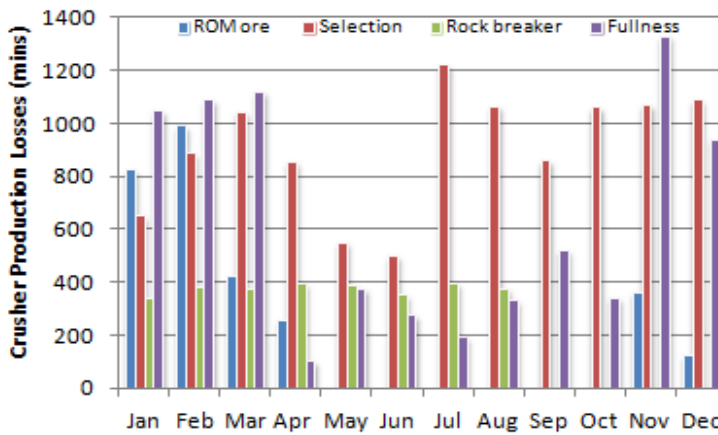
Fig. 10. Change in crusher production losses

There are times in the crushing plant, in which the system is non-operational and keeps downtime associated with mechanical repair, corrective/ preventive maintenance, instrumental and operational delays. Figure 11 shows the change in crusher down times. It is shown that the down times induced by maintenance, operational, mechanical and instrumental were respectively 2862, 5049, 2015 and 328 minutes. The most down times are caused by operational issues such as daily clean-up, chute plugs, crusher plugs and settings (close side setting which enables the production of products in desirable size). Operators have to regularly clean the cone crusher and bottom deck screen chutes for 30 minutes during shift.

Attention must be paid that operators need to check a number of equipment set-ups if their functions are running well. In fact, there has to be a clearance distance of 90 mm between fixed and moving jaws for jaw-type crushers. This clearance distance gets larger when wear appears on the jaws. The shims are mounted to the studs, which are holding the jaws to lessen the clearance to 90 mm, when it reaches more than 120 mm. As mantle wears, the bowl is also tightened in order to increase the pressure on the mantle. The main objective of taking this action is to take mantle closer to the

bowl since crushing action is accomplished between the mantle and bowl. This is also known as the adding bar.
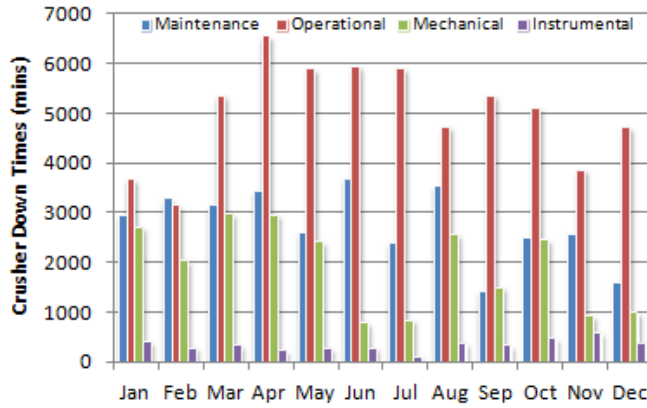
Fig. 11. Change in crusher down times

Figure 12 illustrates the change in metal alarms, which are considered as one of down times experienced in the crushing plant. Data is presented monthly as both count and time. Considering that each metal alarm takes five minutes, the average count number and time of metal alarms were respectively 520 and 43 hours. The total number of the metal-induced alarms corresponded to 22 days during which the plant was not running. To end up the number of metal alarms, a project was initiated recently to sort metals within ores stockpiled in the bins. The preliminary results prove that crusher performance is getting superior.
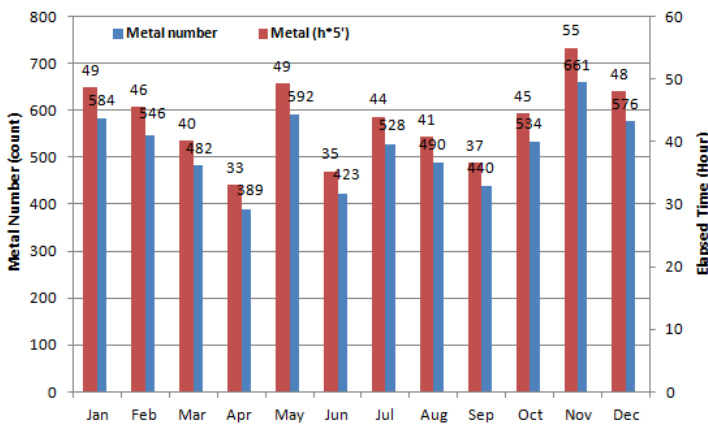
Fig. 12. Change in metal alarms as a function of count and time

One of contributions behind metal sorting at stockpile is also that the number of damages to both, belt conveyors and crushers, causing belt cuts and crusher blockages has dropped significantly. This makes the equipment to remain in the operation, which increases their availability and utilization rates. The non-ore material selection project will also decrease both cone crusher and double deck screen plugs, as shown clearly in Fig. 13.

Fig. 13. Photos showing crusher and screen plugs

Due to the fact that ores entering the circuit is metal, plastic, and wooden free, the apertures of screens, and the chutes of cone crusher and transfer house will never block. This first helps to reduce circulating load and then increases the capacity of crushing plant. Overall, sticky, woody and plastic materials plug chutes and damage the equipment. This project will eventually help to maximize profit, increase the product quality and equipment efficiency.

Conclusions

This paper shows factors that affect the performance of crushing plant operations at the Cayeli Mine (Rize, Turkey). There are three main factors of influence: ore characteristics, equipment and operation. Besides that other factors can contribute positively to the overall crushing performance, if they are well managed by experienced operators. However, due to the fact that ore properties should remain the same during ore processing, its control may become difficult for yield and quality of a product. In controlling a crushing plant performance, an operator must consider these three factors at the same time since one may change quality of the end product to a

great extent, while the others have a lesser effect on the product. Based on the results of the present study, the following conclusions can be drawn.

1. Crusher settings play a leading role in achieving product quality. Regular controls can augment the performance of crushing plant operations.
2. Daily crusher records will let the operator to better realize the actual bottlenecks behind production, and state a way of solution for efficiency.
3. An optimal ore blending will decrease appreciably the need of corrective and preventive maintenance, thus reaching higher operating availability.
4. Sorting a non-ore material within ores, which travels over the plant, is of great importance in increasing the crushing performance.

This paper shows that a newly-started reporting data for the crushing plant will bring a new outlook in assessing the performance of production units in terms of availability and utilization rates.

Acknowledgement

References

ASBJORNSSON G., HULTHEN E., EVERTSSON M., 2012. *Modelling and dynamic simulation of gradual performance deterioration of a crushing circuit – Including time dependence and wear*, Minerals Engineering, Vol. 33, 13–19.

BEERKIRCHER G., O'BRYAN K., LIM K., 2003. *Selection and sizing of secondary and tertiary cone crushers*, Mineral Processing Plant Design, Practice, and Control – Vol. 2, (eds: A.L. Mular, D.J. Barratt, D. N. Halbe), SME, 621–627.

BENGTSSON M., SVEDENSTEN P., EVERTSSON M., 2009. *Improving yield and shape in a crushing plant*, Minerals Engineering, Vol. 22, 618–624.

BOYD K., 2003. *Crushing plant design and layout considerations*, Mineral Processing Plant Design, Practice, and Control – Vol. 2, (eds: A.L. Mular, D.J. Barratt, D. N. Halbe), SME, 669–697.

DRZYMALA J., 2007. *Mineral Processing: Foundations of theory and practice of minerallurgy* (1st Edition), Wroclaw University of Technology, Poland.

GUIMARAES M.S., VALDES J.R., PALOMINO A.M., Santamarina J.C., 2007. *Aggregate production: fines generation during crushing*, International Journal of Mineral Processing, Vol. 81, No. 15, 237–247.

ITAVUO P., 2009. *Dynamic modelling of a rock process*, M.Sc. Thesis, Tampere University of Technology, Finland, 1–112.

LINDQVIST M., 2008. Energy considerations in compressive and impact crushing of rock, Minerals Engineering, Vol. 21, No. 9, 631–641.

MAJOR K., 2003. *Types and characteristics of crushing equipment and circuit flowsheets*, Mineral Processing Plant Design, Practice, and Control – Vol. 2, (eds: A.L. Mular, D.J. Barratt, D. N. Halbe), SME, pp. 566-583.

SCHONERT K., 1996. *The influence of particle bed configurations and confinements on particle breakage*, International Journal of Mineral Processing, Vol. 44–45, No. 3, 1–16.

SVEDENSTEN P., EVERTSSON M., 2004. *Crushing plant optimisation via a genetic evolutionary algorithm*, Minerals Engineering, Vol. 18, 473–479.

UTLEY R.W., 2003. *Selection and sizing of primary crushers*, Mineral Processing Plant Design, Practice, and Control – Vol. 2, (eds: A .L. Mular, D.J. Barratt, D.N. Halbe), SME, pp. 584-605.

VIILO K., 2011. *Crushing and Screening Handbook,* 5th ed., Metso Minerals, Tampere, Finland.

WILLS B.A., NAPIER-MUNN T., 2006. *Wills' Mineral Processing Technology* (7th Edition), Burlington: Butterworth-Heinemann (Elsevier).

THERMODYNAMICS AND ADSORPTION STUDIES OF DYE (RHODAMINE-B) ONTO NATURAL DIATOMITE

Menderes KOYUNCU *, Ali Rıza KUL **

*Department of Textile, Van Vocational School, Yuzuncu Yil University, Van, Turkey, menderes@yyu.edu.tr
**Department of Chemistry, Science Faculty, Yuzuncu Yil University, Van, Turkey

Abstract: Thermodynamics and adsorption studies were conducted with a dye of rhodamine-B on natural diatomite. Adsorption of the dye was investigated with an initial dye concentration at pH 8±0.2, 303, 313 and 323 K. The adsorption experiments were carried out isothermally at three different temperatures. The Langmuir and Freundlich isotherm models were used to describe the equilibrium data and the results were discussed in details. The kinetic data agreed with the pseudo-first order model with rate constants (k_2) in the range of $3.05–1.59.10^{-1}$ g/mg min. The thermodynamic parameters such as standard free energy, entropy change and enthalpy were calculated for natural diatomite. These values showed that adsorption of rhodamine-B on natural diatomite was a spontaneous and endothermic process.

Keywords: diatomite, rhodamine B, adsorption, thermodynamics, Langmuir isotherm, Freundlich isotherm

Introduction

Synthetic dyes are widely used in many industries such as textiles, paper, plastics. Wastewater from textile is polluted by dyes. These colored effluents are known to be carcinogenic and highly toxic (Uzun, 2006; Ertas et al., 2010). The unwanted dye pollutions have to be removed from wastewaters before being discharged into the environment. For this reason, the most common methods available for color removal from waste water are coagulation and flocculation (Moi Pang, et al., 2001) and biomaterials (Papic et al., 2004). The removal of dyes from the aqueous system was a technological challenge for many decades.

A considerable research was conducted on the removal of dyes from wastewater effluent using adsorption techniques with different adsorbents such as activated carbon (Chandra et al., 2007), bentonite (Tahir and Nassem, 2007; Koyuncu, 2009), sepiolite (Dogan et al., 2006), silica (Blitz, 2007; Jesionowski, 2005), fly ash (Eren and Acar, 2006), palm-fruit bunch particles (Mamdouh and Yehiam, 1997), diatomite (Khra-

isheh, 2005; Koyuncu, 2012; Xux, 2012; Junxiong et al., 2012), TiO_2-supported diatomite (Eftekhari et al., 2010; Khraisheh et al., 2005) and other low-cost adsorbents.

Diatomite is an siliceous sedimentary rock, which has an amorphous form of silica ($SiO_2 \cdot nH_2O$). Diatomite contains a small amount of microcrystalline material, and is available in various locations around the world. Diatomite also received attention for its unique combination of physical and chemical properties such as high permeability and porosity, small particle size, large surface area, low thermal conductivity, chemical stability, and its low-cost material for the color removal of textile wastewater (Chan et al., 2011). The silica surface contains silanol groups that spread over matrix of the silica. The silanol group is an active one, which tends to reach many polar organic compounds and various functional groups (Al-Ghouti et al., 2003; Khraisheh et al., 2005; Al-Ghouti et al., 2005). A preliminary study appointed the applicability of using diatomite as a low-cost material for removal of textile wastewater. The diatomite surface is terminated by OH groups and oxygen bridges (Si-OH, $Si{\stackrel{\nearrow OH}{\searrow OH}}$), which act as adsorption sites. In the adsorption processes, it is important to know characteristic of these different adsorption sites (Khraisheh et al., 2005).

In this study, different temperatures of adsorption onto diatomite were attempted, and the effect on dye removal from the aqueous solution was investigated. The experiments were conducted at pH 8±0.2, and the initial dye concentration in the temperature range of 303–323 K was tested. The adsorption capacity and mechanisms as well as the thermodynamic parameters were investigated.

Material and methods

Materials

Diatomite samples were obtained from the Caldiran region of Van/Turkey. The chemical analysis of the diatomite obtained by a XRF technique revealed a chemical composition. The physical properties of the diatomite are given in Table 1. The natural diatomite sample, which was powdered by pounding in a porcelain mortar, was washed with distilled water and dried in an oven at 105 ºC. Rhodamine-B (Rh-B) as a dye was obtained from textile corporation (İstanbul/Turkey). The structural form of rhodamine-B is given in Fig. 1. A Rh-B has the maximum absorption wavelength at 553.7 nm. The maximum absorption wavelength of Rh-B was determined by finding out absorbance at the characteristic wavelength using a double beam UV-visible spectrophotometer.

Adsorption experiments

Adsorption was carried out on RhB by mixing 1.0 g of the natural diatomite samples with initial concentrations of 20 mg/dm³, 40 mg/dm³, and 60 mg/dm³. The mixtures were shaken in a thermally controlled automatic shaker at 120 rpm, at temperatures of 303 K, 313 K, and 323 K for 15, 30, 60, 90, and 120 minutes until the equilibrium

Table 1. Chemical composition and physical properties of natural diatomite

Chemical composition	%
SiO_2	69.70
Al_2O_3	11.50
Fe_2O_3	4.40
TiO_2	0.65
Na_2O	0.80
K_2O	1.40
Loss on ignition	11.55
Physical properties	
Color: Cream	
pH 8±0,2	
Particle size 63 μm	
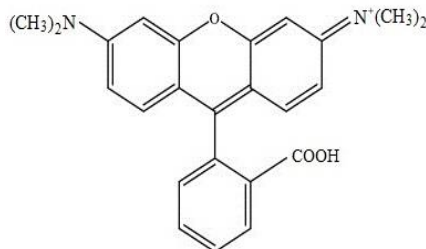
Fig. 1. Chemical structure of rhodamine B

conditions were reached. The concentration of the dye in the aqueous solutions after adsorption was measured by using a UV-vis (Shimadzu UV- Vis 1240) spectropho-tometer. The measurements of the pH values of the dye solutions were determined by using a pH 211 microprocessor pH meter (HANNA Instruments). The percentage of adsorption was estimated using following equation (Xiangheng et al., 2012) :

$$\% \text{ Adsorption} = \frac{C_i - C_e}{C_e} \cdot 100 \qquad (1)$$

where C_i and C_e are initial and equilibrium concentrations (mg/dm^3), respectively.

Thermodynamic parameters

The thermodynamic parameters such as standard Gibbs fee energy (ΔG^0), entropy change (ΔS^0) and enthalpy (ΔH^0) were calculated using following equations (Laidler and Meiser, 1999; Caliskan et al., 2011):

$$K_d = \frac{C_i - C_e}{C_e} \cdot \frac{V}{m} \tag{2}$$

$$\ln K_d = \frac{\Delta S^o}{R} - \frac{\Delta H^o}{RT} \tag{3}$$

$$\Delta G^0 = \Delta H^0 - T\Delta S^0 \tag{4}$$

where K_d is the equilibrium constant, C_i initial concentration (mg/dm^3), C_e equilibrium concentration, V volume (cm^3), m of the diatomite (g), T (Kelvin), and R gas constant (8.314 J/mol). The changes in enthalpy (ΔH^0) and entropy (ΔS^0) were determined from the slope and intercept of the plots of $\ln K_d$ versus $1/T$. The Gibbs free energy (ΔG^0) was calculated using Eq (4).

Kinetic studies

Kinetic studies were carried out using a thermostated shaker with polyethylene tubes at 303 K. A 0.1 g sample of natural diatomite was added to 10 cm^3 of RhB solution (20, 40 and 60 mg/dm^3) and at 303 K temperature between 1–150 minutes (time required to achieve an equilibrium conditions). The samples were analyzed by using the UV-vis (Shimadzu UV-Vis 1240) spectrophotometer. The adsorption experiments were conducted by using three different initial concentrations of RhB solution (20, 40 and 60 mg/dm^3). The amounts of RhB adsorbed at various time periods (q_t) were determined by:

$$q_{t=} \frac{(C_i - C_t)V}{m} \tag{5}$$

where C_i is the initial concentration of RhB, C_t concentration of RhB present in the aqueous solution after time t (min), V volume of solution (dm^3), and m is a mass of adsorbent (mg).

Results and discussion

Effect of initial dye concentration

The relative RhB removal by the adsorbents as a function of RhB concentration was studied (ranging from 20 to 60 mg/dm^3, at pH 8 ± 0.2, at 323 K). Figure 2 shows the effect of the initial dye concentration on adsorption. The equilibrium adsorption capacity increases with the increasing the initial RhB concentration. The RhB concentrations of 20 mg/dm^3, 40 mg/dm^3, and 60 mg/dm^3 increase the removal to 78.97%, 82.19%, and 85.51%, respectively. This increase in the proportion of adsorption may be probably due to the equilibrium shift during the adsorption process, and which may result from the increased number of ions competing for the available binding sites on

the surface of diatomite (Franco, 2010; Xue et al., 2010; Calıskan et al., 2011). Adsorption of the dye was a little increase for concentrations higher than 60 mg/dm^3. It indicates that the saturation of adsorption sites was achieved. It can be seen that the rate of adsorption decreases with time and gradually reaches equilibrium. In Figure 2, where measurements were undertaken over a period of 15-120 min in all cases, the contact time of 120 min was sufficient to ensure, that the adsorption equilibrium was attained. The arithmetic mean of adsorption and standard deviation (σ) were found to be 20 mg/dm^3 73.71 and 7.57 for 20 mg/dm^3, 76.94, and 8.80 for 40 mg/dm^3, 79.26, and 8.88 for 60 mg/dm^3, respectively.
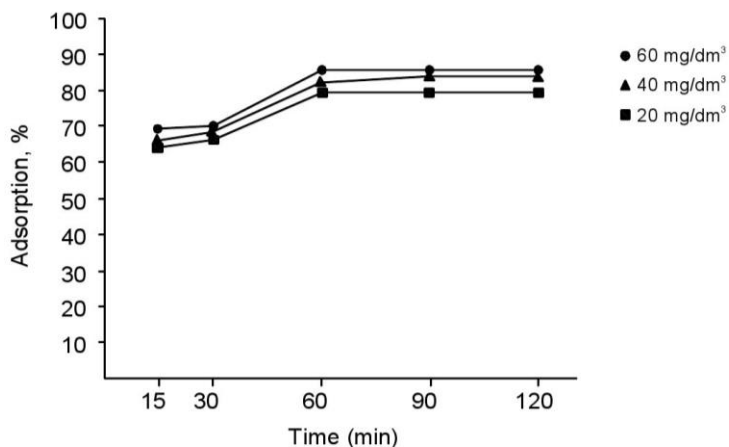
Fig. 2. Effect of contact time and initial dye concentration on dye adsorption.
Natural diatomite dose 1g/ dm^3 (pH 8 ± 0.2 at 323 K)

Effect of temperature

The temperature has two major effects on the adsorption process. Higher temperature increases the rate of diffusion of the adsorbate molecules across the external boundary layer and in the internal pores of the adsorbent particle, owing to decrease in the viscosity of the solution. In addition, temperature changing will change the equilibrium capacity of the adsorbent for the particular adsorbate. In this case of study, a series of experiments was conducted at 303, 313, and 323 K to study the effect of temperature on the adsorption rate.

Adsorption of Rh-B onto diatomite at 303, 313, and 323 K is shown in Fig. 3. The results indicate that adsorption increases with the temperature. It indicates the endothermic nature of the adsorption process. Similar results were also reported for Rh-B adsorption onto acid-heat activated rectorite (Xiangheng et al., 2012), kaolinite (Khan and et al., 2012) and calcined diatomite (Yusan et al., 2012).

The standard deviations (σ) at 303, 313, and 323 K were found to be 0.55, 7.72 and 0.98, 14.23 and 1.25, and 15.12, respectively.
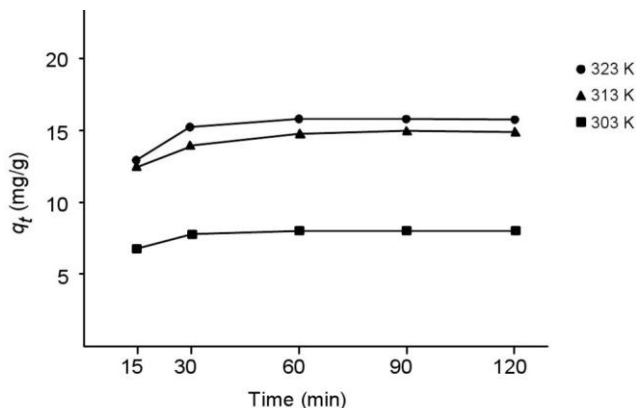
Fig. 3. Effect of temperature on adsorption of Rh-B onto natural diatomite

Adsorption isotherms

Langmuir isotherm

In the solid/liquid adsorption process, adsorption of the solute is usually characterized by either mass transfer (boundary layer diffusion) or intraparticle diffusion or even both (Ghosh and Bhattacharyya, 2002).

The adsorption data of Rh-B removal from natural diatomite was analyzed by the Freundlich and Langmuir isotherm models. The Langmuir isotherm model is valid for monolayer adsorption. The linear equation of the Langmuir isotherm is (Dogan et al., 2006):

$$\frac{C_e}{q_e} = \frac{1}{bq_m} + \frac{1}{q_m}C_e \qquad (6)$$

where, C_e is the equilibrium concentration of RhB in the solution, q_e amount of Rh-B adsorbed at equilibrium, q_m Langmuir adsorption capacity, and b Langmuir constant.

Figure 4 shows the relationship between C_e/q_e and C_e for the adsorption of RhB onto the natural diatomite at 303, 313, and 323 K. The slope calculation and intercept of the linear plots give the values of q_m and b.

The values of the Langmuir constants and coefficient determination R^2 are given in Table 1. The Langmuir adsorption capacity (q_m) was found to be 8.13, 9.52, and 10.21 mg/g at different temperatures (303, 313 and 323 K). The essential characteristic of the Langmuir isotherm can be expressed by the equilibrium parameter and dimensionless constant (R_L) using equation:

$$R_L = \frac{1}{1+bC_o} \qquad (7)$$

where R_L can be $0 < R_L < 1$.
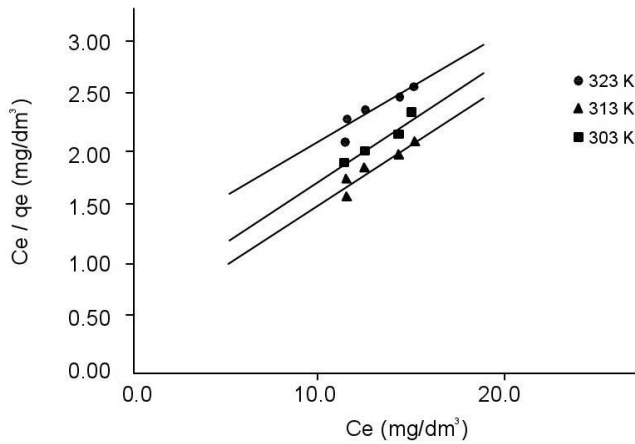
Fig. 4. Langmuir adsorption isotherm plots for adsorption of RhB
onto natural diatomite at different temperatures

Table 1. Isotherm parameters for adsorption of RhB onto natural diatomite

Model	Isotherm Constants	303 K	313 K	323 K
Langmuir	q_m	8.13	9.52	10.21
	b	0.35	0.19	0.15
	R_L	0.14	0.21	0.25
	R^2	0.99	0.99	0.99
Freundlich	K_f	2.45	2.73	3.85
	n	1.61	1.48	1.44
	R^2	0.99	0.99	0.99

The dimensionless separation factor (R_L) was found to be in the range of 0 to 1, indicating that adsorption of Rhodamine-B is favorable for natural diatomite (Freundlich, 1906; Ho and Mckay, 1999; Rahchamani and Zavvar Mousavi, 2011).

The adsorption capacity (q_m) of natural diatomite was found to be 10.21 mg/g. Similar results were also reported for Rh-B adsorption, such as banana pith (Anandkumar and Madal, 2011), cellulose-based (Aksu and Dönmez, 2003) acid activated mango (Namasivayan et al., 1993) and activated carbon (Annadurai et al., 2002).

Freundlich isotherm

The Freundlich isotherm assumes an empirical equation based on the heterogeneous surface of adsorbent. The linear form of the Freundlich isotherm is expressed as (Khan et al., 2011):

$$\log q_e = \log K_f + n \log C_e \tag{8}$$

where K_f is the Freundlich coefficient related to adsorption capacity, and n relates to adsorption intensity. The values of the Freundlich constants were obtained from the linear correlations between the values of log qe and log C_e. The values of K_f, n and coefficient determination R^2 are collected in Table 1. In the Freundlich adsorption constant, n should be between 1 and 10 for beneficial adsorption (Unuabonah et al., 2007; Vasu, 2008). Table 1 shows that n values are in the range of 1 to 10 for natural diatomite and R^2 is 0.99. It means that adsorption of Rh-B on natural diatomite can be described by the Freundlich model.
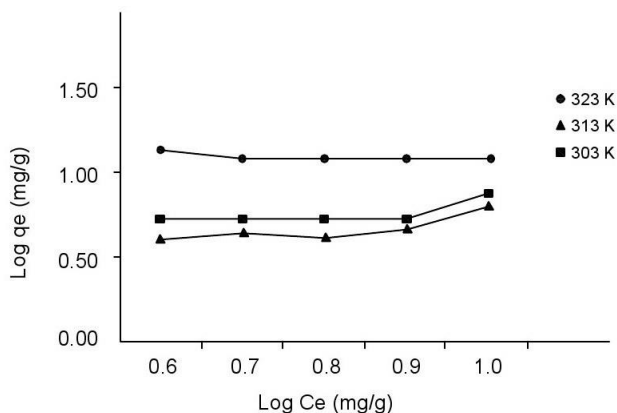
Fig. 5. Freundlich adsorption isotherm plots for adsorption of RhB
onto natural diatomite at different temperatures

Thermodynamic parameters of adsorption

The thermodynamic parameters (ΔG^0, ΔH^0 and ΔS^0) are presented in Table 2. The Gibbs free energy is calculated for adsorption of Rh-B on natural diatomite using Eq. (4). The values of ΔH^0 and ΔS^0 were determined from the slope and intercept from the plot of $1/T$ versus $\ln K_d$ given in Eq. (3), respectively.

The ΔG^0 value is negative for Rh-B on natural diatomite and it indicates that adsorption is spontaneous. The ΔG^0 decreases with temperature. Furthermore, better adsorption is obtained at higher temperatures (Khan et al., 2012). The positive values of the enthalpy change (ΔH^0) indicates that the adsorption process is endothermic. When ΔH^0 is lower than 40 kJ/mol the type of adsorption can be accepted to be a physical process. It indicates that adsorption is physical by nature and involves weak forces of attraction (Khan et al., 2012; Rahchamani et al., 2011). The positive value of ΔS^0 shows the increasing randomness at the solid/solution interface during adsorption of RhB on the adsorbents. The positive mean values of ΔS^0 may be due to some structural changes in the adsorbate and adsorbents during the adsorption process from the aqueous solution (Unuabonah et al., 2007).

Table 2. Thermodynamic parameters for the adsorption of rhodamine B onto natural diatomite

Initial Concentration mg/dm^3)	ΔH^0 (kJ/mol)	ΔS^0 (kJ/mol K)	ΔG^0 (kJ/mol)		
			303 K	313 K	323 K
20	7.68	25.81	–0.140	–0.399	–0.657
40	6.70	24.74	–0.800	–1.040	–1.290
60	7.10	25.11	–0.508	–0.759	–1.010

Adsorption kinetics

The experimental data relating to adsorption of RhB onto natural diatomite was investigated using the Lagergren pseudo-first and pseudo-second order equation (Aivalioti et al., 2010; Chan et al., 2011):

$$\log (q_e - q_t) = \log q_e - \frac{k_1 t}{2.303} \tag{9}$$

$$\frac{t}{q_t} = \frac{1}{k_2 q^2} + \frac{1}{q_e} t \tag{10}$$

where, q_e is the amount of Rh-B adsorbed at equilibrium (mg/g), q_t amount of Rh-B adsorbed at various times, t time of adsorption duration, and k_1 is a rate constant of the equation (min^{-1}).

The calculations were done for 20, 40 and 60 mg/dm^3 RhB solution initial concentration at 303 K. The $k1$ and q_e were calculated from the slope and intercept of the plots of log $(q_e - q_t)$ versus t according to the pseudo-first-order model (Fig. 6) and t/q_t versus t according to the pseudo-second-order model (Fig. 7) as well as q_e and k_2 from the slope and intercept were calculated. The kinetic parameters are given in Table 3. The the q_e values calculated from the pseudo-second-order model are match qe experimental results. The R^2 values were between 0.995 and 0.998. The linear regression correlation coefficient values for pseudo- second-order model were found to be higher than those of the first-order model. Higher R^2 values confirm that the adsorption data are well represented by the pseudo-second-order kinetics. The calculated qe values also agree very well with the experimental data in the case of pseudo-second-ordel kinetics model. Similar kinetic results were reported in adsorption of BTEX, MTBE and TAMI by natural and modified diatomite (Aivalioti et al., 2010), comparative study of lead sorption onto natural perlite, dolomite and diatomite (Irani et al., 2011), adsorption behavior of direct red 12B and rhodamine B from water onto surfactant modified coconutcoir pith (Sureshkumar and Namasivayam, 2008) and application of activated carbon derived from scrap tires for adsorption of rhomine B (Shuangxi and Tanzhu, 2010).
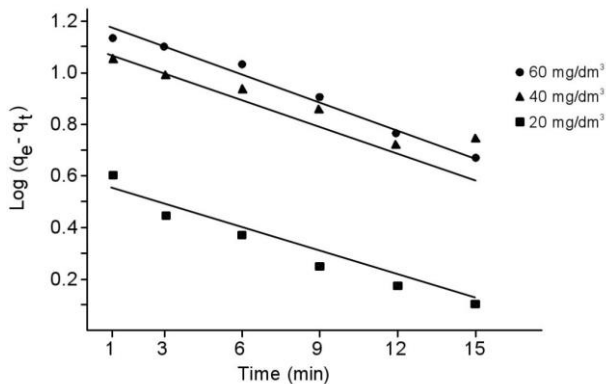
Fig. 6. Pseudo-first-order plots for adsorption of Rhodamine B onto natural diatomite
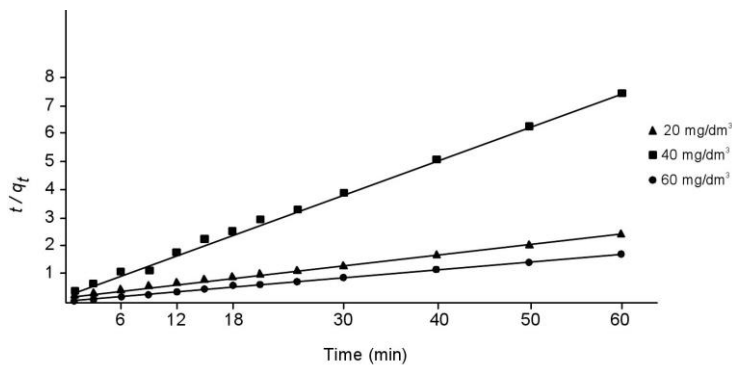
Fig. 7. Pseudo-second-order plots for adsorption of rhodamine B onto natural diatomite

Table 3. Kinetic parameters for adsorption of rhodamine B onto natural diatomite

Kinetic model	Kinetic parameters	Concentration (mg/dm^3)		
		20	40	60
Pseudo-first order	k_1	$5.68 \cdot 10^{-1}$	$10.75 \cdot 10^{-1}$	$12.23 \cdot 10^{-1}$
	q_e (calc.)	1.32	1.09	1.07
	q_e (exp.)	8.06	24.67	34.11
	R^2	0.974	0.981	0.979
Pseudo-second order	k_2	$3.05 \cdot 10^{-1}$	$1.59 \cdot 10^{-1}$	$0.58 \cdot 10^{-1}$
	q_e (calc.)	3.72	12.02	16.59
	q_e (exp.)	8.06	24.67	34.11
	R^2	0.998	0.992	0.995

Conclusion

The adsorption of the dye (rhodamine-B) by natural diatomite was investigated. It was found that natural diatomite is an effective adsorbent for removal of Rh-B from wastewater due to its short adsorption time and its natural pH (8.0±2). The thermodynamic parameters (ΔG^o, ΔH^o and ΔS^o) were calculated. It was shown that adsorption of Rh-B dye by natural diatomite is both endothermic and spontaneous. The removal of Rh-B by the natural diatomite was controlled by the initial dye concentration at natural pH and different temperatures. The adsorption data were well fitted by both Langmuir and Freundlich models. The maximum adsorption was found to be 10.21 mg/g (for initial concentration 20 mg/dm^3, temperature 323 K). The adsorption kinetics of Rh-B can be well described by the pseudo-second-order model. As a result, the natural diatomite can be used as a highly effective low-cost adsorbent for the removal of Rh-B from an aqueous solution.

References

AIVALIOTI M., VAMVASAKI I., GIDARAKOS E., 2010, *Adsorption of BTEX, MTBE and TAMİ on natural and modified diatomite*, Jhazmat, 207–208, 117–127.

AKSU Z., DONMEZ D., 2003, *A comparative study on the bisorption characteristics of some yeasts for remazol blue, reactive dye*, Chemosphere, 50, 1075–1083.

AL-GHOUTI M.A., KHRAISHEH M.A.M., ALLEN S.J., AHMED M.N., 2005, *Thermodaynamic behavior and effect of temperature on the removal of dyes from aqueous solution using modified diatomite, a kinetic study*, J.Colloid Inferface Sci. 287.

AL-GHOUTI M.A., KHRAISHEH M.A.M., ALLEN S.J., AHMED M.N., 2003, *The removal of dyes from textile waste water a study of the physical characteristic, and adsorption mechanisms of diatomeceous earth*, J .Environ. Manage. 69 (3), 229–238.

ANANKUMAR J., MADAL B., 2011, *Adsorption of Chromium (V) and Rhodamine B by surface modified tannery waste kinetic, mechanistic and thermodynamic studies*, Jhazmat, 186 (2–3), 1088–1096.

ANNADURAİ G.R., YUANG S., LEE D.J., 2002. *Use of cellulose– based wastes for adsorption of dyes from aqueous solutions*, Jhazmat, B92, 263–274.

BLITZ I.P., 2007, *Functionalized silicas: Structural characteristics and adsorption of Cu (II) and Pb (II)* Coll.Surface A: Physicochem. Eng. Asp. 307, 83–92.

CALISKAN N., KUL A.R., ALKAN S., GOKIRMAK E., ALACABEY I., 2011, *Adsorption of zinc (II) on diatomite and manganese-oxide-modified diatomite: a kinetic and equilibrium study*, J.hazmat. 193, 27–36

CHAN M., 2011, *Study on adsorption and desorption properties of the starch grafted p- tert- butyl-calix[n] arene for butyl rhodamine B solution*, Jhazmat.185, 914–921.

CHANDRA T.C., MIRNA, M.M., SUDARYANTO, Y., ISMADJI S., 2007. *Adsorption of basic dyes onto activated carbon prepared from durian shell: studies of adsorption equilibrium and kinetics*, Chem.Eng.J. 127, 121–129.

DOGAN M., ALKAN M., DEMİRTAŞ O., OZDEMİR Y.,OZMETİN C., 2006, *Adsorption kinetics of maxilon blue GRL onto sepolite from aqueous solutions*, Chem. Eng. J. 124, 80–101.

EFTEKHARI S., HABIBI YANGSEH A., SOHRABNEZHAD SH., 2010, *Application of AIMCM-41 competitive adsorption of methylene blue and rhodamine B thermodynamic and kinetic studies*, J.Hazmat. 178 (1–3), 349–355.

EREN Z., ACAR F.N., 2006, *Removal of reactive black 5 from aqueous solution: equilibrium and kinetic studies*, Desalination. 194, 1–10.

ERTAS M., ACEMİOĞLU B., ALMA M.H., USTA M., 2010, *Removal of methylene blue from aqueous solution using cotton stalk, cotton waste and cotton dust*, J.Hazmat. 183 (8), 421–427.

FRANCO, F., 2010, *Adsorption of methylene blue on magnesium silicate; kinetics, equilibria and comparison with other adsorbents*, J. Environ. Sci. 22, 467–473.

FREUNDLICH H.Z., 1906, *Over the adsorption ın solution*, J. Physical Chem. 57A, 385–470.

GHOSH, D., BHATTACHARYYA, K.G., 2002, *Adsorption of methylene blue on kaolinite*, Appl. Clay. Sci., 20 295–300

HO Y.S., MCKAY G., 1999, *Pseudo-second-order model for sorption process*, Process Biochem. 34 451–465.

IRANI M., AMJADI M., MOUSAVIAN M.A., 2011, *Comparative study of lead sorption onto natural perlite, dolomite, and diatomite*, Chem. Eng. J. 178, 317–323.

JESIONOWSKI T., 2005, *Characterization of pigments obtained by adsorption of C.I basic blue 9 and C.I acid orande 52 dyes onto silica particles precipitated via the emulsion route*, Dyes and Pigments. 67, 81–92.

JUNXIONG L., WANG L., SUN C., 2012, *Influence factors and kinetic study on photocatalytic degradation of Rhodamine B by Fe-doped TiO$_2$/diatomite composite*, Advanced Materials Research 535 (537), 2209–2213.

KHA T.A., DAHIYA S., IMRAN A., 2012. *Use of kaolinite as adsorbent: Equilibrium, dynamics and thermodynamic studies on the adsorption of Rhodamine B from aqueous solution*, Appl. Clay. Sci. 69 58–66.

KHAN T.A., SHARMA S., ALI L., 2011, *Adsorption of rhodamine B dye from aqueous solution onto activated mango (magnifera indica) leaf powder equilibrium, kinetic and thermodynamic studies*, J. of Toxicolgy and Environ.Health Sci. 3 (10), 286–297.

KHRAISHEH M.A.M., AL-GHOTI M.A., ALLEN S.J., 2005, *Effect of OH and silanol groups in the removal of dyes from aqueous solution using diatomite*, Water Research, 39, 922–932.

KHRAISHEH M.A.M., ALGHOUTI M.S., 2005, *Enhanced dye adsorption by micro emulsion– modified calcined diatomite*, Adsorption, 11(5–6), 547–559.

KOYUNCU M., 2009, *Adsorption properties of basic dyes (Maxilon Red and Maxilon Yellow GRL) onto bentonite*, Asian J. Chem. (21) 5458–5465.

KOYUNCU M., 2012, *Colour removal from aqueous solution of tar- chromium green 3G dye using natural diatomite*, Physicochem. Probl. Miner. Process. 48 (2), 485–494.

LAIDLER K.J., MEİSER J.M., 1999. *Physical Chemistry*, Houghton Mifflin, New York, p. 852.

MAMDOUH M., NASSAR M.Y., 1997, *Removal of different basic dyes from aqueous solutions by adsorption on palm fruit bunch particles*, Chem. Eng. J 661 233–226.

MOI PANG F., KUMAR P., TENG T.T., MOHD OMAR A.K., WASEWAR K.L., 2011, *Removal of lead, zinc and iron by coagulation-flocculation*, JTICE. (309), 7.

NAMASIVAYAN C. N., KANCHANA R.T., 1993, *Yamuna, Waste banana pith as adsorbent for the removal of rhodamine-B from aqueous solution*, Waste Manage. 13, 89–95.

PAPIC S., KOPRIVANAC N., BOZIC A.L., METERS A., *Removal of some reactive dyes from synthetic wastewater by combined Al (III) coagulation7carbon adsorption process*, Dyes Pigments (73) 291–298.

RAHCHAMANI J., ZAVVARMOUSAVI H., BEHZAD M., 2011, *Adsorption of methyl violet from aqueous solution by polyacrylamide as an adsorbent. ısotherm and kinetic studies*, Desalination, 267, 256–260.

SHUANGXI L.L., TANZHU L., 2010, *Application of activated carbon derived from scrap tires for adsorption of Rhodamine B*, J. Environ. Sci. 22 (8), 1273–1280.

SURESHKUMAR M.V., NAMASIVAYAM C., 2008, *Adsorption behavior of direct Red 12B and Rhodamine B from water onto surfactant- modified coconutcoir pith, colloids and surfaces* A: Physicochem. and Eng. Aspects. 317 (1–3), 277–283.

TAHIR S.S., NASEEM R., 2007, *Removal of Cr(III) from tannery waste water by adsorption onto bentonite clay*, Separation of purification Tech, 53, 312–321.

UNUABONAH E.I., ADEBOWALE K.O., OLU-OWOLABI B.I., 2007, *Kinetic and thermodynamic studies of the adsorption of lead (II)ions onto phosphate-modified kaolinite clay*, Jhazmat. 144, 386–395.

UZUN I., 2006, *Kinetics of the adsorption of reactive dyes by chitosan*, Dyes and pigments, 70 (2) 76–83.

VASU A.E., 2008, *Studies on the removal of Rhodamine B and malachite green from aqueous solutions by activated carbon*, E–J of Chem.5, 844–852.

XIANGHENG X., XISHENG H., YONGHONG Z., 2012, *Adsorption properties of acid– heat activated rectorite for Rhodamine B removal: equilibrium, kinetic studies*, Des. and Water Treat. 37, 259–267.

XUE A.L., ZHOU S.Y., LU X.P., HUN P.F., 2010, *Adsorption of reactive dyes from aqueous solution by silylated palygorskite*, Appl. Clay.Sci. 48, 638–640.

XUXCHEHWUO S., 2012, *Surface molecular imprinting on polypropylene fibers for rhodamine B selective adsorption*, J. Collod Interface Sci., 385 (1), 193–201.

YUSAN S., GOK C., ERENTURK S., AYTAS S., 2012, *Adsorption removal of thorium (IV) using calcinated and flux calcinated diatomite from Turkey: Evaluation of equilibrium, kinetic and thermodynamic data*, Appl. Clay Sci. 67–68, 106–116.

RECYCLING OF COLEMANITE TAILINGS USING THE JAMESON FLOTATION TECHNOLOGY

Ali UCAR*, Oktay SAHBAZ*, Senem KERENCILER*, Bahri OTEYAKA**

* Dumlupinar University, Mining Engineering Department, Kutahya, Turkey, oktay.sahbaz@dpu.edu.tr
** Osmangazi University, Mining Engineering Department, Eskisehir, Turkey

Abstract: In this study, beneficiation of colemanite minerals from tailings of the Emet Boron Processing Plant using a laboratory scale Jameson flotation cell was investigated in detail. Effect of some working parameters of the Jameson cell such as jet length, plunging depth of downcomer, and bias factor was studied for the flotation performance of colemanite. The results showed that all parameters showed a significant effect on colemanite flotation using the Jameson cell which was the first time used in boron flotation with a negative bias factor. The results also indicated that a high recovery could be obtained with a worthy grade values by the negative bias factor. According to the results obtained at the bias factor of -0.3, jet length of 3 cm, and plunging depth of 20 cm, B_2O_3 content of the sample increased to approximately 46% from 36.8% with a recovery of 98.47%.

Keywords: colemanite tailing, flotation, Jameson cell

Introduction

Boron is a very important raw material for more than 200 different industries. Boron concentrates, by-products and refined products are widely used in many sectors. Major boron reserves in the world are located in Turkey, and this includes about 72% of the total world's boron reserves of colemanite, tincal and ulexite (Helvacı and Alonso 2000). These reserves provide a significant economic potential for Turkey when boron content of concentrate is increased by various techniques including physical and physico-chemical methods. Therefore, it is necessary to produce a clean product by removal of gangue minerals, and also prevent loss of boron to slurry ponds. Particularly, montmorillonite type of clay is a major source of gangue minerals in boron reserves (Ozdemir and Celik 2010). Therefore, separation of boron minerals from montmorillonite is the most significant beneficiation process for increasing the quality of concentrate.

Boron beneficiation process conventionally includes a series of steps: washing, scrubbing, and classification. In Turkey, these series of methods have been utilized together to obtain concentrate with high boron content depending on the particle size. Moreover, the performance of the beneficiation methods for coarse particles is relatively high. On the other hand, the performance of physical methods decreases as the feed size gets finer. Therefore, particles finer than 150-200 µm are directly discharged to the slurry pond, and these particles have 20-26% of B_2O_3 (Gul et al. 2006; Kerenciler 2008; Ucar and Yargan 2009). Unfortunately, this causes not only economical loss but also environmental problems. For this reason, many studies have been performed to beneficiate boron minerals from the slurry ponds (Ucar and Yargan 2009). According to these studies, flotation is one of the most suitable methods for the beneficiation of the boron minerals from the slurry pond.

Previous studies indicated the importance of two points which must be taken into a consideration for boron flotation. The first one is the high possibility of slime coating on fine size particles (Yarar 1971; Celik et al. 2002; Ozdemir and Celik 2010; Ozkan and Acar 2004). The second one is the using suitable equipment having a high-performance for flotation of relatively fine particles (Ucar and Yargan 2009). According to the flotation mechanism and its theory, there is definitely a need for fine air bubbles in the flotation of fine and coarse particles (Sahbaz 2010). In this context, slime removal should be performed before flotation is carried out, and, the Jameson flotation cell will be a suitable device due to its high performance in processing of many ores because it produces fine sized air bubbles (400-1000 µm) (Sahbaz et al. 2012; Evans et al. 1995).

The aim of this study is to investigate the beneficiation of colemanite minerals from tailing of the Emet-Espey Boron Processing Plant (Kutahya-Turkey) using a Jameson flotation cell, and to investigate the effects of bias factor, jet length, and plunging depth for the flotation performance.

Materials and methods

Materials

The sample used in this study was obtained from fine tailings (-3 mm) of Emet Etibor Genaral Directorate of the Concentration Plant located in Kutahya-Emet, Turkey. The main mineral of these boron deposits is colemanite, and has a reserve of approximately 1.6 petagram with the B_2O_3 content from 28 to 30% (Eti Mine 2011). The Emet-Espey Boron Processing Plant has a capacity of 300 gigagram/year, and a total concentrate production of 120 Gg/year with a grade of 41% B_2O_3. The tailings from the plant is divided into two groups: coarse (+3 mm) and fine (-3 mm) sized. The tailings of -3 mm, collected as of 150 Gg, have a grade of approximately 26-33%.

The sample was taken from different locations of the tailing, and representatively separated and bagged using sampling methods. The chemical analysis of the sample tailing is presented in Table 1. As seen in Table 1, the B_2O_3 content of the tailing is

determined as 26.33%. Besides boron mineral colemanite, montmorillonite, illite, quartz, calcite, dolomite, and sanidine were found as gangue minerals in the tailing sample (Ucar and Yargan 2009). In addition, arsenic (yellow colour), realgar (red colour), and orpiment minerals were detected in the macroscopic and microscopic examinations.

Table 1. Chemical analysis of the sample

Components	Content, %
B_2O_3	26.3
CO_2	11.3
Na_2O	0.191
MgO	6.29
Al_2O_3	8.3
SiO_2	25.7
P_2O_5	0.128
SO_3	0.953
K_2O	2.38
CaO	13
Fe_2O_3	2.85
As_2O_3	0.448
SrO	0.612
TiO_2	0.33

A 150+38 µm size fraction was used in this study in order to prevent the negative impact of slime in flotation experiments. After the removal of slime, B_2O_3 content of the tailing increased to 36.8% from 26.3%. In the case of the flotation experiments, a commercial corn starch, R801 (Cytec Co), and MIBC were used as depressant, collector (sulphonate type), and frother, respectively. Additionally, tap water was used in these experiments.

The flotation studies were carried out using a Jameson cell (Fig. 1) which was designed by Prof. Dr. Bahri Oteyaka with the help of Prof. Dr. Graeme Jameson in 2003. In this system, there is a centrifugal type pump to feed from conditioning tank through downcomer with pulp pressure (90-150 kPa), a peristaltic pump for washing water, a manometer to measure the pressure, an air flow sensor (anemometer) to measure feed, tailing flow-meters, and the amount of air entering to the system.
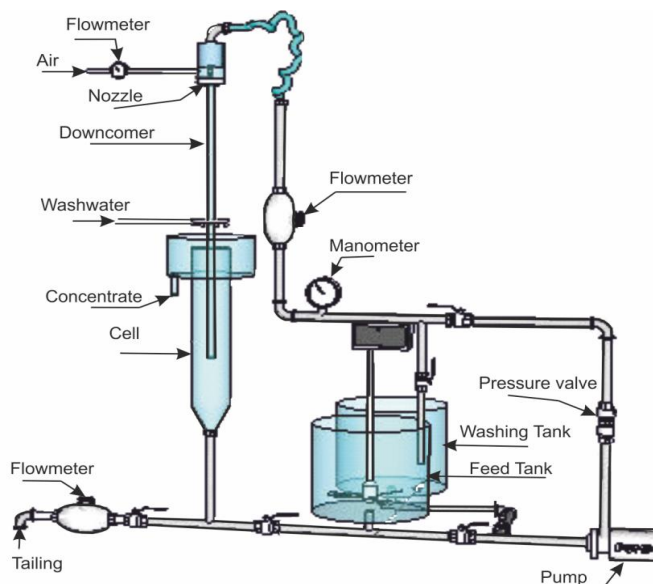
Fig. 1. Jameson flotation cell and equipments

The technical properties of the Jameson flotation cell are given below:

- cell (transparent plexiglas) diameter (D_C): 20 cm
- owncomer diameter (D_D) and length (L_C): 2 cm and 180 cm
- nozzle (stainless cast steel) Diameter (D_N): 0.4 cm.

In the experimental studies, the sample was first conditioned in a conditioning tank by adding the required reagents. In the meantime, 80 dm^3 of washing water tank was filled with the water. Then, the pulp was mixed with frother, and fed to the device where the operating parameters were set (such as a flow rate of feed and waste with by-pass system, air flow, and jet length). Then, the pulp supply valve was opened (by closing the valves between washing water tank and feeding pump), and the cell was fed with pulp approximately for 1 min. A minute later, pulp supply valve was closed, and the washing water tank valve was opened again to get the remaining floating and sinking particles in the cell. Finally, the system was fed only with water, and then the feeding was terminated until clean foam (demineralised air bubbles) came from the top of the cell.

Methods

Flotation experiments

Flotation is a complex beneficiation process realized in three-phase system using physicochemical surface property differences of minerals. For understanding flotation, physicochemical properties of particle surface and interface between phases must be known very well. One of these features is zeta potential profile of colemanite and its zero point of charge (zpc). As known from the literature, the zpc of the colemanite was

found between pH 10-10.5 (Yarar 1971; Celik et al. 2002; Ucar and Yargan 2009; Ozdemir and Celik 2010). Meanwhile, colemanite showed a buffer feature at around pH 9. Moreover, sulphonate as a collector was used at this pH in these studies (Yarar 1971; Gul et al. 2006). It is important to note that the flotation behaviour of the colemanite was examined using a mechanical flotation cell in these studies. However, in this study, the Jameson flotation cell was used for the flotation experiments. Additionally, R801 and starch was used as a sulphonate type collector and depressant, respectively. Other parameters and values are given below. The flotation experiments were carried out in a single-stage and open-circuit. The parameters and the values used for the flotation experiments were: conditioning time (t_k) 2 +5 min, pulp flow 11.4 dm^3/min, washing water flow rate (Q_{ys}) 1.9 dm^3/min, solid ratio (%N) 2.5%, air velocity (V_h) 27 cm/sec, amount of frother (Q_K) 60 ppm, amount of collector (Q_T) 3.500 g/Mg, depressant 800 g/Mg, jet length (L_j) 2-9 cm, plunging depth 20 - 50 cm.

Results and discussion

Results

Effect of jet length

Jet length is defined as a distance between point where pulp jet starts to mix with air in the downcomer and tip of the nozzle. This parameter determines the amount of air entrained to the cell referred as gas hold-up. It varies depending on the entrained air volume, and hold-up changes in the downcomer. The hold-up values from the various jet lengths were determined as 41% (3 cm), 45% (6 cm), and 48% (9 cm) by the use of the procedure given by Harbort et al. (2002). The flotation experiments were carried out at these values, and the results are shown in Fig. 2.
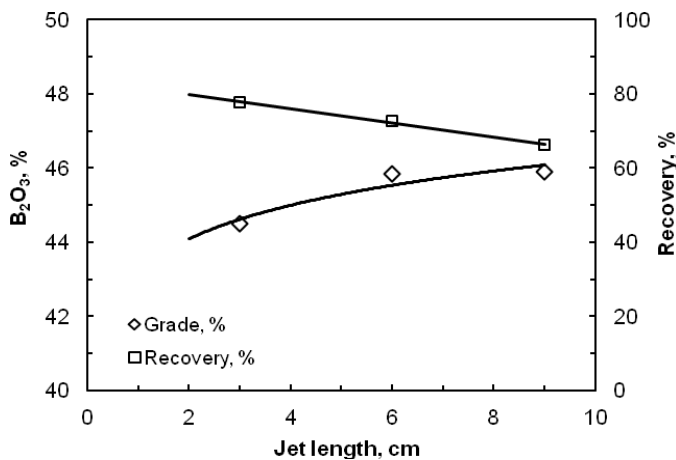
Fig. 2. Effect of jet length on grade-recovery (solid ratio: 2.5%, collector amount: 3500 g/Mg, plunging length: 40 cm, bias factor: +0.3, frother amount: 60 ppm)

As seen in Fig. 2, the flotation recovery decreased with the increase in the jet length. This can be attributed to the increase of the hold-up which caused the turbulence increase in the downcomer, hence this negatively affected the recovery (Oteyaka and Soto 1995; Sahbaz 2010). In addition, it is thought that the average bubble size increased with the increase in the hold-up, and hence probability of collision between particle and bubble started to decrease. Moreover, the turbulence at the end of the downcomer in the separation tank increased with the increasing of hold-up (Sahbaz 2010). Therefore, bubble-particle aggregate which occurred in the downcomer detached, and recovery decreased. The suitable jet length was found to be 3 cm for the colemanite sample.

Effect of plunging length

One of the other important parameters for the colemanite flotation using the Jameson cell is the plunging length of the downcomer at the separation tank. As the plunging length increases, water pressure applied in the cell increases on cross-sectional surface area of the pulp (aggregates + hydrophilic particles) coming out of the downcomer. In order to investigate the effect of this pressure on the recovery and grade, the flotation experiments were carried out at 4 different plunging lengths of the downcomer (e.g. 20 cm, 30 cm, 40 cm, and 50 cm), and the results are shown in Fig. 3.

As shown in Fig. 3, depending on the increase of plunging length, the recovery decreased while there was no noteworthy change in the grade. The reason for this could be related to a reduced flotation probability due to a poor stability of the bubble-particle aggregate because relatively coarse particles are easily affected any change in turbulence (Cinar et al. 2007). As clearly seen in Fig. 3, the most suitable plunging length for the downcomer is in the range between 20 and 30 cm. At this depth, a concentrate with B_2O_3 grade of 43.4% was obtained with a recovery of 92.78%.
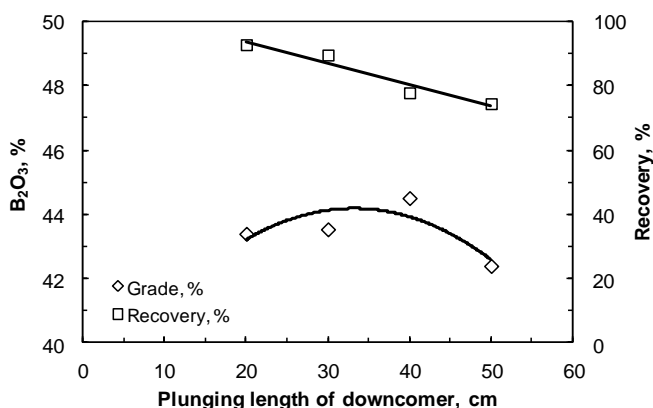
Fig. 3. Change of grade-recovery depending on the plunging depth (solid ratio 2.5%, collector amount 3500 g/Mg, jet length 3 cm, bias factor +0.3, frother amount 60 ppm)

Effect of bias factor

Fraction of the wash water flowing downward to report to the tailing stream which is called the bias factor is one of the variable contributing to the attainment of performance of the Jameson cell (Sahbaz et al. 2008). The bias factor is not only the parameter responsible for the formation of froth zone but also is maintained to limit the entrainment of fine hydrophilic particles into the froth phase. Production of a clean concentrate is greatly helped by the increased froth depth and the increasing bias factor (Cinar et al. 2007). As given in Eq. 1, the bias factor (BF) is defined as a ratio of the difference between tailing (Q_A) and the feed flow rate (Q_B) to the washing water flow (Q_{WW}) (Mohanty and Honaker 1999; Patwardhan and Honaker 2000).

$$BF= (Q_A - Q_B)/Q_{WW} \qquad (1)$$

The *BF* is generally positive in the fine-grained minerals flotation (-100 µm) in order to prevent entrainment of hydrophilic minerals. For the purpose of present investigation, four different positive *BF*'s (+0.3, +0.4, +0.5, and +0.7) were evaluated for the colemanite sample. The feed and washing water rates were fixed, and tailing rate was changed during the experiments to obtain the *BF* values used in the present study. On the other hand, negative bias was used for coarse-grained minerals flotation (Oteyaka and Soto 1995). Meanwhile, the *BF* must be close to zero or negative in order to increase recovery. Therefore, flotation experiments were also carried out at negative bias factor values (–0.1, –0.2 and –0.3). The results are shown in Figs. 4 and 5.
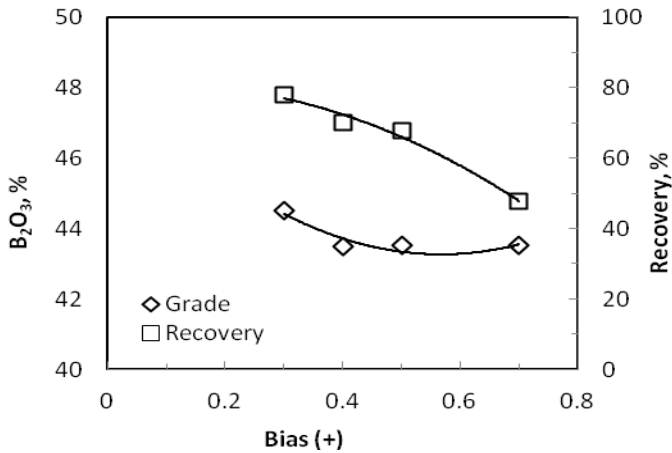
Fig. 4. Change of grade-recovery depending on the positive bias (solid ratio 2.5%, collector amount 3500 g/Mg, plunging length 40 cm, jet length 3 cm, frother 60 ppm)

Figure 4 shows the recovery and grade values as a function of positive bias values. The increase of positive BF provided the increase in the froth thickness caused the

recovery decreased. In addition, there was not significant change in the grade of the float product. The thick froth zone acted as a barrier for large particles even though some of them were hydrophobic. Under the washing water and dense bubble environment, it became difficult for the particles to move up, and hence bubble particle detachment occurred. As a result of these experiments, a product with 44.51% of B_2O_3 was obtained with a recovery of 77.83% at 0.3 positive bias factor value.

In addition, the flotation results as a function of negative bias values are presented in Fig. 5. As shown in Fig. 5, the flotation recovery sharply increased with the increase in the bias values. The results indicated that a colemanite concentrate with 45.42% of B_2O_3 was obtained with a recovery of 98.47% at 0.3 of the negative bias value. Moreover, the positive role of rising water with the increase of buoyancy played a positive role for the grade and recovery increase in the absence of froth zone. Furthermore, it must be taken into a consideration that there was not any particle in slime size which may be dragged into the concentrate in the case of negative bias values. Therefore, there was no significant change in the grade while the recovery increased.
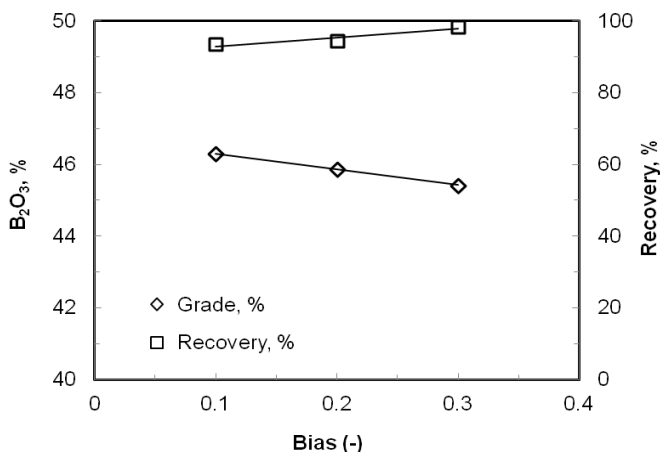
Fig. 5. Grade and recovery relation in accordance with negative bias (solid ratio 2.5%, collector 3500 g/Mg, plunging length 20 cm, jet length 3 cm, frother 60 ppm)

One of the most important indicators of flotation performance is selectivity obtained from upgrading curves such as Halbich's, Fuerstenau's, and other (Duchnowska and Drzymala 2013; Drzymala et al. 2013). In this study, Halbich's grade-recovery curve was used, and the results are seen in Fig. 6. It can be stated that it is possible to increase the flotation recovery up to 98% with no loss in the grade. In Fig. 6, the circle shows the upgrading of colemanite at the different jet lengths while triangle and square shows the upgrading at plunging depth and negative BF, respectively.
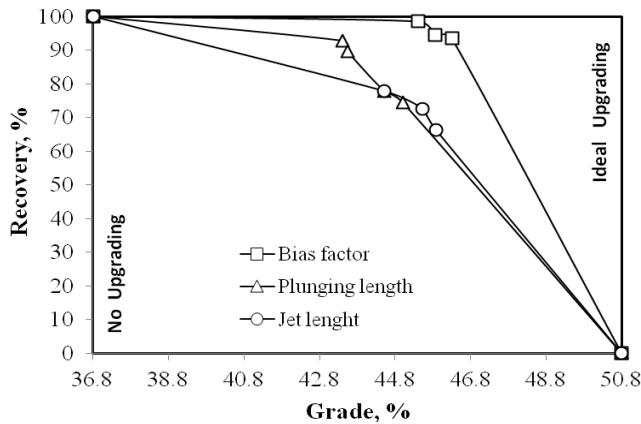
Fig. 6. Upgrading curves for effect of parameters

As seen from Fig. 6, a final concentrate with B_2O_3 of 46% was obtained with a recovery of 99%. This result indicated that a colemanite product can be beneficiated from the tailings with a grade of more than 40% which is much higher than that of product obtained using a classical physical separation including scrubbing and classification. It can also be concluded that if the plunging depth of the downcomer is reduced, and negative bias factor is chosen while jet length is reduced, the process recovery can be increased.

Conclusions

In this study, a Jameson flotation cell was applied to separate colemanite from the fine tailing of the Emet-Espey slurry pond. The final concentrate having 45.42% of B_2O_3 was obtained from the feed having 36.8% B_2O_3 content with the recovery of 98.47%. Based on the results obtained from this study we can conclude that

- operating parameters of the Jameson cell showed a significant impact on the flotation recovery. The negative bias factor has a more pronounced effect in terms of recovery. It is the operating parameter to be considered specifically for the coarse particle and the feed without slime,
- the Jameson flotation cell has been used for the first time for the colemanite flotation, and a high flotation recovery and grade were gained,
- it is convenient to use positive bias in flotation of fine-grained (- 100 µm) minerals, and the negative bias in flotation of grains over the size of 100 µm without slime problems,
- colemanite can be beneficiated from the tailings of the Emet Processing Plant with the grade of more than 40%,

- in addition, plunging depth of the downcomer should be reduced, and negative bias factor should be applied to increase the recovery of the process.

This study clearly indicated that colemanite tailings without slime can be successfully beneficiated with a high recovery using the Jameson cell with a negative bias factor. Further research will be conducted to beneficiate the finer size (-38 µm) fraction.

Acknowledgements

References

CELIK M.S., M. HANCER, J.D. MILLER, 2002, *Flotation chemistry of boron minerals*, Journal of Colloid and Interface Science, 256, 121–131.

ETI MINE, 2011, *Boron Sector Report* (In Turkish), Eti Mine Work General Management, Ankara, Turkey.

EVANS G.M., ATKINSON B.W., JAMESON G.J., 1995, *The Jameson Cell,* Flotation Science and Engineering, Edited by K.A. Matis, 331-363.

DUCHNOWSKA M., DRZYMALA J., 2012, *Self-similarity of upgrading parameters used for evaluation of separation results*, International Journal of Mineral Processing, 106 -109, 50-57.

DRZYMALA J., KOWALCZUK P.B., OTENG-PEPRAH M., FOSZCZ D., MUSZER A., HENC T., LUSZCZKIEWICZ A., 2013, *Application of the grade-recovery curve in the batch flotation of Polish copper ore*, Minerals Engineering, 49, 17-23.

GUL A., KAYTAZ Y., ONAL G., 2006, *Beneficiation of colemanite tailings by attrition and flotation,* Proceedings of Xth International Mineral Processing Symposium, Istanbul, Türkiye.

HELVACI AND ALONSO, 2000. *Borate deposits of Turkey and Argentina: A summary and geological comparison*, Turkish Journal of Earth Sciences, 9, 1-27.

HARBORT G.J., MANLAPIG E.V. VE DEBONO S.K., 2002, *Particle collection within the Jameson cell downcomer,* Trans. IMM Section C, V. 111/Proc. Australas IMM, V. 307.

KERENCILER S., 2008, *Investigation of beneficiation of Emet Espey boron plant tailings using a Jameson Flotation Column* (In Turkish), M.Sc. Thesis, Dumlupinar University, Kutahya, Turkey.

MOHANTY M.K., HONAKER R.Q., 1999. *Performance optimization of Jameson flotation technology for fine coal cleaning*, Minerals Engineering, 12(4), 367-381.

OTEYAKA B., SOTO H., *Modelling of negative bias column for coarse particles flotation,* Minerals Engineering, 1995, 8, 91-100.

OZDEMIR O., CELIK M.S., 2010, *Surface properties and flotation characteristics of boron minerals,* The Open Mineral Processing Journal, 3, 2-13.

OZKAN Ş.G., ACAR A., 2004, *Investigation of impact of water type on borate flotation,* Water Research, 7, 1773-1778.

PATWARDHAN A., HONAKER R.Q., 2000, *Development of a carrying-capacity model for column froth flotation*, International Journal of Mineral Processing, 59, 275-293.

SAHBAZ O., OTEYAKA B., KELEBEK S., UCAR A., DEMIR U., 2008, *Separation of unburned carbonaceous matter in bottom ash using Jameson cell*, Separation and Purification Technology, 62(1), 103-109.

SAHBAZ O., 2010, *Modification of downcomer in Jameson cell and its effect on performance* (In Turkish), Ph.D. Thesis, Dumlupinar University, Department of Mining Engineering, Kutahya, Turkey.

SAHBAZ O., ERCETIN U., OTEYAKA B., 2012, *Determination of turbulence and upper size limit in Jameson flotation cell by the use of computational fluid dynamic modelling,* Physicochemical Problems of Mineral Processing., 49 (2), 535-546.

UCAR A., YARGAN M., 2009, *Selective separation of boron values from the tailing of a colemanite processing plant*, Separation and Purification Technology, 68(1), 1–8.

XSTRATA TECHNOLOGY, 2005, Jameson cell, http://xstratatech.com/doc/jc_brochure_2004/ 001. pdf.

YARAR B., 1971, *Evaluation of colemanite mineral by flotation method* (In Turkish), The Scientific and Technological Research Council of Turkey (TUBITAK), Engineering Research Group (MAG), Ankara, Turkey.

LEACHING OF CHALCOPYRITE CONCENTRATE IN HYDROGEN PEROXIDE SOLUTION

Tevfik AGACAYAK[*]**, Ali ARAS**[*]**, Salih AYDOGAN**[*]**, Murat ERDEMOGLU**[**]

[*] Selcuk University, Mining Engineering Department, 42075 Konya, Turkey, tevfik@selcuk.edu.tr
[**] Inonu University, Mining Engineering Department, 44280 Malatya, Turkey

Abstract: The leaching conditions of chalcopyrite ($CuFeS_2$) concentrate in a hydrogen peroxide medium were investigated by studying the effects of its leaching parameters, such as stirring speed, temperature, hydrogen peroxide concentration and the particle size of the concentrate on Cu extraction. It was found that stirring speed has no effect on the leaching. Copper extraction from chalcopyrite is directly proportional to hydrogen peroxide concentration, but the extraction decreases at temperatures above 60°C. The maximum copper extraction was obtained with the following conditions without stirring: 240 min of leaching time, 3.0 M hydrogen peroxide concentration, 40°C leaching temperature and 53-75 μm particle size fraction.

Keywords: chalcopyrite, dissolution, hydrogen peroxide, leaching, extraction

Introduction

Chalcopyrite ($CuFeS_2$) is the most important commercial copper sulphide mineral and is the principal source of commercially produced copper. It is generally associated with other sulphide minerals such as galena (PbS), sphalerite (ZnS) and pyrite (FeS_2). In conventional technology Cu is recovered from $CuFeS_2$ concentrates by crushing, beneficiation concentration, roasting and smelting techniques, followed by electrorefining and electrowinning operations (Habashi, 1978). Approximately 80-85% of the total world copper production is carried out through pyrometallurgical processes that produce SO_2 gas (Antonijević et al., 2004). Hydrometallurgical methods were developed opposed to the classic pyrometallurgical routes due to stringent regulations on SO_2 emission (Habashi, 1999; Antonijević et al., 2004). Although SO_2 gas is used in the production of sulphuric acid, it causes storage and transportation problems.

Chalcopyrite is the most abundant copper mineral and the most refractory and difficult to leach (Plumlee, 1999; Vanhanen, 1999). For that reason, numerous

leaching studies have been performed by many researchers using various oxidants in acidic media, such as cupric ion (Liddicoat and Dreisinger, 2007; Al-Harahsheh et al., 2008; Yevenes et al., 2010; Skrobian et al., 2005; Lundstrom et al., 2005; Tchoumou and Roynette, 2007), ferric ion (Al-Harahsheh et al., 2008; Akcil and Ciftci, 2002; Dutrizac, 1990; Hirato et al., 1987; Yoo et al., 2010; Cordoba et al., 2008; Nazari and Asselin, 2009), dichromate ion (Antonijevic et al., 1994; Aydogan et al., 2006; Altundogan et al., 2004), nitrate ion (Sokic et al., 2009), hydrogen peroxide (Balaz and Briancin, 1990; Antonijevic et al., 2004; Mahajan et al., 2007; Turan and Altundogan, 2013), hypochlorite (Ikiz et al., 2006) and oxygen (Padilla et al., 2007; Puvvada and Murthy, 2000). Among these agents, hydrogen peroxide is a strong and environmentally safe oxidizing agent. It is reported that hydrogen peroxide produces no reaction products apart from water during the oxidation of sulphide minerals (Antonijevic et al., 2004). Oxidative dissolution of chalcopyrite in hydrogen peroxide solutions can be summarised as follows (Dold, 2005):

$$2CuFeS_2 + 17/2O_2 + 5H_2O \leftrightarrow 2Cu^{2+} + 2Fe(OH)_3 + 4SO_4^{2-} + 4H^+ . \qquad (1)$$
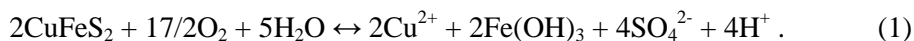
The reactions that take place in Cu extraction from chalcopyrite concentrate are (Habashi, 1999):

$$2CuFeS_2 \leftrightarrow 2Cu^{2+} + 2Fe^{2+} + 4S^{2-} \qquad (2)$$

$$H_2O_2 \leftrightarrow H_2O + 1/2O_2 \qquad (3)$$

$$2Fe^{2+} + 1/2O_2 + 5H_2O \leftrightarrow 2Fe(OH)_3 + 4H^+ \qquad (4)$$

$$4S^{2-} + 8O_2 \leftrightarrow 4SO_4^{2-} . \qquad (5)$$

Elemental sulphur is stable in an acid medium, but it oxidizes slowly in water at high temperatures (above 150°C) with oxygen pressure to form sulphuric acid (Habashi, 1999):

$$S + 3/2O_2 + H_2O \leftrightarrow H_2SO_4. \qquad (6)$$
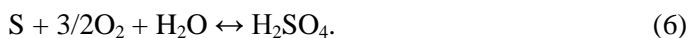
The present paper, aims to investigate the effects of leaching parameters such as stirring speed, temperature, hydrogen peroxide concentration and particle size, on the dissolution of chalcopyrite in an oxidative medium (only with hydrogen peroxide solution). Copper ions were extracted selectively from chalcopyrite concentrate at atmospheric pressure and lower temperature with a high recovery. Generally, chalcopyrite leaching studies were carried out using a combination of different media. Mahajan et al. (2007) and Antonijevic et al. (2004) obtained copper extraction in a mixture of H_2O_2–H_2SO_4–ethylene glycol and a H_2SO_4–H_2O_2 medium, respectively.

Material and methods

Material

Samples of the chalcopyrite concentrate were taken from the Menka Flotation Plant (Sivas, Turkey), where the $CuFeS_2$–PbS–ZnS complex ore is enriched. The particle size of the concentrate was –212 μm. The concentrate was wet sieved to obtain 212×106, 106×75 and 75×53 particle size fractions. The chemical analysis of each size fraction is given in Table 1.

Table 1. Chemical analysis of chalcopyrite concentrate (wt.%)

Particle size (μm)	Cu (%)	Fe (%)	Zn (%)	Pb (%)	S (%)	Others (%)
212×106	23.52	23.17	1.01	1.13	27.27	23.9
106×75	26.91	26.56	1.46	1.70	31.48	11.89
75×53	24.90	25.16	2.42	3.08	30.57	13.87

Experimental procedure

A Pyrex beaker of 1 dm^3 was used as a leaching reactor placed in a temperature-controlled water bath and closed with a rubber cover. Stirring was carried out by a Heidolph RZR 2021 model mechanic stirrer equipped with a Teflon-covered propeller. A 2 g/dm^3 chalcopyrite sample with a fraction size of 75×53 μm was used for all experiments. Then, the stirring speed was raised to 600 rpm, the temperature was varied in the range of 30–70 °C, the hydrogen peroxide concentration was in the range of 0.5–3.0 M and the particle size range was 212×106, 106×75 and 75×53 μm. The amount of Cu in the leaching solution was determined using a GBC SensAA model flame atomic absorption spectrometer (AAS). For this purpose, 1 cm^3 of leaching solution was withdrawn from the reactor at various time intervals and diluted with water to 100 cm^3 in a volumetric flask. Distilled water and reagent grade chemicals were used for all required solutions.

Results

Effect of stirring speed

The effect of stirring speed on the dissolution of chalcopyrite was investigated at different stirring speeds that ranged from 0 to 600 rpm in a 2.0 M H_2O_2 solution at 50 °C (Fig. 1). It can be seen from Fig. 1 that the Cu extraction was independent of the stirring speed. Thus, all subsequent experiments were carried out without stirring except for homogenizing the solution prior to the sampling for the Cu analysis.
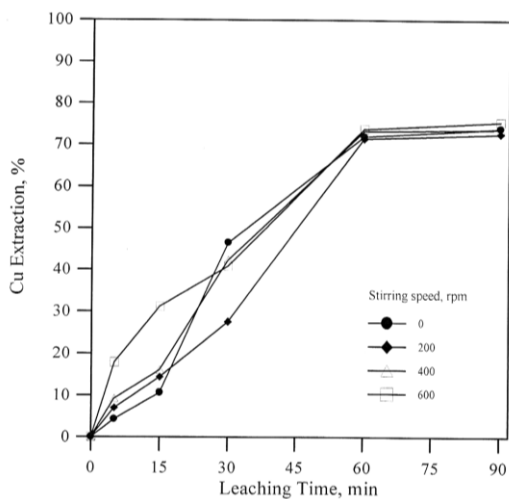
Fig. 1. Effect of stirring speed on chalcopyrite dissolution.
Conditions: 2.0 M H_2O_2, 50°C, 2 g/dm^3 (75×53 µm) chalcopyrite concentrate

Effect of temperature

The experiments were carried out in the 30–70°C temperature range in the solutions containing 2.0 M H_2O_2 (Fig. 2). It can be seen in Fig. 2 that the Cu extraction obtained in 90 min of leaching time reached above 80% at 40 °C. However, in the 90–240 min leaching time interval, Cu extraction reached almost stable values. In addition, it decreased with increasing temperature in the range of 50–70 °C compared to lower
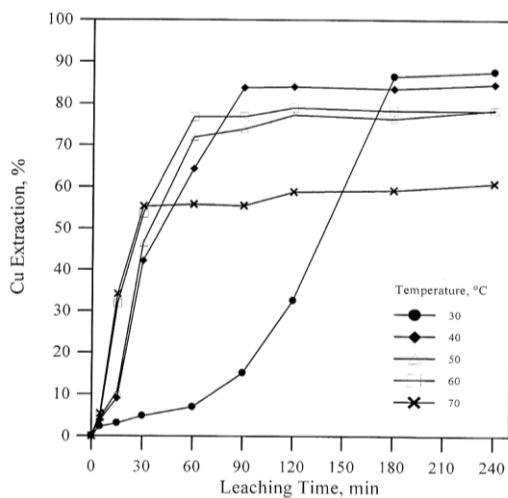
Fig. 2. Effect of temperature on chalcopyrite dissolution.
Conditions: 2.0 M H_2O_2, 2 g/dm^3 (75×53 µm) chalcopyrite concentrate, no stirring

temperatures. These findings suggest that the decomposition of hydrogen peroxide happens more readily at higher temperatures (Antonijevic et al., 1997; Mahajan et al., 2007). Antonijevic et al. (1997) reported that the accelerated decomposition of hydrogen peroxide was above 60 °C.

Effect of H_2O_2 concentration

The experiments were carried out in solutions containing various H_2O_2 concentrations at 40°C. The results are given in Fig. 3. Cu extraction increased with increasing H_2O_2 concentration within a 240 min leaching time. However, in the 90-240 min leaching time interval, Cu extraction almost reached stable values for the solutions containing 2.0 and 3.0 M H_2O_2. In addition, the Cu extraction rate decreased for the solutions containing 0.5 and 1.0 M H_2O_2.
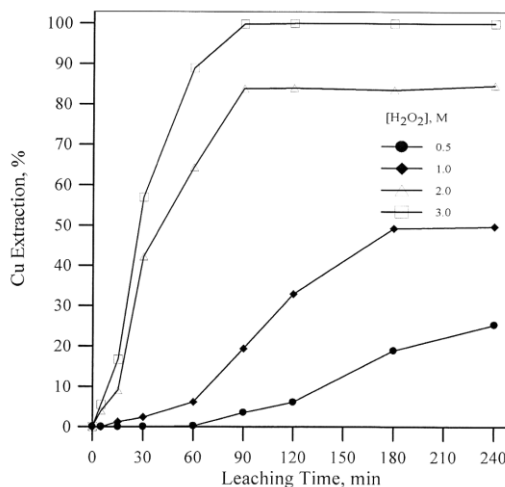
Fig. 3. Effect of H_2O_2 concentration on chalcopyrite dissolution.
Conditions: 40 °C, 2 g/dm^3 (75×53 µm) chalcopyrite concentrate, no stirring

Effect of particle size

The experiments were carried out using three different particle size fractions in the solutions containing 3.0 M H_2O_2 at 40°C. The results are given in Fig. 4. Cu extraction increased with decreasing particle size because of the increase in surface area at unit weight.

Discussion

According to the XRD analysis (Fig. 5), the chalcopyrite concentrate used in the leaching experiments contained mainly chalcopyrite and pyrite. After leaching, the
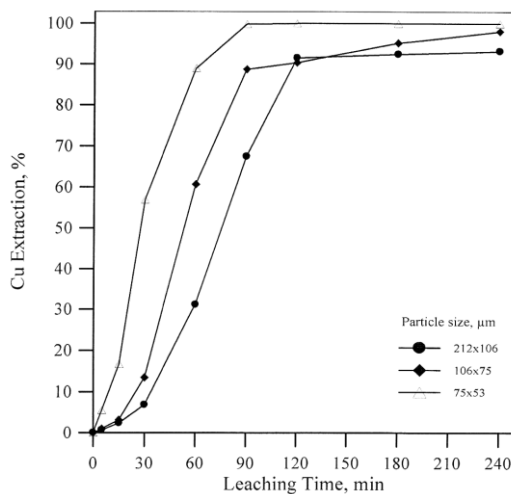
Fig. 4. Effect of particle size on chalcopyrite dissolution.
Conditions: 3.0 M H_2O_2, 40 °C, 2 g/dm^3 (75×53 µm) chalcopyrite concentrate, no stirring

major mineral determined in the residue was chalcopyrite. Pyrite was almost absent. In addition, no elemental sulphur was detected, at least in its crystal form. In addition, elemental sulphur production was not observed during the leaching experiments. However, amorphous iron compounds were observed with an optical microscope (Fig. 6). In the leaching solutions, approximately 5% Fe extraction was achieved. Therefore, it was concluded that rather than the iron existing in the chalcopyrite, the iron in the pyrite is extracted. In order to confirm this, pyrite leaching experiments were performed under conditions identical to those of the chalcopyrite leaching experiment, and this phenomenon was supported by the XRD results (Fig. 7).
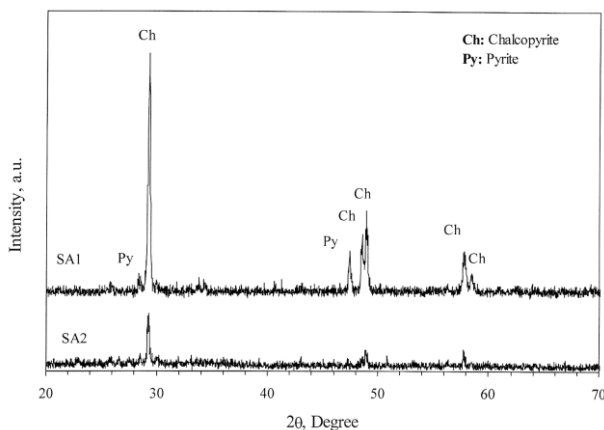
Fig. 5. XRD patterns for the chalcopyrite concentrate (SA1)
and the residue obtained after the leaching (SA2)
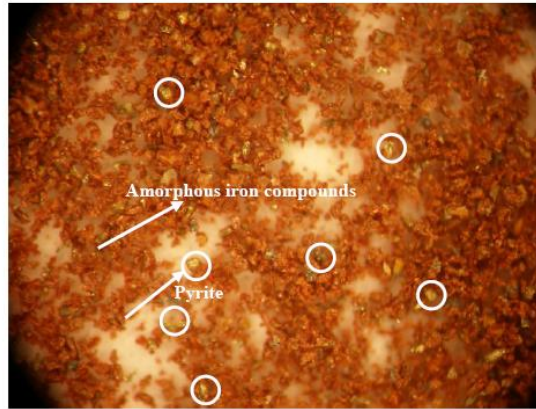
Fig. 6. Microscopic photograph of chalcopyrite concentrate after hydrogen peroxide leaching
Conditions: 3.0 M H_2O_2, 40°C, 2 g/cm^3 (75x53 µm) chalcopyrite concentrate, no stirring
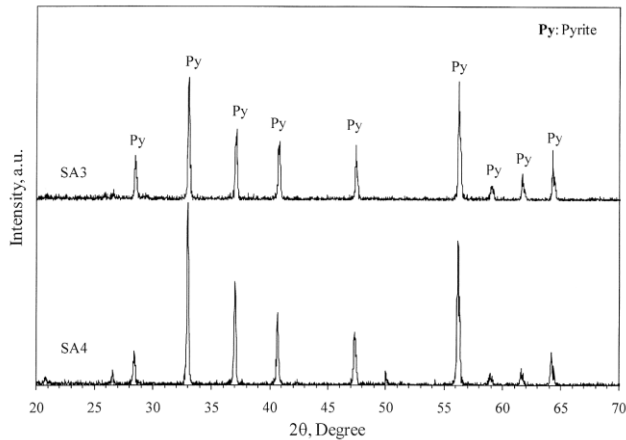
Fig. 7. XRD patterns for a pyrite concentrate before (SA3) and after (SA4) the leaching

During the leaching, a clear pH decrease was observed (Fig. 8) from the beginning of the experiment. Hence, it was concluded that the reaction produces acid in the solution. The dissolution of pyrite in hydrogen peroxide occurred in the reaction as follows:

$$FeS_2 + 7.5H_2O_2 \leftrightarrow Fe^{3+} + 2SO_4^{2-} + H^+ + 7H_2O. \tag{7}$$
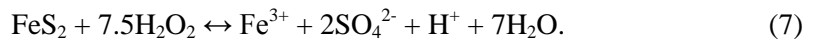
The potential-pH diagram for sulphur is given in Fig. 9 (Habashi, 1999). Figure 9 shows that sulphate ions occurred in the oxidizing conditions achieved in this study. Besides, by adding $BaCl_2$ to the centrifuged leach solution, it was proved that sulphate ions existed in the leach solution, and white barium sulphate precipitate was observed.
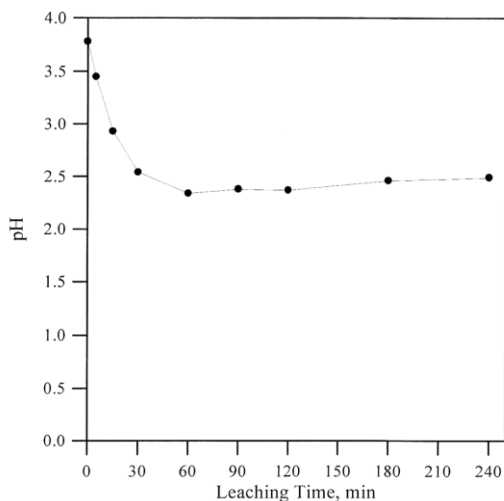
Fig. 8. Variation of pH with leaching time. Conditions: 3.0 M H_2O_2, 40°C,
2 g/dm^3 (75×53 μm) chalcopyrite concentrate, no stirring
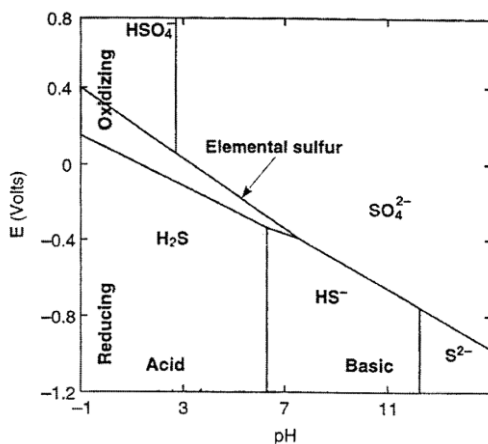
Fig. 9. Potential-pH diagram for sulphur (Habashi, 1999)

Conclusions

In this study, the extraction of Cu from chalcopyrite concentrate in hydrogen peroxide solutions was studied. It was determined that the dissolution process was independent of the stirring. In general, the Cu extraction rate increased with increasing temperatures during the early times of the leaching period. However, it decreased prolonged periods of times, due to the decomposition of hydrogen peroxide at higher temperatures. Cu extraction increased with increasing H_2O_2 concentration in the 240 min leaching time. However, in the 90–240 min leaching time interval, it reached

stable values for the solutions containing 2.0 and 3.0 M H_2O_2, respectively. Cu extraction increased with decreasing particle size because of the increase in surface area at unit weight. Optimum leaching conditions of chalcopyrite concentrate in H_2O_2 solution were found as: H_2O_2 concentration: 3.0 M, leaching temperature: 40 °C, stirring speed: 0 rpm; particle size: 75×53 µm. Under these conditions, copper recovery may be as high as 99%. In the studied conditions, it was determined that Cu extraction from chalcopyrite concentrate is possible and iron ions dissolved from chalcopyrite and precipitated. In addition, the pyrite mineral that was present in the concentrate dissolved; thus, the XRD analyses supported these results.

References

AKCIL A., CIFTCI H., 2002. *A study of the selective leaching of complex sulphides from the Eastern Black Sea Region, Turkey*. Minerals Engineering 15 (6), 457–459.

AL-HARAHSHEH M., KINGMAN S., AL-HARAHSHEH A., 2008. *Ferric chloride leaching of chalcopyrite: Synergetic effect of CuCl2*. Hydrometallurgy 91, 89–97.

ALTUNDOGAN H.S., BOYRAZLI M., TUMEN F., 2004. *A study on the sulphuric acid leaching of copper converter slag in the presence of dichromate*. Minerals Engineering 17, 465–467.

ANTONIJEVIC M.M., JANKOVIC Z.D., DIMITRIJEVIC M.D., 1994. *Investigation of the kinetics of chalcopyrite oxidation by potassium dichromate*. Hydrometallurgy 35, 187–201.

ANTONIJEVIC M.M., DIMITRIJEVIC M., JANKOVIC Z., 1997. *Leaching of pyrite with hydrogen peroxide in sulfuric acid*. Hydrometallurgy 46, 71–83.

ANTONIJEVIC M.M., JANKOVIC Z.D., DIMITRIJEVIC M.D., 2004. *Kinetics of chalcopyrite dissolution by hydrogen peroxide in sulphuric acid*. Hydrometallurgy 7, 329–334.

AYDOGAN S., UCAR G., CANBAZOGLU M., 2006. *Dissolution kinetics of chalcopyrite in acidic potassium dichromate solution*. Hydrometallurgy 81, 45–51.

BALAZ P., BRIANCIN J., 1990. *Leaching and properties of mechanically activated chalcopyrite.* Fizykochemiczne problemy mineralurgii 22, 193–200.

CORDOBA E.M., MUNOZ J.A., BLAZQUEZ M.L., GONZALEZ F., BALLESTER A., 2008. *Leaching of chalcopyrite with ferric ion. Part I: General aspects*. Hydrometallurgy 93, 81–87.

DOLD B., 2005. Basic *Concepts of Environmental Geochemistry of Sulfide Mine-Waste*. XXIV Curso Latinoamericano de Metalogenia UNESCO–SEG, Lima, Peru.

DUTRIZAC J.E., 1990. *Elemental sulfur formation during the ferric chloride leaching of chalcopyrite*. Hydrometallurgy 23, 153–176.

HABASHI F. 1978. *Chalcopyrite, its Chemistry and Metallurgy*, McGraw-Hill, New York.

HABASHI F., 1999. *A Textbook of Hydrometallurgy*. Métallurgie Extractive Québec, second edition, 750 p. Canada.

HIRATO T., MAJIMA H., AWAKURA Y., 1987. *The leaching of chalcopyrite with ferric sulphate*. Metall. Trans. B 18B, 489–496.

IKIZ D., GULFEN M., AYDIN A.O., 2006. *Dissolution kinetics of primary chalcopyrite ore in hypochlorite solution*. Minerals Engineering 19, 972–974.

LIDDICOAT J., DREISINGER D., 2007. *Chloride leaching of chalcopyrite*. Hydrometallurgy 89, 323–331.

LUNDSTROM M., AROMAA J., FORSEN O., HYVARINEN O., BARKER M.H., 2005. *Leaching of chalcopyrite in cupric chloride solution*. Hydrometallurgy 77, 89–95.

MAHAJAN V., MISRA M., ZHONG K., FUERSTENAU M.C., 2007. *Enhanced leaching of copper from chalcopyrite in hydrogen peroxide–glycol system*. Minerals Engineering 20, 670–674.

NAZARI G., ASSELIN E., 2009. *Morphology of chalcopyrite leaching in acidic ferric sulfate media*. Hydrometallurgy 96, 183–188.

PADILLA R., VEGA D., RUIZ M.C., 2007. *Pressure leaching of sulfidized chalcopyrite in sulfuric acid–oxygen media*. Hydrometallurgy 86, 80–88.

PLUMLEE G.S., 1999. The *environmental geology of mineral deposits*. In: Plumlee, G. S. and Logsdon, M.J. (Eds.) Reviews in Economic Geology, The environmental geochemistry of ore deposits. Part A: Processes, Techniques, and Health Issues, v. 6A, 71–116.

PUVVADA G.V.K., MURTH, D.S.R., 2000. *Selective precious metals leaching from a chalcopyrite concentrate using chloride/hypochlorite media*. Hydrometallurgy 58, 185–191.

SKROBIAN M., HAVLIK T., UKASIK M., 2005. *Effect of NaCl concentration and particle size on chalcopyrite leaching in cupric chloride solution*. Hydrometallurgy 77, 109–114.

SOKIC M.D., MARKOVIC B., ZIVKOVIC D., 2009. *Kinetics of chalcopyrite leaching by sodium nitrate in sulphuric acid*. Hydrometallurgy 95, 273–279.

TCHOUMOU M., ROYNETTE M., 2007. *Leaching of complex sulphide concentrate in acidic cupric chloride solutions*. Trans. Nonferrous Met. Soc. China 17, 423–428.

TURAN M.D., ALTUNDOGAN H.S., 2013. *Leaching of chalcopyrite concentrate with hydrogen peroxide and sulfuric acid in an autoclave system*. Metallurgical and Materials Transactions 44B, 809–819.

VANHANEN M.R., 1999. *Finnish expert report on best available techniques in copper production and by-production of precious metals*. The Finnish Environment, Finland.

YEVENES L.V., MIKI H., NICOL M., 2010. *The dissolution of chalcopyrite in chloride solutions: Part 2: Effect of various parameters on the rate*. Hydrometallurgy 103, 80–85.

YOO K., KIM S., LEE J., ITO, M., TSUNEKAWA M., HIROYOSHI N., 2010. *Effect of chloride ions on leaching rate of chalcopyrite*. Minerals Engineering 23, 471–477.

REGIONAL FEATURES ANALYSIS OF PLUGGED HOLES OF DENSE PHASE GAS-SOLID SEPARATION FLUIDIZED BED

Bo ZHANG, Yuemin ZHAO, Zhenfu LUO, Shulei SONG, Chenlong DUAN, Liang DONG

School of Chemical Engineering and Technology, China University of Mining and Technology, 221116, Xuzhou, China, ymzhao_paper@126.com, clduan@cumt.edu.cn

Abstract: In contrast to traditional coal separation, dry separation does not require water and does not cause water pollution. Dense phase gas–solid fluidized beds are used for dry separation. The plugged holes in the air distributor should be tested to ensure the stability of these beds for particle separation. The pressure fluctuation is sensitive to these plugged holes. This sensitivity can be tested and diagnosed by determining the standard deviation of the pressure fluctuation. In areas with partial blockage, that is the areas with weak fluidization, a decrease in the volume fraction of the particles and in the pressure differences in the transverse of the bed results in an increase of the standard deviation of the pressure fluctuation, thereby stimulating the lateral mixing of medium-sized particles. The standard deviation and the mixing intensity decrease axially. The value of sensitivity of the plugged holes in the air distributor decreases as the height of the bed increases. The features of air distributors affect the surrounding areas. The distribution law determining the influence of plugged holes on the beds is symmetrical. As the blockage of the fluidized bed distributor region increases, the mean square error of the pressure fluctuation in the related regions increases. The intensity of the effect is proportional to the distance to the plugged holes.

Introduction

Coal plays a predominant role in China's energy consumption structure (National Bureau of Statistics of China, 2012). As the main energy source, coal will make great contributions to the national economic development for a long time (IBGE census, 2011). Meanwhile, it will also bring serious environmental pollution for its raw coal of poor quality, and high ash and sulfur content. Low ash coal with less than 10% ash

content accounts for 15%-20% of recoverable deposits. High sulfur content coal with more than 1% sulfur content accounts for 33% of the total. Coal preparation is an economic and effective method to reduce smoke dust and SO_2. It is the prerequisite of deep processing of coal and one of key technologies of energy conservation and emission reduction (World Energy Council, 2010). More than two-thirds of coal resources in China are distributed in arid areas. As the coal mining is transferred to arid areas, wet coal preparation is under restrictions. Moreover, because of ample lignite resources which are easy to slime, it is inappropriate to adopt wet separation. Therefore, it is necessary to develop effective dry separation (Chen and Yang, 2003, Dong et al., 2013 and Luo et al., 2008).

Compared to traditional coal separation, dry separation does not need water and will not cause water pollution. Coal dry beneficiation with air dense medium fluidized bed, an effective dry separation, is the research focus and difficulty in the field of coal dressing (Breuer et al., 2009; Sampaio et al., 2008; Weinstein et al., 2007 and Prashant et al., 2010). The performance of air distributors of dense phase gas-solid separation fluidized bed is vital to the stability of the separation of beds (Luo et al., 2002; Macpherson et al., 2011; Zhao et al., 2010a, 2010b, 2011). During the process of separation, plugged holes always appear in the part of air distributor. However, documents about the forecast and influence of blocking areas in dense phase gas-solid separation fluidized bed are still rare (Oshitani et al., 2012 and Wang et al., 2013). For the points of pressure waves, fluctuation signals of the absolute pressure include the pressure fluctuations and pressure fluctuation of bed caused by partial bubble motion and the spreading of pressure fluctuation. (Song et al., 2012; Oshitani et al., 2010; Yoshida et al., 2011) This paper uses statistic analysis to analyze pressure fluctuation signals of dense phase gas-solid separation fluidized bed, forecast the areas of plugged holes, and explore basic features of pressure fluctuations and mean square deviations in blocking areas in air distributors

Characterization methods

The mean value of pressure is

$$\overline{P} = \frac{1}{n}\sum_{i=0}^{n} P_i$$

while the mean square deviation of pressure fluctuation is

$$\Delta P = \sqrt{\frac{1}{n-1}\sum_{i=1}^{n}(P_i - \overline{P})} \ .$$

Taking pressure fluctuation of fluidized beds as the standard of judging the fluidization quality and the stability of beds, the sensitivity of different positions of fluidized beds to plugged holes can be judged from D-value of mean square of pressure fluctuation around plugged holes in air distributors :

$$S = \frac{\Delta P_b - \Delta P_a}{\Delta P_a} .$$

In this formula, P_i, $\overline{P}$ and ΔP represent instantaneous value, mean value and mean square deviation separately. ΔP_a and ΔP_b separately represent the mean square in front and back of air distributors.

Equipment and characteristics of materials

Equipment

This paper uses the model machine of dense phase gas-solid fluidized bed separator with 280 mm diameter and 500 mm height under the normal pressure. As seen in Fig 1, the whole system is made up of air supply system, air flow control system, fluidized bed model, dust pelletizing system, differential pressure measuring installation and data acquisition system. The fluidized bed consists of the upper chamber, air distributor and lower chamber. For test and observation, the upper chamber is made up of organic glasses. The air distributor is a group of steel multi-orifices with 3mm aperture. Two-double industrial filter cloth between multi-orifices at the bottom is used as air distributor. In order to study the features of partial blocking areas in the air distributor of dense phase gas-solid separation fluidized bed, the round air distributor is homogeneously divided into eight regions which are marked as A, B, C, D, E, F, G
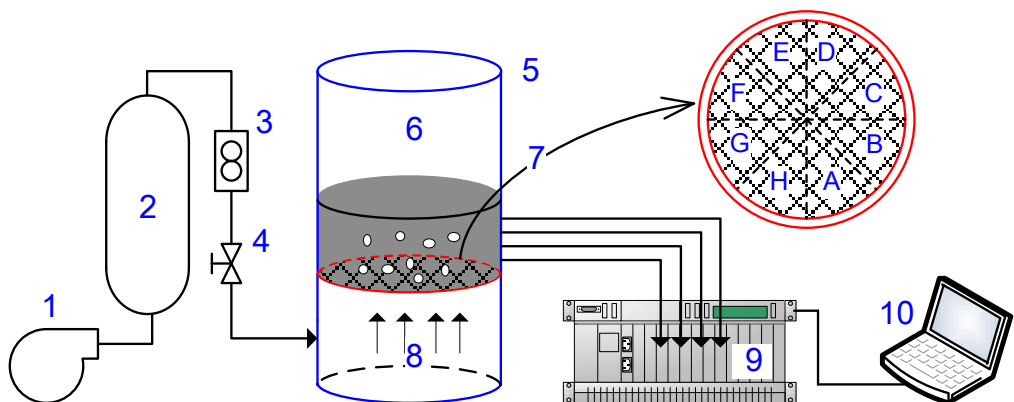
Fig. 1. The model device of gas-solid fluidized beds for separation and the partition of air distributors: 1 – Roots blower, 2 – Air-drum, 3 – Rotameter, 4 – Blast gate, 5 – Model of gas-solid fluidized bed, 6 – Fluidized bed, 7 – Air distributor, 8 – Air chamber, 9 – Data acquisition system, 10 – Computer

and H. Region A is a problem area due to plugged holes while other areas are associated areas influenced by the plugged holes. The pressure is measured by a JYB-G intelligent pressure transmitter, then converted to the pressure signal through the amplifier and finally achieves transformation between voltage signals and digital signals, stores computer information and processes data through the original Lab Jack U12 data acquisition device. The height of the fluidized bed is 200 mm. Fig 1 shows the height of test points in corresponding areas of partitions of air distributors.

Characteristics of materials

Geldart B magnetite powder with wide size fraction and high density which used in coal separation as the medium solid particle was used in the tests. True density is 4200 kg/m^3 and bulk density is 2470 kg/m^3. The particle size of main fractions ranges from 0.074 mm to 0.300 mm. Its magnetic material content is 99.71% and saturation magnetization is 77.21 A·m^2/kg. The magnetite powder is screened by sieve shaker. The result can be seen from Table 1. The distribution range of the main particle size of magnetite powder is 0.15–0.10, 0.20–0.15, 0.01–0.074 and 0.30–0.20 mm. These four particle size fractions account for 91.77% of the whole. For there are little particles whose diameters are more than 0.300 mm or less than 0.074 mm, this research uses dominant size fraction as medium particles of fluidized beds. Moreover, the magnetic material content of Geldart B magnetite powder approaches 100%, with high purity and intensive magnetization and is beneficial to the formation of homogeneous and stable fluidized beds.

Table1. Particle size distribution of the medium solid (Geldart B)

size fraction (mm)	magnetite powder productivity (%)	size fraction (mm)	magnetite powder productivity (%)
1.00–0.63	0	0.15–0.10	28.95
0.63–0.50	0	0.10–0.074	24.69
0.50–0.30	3.77	0.074–0.05	1.79
0.30–0.20	10.59	–0.05	2.67
0.20–0.15	27.54	Total	100

Results and discussion

Stability and sensitivity at various bed heights

Researchers in the field of fluidization have adopted several methods to analyze the pressure signals in fluidized beds. These methods include statistical analysis (time domain), frequency analysis (frequency domain), and non-linear analysis (such as chaotic method) (Chen et al., 2006; Bi et al., 1996; Croxford et al., 2011). The mean

value and mean square deviation of the pressure fluctuation at the test points of the fluidized bed reflect the characteristics of gas–solid two-phase flow in the fluidized beds (Table 2). This study conducts a detailed analysis of the influence of the stability of fluidized beds and the regional statistical characteristics caused by partially plugged holes. As shown in Fig. 2, regions A, B, C, and D are selected as the objects of study to analyze the mean square deviations and sensitivity of the pressure fluctuation at different heights of the bed.

Table 2. The height of test points

Test Point	Distance from air distributor /mm	Test Point	Distance from air distributor /mm
1	180	3	80
2	130	4	30

In the experiment, superficial fluidization velocity is fixed at 1.50 U_{mf} (minimum fluidization velocity). The mean square deviations of the pressure fluctuation in region A are observed as 0.00248, 0.00304, 0.00247, and 0.00189 when none of the holes in the air distributor are plugged. The mean square deviations of the pressure oscillation at a bed height of 80 mm are higher than those in any other area. These deviations further increase to 0.00399 when the plugged holes cover 75% of the air distributor. Sensitivity S is less than that at a bed height of 30 mm. Sensitivity S of the plugged holes in regions B, C, and D decreases with increasing bed height. The fluidized gas is generally considered to initially enter the bed in the form of jet flow. The influence of plugged holes is increased when planar porous plates are used as fluidized beds.

The mean square deviations of the pressure fluctuation in the fluidized region increases axially, reaching a maximum and then dropping down when no holes are plugged. Less pressure fluctuation occurs at the top than the bottom of the bed. The mean square deviation, rather than the mean value, in all of the areas is significantly influenced by plugged holes under the same superficial fluidization velocity. Consequently, the stability of the bed is reduced. Pressure fluctuations are primarily caused by forward flow regions at the bottom of the bed and bubble movement. At the same gas speed, partially plugged holes cause uneven air distributors, resulting in an increased intensive forward flow region at the bottom of the bed and bigger bubbles. Moreover, plugged holes decrease the mean square deviation of the pressure fluctuation at the middle and bottom of the bed. The mean square deviation of the pressure fluctuation at the forward flow region is approximately equal to and is consistent with the changes in speed along the height of the bed.

The analysis of the mean square deviations of the pressure fluctuation at various heights of the bed in the region A and the related regions B, C, and D reveal that sensitivity S of the plugged holes in air distributors decreases with increasing bed height. The changes in pressure fluctuation caused by plugged holes are more obvious near the air distributor, that is, the value of *S* increases as the test point approaches the

air distributor. Thus, a 30 mm height is selected as the test height in this study. The standard deviation of the pressure fluctuation in region A increases initially and then decreases axially (the height of the bed).
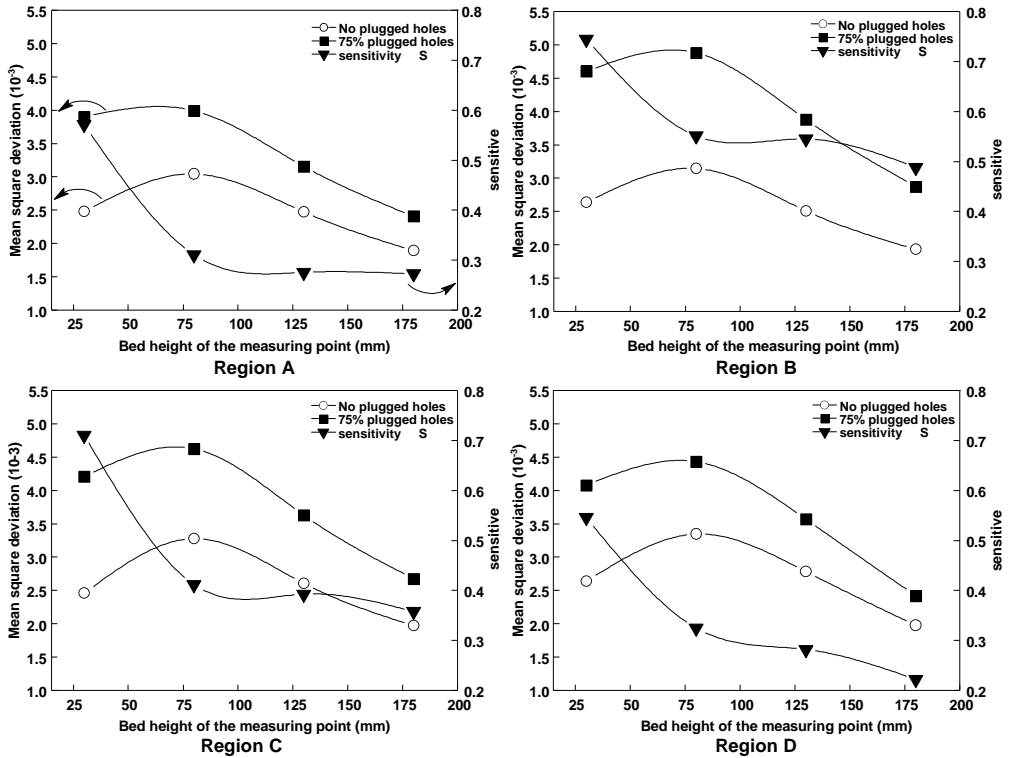
Fig. 2. Mean square deviation of pressure fluctuation and sensitivity

Influence of gas velocity on plugged holes

This study analyzes the distribution law of bed instability caused by plugged holes at various fluidized gas velocities. As shown in Fig. 3 the percentage of plugged holes in area A is 75%, and the measuring point is at a bed height of 30 mm. At this measuring point, the superficial gas velocities are U_{mf}, 1.25 U_{mf}, 1.5 U_{mf}, and 1.75 U_{mf}. As shown in Fig. 1, A is the problem area, and the other areas are associated areas influenced by the plugged holes. The superficial gas velocity increases with an increase in the mean square deviation of the pressure fluctuation in region A, suggesting that pressure fluctuation in the bed is becoming increasingly severe. The pressure fluctuations in the adjacent related regions H and B are greater than that in region A. These fluctuations in regions H and B symmetrically and progressively decreases to the sides from region A. These findings suggest that the distribution law of the influence of the plugged holes is symmetrical from the blockage problem area, and the influence of the partial blockage problem in the air distributor progressively decreases in the form of diffusion.

The experiment shows that the pressure caused by plugged holes varies at different lateral positions at the bottom of the bed layer. Bubbles with significant lateral movement appear in regions B and H. These bubbles improve the particle cross-mixing in the fluidized beds. The mean square deviation of the pressure fluctuation in region A is significantly greater than those of the two sides. Region A exhibits weak fluidization and the other two regions exhibit strong fluidization because of the difference in speed between the two sides of the fluidized gas velocities. An ascending medium stream can be observed because of the entrainment of air bubbles. The influence of the blockage problem is reportedly beneficial to the dense particle phase at the bottom of the weak fluidization region, which exhibits a significant downward trend under its own weight. Particles in strong fluidized regions turn entrained bubbles upward again. The bubble activity on the bed layer of region A is relatively weak, resulting in decreased medium flow, which in turn results in large-scale horizontal diffusion flow of particles within the fluidized bed.
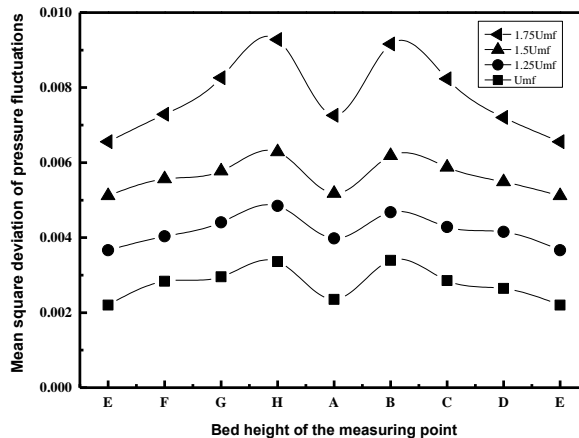
Fig. 3. The mean square deviation of pressure fluctuations with different gas velocity

A modified air distributor has been used in the distributor section, for uniform mixing of the gas moving as fine bubbles to the fluidizing section (Jena et al., 2009). The bottom zone of using three types of distributor plates (Paiva et al., 2004.) and hydrodynamic characteristics (Sobrino et al., 2009) are investigated by obtaining measurements of pressure and radial voidage profiles. A technique (Paiva et al., 2004.) to estimate the porosity fluctuations of the dense phase in the bottom of the bed is also proposed. But these studies focus on the performance of the new type of gas distributor and ignore the blocking problem and stability in the long run. The blockage area prompts strong particle disturbance at the bottom of the bed layer (Fig. 4). The mixing action only partially occurs at the intersection of the blockage areas and the regions with strong fluidization. The horizontal velocity of the particles is very low. Mixing is weak in the bed. Fraction differences exist between the particles and the signal feature (Fig.

3), because of the influence of the plugged holes suggesting that the mean square deviation of the pressure fluctuations on both sides progressively decreases as the areas of regions B and H increase. The decrease in mean square deviation is more obvious with an increase in fluidized gas velocity.

This experiment proves that the partial plugging of holes in specific areas cause lateral bubble movement in dense phase gas–solid separation fluidized beds. By analyzing the plugged holes in this area, the following factors can be revealed: the strong and weak fluidized regions, the differences in the volume fraction of particles, the pressure difference in the transverse of beds, the increase in the standard deviation of pressure fluctuations, and the strengthening of the lateral mixing of medium particles. The emergence of two or more strong fluidized regions near the blockage areas can be considered a means of judging its regional features.
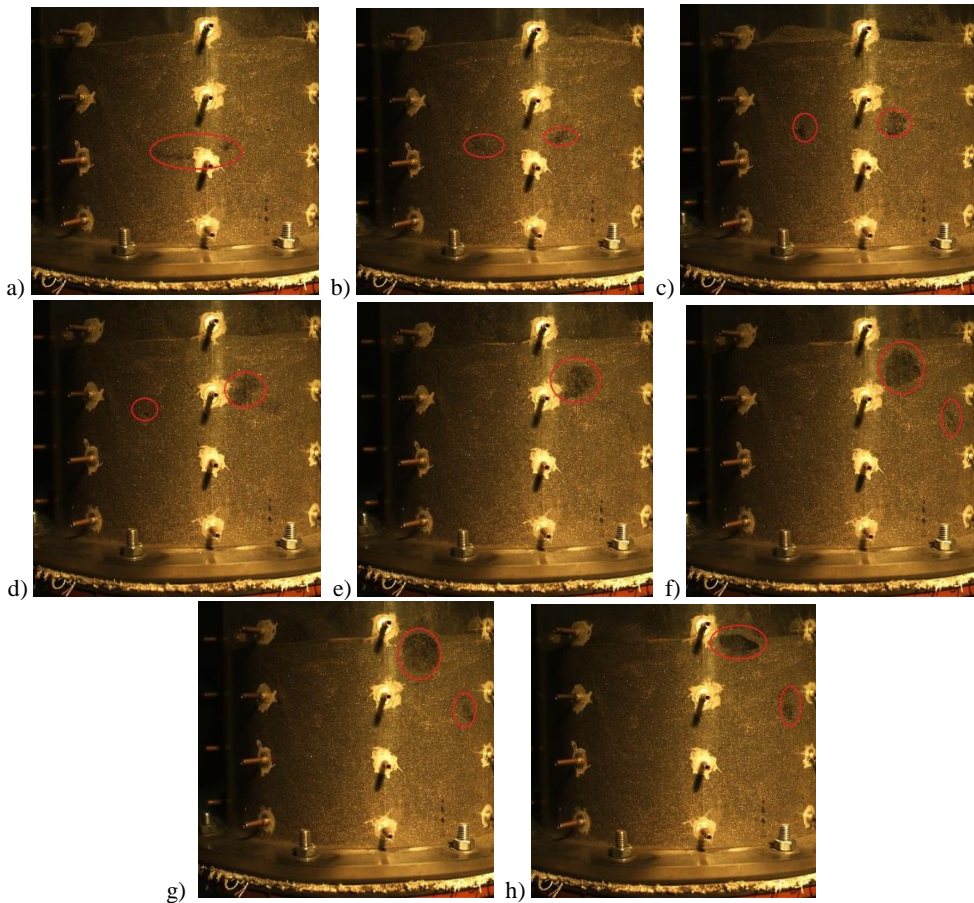
Fig. 4. Bubble behavior caused by plugged holes in air distributors

Influence of blockage area on stability

Previous studies (Schaaf et al., 2002; Lim et al., 2007 and Martin et al., 2011) have mostly focused on the pressure drop and structure of air distributors for dense phase gas–solid fluidized bed. The blockage area is a major factor that influences the regional characteristics of air distributors in a dense phase gas–solid separation fluidized bed. This study analyzes the blockage area of a bed under $1.75U_{mf}$ of gas velocity.

The height of the fluidized bed is 200 mm, and the measuring point is from an air distributor at a bed height of 30 mm. The distribution law, which is affected by the plugged holes on the bed, is symmetrical to the blocked regions; thus, this study merely analyzes the macro-signal features of the blocked regions A, B, C, and D. As shown in Fig. 5, in Area A, the mean square deviation of the pressure fluctuations of the bed first increases and then decreases as the number of plugged holes increases. Increasing the number of plugged holes causes a decrease in average fluidized gas velocity and results in the non uniformity of wind velocity distribution; thus, the uniformity of the average fluidized gas velocity and the wind velocity distribution is considered the main factor influencing the stability of bed. Increasing the number of plugged holes also results in the uneven distribution of gas velocity, which causes the pressure differences near the air distributor and the increase in pressure fluctuation.

When the percentage of plugged holes increase from 0% to 25%, the effect of the non uniformity of gas velocity distribution is significantly more obvious than the effect of the decrease in the average fluidized gas velocity. Therefore, the mean square deviation of the pressure fluctuation increases as the percentage of plugged holes in this range increases. When the percentage of plugged holes increases from 25% to 50%, the effect of the average fluidized gas velocity intensifies as the velocity decreases. However, the non uniformity of wind velocity distribution is still a major factor influencing the bed stability near the air distributor. When the percentage of plugged holes increases from 50% to 75%, the fluidized air velocity becomes the major factor influencing pressure fluctuation. The fluidized gas velocity in this region sharply decreases, and the heterogeneity of wind velocity distribution is improved; thus, the effect of the non uniformity of wind velocity distribution on the bed gradually becomes less significant than the effect of the decrease in fluidized gas velocity. When the percentage of the plugged holes increases from 75% to 100%, the fluidized air velocity becomes increasingly smaller. The mean square deviation of the pressure fluctuation and the disturbance of medium-sized particles begin to decline at the bottom of the bed, thereby gradually improving the stability of the bed.

Region B is the nearest to region A among all the relevant regions. Thus, this region has greatest pressure fluctuation and the most obvious variation in sensitivity. As shown in Fig. 5, the mean square deviation of the pressure fluctuation increases as the blockage area increases. When the percentage of plugged holes ranges between 25% and 75%, the variation rate of the mean square deviation of the pressure fluctuation is smaller than that of the blocking percentages ranging from 0% to 25% and from 75% to 100%.
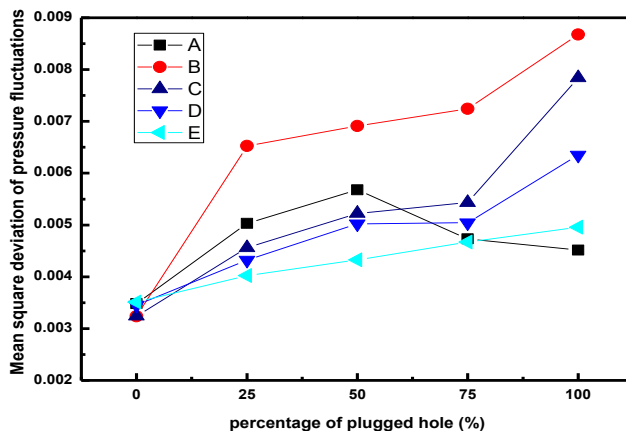
Fig. 5. Plugging hole area of fluidized bed pressure fluctuation variance

The effect of distributor hole-size on the bubble hydrodynamics (M et al., 2007) air distributor geometry (the opening fraction, different hole size and number) (Seong et al., 2005) on the fluidization characteristics were studied. An attempt has been made to study the stability characteristics of different cross-sectional shapes of fluidized bed having same cross-sectional area (Sahu et al., 2013). But they did not consider the blockage area and relevant regions stability characteristics. The paper researched the blockage area characteristics and the rule of relevant regions the stability characteristics. The mean square deviation of the pressure fluctuation in all the relevant regions is mainly prompted by the varying pressures in the blocked areas and the variations in fluidized air velocity, which together lead to the variations in fluidized air velocity in the relevant regions. Moreover, the mean square deviation in pressure fluctuation increases as the blocking acreage increases. The order of the effect intensity of region B, C, D, and E corresponds with their respective distances from region A.

Conclusion

This research suggests the plugged holes in the air distributor should be tested to ensure the stability of these beds for particle separation. The pressure fluctuation is sensitive to these plugged holes. The sensitivity can be tested and diagnosed by determining the standard deviation of the pressure fluctuation. The pressure fluctuations signal is a way to present its macro-signal features of the interaction in the bottom of the bed. In areas with partial blockage, that is the areas with weak fluidization, a decrease in the volume fraction of the particles and in the pressure differences in the transverse of the bed results in an increase in the standard deviation of the pressure fluctuation, thereby stimulating the lateral mixing of medium-sized particles. The standard deviation and the mixing intensity decrease axially. The value of sensitivity (S) of the plugged holes in the air distributor decreases as the height of the bed increases. The blocking area not only

occurs partially, but often there are different degrees of blocking in the whole. The uneven distribution law of density is caused by blocking. All these parameters should be explore and a further analysis is needed.

Regional features of plugged holes is that the standard deviation of the pressure fluctuation in region A increases initially and then decreases axially (the height of the bed), the mean square deviation of the pressure fluctuations on both sides progressively decreases as regions B and H (nearby problem region) increase, the order of the effect intensity of region B, C, D, and E corresponds with their respective distances from region A. The features of air distributors affect the surrounding areas. The intensity of the effect is proportional to the distance to the plugged holes. The regional features were used to detect gas distributor plugged holes and uneven distribution of gas in the industrial fluidized bed.

Acknowledgements

References

BI H.T., GRACE J.R., 1996.*Radial pressure difference and their fluctuations in dense fluidized beds*. Chemical Engineering Science, 51(4):663–665.

BREUERH., SNOBYR.J., MSHRA S., BISWAL D., 2009. *Dry coal jigging - a suitable alternative for Indian power coals*. Journal of Mines, Metals and Fuels, 57(12): 425-428.

CELIA SOBRINO, NAOKO ELLIS, MERCEDES D.V., 2009. *Distributor effects near the bottom region of turbulent fluidized beds*. Powder Technology, 189:25–33.

CHEN Q., YANG Y. 2003. *Development of dry beneficiation of coal in China*. Coal Preparation: A Multinational Journal, 23(1–2): 3–12.

CHEN Y.G, TIAN Z.P., MIAO Z.Q., 2006. *Analysis of the pressure fluctuations in binary solids circulating fluidized bed*. Energy Conversion and Management 47:611–623.

DONG L., ZHAO Y.M., LUO Z.F., DUAN C.L., WANG Y.W., YANG X.L., ZHANG B., 2013. *A model for predicting bubble rise velocity in a pulsed gas solid fluidized bed*, International Journal of Mining Science and Technology, 23:227–230.

JENA H.M., SAHOO B.K., ROY G.K., MEIKAP B.C., 2009. Statistical analysis of the phase holdup characteristics of a gas–liquid–solid fluidized bed. The Canadian Journal of Chemical Engineering, 87(2):1–10.

IBGE CENSUS.2011.*Statistical handbook of the BRICS2011*. Beijing: China Statistics Press.

PAIVA J.M., PINHO C., FIGUEIREDO R., 2004. *The influence of the distributor plate on the bottom zone of a fluidized bed approaching the transition from bubbling to turbulent fluidization*. Chemical Engineering Research and Design, 82(A1): 25–33

LIM C., GILBERTSON M., HARRISON A., 2007. *Bubble distribution and behaviour in bubbling fluidized beds*. Chemical Engineering Science. 62 (1–2), 56–69.

LUO Z.F., FAN M.M., ZHAO Y.M., TAO X.X.,CHEN Q.R.,CHEN Z.Q., 2008. *Density-dependent separation of dry fine coal in a vibrated fluidized bed*. Powder Technology,187(2): 119-123.

LUO Z.F., ZHAO Y.M., CHEN Q.R., FAN M.M., TAO X.X., 2002. *Separation characteristics for fine coal of the magnetically fluidized bed*. Fuel Processing Technology, 79(1): 63–69.

NATIONAL BUREAU of STATISTICS of CHINA. 2012. *The 2011 national economic and social development statistics bulletin of the People's Republic of China (PRC)*. Beijing: National Bureau of Statistics of China.

MACPHERSON S.A., IYESON S.M., GALVIN K.P., 2011. *Density-based separation in a vibrated Reflux Classifier with an air-sand dense-medium: Tracer studies with simultaneous underflow and overflow removal*. Minerals Engineering, 24(10): 1046–1052.

MARTIN L, BRIONGOS JV, NE STOR G.H., 2011. *Detecting regime transitions in gas–solid fluidized beds from low frequency accelerometry signals*. Powder Technology. 207:104–112.

M. A. A., MOSES T., VISHNU P., 2007. *Simulations of bubble column reactors using a volume of fluid approach: effect of air distributor*. The Canadian Journal of Chemical Engineering, 85(6):290–301.

OSHITANI J., FRANKS G.V., GRIFFIN M.,2010. *Dry dense medium separation of iron ore using a gas–solid fluidized bed*.Advanced Powder Technology, 21(5): 573-577.

OSHITANI J., ISEI Y., YOSHIDA M., GOTOH K., FRANKS G., 2012.*Influence of air bubble size on float–sink of spheres in a gas–solid fluidized bed*. Advanced Powder Technology, 23(1): 120-123.

ORHAN E.C., ERGUN L., ALTIPARMAK B., HONAKER R Q., 2010. *Application of the FGX separator in the enrichment of catalagzi coal: a simulation study*. International Coal Preparation Congress 2010 Lexington, KY; SME: 562-570.

PRASHANT D., XU Z., SZYMANSKI J., HONAKER R.Q., BODDEZ J., 2010. *Dry cleaning of coal by a laboratory continuous air dense medium fluidized bed separator*. International Coal Preparation Congress 2010 Lexington, KY; SME: 608-616.

SAMPAIO C.H., ALIAGA W., PACHECO E.T., PETTER E., WOTRUBA H., 2008. *Coal beneficiation of Candiota mine by dry jigging*. Fuel Processing Technology, 89(2): 198-202.

SAHU A.K., TRIPATHY A, BISWAL S.K., 2013.*Study on particle dynamics in different cross sectional shapes of air dense medium fluidized bed separator*. Fuel, 111: 472–477

SEONG Y.S., DONG H. L., GUI Y. H., DUK J.K., SANG J. S., SANG D.K., 2005. *Effect of air distributor on the fluidization characteristics in conical gas fluidized beds*. Korean Journal of Chemical Engineering, 22(2), 315-320.

SONG S.L., ZHAO Y.M., LUO Z.F., TANG L.G., 2012. *Motion behavior of particles in air–solid magnetically stabilized fluidized beds for separation*, International Journal of Mining Science and Technology,22:725–729

VAN DER SCHAAF, J., SCHOUTEN, J., JOHNSSON, F., VAN DEN BLEEK, C., 2002.*Non-intrusive determination of bubble and slug length scales in fluidized beds by decomposition of the power spectral density of pressure time series*. International Journal of Multiphase Flow, 28, 865–880.

WANG S., HE Y.Q., HE J.F., GE L.H.,LIU Q., 2013. *Experiment and simulation on the pyrite removal from the recirculating loadofpulverizer with a dilute phase gas–solid fluidized bed*, International Journal of Mining Science and Technology ,23:01–305.

WEINSTEIN R., SNOBY R., 2007.*Advances in dry jigging improves coal quality*. Mining Engineering, (1): 29-34.

WORLD ENERGY COUNCIL, 2010.*Water for Energy*. London: WEC.

YOSHIDA M., OSHITANI J., TANI K., GOTOH K., 2011. *Fluidized bed medium separation (FBMS) using the particles with different hydrophilic and hydrophobic properties*. Advanced Powder Technology, 22(1): 108-114.

ZHAO Y.M., TANG L.G., LUO Z.F., LIANG C.C., XING H.B., WU W.C., DUAN C.L., 2010a. *Experimental and numerical simulation studies of the fluidization characteristics of a separating gas-solid fluidized bed*. Fuel Processing Technology, 91(2): 1819-1825.

ZHAO Y.M., LIU X.J., LIU K.L., LUO Z.F., WU W.C., SONG S.L., TANG L.G., 2011. *Fluidization characteristics of a gas-paigeite-powder bed to be utilized for dry coal beneficiation*. International Journal of Coal Preparation and Utilization, 31(3-4): 149-160.

ZHAO Y.M., LUO Z.F., CHEN Z.Q., TANG L.G., WANG H.F., XING H.B., 2010b. *The effect of feed-coal particle size on the separating characteristics of a gas-solid fluidized bed*. Journal of the South African Institute of Mining and Metallurgy, 110(5): 219-224.

CARBON DIOXIDE SEQUESTRATION DURING SHALE GAS RECOVERY

Andrzej ROGALA, Katarzyna KSIEZNIAK, Jan KRZYSIEK, Jan HUPKA

Chemical Technology Department, Chemical Faculty, Gdansk University of Technology, Gdansk, Poland,
andr.rogala@gmail.com

Abstract: This paper presents literature on theoretical and practical aspects of gas production from shale using carbon dioxide fracturing. Development of technical and environmental aspects of carbon dioxide fracturing technologies is also considered. Patents applicable to carbon dioxide fracturing are reviewed. In this work experiments were also conducted to verify possibility of carbon dioxide sequestration in the shale gas reservoirs. Carbon dioxide and methane (CH_4) storage capacity was measured as Langmuir volumes. The adsorption capacities depend on content of organic matter in the shale rocks and pressure. The obtained results indicate that developing of carbon dioxide fracturing is reasonable.

Keywords: shale gas, fracturing, unconventional gas resources, CO_2 fracturing

Introduction

Hydraulic fracturing (HF) is the main method of shale gas recovery. It is based on pumping fracturing fluid into a borehole under very high pressure to create fractures and stimulate reservoir for gas production (Howard, 1970). The fracturing fluid consists mainly of water and proppant (99.5%) and chemical additives (0.5%). Proppant is a material which prevents fractures from closing. Usually it is sand, sometimes ceramic material or resin coated sand (Mader, 1989). Chemicals are used to stimulate a reservoir and have various tasks in the fracturing fluids, they are: friction reducers, acids, corrosion inhibitors, biocides, iron control agent, gelling agent, cross-linker, breaker, KCl, NaCl. The hydraulic fracturing technologies, despite many years of use and numerous improvements, still have many problems. These are compatibility between fracturing fluid and reservoir rock and oil (Lal, 1999), water and waste water management, environmental costs, investment costs, risk of ground and surface water contamination, methane emission to atmosphere (USEPA, 2011), and wide social perception influenced by media. A continuous technology

improvement is a natural trend in many research activities and introduction to the oil and gas field.

Table 1. Cation exchange capacity of clay minerals
(Eslinger and Pevear, 1988; Martin and Dacy, 2004)

Mineral	CEC [meq/100 g]
Smectite	80–150
Illite	10–40
Kaolinite	10–100
Chlorite	< 10
Hydrous Mica	10–40

A fracturing industry has identified a problem of compatibility between fracturing fluid and reservoir, especially containing water sensitive shales with smectite and illite. These minerals have tendency to bond high amount of water and swell/expansion. This phenomenon results in propped fractures reduced frac flow capacity and decrease of gas or oil flow in consequence. In Table 1 it can be found that smectite has much greater cation exchange capacity CEC than illite. Both of them have higher CEC than kaolinite and chlorite. CEC is closely connected with ability of a mineral (especially clay) to bind water. A greater value of CEC means that more water can be trapped in a clay structure and swell more intensively. The mechanism and understanding the water capillary forces is the subject of research worldwide. This is particularly important for Polish gas-bearing shale, which contains significant amount of smectite and illite. First fracturing works done in Poland showed that swelling clays significantly impede HF operations (PAP, 2013). The consequence of these problems is to develop wide range of technologies alternative to water based HF of shale oil and gas reservoirs that are water sensitive. The fracturing technology development is focused on water either reduction or elimination in the fracturing fluid. The application of shale inhibitors in water-based fracturing fluids is very expensive and due to shale anisotropy is not very well predictable. The best known technologies are: liquid carbon dioxide fracturing, nitrogen fracturing, carbon dioxide/nitrogen-based foam fracturing, gelled methanol fracturing and liquefied propane fracturing (Rogala, 2013). All these methods are designed to maintain compatibility between fracturing fluid and clay minerals containing expanding smectite and swelling illite (Ahn and Peacor, 1986). This approach allows to eliminate potential fracture closing by smectite and illite, which decides about the fracturing quality and overall frac conductivity.

Carbon dioxide fracturing

A widespread interest in the use of carbon dioxide (CO_2) in shale gas recovery is associated with the low price, general accessibility and its specific properties. Moreover, the United Nation policy of imposing money penalties for exceeding the limits of CO_2 emission to the atmosphere, further stimulates the use of this gas in the industry. As it is shown in Fig. 1, critical parameters of CO_2 are relatively small. Due to very high gaseous CO_2 injection pressure during fracturing and temperature in the reservoir about 80 °C, CO_2 becomes supercritical at the depth of 800 m and fluid, having much higher viscosity and density than gas. Supercritical CO_2 is completely compatible with the reservoir rock and reservoir fluid. In addition, CO_2 after contact with formation water, forms acidic species, leading to lowering pH. This property prevents creation of iron hydroxides, presence of which may plug slippage and reduce the frac conductivity (Economides et al., 2000). The same parameters of operation are not possible by using nitrogen, the gas that was also tested on wells. It has not only higher values of critical parameters, but also requires the use of high pressure equipment operating under higher pressure causing greater problems than in the case of CO_2.

The first carbon dioxide fracturing technology was patented in 1982 (Bullen and Lillies, 1982). This method is well-established and has been repeatedly modified. It is commonly used for dry fracturing in water sensitive formations. It involves injecting sand with liquid CO_2 as a carrier fluid for a proppant being mixed in a pressurized blender without the addition of water or other auxiliary compounds, except gelling additive. The proppants are synthetic or natural particles such as sand, resin coated sand or sintered bauxite ceramics, used in oil and gas industry to keep fractures opened. CO_2 on the surface is liquefied at a pressure of 1.4 MPa and a temperature of −34.5 °C. The proppant is added directly to a liquid CO_2 under these conditions on the surface using specialised equipment. The liquid CO_2 viscosity is about 5 cP and therefore, allows to increase viscosity to carry the proppant in propagated fracture. After stabilization of temperature and pressure, CO_2 partly dissolves in residual water and liquid hydrocarbon deposits.
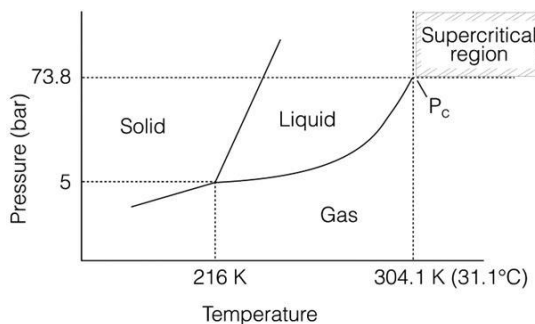
Fig. 1. Phase diagram of carbon dioxide (Ginty et al., 2005)

One of the most important advantage of liquid CO_2 fracturing is elimination of conditional formation damage normally related with the fracturing fluids. Another one is rapidly clean-up process and evaluation of the well following fracturing (Lilliesand King, 1982).

In Canada, only up to late 1990', there were more than 1200 tests, accomplished with success (Wright, 1998). The technology was also used in the USA for Devonian shale in East Kentucky and West Pennsylvania, Texas and Colorado (Arnold, 1998). It was observed that the average gas production in some wells was as much as five-fold greater than in the case of production using conventional HF treatments.

The main problem related with carbon dioxide fracturing (also using nitrogen or CO_2/N_2 mixture) is its transport in the liquid state and storage in pressurized tanks. In particular, the loss of CO_2 to the atmosphere should be avoided because of eventual impact on global warming. CO_2 fracturing keeps clays (smectite and illite) stabilized and prevents metal leaching and chemical interactions between fracturing fluid and reservoirs. The greatest successes in the CO_2 fracturing were recorded in Canada and in the former Soviet Union in late eighties (Luk and Grisdale, 1994).

Technologies of shale gas recovery based on carbon dioxide

Since the first carbon dioxide fracturing technology was developed, there were many attempts to use carbon dioxide in shale gas recovery. The following are the most promising solutions of problems associated with classical liquid carbon dioxide fracturing.

In 1987 a new composition of liquid CO_2 fracturing fluid was described by Canadian Fracmaster (Bullen et al., 1987). Alkene oxide additive was used (preferably propylene oxide) in the presence of a catalyst, producing in the reservoir random copolymer having a molecular weight of 20000 – 150000 and similar in structure to the polycarbonate (IR spectrum showed interleaved carbonate bond). The presence of this compound in an amount of 1.5–3.5% (wt) of the fracturing fluid significantly increased the viscosity and improved fracturing parameters. In addition, it was decomposed at normal temperature and pressure at the time from 24 to 48 hours and much faster under reservoir conditions, so that did not leave any undesirable chemical compounds in the shale formations.

At the end of 1980', a method of fracturing low permeability fields with a mixture of liquid hydrocarbons and CO_2 was developed (Mzik, 1989). The idea was the result of the observation that an oil viscosity increased more rapidly with increasing temperature than the mixtures of any suitable polymer, and additionally was miscible with liquid carbon dioxide. A mixture of hydrocarbons for the preparation of the proposed fracturing fluid was obtained by mixing petroleum products from the light and medium distillates and aromatic compounds. A mixture of hydrocarbons should have the following properties: average molecular weight of less than 200, content of at least 70% of the C5–C14 fraction, at least 8% by weight, aromatics solidification temperature below –40 °C, and density from 0.77 to 0.85 g/cm^3 at 15 °C. The

fracturing fluid should consist of 95 to 15% liquid CO_2 and 5–85% of hydrocarbons. The proposed fracturing fluid is very simple, safe in use, and it can be injected using a conventional equipment for fracturing, also with the addition of proppant. The use of such a fluid, resulting in fractures with larger width than in case of use only liquid CO_2,also greatly facilitates the purification of the hole. In addition, the well clean-up is much faster.

A common problem connected with the liquid CO_2 is the presence of ice during the fracturing operation. If the wellhead pressure rapidly drops, CO_2 in such conditions may result in ice formation in a form of hydraulic head and pipes, which eventually restricts the gas flow. Therefore, it was decided to optimize the process by adding nitrogen to the CO_2 gas, which not only prevents ice build-up but also reduces the cost of operating the well (Gupta et al., 1998). A little different solution of this problem was proposed by Tudor (1999). He described a fluid consisting of 100% liquid carbon dioxide, 100% gaseous nitrogen and proppant. Contrary to expectations, the new method of liquid CO_2/N_2 treatments resulted in actual lowering the surface treatment pressures at equivalent volumetric rates, which reduced pumping costs and yield-improved leak-off characteristics.

One of the most important factor during shale gas recovery is concentration of proppant in the fracturing fluid. Nowadays, it should be about 0.48 kilograms per cubic decimeter and there is a problem to reach this value using non-aqueous fracturing technologies. Therefore Luk and Grisdale (1996) proposed to connect hydraulic/alcohol/hydrocarbon fracturing with carbon dioxide fracturing. They made two phase fracturing fluids able to have enough the maximum proppant concentration. A part of the proppant volume is added to liquid carbon dioxide and rest to water alcohol or hydrocarbon. Then, two systems are mixed together. The resulting fluid is much more compatible with reservoir than the classical fracturing fluids, especially with water sensitive shales. A high concentration of the proppant provides a high gas flow through the fractures.

US Patent 6729409 (2004) describes a method of using two-phase fracturing fluid in which the liquid phase is carbon dioxide and gaseous phase is nitrogen. In the liquid phase a nonfunctional non-ionic fluorochemical stabilizer was used. This technology can be used to stimulate unconventional hydrocarbon reservoirs of both oil and gas-bearing. The main advantage is a greater increase of fracturing fluid viscosity than in fluids of similar methods. It has positive impact on the maximum proppant concentration in fracturing fluid and gas flow through fractures.

In 2010 a new method of stimulation of shale formations using the carbon dioxide-based fracturing fluid, having viscosity below 10 mPa·s and share rate about 100/s,was invented (Kubala, 2010). The treatment fluid is injected into a borehole under a pressure higher than the reservoir pressure. The concentration of carbon dioxide is from 70% by mass to near 100%. There can be also used some surfactant, especially fluoropolymeric. Fracturing fluid can be aqueous, almost non-aqueousor non-aqueous. This technology leads to better fracturing parameters, fracturing fluid is more

compatible with reservoir, the concentration of proppant can be higher than in other methods, as a result, the gas flow is also higher.

Mack (1999) proposed a shale gas fracturing technology, which is a modification of the hydraulic fracturing and carbon dioxide fracturing. A part of classical fracturing fluid is replaced by a mixture of nitrogen and carbon dioxide in a volume ratio from 1:5 to 1:4. Carbon dioxide is supplied as a liquid, whereas nitrogen is supplied as a gas. The proppant is added to the fracturing fluid together with a mixture of CO_2 and N_2. The surfactants and foam stabilizers are also added to the mixture. When the fluid is at the bottom of the borehole, carbon dioxide achieves the supercritical state because of a high temperature in the reservoir. Then, the foam is formed and intensifies the process of fracturing. The resulting fracturing fluid has much lower flow resistance in the reservoir, enabling lower power consumption by the pumps used for fracturing. Moreover, there is a compatibility between fracturing fluid and reservoir.

Comparison of liquid carbon dioxide fracturing and hydraulic fracturing

Table 2 shows the most important factors pertaining to shale gas recovery. The comparison between water-based hydraulic fracturing and liquid carbon dioxide fracturing was made.

Table 2. A comparison of hydraulic fracturing with CO_2 fracturing technology. N and Y mean no and yes, respectively. *Average data from field applied technology by Jan Krzysiek (unpublished)

Consideration	Hydraulic Fracturing	Liquid CO_2 Fracturing
environmentally friendly	N	N
fluid availability	?	Y
fluid recycling	Y	possible or useless
chemicals used	Y	reduced or eliminated
reservoir compatibility	biggest problem	Y
fracture creation	Y	Y
proppant carrying	Y	Y
recovery to pipeline	N	N
heavy metals flowback	Y	N
frac cost	1	$\gg 1$*
fluid left in formation	Y	N
well clean up	Y	Y
frac geometry predictability	N	N
tilting stress development	Y	Y
zone water in flux risk	1	> 1*
fracture length	1	> 1*
fraced well performance	1	$\ll 1$*
local road damage risk	Y	Y
environmental risk	Y	Y
NO_x and CO_2 in pumping	Y	Y
return on investment	1	< 1*

As shown in Table 2, carbon dioxide fracturing seems to be a method allowing elimination of water-based hydraulic fracturing which is not the most optimal. The main problems with this technology are economic and technological, that is the very long return on investment time and fact that expanding in reservoir carbon dioxide is extremely difficult to control. Presently, this method cannot be used in the deep wells, which occur in Poland.

Sequestration of carbon dioxide in shale gas reservoirs

One of the latest proposed solution is the conjugated hydrocarbon gas recovery and simultaneous storage of CO_2 in horizontal small diametrical wells made in a single horizontal well. The team, led by Niezgoda (WAT, 2012) proposed a method based on the stimulation of the reservoir using liquid carbon dioxide with the addition of proppant. The fracturing is achieved by pressure from supercritical CO_2 caused by reservoir temperature. Return on investment (ROI) as a prime target of investors is questionable. The inventors claimed that the efficiency of borehole can increase about 60 - 80% compared to 15% in the case of hydraulic fracturing. Unfortunately, negligible information about innovative solutions does not allow objectively evaluate possibility of carbon dioxide sequestration during the shale gas recovery. Nevertheless, the idea of the technology seems to be one of the best possible alternatives to hydraulic fracturing. Carbon dioxide sequestration during shale gas recovery could significantly change the importance of carbon dioxide place in the unconventional hydrocarbons resources market. This kind of technology is also supported by the Kyoto Protocol about reduction of global CO_2 concentration in the atmosphere (UNFCCC, 1997). Especially due to the prolongation of its duration until 2020 (UNFCCC, 2012). The results of these documents are EU actions to promote sequestration of CO_2. Therefore, there were conducted tests to evaluate possibility of carbon dioxide sequestration in the shale gas reservoirs.

Experimental

In this work experiments were conducted to verify possibility of carbon dioxide sequestration in the shale gas reservoirs. The carbon dioxide and methane (CH_4) storage capacities were measured as Langmuir volumes. Adsorption analyses were performed using the high-pressure volumetric adsorption. Isotherms were measured on a custom-made apparatus based on Boyle's law. Langmuir coefficients were determined using specialized computer software. To find the relationship between the gases storage capacity and content of organic matter in the shale reservoirs, the total organic carbon TOC analysis was also conducted.

The research was based on shale rock samples derived from the Ordovician (O1 and O2) and Lower Silurian (S1) period. The shale is a source rock for unconventional hydrocarbon fields in the Baltic Basin. The determined TOC values of shale rock

samples and Langmuir coefficients for carbon dioxide and methane adsorption are shown in Table 3.

Table 3. Gas storage capacity and total organic carbon for collected samples

Sample	Formation	Langmuir Coefficients		Langmuir Coefficients		TOC [%]
		CH_4 [m^3_s/1000kg]	CH_4 [MPa]	CO_2 [m^3_s/1000kg]	CO_2 [MPa]	
O1	Ordovician	0.1412	1.216	0.9711	1.750	1.58
O2	Ordovician	0.9812	3.041	1.9113	2.211	2.92
S1	Lower Silurian	2.1401	7.122	4.0443	6.421	3.70

m^3_s – standard cubic meter

The shale rock adsorption capacity measured by means of the Langmuir volumes ranges from 0.97 to 4.04 standard cubic meters of CO_2 per 1000 kg of shale rock at the Langmuir pressures ranging from 1.75 to 6.42 MPa. The Langmuir volumes for CO_2 are much higher than for CH_4 which ranged from 0.14 to 2.14 standard cubic meters of CH_4 per 1000 kg of shale rock at the Langmuir pressures ranging from 1.22 to 7.12 MPa. The TOC values of tested samples ranged from 1.60 to 3.70%, sample O1 has the lowest TOC value and also the lowest Langmuir volumes, in particular pressures, whereas sample S1 has the highest TOC value, it also has the highest Langmuir volumes. To properly compare the adsorption capacity data, three pressure conditions were selected: 1.4, 2.8, and 4.2 MPa. The data are presented in Table 4.

Table 4. Summary of CO_2 and CH_4 adsorption capacity
in standard cubic meter per 1000 kg at selected pressures

Sample	Formation	Adsorbed substance	Absolute Pressure [MPa]		
			1.4	2.8	4.2
O1	Ordovician	CH_4	0.0852	0.1172	0.1450
		CO_2	0.3996	0.5881	0.7014
O2	Ordovician	CH_4	0.2721	0.4341	0.5298
		CO_2	0.9772	1.2975	1.4181
S1	Lower Silurian	CH_4	0.3186	0.5695	0.7753
		CO_2	1.4190	2.5233	3.3884

At a constant pressure of 1.4 MPa, the measured CO_2 adsorption capacity ranged from 0.40 to 1.42 m^3/1000 kg whereas methane adsorption capacity ranges from 0.09 to 0.32 m^3/1000 kg. At 2.8 MPa, the CO_2 adsorption capacity ranges from 0.59 to 2.52 m^3/1000kg and methane from 0.12 to 0.57 m^3/1000 kg. At 4.2 MPa for CO_2 it ranges from 0.70 to 3.39 m^3/1000 kg, while for CH_4 from 0.15 to 0.78 m^3/1000 kg. The

adsorption capacities of CO_2 for the tested samples at the selected pressures are presented in Fig. 2. Figure 2 shows that, the higher absolute pressure during absorption, the higher adsorption capacity. Taking into account the fact that the fracturing pressure is about 100 MPa or higher, it may be assumed that the CO_2 adsorption capacity during shale gas recovery is much higher than in the presented results.
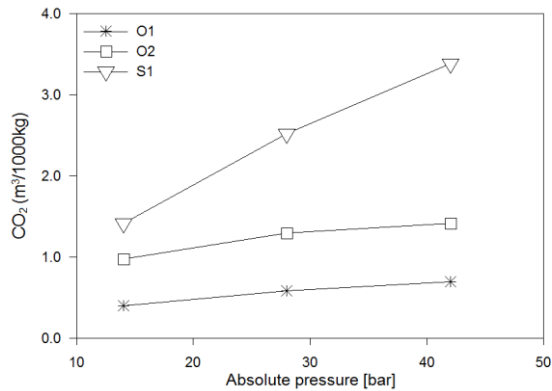
Fig. 2. Adsorption capacities of shale samples at selected pressures (1 bar = 0.1 MPa)

Conclusions

Considering economic, environmental and safety reasons, liquid carbon dioxide fracturing seems to be the most promising alternative to the hydraulic fracturing method. This may be warranted by the properties of this substance, which is non-toxic, non-flammable and it can be easily converted into a liquid state. Over the years carbon dioxide was used in foam fracturing, fracturing using mixtures of carbon dioxide with nitrogen or hydrocarbons as well as liquid carbon dioxide. All these fracturing fluids contained the proppant. There are major advantages of carbon dioxide fracturing:

- elimination of potential formation damage normally associated with fracturing fluids,
- the gas can be removed easily and the clean-up process is fast,
- CO_2 fracturing keeps clays (smectite and illite) stabilized and prevents metal leaching and chemical interactions,
- possibility of elimination of chemical additives,
- possibility of CO_2 sequestration (green technology),

and also disadvantages:

- a very expensive equipment,
- the ice presence in the hydraulic head and pipes, what eventually results in clogging gas flow,

- problems with transport in liquid state and stored in pressurized containers,
- possible loss of CO_2 – eventual impact on the global warming,
- a very long time of return on investment.

The following conclusions from the research of carbon dioxide sequestration in shale reservoirs can be drawn.

1. Langmuir volumes of carbon dioxide are much higher than volumes of methane under given conditions. It suggests that the volume of carbon dioxide possible to be sequestrated should be greater than adsorbed (not total) methane.
2. For maximum tested constant pressure of 4.2 MPa, CO_2 the adsorption capacity ranges from 0.70 to 3.39 m^3/1000 kg. This capacity should be much higher during carbon dioxide fracturing because of higher injection pressure. Thus, the sequestration should occur with a higher efficiency.
3. The TOC values of tested samples range from 1.60 to 3.70%
4. The adsorption capacities of CO_2 and CH_4 depend on content of organic matter in the shale rocks. The shale rocks with higher TOC values can absorb much more CO_2 and reservoirs can be more capacious for carbon dioxide sequestration.
5. To properly evaluate the possibility of carbon dioxide sequestration during carbon dioxide fracturing, further research is necessary. Precise estimates of geological deposits and detailed economic analysis are also required.

Taking into account the financial implications of not observing the limits of CO_2 emissions, cost-effectiveness of carbon dioxide can significantly increase in future. The Kyoto protocol and the European Union policies cause that the development of carbon dioxide fracturing can be very important. However, a long-term study and improvements of this technology are necessary.

Acknowledgments

References

AHN J.H., PEACOR D.R., 1986, *Transmission electron microscope data for rectiorite: Implications for the origin and structure of "fundamental particles"*, Clays and Clay Minerals, No. 34, 180–186

ARNOLD D.L., 1998, *Liquid CO2 – sand fracturing: the dry frac*, Fuel and Energy Abstracts, Vol. 39, No. 3, 185–185

BULLEN R.S., LILLIES A.T., 1982, *Carbon dioxide fracturing process and apparatus*, US Patent No. 4374545

BULLEN R.S., MZIK J., RICHARD J.P., 1987, *Novel compositions suitable for treating deep wells*, US Patent No. 4701270

ECONOMIDES M.J., NOLTE K. G., AHMED U., 2000, *Reservoir stimulation*, Chichester: Wiley

ESLINGER E., PEVEAR D., 1988, *Clay Minerals for Petroleum Geologists and Engineers*, Society of Economic Paleontologists and Mineralogists, SEPM Short Course Notes, No. 22, (Tulsa, 1988)

GINTY P.J., WHITAKER M.J., SHAKESHEFF K.M., HOWDLE S.M., 2005, *Drug delivery goes supercritical*, Materials today, Vol. 8, No. 8, 42–48

GUPTA D.V. S., BOBIER D.M., 1998, *The History and Success of Liquid CO_2 and CO_2/N_2 Fracturing System*, Canadian Fracmaster Ltd., SPE Gas Technology Symposium (Calgary, Alberta, Canada 15th–18th March 1998)

GUPTA D.V.S., PIERCE R.G., SENGER ELSBERND C.L, 2004, *Foamed nitrogen in liquid CO_2 for fracturing*, US Patent No. 6729409

HARRIS P.C., KLEBENOW D.E., KUNDERT D.P., 1989, *Constant internal phase design improves stimulation results*, SPE Paper 17532

HOWARD G. C., FAST C. R., 1970, *Hydraulic Fracturing*, SPE of AIME, pp. 210

KARGBO D.M., WILHELM R.G., CAMPBELL D.J., 2010, *Natural Gas Plays in the Marcellus Shale: Challenges and Potential Opportunities*, Environmental Scientific Technology, No. 44, 5679–5684

KRZYSIEK J., 2012, *Is Polish Shale Gas posing challenge to players and researchers?*, Workshop Abstract Proceedings, Interfacial Phenomena in Theory and Practice, VII Summer School (Sudomie June 24th- 30th 2012)

KUBALA G., MACKAY B.A., 2010, *Use of carbon-dioxide-based fracturing fluids*, US Patent No. 7726404

LAL M., 1999, *Shale Stability: Drilling Fluid Interaction and Shale Strength*, SPE Paper 54356, SPE Latin American and Caribbean Petroleum Engineering Conference (Caracas, Venezuela 21st - 23rd April 1999)

LILLIES A. T., KING S.R., 1982, *Sand Fracturing With Liquid Carbon*, Publisher Society of Petroleum, DOI 10.2118/11341

LOKHANDWALA K.A., JARIWALA A., 2005, *Natural gas treatment process for stimulated well*, US Patent No. 7537641

LUK S. W. M., GRISDALE J. L., 1996, *High proppant concentration/high CO_2 ratio fracturing system*, US Patent No. 5515920

MADER D. et al., 1989, *Hydraulic proppant fracturing and gravel packing*, Elseviewer Science Publishers B. V., Vol. 26, 0-444-41625-0 (series)

MACK D. J., 1991, *Fracturing process using carbon dioxide and nitrogen*, US Patent No. 5069283

MARTIN P., DACY J., 2004, *Effective Qv by NMR core tests*, SPWLA 45th Annual Logging Symposium (June 6th - 9th 2004)

MZIK J., 1989, *Fracturing process for low permeability reservoirs employing a compatible hydrocarbon-liquid carbon dioxide mixture*, US Patent No. 4825952

PAGE J. C., MISKIMINS J.L., 2009, *A Comparison of Hydraulic and Propellant Fracture Propagation in a Shale Gas Reservoir*, Journal of Canadian Petroleum Technology, Vol. 48 No. 5, pp. 26 - 30

PAP, 2013, *Eksperci: PGNiG ma problemyze szczelinowaniem w poszukiwaniu gazu*, [Online] <http://www.biznes.pl>Recovered: June 15th 2013

REIDENBACH V. G., HARRIS P. C., LEE Y. N., LORD D. L., 1986, *Rheological Study of Foam Fracturing Fluids Using Nitrogen and Carbon Dioxide*, SPE, DOI 10.2118/12026-PA

ROGALA A., KRZYSIEK J., BERNACIAK M., HUPKA J., 2013. *Non-aqueous fracturing technologies for shale gas recovery*, Physicochemical Problems of Mineral Processing, Vol. 49, No. 1, 313–322

TUDOR R., 1999, *Nitrogen/carbon dioxide combination fracture treatment*, US Patent No. 5883053

UNITED NATIONS FRAMEWORK CONVENTION ON CLIMATE CHANGE (UNFCCC), *Doha Climate Gateway CMP8 Decisions* (Doha 2012)

UNITED NATIONS FRAMEWORK CONVENTION ON CLIMATE CHANGE (UNFCCC), *The Kyoto Protocol*(Kyoto 1997)

United States Environmental Protection Agency (USEPA), 2011, *Plan to Study the Potential Impacts of Hydraulic Fracturing on Drinking Water Resources*

Wright T.R., 1998, *Frac technique minimizes formation damages Dry Frac*, [Online] <http://findarticles.com/p/articles/mi_m3159/is_n1_v219/ai_20387355/>Recovered: June 20th 2013

WAT (Wojskowa Akademia Techniczna), 2012, *Sposób sprzężonego wydobycia węglowodorów gazowych i magazynowania CO_2 z poziomych odwiertów małośrednicowych wykonanych w pojedynczym odwiercie pionowym*, Patent Office of Poland, patent application No. P.398228

EVALUATION OF PYRITIC TAILINGS FROM A COPPER CONCENTRATION PLANT FOR CALCAREOUS SODIC SOIL RECLAMATION

Gulsen TOZSIN[*], Ali Ihsan AROL[**], Gokhan CAYCI[***]

[*] Department of Mining Engineering, Ataturk University, 25400, Erzurum, Turkey; gulsentozsin@gmail.com
[**] Department of Mining Engineering, Middle East Technical University,06800,Ankara,Turkey
[***]Department of Soil Science and Plant Nutrition, Ankara University, 06110, Ankara, Turkey

Abstract: This study was aimed to investigate the feasibility to use waste pyrite and sulphuric acid produced from waste pyrite for the reclamation of calcareous sodic soils. The final aim is to displace Na from an exchange complex and replace it with Ca, leading to a decrease in pH and exchangeable sodium percentage (ESP) and an improvement of soil structure. A fertility of the soil may also be enhanced by this technique since waste pyrite can be rich in several micronutrients. An additional advantage to this strategy is that waste pyrite is inexpensive and readily available in large quantities, by contrast to gypsum. In this study, column-leaching tests were carried out to evaluate a change in soil properties upon addition of gypsum and pyritic tailing amendments from a copper concentration plant. An availability of essential micronutrients for a plant growth (Fe, Cu, Zn and Mn) and hazardous potential of pyritic tailings in terms of heavy metal contamination were taken into account. Gypsum, powder waste pyrite and sulfuric acid produced from waste pyrite were applied to the soil with reference to the gypsum requirement (GR) of the soils. The results showed that application of waste pyrite with a dose of 44.74 megagrams per ha was superior to gypsum of 55.20 Mg/ha dose in terms of exchangeable sodium percentage (ESP) in 42 weeks. In addition, application of all the concentrations of sulfuric acid produced from waste pyrite also decreased the ESP values. The best values with sulfuric acid were obtained with a dose of 35.31 Mg/ha in 26 weeks. It was observed that the content of all micronutrients in the soil increased significantly (P<0.01) with waste pyrite and sulfuric acid applications. The levels of the micronutrients after treatments can be classified sufficient for the plant growth except for the iron level with the minimum dose of sulfuric acid application 17 Mg/ha. The heavy metal content in the soil after treatment with the pyritic tailings was found to be lower than the legal limit values. Thus, waste pyrite can be effectively used since rapid amelioration of calcareous sodic soils is possible with no deleterious heavy metal contamination.

Keywords: waste pyrite, gypsum, pyrite oxidation, column leaching test, sodic soil, reclamation

Introduction

The problem of soil sodicity (alkalisation) is extensively spread in many countries in the world. This is more vital for developing countries where a sodicity hinders agricultural production or even makes it impossible (Qadir et al., 2006; Brinck and Frost, 2009). Sodic soils contain sufficient exchangeable sodium to affect the plant growth adversely. According to the United States Salinity Laboratory these soils have an exchangeable sodium percentage ESP more than 15, pH of saturated soil paste (pHs) more than 8.5 and electrical conductivity of saturation extracts (ECe) less than 4 dS m^{-1} (Richards, 1954). Soil alkalisation frequently lead to deterioration and complete abandonment of agriculture and hence to a great economic damage.

Gypsum has been known to be an amelioration agent for sodic soil for more than 100 years; however, it has been used only rarely because of the high cost involved in the exploitation, transportation and crushing (Wang et al., 2008). Tailings from sulfide mines, on the other hand, usually contain large amount of pyrite (FeS$_2$) which is the main source of acid rock drainage and pollute the environment. Pyrite waste must be disposed off under strictly controlled conditions (Pulles et al., 1996; Jovanovic, 1998; Annandale et al., 1999). It has a great potential for restroring the productivity of calcareous sodic lands and improving the fertility of the soil. Oxidation of pyrite leads to the production of sulfuric acid, which reacts with native CaCO$_3$ to produce soluble Ca to replace adsorbed Na from the exchange complex of sodic soil and brings down to pH and ESP (Tiwari et al., 1988; Qadir et al., 1996; Qadir and Oster, 2004). The exchange of Ca with Na in the soil exchange complex results in flocculation of soil particles and the restoration of porous structure and high permeability of soil (Chun et al., 2001).

Pyrite can be also used as a source of micronutrients needed for a plant growth, particularly Fe, Cu, Zn and Mn. Therefore, it can be used as a fertilizer in calcareous sodic soils where these elements are deficient.

A comparison of gypsum vs. pyrite and sulfuric acid in reclamation of sodic soils indicated good possibilities of utilizing pyrite and sulfuric acid for sodic soil amelioration (Somani, 1994; Castelo Branco et al., 1999; Mace et al., 1999). This study was planned to compare the effectiveness of gypsum, waste pyrite from a copper concentration plant and suphuric acid produced from waste pyrite in reclaiming sodic soils. For this purpose, Na and sodium adsorption ratio (SAR) of the leachates, pH, ESP and heavy metal content of soils as well as essential micronutrient content of soil for the plant growth were investigated.

Materials and methods

Materials

The surface soil (0–15 cm) from Saraykoy, Ankara, Turkey was used in this study. The soil samples were air-dried, blended and ground to pass through a 2 mm sieve in a

laboratory. Relevant properties of the as-received soil are presented in Table 1. This soil is classified as non-saline (EC = 2.85 dS m^{-1}), sodic (ESP = 83.33) (Richards, 1954), moderately calcareous (CaCO$_3$ = 9.18%) with low organic matter content (0.71%) (Ulgen and Yurtsever, 1974). The level of available micronutrients determined by a DTPA method was 1.75 mg kg^{-1} Fe, 0.29 mg kg^{-1} Cu, 0.07 mg kg^{-1} Zn and 3.53 mg kg^{-1} Mn. These levels of Fe, Zn and Mn are classified as marginal for the plant growth (Follet and Lindsay, 1970; Lindsay and Norwell, 1978; FAO, 1990). The heavy metal content of the soil is lower than the limit values set by Turkish Soil Contamination Regulation (2001) (Table 2).

Table 1. Relevant properties of calcareous sodic soil before the experiment

EC (dS m^{-1})	pH	Bulk density (g cm^{-3})	CEC (mmol$_c$ 100g^{-1})	CaCO$_3$ (%)	Organic matter (%)	Boron (mg kg^{-1})
2.85	9.27	1.22	38.52	9.18	0.71	8.87

ESP (%)	DTPA-extractable (mg kg^{-1})			
	Fe	Cu	Zn	Mn
83.33	1.75	0.29	0.07	3.53

Table 2. Heavy metal content of calcareous sodic soil

Element	Concentration (mg kg^{-1} soil)	Limit values[*] (mg kg^{-1} soil)
Cr	24.59	100
Co	3.20	20
Ni	20.78	75
Cu	14.40	140
Zn	61.32	300
Pb	20.89	300
Mo	2.19	10
Cd	0.12	3
Fe (%)	4.08	–

[*]according to Turkish Soil Contamination Regulation (2001)

Waste pyrite used as an amendment was taken from the tailings stream of Kure Copper Concentration Plant, Turkey. A sulfur content of pyrite was found to be 44% using the methods outlined in Turkish Standards Institution (1987). A heavy metal content of waste pyrite is given in Table 3.

Table 3. Heavy metal content of waste pyrite

Element	Cr	Co	Ni	Cu	Zn	Pb	Mo	Cd	Fe (%)
Concentration (mg kg^{-1} pyrite)	21.22	824	61.73	6886	781.25	202.54	<2.40	<0.54	40.70

The oxidation experiment of waste pyrite was performed by aerating a suspension of 400 g of waste pyrite in 15 dm^3 of water placed in a 25 dm^3 polypropylene container for 25 days at room temperature (22–24 °C). The suspension was stirred by injecting the air through a polyethylene container. Ferric iron (Fe^{3+}) from oxidation of pyrite precipitates as a solid ferric hydroxide and forms sulfuric acid from four H^+ generated for each iron atom initially present as pyrite (1) (Somani, 1994):

$$FeS_2 + 15/4 O_2 + 7/2\ H_2O \rightarrow Fe\ (OH)_3 + 2H_2SO_4. \tag{1}$$

The sulfate concentration of sulfuric acid produced from waste pyrites is 10.02 g/dm^3 (Richards, 1954). The heavy metal content of sulfuric acid produced from waste pyrites is given in Table 4.

Table 4. Metal content of sulfuric acid produced from waste pyrite

Element	Cr	Co	Ni	Cu	Zn	Pb	Mo	Cd	Fe
Sulfuric acid solution (mg/dm^3)	0.55	9.10	0.95	81	35.70	0.86	<0.008	<0.003	2286

Pure powder gypsum ($CaSO_4 \cdot 2H_2O$) (Merck, 102161) was used as an amendment for the comparison of the effectiveness of waste pyrite.

Methods

Column leaching tests were carried out to estimate amount of leaching needed for the removal of excess soluble salts, to determine the response of soils to the addition of gypsum, waste pyrite and sulfuric acid, and to find the changes in the soil properties such as pH and ESP after leaching.

The leaching study was conducted with packed sodic soil columns treated gypsum, waste pyrite and sulfuric acid produced from waste pyrite. Polyvinyl chloride (PVC) columns with a diameter of 10 cm and a length of 35 cm were hand packed with air-dried and homogenized sodic soils (<2 mm) to a depth of 20 cm (Fig. 1).

Fig. 1. Photos of the column test set-up

The experimental layout was a randomized design with four doses of pyrite and sulfuric acid and one dose of gypsum with four replicates per dose. Gypsum, waste pyrite and sulfuric acid were applied to the soil on the basis of gypsum requirement (GR) of the soils (FAO, 1988). The minimum dose of pyrite addition level, 23.74 Mg/ha)(megagrams per hectare) (Pyrite 1 = GR) was calculated on the basis of gypsum requirement (GR), 55.2 Mg/ha, to reduce ESP to 15%. Randomly selected higher levels of pyrite addition, namely 31.96 Mg/ha (Pyrite 2), 39.63 Mg/ha (Pyrite 3) and 44.74 Mg/ha (Pyrite 4) (Table 5) were also applied to make up for the possible incomplete pyrite oxidation. In the application of sulfuric acid produced from waste pyrite, 31.46 Mg/ha of H_2SO_4 was assumed to be equivalent to 55.20 Mg/ha of gypsum (FAO, 1988). In this study, 17 Mg/ha (H_2SO_4–1), 19.62 Mg/ha (H_2SO_4–2), 23.54 Mg/ha (H_2SO_4–3), 26.15 Mg/ha (H_2SO_4–4) and 35.31 Mg/ha (H_2SO_4–5) of H_2SO_4 (Table 5) were tested to determine the effectiveness of sulfuric acid in reclamation of the calcareous sodic soil.

Table 5. Soil amendments and application rates

Soil Amendment	Application rate (t/ha)	Soil Amendment	Application rate (Mg/ha)
Gypsum	55.20	$H_2SO_4^-1$	17.00
Pyrite 1 (=GR)*	23.74	$H_2SO_4^-2$	19.62
Pyrite 2	31.96	$H_2SO_4^-3$	23.54
Pyrite 3	39.63	$H_2SO_4^-4$	26.15
Pyrite 4	44.74	$H_2SO_4^-5$	35.31

* GR: gypsum requirement of the soil

Pyrites undergo rapid oxidation when they are surface applied on the moist soils. Therefore, pyrite of predetermined doses was evenly spread on the moist soil surface as thinly as possible. In order to facilitate the oxidation of pyrite and ensure the supply of sufficient oxygen, the soil surface with pyrite was moistened until soaked by water spraying every 24 hours for 5 weeks in a similar way to Tiwari and Sharma (1989). The gypsum amendment was incorporated into the soil before packing. Sulfuric acid was applied onto the soil surface after packing. After the amendment applications, the columns were leached by a ponding method with tap water (EC = 1.21 dS m^{-1}, SAR = 1.66) with a hydraulic head of 10 cm (785 cm^3 water) in the columns at the certain intervals. Leaching dissolved and carried the amendments downward and removed the soluble salts. The leachate were collected and analyzed for Na and SAR to determine the effectiveness of amendments.

Analysis

The samples were air-dried and ground to pass a 2 mm sieve. The soil pH was measured in the saturated soil paste and EC was measured in the saturation extract (Richards, 1954; Rhoades, 1982a). A dry bulk density of soil was analyzed according

to Tuzuner (1990). A cation exchange capacity (CEC) of the soil was determined by a Na acetate method (1M NaOAc at pH 8.2) (Rhoades, 1982b). A content of $CaCO_3$ was determined using a calcimeter (Nelson, 1982). Organic matter content was determined by a dichromate oxidation method (Nelson and Sommers, 1982). Boron was analyzed using a carmine solution (Richards, 1954). Soluble cations and anions, and exchangeable cations were determined using the methods described by Richards (1954). Fe, Cu, Zn and Mn were measured by an atomic absorption spectrophotometer after extraction using a DTPA solution (Lindsay and Norwell, 1978). The total trace elements in soils were determined by digestion with nitric acid using by an inductively coupled plasma mass spectrometry. ESP was calculated using the formula $(100 \cdot Na_x/CEC)$ (Na_x: exchangeable sodium (mmol 100 g^{-1})). SAR was determined using the formula $(Na/[(Ca+Mg)/2]^{1/2})$ (Na, Ca, Mg: soluble cations (mmol/dm^3)) (FAO, 1988). Statistical analyses were performed using MINITAB 15.1 software (Minitab Inc., 2007).

Results and discussion

Leachate properties

The leachate from the test columns were analyzed after full cycle (collection of 785 cm^3 leachate for each cycle) of the leaching tests. Na and SAR in the leachates of the soil were measured to evaluate the efficiency of the amendments.
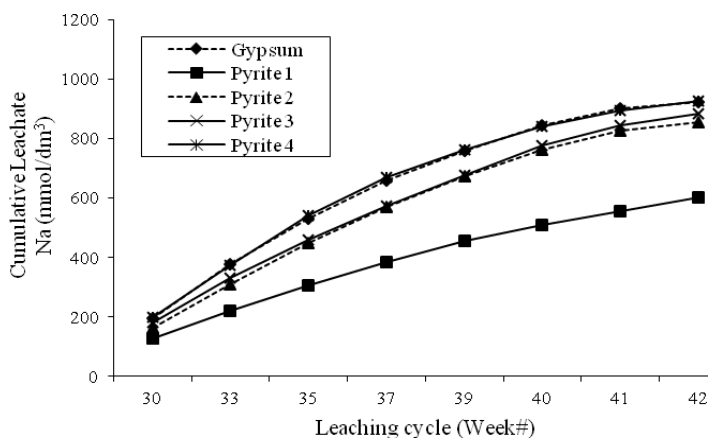
Fig. 2. Na in leachates from calcareous sodic soil columns treated with gypsum and waste pyrite

The solubility of salts enhanced removal of Na into the leachate of the calcareous sodic soil as a result of ion exchange. Exchangeable Na was replaced with Ca ions. Becoming soluble, it was removed from the soil during the leaching processes. For the soil treated with waste pyrite, the soil solution (leachate) was collected taking into account the SAR values of treated soils after 30, 33, 35, 37, 39, 40, 41 and 42 weeks

after start of irrigation. The concentration of Na leaching, 926.17 mmol/dm^3, was the highest with the Pyrite 4 dose followed by 921.33 mmol/dm^3 with the gypsum application on the last leachate (Fig. 2). This result indicates that it is necessary to use almost twice the amount of pyrite than that calculated to be equivalent to minimum gypsum level.

For the soil treated with sulfuric acid, the leachates were collected after 15, 17, 19, 21, 23, 24, 25 and 26 weeks after the start of irrigation. The highest concentraton of Na leaching, 1096.25 mmol/dm^3, was observed for the H_2SO_4-5 application (Fig. 3).
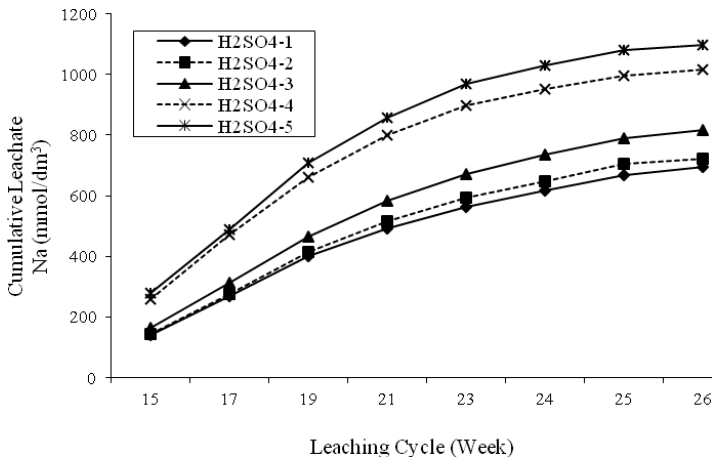
Fig. 3. Na in leachates from calcareous sodic soil columns treated with sulfuric acid
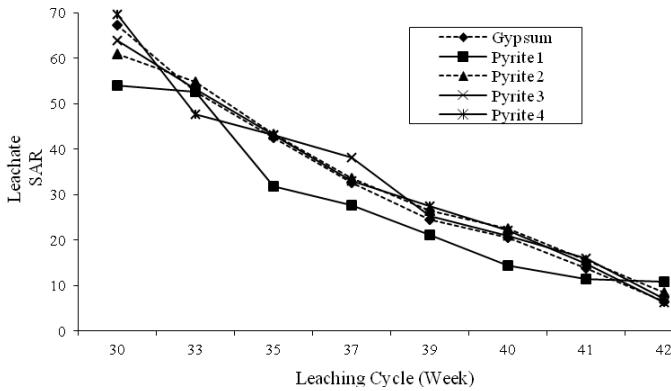
Fig. 4. SAR values in leachates from calcareous sodic soil columns
treated with gypsum and waste pyrite

SAR is the ratio of sodium (detrimental element) to the combination of calcium and magnesium (beneficial elements). In the other words, SAR is the measure of the sodicity of soil and shows the efficiency of leaching process on soil remediation. After

eight leaching cycles, SAR of all soils was lower than 12. This value separates the sodic soil from the non-sodic soils (Richards, 1954). For the soil treated with waste pyrite, SAR value 6.35, was the lowest with Pyrite 4 dose followed by 6.42 with the gypsum application on the last leachate (Fig. 4).

For the soil treated with sulfuric acid, the lowest SAR value 5.11 was observed for the H_2SO_4–5 application (Fig. 5).
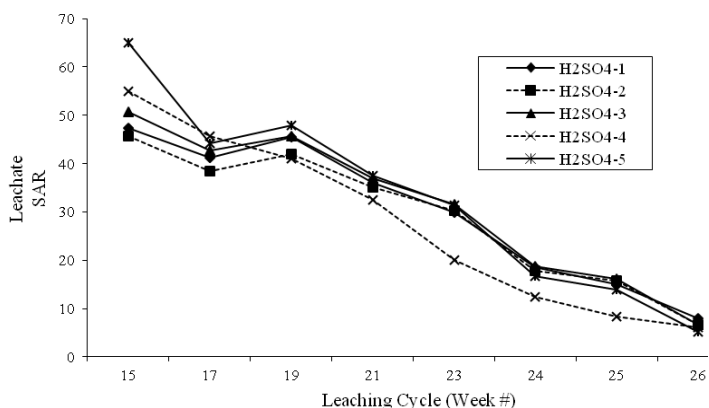
Fig. 5. SAR values in the leachates from calcareous sodic soil columns treated with sulfuric acid

Soil properties after leaching

The results indicated that gypsum for all application doses of waste pyrite and sulfuric acid produced from waste pyrite, had a significant effect on EC, ESP, $CaCO_3$, organic matter and boron content at the $P<0.01$ level in the soil treated with waste pyrite (Table 6) and had a significant effect on ESP, $CaCO_3$, organic matter at the $P<0.01$ level and boron at the $P<0.05$ level in the soil treated with sulfuric acid (Table 7).

Table 6. Physical and chemical properties of the soil before and after gypsum and waste pyrite treatment

Treatments	EC (**) (dS m^{-1})	pH (NS)	ESP (**)	CaCO$_3$ (**) (%)	O.M. (**) (%)	Boron (**) (mg kg^{-1})
Untreated Soil	2.85	9.27	83.33	9.18	0.71	8.87
Gypsum	2.05±0.02bc	7.78±0.07	12.26±0.04c	8.12±0.20a	0.76±0.03d	1.03±0.02c
Pyrite 1	2.27±0.02a	7.92±0.02	14.92±0.49a	7.59±0.07b	0.84±0.03d	1.63±0.03a
Pyrite 2	2.11±0.02b	7.87±0.08	14.63±0.15ab	7.14±0.05c	1.12±0.05c	1.30±0.01b
Pyrite 3	2.09±0.02bc	7.85±0.01	13.59±0.38b	6.27±0.05d	2.29±0.01b	1.26±0.08b
Pyrite 4	2.02±0.02c	7.77±0.05	11.77±0.22c	6.22±0.04d	2.65±0.04a	1.00±0.02c

Values represents means ± standard errors, same letter in each category were not different at $P < 0.01$(**) significant level
NS: not significant

Table 7. Physical and chemical properties of the soil before and after sulfuric acid treatment

Treatments	EC (NS) (dS m^{-1})	pH (NS)	ESP (**)	CaCO3 (**) (%)	O.M. (**) (%)	Boron (*) (mg kg^{-1})
Untreated Soil	2.85	9.27	83.33	9.18	0.71	8.87
H$_2$SO$_4$–1	2.06±0.01	7.51±0.08	14.34±0.33a	8.82±0.01a	1.11±0.01d	1.17±0.03a
H$_2$SO$_4$–2	2.05±0.01	7.46±0.09	13.65±0.33a	6.71±0.14b	1.12±0.01d	1.08±0.02ab
H$_2$SO$_4$–3	2.04±0.01	7.42±0.14	12.16±0.25b	6.00±0.14c	1.14±0.01c	1.06±0.03ab
H$_2$SO$_4$–4	2.04±0.01	7.34±0.04	9.39±0.03c	5.65±0.01c	1.30±0.01b	1.05±0.02ab
H$_2$SO$_4$–5	2.04±0.01	7.28±0.03	9.33±0.18c	5.65±0.14c	1.54±0.01a	1.00±0.03b

Values represents means ± standart errors, same letter in each category were not different at P < 0.05(*) and P < 0.01(**) significant levels. NS: not significant.

EC decreased in all the treated soil due to removal of salts by the leaching processes. The initial EC of untreated soil was 2.85 dS m^{-1}, which is well below the value of 4 dS m^{-1} separating the non-saline soils from the saline soils (Richards, 1954), and it was further reduced at the end of leaching (Table 6 and 7). The pH of untreated soil was 9.27 and higher than threshold value of 8.5 (Richards, 1954). Upon treatment the pH values of soil were reduced to 7.77–7.92 in the waste pyrite treated soil and 7.28–7.51 in the sulfuric acid treated soils.

All treatments had the ameliorative potential to lower the soil ESP below 15%. After leaching, ESP decreased from 83.33% down to 15% separating the sodic soils from the non-sodic soils (Richards, 1954). The maximum decrease of ESP was observed in Pyrite 4 dose (11.77%) and followed by gypsum (12.26%) applications in the waste pyrite treated soil (Table 6) and observed in H$_2$SO$_4$–5 (9.33%) and followed by H$_2$SO$_4$–4 (9.39%) applications in the sulfuric acid treated soil (Table 7).

Dissolution of CaCO$_3$ is clearly seen in the waste pyrite and sulfuric acid treated soils. The more the pyrite and sulfuric acid addition, the more CaCO$_3$ dissolution and therefore the less CaCO$_3$% in the soil was left. The organic content of soils increased after all applications. The soil organic matter content of less than 2% has a low infiltration and low productivity (Ulgen and Yurtsever, 1974). By adding increasing dose of waste pyrite and sulfuric acid, the organic matter content in the soil increased but only with Pyrite 3 (2.29%) and Pyrite 4 (2.65%) doses of waste pyrite applications the value reached above 2% (Table 6). Accumulation of boron in plants at toxic levels may result in plant injury or reduced growth and even death (FAO, 1988). The limit value of boron is 1.5 mg kg^{-1} in a saturated paste extract of soil for sensitive plants according to U.S. Salinity Laboratory (Richards, 1954). Boron decreased to well below 1.5 mg kg^{-1} with the all applications due to leaching except for the Pyrite 1 dose (1.63 mg kg^{-1}) application.

The heavy metal content of soils after treatment with gypsum, Pyrite 4 dose (maximum dose of waste pyrite) and H$_2$SO$_4$-5 (maximum dose of H$_2$SO$_4$) applications are given in Table 8. It was found that all values are within the tolerance limit of soil according to Turkish Soil Contamination Regulation (2001).

Table 8. Heavy metal content of calcareous sodic soil
before and after treated with Pyrite 4 dose and H_2SO_4–5

Element	Untreated soil (mg kg^{-1} soil)	Pyrite 4 treatment (mg kg^{-1} soil)	H_2SO_4–5 treatment (mg kg^{-1} soil)	Limit values* (mg kg^{-1} soil)
Cr	24.59	32.40	62.70	100
Co	3.20	16.08	15.70	20
Ni	20.78	33.40	42.50	75
Cu	14.40	128.90	105.50	140
Zn	61.32	94.67	177.36	300
Pb	20.89	35.24	28.28	300
Mo	2.19	3.54	3.11	10
Cd	0.12	0.58	0.45	3
Fe (%)	4.08	8.04	6.28	-

*according to Turkish Soil Contamination Regulation (2001)

Table 9. Essential micronutrient content of soil for plant growth before and after waste pyrite and sulfuric
acid treatment

	DTPA-extractable	Untreated soil	Pyrite 1	Pyrite 2	Pyrite 3	Pyrite 4	Sufficient level
Waste Pyrite Applications	Fe (mg kg^{-1})	1.75	8.55±0.09d	10.71±0.22c	14.86±0.40b	19.33±0.26a	> 4.5[1]
	Cu (mg kg^{-1})	0.29	1.45±0.07d	3.24±0.09c	6.68±0.11b	8.80±0.06a	> 0.2[2]
	Zn (mg kg^{-1})	0.07	1.70±0.04b	1.94±0.04ab	2.06±0.05a	2.08±0.12a	0.7 - 2.4[3]
	Mn (mg kg^{-1})	3.53	20.01±0.71cd	28.34±0.88b	22.16±0.80c	35.48±0.54a	14 – 50[3]

	DTPA-extractable	Untreated soil	H_2SO_4⁻1	H_2SO_4⁻2	H_2SO_4⁻3	H_2SO_4⁻4	H_2SO_4⁻5	Sufficient Level
Sulfuric acid Applications	Fe (mg kg^{-1})	1.75	3.61±0.09d	7.36±0.06c	7.25±0.10c	8.12±0.03b	11.07±0.20a	> 4.5[1]
	Cu (mg kg^{-1})	0.29	3.84±0.04e	8.19±0.06d	9.65±0.06b	9.21±0.04c	9.90±0.06a	> 0.2[2]
	Zn (mg kg^{-1})	0.07	1.14±0.04c	1.55±0.07b	1.97±0.04a	1.95±0.06a	2.10±0.30a	0.7 - 2.4[3]
	Mn (mg kg^{-1})	3.53	14.94±0.05d	17.35±0.27c	25.08±0.19b	25.42±0.87b	29.76±0.36a	14 – 50[3]

Values represents means ± standard errors, same letter in each category were not different at P < 0.01
significant level.
[1] Lindsay and Norvell, 1978, [2] Follet and Lindsay, 1970, [3] FAO, 1990.

The level of available micronutrients essential for the plant growth was determined
by the DTPA method. It was observed that all the micronutrient in the soil increased
significantly (P < 0.01) with waste pyrite and sulfuric acid applications (Table 9). The
levels of the micronutrients after treatments can be classified sufficient for plant the
growth except for the iron level with the minimum dose of sulfuric acid application,
H_2SO_4–1 (Follet and Lindsay, 1970; Lindsay and Norvell, 1978; FAO, 1990). The
micronutrient analysis was not done for gypsum tests because the gypsum material
was a purified chemically.

Conclusions

All amendments tested in this study were effective in calcareous sodic soil reclamation. The application of waste pyrite with a dose of 44.74 Mg/ha (Pyrite 4) was superior to the gypsum of 55.20 Mg/ha dose in terms of ESP in 42 weeks. ESP decreased from 83.33% to 11.77% with the application of waste pyrite of 44.74 Mg/ha dose and from 83.33% to 12.26% with the application of gypsum of 55.20 Mg/ha dose. In addition, the application of all concentrations of sulfuric acid produced from waste pyrite also decreased the ESP values. The best values with sulfuric acid were obtained with a dose of 35.31 Mg/ha in 26 weeks. The application of waste pyrite or sulfuric acid to the soil resulted in the increased availability of DTPA-extractable Fe, Cu, Zn and Mn which are essential for the plant growth. The pyrite does not appear to lead to pollution or toxic problems in the soil. Thus, the use of pyrite, by the product or waste from the copper concentration plants may be the useful amendment and effective fertilizer in the calcareous sodic soils.

Acknowledgements

References

ANNANDALE, J.D., JOVANOVIC, N.Z., BENADE, N., TANNER, P.D. (1999) *Modelling the long-term effect of irrigation with gysiferous water on soil and water resources*, Agriculture, Ecosystems & Environment, Vol. 76, 109–119.

BRINCK, E., FROST, C. (2009) *Evaluation of amendments used to prevent sodification of irrigated fields*, Applied Geochemistry, Vol. 24, 2113–2122.

CASTELO-BRANCO, M.A., SANTOS, J., MOREIRA, O., OLIVEIRA, A., PEREIRA, P.F., MAGALHAES, I., DIAS, S., FERNANDES, L.M., GAMA, J., VIEIRA E SILVA, J.M., RAMALHO, R.J. (1999) *Potential use of pyrite as an amendment for calcareous soil*, Journal of Geochemical Exploration, Vol. 66, 363–367.

CHUN, S., NISHIYAMA, M., MATSUMOTO, S. (2001) *Sodic soil reclaimed with by-product from flue gas desulfurization: corn production and soil quality*, Environmental Pollution, Vol. 114, 453–459.

FOLLETT, R.H., LINDSAY, W.L. (1970) *Profile distribution of zinc, iron, manganese and copper in Colorado soils*, Colorado Exper State Bull, No:110.

FOOD AND AGRİCULTURE ORGANİZATİON OF UNİTED NATİONS (FAO). (1988) *Salt-affected soils and their management*, Soil bulletin 39, Rome, Italy.

FOOD AND AGRICULTURE ORGANIZATION OF UNITED NATIONS (FAO). (1990) *Micronutrient assessment at the country level*, Soil bulletin 63, Rome, Italy.

JOVANOVIC, N.Z., BARNARD, R.O., RETHMAN, N.F.G., ANNANDALE, J.G. (1998) *Crops can be irrigated with lime-treated acid mine drainage*, Water SA, Vol. 24, 113–122.

LINDSAY, W.L., NORWELL, W.A. (1978) *Development of a DTPA soil test for zinc, iron, manganese and copper*, Soil Science Society of America Journal, Vol. 42, 421-428.

MACE, J.E., AMRHEIN, C., OSTER, J.D. (1999) *Comparison of gypsum and sulfuric acid for sodic soil reclamation*, Arid Soil Research and Rehabilitation, Vol. 13, 171–188.

MINITAB 15.1. (2007) *Minitab Inc State College*, Pennsylvania.

NELSON, D.W., SOMMERS, L.E. (1982) *Total carbon, organic carbon and organic matter,* In: MILLER, R.H., KEENEY, D.R. (Eds.), Methods of Soil Analysis, American Society of Agronomy, Madison, 539–549.

NELSON, R.E. (1982) *Carbonate and gypsum*. In: MILLER, R.H., KEENEY, D.R. (Eds.), Methods of Soil Analysis, American Society of Agronomy, Madison, 181-197.

PULLES, W., HEATH, R., HOWARD, M. (1996) *A Manual to assess and manage the impact of gold mining operations on the surface water environment (Pretoria, South Africa)*, Water Resources Commission, Report No. TT 79/96.

QADIR, M., QURESHI, R.H., AHMAD, N. (1996) *Reclamation of a saline-sodic soil by gypsum and Leptochloa fusca*, Geoderma, 74 (3-4), 207–217.

QADIR, M., OSTER, J.D. (2004) *Crop and irrigation management strategies for saline-sodic soils and waters aimed at environmentally sustainable agriculture*, Science of The Total Environment, Vol. 323, 1–19.

QADIR, M., NOBLE, A.D., SCHUBERT, S., THOMAS, R.J., ARSLAN, A. (2006) *Sodicity-induced land degradation and its sustainable management: problems and prospects*, Land Degradation and Development, Vol. 17, 661–676.

RHOADES, J.D. (1982a) *Soluble salts*, In: PAGE, A.L. (Ed.), Methods of Soil Analysis, Agronomy Monograph, Madison, 167–178.

RHOADES, J.D. (1982b) *Cation exchange capacity*, In: PAGE, A.L., MILLER, R.H., KEENEY, D.R. (Eds.), Methods of Soil Analysis. American Society of Agronomy, Madison, 149-157.

RICHARDS, L.A. (1954) *Diagnosis and improvement of saline and alkali soils*, Agricultural Handbook 60, Washington.

SOMANI, L.L. (1994) *Use of pyrites in agriculture for soil fertility and alkali amelioration*, Udaipur, Agrotech Publish.

TIWARI, K.N., KUMAR, A., CARTER, M.R., GUPTA, U.C. (1988) *Evaluation of sedimentary iron pyrites as an ameliorant for a saline-sodic soil in Uttar Pradesh, India*, Arid Soil Research and Rehabilitation, Vol. 3, 361–368.

TIWARI, K.N., SHARMA, D.N. (1989) *Soil salinity research, AICRP on management of salt affected soils*, C. S. Azad University of Agricultural and Technology, Kanpur.

TURKISH SOIL CONTAMINATION REGULATION. (2001) *Turkey Ministry of Environment and Forest*, Ankara, Turkey.

TURKISH STANDARDS INSTITUTION (TSI). (1987) *Copper and copper alloys, Determination of sulfur content-Combustion Titrimetric Method*, Ankara, Turkey.

TUZUNER, A. (1990) *Laboratory handbook of soil and water chemical methods*, Republic of Turkey Ministry of Agriculture, Forestry and Village Affairs, General Directorate of Rural Services, Ankara, Turkey.

ULGEN, N., YURTSEVER, N. (1974) *Fertilizer and fertilization guide of Turkey*, Soil and Fertilizier Research Institute, Publication No:28, Ankara, Turkey.

WANG, S.J., CHEN, C.H., XU, X.C., LI, Y.J. (2008) *Amelioration of alkali soil using flue gas desulfurization byproducts: Productivity and environmental quality*, Environmental Pollution, Vol. 151, 200–204.

PHYSICAL PURIFICATION OF DIATOMITE BASED ON LAMINAR-FLOW CENTRIFUGAL SEPARATION

Xiaoping YANG, Zhiming SUN, Shuilin ZHENG

School of Chemical and Environmental Engineering, China University of Mining and Technology (Beijing), Beijing 100083, China, yxp@cumtb.edu.cn, Tel.: +86-13718182908

Abstract. Natural diatomaceous earth or diatomite of good quality becomes rare and a demand for it increases every year. In this paper, we develop a novel method based on laminar-flow centrifugal separation to purify mid- and low-grade diatomite for industrial production purposes. Effects of the drum cone angle, drum speed, feeding concentration, feeding flow rate and feeding time on separation were investigated experimentally. The interdependency of these variables was studied using a response surface experiment. Operating conditions of a laminar-flow centrifugal separator were further optimized. Results showed that the feeding flow rate had a great influence on a silicon dioxide content of diatomaceous in concentrate and tailing. The optimal separation results were achieved as 87.5 wt.%, of SiO_2 content of diatomaceous in concentrate and 6.98 wt.% in tailing. The optimal operating conditions included the drum cone angle of 0.0087 rad, the drum speed of 89.62 rad/s, the feeding concentration of 24.66 wt.%, the feeding flow rate of 2.33×10^{-4} m^3/s, and the feeding time of 90 s. A scanning electron microscopy (SEM) clearly indicated that the pore blockage on the surface of diatoms was cleared out. The variation about the breakage rate of diatom shells was lower than 5% through the pilot purification production line. The characterization of original diatomite and derived products after purification were determined by X-ray diffraction (XRD). The results indicated that the impurity content of purified diatomite was improved significantly.

Keywords: diatomite, physical purification, laminar-flow centrifugal separation, response surface experiment

Introduction

Diatomaceous earth or diatomite is a powder and a non-metallic mineral. The main components are diatoms, which are very small (generally < 100 μm) algae. Many diatoms form colonies, which are deposited in the bottom sediments, along with clay, quartz and other minerals. Diatomite is formed over hundreds of millions of years of accumulation and the geological transition of the mixed minerals. Skeletal diatomite has special physical and chemical characteristics, namely a large specific surface area

and high adsorption capacity. A microscopy analysis reveals the presence of numerous fine microscopic pores, cavities and channels (Martinovic et al., 2006; Ibrahim and Selim, 2011, 2012). The unique cell-wall structure of diatom means that diatomite is widely used in the fields of chemical engineering, environmental engineering, constructional material, agriculture and industrial filtration (Zheng, 2009; Koyuncu, 2012). The demand for this nonrenewable resource increases annually with a rapid industrial development. Though diatomite resources in China are rich, natural and high grade diatomite mines are becoming exhausted. Applications for mid- and low-grade diatomite are limited because of the impurities in the mineral. Beneficiation of diatomite is necessary to enrich the diatomaceous shell and eliminate the clay, quartz, metal oxide minerals and organic matter from a run-of-mine. However, the special microscopic structure of diatom makes it difficult to purify diatomite.

There are many methods to purify diatomite, which include dry classification, wet gravity preparation, acid leaching, magnetic separation, hot flotation and calcinations. The complexity of the flow sheet and effects of purification depend on the planned application of diatomite. Dry classification involves drying a crude ore, crushing it and then putting it through several stages of cyclone classification (Zheng, 1994). An overflow of the cyclone is tailings and an underflow is diatom and a coarse sand. Further classification produces a diatomite concentrate with different quality. Wet gravity preparation involves completely dispersing diatoms and the impurities after scrubbing the mixture of diatomite and water, and subsequent stratifying the diatomaceous slurry by natural gravity settling in a slot-type pool (Zheng, 1994; Wang and Wang, 1995; Zheng et al., 1997; Meng, 1999; Shi et al., 2001; Martinovic et al., 2006; Mohamed, 2009). The coarser material that settles quickly is the diatomite concentrate and the suspended particles in the slurry are clay minerals. Acid leaching involves mixing and agitating a hydrofluoric and sulfuric acid solution with the diatomaceous raw earth (or concentrate processed by wet gravity preparation) (Wang, 1980; Yang and Zhang, 1991; Wang et al., 1995; Li et al., 1997; Qiu et al., 2001; Franca et al., 2003; Gu, 2003; Wang et al., 2006; Zheng et al., 2006; Osman et al., 2009). The impurities such as aluminum oxide (Al_2O_3), ferric oxide (Fe_2O_3), calcium oxide (CaO) and magnesium oxide (MgO) became soluble sulfate. The remaining insoluble component is siliceous diatomite. A high-grade diatomite concentrate is obtained through filtration, washing and drying the insoluble component. The disadvantages of acid leaching are high cost and the production of large quantities of waste acid. Diatomite with high iron content can be purified by magnetic separation (Videnov et al., 1993; Ma et al., 2012). A hot flotation method introduces steam into the scrubbed diatomite slurry with a concentration of 17–18 wt.%, while maintaining the slurry temperature between ~333–343 K (Shi and Zhang, 1993). The diatomite remains and impurities are stratified under these conditions. Diatomite is calcined at ~873–1073 K to vaporize the organics from the raw earth (Wang et al., 2006). Integral flow sheets, which are a combination of the methods mentioned above, are applied to

further purification of diatomite (Shi and Zhang, 1993; Ding et al., 1995; Cui et al., 1996; Yuan, 2001; Gu et al., 2003; Wang et al., 2006; Zheng et al., 2006).

Among methods mentioned above, wet gravity preparation is the simplest, most environmentally friendly and most effective. However, at present the industrial application of this method relies on natural gravity settling in slot-type pools to separate diatoms and impurities, which has associated problems of low efficiency and productivity, high labor intensity and unstable product quality. To overcome these problems, we submit the method of laminar-flow centrifugal separation to process mid- and low-grade diatomite. Based upon the differences in particle size and hardness between diatoms and impurities, the run-of-mine is scrubbed by adding water and a dispersant agent at set proportions to increase the dispersion difference between diatoms and the minerals (e.g., montmorillonite) in the water, and to stratify the constituents of diatomite. A screening process is implemented to separate the coarse quartz, feldspar and metal oxide minerals. The undersize slurry enters the laminar-flow centrifugal separator to separate the diatom shells from impurities. The sedimentary deposit is the diatomite concentrate, whereas the overflow (i.e. fine-grade component) is the clay minerals (Zheng, 1994; Zheng et al., 1997). Laminar-flow centrifugal separation is promising as an improved method to purify diatomite since a centrifugal acceleration is hundreds of times greater than a gravity acceleration. In this paper, we study the influence of process and structure parameters of the laminar-flow centrifugal separator on the characteristics of the purified diatomite concentrate. Our goal is to determine the optimal operating condition and operational mode of the separator.

Materials and methods

Materials

The run-of-mine was obtained from the disused diatomite mine in Liudaogou, Linjiang City, China. Table 1 lists the main chemical composition of diatomite. The silicon dioxide (SiO_2) content in the run-of-mine is 80.17 wt.%. It is the typical clayey second-grade diatomite. A diatom morphology was examined with a SEM S-3500N scanning electronic microscope (SEM), as shown in Fig. 1. The diatom types present according to the surface shape as shown in Fig. 1 are mainly disc diatoms, as well as a small number of cymbiform diatoms, straight chain diatoms, and debris from striated diatoms. The shape of diatom is not perfect, with small and broken diatom shells attached on the surface. Complete diatom frustules (cell walls) measure ~20–50 μm in diameter.

Experiment diagram

Figure 2 shows a pilot-scale experimental technical flow sheet of the laminar-flow centrifugal separation. In Figure 2, number 1 indicates a separator specially designed

for purifying the diatomaceous earth. The drum end with a short diameter is connected with the base plate, which is fixed on the main axis. The feeding pipe extends into the drum. The separated products discharge from the large end of the drum, with a diameter of 0.8 m. The inclined length of drum's inner wall is 0.6 m. The maximum speed of the drum is 157 rad/s. The actual speed can be changed on-line. The maximum separation factor is 1000, which is computed by dividing the centrifugal acceleration by the gravity acceleration. The panel in the slurry current direction changing box (6 or 7) is driven by an electromagnet operated by the controller, to fulfill the conversion of the slurry flowing direction.

Table 1. Chemical composition of raw diatomite from Liudaogou, Linjiang City, China

Components	SiO_2	Al_2O_3	Fe_2O_3	TiO_2	CaO	MgO	K_2O	Na_2O	Loss-on-ignition
Content (wt.%)	80.17	5.72	2.48	0.31	0.35	0.64	0.96	0.39	8.31
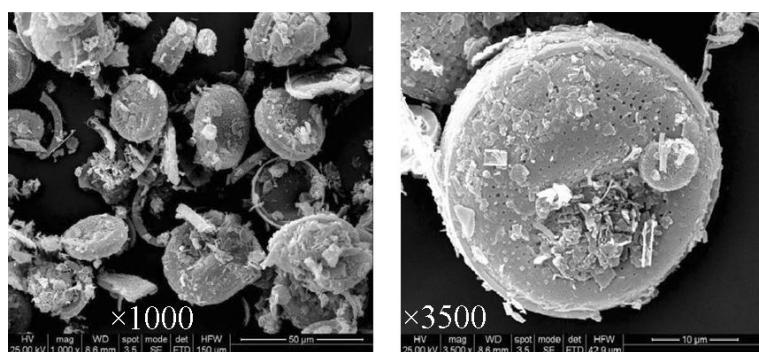
Fig. 1. SEM of the raw diatomite
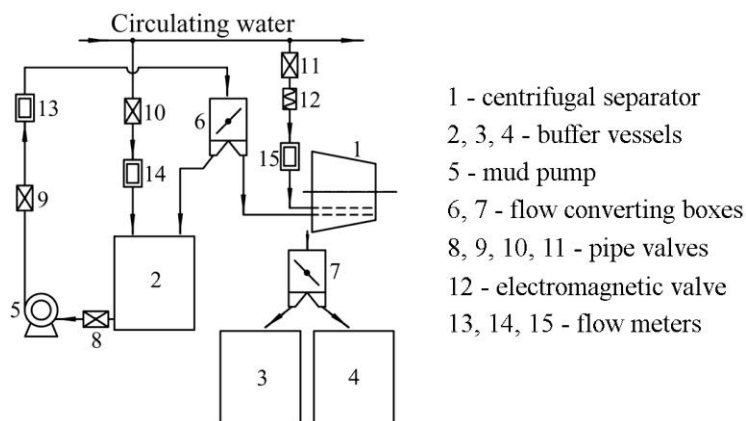
Fig. 2. Pilot-scale experiment flow sheet

1 - centrifugal separator
2, 3, 4 - buffer vessels
5 - mud pump
6, 7 - flow converting boxes
8, 9, 10, 11 - pipe valves
12 - electromagnetic valve
13, 14, 15 - flow meters

The working mode of the laminar-flow centrifugal separator includes four stages: feeding, interval, washing and resting. The raw slurry in the buffer vessel 2 in Fig. 2 is carried by the mud pump 5 to the slurry current direction changing box 6. The panel is set at the zero position, so the slurry flows back to the buffer vessel 2. The feeding stage starts after the drum speed reaches the target speed, at which time the panel changes to the opposite position. Now, the slurry flows into the laminar-flow centrifugal separator. The diatomaceous concentrate deposits on the inner wall of the drum because of the centrifugal force. The tailings flow out of the separator and enter the tailings buffer vessel 4 through the slurry current direction changing box 7. After time t_1 the process reaches the interval stage and the panel in the slurry current direction changing box 6 is reset to the zero position. This stage lasts time t_2 to ensure the slurry in the feeding pipe flows into the separator and the tailings in the separator flow into tailings buffer vessel 4. Now, the washing stage occurs. The panel in the slurry current changing box 7 moves to the opposite position. The electromagnet 12 turns on to open the circulating water. The diatomaceous concentrate on the inner wall of the drum is washed off, and enters into concentrate buffer vessel 3. The electromagnet 12 for washing water is turned off after time t_3. After waiting for time t_4, the panel in the slurry current changing box 7 is reset to the zero position. Then, the next separation cycle commences.

Content analysis

A multi-element express analyzer DHF82 was used to analyze the chemical composition, mainly SiO_2, Fe_2O_3 and Al_2O_3 contents of raw diatomite and purified concentrates. The crystalline phase identification of samples was undertaken by a PANalytical X'Pert PRO X-ray diffractometer employing CuKα radiation at a goniometer rate of $2\theta= 4°/min$. It is common to choose SiO_2 content as the criterion to evaluate the quality grade of diatomite. The content of SiO_2 for the first class diatomite is over 85 wt.%. High-grade diatomite contains a minimum of SiO_2 content about 95 wt.%. The change in the surface morphology for the separated diatomite in contrast with the raw ore was observed by SEM. The breakage rate of the diatom shell through physical purification was quantified as the total diatom numbers 500 divided by the broken diatom numbers. Counts were performed with the JX-2000 image analyzer in the best observation field. The more complete the diatom shell construction, the more valuable diatomite for high-end and specialized field applications.

Results and discussion

Effects of drum speed and cone angel on purification

Figure 3 shows the changes in product concentration of the laminar-flow centrifugal separator with feeding time (75 s, 90 s) and cone angle (0.07 rad, 0.0087 rad) at a

fixed feeding concentration of 24 wt.%, feeding flow rate of $2 \cdot 10^{-4}$ m³/s, washing water pressure of $4 \cdot 10^{5}$ Pa, washing water flow rate of $5 \cdot 10^{-4}$ m³/s and washing time of 20 s. From Figure 3 it can be seen that when the cone angle is 0.07 rad, the diatomite concentration in tailing is > 8.5 wt.% (Fig. 3 a) and for the concentrate it is less than 4.0 wt.% (Fig. 3 b), which does not increase even with prolonged feeding time. However, when the cone angle is changed to 0.0087 rad, the concentrate concentration clearly increases at the same drum speed. It reaches 7.0 wt.% even at a lower drum speed of 83.73 rad/s (Fig. 3 b). The cone angle of drum determines the inner surface area, inclination length and particle movement route. This cone angle affects the axial force and acceleration of particles, as well as the moving speed of diatomite slurry in the radial and axial direction, and motion track. The larger the cone angle, the faster the slurry passes through. Therefore, at this cone angle some part of the slurry directly flows out of the drum without separation and moves into the tailings. This condition leads to a thinner deposit on the inner wall in the laminar-flow centrifugal separator. When the cone angle is 0.07 rad, the drum speed and the feeding time have less influence on the deposit thickness. This phenomenon was verified by examining the inner wall of the drum after the separator was stopped. Under the same working conditions, the concentrate recovery should be low and the separation effect should be worse if the concentration of diatomite concentrate is low. The most diatomaceous concentrate flowed with the overflow into the tailings. Therefore, the subsequent experiment was carried out under a cone angle of 0.0087 rad.
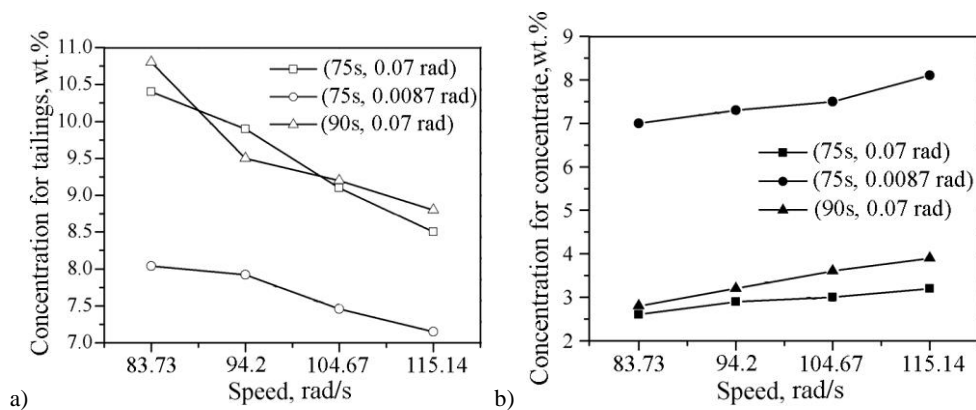
Fig. 3. Influence of cone angle and drum speed on laminar-flow centrifugal separation

Single factor experimentation

The experiments compare the separation effects of the laminar-flow centrifugal separator at different drum speeds. The tests were carried out with the cone angle at 0.0087 rad, raw slurry concentration at 24 wt.%, feeding flow rate at $2 \cdot 10^{-4}$ m³/s, feeding time at $t_1 = 75$ s, interval time at $t_2 = 6$ s, washing time at $t_3 = 22$ s, resting time at $t_4 = 6$ s, washing water pressure at $4 \cdot 10^{5}$ Pa, and washing water flow rate at

$5 \cdot 10^{-4}$ m³/s. The results are shown in Figs. 4(a) and 4(b). With the increase in drum speed, the SiO_2 content in the diatomaceous concentrate also increases, but the concentration in tailings decreases. It shows that the centrifugal force of the particle depends on the drum speed. The separation factor increases as the drum speed increases, which speeds up the settlement of the particles. However, the separating effects of the diatomaceous slurry are also influenced by particle size and particle density. The drum speed of 31.42–52.36 rad/s is enough to separate the fine metallic minerals. However, since the apparent density for diatomite is $0.58–0.65 \times 10^3$ kg/m³, far less than that of fine metallic minerals (Zheng, 2009), the separation of diatomite needs a higher drum speed in laminar-flow centrifugal separation.
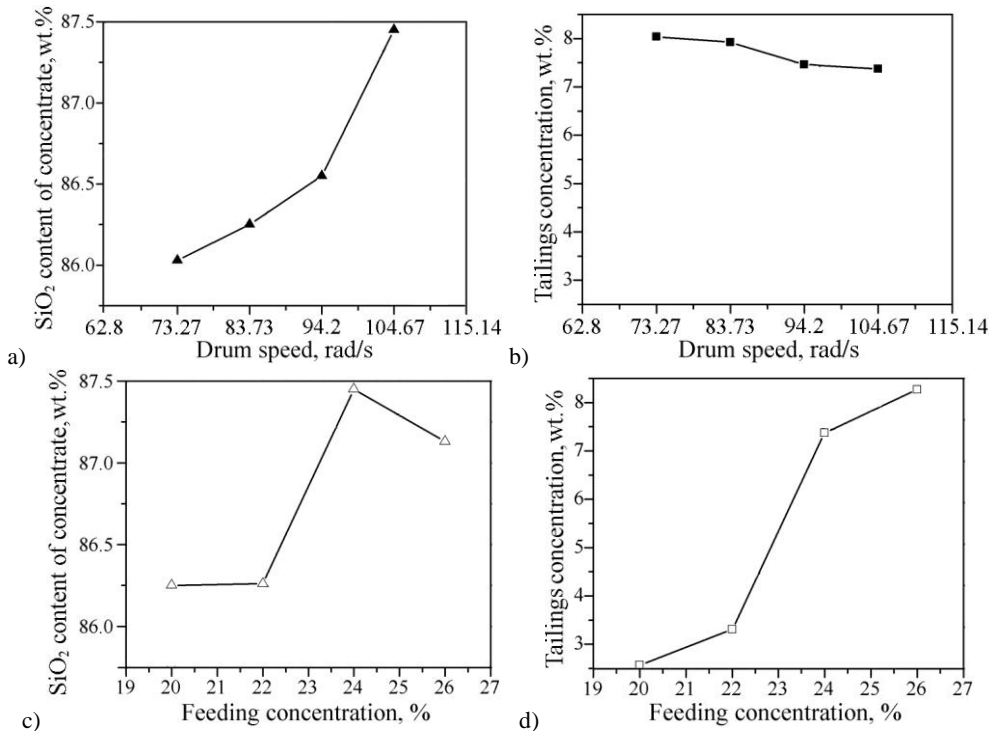
Fig. 4. Influence of drum speed and feeding concentration on laminar-flow centrifugal separation

In this paper we study the influence of different feeding concentrations on the separating effect based on the experimental conditions discussed above (Figs. 4 (c) and (d)). The results indicate that with the increase in the feeding concentration, the SiO_2 content of concentrate first increases and then decreases when the feeding concentration surpasses 24 wt.%. However, the tailings concentration increases with the feeding concentration. If the slurry concentration increases, the fluidity degrades and the viscosity increases. Further, stratification becomes slow. Therefore, the

processing capacity increased, but part of deposited concentrate flowed out, which led to a decrease in the SiO_2 content.

Figure 5 shows the relationship between SiO_2 content in concentrate and tailings concentration with different feeding times and feeding flow rates. If the feeding time is prolonged from 45 s to 60 s, the SiO_2 content of concentrate increases by 2.17 wt.% (Fig. 5 a). However, the increase is very small with further prolonging the feeding time. The tailings concentration also increases with the feeding time and then remains stable (Fig. 5 b). This result shows that it is helpful to purify diatomite by increasing the feeding time to a certain degree. Once the deposit thickness on the inner wall reaches a certain extent, the protracted feeding time only increases the processing capacity and does not improve the SiO_2 content in concentrate. In addition, the experiments show that the tailings concentration increases with the increase in feeding flow rate (Fig. 5 c). However the SiO_2 content in concentrate increases with the increase of the feeding flow rate, and then decreases after the feeding flow rate reaches $2 \cdot 10^{-4}$ m^3/s (Fig. 5 d). It shows that too high a feeding flow rate will lead to diatom loss under this separation condition.
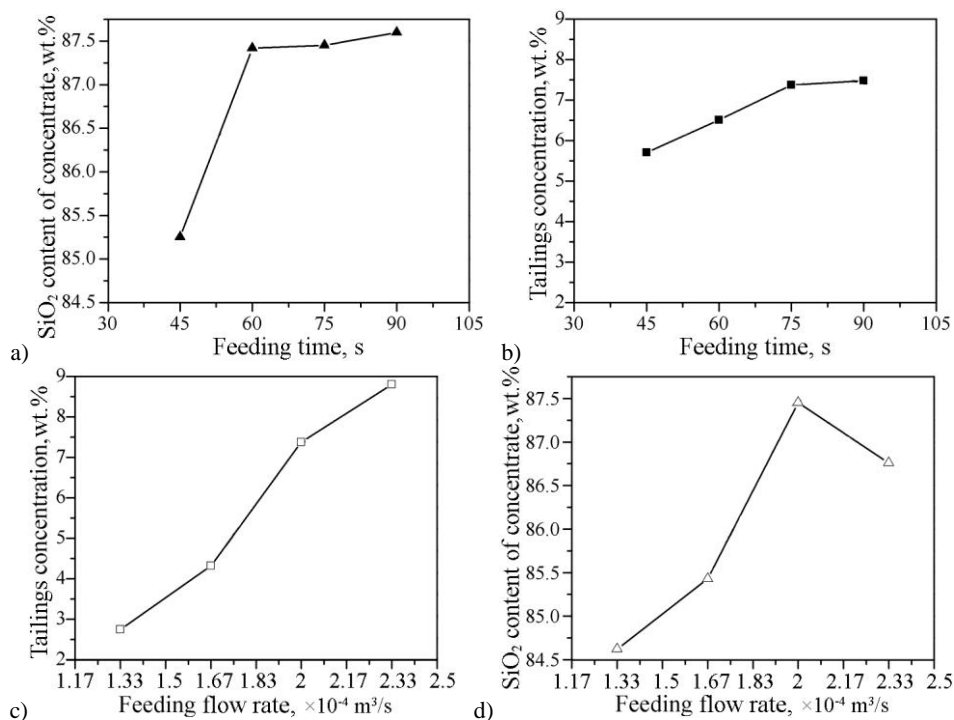
Fig. 5. Influence of feeding time and feeding flow rate on laminar-flow centrifugal separation

Response surface experiment

In order to search for the optimal separation condition of the laminar-flow centrifugal separator, a 4-factor × 3-level response surface experiment, including three central points, was designed to study the influence of drum speed, feeding concentration, feeding flow rate and feeding time on the separating effects based on the single factor experimentation. Table 2 lists the factor and level parameters while Table 3 presents the response surface design and results. The linear model analysis of the standard least squares fitting showed that the influential sequence of the technical parameters on the silicon dioxide content of concentrate from high to low was: feeding flow rate, feeding concentration, drum speed, and feeding time. The feeding flow rate had the most significant influence. The influential sequence for the tailings concentration from high to low was: feeding concentration, feeding flow rate, feeding time, and drum speed. From all these parameters, the feeding concentration and the feeding flow rate had the most significant influence. Therefore, the feeding flow rate had the strong influence on both the silicon dioxide content of concentrate and the tailings concentration.

Table 2. Factors and their levels

Levels	Feeding concentration (wt.%)	Drum speed (rad/s)	Flow rate ($\times 10^{-4}$ m^3/s)	Feeding time (s)
1	22	83.73	1.67	60
2	24	94.20	2.0	75
3	26	104.67	2.33	90
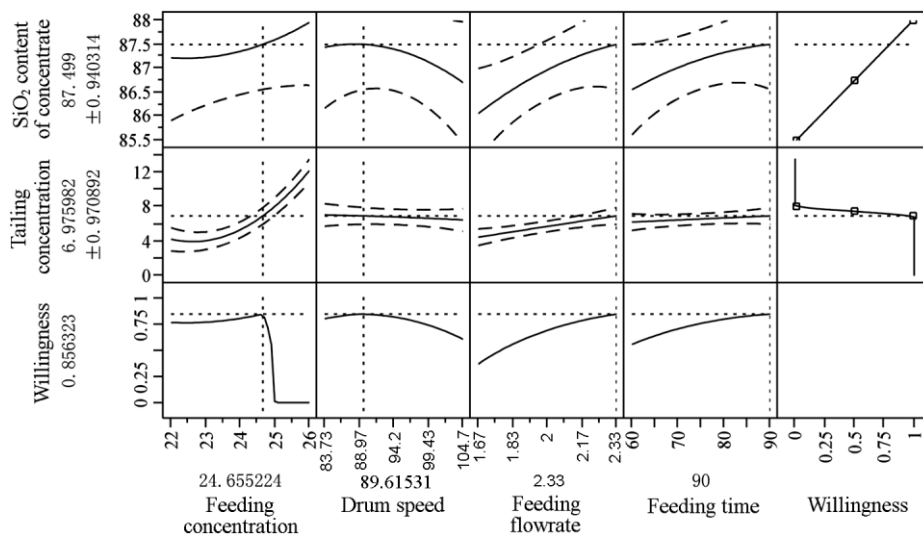
Fig. 6. Prediction profiler for optimal configuration

Table 3. Response surface design and results

No.	Feeding concentration (wt.%)	Drum speed (rad/s)	Flow rate ($\times 10^{-4}$ m³/s)	Feeding time (s)	SiO$_2$ content of concentrate (wt.%)	Tailings concentration (wt.%)
1	22	83.73	2.0	75	86.21	3.22
2	22	94.20	1.67	75	86.18	2.0
3	22	94.20	2.0	60	86.11	2.75
4	22	94.20	2.0	90	86.55	3.23
5	22	94.20	2.33	75	87.58	4.42
6	22	104.67	2.0	75	87.29	3.11
7	24	83.73	1.67	75	85.98	2.62
8	24	83.73	2.0	60	85.67	3.79
9	24	83.73	2.0	90	85.92	4.61
10	24	83.73	2.33	75	86.93	4.63
11	24	94.20	1.67	60	86.64	2.11
12	24	94.20	1.67	90	86.17	2.81
13	24	94.20	2.0	75	87.49	3.71
14	24	94.20	2.0	75	86.84	4.08
15	24	94.20	2.0	75	86.55	3.48
16	24	94.20	2.33	60	86.64	4.15
17	24	94.20	2.33	90	87.29	4.93
18	24	104.67	1.67	75	86.42	2.59
19	24	104.67	2.0	60	87.51	2.96
20	24	104.67	2.0	90	86.71	4.01
21	24	104.67	2.33	75	86.17	5.17
22	26	83.73	2.0	75	87.13	10.78
23	26	94.20	1.67	75	86.63	8.68
24	26	94.20	2.0	60	87.28	10.17
25	26	94.20	2.0	90	87.93	10.7
26	26	94.20	2.33	75	87.57	12.03
27	26	104.67	2.0	75	87.13	8.27
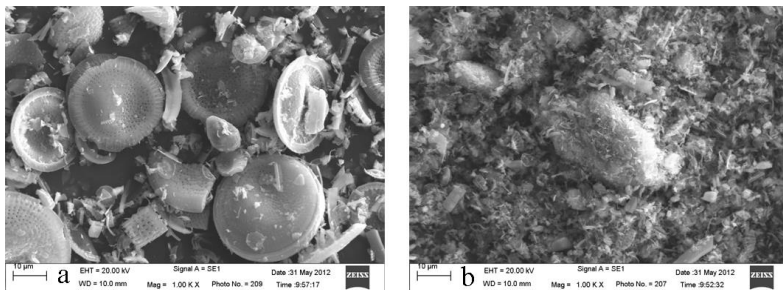
Fig. 7. SEM comparison of the diatomite purification (a: concentrate, b: tailings)

The experimental goal was to find the optimal separation condition to purify diatomite with the laminar-flow centrifugal separator. The requirement is that the SiO_2 content in concentrate is greater than 85 wt.% (the first-grade earth standard) and the tailings concentration is not too low. A low tailings concentration indicates that some clay minerals were deposited on the inner wall of the drum due to centrifugal force, and then entered into the diatomaceous concentrate resulting in decreasing the concentrate grade. Therefore, these two factors should be considered at the same time during the evaluation. The optimal parameter combination was obtained by the model prediction profiler according to the maximum willingness (Fig. 6), that is the feeding concentration 24.66 wt.%, drum speed 89.62 rad/s, feeding flow rate $2.33 \cdot 10^{-4}$ m^3/s, and feeding time 90 s. The predicted results were: SiO_2 content of 87.5 ± 0.94 wt.% and tailings concentration of 6.98 ± 0.97 wt.%.

A continuous running experiment was carried out based on the optimal combination above. The results were: SiO_2 content = 87.41 wt.%, Al_2O_3 content = 3.81 wt.%, Fe_2O_3 content = 1.64 wt.%, and tailings concentration = 6.14 wt.%. The SEM results from the diatomaceous concentrate and the tailings through beneficiating are shown in Fig. 7. The pore blockages in the diatom frustules are obviously improved by laminar-flow centrifugal separation.

The analysis with a graphic granulometer showed that the breakage rate for the diatomaceous raw mineral was 67.4%, for the feeding raw diatomite 69.4%, and for the separated diatomaceous concentrate 63.5%. The breakage rate of diatoms after being scrubbed increased by 1.9%, but it decreased by 5.8% after separation with the laminar-flow centrifugal separator. This probably was due to broken diatoms entering the overflow and becoming the tailings, because their diameter was close to that of clayey minerals. Therefore, it can be seen that the diatomaceous raw minerals themselves were fragmentary. The breakage rates had no prominent change after physical separation, but the breakage rate of the diatomaceous concentrate decreased when compared with raw diatomite. The destruction to the diatom frustule was very small by using the physical preparation method reported in this paper.

Mineralogical analysis

X-ray diffraction (XRD) is one of the most useful techniques to study the structural geometry and texture of impurities in diatomite. The XRD patterns of raw diatomite before purification and different products (oversized product, centrifugal overflow and centrifugal sediment) obtained after purification are given in Fig. 8. It shows an essentially amorphous phase, but a significant amount of crystalline phases is also found in raw diatomite. The XRD pattern shows the high content of amorphous SiO_2. The main impurities in the raw sample can be divided into two types. One type is clay minerals such as montmorillite, kaolin and muscovite, and the second type is crystalline silicious sands, such as quartz and feldspar. The main mineral composition of the oversized product is coarse feldspar and quartz, which agrees with our expectations. The typical XRD patterns of clay minerals such as montmorillite, kaolin

and muscovite appear in the centrifugal overflow, determined as the tailings. The purified powder sample exhibits less crystalline structure after purification. From Figure 8, it can be seen that a high-grade amphorous silica material with less crystalline structure is obtained after purification.
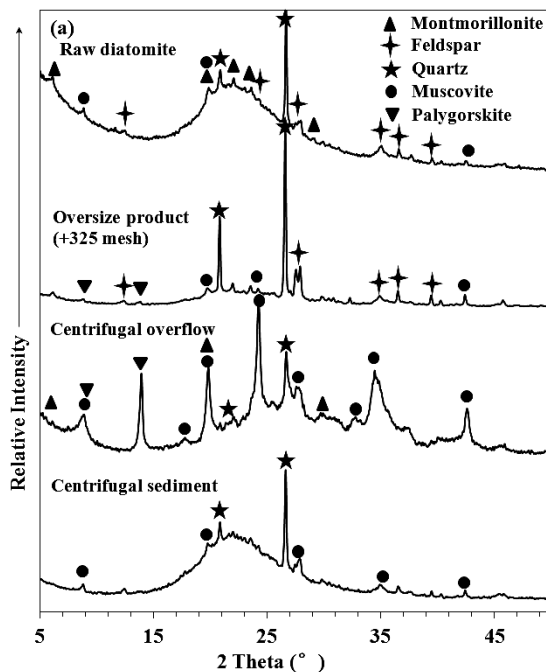
Fig. 8. XRD patterns of raw diatomite and different products obtained after purification

Conclusions

High grade diatomite can be successfully prepared from mid- and low-grade raw diatomite through physical purification by the laminar-flow centrifugal separator. The following salient conclusions related to centrifugal settling treatment and preparation of diatomite powders can be advanced.

A single factor experimentation shows that the SiO_2 content increases with increasing the drum speed, feeding concentration and feeding flow rate. However, SiO_2 content decreases when the feeding concentration exceeds 24 wt.% or the feeding flow rate is faster than $2 \cdot 10^{-4}$ m^3/s.

A response surface experiment indicates that the influential sequence of technical parameters on the SiO_2 content in concentrate is feeding flow rate > feeding concentration > drum speed > feeding time. The feeding flow rate has the most significant influence. The influential sequence for the tailings concentration is feeding concentration > feeding flow rate > feeding time > drum speed. From all these

parameters, the feeding concentration and the feeding flow rate have the most significant influence.

The optimal parameter combination for diatomite separation was obtained by the model prediction profiler according to maximum willingness. The optimal combination was the feeding concentration 24.66 wt.%, drum speed 89.62 rad/s, feeding flow rate $2.33 \cdot 10^{-4}$ m^3/s and feeding time 90 s. The predicted results were: SiO_2 content = 87.5 ± 0.94 wt.% and tailings concentration = 6.98 ± 0.97 wt.%.

The feasibility of this method was demonstrated by the pilot-scale continuous production, based on the optimal parameter combination above. The SiO_2 content in concentrate was 87.41 wt.%. The SEM analysis of the diatomaceous concentrate indicated that the pore blockages in the diatom shell were clearly improved by laminar-flow centrifugal separation. Graphic granulometry indicated that the breakage rate was not markedly changed using this method.

Acknowledgements

References

CUI, T. S., WU H. H., ZHOU Z. G., 1996, *Research on mineral processing technology of low grade diatomite of Shuangjiang in Yunnan*, Journal of Guilin institute of technology, 16(3), 313–316.

DING H., LIN H., CUI T. S., 1995, *Yunan Low grade diatomite purifying*, Multipurpose utilization of mineral resources, (4), 12–14.

FRANCA S. C. A, MILLQVIST M. T., LUZ A. B., 2003, *Beneficiation of Brazilian diatomite for the filtration application industry*, Minerals & Metallurgical Processing, 20 (1), 42–46.

GU J. C., 2003, *The study on the mechanism in purification of diatomite ore by microwave Strengthening* (Doctoral dissertation), Sichuan University, Chengdu, China.

GU J. C., LIU Y. C., ZHANG Y. X., 2003, *Research on purifying the diatomite*, Non-metallic Mines, 26(1), 46–47.

IBRAHIM S. S., SELIM A. Q., 2011, *Evaluation of Egyptian diatomite for filter aid applications*, Physicochemical Problems of Mineral Processing, 47, 113–122.

IBRAHIM S. S., SELIM A. Q., 2012, *Heat treatment of natural diatomite*, Physicochemical Problems of Mineral Processing, 48(2), 413−424.

KOYUNCU M., 2012, *Colour removal from aqueous solution of tar-chromium green 3g dye using natural diatomite*, Physicochemical Problems of Mineral Processing, 48(2), 485–494.

LI J., 1974, *Laminar-flow centrifugal separator*, Nonferrous Metals (Extractive Metallurgy), (2), 5–13.

LI Y., ZHENG S. L., XIA Q. L., DU Y. C., 1997, *Study of preparing fine pure active silica powder from diatomite*, Conservation and utilization of mineral resources, (6), 17–19.

MA S. Y., ZHOU Y. Y., LI X. J., 2012, *Technology research of magnetic separation on iron-removal of Jilin diatomite*, China Non-Metallic Minerals Industry, 96(3), 13–15.

MARTINOVIC S., VLAHOVIC M., BOLJANAC T., PAVLOVIC L., 2006, *Preparation of filter aids based on diatomite*, Internal Journal of Mineral Processing, 80, 255−260.

MENG X. Y., 1999, *Study on dressing of clayey diatomite*, Conservation and utilization of mineral resources, (1), 36–37.

MOHAMED I. A., 2009, *Characterization and process development of the Nile diatomaceous sediment*, Internal Journal of Mineral Processing, 92, 128–136.

OSMAN S., REMZI G., CEM O., 2009, *Purification of diatomite powder by acid leaching for use in fabrication of porous ceramics*, International Journal of Mineral Processing, 93, 6–10.

QIU D. Y., SHENG G. Y., WU X. H., 2001, China Patent No. 01129546, Beijing: State Intellectual Property Office of the P. R. C.

SHI D. M., ZHANG Z. H., 1993, *Experiment research on Yunan Xundian diatomite purifying*, Non-metallic Mines, 16(1), 7–10.

SHI X. Z., YU D. S., WANG F. X., 2001, China Patent No. 00112041, Beijing: State Intellectual Property Office of the P. R. C.

VIDENOV N., SHOUMKOV S., DIMITROV Z., 1993, *Beneficiation of diatomites by high gradient magnetic separation*, International Journal of Mineral Processing, 39(3–4), 291–298.

WANG L. J., ZHENG S. L., CHEN J. T., SHU F., 2006, *Study on purification & adsorption of diatomite*, Non-metallic Mines, 29(2), 3–5.

WANG X. M., 1980, *Experiment report on producing activated white clay from diatomite*, Zhejiang Chemical Industry, 4, 36–41.

WANG X. Q., WANG Q. H., 1995, China Patent No. 94108311, Beijing: State Intellectual Property Office of the P. R. C.

WANG Z. M., MA X. F., SUN W. T., WANG X. X., 1995, *Research on acid treatment to purify the diatomite and the waste acid utilization*, Non-metallic Mines, 18(1), 16–19.

YUAN P., 2001, *Study on purification of diatomite and its surface hydroxyl groups and acid sites* (Doctoral dissertation), Guangzhou Institute of Geochemistry, Chinese Academy of Sciences, Guangzhou, China.

YANG Y. K., ZHANG Y. N., 1991, China Patent No. 90100675, Beijing: State Intellectual Property Office of the P. R. C.

ZHENG S. L., 1994, *Purification research on clayey diatomite in China*, Non-metallic Mines, 17(4), 24–51.

ZHENG S. L., 2009, *Non-metallic mineral preparation and application* (2nd ed.), Beijing: Chemical Industry Press, 141–142.

ZHENG S. L., LI Y., DU Y. C., XIA Q. L., 1997, *Purification technology research on clayey diatomite for one mine in Jilin*, Non-metallic Mines, 20(4), 49–50.

ZHENG S. L., WANG L. J., SHU F., CHEN J. T., 2006, *Effect of calcining and sulfuric acid treatment on properties of diatomite*, Journal of the Chinese Ceramic Society, 34(11), 82–68.

APPLICATION OF MULTI-PARAMETER DATA VISUALIZATION BY MEANS OF AUTOASSOCIATIVE NEURAL NETWORKS TO EVALUATE CLASSIFICATION POSSIBILITIES OF VARIOUS COAL TYPES

Dariusz JAMROZ

AGH University of Science and Technology, Faculty of Electrical Engineering, Automatics, Computer Science and Biomedical Engineering, Department of Applied Computer Science, al. Mickiewicza 30, 30-059 Krakow, Poland, jamroz@agh.edu.pl

Abstract: The significance of data visualization in modern research is growing steadily. In mineral processing scientists have to face many problems with understanding data and finding essential variables from a large amount of data registered for material or process. Hence it is necessary to apply visualization of such data, especially when a set of data is multi-parameter and very complex. This paper puts forward a proposal to introduce the autoassociative neural networks for visualization of data concerning three various types of hard coal. Apart from theoretical discussion of the method, the empirical applications of the method are presented. The results revealed that it is a useful tool for a researcher facing a complicated set of data which allows for its proper classification. The optimal neural network parameters to successfully separate the analyzed three types of coal were found out for the analyzed example.

Introduction

Multidimensional statistical analysis can be divided into many types. Besides typical approximations or searching for a regressive equation with the use of numerous modern methods (Ahmed and Drzymala, 2005; Brozek and Surowiak, 2005; 2007; 2010; Drzymala, 2007; 2009; Gawenda et al., 2005; Niedoba, 2009; 2011; 2013b; Niedoba and Surowiak, 2012; Saramak, 2011; 2013; Snopkowski and Napieraj, 2012; Tumidajski, 1997; Tumidajski and Saramak, 2009), there are also many data-mining methods which are widely used. One of them includes visualization methods aimed at recognition of differences and similarities between analyzed sets of data. This is

frequently a very significant issue in mineral processing where processes are feature-dependent.

Owing to the methods of multidimensional data visualization through the transformation of multidimensional space into two-dimensional, it is possible to show multi-parameter data on the computer screen, thus making it possible to carry out a qualitative data analysis in the most natural way for a human being – by a sense of sight. One of the methods involves using autoassociative neural networks. This method was used in the paper to present and analyze a set of seven-parameter data describing samples of three various coal types: 31, 34.2 and 35 (according to Polish classification of coal types). It was decided to examine whether the amount of data is sufficient for the proper classification of coal types. The application of various methods to analyze recognition possibilities of various coal features is becoming an interesting issue. Recently, different visualization methods have been investigated such as observational tunnels method (Jamroz and Niedoba, 2014; Niedoba and Jamroz 2013). However, the application of autoassociative neural networks to evaluate the possibility of proper identification of coal type is a novel sort of approach.

Previous investigations conducted by means of observational tunnels method (Jamroz and Niedoba 2014) showed that not only analyzed data are correlated but also that only three parameters are sufficient to correct recognition of coal type. Furthermore, it was stated that occurrence of high linear correlation coefficient between two parameters does not mean the possibility of replacing one parameter by another one. However, the main reason of applying autoassociative neural networks in this paper is that this method allows some significant parameters without any additional analysis. It is not necessary to check which parameters are significant or to check which of them are correlated – in fact any additional analyzes are not necessary. The result is achieved immediately in the very suitable way for the researcher – by sight sense. This is because for neural network is not important if it has 3, 7 or 20 inputs. Sight sense is a mechanism which was developed by nature during many thousands of years. Everyone who performs image recognition knows that it is easier to observe, for example, a figure and state if it presents, for example, a giraffe than to write a program (using many various known or unknown methods) which is capable to recognize this animal on the basis of a photo. That is why connection of autoassociative neural network creating two-dimensional figure and our personal neural network (brain) analyzing this figure by sense of sight can give more readable results. So, it is much easier to check whether the points being part of various fractions can be separated by not complicated curve (like polynomial of low degree) or not than check it by means of selected analysis. Additionally, because autoassociative neural networks are non-linear methods then their abilities and clearness of results are much bigger than the ones of simple linear methods. Within previously conducted works the analyzes of multi-parameter coal data were performed by means of many methods: observational tunnels method (Niedoba and Jamroz 2013; Jamroz and Niedoba 2014), Kohonen network, multidimensional scaling (Jamroz 2014b), relevance maps, PCA

(Niedoba 2014) and autoassociative neural networks. By means of all these methods the satisfying results were obtained for coal and they are described in several papers. The detailed comparison of these methods efficiency is in progress.

General visualization principles of multi-parameter data

Only multi-parameter analysis of many features describing grained material gives sufficient information about the researched material. A number of methods can be applied for this purpose, including visualization methods. Based on a big collection of data it is often impossible to observe significant differences. Multi-parameter visualization, by contrast, gives a chance to do it. There are many techniques of multi-parameter visualization. The following methods of data visualization should be mentioned: grand-tour method (Asimov 1985), the method of principal component analysis (Hotelling, 1933; Jolliffe, 2002; Niedoba, 2014), the use of neural networks for data visualization (Kohonen, 1989; Jain and Mao, 1992; Aldrich, 1998), a parallel coordinates method (Inselberg 2009), multidimensional scaling (Kruskal, 1964; Jamroz, 2014b), the scatter-plot matrices method (Cleveland, 1984), method using the so-called relevance maps (Assa et al., 1999), method of observational tunnels (Jamroz, 2001; 2014a; Jamroz and Niedoba, 2013; 2014). The visualization of multidimensional solids is also possible (Jamroz, 2001; 2009).

Experiment

Three types of coal, types 31 (energetic coal), 34.2 (semi-coking coal) and 35 (coking coal) according to the Polish classification, were used in the investigation (Olejnik et al., 2010). Seven-parameter data consisted of 205 samples, including 72 samples of coal, type 31, 61 samples of coal, type 34.2 and 72 samples of coal, type 35. The whole set of data used in this paper can be found in (Niedoba, 2013a). They were obtained from three different Polish coal mines. Subsequently, all of them were initially screened on a set of sieves of the following sizes: -1.00, -3.15, -6.30, -8.00, -10.00, -12,50, -14.00, -16.00 and -20.00 mm. Then, the size fractions were additionally separated into density fractions by separation in dense media using zinc chloride aqueous solution of various densities (1.3, 1.4, 1.5, 1.6, 1.7, 1.8 and 1.9 g/cm^3). The fractions were used as a basis for further consideration and additional coal features were determined by means of chemical analysis. For each density-size fraction such parameters as combustion heat, ash contents, sulfur contents, volatile parts contents and analytical moisture were determined, making up, together with the mass of these fractions, seven various features for each coal type. Examples of data were presented in Table 1 showing the data for density-size fractions 1.00-0.50 mm for type 31 of coal.

Table 1. Data for density-size fraction 1.00-0.50 mm – coal type 31

Density [g/cm^3]	Mass	Combustion heat [cal]	Ash contents [%]	Sulfur contents [%]	Volatile parts contents V^a	Analytical moisture W_a
<1.3	4187.8	7367	1.25	0.63	36.02	4.15
1.3–1.4	2864	7021	3.35	0.66	32.14	4.33
1.4–1.5	310	5939	18.78	1.33	27.54	2.55
1.5–1.6	102.3	5547	23.83	1.66	26.87	2.80
1.6–1.7	111.9	4911	30.54	1.91	25.98	2.65
1.7–1.8	91.3	4177	39.94	1.93	25.17	2.35
1.8–1.9	80.9	3462	47.43	1.74	24.00	2.29
>1.9	1051.8	762	82.20	1.72	13.05	1.14

Autoassociative neural networks

Method description

Autoassociative neural networks are an example of self-organizing neural networks which learning process occurs without the teacher. When applied to visualization of multi-parameter data, the network has *n* inputs, one of indirect layers consisting of 2 neurons and *n* outputs. The number of network inputs and outputs is equal to the number of parameters of the analyzed data. The network is learnt by error backward propagation method.
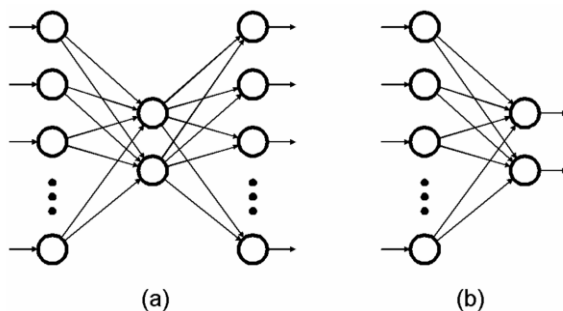
Fig. 1. Structure of autoassociative neural network used for multi-parameter data visualization.
(a) network training for receiving signals on outputs possibly closest to signals on inputs,
(b) transformation of input signal in location on two-dimensional screen
with the use of a fragment of previously learnt network

As a result of learning process, the same signals should impact both the outputs and inputs of neural networks. The described network is based on a change of input n-dimensional space *B* into two-dimensional space *Y* and then back into *n*-dimensional space B^* in the most similar way to *B*. The data going through the layer of two neurons, which outputs represent two-dimensional space *Y*, is compressed by network,

thus resulting in a two-dimensional preservation of certain individual features of original data from space B, which allows for reconstruction of the data.

When the learning process is over, the data visualization can be started. It consists in providing input to each data vector x on the neural network and projecting two-dimensional point representing it (on the basis of data from hidden layer consisting of two neurons). The location of this point is determined by two coordinates taken directly from the outputs of two neurons which constitute indirect layer and represent (in a compressed way) space *B*. A general working scheme by learning and visualization of such network has been presented in Figure 1.

Algorithm

A set of input data consists of elements described by n features. It can be then treated as a set of n-parameter vectors. The visualization based on autoassociative neural networks involves two stages.

I) Self-organization of network. In this stage all neuron weights are calculated on the basis of input data (Fig. 1a). The algorithm developed to fulfill this stage includes:

1. scaling of input data in order to ensure that the neural network can reproduce it as a result of the learning process. Individual features representing data parameters were scaled so fit the network output permissible range. In order to calculate the value of neuron output the function of hyperbolic tangent was used (described in equations (1) and (2)). So, the values of network outputs are within the range (-1, 1). It was decided then to scale the individual coordinates (features) of data sets to range (-0.9, 0.9),

2. randomization of all weights $w_{i,j,k}$ for all neurons (where $w_{i,j,k}$ is the weight of kth input of neuron located in i^{th} network layer on j^{th} position). Each weight was assigned to a value within the range (-0.5, 0.5) by applying plate probability distribution.

The next points 3-7 are carried out for each of input data vector ITER times (ITER is a parameter accepted in a given moment):

3. the output values for all neurons located in first layer are calculated for the next wth vector of input data. The weight is associated for an input of every neuron in the network. An input signal has an influence upon output signal. Additionally, the value of output signal depends on an additional weight (with adopted index 0) which determines component constant. To each neuron the $n+1$-parameter weight vector is assigned, where n is the number of network inputs. The value of output of first layer neuron is calculated according to the formula:

$$y_{1,j} = g\left(w_{1,j,0} + \sum_{k=1}^{n} w_{1,j,k} x_{k,w} \right) \tag{1}$$

where: g – adopted non-linear function, n – number of network inputs, $y_{i,j}$ – value of output of neuron located on i^{th} layer of network on j^{th} position (for the first layer of neurons the value of i is equal to 1), $w_{i,j,k}$ – weight of kth input of neuron located on i^{th} network layer on j^{th} position, $x_{k,w}$ – k^{th} feature of wth part of input data set (k^{th} coordinate of wth data vector). Application of non-linear function g in Eq. (1) allows to increase the calculating possibilities of neural network. In conducted experiments the hyperbolic tangens function was used as this function.

4. The values are calculated for all neurons' outputs located in all individual network layers. The calculations of neurons' outputs in the next layer can always be followed by the calculation of neuron values from the previous layer. This can take place because the values of previous layer outputs constitute at same time inputs for the next layer of neurons. In this way the values of all neurons in all layers are calculated.

$$y_{i,j} = g\left(w_{i,j,0} + \sum_{k=1}^{size(i-1)} w_{i,j,k}\, y_{i-1,k} \right) \tag{2}$$

where: size $(i–1)$ – number of neurons in $i–1$ layer, $y_{i,j}$ – output value of neuron located in i^{th} network layer on j^{th} position, $w_{i,j,k}$ – weight of kth input of neuron located in i^{th} network layer on j^{th} position, g – adopted non-linear function, the same as in equation (1).

5. For the purpose of calculating the errors of network output, it is necessary to obtain the difference between network input values (what is supposed to be obtained) and output values obtained on the last layer of neurons. This difference is then multiplied by a derivative of function g adopted in equations (1) and (2), which is the derivative of hyperbolic tangens function, obtaining:

$$\delta_{i,j} = \left(1 - y_{i,j}^{\,2}\right)\!\left(x_{j,w} - y_{i,j}\right) \tag{3}$$

where: $\delta_{i,j}$ – calculated error value of output of neuron located in i^{th} network layer on j^{th} position (in this equation i means the number of last network layer), $y_{i,j}$ – output value of jth neuron of ith layer, $x_{j,w}$ – j^{th} feature of wth part of input data set.

6. The errors of neurons' outputs from other network layers, individually from the penultimate to the first layer, are calculated as following:

$$\delta_{i,j} = \left(1 - y_{i,j}^{\,2}\right) \sum_{k=1}^{size(j+1)} \left(\delta_{i+1,k}\, w_{i+1,k,j}\right) \tag{4}$$

where: $\delta_{i,j}$ – calculated error value of output of neuron located on i^{th} network layer on j^{th} position, $w_{i+1,k,j}$ – weight of jth input of kth neuron from $i+1$ layer, size $(j+1)$ – number of neurons located in layer $j+1$, $y_{i,j}$ – output value of jth neuron from i^{th} layer.

7. Modification of neuron network weights on the basis of previously calculated errors. The modification was adopted according to the formula:

$$\widetilde{w}_{i,j,k} = w_{i,j,k} + \eta \delta_{i,j} y_{i-1,k} \tag{5}$$

where: $w_{i,j,k}$ – weight of kth input of jth neuron from i^{th} layer, $\widetilde{w}_{i,j,k}$ – weight $w_{i,j,k}$ after change, $\delta_{i,j}$ – value of error of jth neuron output from i^{th} layer, $y_{i-1,k}$ – value of output of kth neuron from $i+1$ layer, η – speed of learning, the constant 0.01 was adopted.

II) Projection of image (Fig. 1b). Points 1-2 are realized for each input data vector.

1. The values of outputs of following neuron layers are calculated for next wth input data vector. The calculations of the values of next neuron layers are conducted until the output value of determined two-neuron layer is found. Which layer it is should be assumed at the beginning during the construction of neural network. Let us assume that values obtained from outputs of these two neurons are u and v.

2. The symbol representing fraction of wth data vector is drawn on screen in point of coordinates (u, v). The values u and v are within the range (-1, 1) – it occurs from the previously accepted hyperbolic tangent function in equations (1) and (2).

The image of "locations" through which the data representing individual coal fractions flow is created in this way.

Results and discussion

During investigation the analysis was performer for various parameters. Such parameters were searched by which neural network is able to group coal data in the possibly best way. Some obtained parameters need to be accepted as constants – for example, number of network layers and non-linear function g (on which basis neuron outputs are calculated). For further analysis of coal data is sufficient to select initial, random values of all neurons weights generated by pseudo-random generator of values and value of parameter ITER – meaning number of learning repeats. Choice of other set of values generated by random numbers generator is not a problem. However, choice of the moment of stopping learning process requires experience and knowledge of neural networks functioning way.

Neural networks are very specific. They are being learnt till the moment when they will recognize correctly. If learning process is too short then it will be insufficiently well prepared. However, in practice of artificial neural networks the phenomenon of network "over-learning" exists when the learning process lasts to long. It happens because algorithm tries more and more adequately fit function realized by network to samples and this causes that this function becomes very complex, with large number of extremes – as a result it will recognize samples being outside learning set incorrectly. Example of function being realized by correctly learnt network and by "over-learnt" network is presented on Figure 2. That is why at certain moment when

neural network is already learnt, the learning process should be stopped. In purpose of checking if network was learnt, various criteria can be searched. Figure 3 shows relation between network error and parameter ITER. This error is calculated as mean squared error of difference between individual inputs and outputs of the network for all samples and network inputs. This graph was obtained for data containing 3 types of coal, showed on Figs 5–6. In case of this data for ITER = 5 this error was equal to 0.104462, for ITER = 30 it was equal to 0.028714 and for ITER = 9000 it was equal to 0.006332.
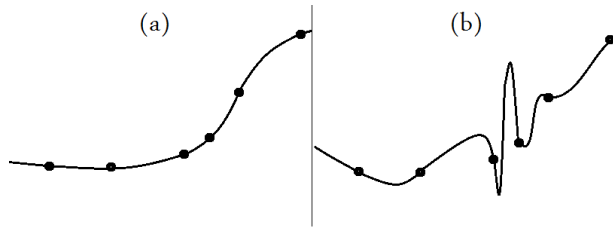
Fig. 2. Examples of two functions of one variable being realized by the same neural network learnt on the basis of the same set consisted of 6 points. Part (a) shows function realized by network learnt correctly, part (b) shows function realized by "over-learnt" network
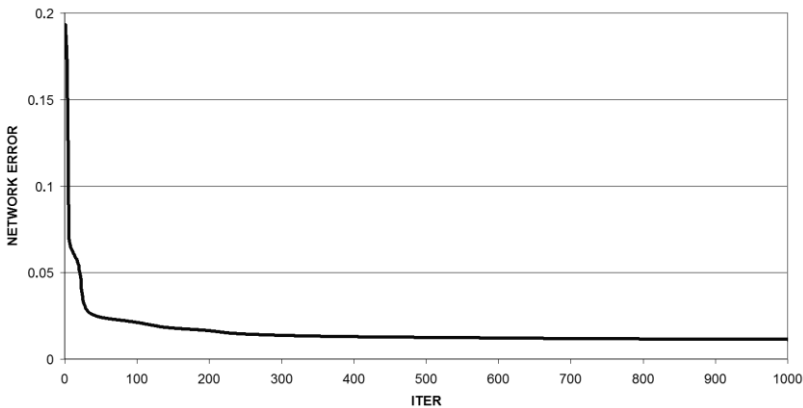
Fig. 3. Relation between network error and ITER parameter. Error is calculated as mean square error of difference between individual inputs and outputs of the network for all samples and network inputs

In practice, this graph does not give much because it always presents function which lowers till certain limit. Additionally, in case of neural networks, as it was mentioned before, during learning process till certain moment we achieve better and better results and then, despite that error still lowers, network becomes "over-learnt". Thus, if views from which occurs that separation is possible were obtained it means that in analyzed data (in chosen parameters) information allowing proper recognition gathers. In case if analyzed data (containing chosen 7 parameters) do not contain information necessary to identify coal type then independently on learning process

length is not possible to achieve views showing that data of various fractions are located in other part of the figure. It should be remembered that during network learning no information about what fraction is represented by the sample is provided. That means that during learning process network does not know if any two samples represent the same fraction or various ones. Only after ending of learning process (during plotting) each sample is assigned with number of fraction of which it is part. This is done in purpose of checking if network assigned to each fraction other part of the 2-D space (graph).

Based on assumptions put forward in the previous chapter a computer software was developed to visualize seven-parameter data describing various types of coal. The software was developed C++ language by means of Microsoft Visual Studio. The experiment led to a conclusion that the best results from the analysis of data describing various coal types were yielded by a 6-layer neural network. Three layers serve to compress data from seven to two parameters while the other three serve to decompress from two to seven parameters. The third layer consists of two neurons (their outputs serve to visualization) and each of the remaining layers consists of 7 neurons. In Figure 4 the topology of network was shown. The outputs of neurons $y_{3,1}$ and $y_{3,2}$ are the outputs of two-neuron layer on which the visualization was based. Full information is transferred through these two signal outputs, which is necessary to reconstruct seven-parameter input data. This is why on the basis of these outputs, it is possible to read the coordinate values of the point located on plane which represent seven-parameter input data vector.
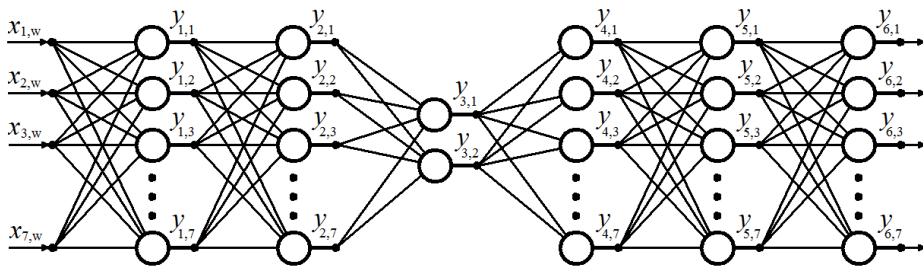
Fig. 4. Topology of autoassociative neural network with the best results. Three layers serve to compress data and three to reproduce data. Outputs $y_{3,1}$ and $y_{3,2}$ of the layer consisting of two neurons serve to visualize seven-parameter data

The obtained results were presented in Figures 5-9. The views show a way of compression of seven-parameter data by neural network to two parameters determined by outputs $y_{3,1}$ and $y_{3,2}$ of the network. The compression must allow for a reconstruction of seven-parameter input data by the last three network layers, hence it should contain all information needed for this purpose. In this way it is possible to see all significant features of seven-parameter data on two-dimensional screen.
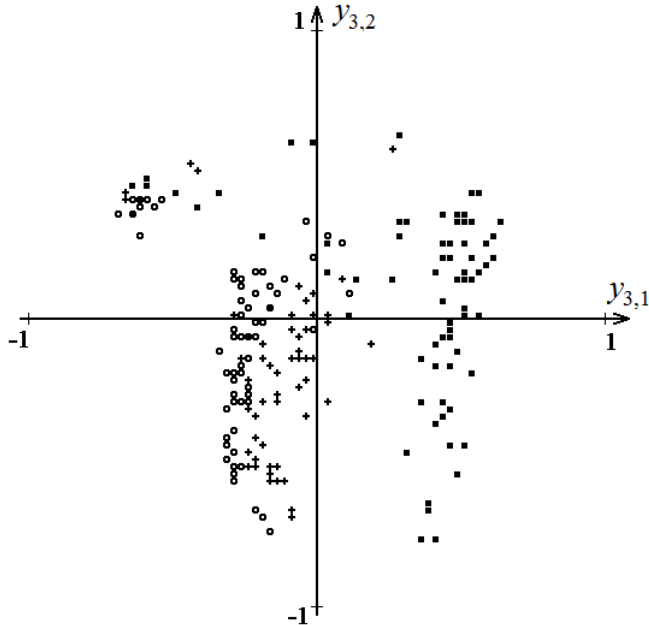
Fig. 5. A presentation of seven- parameter data representing three various coal types by parameter ITER=30 shown by neural network with two signals $y_{3,1}$ and $y_{3,2}$. Signals representing samples of coal type 31 were marked with (■), (+) – samples of coal type 34.2, (o) – samples of coal type 35

Figure 5 shows the view obtained by parameter ITER=30. The adopted ITER value means that the self-learning process network was conducted for each input data vector 30 times. Figures 5-6 show how the network evolves. It can be seen that the signals which are a reply to data representing the same coal types start to occupy separated subareas and groups. In Figure 5 it can be noticed that by small value of parameter ITER=30, the signals representing the same types start to group. However, in some parts of the space, the signals of various coal types still overlap. In Figure 6 (ITER=9000) it can be observed that signals which are a reply to data representing samples of certain coal type gather. It can be seen that these gatherings can be separated. The clearness of the signal space division grows along with the increase of ITER parameter, so with the network learning process. It should be pointed out that the information of data vectors affiliation to certain fractions was not taken into account during self-learning of the network (calculating of weights). Therefore, the grouping of signals (i.e. those that go through layer consisting of two neurons) representing a certain fraction depends only on certain data properties noticed by the network.

In order to achieve even more clear results, it was decided to make a presentation of the same data in other way by means of autoassociative neural network. An examination was conducted how network will allocate signals to data representing coal types in pairs. Figure 7 depicts network data on coal types 34.2 and 35. It is even

more clear that signals representing coal type 34.2 gather in aggregations which can be easily separated from signals representing samples of coal type 35.
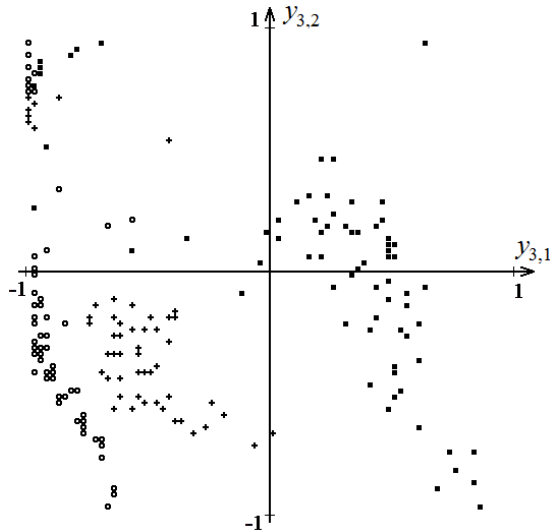
Fig. 6. A presentation of seven-parameter data representing three various coal types by parameter ITER = 9000 shown by neural network with two signals $y_{3,1}$ and $y_{3,2}$. Signals representing samples of coal type 31 were marked with (■), (+) – samples of coal type 34.2, (o) – samples of coal type 35
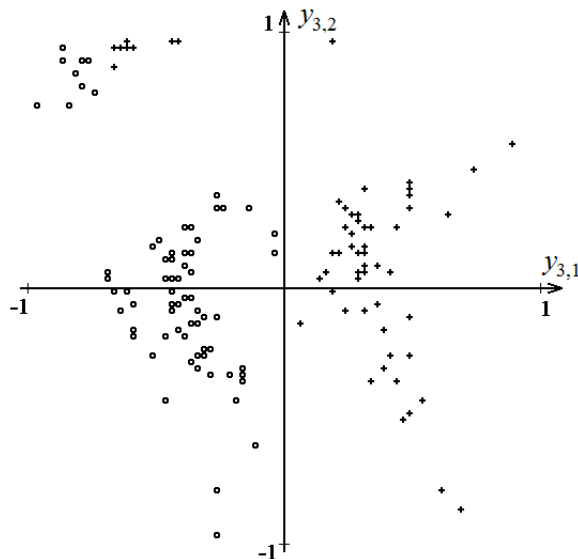
Fig. 7. A presentation of seven-parameter data representing three various coal types by parameter ITER=4000 shown by neural network with two signals $y_{3,1}$ and $y_{3,2}$. Signals representing samples of coal type 34.2 were marked with (+) –, (o) – samples of coal type 35

Figure 8 depicts the way how neural network presents data representing coal types 31 and 35. It is also clear that signals representing samples of coal type 31 gather in aggregations which can be easily separated from signals representing samples of coal type 35. Figure 9 shows the way how network presents data representing coal types 31 and 34.2. It can be clearly seen that signals representing samples of coal type 31 gather in aggregations which can be easily separated from signals representing samples of coal type 34.2.
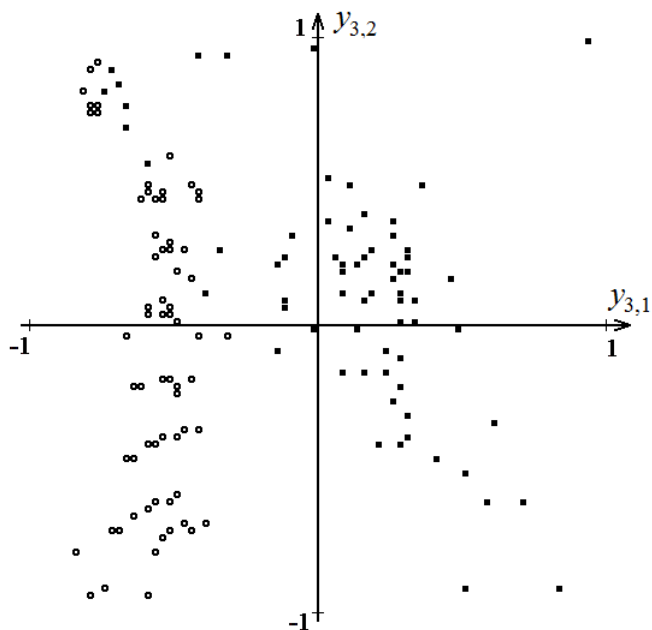
Fig. 8. A presentation of seven-parameter data representing three various coal types by parameter ITER=17120 shown by neural network with two signals $y_{3,1}$ and $y_{3,2}$. Signals representing samples of coal type 31 were marked with (■), (o) – samples of coal type 35

If it is possible to confirm the possibility of separation of coal samples, type 34.2 from coal type 35 (Fig. 7), the possibility of separation of coal samples, type 31 from coal type 35 (Fig. 8) and, furthermore, the possibility of separation of coal samples, type 31 from coal type 34.2 (Fig. 9) is also confirmed, then it can be stated that the samples of all three types of coal can be separated from each other. The application of multi-parameter data visualization by means of autoassociative neural networks allows to arrive at a conclusion that the information about seven-parameter input data describing samples of three coal types is sufficient for their proper classification.
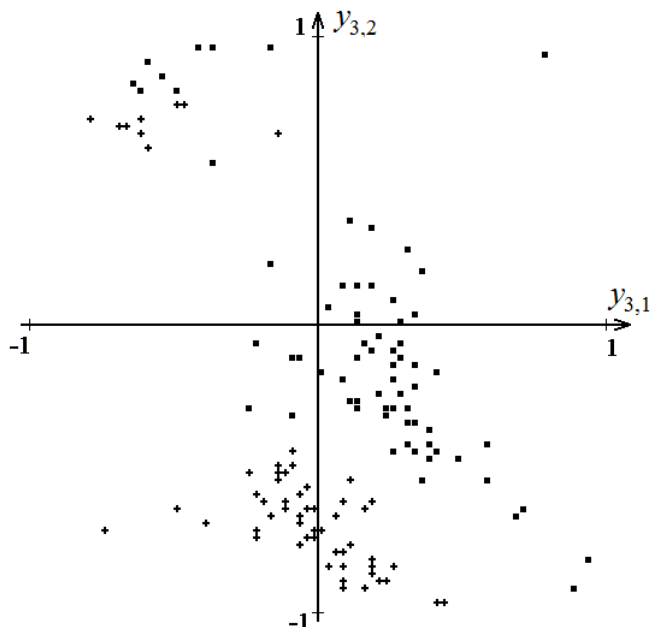
Fig. 9. A presentation of seven-parameter data representing three various coal types
by parameter ITER =5230 shown by neural network with two signals $y_{3,1}$ and $y_{3,2}$, show. Signals
representing samples of coal type 31 were marked with (■), (+) – samples of coal type 34.2

Conclusions

The conducted experiments involving the visualization of seven-parameter data
visualization by means of autoassociative neural networks allowed to draw the
following conclusions.
1. Visualization of seven-parameter data by means of autoassociative neural networks
   allows to state that the information in analyzed seven-parameter data is sufficient
   for the proper classification of coal types 31, 34.2 and 35.
2. Even the presentation of three types of coal in one Figure allows to state that signals
   representing samples of coal of certain type gather in aggregations which can be
   easily separated. It occurs that data contains information sufficient for the proper
   classification of coal types.
3. Presentation of data representing various coal types in pairs by means of
   autoassociative neural networks allows to obtain even more clear results.
4. The best results were obtained by means of neural network consisting of 6 layers.
   Three layers served to compress data from 7 to 2 parameters and three layers
   served to decompress from 2 to 7 parameters. Third layer which comprised two
   neurons, which outputs served for visualization purposes, and each of the
   remaining layers consisted of 7 neurons.

5. Clearness of results grows along with the learning progress of neural network (growth of parameter ITER value).
6. Whether the results are clear highly depends on adopted parameters. The change of these parameters results in different allotment of individual areas of signal space by neural network to data representing various types of coal.
7. Some sort of problem arising from such visualization is the necessity of selecting parameters in order to obtain a view which clearly presents the searched information. It should be noticed that during conducted experiments the views obtained by means of neural networks ranged from 3 to 8 layers. These views were obtained by ITER parameter value equal from 1 to 30000. The experiments were conducted for various initial ranges of weights. The results presented in the paper include the clearest ones from the all obtained.

Acknowledgements

References

Ahmed H.A.M., Drzymala J.: *Two-dimensional fractal linearization of distribution curves*, Physicochemical Problems of Mineral Processing, vol. 39, 129–139, 2005.

Aldrich C., *Visualization of transformed multivariate data sets with autoassociative neural networks*. Pattern Recognition Letters, Volume: 19, Issue: 8, June, 1998, 749–764.

Asimov D., *The Grand Tour: A Tool for Viewing Multidimensional Data,* SIAM Journal of Scientific and Statistical Computing, 128–143, vol. 6, No, 1985.

Assa J., Cohen-Or D., Milo T., *RMAP: a system for visualizing data in multidimensional relevance space,* Visual Computer, vol.15, no.5, 217–34. Publisher: Springer-Verlag, Germany, 1999.

Brozek M., Surowiak A., *Argument of Separation at Upgrading in the Jig*, Archives of Mining Sciences, vol. 55, 21–40, 2010.

Brozek M., Surowiak A., *Effect of Particle Shape on Jig Separation Efficiency*, Physicochemical Problems of Mineral Processing, vol. 41, 397–413, 2007.

Brozek M., Surowiak A., *The Dependence of Distribution of Settling Velocity of Spherical Particles on the Distribution of Particle Sizes and Densities*, Physicochemical Problems of Mineral Processing, vol. 39, 199–210, 2005.

Cleveland W.S., McGill R., *The many faces of a scatterplot*, Journal of the American Statistical Association, vol.79, 807–822. 1984.

Drzymala J., *Mineral processing: foundations of theory and practice of minerallurgy,* Oficyna Wydawnicza Politechniki Wrocławskiej, Wrocław, 2007.

Drzymala J., *Basics of minerallurgy,* Oficyna Wydawnicza Politechniki Wrocławskiej, 2009. [in Polish]

Gawenda T., Saramak D., Tumidajski T., *Regression models of rock materials crushing in jaw crushers*, Scientific Issues of Civil Engineering and Environmental Engineering Faculty of Koszalin University of Science and Technology, series: Environmental Engineering, no 22, 659–670, 2005. [in Polish]

Hotelling H., *Analysis of a complex of statistical variables into principal components*, Journal of Educational Psychology, vol. 24, 417–441, and 498–520, 1933.

Inselberg A., *Parallel Coordinates: VISUAL Multidimensional Geometry and its Applications*, Springer, 2009.

Jain A.K., Mao J., *Artificial neural network for non-linear projection of multivariate data*. In: Proc. IEEE Internat. Joint Conf. On Neural Networks, Baltimore, MD, vol. 3, 335–340, 1992.

Jamróz D., Niedoba T., *Application of Observational Tunnels Method to Select Set of Features Sufficient to Identify a Type of Coal*, Physicochemical Problems of Mineral Processing, vol 50(1), 185–202, 2014.

Jamroz D., *Visualization of objects in multidimensional spaces*, Doctoral Thesis, AGH, Kraków, 2001. [in Polish]

Jamroz D., *Multidimensional labyrinth - multidimensional virtual reality*. [In:] Cyran K., Kozielski S., Peters J., Stanczyk U., Wakulicz-Deja A. (eds.), Man-Machine, Interactions, AISC, Heidelberg, Springer-Verlag, vol. 59, 445–450, 2009.

Jamroz D., *Application of Multidimensional Data Visualization in Creation of Pattern Recognition Systems*, In: Gruca A., Czachórski T., Kozielski S. (eds.), *Man-Machine, Interactions 3*, AISC, Switzerland, Springer International Publishing, vol. 242, 443–450, 2014a.

Jamroz D., *Application of multidimensional data visualization by means of multidimensional scaling to qualitative classification of various types of coal*, Archives of Mining Sciences, paper in printing, 2014b.

Jolliffe I.T. *Principal Component Analysis*, Series: Springer Series in Statistics, 2nd ed., Springer, NY, 2002.

Kohonen T., *Self Organization and Associative Memory*, Springer-Verlag, 1989.

Kruskal J. B., *Multidimensional scaling by optimizing goodness of fit to a nonmetric hypothesis*, Psychometrika, vol. 29, 1–27, 1964.

Lyman G. J., *Application of Line-Length Related Interpolation Methods to Problems in Coal Preparation – III: Two dimensional Washability Data Interpolation*, Coal Preparation, vol. 13, 179–195, 1993.

Niedoba T., Jamroz D., *Visualization of multidimensional data in purpose of qualitative classification of various types of coal*, Archives of Mining Sciences, vol. 58, iss. 4, 1317–1333, 2013.

Niedoba T., *Multidimensional distributions of grained materials characteristics by means of non-parametric approximation of marginal statistical density function*, AGH Journal of Mining and Geoengineering, iss. 4, 235–244, 2009 [in Polish].

Niedoba T., *Multidimensional characteristics of random variables in description of grained materials and their separation processes,* Wydawnictwo Instytutu Gospodarki Surowcami Mineralnymi i Energią PAN, Kraków, 2013a [in Polish].

Niedoba T., *Statistical analysis of the relationship between particle size and particle density of raw coal*, Physicochemical Problems of Mineral Processing, vol. 49, iss. 1, 175–188, 2013b.

Niedoba T., *Multi-parameter data visualization by means of principal component analysis (PCA) in qualitative evaluation of various coal types*, Physicochemical Problems of Mineral Processing, vol. 50, iss. 2, 575–589, 2014.

Niedoba T., Surowiak A., *Type of coal and multidimensional description of its composition with density and ash contents taken into consideration*, in Proceedings of the XXVI International Mineral Processing Congress, vol. 1, 3844–3854, 2012.

Niedoba T., *Three-dimensional distribution of grained materials characteristics*, in Proceedings of the XIV Balkan Mineral Processing Congress, Tuzla, Bosnia and Herzegovina, vol. 1, 57–59, 2011.

Olejnik T., Surowiak A., Gawenda T., Niedoba T., Tumidajski T., *Multidimensional coal characteristics as basis for evaluation and adjustment of its beneficiation technology*, AGH Journal of Mining and Geoengineering, vol. 34, iss. 4/1, 207–216, 2010. [in Polish]

Saramak D., *Mathematical models of particle size distribution in simulation analysis of High-pressure grinding rolls operation*, Physicochemical Problems of Mineral Processing, vol. 49(1), 495–512, 2013.

Saramak D., *Technological Issues Of High-Pressure Grinding Rolls Operation In Ore Comminution Processes*, Archives of Mining Sciences, vol. 56, no 3, 517–526, 2011.

Snopkowski R., Napieraj A., *Method Of The Production Cycle Duration Time Modeling Within Hard Coal Longwall Faces*, Archives of Mining Sciences, vol. 57, no. 1, 121–138, 2012.

Tumidajski T., Saramak D.: *Methods and models of mathematical statistics in mineral processing*, Wydawnictwo AGH, Kraków, 2009. [in Polish].

Tumidajski T.: *Stochastic analysis of grained materials properties and their separation processes*, Wydawnictwo AGH, Kraków, 1997. [in Polish].

RECOVERY OF VALUABLE METALS FROM ZINC PLANT RESIDUE THROUGH SEPARATION BETWEEN MANGANESE AND COBALT WITH N-N REAGENT

Davood MORADKHANI[*]**, Behzad SEDAGHAT**[**]**,
Mostafa KHODAKARAMI**[**, ***]**, Ilnaz ATAEI**[**]

[*] Faculty of Engineering, University of Zanjan, Zanjan, Iran
[**] Research and Engineering Company for Non-ferrous Metals (RECo.), Zanjan, Iran
[***] Faculty of Engineering, Imam Khomeini International University, Qazvin, Iran,
     mostafakhodakarami@gmail.com

Abstract: Recovery and separation of cobalt and manganese from one of zinc plant residues (ZPR), namely hot filter cake (HFC) using a hydrometallurgical process was studied. The process is carried out in four steps as follows: (1) washing zinc, (2) reductive leaching with hydrogen peroxide, (3) cadmium cementation with zinc powder and (4) separation of cobalt from manganese with beta naphthol. In this research, the separation between manganese and cobalt from the HFC using N-N reagent was investigated. The influence of several parameters on the course of the reaction such as N-N quantity, pH, temperature and reaction time was also examined. The optimum separation conditions were found to be N-N quantity: 8 times of stoichiometric value, time: 30 min, temperature: 25 °C and pH = 1.5. Using the optimized conditions, the cobalt and manganese precipitation was nearly 99% and 0%, respectively. A kinetic study of manganese precipitation through N-N reagent has been carried out to assess the effect of kinetics parameters. The data obtained for the leaching kinetics indicated that the precipitation of manganese is an ash diffusion controlled reaction and the reaction activation energy is equal to 1.4kJ/mol.

Keywords: zinc plant residue, manganese, cobalt, beta naphthol, kinetics

Introduction

The production of non-ferrous metals from primary and secondary material results in the generation of a wide variety of wastes and residues. They are a result of metals separation that is necessary for the production of pure metals from complex sources. These wastes and residues result from different stages of processing as well as from the flotation, slags, slimes and flue dusts systems (Florijn et al., 1993, Hatch, 2000, Ross, 1994, Wentz, 1989). These wastes are activated through certain processes such

as grinding, leaching, roasting, smelting, quenching, etc. Exposure of these wastes to atmospheric oxygen and moisture results in solubilization of toxic metals which may dramatically affect the water quality and biological life in surface waters. The potential release of toxic heavy metals from such by-products and waste materials to the surface and ground water is of particular concern (Altundogan et al., 1992, Tumen, 1988, Tumen et al., 1991; 1992).

The hydrometallurgical processes are environmentally and economically more suitable to treat even low zinc containing materials on small scale. They can process secondaries containing different impurities. Zinc oxide ores are usually concentrated through flotation or gravity, where the metal recovery is low and the operating cost is high (Jha et al., 2001, Safarzadeh et al., 2005). Different studies have been carried out throughput the world to recover valuable metals from zinc plant residues (ZPR). For example, Kul and Topkaya (2008) studied the recovery of germanium and other valuable metals from ZPR of Cinkur Zinc Plant. In another study, Wang and Zhou (2002) recommended a hydrometallurgical process for the production of cobalt oxide after inspecting the recovery of cobalt from ZPR. Raghavan et al. (2000) described hydrometallurgical processing of lead-bearing materials generated at zinc plants. In their approach, lead sulfate residue was treated with brine solution and then lead was cemented-out from resultant filtrate using aluminum scrap. With initial lead ion concentration of 4.5 g/dm^3, 97.1% of lead was extracted. Abdollahi et al. (2006) extracted zinc and lead from Iranian zinc plant residues using brine-leaching method. They blended the residue with H_2SO_4 at 70 ^{o}C and then for lead recovery, after zinc extraction, the residual solid was subjected to brine leaching with NaCl. Lead content of brine-leaching filtrate was cemented by metallic aluminum. Cementation efficiency for lead content of 16.36 g/dm^3 was about 97–98%. The brine leaching of lead-bearing ZPR of NILZ plant was reported (Farahmand et al., 2009). Safarzadeh et al. (2009) studied the recovery of Zn, Ni and Cd from Ni-Cd residue. Under the optimum collective leaching conditions, t: 150 min, T: 45 ^{o}C, stirring speed: 500 rpm, S/L: 1/13 and pH = 1.3–1.5, the maximum metal recoveries were 99.95%, 98.30% and 97.50% for Zn, Cd and Ni, respectively. Also cementation efficiencies for cadmium and nickel were 98.95% and 99.98%, respectively.

Eivazi et al. (2008) reported the best condition for extraction of zinc, cobalt and manganese from ZPR of NILZ plant. Their process included: washing at optimum conditions: pH = 3, S: L ratio of 1:4, 40 ^{o}C, 90 min; Reductive leaching with: 20 g/dm^3 sulfuric acid, S: L of 1:10, 3%(V/V) hydrogen peroxide and ambient temperature; separation of zinc, manganese and cobalt by solvent extraction using 20%D2EHPA+5%TBP in kerosene, 25 ^{o}C and O: A ratio of 1:1. Zinc was separated from manganese and cobalt at pH = 1.5. Then, manganese was purified from cobalt at pH = 2.9.

In the zinc plant located in Zanjan, Iran, a leach-electrolysis process is practiced for zinc production. In this process, number of filter cakes is generated daily as by-products. These wastes are stored for valuable elements' recovery in the future and

dumped in open stockpiles where they may lead to heavy metal pollution problems. In these plants three types of wastes are produced: leaching filter cake, Co purification filter cake (or Hot Filter Cake) and Ni-Cd purification filter cake. All of the filter cakes have high levels of heavy metals (Sedaghat et al., 2008).

In this study the possibility of separation of manganese and cobalt with N-N reagent from zinc plant residues (Co filter cake) has been studied. The first step in the metals recovery experiments was the low sulfuric acid washing of Co filter cake samples. After obtaining the pregnant wash solution with the optimum washing recoveries, the solution was leached with hydrogen peroxide in order to recover cobalt and manganese. Subsequently, cadmium was removed from pregnant solution with zinc powder. Finally, manganese and cobalt were separated with N-N reagent. Hence, the objectives of this study was to investigate the role of main factors such as N-N quantity, temperature, pH and reaction time, and also to determine what process controlled the rate of the dissolution of Mn or what kinetic model could be applied. At last, a conceptual flowchart diagram of the process for extraction of valuable metals from zinc plant residue was proposed.

Experimental

Materials and methods

Cobalt filter cake for the leaching study was obtained from Sane Rooy Co., Zanjan, Iran. After drying, the filter cake was ground and homogenized. The chemical analysis was carried out with a Perkin-Elmer AA300 model atomic absorption spectro-photometer. The chemical analysis of the filter cake is given in Table 1. As can be seen from Table 1, the filter cake is mostly composed of zinc and manganese.

Table 1. Chemical analysis of the Co purification filtercake

Content [wt.%]					
Co	Mn	Zn	Ni	Cd	Ca
1.19	9.1	14.66	0.07	0.35	6.64

Separation between manganese and cobalt was examined encompassing four parameters of pH, temperature, N-N quantity and contact time using beta naphthol. For each parameter six levels were chosen as shown in table 2.

Table 2. Special parameters in separation of manganese and cobalt

Parameters	Units	Level 1	Level 2	Level 3	Level 4	Level 5	Level 6
pH	–	1.5	2	2.5	3	3.5	4
Temperature	ºC	25	40	50	60	70	80
N-N quantity	-	6	7	8	9	10	11
Time	Min	15	30	45	60	75	90

Procedure and equipment

Experiments were carried out in a glass beaker of 1 dm^3 volume equipped with a mechanical stirrer submerged in a thermostatic bath. Mechanical stirrer (Heidolf RZR 2020) had a controller unit and the bath temperature was controlled using digital controller (within ±0.5 ^{o}C). For minimizing aqueous loss when the system is heated, a reflux condenser mounted on top of the cell. After adding 1liter of solution to the reaction vessel and setting the temperature at the desired value, a specific weight of additives were added to the reactor while stirring the content of the reactor at a certain speed. At the end of the reaction period, the contents of the beaker were filtered and the amounts of manganese and cobalt in the filtrate were analyzed.

Results and discussion

Washing of zinc

Based on the results from washing experiments in the previous study (Eivazi et al., 2008) for zinc removal, the following optimum washing conditions were chosen: H_2SO_4 concentration 200 g/dm^3 , 25 ^{o}C, the liquid to solid ratio (L/S) 8:1, pH = 1 and reaction time: 120 min. Using the optimized conditions, the zinc recovery was nearly 96%. After completion of the washing experiment, the washing residue was filtered, washed, dried and weighed. The analytic result of the washed filter cake is given in Table 3.

Table 3. Chemical analysis of the washed filter cake

Content [wt.%]					
Co	Mn	Zn	Ni	Cd	Ca
1.31	11.13	1.77	0.04	0.27	12.36

Reductive leaching with hydrogen peroxide

After sulfuric acid leaching in washing stage, the obtained filter cake was subjected to reductive leaching to investigate the recovery of cobalt and manganese. Cobalt and manganese dissolution is easily performed from ZPR using dilute sulfuric acid solutions containing hydrogen peroxide as a reducing agent. The most suitable conditions were investigated by Eivazi et al. (2009), as follows: sulfuric acid concentration: 30 g/dm^3, amount of hydrogen peroxide: 3% (V/V), pulp density: 100 g/dm^3, leaching time: 45 min and ambient temperature. Based on the optimum conditions, more than 90% of Co, Mn and Zn could be extracted. The chemical analysis of the achieved filtrate in this stage is shown in Table 4.

Table 4. Chemical analysis of the filtrate

Content [g/dm^3]			
Co	Mn	Zn	Cd
1.18	8.58	1.45	0.035

Cadmium cementation with zinc powder

Based on the results from cadmium cementation experiments in the previous study for cadmium removal, the following optimum conditions were chosen: pH = 3.5, Temperature: 25 ^{o}C, stirring speed: 100 rpm, zinc powder: 10 time of stoichiometric quantity of cadmium and reaction time: 30 min. Based on the optimized conditions, nearly 97% of cadmium was removed.

Separation between manganese and cobalt using N-N reagent

Preparation of N-N reagent

To make N-N reagent, three materials such as beta naphthol, sodium nitrite and sodium hydroxide were used. The nitrosation reaction of beta naphthol is generally shown as follows:

$$C_{10}H_7OH + NaNO_2 \rightarrow HO\text{-}C_{10}H_6\text{-}NO + NaOH$$
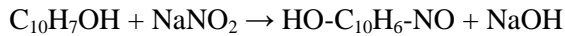
The ratio of beta naphthol, sodium nitrite and sodium hydroxide in weight has been decided as follows: beta naphthol: 144 g, $NaNO_2$: 69 g and NaOH: 40 g. Since beta naphthol is hardly soluble in cold water, beta naphthol, sodium nitrite and sodium hydroxide were mixed with cold water and heated to 70 ^{o}C through agitation for two hours.

Investigation of effective parameters

Effect of pH

Experiments were carried out to investigate the effect of pH on the separation of manganese and cobalt. As can be seen in Fig. 1, maximum separation between manganese and cobalt is in pH of 1.5. In this pH, recovery of manganese and cobalt was 94.56% and 0% respectively. Therefore, to investigate the other separation parameters, the pH = 1.5 was chosen for the optimum pH.
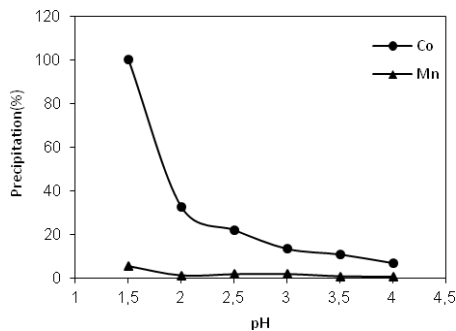
Fig. 1. Effect of pH on the separation of manganese and cobalt for various pH
(N-N quantity: 8 times of stoichiometric value; temperature: 25 ºC;
time: 15 min; stirrer speed: 900 rpm)

Effect of N-N quantity

The effect of N-N quantity on the separation between manganese and cobalt was investigated in the range of 6 to 11 times of stoichiometric value. The results are presented in Fig. 2. As it can be seen in Fig. 2, separation of manganese and cobalt increases with N-N quantity. The maximum manganese and cobalt recovery at N-N quantity equal to 8 times of stoichiometric value after 15 min were 94.56 and 0%, respectively. Therefore, the N-N quantity equal to 8 times of stoichiometric value was chosen for the optimum N-N quantity to investigate the other parameters.
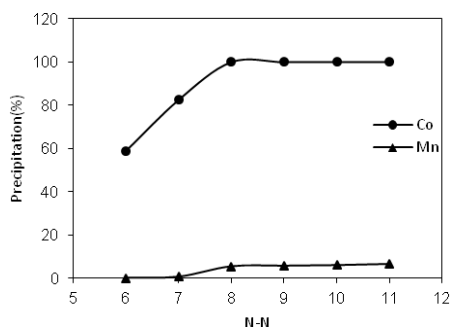
Fig. 2. Effect of N-N quantity on the separation of manganese and cobalt
for various N-N amount (pH = 1.5; temperature: 25 ^{o}C;
time: 15 min; stirrer speed: 900 rpm)

Effect of reaction time

Experiments were carried out to investigate the effect of reaction time on the separation between manganese and cobalt. As it shown in Fig. 3, the optimum precipitation of the cobalt and manganese were 99% and 0%, respectively, at reaction time of 30 min. Therefore, the time: 30 min was chosen as optimum time.
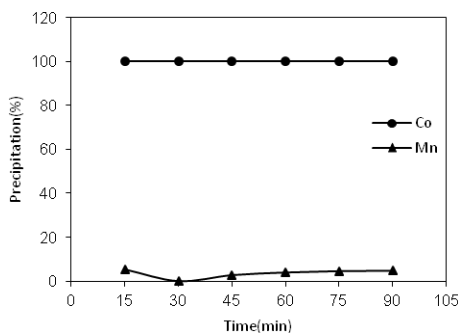
Fig. 3. Effect of reaction time on the separation of manganese
and cobalt for various times (N-N quantity: 8 times of stoichiometric value;
temperature: 25 ºC; stirrer speed: 900 rpm; pH = 1.5)

Effect of temperature

Figure 4 shows the effect of temperature on the separation between manganese and cobalt. As it shown in Fig. 4, increasing the temperature up to 40 $^{\circ}$C resulted in a decrease in manganese recovery. The maximum recovery of Mn was noticed in the temperature of 25 $^{\circ}$C that was equal to 99%.
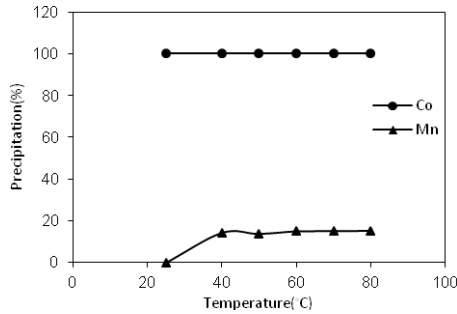
Fig. 4. Effect of temperature on the separation of manganese and cobalt
for various times (N-N quantity: 8 times of stoichiometric value;
time: 30 min; stirrer speed: 900 rpm; pH = 1.5)

Kinetics of separation between manganese and cobalt

The shrinking core model (SCM) was used to describe the leaching reaction. Therefore, three different models can be considered as reaction mechanism with their constant rate equations which will be discussed in the following section.

Film diffusion control for spherical particles

The fraction of manganese reacted at any time, *t*, in a film diffusion control situation can be calculated from the following equation (Levenspiel, 1999):

$$X_{Mn} = kt \qquad (1)$$
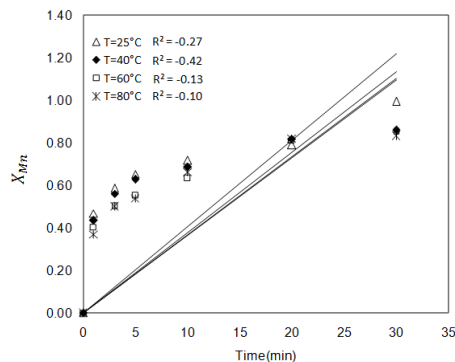
Fig. 5. Plot of X_{Mn} vs. time for different temperatures (N-N quantity: 8 times
of stoichiometric value; time: 30 min; stirrer speed: 900 rpm; pH = 1.5)

where X_{Mn} stands for the fraction of manganese reacted and k (min^{-1}) is reaction rate constant. Based on the experimental data shown in Fig. 5, the left-hand side of Eq. (1) is plotted against time. The values of the correlation coefficient R^2 for linearity of the plot are very far from the normal state. At all of the temperatures, the experimental data deviates further from a linear form. None of the straight lines can be considered close enough to fit the experimental data to suggest a film diffusion model for the process.

Ash diffusion control for spherical particles

Diffusion of Mn^{2+} through the blanket of ash at any time, t, can be calculated from the following equation (Levenspiel, 1999):

$$1-3(1-X_{Mn})^{2/3}+2(1-X_{Mn})=kt. \tag{2}$$

In order to test the possibility of diffusion through the ash, the left hand side of Eq. (2) was plotted against time (Fig. 6). It is obvious that the data are well fitted to the corresponding lines. Therefore, the diffusion through the ash could be rate determining step in the process.
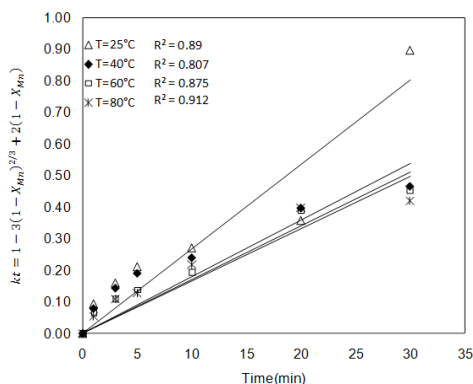
Fig. 6. Plot of $1-3 (1-\alpha)^{2/3}+2(1-\alpha)$ vs. time for different temperatures (N-N quantity: 8 times of stoichiometric value; time: 30 min; stirrer speed: 900 rpm; pH = 1.5)

Chemical reaction control for spherical particles

The fraction of manganese reacted at any time, t, in a chemical reaction control process can be calculated from the following equation (Levenspiel, 1999):

$$1-(1-X_{Mn})^{1/3}=kt. \tag{3}$$

The left-hand side of Eq. (3) is plotted against reaction time in Fig. 7. By comparing Figs. 5–7, it is indicated that the R^2 values for Fig. 6 are closer to 1 than those of Figs. 5 and 7. Therefore the data can be correlated to an ash diffusion control model and diffusion of Mn^{2+} through the blanket of ash controls the reaction rate.
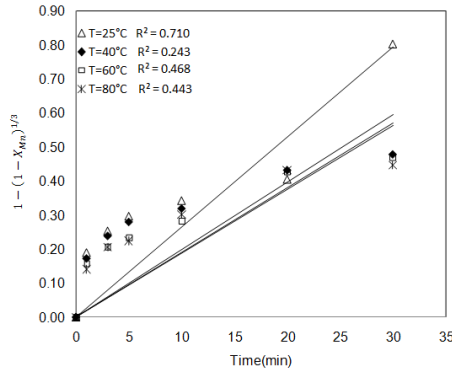
Fig. 7. Plot of $1- (1-\alpha)^{1/3}$ vs. time for different temperatures (N-N quantity: 8 times of stoichiometric value; time: 30 min; stirrer speed: 900 rpm; pH = 1.5)

Activation energy

The temperature dependence of the reaction rate constant (k) can be calculated from the Arrhenius equation (Levenspiel, 1999):

$$k=A \, \exp\left(\frac{-Q}{RT}\right) \tag{4}$$

where A represents the frequency factor; Q (kJ/mol) is the activation energy of the reaction; R is the universal gas constant and T is the absolute temperature. The values of k at different temperatures can be calculated from the slope of the lines shown in Fig. 6. The results obtained from Figs. 5–7 indicate that the dissolution rate of manganese is controlled by the diffusion and not by surface chemical reactions. Generally, a high value of activation energy indicates that the process is "strongly" influenced by temperature and, therefore, the rate-controlling step could be the
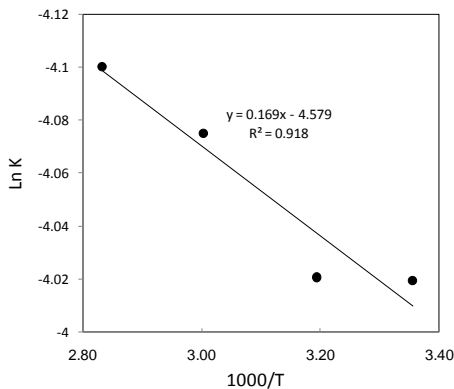
Fig. 8. Arrhenius plot of reaction rate against reciprocal temperature (N-N quantity: 8 times of stoichiometric value; time: 30 min; stirrer speed: 900 rpm; pH = 1.5)

reaction at the solid surface. Conversely, a low value of activation energy indicates that the process is "weakly" influenced by the temperature and the rate-controlling step could be the mass transport of reagents or products through the reaction product. Arrhenius plot considering the apparent rate constants was obtained by applying Eq. 2 to leaching experimental data. As can be seen in Fig. 8, the calculated activation energy was 1.4 kJ/mol which clearly suggests ash diffusion control for the process.
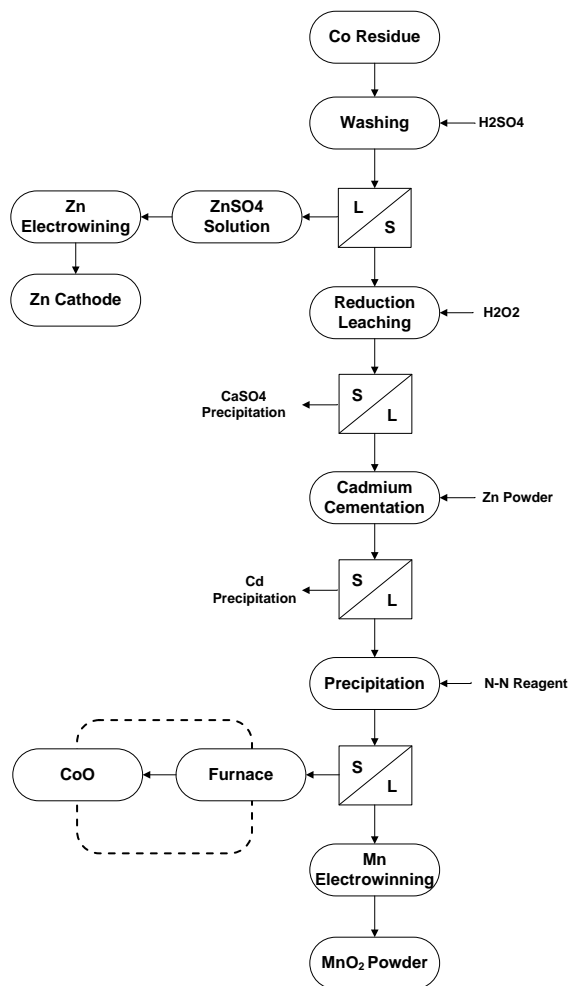
Fig. 9. Flow diagram for the recovery of zinc, manganese and cobalt from zinc plant residues

Working flow sheet

Finally, taking the findings of this study into account, a simplified flow diagram (Fig. 9) was proposed for the process, showing the successive stages based on the process conditions. The laboratory scale experiments including washing by dilute sulfuric

acid, reductive leaching with hydrogen peroxide, cadmium cementation with zinc powder and separation between manganese and cobalt by N-N reagent were performed in order to produce several valuable products from zinc plant residue. Zinc has been recovered from hot filter cake by washing. Filtrate of this stage was sent for electrowining to produce zinc cathode. Residue from previous stage has been leached with hydrogen peroxide for recovering manganese and cobalt. In this stage there was a residue including $CaSO_4$. Filtrate has been used for cadmium removal with zinc powder. Residue of this stage contains cadmium with high grade. Filtrate had manganese and cobalt. Separation between above-mentioned elements was carried out with N-N reagent. After filtration, residue contains cobalt along with beta naphthol. Beta naphthol was burned by furnace and then cobalt oxide was achieved. After cobalt removal, manganese can be recovered from solution by electrowining.

Conclusion

In this research, a hydrometallurgical process has been applied for recovery of valuable metals from Hot Filter Cake of zinc production plant. This process has several stages including: (1) washing zinc, (2) reductive leaching with hydrogen peroxide, (3) cadmium cementation with zinc powder and (4) separation between cobalt and manganese with N-N reagent. This study has mainly focused on the separation of manganese and cobalt from ZPR with N-N reagent. The effect of operating conditions such as N-N quantity, time, pH and temperature on separation between manganese and cobalt was studied. As a result, the ultimate optimum leaching conditions were found to be time: 30 min, temperature: 25 ℃, stirring speed: 900 rpm, N-N quantity: 8 times of stoichiometric value and pH = 1.5. Under this condition, precipitation of cobalt and manganese were 99% and 0%, respectively. Finally, the final precipitate was burned to remove beta naphtol and then cobalt oxide was achieved. A shrinking core model can be used to describe the dissolution kinetics of ZPR in dilute sulfuric acid solution. The dissolution process was found to be controlled by diffusion through a product layer. The activation energy of the dissolution process was found to be 1.4 kJ/mol in the temperature range of 25–80 ℃. The low value of activation energy predicts that Mn extraction should be less sensitive to temperature.

Acknowledgements

References

Abdollahi P., Moradkhani D., Behnian D., Yozbashizadeh H., 2006, *Lead recovery from Iranian zinc plant residue using brine leaching method*. Proceedings of XXII International Mineral Processing Congress, Istanbul Turkey, 1515–1520.

Altundogan H.S., Ozer A., Tumen F., 1992, *Bakir Curuflarinin Asidik Ortamlardaki Agir Metal Cozunurlukleri*, VIII. Kimya ve Kimya Muhendisligi Sempozyumu, 7-11 Eylul 1992. Istanbul, Vol IV, 195–200.

Eivazi A.R.H., Alamdari E. K., Moradkhani D., 2008, *Dissolution kinetics of zinc from zinc plant residue*. In: Young, C.A., (Eds.), Hydrometallurgy 2008, Proceedings of the 6th International Symposium. The Minerals, Metals and Materials Society, Vancouver, Canada, 196–200.

Eivazi A.R.H., Heidari N., Alamdari E.K., Darvishi D., Moradkhani D., 2009, *Dissolution of Co, Mn and Zn from zinc plant residue in H_2O_2-H_2SO_4-H_2O medium*, The 2009's Fifth International conference on Hydrometallurgy, Zhangjiajie, Hunan Province, China.

Eivazi A.R.H., Moradkhani D., Alamdari E.K., Darvishi D., 2008, *Solvent extraction separation of zinc, manganese and cobalt in sulfate solutions by D2EHPA*, International Solvent Extraction Conference, B.A. Moyer, Eds., Vol. I, Tucson, Arizona, USA, 233–238.

Farahmand F., Moradkhani D., Safarzadeh M.S., Rashchi F., 2009, *Brine leaching of lead bearing zinc plant residues: process optimization using orthogonal array design methodology*. Hydrometallurgy 95, 316–324.

Florijn P.J., Van Beusichem M L., 1993, *Uptake and distribution of cadmium in maze inbred lines*, Plant Soil 150, 25–32.

Hatch, 2000, *Review of Environmental Releases for the Base Metals Smelting Sector*, PR36242.002.

Jha M.K., Kumar V., Singh R.J., 2001, *Review of hydrometallurgical recovery of zinc from industrial wastes*. Resour. Conserv. Recycl, 33, 1–22.

Kul, M., Topkaya, Y., 2008, *Recovery of germanium and other valuable metals from zinc plant residues*, Hydrometallurgy, Vol. 92, Issue 3-4, 87–94.

Levenspiel O., 1991, *Chemical Reaction Engineering*, 3rd Edn. John Wiley and Sons, New York.

Raghavan R., Mohanan P.K., Swarnkar S.R., 2000, *Hydrometallurgical processing of lead-bearing materials for the recovery of lead and silver as lead concentrate and lead metal*. Hydrometallurgy 58, 103–116.

Ross S.M., 1994, *Toxic metals in soil–plant systems*. John Wiley & Sons, Chichester, UK.

Safarzadeh M.S., Moradkhani D., Ashtari P., 2009, *Recovery of zinc from Cd–Ni zinc plant residues*. Hydrometallurgy, 97, 67–72.

Safarzadeh M.S., Moradkhani D., Ojaghi-Ilkhchi M., 2005, *Fall, Feasibility studies on the production of cadmium in Iran*. Report no. 202, R&D Center, Iranian Zinc Mines Development Company, Zanjan (in Persian).

Sedaghat B., Moradkhani D., Khodadadi A., Eivazi Hollagh A.R., Koleini S.M.J., 2008, *Study of the effective parameters to transport of hazardous waste from zinc leaching plant to environment*, Hydrometallurgy 2008, Proceedings of the Sixth International Symposium.

Tumen F., 1988, *A Study on the Solubility of Lignite Fly Ash*, Doga TU J. Chem, 12(1), 88–96.

Tumen F., Bildik M., Boybay M., Cici M., Solmaz B., 1992, *Ergani Bakir Isletmesi Kati Atiklarinin Kirlilik Potansiyeli*, Doga Tr. J. of Engineering and Environmental Sciences, 16: 43–53.

Tumen F., Boybay M., Solmaz B., Cici M., Bildik M., 1991, *Elazig Ferrokrom Fabrikasi ve Keban Simli-Kursun Isletmesi Kati Atiklarinin Kirlilik Potansiyeli*, Doga Tr. J. of Engineering and Environmental Sciences, 15: 464–485.

Wang Y., Zhou C., 2002, *Hydrometallurgical process for recovery of cobalt from zinc plant residue*", Hydrometallurgy, Vol. 63, Issue 3, 225–234.

Wentz C. A., 1989, *Hazardous Waste Management*, McGraw-Hill, NewYork.

RELATIONSHIP BETWEEN FLOTATION AND Fe/Mn RATIO OF WOLFRAMITE WITH BENZOHYDROXAMIC ACID AND SODIUM OLEATE AS COLLECTORS

Siyuan YANG[*,**], Qiming FENG[*], Xianyang QIU[**], Yude GAO[**], Zhenfu XIE[*]

[*] School of Mineral Processing and Bioengineering, Central South University, Changsha, China, qmfeng@126.com

[**] Guangzhou Research Institute of Non-ferrous Metals, Guangzhou, China

Abstract: Several studies revealed that flotation of wolframite changes with different Fe/Mn ratios, but they did not reach a consensus. This relationship in the presence of benzohydroxamic acid (BHA) and sodium oleate (NaOl) as collectors was studied in this paper through comparison of probability distribution curve of wolframite with different Fe/Mn ratios between the raw ore and the flotation concentrate, the pure mineral flotation and solution chemistry of flotation. The results showed that wolframite with high Fe/Mn ratio showed higher flotation with BHA as a collector while the flotation behavior of wolframite was completely opposite with NaOl as a collector. Besides, the calculations of chemical equilibrium in the solution were plotted as $\Delta G°$-pH graphs. The results revealed that the flotation of wolframite may be determined by the interaction between BHA and ferric(II) ion or between NaOl and manganous ion. From the perspective of collector mixture, the results also explain the high collecting capability of the BHA/NaOl collector mixture, which can be defined as "functional complementation".

Introduction

Since the discovery tungsten in the last quarter of 18th century, tungsten-based products have been used in a wide range of applications from daily household necessities to highly specialized components of modern science and technology (Koutsospyros et al. 2006; Amer 2000). Most tungsten ores contain less than 1% of WO_3 nowadays (Luo et al. 2003) and wolframite is the common tungsten mineral constituent of economic ore deposits. The traditional ways of wolframite recovery include gravity separation and magnetic separation, while flotation has become an

important method in mineral processing for fine and complex wolframite ore resources, which can be hardly processed by traditional ways (Pradip 1996).

Previous investigations on wolframite flotation have focused on flotation reagents or agglomeration (Srinivas et al. 2004; Hu et al. 1997; Wei et al. 1986; Kelsall and Pitt 1987), but ignore composition, which is also an important factor in wolframite flotation. An empirical formula of wolframite is $(Fe,Mn)WO_4$, an intermediate between two end-members: ferberite $(FeWO_4)$ and huebnerite $(MnWO_{4)}$ (Hsu 1976). The relationship between flotation and component of wolframite has been rarely investigated by researches. Some researchers consider that flotation of wolframite may be determined by manganium(II) ions (Mn^{2+}) of wolframite surface using 1-nitroso-2-naphthol or sodium oleate (NaOl) as a collector (Mclaren 1943; Wang 1986). However, ferric(II) ions (Fe^{2+}) on the surface of wolframite also may react with other collectors.

There are several shortages in previous investigations. First, the flotation of wolframite with different components has not been studied to this point, and, it is necessary for its practical significance. Second, benzohydroxamic acid (BHA) has never been chosen as a collector in existing research, which was already used in Shizhuyuan mine in Hunan Province, China. Noticeably, the Shizhuyuan mine is well-known for its complex and fine wolframite ore (Lu et al. 2003). Third, flotation of wolframite differs at varying Fe/Mn ratio, and may change with collectors. However, this phenomenon has never been linked to the use of BHA/NaOl collector mixture which collecting capability is already proved better than single collectors. There are several explanations for the high efficiency of collector mixtures such as co-adsorption or selective attachment and spreading (Vidyadhar and Hanumantha Rao 2006; Wang et al. 2006) while in wolframite flotation, the high collecting capability of BHA-NaOl collector mixture may be caused by their different collecting capabilities for wolframite, which can be defined as "functional complementation".

In this paper, BHA/NaOl as collectors were adopted to study the relationship between floatability and Fe/Mn ratio of wolframite, and hence the high collecting capability of BHA/NaOl collector mixture in flotation was explained. Probability distribution curves of wolframite with different Fe/Mn ratios between the raw ore and the flotation concentrate, pure mineral flotation and solution chemistry of flotation were compared, respectively.

Materials and methods

Samples and reagents

The wolframite raw ore was obtained from the Miantuwo mine in Guangdong Province, China. It was dry-ground in a porcelain mill, and then screened to -74+38 μm by a sieve. The mineral composition of the wolframite ore selected for experiments was characterized by a MLA-650 mineral liberation analyzer (FEI

Company), and the results are presented in Tables 1 and 2. According to Table 1, wolframite is the main component of tungsten ore, accounting for 94.77%, and thus chemical analysis of WO_3 can be used as an effective way to identify the grade of wolframite. Table 2 shows that the gangue of the Miantuwo wolframite ore is simple because the main existing forms are quartz (83.59%), mirrorstone (8.42%), and orthoclase (3.9%).

Table 1. Occurrence state of tungsten in Miantuwo raw ore

Mineral	WO_3 (%)	Relative Proportion (%)
Wolframite	0.598	94.77
Sheelite	0.0329	5.23
Total	0.631	100.00

Table 2. Mineral component of Miantuwo raw ore

Mineral	Content (%)	Mineral	Content (%)	Mineral	Content (%)
Wolframite	0.731	Orthoclase	3.9	Chlorite	0.13
Sheelite	0.038	Limonite	0.21	Kaolinite	0.58
Quartz	83.59	Biotite	0.21	Magnetite	0.39
Mirrorstone	8.42	Molybdenite	0.21	Other Minerals	0.772
Fluorite	0.3	Albite	0.52		

On the other hand, the pure minerals of wolframite were obtained from the Yaoling mine in Guangdong and Hukeng mine in Jiangxi Province of China. After the selection by repeated elutriation and dry magnetic separation, they were dry-ground with a porcelain mill, and screened to -74+38 μm by sieves. Yaoling and Hukeng wolframite were assayed to contain 72.20% and 72.30% WO_3 with a Fe/Mn ratio of 1.672 and 0.205, respectively.

BHA used as a collector is 95% pure, while the other collector NaOl, and the pH regulator are analytically pure. Terpineol used as a frother and sodium silicate used as a regulator are commercially pure. Double distilled water was used for all tests.

Experiments and Methods

Flotation tests

The flotation tests were carried out using a XFG-type laboratory flotation machine (0.5 dm^3 flotation tank) with a fixed impeller speed at 1800 rpm. The slurry was prepared by adding 125 g of wolframite to 500 cm^3 of distilled water, and then adjusted to the desired pH by adding a 10% mass fraction of sodium carbonate stock solution. After that, the collector mixtures (BHA and NaOl), depressor (sodium silicate), and frother (terpineol) were added to the slurry as experiments required with

conditioning period of 3, 3, and 1 min respectively. The flotation concentrates were then collected in 3 min. Both the floated and the unfloated particles were filtered, dried, weighed, and chemical analyzed to acquire the grade and the flotation recovery of the concentrates.

Micro flotation tests

The micro flotation tests were performed using a XFG-type laboratory flotation machine with a 40 cm^3 flotation tank. The slurry was prepared by adding 2 g of wolframite to 40 cm^3 of distilled water, and agitated for 1 min. Then, the pH of the slurry was adjusted to the desired value by adding a 0.5 mol/dm^3 HCl or NaOH stock solution. After that, the slurry was conditioned for 3 and 1 min, respectively, after adding the collector or frother, and the flotation time was kept as 3 min. The concentrate and the tailings were filtered, dried, and weighed to calculate the flotation recovery of wolframite.

Electron probe X-ray microanalysis

The precise contents of Fe and Mn in wolframite for each test sample was detected by an electron probe micro analyzer (EPMA), which is widely used in precise detection of composition of mineral particles (Pownceby et al. 2007; Chryssoulis and Dimov 2004; Jercinovica et al. 2008). The raw wolframite ore and the flotation concentrate were enriched by repeated elutriation to obtain an appropriate testing sample. About thirty wolframite particles of each sample were tested and divided into 10 intervals to draw probability distribution curves. All the samples were measured under almost 0 mm beam spot, 2×10^{-8} A, and 20 kV using JXA-8100 EPMA.

Results and discussion

Flotation tests

Figure 1 shows the probability distribution curves of different Mn/Fe ratios of wolframite for the raw ore. Clearly, the wolframite with high Fe content (Fe/Mn > 1) accounted for a larger proportion which is 69.3% (area ratio, similarly hereinafter), and the distribution of components in entire wolframite particles showed a great difference. The different Fe/Mn ratios of wolframite were distributed in the whole 10 intervals, and the largest highest relative frequency of it was only accounted for 0.2.

The results of wolframite flotation at the same dosage but different BHA-to-NaOl ratios are shown in Fig. 2. The recovery and the grade of wolframite are 57.27% and 12.38%, respectively, with BHA as a single collector, and 55.13% and 1.34%, respectively, with NaOl as a single collector. Besides, the separation efficiency was significantly improved when the collector mixture of BHA and NaOl was used, especially at the ratio of 3:1 where the recovery and the grade of wolframite reached to 89.47% and 6.37%, respectively.
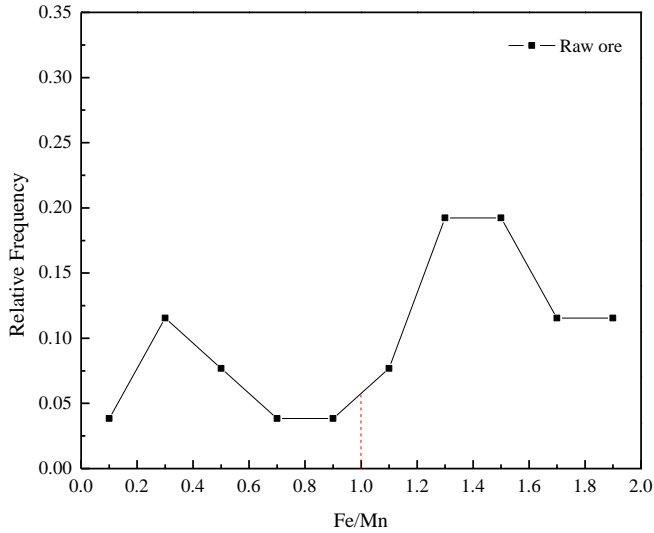
Fig. 1. Probability distribution curve of wolframite with different Fe/Mn ratios in raw ore
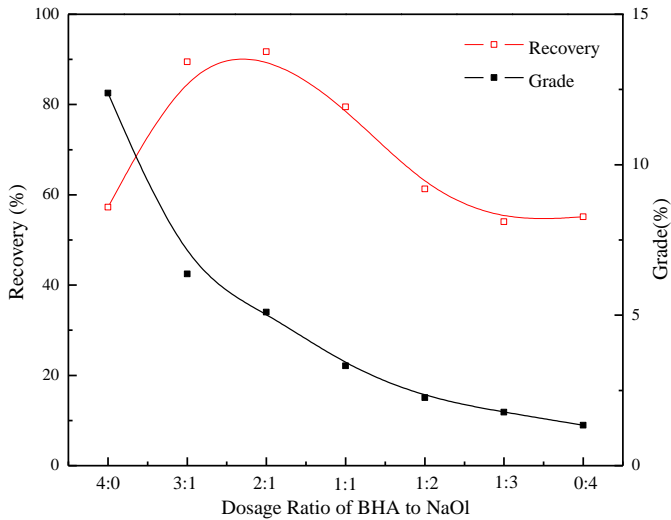
Fig. 2. Relationship between dosage ratios of collectors and collecting capability of Miantuwo wolframite ore (NaOl = 150 mg/dm^3, sodium silicate = 125 mg/dm^3, terpineol = 10 mg/dm^3; pH = 10±0.1)

Figures 3 and 4 show the probability distribution curves of wolframite at different Fe/Mn ratios using BHA and NaOl as a single collector, respectively. On one hand, the distribution of wolframite with high Mn content (Fe/Mn < 1) in concentrate considerably increased compared to that of the raw ore using NaOl as a collector. The percentage of wolframite with high Mn content increased from 30.7% for the raw ore to 43.3% in the concentrate which indicated that the floatability of wolframite

increased with manganese content in the mineral. On the other hand, the flotation behavior of wolframite was completely opposite when BHA as a collector was used. The percentage of wolframite with high Mn content decreased from 30.7% for the raw ore to 23.3% in the concentrate. Thus, the separation efficiency of wolframite ore flotation could be drastically improved with the collector mixture of BHA and NaOl which has different collecting capability (shown as Fig. 2).
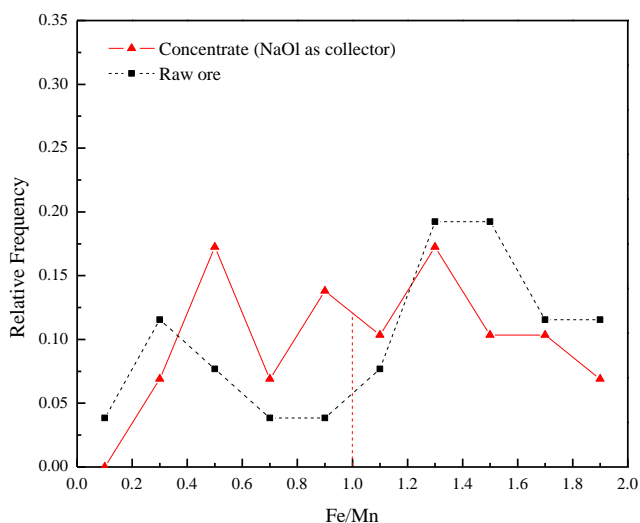
Fig. 3. Probability distribution curve of wolframite with different Fe/Mn ratios with NaOl as a collector (NaOl = 150 mg/dm^3; sodium silicate = 125 mg/dm^3; terpineol = 10 mg/dm^3; pH = 10±0.1)
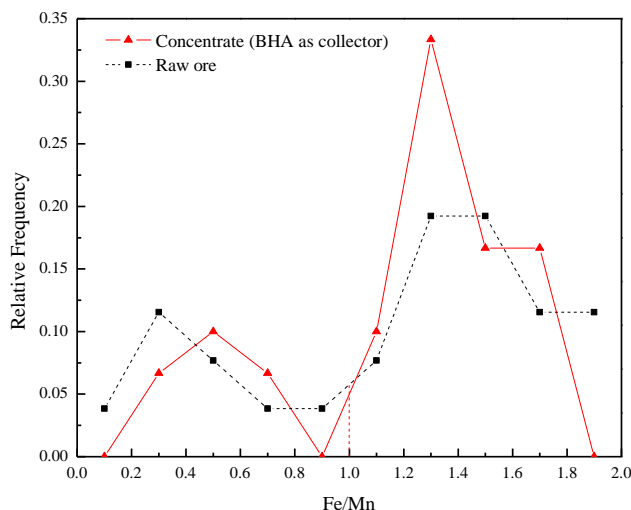
Fig. 4. Probability distribution curve of wolframite with different Fe/Mn ratios with BHA as a collector (BHA= 150 mg/dm^3, sodium silicate = 125 mg/dm^3, terpineol = 10 mg/dm^3; pH = 10±0.1)

In order to further prove the results obtained from this study, the micro flotation tests of wolframite from the Yaoling and Hukeng mine (size fraction: -74+38 μm) were conducted. The results are shown in Figs. 5 and 6, respectively. Evidently, the flotation recovery of Yaoling wolframite (Fe/Mn = 1.672) was significantly higher
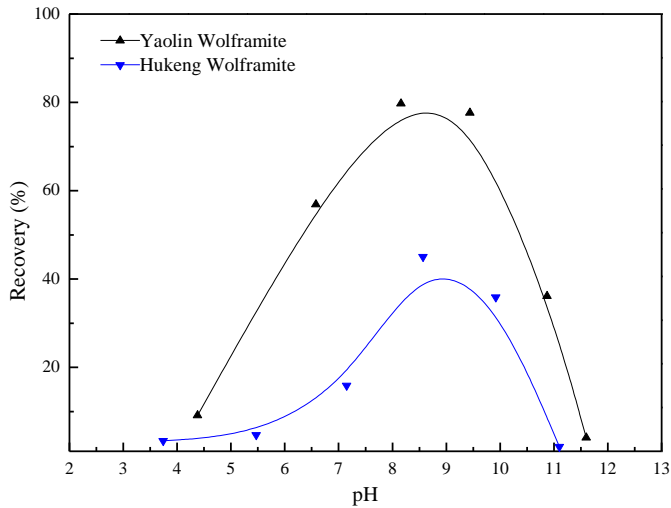
Fig. 5. Flotation recovery of wolframite (size fraction: -74+38 μm) as a function of pH with BHA as a collector (Fe/Mn (Yaoling) =1.672; Fe/Mn (Hukeng) =0.205, BHA = 100 mg/dm^3, MIBC = 20 mg/dm^3)
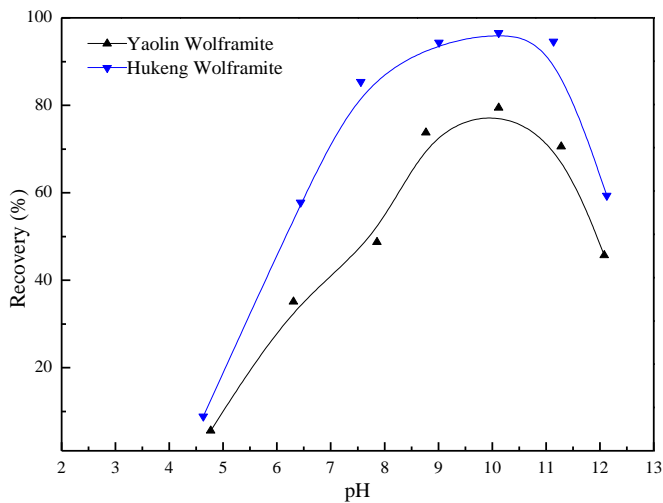
Fig. 6. Recovery of wolframite (size fraction: -74+38 μm) as a function of pH with NaOl as a collector (Fe/Mn (Yaoling)=1.672; Fe/Mn (Hukeng) = 0.205, NaOl = 30.4 mg/dm^3)

than that of Hukeng wolframite (Fe/Mn=0.205) at the studied pH range when BHA as a collector was sued. The maximum recovery of Yaoling wolframite was 79.7% while Hukeng wolframite was only 45.05%. Moreover, the pH range suitable for the flotation increased as well. However, the floatability of wolframite was completely opposite when NaOl as a collector was used. The maximum recovery was 79.45% and 96.6%, for Yaoling wolframite and Hukeng wolframite, respectively.

Calculations of chemical equilibrium in solution

As known from the literature that the role between the flotation reagent and metallic ion on the surface of mineral is related to their interactions in solution (Somasundaran and Wang 2006). The reactions between metallic ions of wolframite and anionic collector ion are considered as follows:

$$Mn^{2+} + 2R^- \Leftrightarrow MnR_{(2s)} \tag{1}$$

$$Fe^{2+} + 2R^- \Leftrightarrow MnR_{(2s)} \tag{2}$$

for BHA, $Ksp_{(MnR2)}=10^{-12.6}$, $Ksp_{(FeR2)}= 10^{-15.1}$. For NaOl, $Ksp_{(MnR2)}=10^{-15.3}$, $Ksp_{(FeR2)} = 10^{-15.4}$. Ksp stands for solubility product. In addition, the second reaction of R^- with a proton is given below:

$$H^+ + R^- \Leftrightarrow HR; K^H = [HR]/[H^+][R^-] \tag{3}$$

K^H is equal to $10^{-8.9}$ and 10^{-6} for BHA and NaOl respectively (Galvez et al. 2005; Somasundaran and Wang 2006).

Hydrolysis of metallic ions (Sillen and Martell 1964):

$$Mn^{2+} + OH^- \Leftrightarrow Mn(OH)^+$$

$$K_1 = \frac{[Mn(OH)^+]}{[Mn^{2+}][OH^-]} = 10^{3.4} \tag{4}$$

$$Mn^{2+} + 2OH^- \Leftrightarrow Mn(OH)_{2(s)}$$

$$K_s = [Mn^{2+}][OH^-]^2 = 3.9 \times 10^{-14} \tag{5}$$

$$Fe^{2+} + OH^- \Leftrightarrow Fe(OH)^+$$

$$K_1 = \frac{[Fe(OH)^+]}{[Fe^{2+}][OH^-]} = 10^{4.5} \tag{6}$$

$$Fe^{2+} + 2OH^- \Leftrightarrow Fe(OH)_{2(l)}$$
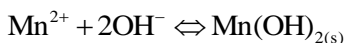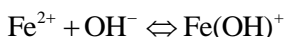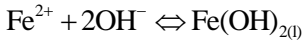
$$K_1 = \frac{[Fe(OH)_2]}{[Fe^{2+}][OH^-]^2} = 10^{7.4} \tag{7}$$

$$Fe^{2+} + 2OH^- \Leftrightarrow Fe(OH)_{2(s)}$$
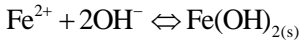
$$K_s = [Fe^{2+}][OH^-]^2 = 2.2 \times 10^{-18} \tag{8}$$

Ksp' is assumed to be the conditional solubility product. From Eqs. (1) to (8), standard free enthalpy for the above reaction can be calculated as (Somasundaran and Wang 2006):

$$\Delta G^\circ = RT \ln Ksp' = RT \ln(Ksp \times \alpha_M \times \alpha_R^2) \tag{10}$$

$$\alpha_M = 1 + K_1[OH] + K_2[OH]^2 + K_s^{-1}[OH]^2 \tag{11}$$

$$\alpha_R = 1 + K^H[H] \tag{12}$$

where α_M is the conditional hydrolysis constant of metallic ions of wolframite and α_R is the second proton constant of collector ions. Then, from Eqs. (9) to (11),

$$\Delta G^\circ = RT \ln((Ksp \times (1 + K_1[OH] + K_2[OH]^2 + K_s^{-1}[OH]^2) \times (1 + K^H[H])^2). \tag{13}$$

According to the data seen above, ΔG–pH graphs for Fe^{2+} and Mn^{2+} on the surface of wolframite with collectors of BHA and NaOl can be plotted and shown in Figs. 7 and 8.
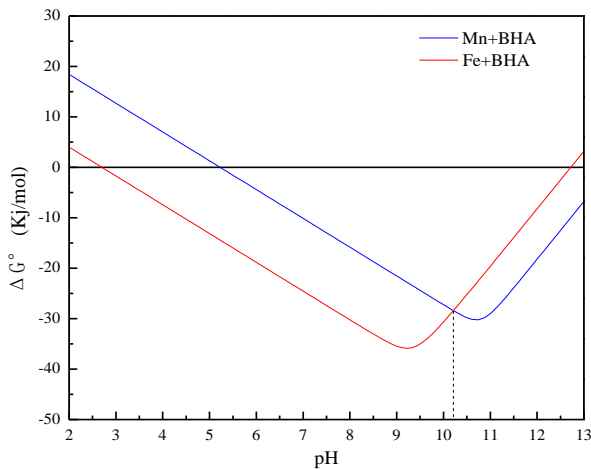
Fig. 7. ΔG° value of BHA reacting with Mg^{2+} or Fe^{2+} as function of pH
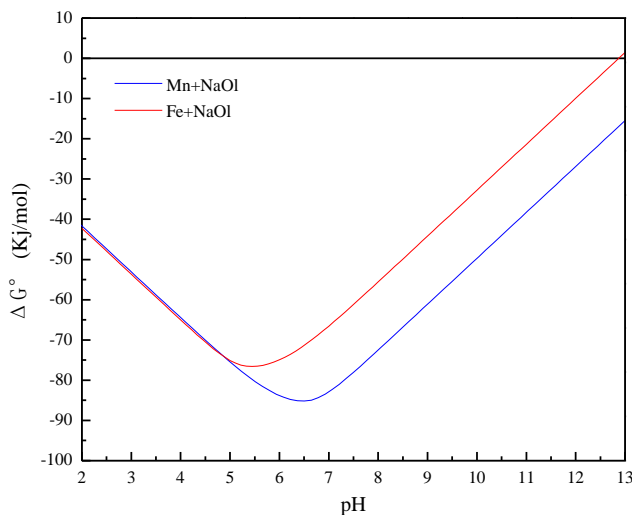
Fig. 8. $\Delta G°$ value of NaOl reacting with Mg^{2+} or Fe^{2+} as function of pH

Figure 7 shows that $\Delta G°$ of Fe^{2+} reacting with BHA is negatively higher compared with Mn^{2+} at less than pH 10.2, which means that BHA prefers to react with Fe^{2+} at that pH range. After that, Mn^{2+} plays a dominant role in the collector system while the $\Delta G°$ is already positively moved which means that solution is too alkali to float. On the other hand, Fig. 8 shows that $\Delta G°$ of Mn^{2+} reacting with NaOl is negatively higher compared with Fe^{2+} at the pH range of 5-13, which is the same pH range of flotation experiment. Therefore, the flotation behavior of wolframite may be determined by the interaction between Mn^{2+} and NaOl. Thus, these thermodynamic data agree with the results obtained from the flotation experiments.

Conclusions

1. Through comparing the probability distribution curve of wolframite with different Fe/Mn ratios for the raw ore and flotation concentrate, the percentage of wolframite with high Mn content (Fe/Mn<1) decreased from 30.7% for the raw ore to 23.3% for the concentrate with benzohydroxamic acid (BHA) as a collector. On the other hand, it increased from 30.7% for the raw ore to 43.3% for the concentrate with sodium oleate (NaOl) as a collector. These results strongly indicate that the flotation of wolframite is determined by iron(II) ions (Fe^{2+}) on the surface of wolframite with BHA while manganium(II) ions (Mn^{2+}) play a dominant role in the collecting system of NaOl.
2. The micro flotation tests showed that the single mineral of wolframite with high Fe/Mn ratio is more floatable with BHA but harder to float with NaOl. This conclusion corresponds to the results of flotation tests of wolframite.

3. $\Delta G°$-pH graphs showed that BHA prefers to react with Fe^{2+} while Mn^{2+} shows higher chemical activity in the collecting system of NaOl, which clearly explain the mechanism of different floatabilities of wolframite with different collectors.
4. The separation efficiency of wolframite ore flotation was significantly improved with the collector mixture of BHA and NaOl. Their different collecting capabilities explain the high collecting capability of the collector mixture which can be defined as "functional complementation".

Acknowledgements

References

AMER A. M., 2000, *Investigation of the direct hydrometallurgical processing of mechanically activated low-grade wolframite concentrate*, Hydrometallurgy, 58(3), 251–259.

CHRYSSOULIS S.L., DIMOV S.S., 2004, *Optimized conditions for selective gold flotation by ToF-SIMS and ToF-LIMS*, Applied Surface Science, 231–232, 265–268.

GÁLVEZ N., RUIZ B., CUESTA R., COLACIO E., DOMÍNGUEZ–VERA J.M., 2005, *Release of iron from ferritin by aceto- and benzohydroxamic acids*, Inorganic Chemistry, 44(8), 2706–2709.

HSU L.C., 1976, *The stability relations of the wolframite series*, American Mineralogist, 61, 944–955.

HU Y., WANG D., XU Z., 1997, *A study of interactions and flotation of wolframite with octyl hydroxamate*, Minerals Engineering, 10(6), 623–633.

JERCINOVICA M.J., WILLIAMSA M.L., LANE E.D., 2008, *In–situ trace element analysis of monazite and other fine–grained accessory minerals by EPMA*, Chemical Geology, 254(3–4), 197–215.

KELSALL G. H., PITT J. L., 1987, *Spherical agglomeration of fine wolframite ((Fe, Mn)WO$_4$) mineral particles*, Chemical Engineering Science, 42(4), 679–688.

KOUTSOSPYROS A., BRAIDA W., CHRISTODOULATOS C., DERMATAS D., STRIGUL N., 2006, *A review of tungsten: from environmental obscurity to scrutiny*, Journal of Hazardous Materials, 136(1), 1–19.

LU H.Z., LIU Y., WANG C., XU Y., LI H., 2003, *Mineralization and fluid inclusion study of the Shizhuyuan W-Sn-Bi-Mo-F skarn deposit*, Hunan Province, China, Economic Geology, 98(5), 955–974.

LUO L., MIYAZAKI T., SHIBAYAMA A., YEN W., FUJITA T., 2003, *A novel process for recovery of tungsten and vanadium from a leach solution of tungsten alloy scrap*, Minerals Engineering, 16(7), 665–670.

MCLAREN, D.C., 1943, *Flotation of tungsten ores*, Canadian Mining Journal, 64, 8–13.

POWNCEBY M.I., MACRAE C.M., WILSON N.C., 2007, *Mineral characterisation by EPMA mapping*, Minerals Engineering, 20(5), 444–451.

PRADIP 1996, *Recent advances in the recovery of tungsten values in the fine and ultrafine size range*, Bulletin of Materials Science, 19(2), 267–293.

SILLÉN L.G., MARTELL A.E., 1964, *Stability constants of metal–ion complexes*, London: Chemical Society, sec. II, ligands.

SOMASUNDARAN P., WANG D., 2006, *Solution chemistry: minerals and reagents* (Vol. 17), Access Online via Elsevier, 8 and 116.

SRINIVAS K., SREENIVAS T., PADMANABHAN N. P. H., VENUGOPAL R., 2004, *Studies on the application of alkyl phosphoric acid ester in the flotation of wolframite*, Mineral Processing and Extractive Metallurgy Review: An International Journal, 25(4), 253–267.

VIDYADHAR A., HANUMANTHA RAO K., 2006, *Adsorption mechanism of mixed cationic/anionic collectors in feldspar–quartz flotation system*, Journal of Colloid and Interface Science, 306(2), 195–204.

WANG D., 1986, *Flotation behavior of wolframite with different components*, Journal of Central South Institute of Mining and Metallurgy, 4, 40–45.

WANG X., NGUYEN A.V., MILLER J.D., 2006, *Selective attachment and spreading of hydroxamic acid–alcohol collector mixtures in phosphate flotation*, International Journal of Mineral Processing, 78(2), 122–130.

WEI D., WEI K., QIU J., 1986, *Hydrophobic agglomeration and spherical agglomeration of wolframite fines*, International Journal of Mineral Processing, 17(3–4), 261–271.

FLOTATION OF LIGNITE PRETREATED BY SORBITAN MONOOLEATE

Wenjun ZHANG, Xiaoyan TANG

Low Carbon Energy Institute, School of Chemical Engineering and Technology, China University of Mining and Technology, Xuzhou 221116, Jiangsu, China, wjzhang_cumt@126.com

Abstract: In this study, sorbitan monooleate was used to pretreat lignite prior to flotation tests. First, the lignite sample and water were mixed with 0%, 0.5%, 1%, 1.5% and 2% (on the basis of the weight of the coal) of sorbitan monooleate to produce five types of flotation slurries. FTIR, XPS and SEM were used to analyze the surface properties of the lignite sample. The flotation tests were used to indicate the improvements in flotation of lignite after the sorbitan monooleate pre-treatment. FTIR and XPS results showed that there are many oxygenated functional groups in lignite such as carboxyl group and hydroxyl groups. Furthermore, SEM results showed that there are many holes on the lignite surface. These holes will be filled with water in the flotation pulp. The flotation results indicated that sorbitan monooleate can improve the lignite flotation at low concentrations of sorbitan monooleate. However, the flotation behavior of lignite deteriorated at higher concentrations of sorbitan monooleate.

Keywords: sorbitan monooleate, flotation, lignite, FTIR, XPS, SEM

Introduction

Flotation is a common and useful method to upgrade fine coals (<0.5 mm). Flotation usually uses the difference in hydrophobicity between coals and minerals to obtain froth product. However, it is recognized that lignite is difficult to float using oily collectors. Atesok and Celik (2000) achieved a remarkable increase in combustible matter recovery and a decrease in ash content using an addition of pitch in dry grinding process of low rank coal. Celik and Seyhan (1995) investigated the effect of heat treatment on the improvement in hydrophobicity of lignite. Lignite hydrophobicity would have a remarkable increase after heat treatment at 105 °C for 4 hr (Cinar, 2009). Ozbayoglu et al. (2009) found that microwave radiation could improve the flotation of lignite since the moisture content in pore or on the surface of lignite could be reduced. Lignite became easy to float as the hydrophobicity of lignite could be raised using microwave treatment. At the same time, Taixi oxidized coal in China is also difficult to float as

oxidized coal surface has some similar properties to lignite surface, and oxidized coal flotation can be improved by pretreatments (Xia et al. 2012, 2013).

In addition, surfactants have been widely applied in improving low rank coal flotation (Yu et al. 1990; Burkin and Bramley 1963; Aston et al. 1981; Chander et al. 1987; Moxton et al. 1987; Jia et al. 2000). Surfactants were added at low concentrations may make coal hydrophobic, whereas, at high concentration, they may make it hydrophilic. The conditions for flotation of lignite of Tuncbilek were investigated to achieve the best flotation performance since flotation conditions always had a significant effect on coal flotation (Sahbaz 2013; Li et al. 2013).

In this study, sorbitan monooleate was used to improve the flotation of Neimeng lignite from China. The effect of different sorbitan monooleate concentrations on flotation performance of lignite was investigated. Fourier Transform Infrared (FTIR), X-ray Photoelectron Spectroscopic (XPS), and Scanning Electron Microscopy (SEM) were used to analyze the surface properties of the lignite. The flotation tests were performed to indicate the improvements in the flotation of the lignite after sorbitan monooleate pretreatment, and FTIR, XPS, and SEM results were used to understand the flotation behavior of the lignite.

Materials and methods

Materials

The coal samples were obtained from Neimeng Province of China. The samples were dry-ground in a laboratory mill to pass 0.074 mm sieve. The proximate analysis of lignite samples can be shown as follows, M_{ad}=8.12%, V_{ad}=20.49%, FC_{ad}=41.31%, A_{ad}=30.08%, S_t=1.67%, where M_{ad} is the moisture content, V_{ad} the volatile content, FC_{ad} the fixed carbon content, A_{ad} the ash content, and S_t is the total sulfur content on a dry basis. Sorbitan monooleate used in this study was supplied by Shanghai in China.

Methods

FTIR, XPS and SEM measurements

A Perkin Elmer Spectrum 2000 model spectrometer was used for the FTIR analyses, and the spectrum was obtained at 2 cm^{-1} resolution, between 4000 and 400 cm^{-1}. FTIR spectrum of lignite was obtained with KBr pellets, prepared with <0.074 mm coal samples and analytical grade KBr. The ratio of the coal to KBr was 1 to 100.

The XPS experiments were carried out at room temperature in an ultra high vacuum (UHV) system with the surface analysis system (ESCALAB 250Xi, America). The base pressure of the analysis chamber during the measurements was lower than 1.0×10^{-7} Pa. Al Ka radiation (hv=1486.6 eV) from a monochromatized X-ray source was used for XPS. For all analyses, the take-off angle of the photoelectrons was 90° and the spot size was 900 μm. The spectra of survey scan were recorded with the pass energy of 100 eV; the energy step size was 1.00 eV. High resolution spectra were recorded with the pass

energy of 20 eV, and the energy step size was 0.05 eV. The data processing (peak fitting) was performed with XPS Peakfit software using a Smart type background subtraction and Gaussian/Lorentzian peak shapes. The binding energies were corrected by setting the C1s hydrocarbon ($-CH_2-CH_2-$bonds) peak at 284.6 eV.

The FEI Quanta 250 SEM was used to analyze the surface morphology of lignite. The magnification times were fixed at 1000, 2000, 4000 and 10000. The coal samples were prepared by surface cleaning using absolute ethyl alcohol. After the surface cleaning, the coal samples were dried in air. Before the SEM, the coal samples were sputter-coated with a layer of gold. The details operating parameters of the SEM were as follows: HV was 30.00 kV; WD was 20.2 mm; Pressure was $1.21.10^{-4}$ Pa; Spot was 2.5.

Flotation tests

Diesel and 2-octanol was used as collector and frother, respectively. The flotation tests were conducted in a 1.5 dm^3 XFD flotation cell using 100 g of coal for each flotation test. The impeller speed of flotation machine was kept as 1910 rpm, and airflow rate was 1.2 dm^3/min. Collector dosage was 10 kg/Mg coal, and frother dosage was 1 kg/Mg. Sorbitan monooleate concentration were as 0%, 0.5%, 1%, 1.5% and 2% (on the basis of the weight of the lignite).

For each test, the pulp was first agitated in the flotation cell for 1 min, and second sorbitan monooleate was added, and agitated for an additional 3 min. After this, diesel was added to the pulp, and agitated for another 3 min. Then, the frother was, and the pulp was conditioned for an additional minute. At last, the air inlet was opened and the froth product was collected.

The flotation concentrate was analyzed by three indexes: Combustible matter recovery, Flotation efficiency index, and Ash content. Eq. (1) and (2) were used to calculate the combustible matter recovery and flotation efficiency index for the flotation experiments:

$$Combustible\ Matter\ Recovery\ (\%) = \frac{M_C(100 - A_C)}{M_F(100 - A_F)} \cdot 100 \tag{1}$$

$$Flotation\ Efficiency\ Index\ (\%) = \frac{M_C(A_F - A_C)}{M_F A_F(100 - A_F)} \cdot 100 \tag{2}$$

where M_C is weight of the concentrate (%), M_F weight of the feed (%), A_C the ash content of the concentrate (%), and A_F is the ash content of the feed (%).

Results and Discussion

FTIR, XPS and SEM analysis

As shown in Fig. 1, FTIR spectrum of lignite shows that C-C, CH_3 and CH_2 stretching vibration region are characterized by peaks at 2920 cm^{-1} and 2850 cm^{-1}. The peak at

1384 cm^{-1} may be -CH$_3$ stretching vibration. The peaks around 1100 cm^{-1}, 1190 cm^{-1} and 1035 cm^{-1} may be attributable to C-O-C vibration (Sun et al. 2010). The peaks at 3420 cm^{-1} is for OH, at 1620 cm^{-1} is for C=O or COOH. The peaks around 697 cm^{-1} and 915 cm^{-1} indicate the presence of benzene rings. However, the major hydrophobic functional groups at 1430 cm^{-1} for R-H and at 3030 cm^{-1} for aromatic hydrogen groups cannot be found in this spectrum (Yuh and Wolt 1983; Jena et al. 2008). The peaks around 3600 cm^{-1} may be attributed to the moisture content in lignite. It indicates that lignite has few hydrophobic functional groups but many oxygen containing functional groups on its surface. Therefore, lignite is difficult to float with common oily collectors.
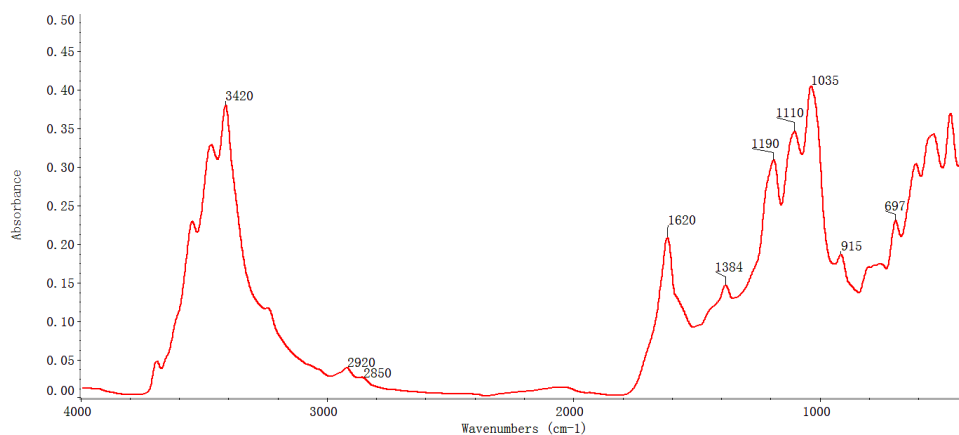
Fig. 1. FTIR spectrum of lignite

The binding energies corresponding to appropriate peaks in coals are as follows. C1s peaks at binding energies of 284.6 eV, 286.1 eV, 287.6 eV and 289.1 eV are corresponding to the following groups: C-C or C-H, C-O (alcohol, phenol or ether), C=O (carbonyl or chinone) or O-C-O (in low rank coals) and COO$^-$ (carboxyl) (Desimoni et al. 1990, 1992; Fiedler and Bendler 1992; Xia and Yang, 2013a, 2013b).

The C1s peaks are fitted as shown in Fig. 2. The relative contents of carbon forms on the surface of lignite are calculated. The content of C-C and C-H groups is 5.64%. The content of C-O group is 60.75%. The content of C=O group is 25.65% and the content of COOH group is 7.96%. Hydrophilic functional groups are C=O, C-O and COOH. Hydrophobic functional groups are C-H and C-C. The content of hydrophobic functional groups is very small while that of hydrophilic functional groups is very high. Hydrophilic functional groups will be bonded with water by hydrogen bond, and lignite coal surface will be covered by a thick hydration shell in flotation pulp. Therefore, lignite is difficult to float.

As shown in Fig. 3, surface morphology of lignite is rough with lots of holes. Lignite surface is like a honeycomb. These holes will be filled with water in flotation pulp. Lignite surface will be covered by a thick hydration shell in flotation pulp and become hydrophilic. Therefore, lignite is difficult to float.
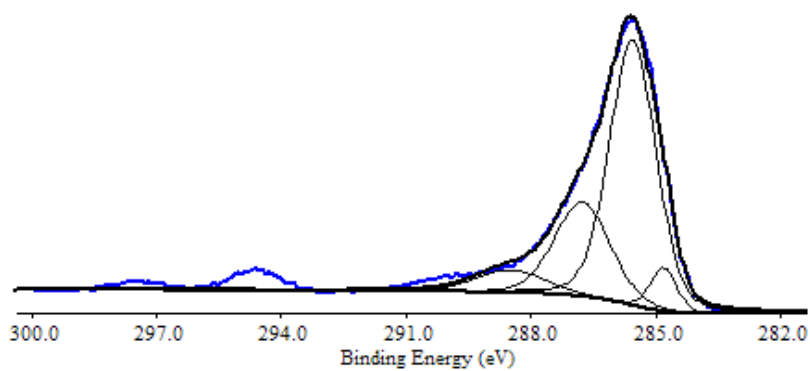
Fig. 2. C1s peaks of lignite
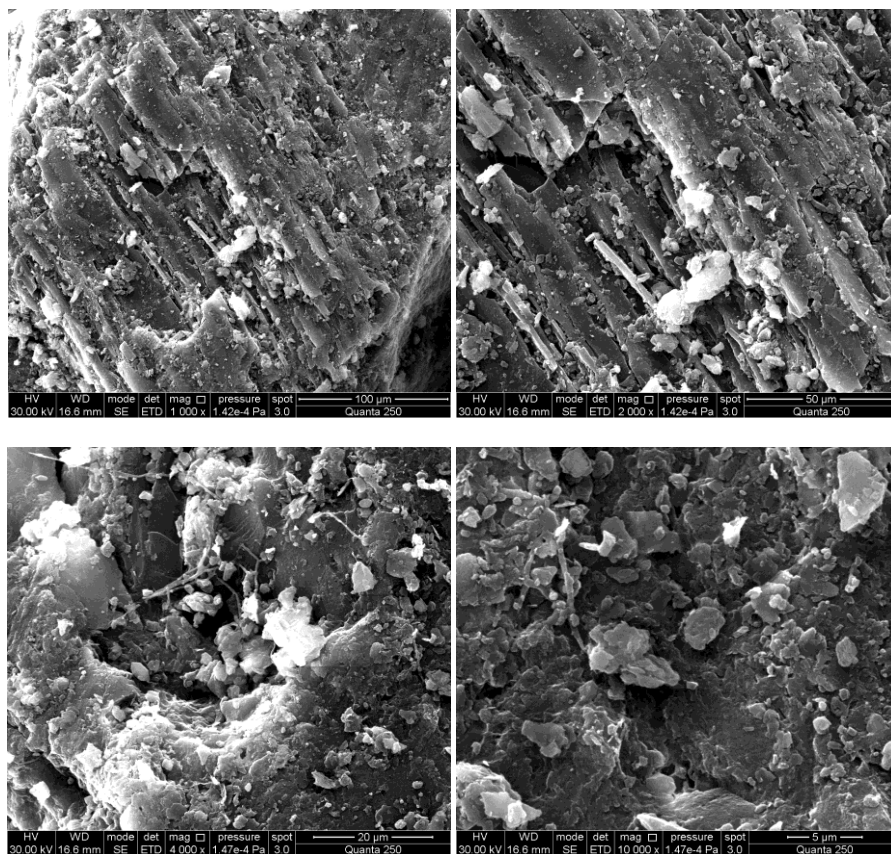
Fig. 3. SEM results of lignite surface

Flotation Experiments

Figure 4 shows that both combustible matter recovery and flotation efficiency index increase with the increase of sorbitan monooleate dosage while sorbitan monooleate dosage is less than 1%. However, both of them decrease with the increase of sorbitan monooleate dosage while it is more than 1%. Sorbitan monooleate can cover lignite surface. It indicates that lignite hydrophobicity may be enhanced by sorbitan monooleate at low concentrations and decreased at high concentrations. In addition, the viscosity of flotation pulp may be increased by a high sorbitan monooleate concentration. A higher viscosity of flotation pulp has a bad effect on flotation recovery. Therefore, lignite particles cannot be easy to float by bubbles in a higher viscosity. Meanwhile, the probable mechanism for decreasing flotation efficiency at higher concentrations of sorbitan monooleate may be a production of bilayer adsorption. Under a higher concentration of sorbitan monooleate, the sorbitan monooleate may cover the coal surface as a bilayer. Therefore, the flotation performance may be damaged by higher concentrations of sorbitan monooleate.

From the ash content in Fig. 4, the ash content has an opposite change compared with the changes of the combustible matter recovery and flotation efficiency index. The lowest ash content is obtained at sorbitan monooleate concentration of 1%.
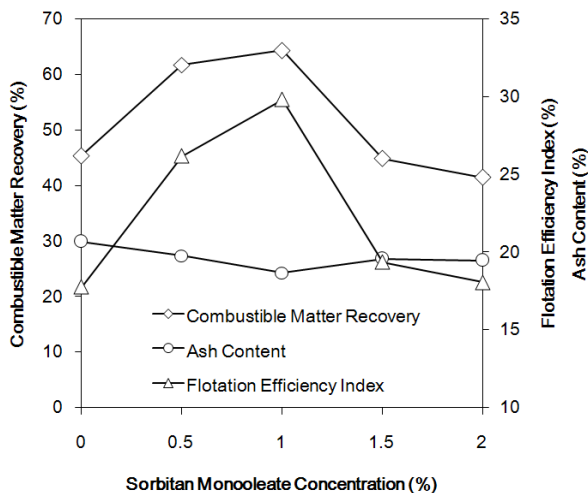
Fig. 4. Flotation results of lignite pre-treated by sorbitan monooleate

Conclusions

FTIR and XPS results show that there are many oxygenated functional groups in lignite such as carboxyl group and hydroxyl groups. SEM result shows that there are many holes on lignite surface. These holes will be filled with water in flotation pulp. Lignite has few hydrophobic functional groups but many oxygen containing functional groups

on its surface. It indicates why lignite is difficult to float with common oily collectors. Therefore, sorbitan monooleate was used to enhance the flotation recovery of lignite.

Flotation performance of lignite can be enhanced by sorbitan monooleate. The optimal sorbitan monooleate concentration was 1% in this paper. Higher sorbitan monooleate concentration showed an opposite effect on the flotation performance of lignite. Under a higher concentration of sorbitan monooleate, the sorbitan monooleate may cover the coal surface as a bilayer. In addition, the viscosity of flotation pulp may be increased by a high sorbitan monooleate concentration. A higher viscosity of flotation pulp also showed a bad effect on the flotation recovery.

Acknowledgements

References

ASTON J.R., DEACON M.J., FURLONG D.N., HELY T.W., LAU A.C.M., 1981, *The chemistry of non-ionic surfactants, preparation processes*, Proceedings of the first Australian coal preparation congress, Newcastle, Australia, 358–378.

ATESOK G., CELIK M.S., 2000, *A new flotation scheme for a difficult-to-float coal using pitch additive in dry grinding*, Fuel, 79(12), 1509-1513.

BURKIN A.R., BRAMLEY J.V., 1963, *Flotation with insoluble reagents II, effect of surface active reagents on the spreading of oil at coal–water interface*, Journal of Applied Chemistry, 13, 417–422.

CELIK M.S., SEYHAN K., 1995, *Effect of heat treatment on the flotation of Turkish lignites*, International Journal of Coal Preparation and Utilization, 16, 65–79.

CHANDER S., MOHAL B., APLAN F.F., 1987, *Wetting behavior of coal in the presence of some non-ionic surfactants*, Journal of Applied Chemistry, 13, 205–216.

CINAR M., 2009, *Floatability and desulfurization of a low-rank (Turkish) coal by low-temperature heat treatment*, Fuel Processing Technology, 90(10), 1300–1304.

DESIMONI E., CASELLA G.I., MORONE A., SALVI A.M. 1990, *XPS determination of oxygen-containing functional groups on carbon-fibre surfaces and the cleaning of these surfaces*, Surface and Interface Analysis,15, 627–634.

DESIMONI E., CASELLA G.I., SALVI A.M. 1992, *XPS/XAES study of carbon fibres during thermal annealing under UHV conditions*, Carbon, 30, 521–526.

FIEDLER R., BENDLER D. 1992, *ESCA investigations on Schleenhain lignite lithotypes and the hydrogenation residues*, Fuel, 71, 381–388.

JENA M.S., BISWAL S.K., RUDRAMUNIYAPPA M.V., 2008, *Study on flotation characteristics of oxidised Indian high ash sub-bituminous coal*, International Journal of Mineral Processing, 87, 42–50.

JIA R., HARRIS G.H., FUERSTENAU D.W., 2000, *An improved class of universal collectors for the flotation of oxidized and for low-rank coal*, International Journal of Mineral Processing, 58, 99–118.

LI Y., ZHAO W., XU S., XIA, W., 2013, *Changes of size, ash and density of coal particles on the column axis of a liquid-solid fluidized bed*, Powder Technology, 245: 251–254.

MOXTON N.T., KEAST-JONES B., NICOL S.K., 1987, *Insoluble oils in coal flotation: the effects of surface spreading and pore penetration*, International Journal of Mineral Processing, 21, 261–274.

OZBAYOGLU G., DEPCI T., ATAMAN N., 2009, *Effect of Microwave Radiation on Coal Flotation*, Energy Sources Part A-Recovery Utilization And Environmental Effects, 31(6), 492–499.

SOKOLOVIC J.M., STANOJLOVIC R.D., MARKOVIC Z.S., 2012, *The Effects of Pretreatment on the Flotation Kinetics of Waste Coal*. International Journal of Coal Preparation and Utilization, 32(3), 130–142.

SOKOLOVIC J.M., STANOJLOVIC R.D., MARKOVIC Z.S. 2012, *Activation of oxidized surface of anthracite waste coal by attrition*. Physicochemical Problems of Mineral Processing, 48(1), 5–18.

SAHBAZ O., 2013, Determining optimal conditions for lignite flotation by design of experiments and the halbich upgrading curve, Physicochemical Problems of Mineral Processing, 49(2), 535–546.

SUN W., OUYANG K., ZHANG L., HUA Y., CHEN C., 2010, *Preparation of hydrolyzate of hogwash oil (HHO) and its application in separating diaspore from kaolinite*, Minerals Engineering, 23, 670–675.

XIA W., YANG J., ZHAO Y., ZHU B., WANG Y., 2012, *Improving floatability of Taixi anthracite coal of mild oxidation by grinding*, Physicochemical Problems of Mineral Processing 48 (2), 393–401.

XIA W., YANG J., LIANG C., 2013, *A short review of improvement in flotation of low rank/oxidized coals by pretreatments*, Powder Technology, 237, 1–8.

XIA W., YANG J., 2013a, *Effect of pre-wetting time on oxidized coal flotation*, Powder Technology, 250, 63–66.

XIA W., YANG J., 2013b, *Reverse flotation of Taixi oxidized coal*. Energy & Fuels, 27(12), 7324–7329.

YU Q., YE Y., MILLER J.D., 1990, *A study of surfactant/oil emulsion for fine coal flotation*, Advances in Fine Particles Processing, Springer, 344–355.

YUH S.J., WOLT E.E., 1983, *FTIR studies of potassium catalyst treated gasified coal chars and carbon*, Fuel, 62, 252–255.

ZHOU Z., LI X., LIANG J., LIU J., ZHOU J., CEN K., 2011, *Surface Coating Improves Coal–Water Slurry Formation of Shangwan Coal*, Energy & Fuels, 25(8), 3590–3597.

CONCENTRATION OF CHROMITE
BY MEANS OF MAGNETIC CARRIER
USING SODIUM OLEATE AND OTHER REAGENTS

Yasar UCBAS, Volkan BOZKURT, Kemal BILIR, Halil IPEK

Eskisehir Osmangazi University, Faculty of Engineering and Architecture, Department of Mining Engineering, 26480, Eskisehir, Turkey; corresponding author: vbozkurt@ogu.edu.tr

Abstract: Chromite recovery was studied using a magnetic carrier technology. Heavy media grade magnetite was used as the magnetic carrier. The effect of various reagents such as sodium oleate (NaOl) as a collector and carboxymethyl cellulose (CMC) as well as quebracho tannin as depressants on chromite removal was investigated. The effects of pH and reagent dosages were also determined. First, the zeta potential measurements were performed for different minerals in the absence and presence of NaOl, and then magnetic carrier tests were carried out under conditions based on zeta potential measurements. The magnetic carrier tests performed in the case of individual minerals (i.e. single minerals) showed that chromite (recovery of 95.1%) could be separated from serpentine (recovery of 3.2%) whereas it could not be separated from olivine. The best chromite concentrates containing 42.1% Cr_2O_3 were obtained with a 76% recovery from a synthetic mixtures of chromite and serpentine under optimum test conditions, that is at pH 10.5, 5.10^{-5} M NaOl, 20 g/Mg CMC, 0.5 g magnetite and 500 g/Mg kerosene (the feed contained 27% Cr_2O_3). Slime tailings of Turkish Maadin Company, Kavak Chrome Concentrating Plant in Eskisehir, which contain fine chromite, serpentine and olivine, were also investigated. It was found that chromite could not be satisfactorily recovered from the original slime sample in the presence and absence of NaOl by using the magnetic carrier technology. Additional FTIR studies performed with the investigated minerals showed that NaOl adsorption on chromite was greater than that on serpentine and magnetite minerals. It was also found that NaOl adsorption on serpentine is significantly reduced in the presence of magnetite while it increases only slightly on chromite.

Keywords: chromite, serpentine, magnetite, magnetic carrier, sodium oleate, zeta potential, FTIR

Introduction

The production of fine and ultrafine particles during the size reduction processes is unavoidable in mineral processing systems. The processing of these particles by conventional mineral separation methods is not satisfactory due to the problems associated with particle size. Studies aimed at finding new methods of upgrading of

fine and ultrafine materials began three decades ago (Fuerstenau et al., 1979). Most of these methods are based on the combination of aggregation and flotation processes. Separation of fine particles by magnetic carrier methods have been described in many papers (De Lafour, 1976; Nott, 1978; Schubert, 1980; Cook, 1981; Nott and Price, 1981; Parsonage, 1984, 1988). Selective separation of non-magnetic minerals such as chalcocite, sphalerite and coal from their associated gangue minerals has been described by Schubert (1980). Magnetic coating of iron and titanium bearing gang minerals by fine-sized magnetite particles before magnetic separation has also been applied in kaolinite concentration (Nott, 1978; Cook, 1981; Nott and Price, 1981). Magnetic carrier methods have also found application in water treatment process (De Lafour, 1976). The principle of the method is selective coating of the target mineral surfaces by magnetite particles in an agitated pulp followed by removal of the coated mineral from the pulp using magnetic separation. The factors that affect the coating of the magnetite are zeta potential of minerals and magnetite as well as the presence of adsorbed surfactant layer on the mineral and magnetite surfaces. Separation of many minerals such as apatite, barite, scheelite, magnesite, chromite and iron minerals from calcite, dolomite, serpentine, quartz and corundum minerals has been carried out on laboratory and pilot scales by controlling these parameters (Parsonage, 1984, 1988; Anastassakis, 1999, 2002; Prakash et al., 1999, 2001; Ucbas et al., 2014).

Chromite is primarily used as a refractory material. For this purpose, the Cr_2O_3 content of chromite should be more than 45%. Hence, concentration of chromite is often required. It is usually performed by gravity methods based on differences between the densities of chromite and gangue minerals, especially serpentine and olivine. The fine fraction below 100 μm is usually discarded as gangue due to the process and equipment inefficiencies. Therefore, substantial amount of chromite fines report to the tailings stockpiles in gravity separation plants. This results in resource loss considering the fact that the Cr_2O_3 content of these stocks reaches up to 20%. Since Turkey is one of the leading chromite ore producers in the world, it is obvious that the amount of chromite fines in tailings could be quite large throughout Turkey (Ucbas et al., 2014). Therefore, the utilization of these tailings could contribute to the economy while partially reducing the environmental problems.

Several studies have been attempted to recover chromite from slime stocks using column flotation, high intensity wet magnetic separation (WHIMS), WHIMS/column flotation (Guney et al., 1999; 2001) and multi gravity separation (Ozdag et al., 1994; Cicek and Cocen, 2002) with a limited success. Magnetic carrier technology would well be an alternative method to recover chromite from such stocks (Ucbas et al., 2014).

Approximately 0.3 teragrams of tailings containing 17.36% Cr_2O_3 have been accumulated over the years in stockpiles of Turkish Maadin Company, Kavak Chrome Concentrating Plant located near the city of Eskisehir, Turkey. The aim of this study is to investigate possible concentration of chromite fines from these slime tailings using the magnetic carrier technology.

Materials and methods

Materials

Chromite, serpentine and olivine samples were obtained from the gravity concentration circuit while slime samples were obtained from the tailings stockpiles of Turkish Maadin Company, Kavak Chrome Concentrating Plant. Fine-sized heavy media grade magnetite was supplied by the ELI Manisa Coal Preparation Plant. All samples were, if needed, first crushed, then further ground using ceramic fast mill (Gabrielli Fast Mill 2B) for 60 minutes.

Sodium oleate (NaOl) was used as a collector (>99% Sigma-Aldrich). Quebracho tannin and carboxymethylcellulose (CMC) were used as depressants (Chevron Phillips Chemical Company LP Mining Chemical) and analytical grade HCl and NaOH were used to adjust pH. Deionized water was used in all experiments.

Methods

Sample characterization

The particle size of the samples was measured wet in a Malvern Model 2000 particle size analyzer. Chemical analyses of the samples were performed using X-ray fluorescence spectroscopy (XRF, Spectro X-Lab). Mineralogical analyses of the samples were carried out using X-ray diffraction spectroscopy (XRD, Rigaku Miniflex, 1.54056-CuKα1).

Zeta potential measurements

For determining zeta potentials, electrophoretic mobility measurements of chromite, magnetite, serpentine and olivine were conducted using Zeta-Meter System 3.0+ equipped with a camera system in the absence and presence of NaOl ($2 \cdot 10^{-5}$ M). One gram of samples in 100 cm^3 of solution was conditioned for 10 min after obtaining the preset pH. The slurry was kept unstirred for additional 5 min to let larger particles to settle. The pH was adjusted with diluted HCl or NaOH. Thirty particles were followed through camera at each pH value. The instrument gave the average electrophoretic mobility from which the zeta potential was calculated using the Smoluchowski equation (Eq. 1)

$$\zeta = \frac{4\pi\eta U}{\varepsilon}$$

(1)

where ζ is the zeta potential (mV), η is the viscosity of the medium (poise), U is the electrophoretic mobility (μm/s per V/cm), ε is the dielectric constant.

Magnetic carrier tests

The tests were performed in a 100 cm^3 beaker. A stirrer with a plastic impeller was used to keep the particles in the suspension. The pH was regulated with diluted HCl or NaOH. Initial tests were carried out individually for each mineral (i.e. single

minerals). One gram of the mineral, 0.5 g of magnetite and 500 g/Mg kerosene were conditioned for 10 min at the prefixed pH in the absence and presence of NaOl. After conditioning period, stirrer was stopped. The magnetite and magnetite coated particles were removed by using highly magnetic metal rod. Uncoated particles (i.e. material remained) in the beaker were weighted after filtering and drying them in an oven. The net weight, the weight of uncoated particles subtracted from initial weight, was determined. This value was presented as per cent recovery for the results of magnetic carrier tests. The magnetite coating on the mineral surfaces was removed by ethanol washing for mass balancing purpose. The effects of pH, collector and depressant dosages were studied.

In the case of synthetic mineral mixtures (chromite, serpentine and olivine), equal weight (1 g) of each mineral was used while the procedure was the same as described previously.

FTIR studies

All samples (chromite, magnetite, serpentine, and slime) were prepared according to the zeta potential measurement data and magnetic carrier test procedures described previously. The infrared spectra of the samples were registered after their air drying. The spectra of chromite and serpentine were also registered in the presence of magnetite (sharing the same solution but isolated) for imitating magnetic carrier tests. The FTIR spectra were recorded using a Perkin Elmer 2000 spectrometer equipped with its own Diffuse Reflectance Infrared Fourier Transform (DRIFT). Typical spectrum was an average of 200 scans in the 4000-400 cm^{-1} spectral range with a resolution of 4 cm^{-1} using a deuterated triglycine sulfate (DTGS) detector. At the concentration of collector used, the intensity of the bands with respect to adsorbed layers was low, and the samples were not mixed with KBr since dilution further reduces the sensitivity. Thus, the untreated samples were used as a reference.

Results and discussions

Characterization of samples

The particle sizes of the samples are given in Table 1. It can be seen that magnetite is the finest while olivine is the coarsest mineral in terms of 90% pass. Chemical compositions of the samples are shown in Table 2. The results confirm the purity of the minerals, especially in terms of Cr_2O_3 content for chromite, and SiO_2 as well as MgO contents for serpentine and olivine while Fe_2O_3 and FeO contents for magnetite.

Figure 1 and Table 3 show the XRD analysis of the samples and the values of 2θ characteristic peaks of the pure minerals obtained from X-ray diffraction database, respectively for comparison. The results of this analysis suggested that the 2θ characteristic peak values of the pure minerals were quite consistent with the mineral samples studied, validating the purity of the samples. A comparison of the X-Ray

diffraction of slime and the minerals (Fig. 1) reveals that the slime sample contains all the minerals to a certain extent.

Table 1. Particle size of investigated minerals (Ucbas et al., 2014), olivine and chromite slime

Pass (%)	Magnetite (μm)	Chromite (μm)	Serpentine (μm)	Olivine (μm)	Slime (μm)
%10	2.83	0.26	2.73	2.94	3.91
%50	8.95	6.67	22.84	20.83	42.19
%90	26.29	34.11	173.17	180.67	166.51
%97	42.00	86.25	243.19	263.63	254.61

Table 2. Chemical analysis of investigated minerals (Ucbas et al., 2014), olivine and chromite slime

Oxides (%)	Magnetite	Chromite	Serpentine	Olivine	Slime
Cr_2O_3	0.08	54.00	0.51	0.97	17.36
Fe_2O_3	67.16	16.79	8.23	7.09	8.91
FeO	31.21	-	-	-	-
Al_2O_3	0.44	12.50	0.02	0.01	1.50
SiO_2	0.11	0.02	46.00	33.00	24.09
MgO	0.02	14.95	31.00	42.00	32.21
CaO	0.38	0.14	0.09	0.20	0.34
LOI	-	1.14	13.65	16.31	15.09
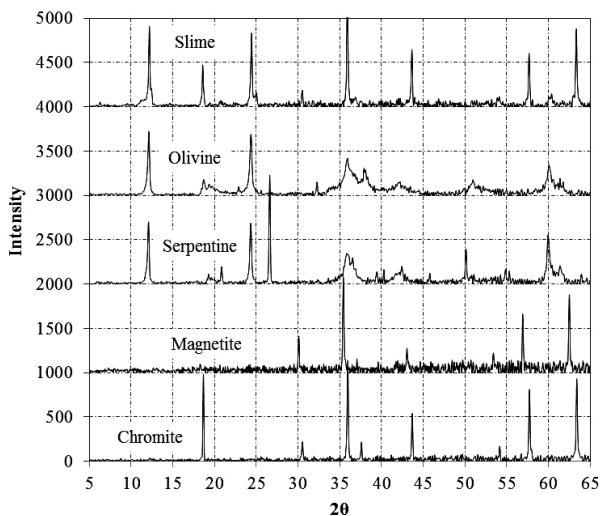
Fig. 1. XRD analysis of investigated minerals (Ucbas et al., 2014), olivine and chromite slime

Table 3. 2θ characteristic peaks of the investigated minerals (Ucbas et al., 2014) and olivine

Minerals	2θ	2θ	2θ
Chromite	35.6(100)	63.7(90)	57.6(90)
Magnetite	35.5(100)	62.7(85)	57.2(85)
Serpentine	12.1(100)	24.4(70)	19.4(50)
Olivine	24.3(100)	35.9(80)	60.8(70)

Zeta potential measurements in the absence of NaOl

The measured zeta potentials of magnetite, chromite, serpentine and olivine at different pH's are shown in Fig. 2. It can be observed that the zero point of charge (zpc) of chromite, magnetite, and serpentine are 7.2, 5.0, and 3.1, respectively (Ucbas et al., 2014). Olivine is positively charged at all pH values studied. Similar zpc values were reported in the literature (Iwasaki et al., 1962; Laskowski and Sobieraj, 1969; Sobieraj and Laskowski, 1973; Smith and Allard, 1983; Atak, 1987; Guney and Atak, 1997; Allesse et al., 1997; Anastassakis, 1999, 2002; Prakash et al., 1999).
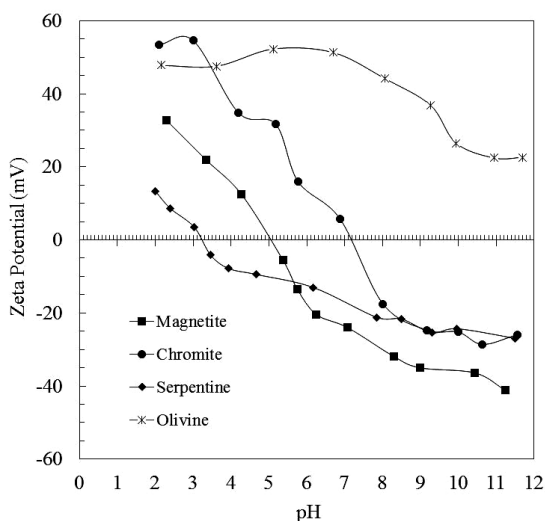
Fig. 2. Zeta potential of magnetite, chromite, serpentine (Ucbas et al., 2014) and olivine

Zeta potential measurements in the presence of NaOl

The measured zeta potentials of magnetite, chromite, serpentine and olivine at different pH in the presence of $2 \cdot 10^{-5}$ M NaOl are shown in Fig. 3. It can be seen that the zeta potential of all minerals decreases towards the negative direction beginning from pH value around 2 and charge reversal takes place at pH values between 2 and 4 for all minerals. The pzc of all minerals shifts to lower pH values as well. This could be explained by binding of oleate anions on cationic surface sites and reducing the net charge of the surfaces through physical adsorption. Above the pzc, where the surface

net charge was negative, zeta potential values of chromite, magnetite and serpentine kept decreasing until reducing its magnitude towards the higher alkaline region. This could be attributed to chemisorption (i.e. complexation of oleate anions with metal hydroxyl species) (Iwasaki et al., 1962; Laskowski and Sobieraj, 1969; Sobieraj and Laskowski, 1973; Smith and Allard, 1983; Atak, 1987; Guney and Atak, 1997; Allesse et al., 1997; Anastassakis, 1999, 2002; Prakash et al., 1999; Fuerstenau and Palmer, 1976; Ananthpadmanabhan and Somasundaran, 1979). However, in the case of olivine, charge reversal takes place at pH around 4 and olivine has net negative surface charge above this pH value. This could be interpreted as the presence of physical adsorption of NaOl onto olivine surfaces.
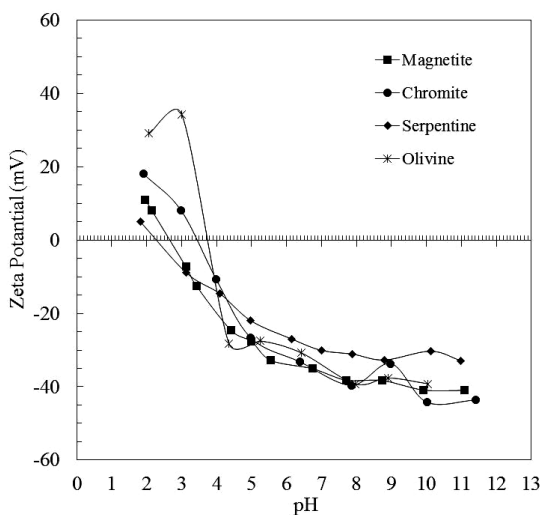
Fig. 3. Zeta potential of minerals in $2 \cdot 10^{-5}$ M NaOl solution

Magnetic carrier tests for single minerals

Magnetic carrier tests in the absence of NaOl

From the results of zeta potential measurements of minerals in the absence of NaOl (Fig. 2), it can be seen that magnetite and serpentine are negatively charged while chromite and olivine are positively charged at the pH range between 5 and 7. This could suggest that chromite and olivine minerals could be coated with magnetite due to the electrostatic attraction. Magnetic carrier tests conducted under these conditions revealed that minerals (chromite, serpentine and olivine) could well be coated with magnetite as predicted but magnetite attachment to minerals were so loose that even a gentle stirring of resulted in the detachment of the magnetite. This demonstrates that electrostatic attraction itself is not enough for effective magnetite coating. Similar results were obtained in the literature (Anastassakis, 1999, 2002; Prakash et al., 1999, 2001; Ucbas et al., 2014). This was attributed to the presence of a thin film of water

between the hydrophilic surfaces of magnetite and minerals. Thin film of water could not be ruptured even though magnetite and mineral particles are very close to each other as a result the particles are easily detached under even gentle stirring conditions (Anastassakis, 1999, 2002).

Magnetic carrier tests in the presence of NaOl

From the zeta potential measurements of minerals in the presence of NaOl (Fig. 3), it is observed that chromite and olivine are positively charged while magnetite and serpentine are negatively charged at pH 3. This could suggest the possible magnetite coating of chromite and olivine through electrostatic attraction, as a result, their separation from serpentine. Magnetic carrier tests were carried out with chromite, olivine and serpentine separately in the presence of $1 \cdot 10^{-4}$ M NaOl at pH 3. Chromite recovery was 95.5% while serpentine recovery was 53%. Olivine recovery was similar (90% <) to chromite recovery suggesting difficulty in separation of chromite from olivine using magnetic carrier. Therefore, further magnetic carrier tests were mainly focused on separation of chromite from serpentine. In order to increase the chromite recovery to target values (> 98%), new tests were performed at increased NaOl dosage ($2 \cdot 10^{-4}$ M). Recovery of chromite was increased up to 99.2% while recovery of serpentine remained similar (54.1%). Obtained recovery values clearly indicated that chromite could not be separated from serpentine selectively under the conditions based on the zeta potential measurements alone. Similar results were observed in previous studies performed by the present authors (Bozkurt et al., 2006; Ucbas et al., 2014). This is attributed to the fact that hydrophobicity of mineral surfaces is more important than the surface charge differences of minerals (i.e. hydrophobic interaction forces dominate the magnetite coating rather than electrostatic interaction forces). The strength of hydrophobic interaction forces was investigated in a study by measuring surface forces between two hydrophobic surfaces (Israelachvili, 1992). It was found that hydrophobic interaction forces are extremely strong due to the rearrangements of hydrogen bond configurations in the overlapping solvation zones as two hydrophobic species come together.

Further magnetic carrier tests were carried out within the pH range of 2-12 in the presence of $5 \cdot 10^{-5}$ M NaOl (Fig. 4, 0.5 g magnetite, 500 g/Mg kerosene). Recovery of chromite increases with an increasing pH while serpentine recovery is decreasing. At pH 10.5, recovery of chromite and serpentine are 94.4 and 14.5% (difference of 74.8%), respectively. In order to improve the difference in chromite and serpentine recoveries, the effect of NaOl dosage on recoveries were investigated further at pH 10.5. However, as seen in Fig. 5 (pH 10.5, 0.5 g magnetite, 500 g/Mg kerosene) the difference in chromite and serpentine recoveries cannot be increased by altering NaOl dosage. Higher chromite recoveries obtained with increasing pH in magnetic carrier tests coincides with the literature knowledge where high chromite and magnetite flotation recoveries were obtained at relatively high concentrations of NaOl solutions at highly alkaline pH values (Iwasaki et al., 1962; Atak, 1987; Guney and Atak, 1997;

Fuerstenau and Palmer, 1976; Ananthpadmanabhan and Somasundaran, 1979). This could be explained by the aggregation of chromite and magnetite (recovery of 94.4%). The lower recoveries obtained with serpentine could be attributed to the less magnetite and serpentine aggregation (recovery of 21.6%) due to the lower adsorption levels of NaOl on serpentine compare to chromite as further confirmed by FTIR studies.
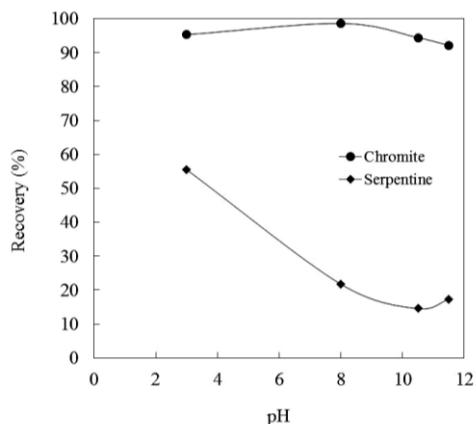
Fig. 4. The effect of pH on recovery   Fig. 5. The effect of NaOl dosage on recovery
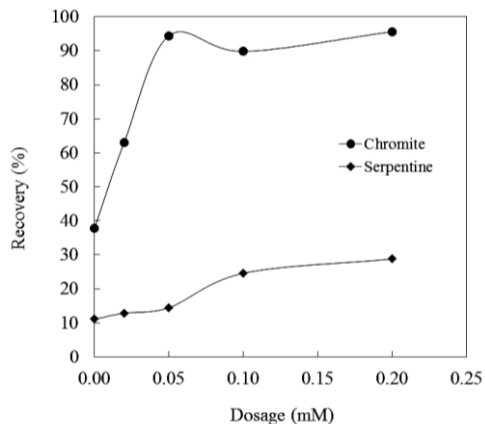
The effects of depressants such as quebracho and carboxymethyl cellulose (CMC) were also investigated for the same aim (Last and Cook, 1952; Bulatovic, 1999). Results of these tests are given in Figs. 6 (pH 10.5, $5 \cdot 10^{-5}$ M NaOl, 0.5 g magnetite, 500 g/Mg kerosene) and 7 (pH 10.5, $5 \cdot 10^{-5}$ M NaOl, 0.5 g magnetite, 500 g/Mg kerosene), respectively. As can be seen from Fig. 6, the difference in recoveries moderately increases at 20 g/Mg quebracho dosage (difference of 83.3%) compare to recoveries obtained in the absence of depressant (difference of 74.8%). Even though the difference is increased, it is not found satisfactory for the selective separation of these minerals.

In the case of tests performed with CMC, the highest difference in chromite and serpentine recoveries is obtained at dosage of 20 g/Mg (Fig. 7). The recovery of chromite is 95.1% while serpentine 3.2% (difference of 91.9%). The difference in recoveries significantly increases, when compared to recoveries obtained in the absence of depressant (Atak, 1987), suggesting the possible separation of these minerals in the presence of CMC. This could be attributed to the depressant effect (blinding agent) of CMC influencing collector adsorption on the minerals (creating negative surfaces on minerals) and inducing particle dispersion (Atak, 1987; Guney and Atak, 1997; Shortridge et al., 2000; Dalvie et al., 2000; Gallios et al., 2007; Laskowski et al., 2007). It can be seen from Figs 6 and 7 that a careful control of depressant dosage is essential since recovery of chromite decreases significantly over certain dosages.

Tests performed with chromite-magnetite and serpentine-magnetite were carried out also with olivine. It was found that the recoveries of olivine were similar to those of chromite obtained in the absence and presence of depressants. This suggested that chromite could not be separated from olivine selectively.
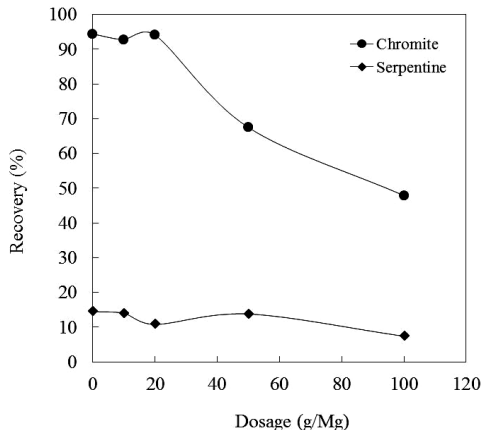
Fig. 6. The effect of quebracho dosage on recovery   Fig. 7. The effect of CMC dosage on recovery
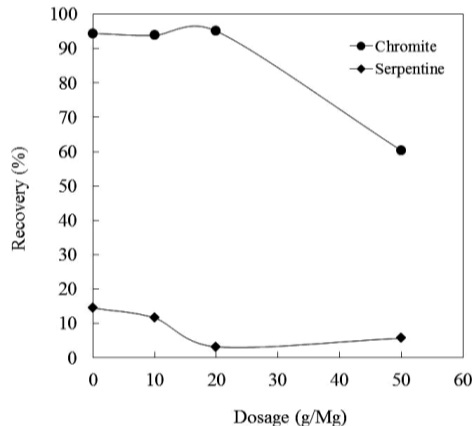
Magnetic carrier tests for mixed minerals and slime tailings

The tests performed with synthetic mixture of chromite and serpentine (1 g each) at pH 10.5, $5·10^{-5}$ M NaOl, 0.5 g magnetite, 500 g/Mg kerosene, 20 g/Mg CMC provided chromite concentrates containing 42.1% Cr_2O_3 with 76% recovery. The feed grade was 27.0% Cr_2O_3. The same conditions applied for the slime sample provided chromite concentrate containing 22.8% Cr_2O_3 with 60.9% recovery. The feed grade of the slime sample was 17.36% Cr_2O_3. This result shows that upgrading is poor and could not be obtained with the industrial chromite slime sample. This could be due to the high olivine content in the slime sample.

The chemistry of NaOl interaction with investigated minerals

FTIR studies in the absence of NaOl

The reference DRIFT spectra of chromite, serpentine, slime and magnetite mineral samples are depicted in Fig. 8. The bands between 3500 and 3750 cm^{-1} are due to the stretching vibrations of the O-H groups. The strong bands between 900 and 1150 cm^{-1} are attributed to the Si-O stretches and Si-O-Si stretching vibration modes (Ucbas et al., 2014). The bands between 500 and 1000 cm^{-1} are assigned to bond between groups II-III transition metal cations in spinel oxides and oxygen anion (Povnnennykh, 1978; Moroz et al., 2001). Strong band observed with magnetite at 570 cm^{-1} is assigned to Fe-O bending vibration (Liese, 1978; Kim et al., 2007).
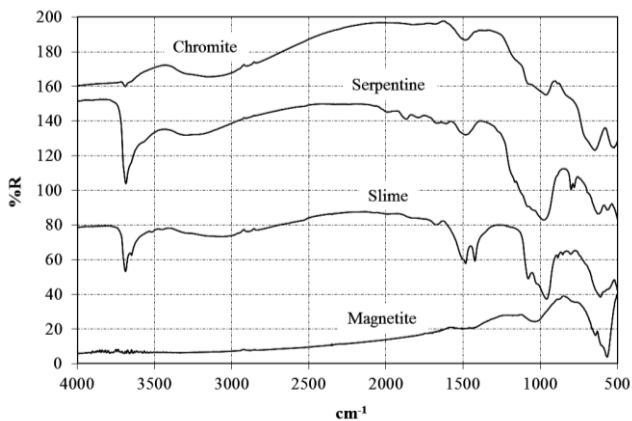
Fig. 8. Reference DRIFT spectra of minerals (Ucbas et al., 2014)
and the slime sample

FTIR studies in the presence of NaOl

The reference infrared spectrum of NaOl is shown in Fig. 9. The characteristic alkyl chain bands at 2920 cm^{-1} and 2850 cm^{-1} are due to asymmetric and symmetric C-H stretching vibrations of CH_2 group, respectively. The weak band at 2945 cm^{-1} is due to an asymmetric C-H stretching vibration of CH_3 group. The bands at lower wavenumbers were assigned to asymmetric (1555 cm^{-1}) and symmetric (1400-1500 cm^{-1}) C=0 (carbonyl) stretching vibrations of carboxylate ion ($RCOO^-$) (Peck et al., 1967; Wensel et al., 1995; Lu et al., 1998; Hamid and Forsberg, 2006).
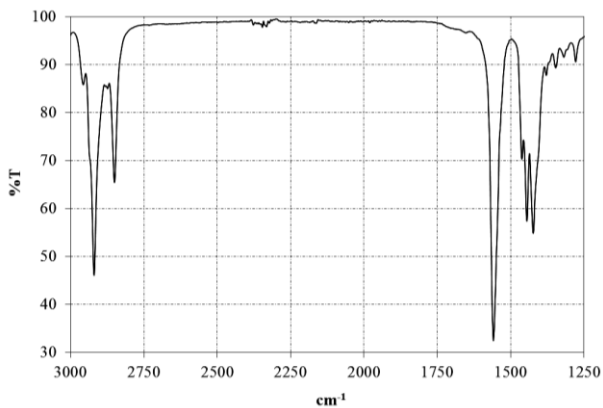
Fig. 9. Reference FTIR spectrum of NaOl

DRIFT spectra for chromite, serpentine and magnetite minerals were acquired at optimum conditions (pH 10.5, $5 \cdot 10^{-5}$ M NaOl) of magnetic carrier tests (Fig. 10). The bands in the presence of NaOl are quiet identical to bands observed at wavenumber of

2920 cm^{-1} and 2850 cm^{-1} with the reference spectrum of NaOl (Fig. 9) indicating adsorption of NaOl on minerals. Furthermore, the band shifts observed, especially more pronounced for chromite compare to serpentine and magnetite minerals due to higher level of collector adsorption, at wavenumbers between 1250 and 1600 cm^{-1} indicates the chemisorption of NaOl (Peck et al., 1967). Bearing in mind that intensities of adsorption bands are quiet reproducible due to the procedure used to acquire spectra of NaOl treated minerals, comparing spectra of minerals in terms of adsorbed band intensities (Fig. 10), it is apparent that NaOl adsorption on chromite is higher than on serpentine and magnetite minerals. However, the presence of some adsorption on serpentine effects separation of minerals negatively as observed in magnetic carrier tests performed under the same conditions.
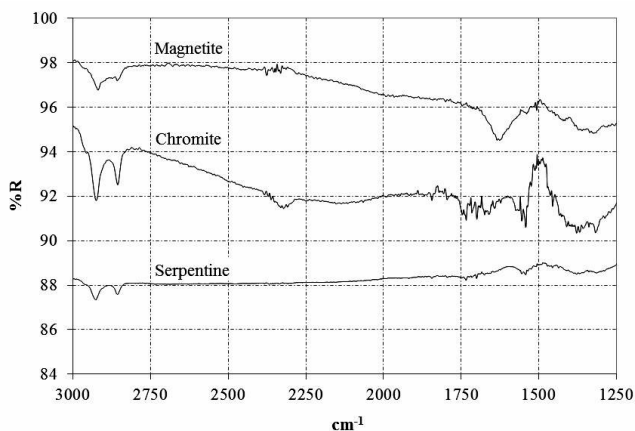
Fig. 10. DRIFT spectra of the minerals in 5·10^{-5} M NaOl
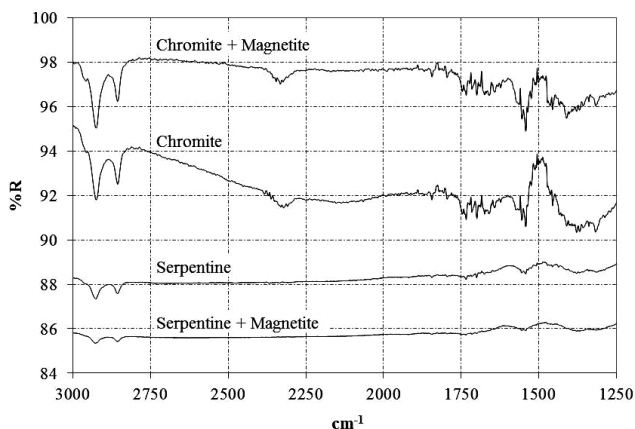
Fig. 11. DRIFT spectra of chromite and serpentine in the presence of magnetite

The spectra of chromite and serpentine were acquired in the presence of magnetite (sharing the same solution but isolated) as well since the magnetic carrier tests were performed in the presence of magnetite. The results are presented in Fig. 11. It can be seen that the amount of NaOl adsorption, indicated by band intensities, on chromite slightly increases when compared to chromite alone. In the case of serpentine, the situation is reversed because the amount of NaOl adsorption is reduced in comparison to serpentine alone. Without strong evidence this could be attributed either to competitive adsorption of NaOl on minerals or the activation of chromite by ions possibly dissolving from magnetite. These results are consistent with magnetic carrier tests performed under the same experimental conditions (Fig. 5).

Conclusions

X-Ray diffraction analysis of the minerals studied revealed that the slime sample contains chromite, serpentine and olivine minerals, to a certain extent. As a result of the magnetic carrier tests, chromite could be separated from serpentine in fine sizes using magnetic carrier technology as confirmed by the tests performed in the case of individual and mixed minerals under the optimal test conditions of $5 \cdot 10^{-5}$ M NaOl in the presence of 20 g/Mg carboxymethyl cellulose at pH 10.5. Chromite separation from serpentine could also be achieved in the presence of quebracho tannin with limited success. However, chromite could not be separated from olivine selectively as confirmed by tests performed in the case of individual and mixed minerals. In addition, it was also realized that separation of chromite from olivine was a challenging research subject. Chromite could not be recovered satisfactorily as well from the original slime sample, perhaps mostly due to the olivine content of it.

The zeta potential and FTIR studies confirmed the chemical nature of the NaOl adsorption on chromite, serpentine and magnetite minerals. The FTIR studies indicated that NaOl adsorption on chromite was higher than those of serpentine and magnetite. It was also found that NaOl adsorption on serpentine declined significantly while that on chromite increased slightly in the presence of magnetite. Thus, selective separation of chromite from serpentine was elaborated further.

Magnetic carrier tests carried out in the absence of NaOl suggested that electrostatic attraction itself was not enough for the successful magnetite coating of minerals. The adsorption of collector onto the mineral surfaces was essential.

It has been demonstrated that the magnetic carrier methods could be used for selective separation of minerals even in fine sizes when their surface could be adapted by proper reagents.

Acknowledgements

References

ALESSE V., BELARDI G., FREUND J., PIGA L., SHEHU N., 1997, *Acidic Medium Flotation Separation of Chromite from Olivine and Serpentine*, Transactions of American Society of Mining Engineers, 302, 26–35.

ANANTHPADMANABHAN K., SOMASUNDARAN P., HEALY T.W., 1979, *Chemistry of Oleate and Amine Solutions in Relation to Flotation*, T. Am. I. Min. Met. Eng. 266, 1–7.

ANASTASSAKIS G.N., 1999, *A Study on the Separation of Magnesite Fines by Magnetic Carrier Methods*, Colloids and Surfaces A: Physicochemical Engineering Aspects, 149, 585–593.

ANASTASSAKIS G.N., 2002, *Separation of Fine Mineral Particles by Selective Magnetic Coating*, Journal of Colloid and Interface Science, 256, 114–120.

ATAK S., 1987, *Adsorption of Oleate on Chromite and Olivine*, Aufbereitungs-Technik, 12, 727-733.

BOZKURT V., UCBAS Y., SONMEZ E., IPEK H., KOCA S., 2006, *Separation of Feldspar Minerals from Quartz Using Magnetic Carrier Technology*. Proceedings of the XXIII IMC, Vol. 2., Onal G., Celik M.S., Arslan F., Atesok G., Guney A, Sirkeci A.E., Yuce A.E., Perek K.T. (eds), Istanbul, Turkey, 963–968.

BULATOVIC S.M.,1999, Use of Organic Polymers in the Flotation of Polymetallic Ores: A Review, Minerals Engineering, 12, 4, 341–354.

CICEK T., COCEN I.,2002, *Applicability of Mozley Multigravity Separator (MGS) to Fine Chromite Tailings of Turkish Chromite Concentrating Plants*, Minerals Engineering, 15, 1–2, 91–93.

COOK J.A. 1981, *Magnetic Beneficiation of Clays Utilizing Magnetic Seeding and Flotation*, British Patent 2092026A.

DALVIE M.A, HARRIS P.J., BRADSHAW D.J., 2000, *The Effect of Polymeric Depressants and Inorganic Dispersants on the Surface Characteristics of Talc*, in: Proceedings of XXI International Mineral Processing Congress, (P. Massacci, Ed.) Elsevier, Amsterdam, B8b-25–B8b-32.

DE LAFOUR C., 1976, *Seeing Principles of High Gradient Magnetic Separation*, Journal of American Water Works Association, 68, 443–446.

FUERSTENAU D.W., CHANDER S., ABOUZEID A.M., 1979, *The Recovery of Fine Particles by Physical Separation Methods*, in: *Beneficiation of Mineral Fines: Problems and Research*, P. Needs, Somasundaran, N. Arbiter (Eds.), AIMMPE Inc., New York, 3–59.

FUERSTENAU M.C., PALMER B.R., 1976, Anionic Flotation of Oxides and Silicates, in: *Flotation - A. M. Gaudin Memorial Volume -*, Volume 1 Chapter 7 - *Fundamentals of Nonmetallic Flotation*, SME Publications, New York, 148–196.

GALLIOS G.P., DELIYANNI E.A., PELEKA E.N., MATIS K.A., 2007, *Flotation of Chromite and Serpentine*, Separation and Purification Technology, 55, 232–237.

GUNEY A., ATAK S., 1997, *Separation of Chromite from Olivine by Anionic Collectors*, Fizykochemiczne Problemy Mineralurgii, 31, 99–106.

GUNEY A, ONAL G., CELIK M.S., 1999, *A New Flowsheet for Processing Chromite Fines by Column Flotation and the Collector Adsorption Mechanism*, Minerals Engineering, 12, 9, 1041–1049.

GUNEY A, ONAL G., ATMACA T., 2001, *New Aspect of Chromite Gravity Tailings Re-Processing*, Minerals Engineering, 14, 11, 1527–1530.

HAMID S.H., FORSBERG K.S.E., 2006, *XPS & FTIR Study of Adsorption Characteristics Using Cationic and Anionic Collectors on Smithsonite*, Journal of Minerals & Materials Characterization & Engineering, 5, 1, 21–45.

ISRAELACHVILI J.N., 1992, *Intermolecular and Surface Forces*, 2nd Edition, Academic Press, London.

IWASAKI I., COKE S.R.B., KIM Y.S., 1962, *Some Surface Properties of and Flotation Characteristics of Magnetite*, Transactions of American Society of Mining Engineers, 223, 113–120.

KIM M.J., LIM B., JEONG Y.K., CHO Y.W., CHOA Y.H.B., 2007, *Surface Modification of Magnetite Nanoparticles for Immobilization with Lysozyme*, Journal of Ceramic Processing Research, 8, 4, 293–295.

LASKOWSKI J.S., SOBIERAJ S., 1969, *Zero Points Of Charge of Spinel Minerals*, Transactions of the Institution of Mining and Metallurgy Section C, 78, C161–C162.

LASKOWSKI J.S., QUI L., O'CONNOR C.T., 2007, *Current Understanding of the Mechanism of Polysaccharide Adsorption at the Mineral/Aqueous Solution Interface*, International Journal of Mineral Processing, 84, 59–8.

LAST I., COOK P., 1952, *Collector Depressant Equilibria in Flotation: II. Depressant Action of Tannic Acid and Quebracho*, Journal of Physical Chemistry, 56, 643–648.

LIESE H.C., 1967, *Mineralogical Notes an Infrared Absorption Analysis of Magnetite*, American Mineralogist, 52, July-August, 1198–205.

LU Y., DRELICH J., MILLER J.D., 1998, *Oleate Adsorption at an Apatite Surface Studied by Ex-Situ FTIR Internal Reflection Spectroscopy*, Journal of Colloid and Interface Science, 202, 1998, 462–476.

MOROZ T., RAZVOROTNEVA L., GRIGORIEVA T., MAZUROV M., ARKHIPENKO D., PRUGOV V., 2001, *Formation of Spinel from Hydrotalcite-Like Minerals and Destruction of Chromite Implanted by Inorganic Salts*, Applied Clay Science, 18, 29–36.

NOTT A.J., 1978, *Magnetic Beneficiation of Clay Using Magnetic Particulate*, US Patent 4087004.

NOTT A.J., PRICE W.M., 1981, Magnetic Beneficiation of Clays using Magnetic Particulate, US Patent 4125460.

OZDAG H., UCBAS Y., KOCA S., 1994, *Recovery of Chromite from Slime and Table Tailings by Multi Gravity Separator*, in: Proceedings of Innovations in Mineral Processing, Sudbury, Canada, 267–78.

PARSONAGE, P., 1984, *Selective Magnetic Coating for Mineral Separation*, Transactions of the Institution of Mining and Metallurgy Section C, 93, C37–44.

PARSONAGE P., 1988, *Principles of Mineral Separation by Selective Magnetic Coating*. International Journal of Mineral Processing, 24, 269–93.

PECK A.S., RABY L.H., WADSWORTH M.E., 1967, *An Infrared Study of the Flotation of Hematite with Oleic Acid and Sodium Oleate*, Transactions of American Institute of Mining and Metallurgical Engineers, 238, 301–07.

POVNNENNYKH A.S., 1978, *The Use of Infrared Spectra for the Determination of Minerals*, American Mineralogist, 63, 956-959.

PRAKASH S., DAS B., MOHANTY J.K., VENUGOPAL R., 1999, *The Recovery of Fine Iron Minerals from Quartz and Corundum Mixtures Using Selective Magnetic Coating*, International Journal of Mineral Proc*essing*, 57, 87–03.

PRAKASH S., MOHANTY J.K., DAS B., VENUGOPAL R., 2001, *Characterization and Removal of Iron from Fly Ash of Talcher Area, Orissa, India*, Minerals Engineering, 14, 1, 123–26.

SHUBERT R.H., 1980, *Magnetic separation of particulate* mixtures, U.S. Patent RE 30.360.

SHORTRIDGE P.G., HARRIS P.J., BRADSHAW D.J., KOOPAL L.K., 2000, *The Effect of Chemical Composition and Molecular Weight of Polysaccharide Depressants on the Flotation of Talc*, International Journal of Mineral Processing, 59, 215–224.

SMITH R.W., ALLARD S.G., 1983, *Effects of Pretreatment and Aging on Chromite Flotation*, International Journal of Mineral Processing, 11, 163–74.

SOBIERAJ S., LASKOWSKI J.S., 1973, *Flotation of Chromite: 1- Early Research and Recent Trends; 2- Flotation of Chromite and Surface Properties of Spinel Minerals*, Transactions of the Institution of Mining and Metallurgy Section C, 82, C207–213.

UCBAS Y., BOZKURT V., BILIR K., IPEK H., 2014, *Separation of Chromite from Serpentine in Fine Sizes using Magnetic Carrier*, Separation Science and Technology, 49, 6, 1–11, DOI: 10.1080/01496395.2013.869602.

WENSEL R.W., PENALOZA M., CROSS W.M., WINTER R.M., KELLAR J.J., 1995, *Adsorption Behavior of Oleate on Mg(OH)$_2$ as Revealed by FTIR Spectroscopy*, Langmuir, 11, 4593–595.

THE ROLE OF ORE PROPERTIES
IN THICKENING PROCESS

Majid UNESI[*], Mohammad NOAPARAST[**], Seiyd Ziaedin SHAFAEI[**], Esmaeil JORJANI[*]

*Tehran Science and Research Branch of Islamic Azad University, Tehran, Iran
** University of Tehran, Tehran, Iran, noparast@ut.ac.ir

Abstract: The role of ore properties (density, particle size, and mineralogy) in thickening process was studied in this research. The shaking table was used to prepare the sample for the tests. The tailings were continuously fed on the table by gravity to separate the tailings in three products as slime, middling and coarse particles. The solid density and particle size of the samples were different. To study the effect of mineralogical properties, the sedimentation behavior of the feed and middling samples were tested. The results showed that the free settling velocity of the feed (2–6 mm/s) was less than that of the middling sample (18–23 mm/s), and the compressibility of middling (density: 0.63–0.86 Mg/m^3) was more than that of feed (density: 0.33–0.47 Mg/m^3). This was due to the amount of clay reduction in the middling sample. The sedimentation behavior of the slime and the coarse samples were also compared in order to study the effect of particle size and density. The settling velocity of the slime and the coarse particles was obtained as 0.1-0.4 and 26 mm/s, respectively, and the maximum underflow density were obtained as 0.35 and 1.57 Mg/m^3, respectively. Therefore, the particle size and density reduction reduced the thickener performance. In order to study the effect of particle size, the sedimentation behavior of the slime and coarse samples were compared, and it was obtained that the settling velocity and underflow density increased with the increasing in the particle size.

Keywords: density, particle size, mineralogy, settling flux, underflow density, thickening

Introduction

Mineral processing techniques are performed in environments which contain a significant amount of water, and in many cases, the most of water is removed with tailings. Therefore, it is necessary to use dewatering equipments such as thickeners in order to avoid environment contamination and water recycling (Burger et al. 1999).

There are many models and experiments which have been presented by researchers to understand the thickening process and to predict the relationship between process parameters. A sedimentation relationship was first proposed by Coe and Clevenger in

1916 which was not practical for flocculated suspensions. Kynch provided a breakthrough in suspension dewatering theory in 1952 which shows that the relationship between concentration and height can be used when the slurry is treated with a flocculating agent. Although the Kynch theory is not suitable for all mineral slurries, it is still used for thickener design calculations. Talmage and Fitch (1955) applied the mathematical approach of Kynch for thickener design and thereafter Yoshioka et al. (1957) obtained the thickener area by using a settling flux. Moreover, Oltmann (1975) suggested a simple empirical approach to the critical flux determination, and hence thickener area. The approximate depth of the thickened sludge layer was readily determined by the method outlined by Osborne in 1977, and the Wilhelm-Naide model (1981) used the underflow concentration to define the unit area which is still used for thickeners design. Also Dahlstrom and Fitch (1985) and Yalcin (1988) proposed a relationship between settling flux and unit area. A graphical method was presented by Kelly and Spottiswood (1989) to determine the settling flux (Buscall et al. 1987). Furthermore, several models have been developed to simulate dewatering behavior by chemical engineers (Bustos et al. 1999, Concha et al. 1996, Deventer et al. 2011). A 1-D model of dewatering was developed by Buscall and White (1987) which quantify the solids volume fraction, the compressive yield stress, and the hindered settling function (Garrido et al. 2003a). In addition, Landman and White (1994) used a phenomenon model which was a combination of empirical and theoretical models, and they described the solid flux function and effective solid stress. They also determined the forces acting on particles in the sedimentation and consolidation process (Garrido et al. 2003b). The BW theory, which was developed by Green (1997), properly modeled the comprehensive yield stress $P_y(\varphi)$ and hindered settling function $R(\varphi)$ in the suspension bed, but not sedimentation above the bed (Gladman et al. 2010). The Kynch theory, developed by Garrido et al. (2003), modeled the sedimentation-consolidation process (Green 1997). Garrido et al. (2003) developed a software for design and simulation of batch and continuous thickening. Thereafter, further studies were conducted by other researchers. An algorithm has been developed by Usher et al. (2005) to account for the underflow concentration and sediment bed from fundamental suspension properties (Landman et al. 1988). The suspension dewatering equations were proposed by Usher et al. (2009) based on the aggregate densification where by aggregate compact and become smaller when subjected to forces in thickening process. They presented the liquid flow velocity around and through aggregates (Lester et al. 2010). The validation of the Usher algorithm was studied by Gladman et al. (2010). They stated that this model was most accurate at the shortest residence times and lowest bed heights, and became poorer for longer residence time and higher beds. This was due to changes in dewatering properties of flocculated aggregates over time which is not adequately considered in the Usher algorithm. Lester et al. (2011) developed the 2-dimensional model of BW. They used the continuity, separation, and transport equations in the modeling. Since solving this model by computational methods was difficult, they used the CFD method

for modeling (Mcfarlane et al. 2005). Van Deventer et al. (2011) developed the Kynch theory which based on aggregate densification behavior. Additionally, the aggregate densification theory was used to predict the final equilibrium bed height by densification rate and bed compression. Also, the relationship between aggregate size and thickening time was obtained (Usher and Scales 2005).

As mentioned above, the role of ore properties has not been studied by researchers, and most of them have focused on the effect of suspension properties in dewatering process. Therefore, the aim of this study was to study the influence of ore properties such as solid density, particle size, and mineralogy on the thickening process in order to better understand the dewatering behavior in these thickeners.

Materials and methods

The tailings obtained from the Sarcheshmeh copper flotation plants in Iran were used for all experiments. As the shaking table could separate the different particles based on their density and size, the tailings samples were initially continuously fed on the table by gravity to separate the tailings in three products as a slime "c", middling "b", and coarse "a". The particle size analysis, XRD and mineralogical studies were carried out to understand the sample properties. The laboratory screens and cylosizer were used for particle size analysis, and the results are shown in Table 1 and Fig. 1. The five Warman cyclosizers were used to analysis the particle size less than 44 μm (i.e. +44, +33, +23, +15, +11, and −11 μm). This cyclosizer worked at 2130 N/m^2 pressure for 20 min. The solid density was determined by a pycnometer (100 cm^3) and the results are presented in Table 2 along with the XRD analysis shown in Fig. 2. The microscopic mineralogical analysis was carried out to find out the metallic minerals in the samples (Table 3). In order to study the effect of the ore properties on the thickening process, the experiments were carried out on the plant conditions. The samples were taken as a suspension from the shaking table and prepared by tailings waste water, hence the thickening behavior can only be attributed to the ore properties. The sample suspension density was measured by Marcy scale and prepared to required density based on experimental conditions. The pH of the sample was kept as 11 which was the pH in the plant.

A high molecular weight of anionic polyacrylamide (NF43U from SNF) was used to flocculate the suspension and prepared at 0.25 g/dm^3 which were the industrial dosage. A 500 cm^3 of cylinder was used to study the thickening behavior and a chronometer was used to record the mud lines at different times.
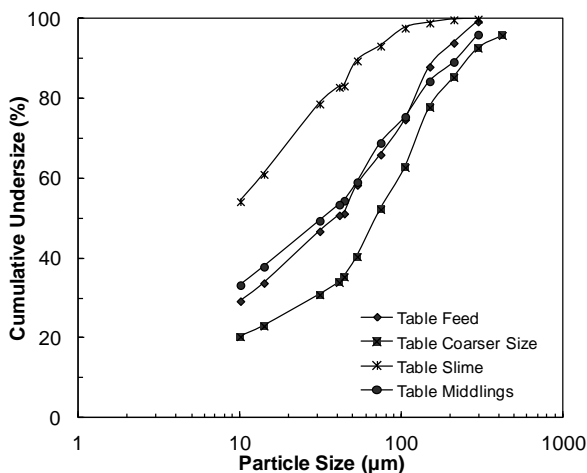
Fig. 1. Particle size distribution of feed, slime, middling, and coarse samples

Table 1. Particle size analysis of the samples

	Feed	Slime	Middling	Coarse
d_{80} (μm)	120	32	120	160
d_{75} (μm)	105	28	105	140
d_{50} (μm)	40	8.5	35	70
d_{25} (μm)	8	2	6	20

Table 2. XRD analysis and solid density of the samples

Minerals	Feed	Slime	Middling	Coarse
aluminum silicate (clinochlore, illite, chamosite, anorthite) (%)	75.6	84.2	43	–
quartz: SiO_2 (%)	22	15.6	53.6	15.6
pyrite: FeS_2 (%)	2.3	-	2.4	84.2
solid density (g/cm^3)	2.8	2.7	2.8	4.7

Table 3. Mineralogical analysis of the samples

Sample	Chalcopyrite	Pyrite	Sphalerite	Hematite	Non-metallic Minerals
Table Feed (%)	0.26	11.621	0	0.302	87.8
Table Slime (%)	0.087	12.244	0	0.392	87.243
Table Middling (%)	0.166	12.352	0.088	0.276	87.066
Table Coarser (%)	1.646	55.256	0.118	0.736	42.243
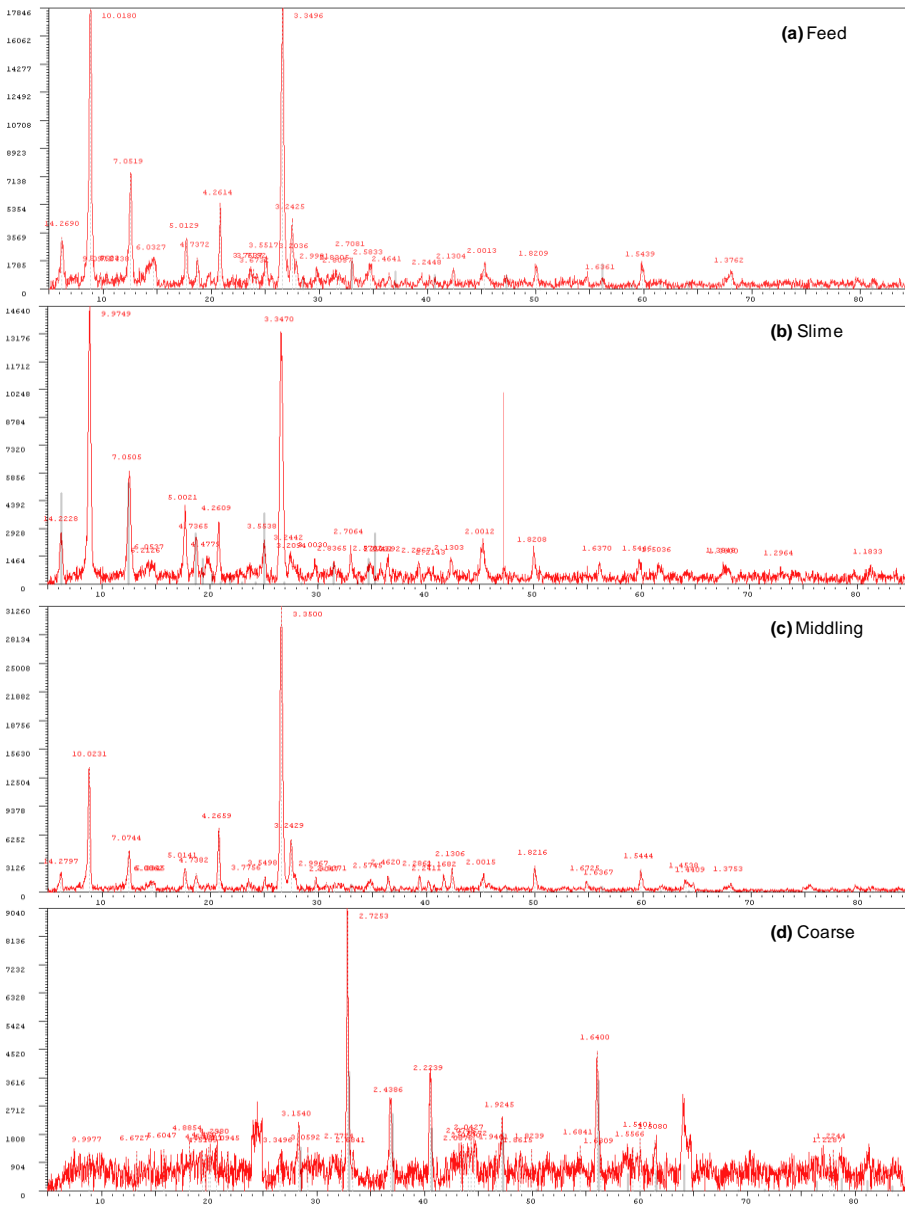
Fig. 2. XRD patterns of (a) feed (b) slime (c) middling (d) coarse samples

Results and discussions

Since the amount of flocculant consumption for the thickening process is usually between 20 and 40 g/Mg, the tests were carried out with a wider range of dosage between 15 and 60 g/Mg. The sedimentation curves for the samples are shown in Figs.

3 to 6. As presented in Tables 2 and 3, the most of the feed is composed of clay minerals and quartz, and the most amount of the slime is composed of clay minerals, but the content of clay minerals in the middle part of the shaking table is significantly lower than the content of them in the feed. In addition, clay minerals were not observed in the coarse sample, and much of them (about 55%) consist of pyrite. The sedimentation tests were performed on the feed and middling in order to investigate the tailings sedimentation behavior in mineralogical view because these two samples have the same solid density as 2.8 g/cm^3 and their d_{80} particle size are similar. In this study, the term "clay" is used as a mineralogical term, i.e. any of a diverse group of fine-grained minerals, not a size fraction.

The negative surface charge (OH$^-$ in alkali solution), swelling characteristics, and small particle size of clay minerals negatively affect the settling behavior of the slimes fraction within the thickening. These factors also affect the rheology of the slurry as it influences the solids concentration and the manner in which the particles stack during settling. As can be seen in Figs. 3 and 5, at different amounts of flocculant, the free settling velocity for the feed sample (2 to 6 mm/s) is much less than that for the middle part sample (18 to 23 mm/s) and in the compaction zone, the compressibility for the middling sample (in concentration range of 0.63 to 0.86 Mg/m^3) is more than that for the feed sample (in concentration range of 0.33 to 0.47 Mg/m^3), which this stems from the reduction of clay content in the middling sample. Also, in Fig. 3, it is observed that by the increasing the flocculant dosage to 30 g/Mg, a good compressibility was obtained in the compaction zone. However, an excessive amount of the flocculant caused the reduction of bed compressibility for the feed sample, and accordingly the final height value in the settling curve increased to 64 mm (for 20 g/Mg) and 68 mm (for 60 g/Mg). The cotton-mode was formed in this zone due to the increasing in the size of the flocks, the networked water was remained inside of the flocks, and therefore the underflow concentration of paste thickeners was reduced. This case was not observed in the middling sample (Fig. 5), and with the increasing of the flocculant dosage, the compressibility increased as well as the free settling velocity and the value of the final height in the settling curve decreased from 43 mm (for 20 g/Mg) to 33 mm (for 60 g/Mg), which could be caused by the interactions between coarse and fine particles in the feed sample, and interaction between the coarse particles in the middling sample.

The packing of the particles on top of each other during settling influences rheology and density of the thickened underflow. The most familiar packing types are referred to as "edge-face" also referred to as "houses of cards" and "face-face" also known as a "band structure" packing relationship (McFarlane et al. 2005). Clays typically stacks into honeycomb structure. The honeycomb packing retains large amounts of water which fills the voids formed by this type of arrangement.

Great effort and highly effective dewatering systems are required to remove the interstitial water therefore the thickener performance will decrease by increasing the clay content in the ore. Since the coarse and high density particles have higher settling

velocity than ones that were fine and lower density, thus they could be divided into two parts in view of settling behavior. Solid density of coarse particles (a) and fine particles (c) were 2.7 and 4.7 g/cm^3, respectively, and this difference at the density values was caused by the existence of clay minerals (aluminosilicates) in part (c) and metallic minerals (such as chalcopyrite and pyrite) in part (a). Since there was much difference between them in terms of size and density, there was also much difference between their settling velocities (Fig. 7).

There is a direct relation between the solid density and amount of metallic minerals. Therefore, the effect of metallic minerals in the settling behavior is defined as higher solid density. In addition, the surface charge on the particles (as mineralogical effects) plays an important role in the flocculation performance. This effect is not significant for the metallic minerals because the higher solid density is much more effective than the surface charge. Therefore, the metallic minerals (as ore properties) are more significant in the settling behavior than the flocculant dosage (operating parameter) because the changes in the flocculant dosage showed no significant effect on the thickening behavior of the sample part (a). In the case of this sample, the little amount of flocculant is needed to improve the clarity of the thickener overflow. It was postulated that the dominant minerals (such as clay and metallic minerals) in the samples would cause affecting the thickener performance. Additionally, part (c) and feed can be compared in a view of the particle size. Although their density was close together, they had different particle size distribution. The effect of this particle size differences was visible in their settling velocities. The smaller size would cause the lower settling velocity, hence that settling velocity for the slime sample was obtained between 0.1 and 0.4 mm/s but that was achieved between 2 and 6 mm/s for the feed (Fig. 7).

Meanwhile, the bed compressibility, which was one of the basic parameters in thickeners, was studied for these two samples. As can be seen in Figs. 4 and 6, the final height for sample (a) was about 19 mm, and for sample (c) was about 85 mm. In other words, the compressibility for sample (a) was very high and for sample (c) was very low, which is due to the parameters such as particle size, density, and mineralogy. With the increasing in the flocculant dosage, the compressibility in part (c) increased (Fig.4) and the final height increased from 92 mm (for flocculant dosage of 15 g/Mg) to 85 mm (for flocculant dosage of 60 g/Mg). The significant increase in the compressibility was observed with the increasing in the flocculant concentration from 15 g/Mg to 35 g/Mg, and from 40 g/Mg to 60 g/Mg. This change was also visible in the free settling zone, and there was no significant effect on the settling velocity, and the compressibility by the increasing in the amount of 5 g/Mg flocculant. The behavior of cotton accumulation of flocks (which was shown in Fig. 3 for feed) was considered minimal in this sample. The increasing in the flocculant dosage showed no effect on its compressibility for the sample part (a) because a high density and large particle sizes of this sample led to little need for the flocculant (Fig. 6).
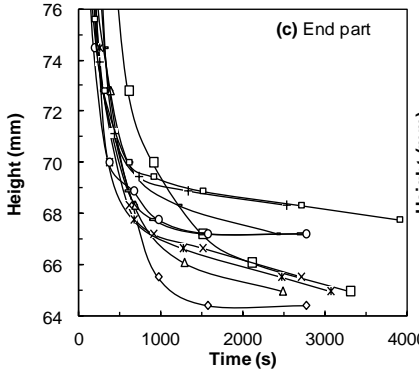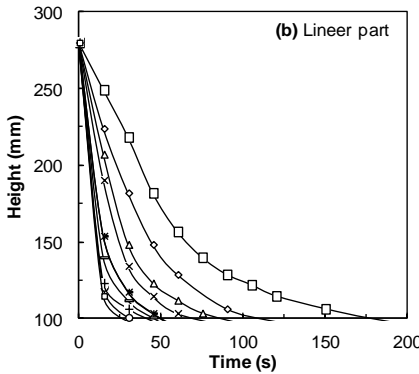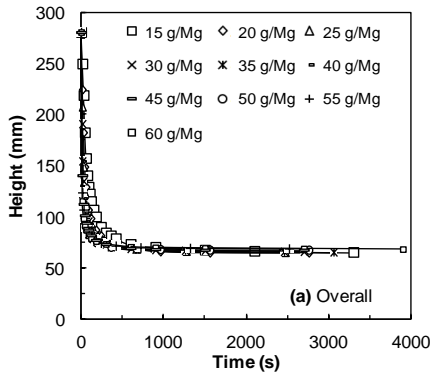
Fig. 3. Feed sedimentation curves
(a) overall (b) linear part (c) end part
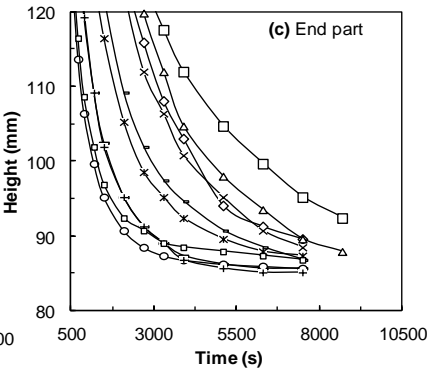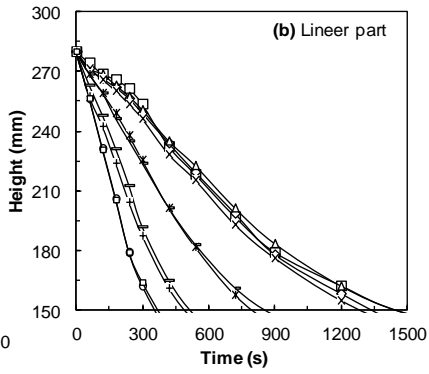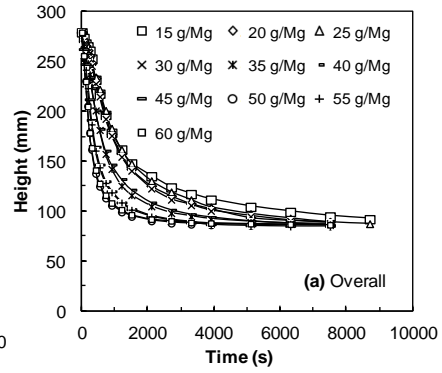
Fig. 4. Slime sedimentation curves
(a) overall (b) linear part (c) end part

Comparing Figs. 3 to 6 indicated that the cotton-mode in the compaction zone, observed only in the feed, can be removed by using this classification because this causes water trapping among the flocks and reduction of underflow concentration in the thickeners and reduces water recovery. Furthermore, with the separation of coarse and high density particles, the consumption of the flocculant for this fraction can be reduced or eliminated.
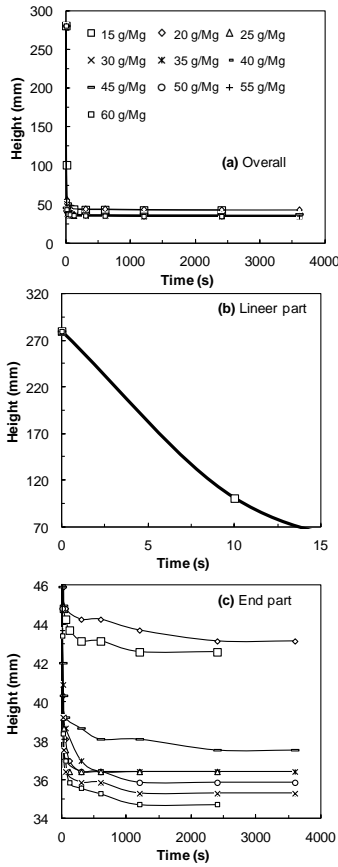
Fig. 5.Middling sedimentation curves
(a) overall (b) linear part (c) end part
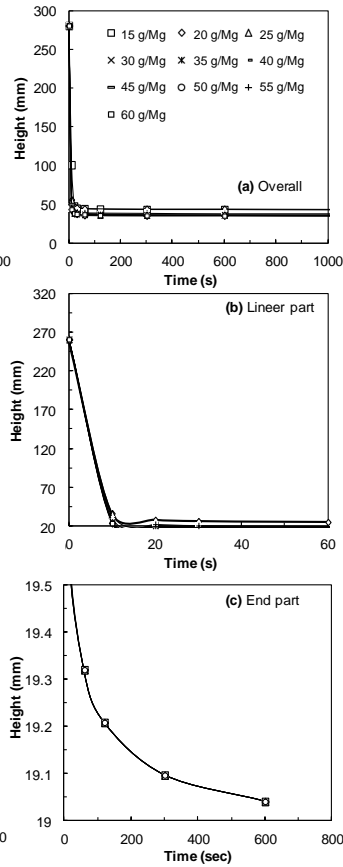
Fig. 6. Coarse sample sedimentation curves
(a) overall (b) linear part (c) end part
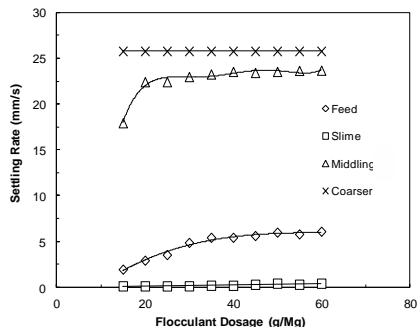
Fig. 7. Free settling curves of the samples

The Wilhelm-Naide model was used in order to compare the settling flux, and the results were shown in Fig. 8. As seen from Fig. 8, the maximum settling flux for the coarse, middling, feed and fine particles were obtained as 120, 55, 9, and 0.25

Mg/m²/h, respectively. Also, the maximum concentrations in the underflow were obtained as 1.57, 0.87, 0.45, and 0.35 Mg/m³, respectively. In other words, the maximum settling flux and concentration in underflow zone for the coarse and the middling parts were more than these amounts in the feed, and for the slime part were less than these amounts in the feed. This is due to changes in the ore properties which were illustrated before. The increasing in the flocculant consumption showed no effect on the settling flux for the coarse particle; it was due to the high density and coarse
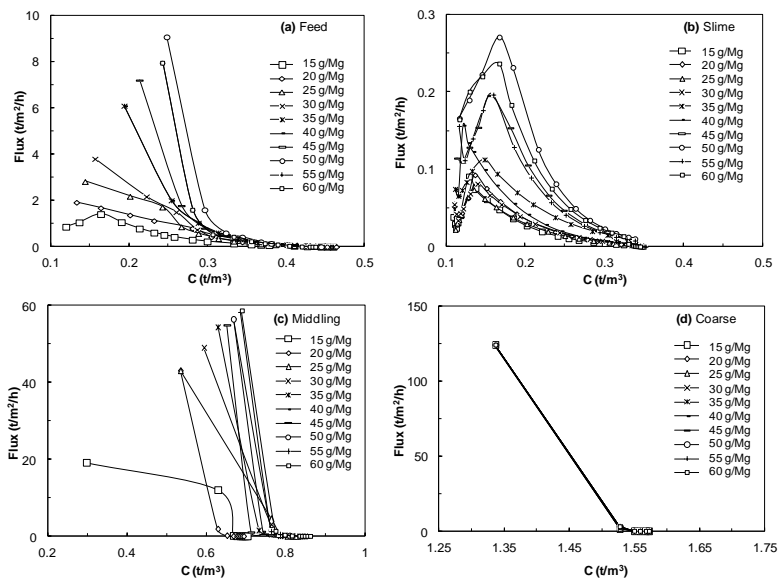
Fig. 8. The settling flux in different underflow density
(a) feed (b) slime (c) middling (d) coarse samples

size of metallic minerals in this part. As can be shown from Fig. 8, the initial flux values of the slime sample changed due to the changes in the settling rate. It means that the flocculant cannot prevail on the initial turbulence which was created because of the low settling velocity of the slimes. Also, this behavior was observed in the feed sample with a low concentration of flocculant (15 g/Mg). Therefore, the minimum amount of required flocculant can be obtained by studying the competition between initial turbulence and settling velocity which can be achieved in the settling flux curve.

According to the measurements and calculations, the weight of solid in the slime, middling, and coarse particle size parts were 46%, 50%, and 4% of the feed, respectively. Thus, half of the feed was transferred to the middling part but it could be understood from Figs. 7 and 8 that a major and effective factor in particles settling was the amount of slime in the feed.

Conclusions

The role of ore properties (density, particle size, mineralogy) in thickening process (settling velocity, bed compressibility, settling flux) were studied in this work using a Sarcheshmeh tailing sample. Initially a shaking table was employed and sample was applied to achieve three different slime, middling, and coarse products. As a result, the free settling velocity of feed (2–6 mm/s) was less than middling sample (18–23 mm/s), and the compressibility of middling (density: 0.63–0.86 Mg/m^3) was more than feed sample (density: 0.33–0.47 Mg/m^3). This was due to the amount of clay reduction in middling sample. Also, it was observed that an excessive amount of flocculant caused reduction of bed compressibility for the feed sample, and the final height value in the settling curve increased to 64 mm (for 20 g/Mg) and 68mm (for 60 g/Mg). The cotton-mode was formed in this zone due to the increasing in the size of the flocks, hence the networked water was remained inside of the flocks, and hence the underflow concentration of the paste thickeners reduced. Therefore, it caused remaining the networked water inside of the flocks and the underflow concentration of the paste thickeners would decrease. This case was not observed for the middling sample, and the compressibility increased with the increasing of flocculant dosage as well as free settling velocity. The value of the final height in the settling curve decreased from 43 mm (for 20 g/Mg) to 33mm (for 60 g/Mg), which could be caused by the interactions between coarse and fine particles in the feed sample, and interaction between the coarse particles in the middling sample.

Also, it was concluded that the clay minerals (aluminosilicates) and metallic minerals (pyrite, chalcopyrite) caused to reduce and to increase the settling velocity, settling flux, and underflow density, respectively, hence the settling velocity of the slime and the coarse particles were obtained as 0.1–0.4 and 26 mm/s, respectively. The maximum flux of the slime and the coarse particles were obtained as 0.25 and 120 Mg/m^2/h, respectively, and the maximum underflow density of slime and coarse particles were obtained 0.35 and 1.57 Mg/m^3. Therefore, the lower particle size and density would reduce the thickener performance. The cotton-mode in the compaction zone, which was observed only for the feed, could be removed by using this classification. Furthermore, with the separation of coarse and high density particles, the consumption of the flocculant for this fraction would be reduced or eliminated. In addition, the effective and major parameter in the sedimentation was the clay content of the feed.

References

BURGER R., BUSTOS M.C., CONCHA F., 1999, *Settling velocities of particulate systems*: 9. *Phenomenological theory of sedimentation processes: numerical simulation of the transient behavior of flocculated suspensions in an ideal batch or continuous thickener*, International Journal of Mineral Processing, 55, 267–282.

BUSCALL R., MCGOWAN I.J., MILLS P.D.A., STEWART R.F., SUTTON D., WHITE L.R., YATES G.E., 1987, *The Rheology of strongly flocculated suspensions*, Non-Newtonian Fluid Mechanics, 24, 183–202.

BUSTOS M.C., CONCHA F., BURGER R., TORY E.M., 1999, *Sedimentation and Thickening*, Kluwer Academic Publishers, Dordrecht, Netherlands, 285.

COE H. S., CLEVENGER G. H., 1916, *Methods for determining the capacities of slime thickening tanks*, Trans AIME, 55, 356–384.

CONCHA F., BUSTOS M.C., BARRIENTOS A., 1996, *Phenomenological Theory of Sedimentation*, Chapter 3 in *Sedimentation of small particles in a viscous Fluid*, Computational Mechanics Publications, Southampton, UK, 51-96.

DAHLSTORM D.A., FITCH E.B., 1985, Mineral Processing Handbook, N.L. Wiess (ed), SME/AIME, Chapter 9, 2-14.

DEVENTER B.G., USHER S.P., KUMAR A., RUDMAN M., SCALES P.J., 2011, *Aggregate densification and batch settling*, Chemical Engineering Journal, 171, 141–151.

GARRIDO P., BURGOS R., CONCHA F., BURGER R., 2003, *Software for the design and simulation of gravity thickeners*, Minerals Engineering, 16, 85–92.

GARRIDO P., CONCHA F., BURGER R., 2003, *Settling velocities of particulate systems*: 14. *Unified model of sedimentation, centrifugation and filtration of flocculated suspensions*, International Journal of Mineral Processing, 72, 57–74.

GLADMAN B.R., RUDMAN M., SCALES P.J., 2010, *Experimental validation of a 1-D continuous thickening model using a pilot column*, Chemical Engineering Science, 65, 3937–3946.

GREEN M.D., 1997, *Characterization of suspensions in settling and compression*, PhD thesis, Department of Chemical Engineering, University of Melbourne Parkville Victoria 3052, Australia.

KELLY E.G., SPOTISSWOOD D.G., 1989, *Introduction to Mineral Processing*, Mineral Engineering Services, Denver.

KYNCH G. J., 1952, *a theory of sedimentation*, Trans Faraday Society, 48, 166–176.

LANDMAN K.A., WHITE L.R., BUSCALL R., 1988, *The Continuous-flow gravity thickener: Steady State Behavior*, AIChE Journal, 34, 239–252.

LESTER D.R., RUDMAN M., SCALES P.J., 2010, *Macroscopic dynamics of flocculated colloidal suspensions*, Chemical Engineering Science, 65, 6362–6378.

MCFARLANE A., BREMMELL K., ADDAIMENSAH J., 2005, *Microstructure, rheology and dewatering behavior of smectite dispersions during orthokinetic flocculation*, Minerals Engineering, 18, 1173.

OLTMANN H.H, 1975, *Filtration and Separation*, 12, 6, 636.

OSBORNE D.G., 1977, *Solid-Liquid Separation*, Chapter 5, L. Svarovsky (ed), Butterworth, London, Boston, 75–99.

TALMAGE W. P., FITCH E.B., 1955, *Industrial and Engineering Chemistry*, 47, 38.

USHER S.P., SCALES P.J., 2005, *Steady state thickener modeling from the compressive yield stress and hindered settling function*, Chemical Engineering Journal, 111, 253–261.

USHER S.P., SPEHAR R., SCALES P.J., 2009, *Theoretical analysis of aggregate densification: Impact on thickener performance*, Chemical Engineering Journal, 151, 202–208.

WILHELM J. H., NAIDE Y., 1981, *Sizing and operating continuous thickeners,* Mining Engineering, 1710–1718.

YALCIN T., 1988, *Bulletin of the Canadian Institute of Metallurgy*, 81, 910, 69.

YOSHIOKA N., HOTTA Y, TANAKA S., NAITO S., TONGAMI S. 1957, *Continuous thickening of homogeneous slurries*, Chemical Engineering, Tokyo, 21, 66-74.

MOBILITY OF SHALE DRILL CUTTINGS CONSTITUENTS

Katarzyna PISZCZ, Justyna LUCZAK, Jan HUPKA

Department of Chemical Technology, Faculty of Chemistry, Gdansk University of Technology, Poland,
katpiszcz@gmail.com

Abstract: This study focuses on the abundance and mobility of metals and trace elements from shale drill cuttings into water, being the main component of the hydraulic fracturing fluid. The relationship between composition of the shale rock and the potential element release during standard water-based leaching tests was characterized by means of X-Ray Fluorescence spectroscopy (XRF). The XRF analysis confirmed the assumption of shales constituents mobility due to the water-rocks interaction. The mobility of studied constituents was expressed by means of variations in content of individual elements. Increased pH of leachates obtained as a result of water based leaching medium indicated releasing of alkaline origin components such as Ca, Rb, Mo, Sr. Measurements of TOC of the leachates indicated low levels of dissolved organic carbon.

Keywords: shale, gas, flowback fluid, liquid residue, leaching, fracturing

Introduction

Production of large amounts of flowback fluid is an important issue in Poland as a potential region for shale gas production. Treatment and recycling of the flowback may pose additional concerns due to leachability of chemicals deposited from the geological formations, which may pose risks to aquatic biota if directly discharged to the environment, and create problems in re-using of the fluid (Fakhru'l-Razi et al. 2009). Leaching is a process by which constituents soluble in liquid migrate from a solid material into an interacting fluid. As a consequence, this phenomenon may lead to formation of liquid waste with characteristics depending on the chemical and physical composition of the shale formation, the operational conditions of fracturing, along with pH, redox potential and composition of the contacting fluid (Heasman et al. 1997). The release of constituents is determined by a confluence of mass transfer mechanisms and chemical processes (Klein 1989).

The longer the hydraulic fluid remains in the reservoir, the more significant the change in composition is. Therefore, the flowback in first few weeks after fracturing is characterized by a high flow rate and composition similar to the liquid introduced into the bed. After this period, the flow rate steadily decrease and the output stream is referred to as liquid residues. These include the remaining part of the fracturing fluid and the reservoir water. Consequently, the liquid composition changes significantly (Tessier et al. 1979). Along with the chemicals introduced with the HFF, the flowback fluid may contain a wide variety of dissolved constituents such as dissolved minerals, dissolved and dispersed oil compounds, salts, metal ions, naturally occurring radioactive materials (NORM), and dissolved gases (Johnson et al. 2008). Therefore, the chemical and physical characteristics of the shale formations and these waters are needed, and the constituents of concern should be identified. These components can make wastewater disposal difficult, and expensive and in addition may impair gas production (Fakhru'l-Razi et al. 2009). Consequently, the flowback may be considered hazardous and require treatment by using suitable technology giving harmless and valuable product to meet environmental regulations and be able to be reused (Calmano et al. 1993).

The elemental and mineralogical characteristics of the shale rocks and flowback fluids has been carried out by various research groups using different analytical methods. Falk and coworkers (2006) used Inductively Coupled Plasma Mass Spectrometry (ICP-MS) and Inductively Coupled Plasma Atomic Emission Spectroscopy (ICP-AES) techniques to observe metals release and changes in pH during leaching test performed with water adjusted to pH 4.0. It was revealed that the concentration of heavy metals in leachate significantly increase in time along with pH decrease (Falk et al. 2006). The release by weathering of selected heavy metals and traces elements was investigated by Peng and co-authors by means of the ICP-MS analytical technique. It was concluded that weathering may be one of the most important sources of environmental contamination with heavy metals and traces elements in areas where black shales are collected and distributed (Peng et al. 2004). Chemical and mineralogical analysis of serpentinite rock samples to characterize the effect of weathering of toxic Cr and Ni metals was examined by Baneschi et al. (2013) by scanning electron microscopy (SEM), electron microprobe (EMP), X-Ray Fluorescence (XRF). To obtain quantitative information about the distribution of trace metals in different mineralogical phases (clay minerals, carbonates, amorphous Fe, Mn oxides, organic matter and other silicates and oxides) a seven-steps sequential extraction analysis was performed. The results suggest that Cr and Ni could be adsorbed by amorphous Mn and Fe hydroxides after the weathering of serpentinites and may be released at different redox conditions, increasing in this way their mobility in the environment (Baneschi et al. 2013). Chapman et al. (2012) tested samples of both hydraulic fracturing fluids and flowback produced during drilling process at Middle Devonian Marcellus Shale wellheads. Investigation was carried out to determine the utility of Sr isotopes in identifying and quantifying the interaction of

produced waters with other waters in the region in the event of an accidental release. The Sr isotope was found out to constitute an extremely sensitive tracer with strong potential as a tool for verification the safety of water disposal, and to determine the origin of total dissolved solids (TDS) in surface and ground waters. Major elements and Sr isotope geochemistry were analyzed by ICP-MS and ICP-AES (Chapman et al. 2012).

Background

Sedimentary shale formations, and as a consequence drill cuttings, are composed mainly of inorganic materials such as clay minerals (illite, smectite, kaolinite, chlorite, biotite, mica), and siliciclastic minerals (quartz, sandstone, feldspar, orthoclase, plagioclase, biotite etc.), though carbonates (dolomite, calcite, limestone ect.) also occur. Shale rocks are enriched in kerogen, a mixture of organic substances, which brake down to form hydrocarbons (Durand 1980). The relative proportions of inorganic and organic materials in generated waste material depend on geology of shale formations varied with organic phase from the drilling fluid used in the vertical and horizontal drilling procedure. The composition of shale rocks as well as some geological properties of selected shale formations in USA, Canada, and Poland were collected and compared in Table 1. The brittle minerals content represented by siliciclastic and carbonate fractions is an important criterion to assess the shales potential for proper respond to hydraulic stimulation and formation of the tree-shaped network of fractures, favorable for gas extraction. Shales with a high percentage of quartz and carbonate as well as presence of illite provide more easily fracturing and breaking to a wide range of small-scale fractures providing numerous flow paths from the matrix to the wellbore. On the contrary, the high amount of ductile clays will result in the deformation of the bed instead of fracturing providing only few induces fractures (Zou et al. 2010). Therefore, shale formations with high quartz and low clay content typically have high Young's modulus and low Poisson's ratio making them more brittle, more prone to natural fractures, and good candidates for proper respond to hydraulic stimulation (Jaeger et al. 2009). The relation between siliciclastic, carbonate minerals and clays content is related with a depositional environment of the shale. It was observed that marine-deposited shales tend to have lower clay content along with higher amount of brittle minerals in comparison to non-marine shales being lacustrine, fluvial deposits as shown in Table 1 (Alexander et al. 2011).

For commercial development deposits with fragile mineral content over 40%, and clay content less than 30% are usually chosen. The average quartz content of shale gas formations in USA is 28–50%, with carbonate content of 4–16%, and total fragile mineral content is on average 46–60% (Zou et al. 2010). In classical example of shale formations Barnett shale in Fort Worth Basin (Texas, USA), being the non-marine deposits, the clay contend is assessed to be 20–50%, siliciclastic minerals 35-50%, and carbonate fractions 0–30%. In comparison, in marine deposited Marcellus shale in

Appalachian Basin (eastern North America, USA) may contain from 20 to even 60% siliclastic minerals, 3–50 carbonate fractions, and lower clay content 10–35% (Bruner et al. 2011). Shale rocks in Poland are mainly marine-deposited formations, however the local structural geology is still poorly understood. Some early shale exploration revealed that quartz content in selected areas can be favorably high (40–80%), however along with high conducive to effective fracture stimulation clay content (30-40%). Further exploration drilling and seismic surveys are still needed to define potential sweet spots in Poland (EIA 2013).

To define the prospective area for development of shale gas, the parameters as total organic content (TOC) as well as thermal maturity are also used. High enough TOC content is required to generate and hold satisfactory gas level for commercial production. General grouping of shales based on TOC content (in wt% of rock) starts from non-source (<0.5), fair (0.5-1.0), good (1.0-2.0), and excellent gas source (>2) (Zhu et al. 2011). The TOC values for shale formations presented in Tab.1 are in the range of 0.5 to even 14 (wt%). For example in Barnett shale gas formation the TOC content was determined to be on average 2–6%, in Marcellus shale 2–10% (Jarvie et al. 2007), and the average TOC value in USA appears to be from 1,3% to 4% wt (Poprawa 2010). The TOC range of Polish samples was recognized to be quite high (1–14%) (EIA 2013). The main stratigraphic targets for shale gas exploration in Poland is approximately 500 m of high resistivity, and the high-TOC. According to the available data, the TOC values are in the range of 2–4% and 6% in Llandovery Baltic Basin section, and Podlasie Basin, respectively. The Upper Cambrian to Tremadocian shale, present only in the northern part of the Baltic Basin, contains high average TOC of 3–12% (EIA 2013).

Thermal maturity of the mineral formation can be indicated by vitrinite reflectance (VR expressed as $\%R_o$) as a measure of degree to which organic metamorphism has progressed. The higher thermal maturity, the lower TOC content of the formation and for hydrocarbon generation VR seems to be more than 0.5%.

The thermal maturity of the oil prone prospective area has a $\%R_o$ greater than 0.7, but less than 1.0%, the wet gas and condensate are between 1.0% and 1.3%, whereas dry gas areas typically have an R_o greater than 1.3% (EIA 2013). For presented in Tab.1 shale formations VR varied between 0.3 and below 4 (Jarvie et al. 2005). The Barnett shale VR, reflecting the beginning of dry gas ($\%R_o = 1.2$), is considerably lower than for Marcellus shale ($\% R_o = 1.6$), and attributed to chemical interactions between petroleum, kerogen, and clay minerals in the shale or to a slow geological heating rate (Bruner et al. 2011).

In Poland $\%R_o$ was observed to be in between 0.85 for Lower Silurian to 1.8 for Upper Cambrian formations in all regions (Lis et al. 2000). The Upper Jurassic and Lower Cretaceous in the Baltic Basin locally have TOC >1.5%, but are thermally immature (R_o 0.5% to 0.7%), therefore were not assessed as potential area for gas exploration. For comparison, the Carboniferous shale in the Fore-Sudetic Monocline

contains 1% to 5% TOC, is located in the dry gas thermal maturity window (R_o of 1.3% to 2.0%), and contains 20% to 60% silica with 2% to 8% total porosity.

As it was mentioned above some bed of shales are known to contain also trace metals (including heavy metals) or even are enriched in metals (Vine and Tourtelot, 1970). Systematic research on metal content in rocks, sediments, waters and biological substances revealed, that organic carbon-rich sediments are often enriched in metals, like Mo, V, Cu, Zn, or U probably due to their abundance in seawater (Goldschmidt 1954; Brumsack 2006). Trace elements can interact both with inorganic and organic compounds of shale formations. According to the Vine and Tourtelot (1970) the trace elements can be divided into connected with detrital minerals (Al, Ti, Ga, Zr, Sc), carbonate formations (Ca, Mg, Mn, Sr), and organic associations (Ag, Mo, Zn, Ni, Cu, Cr, V) (Brumsack 2006).

Tab. 1. Comparison of shale formation components

Shale Formation	TOC (%)	R_o (%)	Component (wt.%)	Chemical Elements
Barnett (USA); Non–marine– deposited shales (1)	2.0–7.0	1.10–2.00	Clay minerals (20–25/50): Illite, Smectite, Kaolinite, Siliciclastic fraction (35–50%): Quartz (40), Feldspar (7), Plagioclase (5) Carbonate minerals (0–30): Calcite, Dolomite, Siderite Other: Pyrite (2–6)	Sr, F, Ba, As, B, Br, U, Ag, Co, Cr, Cu, Mo, Ni, U, V, Zn, Th, Ra^{226}, Ra^{228}
Fayetteville (USA) Non–marine– deposited shales (2)	2.0–9.8	1.20– >4.00	Clay minerals: Chlorite (<5), Illite (20–25) Siliciclastic fraction: Quartz (40–50) Carbonate minerals: Calcite (5–10), Dolomite (5–10)	Fe, Mg, Al, K, Fe, Cr, Th, Zr, Co, Ti
Haynesville (USA) marine–deposited shale (3)	0.5–4.0	2.20–3.20	Clay minerals (25–35%): Illite, Kaolinite, Chlorite (25–35) Siliciclastic fraction (34%): Quartz, Potassium Feldspar, Dolomite, Plagioclase Carbonate minerals: Calcite (5–30%), Dolomite, Fe–Dolomite	Fe, Mg, Al, K, Cr, Zr, V, Co, Ni, U, S
Marcellus (USA) marine–deposited shales (4)	3.0–12.0	1.50–3.00	Clay minerals (10–35%): Illite, Smectite, Biotite, Montmorillonite Siliciclastic fraction (20–60%): Quartz, Muscovite, Feldspar (0–4), Mica (5–13) Carbonate minerals (3–50): Trona Other: Todorokite, Pyrite (5–13)	Ti, Na, Li, Ba Sr, Cs Cr, Mn, Mg, Al, Fe, ^{238}U,
Woodford (USA) marine–deposited shales (5)	1.0–14.0	1.10–3.00	Clay minerals: Illite (13–40%), Kaolinite (1–5%), Chlorite (0–5%) Siliciclastic fraction: Quartz (30–60), Mica, Feldspar (2–10%), Glauconite, Plagioclase (1–4%) Carbonate minerals (6–28%): Calcite (5–11%), Dolomite (0–9%) Other: Pyrite (0–20%), Apatite	Fe, Mg, Al, K, Cr, Pb, Bi, Ti, Cu, Zn, Co, V, Mo, U, S

Shale Formation	TOC (%)	R_o (%)	Component (wt.%)	Chemical Elements
Pierre (Canada) marine–deposited shales (6)	1.0–6.0		Clay minerals (60–70): Smectite (20), Illite (6), Kaolinite (11) Siliciclastic fraction: Quartz (20–43), Orthoclase (2), Plagioclase (7), Feldspar Carbonate minerals (5): Calcite (2), Siderite (2) Other: Pyrite (1)	Fe, Mg, Al, K, Cr, Ti, V, Co, Cu, Pb, Zn, As,
New Albany (USA) (7)	>1.0– 13.00	0.5–1.0	Clay minerals: Siliciclastic fraction: Quartz, Feldspar, Glauconite Carbonate minerals: Dolomite Other: Pyrite, Phosphorite	Fe, P, F, U, Cu, Pb, Zn, Ni, Cd, Co, Mn, Mo, V, Sb, Se
Baltic Basin (8) Poland average	1–6 3.9	1–2.6 0.85–1.8	Clay minerals (30–48/80%) Siliciclastic fraction (25–63%)Clay minerals (30–40%) Siliciclastic fraction: quartz (40–80%)	Ca, K, Na, Mg, Zr, Ti, Fe, Mn, Cr,, Al, V, B, F

* Apatite $Ca_5(PO_4)_3(F,Cl,OH)$ Biotite $K(Mg,Fe)_3(AlSi_3O_{10})(OH,F)_2$
   Calcite $CaCO_3$ Chlorite $(Mg,Fe)_3(Si,Al)_4O_{10}(OH)_2 \cdot (Mg,Fe)_3(OH)_6$
   Dolomite $(CaMg)(CO_3)_2$ Feldspar $(KAlSi_3O_8 - NaAlSi_3O_8 - CaAl_2Si_2O_8)$
   Glauconite $(K,Na)(Fe^{3+},Al,Mg)_2(Si,Al)_4O_{10}(OH)$ Illite $(K,H_3O)(Al,Mg,Fe)_2(Si,Al)_4O_{10}[(OH)_2,(H_2O)]$
   Kaolinite $Al_2Si_2O_5(OH)_4$ Montmorillonite $(Al_2O_3 \cdot SiO_2 \cdot nH_2O)$
   Pyrite Fe_2S Phosphorite $Ca_5(PO_4)_3F$
   Plagioclase $NaAlSi_3O_8 - CaAl_2Si_2O_8$ Siderite $FeCO_3$
   Todorokite $(Na,Ca,K,Ba,Sr)_{1-x}(Mn,Mg,Al)_6O_{12} \cdot 3\text{-}4H_2$

1. (Aydemir 2011), (Orth et al. 1986); 2. (Bai et al. 2012) (Kidder et al. 2003); 3. (Hammes et al. 2012) (Dix et al. 2010); 4. (Harrell et al. 1991) (Onuoha et al. 2011); 5. (Comer 1991) (Harris 2013); 6. (Metwally et al. 2012) (Rader et al. 1961) (Kennedy et al. 2002); 7. (Ettensohn et al. 1981) (Ripley et al. 1990) (Tuttle et al. 2009) 8.(EIA 2013) (Marcinkowski et al. 2013)

Leaching test

The leaching test of rock samples was performed in accordance to the European Standard EN 12457-2 1313, 2002. The tests were conducted in compliance with leaching test for crushed material. One-stage batch test with distilled water at constant liquid to solid ratio (L/S) of 10 and temperature 25 ºC was performed. The rock-water mixture was continuously agitated for 24 hours at 300 rpm/min with the aim of reaching equilibrium conditions. Liquid/solid phase separation was preformed via centrifugation at average RCF = 1456×g for 10 min, followed by pressure filtration in order to obtain the solid material as well as leachate meant for further chemical analysis.

Analytical methodology

Organic matter content in rock samples was determined by ignition at 550 ºC of samples in the muffle furnace. Content of total organic carbon was conducted by Shimadzu TOC-Vcsh Total Organic Carbon Analyzer. Mineralogical characterization was performed by X-ray diffraction using Xpert PRO-MPD, Philips. Elemental analysis of shale rocks before and after leaching was made by a X-Ray Fluorescence Spectrometer (Bruker S8 TIGER Wavelength dispersive X-Ray Fluorescence

WDXRF). Leachates were characterized taking into account total organic carbon content (LiquiTOC Elementar AnalysenSysteme GmbH) and pH (glass electrode ERH-111 and Multifunction Computer Meter, Elmetron).

Results and discussion

The shales used in this study, shown in Fig. 1, were extracted from marine deposits in Baltic Basin formed in Lower Silurian Llandrovery age (Franus et al. 2009). Organic matter content (determined as solids volatile in $550^{o}C$) in shale samples was $3.22\% \pm 0.22$, with total organic carbon $0.85\% \pm 0.03$. Total organic carbon content is much lower than average value for Baltic Basin (4%) mentioned in the report "Technically Recoverable Shale Oil and Shale Gas Resources" published in 2013 by U.S. Energy Information Administration, grouping this bed into fair gas source in terms of its organic richness. According to the period of shale formation, average TOC values for individual sections of the Llandovery Baltic Basin are usually within the range from 1 to 2.5%, whereas Wenlock sections in central, western, and eastern parts of the Baltic Basin usually was determined to be 0.5-1.3%, and 1–1.7% TOC, respectively (Ehlers 1958).

Fig. 1. Picture of studied shale rock material

X-ray diffraction analysis was performed to evaluate the samples detailed mineralogy. The results revealed that the samples cover a wide range of mineralogical composition including mainly clay, siliclastic, and carbonate minerals, as well as other phases. The dominant mineral phase in shale samples was quartz, constituting approximately half of their weight.

X-ray pattern of the powdered shale samples were recorded with Cu target Kα-ray ($\lambda = 1.5406$ Å) in the range $2\Theta = 10$–60 with a 0.02 step interval and 2.0 scan step size for better resolution of the mineral phases as shown in Fig. 2.
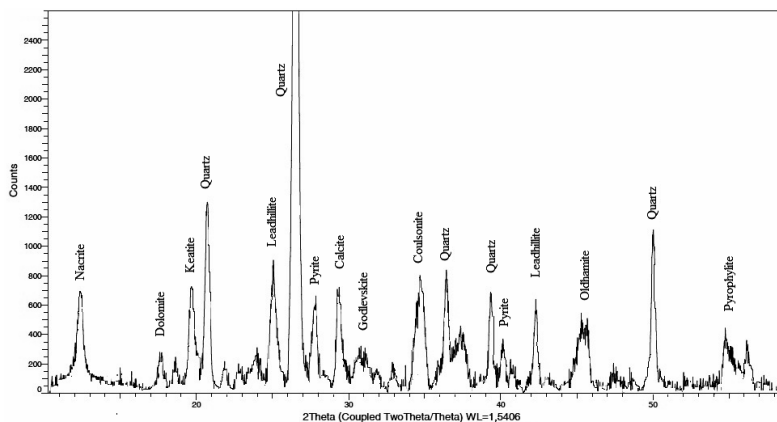
Fig. 2. Diffraction pattern of the shale samples main mineral phases

Furthermore, the X-ray diffraction pattern of the clay components were recorded in the range $2\Theta = 2$–30 with a 0.02 step interval and 2.0 scan step size indicating presence of illite, chlorite and kaolinite or nacrite $Al_2Si_2O_5(OH)_4$ (Fig. 3).
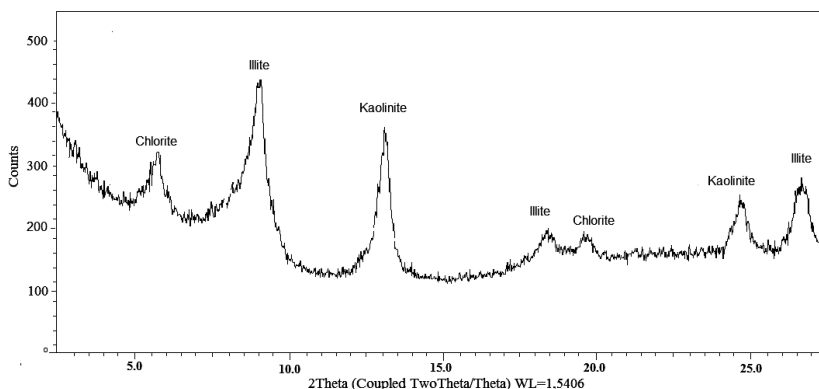
Fig. 3. Diffraction pattern of the clay components

Small proportions of siliciclastic minerals mainly in a form of quartz but also feldspar and micas as muscovite and biotite as well as pyrophyllite $(Al_2Si_4O_{10}(OH)_2)$ were observed.

The carbonate-bearing minerals are present mostly in a form of calcite, dolomite and leadhilite $(Pb_4(SO_4)(CO_3)_2(OH)_2)$. Moreover pyrite and other minerals like godlevskite $(Ni,Fe)_9S_8$, coulsonite (FeV_2O_4), oldhamite (CaS) were observed in minority. The high quartz and low clay content in our samples indicate that the shale may respond favorably to hydraulic stimulation. The XRD mineral analysis results are summarized in Table 2.

Table 2. Mineralogical composition of shale rock samples performed by XRD

Mineral	Component
Clay minerals	chlorite
	illite
	kaolinite (nacrite)
Siliciclastic	quartz (keatite)
	feldspar (plagioclase)
	mica (muscovite/biotite)
	pyrophyllite
Carbonate minerals	calcite
	dolomite
	leadhillite
Other	pyrite
	godlevskite
	coulsonite
	oldhamite

The detailed elemental characteristics of shale rock material was carried out by X-ray fluorescence spectroscopy. The results expressed as the percentage of mass content with experimental errors and lower limit detection are presented in Table 3. The XRF elemental analysis results confirmed that shale samples are composed mainly of aluminosilicate of Ca, Mg, Fe, K, Na forming feldspar, plagioclase, micas and pyrophyllite minerals. These main elements (excluding oxygen) form approximately 46.80 wt% of inorganic fraction. The residue 1.76 wt% is comprised of the elements like Ti, S, V, Mn, Zn, Sr, P, Zr, Cu, Rb, Ni, Cr and Mo, named in this work as trace elements. In comparison to the average geochemistry of earth crust, the studied samples are enriched in Mo, V, Zn, Cu, Ni.

Our results are in agreement with data obtained by Mainali (2012), who examined major and trace elements concentrations in the Hansville shale formation using a hand-held X-ray fluorescence spectroscopy. Cumulative average weight percent of major (Mg, Al, Si, P, S, K, Ca, Ti, Mn, Fe) and trace elements (V, Cr, Co, Ni, Cu, Zn, Th, Rb, U, Sr, Zr, Mo) was about 43% and 0.14% respectively (Mainali 2012). Multiple analysis of minor elements in Pierre Shale was followed by Rader and Grimaldi (1961), and revealed that all samples contained Ti from 0.05 to 0.5%, V, Zn, Cr, Mg in the range from 50 to 500 ppm, Co, Pb, Cu, Ni As from 5 to 50 ppm, and narrow range of 1.0 to 5.0 ppm Se, Mo, U, W.

Leachability of chemical elements from the shale formation to water was investigated by leaching test for crushed material. Constituents migration due to a leaching process of selected grain size fractions was based on determination of the changes in mass concentration of chemical elements against the content in original

Table 3. Elemental analysis of shale rock material by XRF

Element	Conc. [%m/m]	Stat. error [%]	LLD [PPM]
Si	21.99	0.45	64.40
Fe	8.44	0.28	37.20
Al	7.08	0.74	65.80
K	4.08	0.95	32.00
Ca	3.59	1.23	51.30
Mg	1.62	1.42	117.40
Ti	0.63	2.16	27.80
S	0.37	2.86	25.90
Na	0.35	5.16	188.30
Mn	0.14	2.84	23.90
Sr	0.06	3.31	10.40
P	0.05	10.6	41.80
Zr	0.03	3.09	13.90
V	0.03	9.26	42.50
Rb	0.03	3.33	11.30
Zn	0.02	6.33	14.30
Cr	0.02	11.20	34.50
Cu	0.02	11.70	15.90
Ni	0.01	16.70	18.00
Mo	0.01	12.30	11.00

shale samples, measured by XRF spectroscopy. The results of leaching test in respect to particle size fractions, presented in Figs 4-5 revealed that some elements may be released from the shale structure by deionized water. For most of the chemical elements it was shown that the highest weight loss appeared in fraction 1.When analysing main elements, it can be seen that calcium, present in parent rock in amount of 3.6 wt% mainly in siliciclastic and carbonate minerals is leached by water medium to concentration close or below 2 wt%. The Ca^{2+} ions collected in leachates may be identified as easily exchangeable ions located in interlayer sites in clays or as resulting from primary dissolved carbonates. Aluminium and silica compounds are also main elements and occur in variety of minerals (quartz, feldspars, clays) in the parent rock. Despite Al is strongly hydrolysing element, content remain relatively unchanged comparing the parent shale with the leached samples (decreased by 5–11% from an initial value for fraction 2–4), except the first fraction (4.0–2.362 mm), was a 50% decrease of calculated weight. Similar scenario was reported for silica element, were a reduction of 3–10% in weight loss percentage for fraction 2–4, was observed. Concentrations of sodium (0.35 wt%) and potassium (4.1 wt%), bounded in feldspars, clays and oldhamite, also decreased to 0.1–0.25, and 2.6–3.7 wt%, respectively.

Decrease of sodium element may suggest also mass loss of plagioclase. These observations indicated minor leachabilty of Al, Si, Na and K compounds from the sample to aqueous solution in applied leaching conditions. Magnesium content of 1.62 wt%, being present primarily in clays, only slightly declined. The compounds of iron were readily leached from the solids samples irrespective of granularity of the sample (decreased by 10–40% from an initial value). Iron is accumulated in the shales mainly as a sulphide fraction in pyrite, silicate association as chlorite, and to lower extend in godlevskite, oldhamite, coulsonite. The results stays in the contrary to data presented by Lavergren et al. (2009), who observed iron compounds associated mainly with sulphide, Fe-bearing silicates and to some extend with organic material, fractions highly insoluble in water (Lavergren et al. 2009).

When considering trace elements almost all of this elements were easily leached to liquid in the water-based leaching test. In all samples, the exception was sulphur, found to not migrate to aqueous phase probably due to abundance in the insoluble in water piryte form or godlevskite, and oldhamite. The concentration of Zr was unchanged except for a decrease in the fraction 1, which was found to be associated with the residual fractions, whereas abundance of Mn, Zn, Sr, Rb V, Cr, Mo and P compounds indicated limited relative leaching ability from the shale.
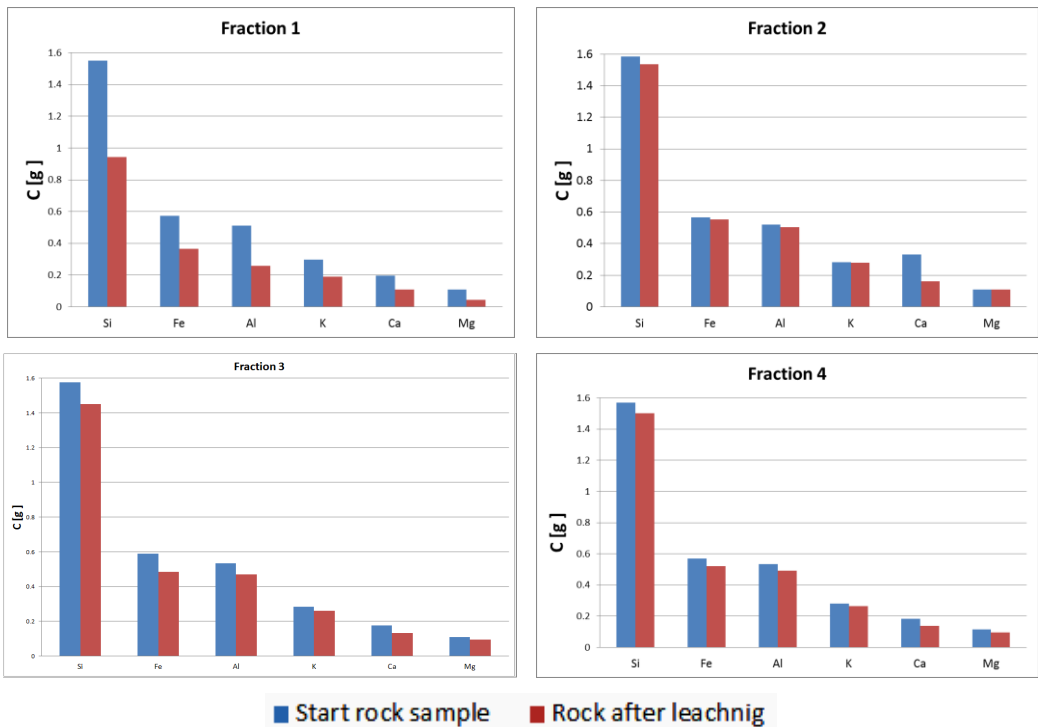
Fig. 4. Changes of shale rock main elements concentration after leaching procedure
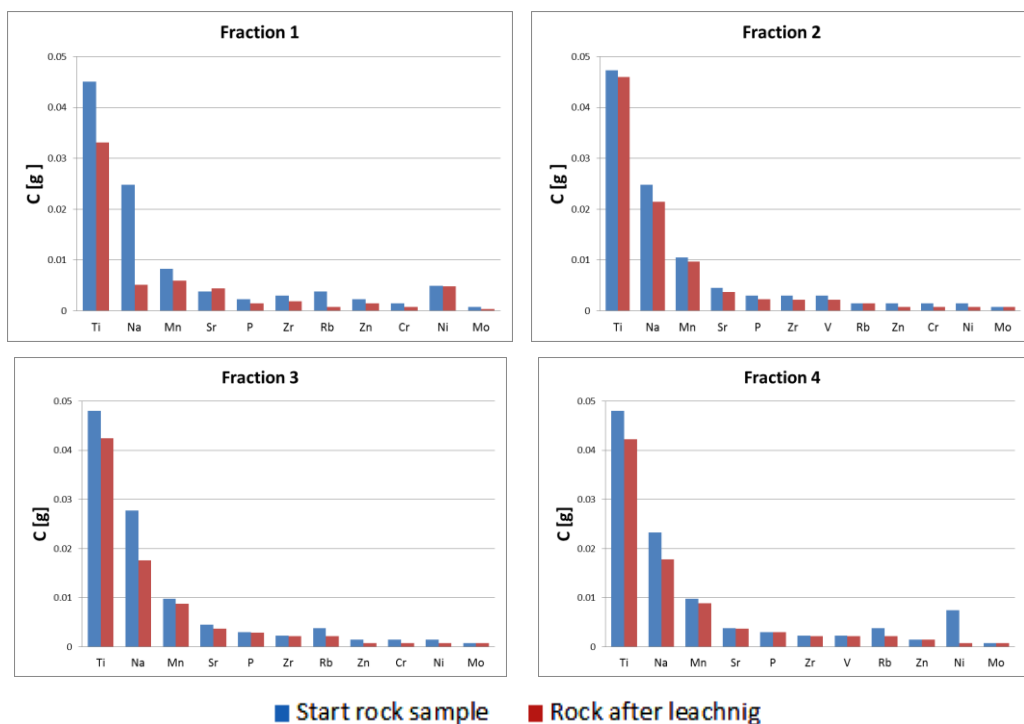
Fig. 5. Changes of shale rock trace elements concentration after leaching procedure

Leachates obtained after the water leaching tests were separated and characterized in respect to total organic carbon content. The relationship between TOC in received leachates and particles size distribution of rock fractions used in experiments is shown in Table 4. It was observed that organic compounds were released to aqueous phase in amount less than 20 ppm of TOC. Generally, the TOC content increase with increasing size distribution of the rock particles due to increasing surface area of the samples.

Table 4. TOC and pH of leachates after water leaching

	Blank	1	2	3	4
TOC [mg/dm^3]	0.02±0.07	8.28±0.12	12.06±0.20	16.06±0.140	16.58±0.17
pH	6.91±0.05	8.40±0.06	8.54±0.06	8.16±0.36	8.51±0.06

Leaching tests performed with deionized water (pH value of 6.91) results in increase of pH of the aqueous solutions to values near 8, comparable for all fraction, due to release of alkaline origin components. Changes in the pH of leaching medium may have high impact on the mobility of heavy metals, the lower pH, the greater solubility of metal ions. Solubility of individual metals may vary with the type of

binding (Heasman et al. 1997). Lower pH values may lead also to carbonates and hydroxides dissolution, when metal ions are displaced by hydrogen ions. Elevated salinity level, on the other side, may shift toward higher pH and lead to competition between dissolved Ca2+ and/or Mg2+ cation. In addition, change redox potential leads to a change in metal binding forms in the solid phase and a decrease in pH-value, which increases the mobility of metal (Calmano et al. 1993).

Conclusions

The shale rock samples from marine deposits in Baltic Basin formed in Lower Silurian Llandrovery age have been characterized in terms of mineral composition as well as main and trace constituents present and transported to aqueous phase, by measurements of geochemically relevant chemical elements calculated weight loss. The X-ray diffraction analysis revealed that main mineral phases in shale are formed by quartz, clays, calcite, micas, pyrophyllite, and dolomite. Pyrite, leadhillite, oldhamite, godlevskite, coulsonite, and feldspar were observed in minority.

The concentration values of twenty elements of shale rock used in the experiments were determined by X-ray fluorescence spectroscopy technique before and after leaching tests. The main elements (mainly Si, Al, Ca, Mg, Fe, K, N) form approximately 46.80 wt% of inorganic fraction, whereas the 1.76 wt% is comprised of the trace elements. The results of water-based leaching test indicate decreasing content of Ca, Ti, Mg, P, V, Zn, Sr, Rb, Ni, Cr, Mo. Considering obtained results it can be expected that produced waste waters may contain mainly constituents as Fe, Al, K, Ca, Mg, Ti, Na and minor Mn, Sr, V, Rb, Cr, Ni and Mo. Determination of the total organic carbon content in leachates revealed a minor leachablity of organic matter from shales towards water. Low TOC in untreated water prevents difficulties with flowback water disposal. The increased pH values are in agreement with the XRF results in respect to alkaline compounds release in all fractions.

The results of this study indicate that many of the shale constituents are potentially leachable, and may create a disposal issue of the flowback water. On the other hand some may stay in drill cuttings, which also need to be properly disposed. Presented studies are a preliminary step for further research with other leaching agents giving wider understanding of a raised problem. Study of shales as a potential precursor of storage material for future possible high level waste disposal should be under investigation.

References

ALEXANDER T., BAIHLY J., BOYER C., CLARK B., WATERS G., JOCHEN V., LE CALVEZ J., LEWIS R., MILLER C.K. and Thaeler J. *Shale gas revolution Oilfield Review* 23(3): 40-55, 2011.

AYDEMIR A. *Comparison of Mississippian Barnett Shale, Northern-Central Texas, USA and Silurian Dadas Formation in Southeast Turkey Journal of Petroleum Science and Engineering* 80(1): 81-93, 2011.

BAI B., ELGMATI M., ZHANG H., WEI M. *Rock characterization of Fayetteville shale gas plays Fuel*, 2012.

BANESCHI I., NATALI C., BOSCHI C., CHIARANTINI L., GUIDI M. (2013). *Investigation of Chromium and Nickel mobility in serpentinite soils and rocks: Impact into groundwaters and influences of carbonation*. EGU General Assembly Conference Abstracts.

BRUMSACK H.-J., *The trace metal content of recent organic carbon-rich sediments: Implications for Cretaceous black shale formation Palaeogeography, Palaeoclimatology, Palaeoecology* 232(2): 344-361, 2006.

BRUNER K.R., SMOSNA R. *A Comparative Study of the Mississippian Barnett Shale, Fort Worth Basin, and Devonian Marcellus Shale, Appalachian Basin. National Energy Technology Laboratory*, DOE/NETL-2011/1478, 2011.

CALMANO W., HONG J., FOERSTNER U., *Binding and mobilization of heavy metals in contaminated sediments affected by pH and redox potential Water science and technology* 28: 223-223, 1993.

CHAPMAN E.C., CAPO R.C., STEWART B.W., KIRBY C.S., HAMMACK R.W., SCHROEDER K.T., EDENBORN H.M. *Geochemical and strontium isotope characterization of produced waters from Marcellus Shale natural gas extraction Environmental science & technology* 46(6): 3545-3553, 2012.

COMER J.B., *Stratigraphic Analysis of the Upper Devonian Woodford Formation, Permian Basin, West Texas and Southeastern New Mexico*, Bureau of Economic Geology, University of Texas at Austin, 1991.

DIX M., SPAIN D., SANO J., RATCLIFFE K., HUGHES S., CASARTA N., BULLER D. (2010). *Application of Whole-Rock Elemental Data in Shale-Gas Development: An Example from the Jurassic Haynesville Formation*. EAGE Shale Workshop 2010.

DURAND B., *Kerogen: insoluble organic matter from sedimentary rocks*, Editions technip, 1980.

EHLERS E.G., *The mechanism of lightweight aggregate formation Am. Ceram. Soc. Bull* 37(2): 95-99, 1958.

EIA. *Technically Recoverable Shale Oil and Shale Gas Resources: An Assessment of 137 Shale Formations in 41 Countries Outside the United States*. Washington, Independent Statistics & Analysis, 2013.

ETTENSOHN F.R., BARRON L.S., *Depositional model for the Devonian-Mississippian black-shale sequence of North America: a tectono-climatic approach*, Kentucky Univ., Lexington (USA). Dept. of Geology, 1981.

FAKHRU'L-RAZI A., PENDASHTEH A., ABDULLAH L.C., BIAK D.R.A., MADAENI S.S., ABIDIN Z.Z., *Review of technologies for oil and gas produced water treatment Journal of Hazardous Materials* 170(2): 530-551, 2009.

Falk H., Lavergren U. and Bergbäck B. *Metal mobility in alum shale from Öland, Sweden Journal of geochemical exploration* 90(3): 157-165, 2006.

FRANUS M., LATOSIŃSKA J. *Wstępna ocena możliwości zastosowania zużytego złoża glaukonitowego jako surowca do produkcji kruszywa keramzytowego Politechnika Lubelska*: 17, 2009.

GOLDSCHMIDT V.M., *Geochemistry. Soil Science*. 78: 156, 1954.

HAMMES U., FRÉBOURG G., *Haynesville and Bossier mudrocks: A facies and sequence stratigraphic investigation, East Texas and Louisiana, USA Marine and Petroleum Geology* 31(1): 8-26, 2012.

HARRELL J.A., BELSITO M.E., KUMAR A., *Radon hazards associated with outcrops of Ohio Shale in Ohio Environmental Geology and Water Sciences* 18(1): 17-26, 1991.

HARRIS N.B., *Trace Elements and Basin Processes: Woodford Shale, Permian Basin, West Texas AAPG 2013 Annual Convention and Exhibition, Pittsburgh, Pennsylvania* 2013.

HEASMAN L., VAN DER SLOOT H., QUEVAUVILLER P., *Harmonization of leaching/extraction tests*, Elsevier Science, 1997.

JAEGER J.C., COOK N.G., ZIMMERMAN R., *Fundamentals of rock mechanics*, 2009.

JARVIE D.M., HILL R.J., POLLASTRO R.M., *Assessment of the gas potential and yields from shales: The Barnett Shale model Oklahoma Geological Survey Circular* 110: 9-10, 2005.

JARVIE D.M., HILL R.J., RUBLE T.E., POLLASTRO R.M., *Unconventional shale-gas systems: The Mississippian Barnett Shale of north-central Texas as one model for thermogenic shale-gas assessment AAPG bulletin* 91(4): 475-499, 2007.

JENG A.S., *Weathering of some Norwegian alum shales, II. Laboratory simulations to study the influence of aging, acidification and liming on heavy metal release Acta Agriculturae Scandinavica B-Plant Soil Sciences* 42(2): 76-87, 1992.

JOHNSON B.M., KANAGY L.E., RODGERS JR J.H., CASTLE J.W., *Chemical, physical, and risk characterization of natural gas storage produced waters Water, Air, and Soil Pollution* 191(1-4): 33-54, 2008.

KENNEDY M.J., PEVEAR D.R., HILL R.J., *Mineral surface control of organic carbon in black shale Science* 295(5555): 657-660, 2002.

KIDDER D.L., KRISHNASWAMY R., MAPES R.H., *Elemental mobility in phosphatic shales during concretion growth and implications for provenance analysis Chemical Geology* 198(3): 335-353, 2003.

KLEIN W., *3.1 Mobility of Environmental Chemicals, Including Abiotic Degradation*, 1989.

LAVERGREN U., ÅSTRÖM M.E., BERGBÄCK B., HOLMSTRÖM H., *Mobility of trace elements in black shale assessed by leaching tests and sequential chemical extraction Geochemistry: Exploration, Environment, Analysis* 9(1): 71-79, 2009.

LIS J., PAMPUCH R., *Spiekanie*, Uczelniane Wydawnictwa Naukowo-Dydaktyczne, Kraków, 2000.

MAINALI P., *Chemostratigraphy And The Paleoceanography Of The Bossier-Haynesville Formation, East Texas Basin, Texas and LA, USA*, 2012.

MARCINKOWSKI B., MYCIELSKA-DOWGIAŁŁO E., *Heavy-mineral analysis in Polish investigations of Quaternary deposits: a review Geologos* 19(1-2): 5-23, 2013.

METWALLY Y.M., CHESNOKOV E.M., *Clay mineral transformation as a major source for authigenic quartz in thermo-mature gas shale Applied Clay Science* 55: 138-150, 2012.

ONUOHA I.E., BILGESU H.I., AMERI S. (2011). *Study of Drilling Fluid Additives and Their Impact on Smectite Inhibition, Marcellus Shale Inhibition, and Filtration and Rheological Properties of Bentonite Based Drilling Fluids*. SPE Eastern Regional Meeting.

ORTH C.J., QUINTANA L.R., GILMORE J.S., GRAYSON R.C., WESTERGAARD E.H., *Trace-element anomalies at the Mississippian/Pennsylvanian boundary in Oklahoma and Texas Geology* 14(12): 986-990, 1986.

PENG B., SONG Z., TU X., XIAO M., WU F., LV H. *Release of heavy metals during weathering of the Lower Cambrian Black Shales in western Hunan, China Environmental Geology* 45(8): 1137-1147, 2004.

POPRAWA P., *System węglowodorowy z gazem ziemnym w łupkach–północnoamerykańskie doświadczenia i europejskie perspektywy Przegląd Geologiczny* 58(3): 216-225, 2010.

RADER L.F., GRIMALDI F.S. *Chemical analyses for selected minor elements in Pierre shale*, US Government Printing Office, 1961.

RIPLEY E.M., SHAFFER N.R., GILSTRAP M.S., *Distribution and geochemical characteristics of metal enrichment in the New Albany Shale (Devonian-Mississippian), Indiana Economic Geology* 85(8): 1790-1807, 1990.

TESSIER A., CAMPBELL P.G., BISSON M., *Sequential extraction procedure for the speciation of particulate trace metals Analytical chemistry* 51(7): 844-851, 1979.

TUTTLE M.L., BREIT G.N., GOLDHABER M.B., *Weathering of the New Albany Shale, Kentucky: II. Redistribution of minor and trace elements Applied Geochemistry* 24(8): 1565-1578, 2009.

VINE J.D., TOURTELOT E.B. *Geochemistry of black shale deposits; a summary report Economic Geology* 65(3): 253–272, 1970.

ZHU Y., LIU E., MARTINEZ A., PAYNE M.A., HARRIS C.E. *Understanding geophysical responses of shale-gas plays The Leading Edge* 30(3): 332–338, 2011.

ZOU C., DONG D., WANG S., LI J., LI X., WANG Y., LI D., CHENG K. *Geological characteristics and resource potential of shale gas in China Petroleum Exploration and Development* 37(6): 641–653, 2010.

OPTIMIZATION OF COAL FLOCCULATION WITH AN ANIONIC FLOCCULANT USING A BOX-WILSON STATISTICAL DESIGN METHOD

Ibrahim SONMEZ[*], Yakup CEBECI[**], Dilek SENOL[***]

* Hitit University, Metallurgical and Materials Eng. Dept., TR-19030 Corum-Turkey, ibrahimsonmez@hitit.edu.tr
** Cumhuriyet University, Mining Engineering Dept., TR-58140 Sivas-Turkey
*** Istanbul University, Mining Engineering Dept., TR-32320 Istanbul-Turkey

Abstract: In this study, the Box-Wilson statistical experimental design method was employed to evaluate suspension pH, salt ($CaCl_2 \cdot 2H_2O$) concentration and anionic flocculant (A-150) amount in flocculation of coal. Response function coefficients were determined by the regression analysis of experimental data and the predictions were found to be in good agreement with the experimental results. The optimum pH, salt ($CaCl_2 \cdot 2H_2O$) concentration and anionic flocculant (A-150) amount were determined as 9.8, 0.0009 M and 791 g/Mg respectively, when minimum turbidity and maximum settling rate are considered.

Keywords: coal, flocculation, anionic flocculant, $CaCl_2 \cdot 2H_2O$

Introduction

Both mechanized coal mining methods and cleaning processes continuously increase the fine coal particle concentration (Hogg, 1980; Pawlak et al., 1985; Kim et al., 1991; Cebeci, 1996; Cebeci et al., 2002) creating problems in dewatering, drying, handling, transportation and storage. Significant quantities of fine coal lost in coal preparation plants result in energy loss and environmental problems (Hogg, 1980; Kim et al., 1991; Cebeci, 1996). Conventional coal beneficiation techniques such as dense-media separation, shaking tables, water-only cyclones are quite inefficient in fine coal processing. Due to the limited success of coal cleaning process, studies have shifted increasingly towards the use of froth flotation, flocculation and oil agglomeration as alternative fine particle processing methods (Kim et al., 1991; Somasundaran 1980; Mehrotra et al., 1983; Hamza et al., 1988).

Flocculation of fine or ultra fine particles using a polymeric flocculant is frequently employed for dewatering or solid-liquid separation process (Somasundaran, 1980; Attia, 1992; Somasundaran and Das 1998; Hogg, 2000). The electrokinetic behavior of the particles affects the recovery and the selectivity in the concentration processes, which depend on the surface properties such as froth flotation, flocculation and oil agglomeration (Cebeci and Sonmez, 2006).

The settling rate and turbidity (or water clarity), which are improved by flocculation, depend heavily on the proper control of both chemical variables (pH, flocculant type, flocculant molecular weight, flocculant amount, charge density, presence of metal ions, ionic strength, zeta potential etc.) and physical factors (mixing conditions, solid concentration, particle surface area, particle size, pulp temperature etc.) (Hogg, 2000; Angle et al., 1997; Ateşok et al., 1988; Clark et al., 1990; Hogg et al., 1993; Su et al., 1998; Besra et al., 2000; Mpofu et al., 2003; Sabah and Cengiz, 2004; Hulston et al., 2004).

In this study, a Box-Wilson statistical experimental design method was used to determine the major operating parameters effects on settling rate, turbidity and zeta potential. This experimental design is a type of response surface methodology, an empirical modeling technique, devoted to the evaluation of the relationship of a set of controlled experimental factors and observed results. This optimization process involves three major steps: performing the statistical design experiments, estimating the coefficients in a mathematical model, and predicting the response and checking the adequacy of the model. It could be beneficial to know whether the Box-Wilson statistical experimental design procedure is applicable to the prediction of important variables such as the settling rate, turbidity and zeta potential in the flocculation of fine coal particles. In order to test the hypothesis, flocculation experiments were carried out using coal waste samples from the Alpagut-Dodurga Coal basin in Corum (Turkey). Regarding the flocculation, pH, $CaCl_2 \cdot 2H_2O$ concentration and anionic flocculant (A-150) were selected as the most relevant independent variables. Settling rate, turbidity, and zeta potential were measured to determine the effects of these independent variables in the experimental design.

Materials and methods

Material

The coal waste sample was obtained from the Alpagut-Dodurga Coal basin in Corum-Turkey. The total ash value was 39.80%. The coal sample was dry-ground to a nominal top size of −53 µm in a rod mill for flocculation tests. The ground coal has 86% passing at 20 µm based on the wet screening results.

The mineral composition was determined by X-ray diffraction (XRD) using a RIGAKU DMAX-III C diffractometer. According to the XRD results of the original coal sample, quartz, calcite, smectite, chlorite and kaolinite were the main mineral matter minerals.

Chemicals

An anionic (A-150) Superfloc synthetic flocculant was obtained from Cyanamid Company. The A-150 polymer used as the flocculant consisted mainly of polyacrylamide and its derivative monomers. The molecular weight was in the range of $5-15 \times 10^6$ g·mol^{-1} (American Cyanamid Company, 1989). A 0.05 M stock solution of $CaCl_2 \cdot 2H_2O$ (147.02 g·mol^{-1}) (Merck) salt was prepared and added into the suspension at the required amount in order to obtain the final desired concentration and investigate the effect on flocculation process. Solutions of HCl (Merck) and NaOH (Carlo Erba) were used to adjust pH. All chemicals used were at least analytical grade.

Flocculation studies

The experiments were carried out in a 400 ml beaker having 4 baffles at the border to create homogeneous slurry during mixing. Mixing was carried out using a Heidolph RZR 2021 model mechanical stirrer. The agitation was provided by a centrally located flat blade turbine impeller (consisting of four blades) at a fixed distance from the bottom of the vessel. Mono-distilled water (pH ~ 6.5) was used in the experiments. The solid concentration was kept constant at 5.0 wt% (w·w^{-1}) for each test and the weight of suspension was subjected to 200 g (10 g coal sample + 190 g water). The mixture was conditioned for 3 minutes before and after adding the salt solution. After adding the A-150 flocculant, the suspension was conditioned for 2 minutes under constant stirring. The A-150 amount was based on the mass ratio of coal on dry basis. After 2 minutes, the stirring speed was reduced to the half of stirring speed for 1 minute to allow floc growth. Then, the suspension was transferred into a 500 cm^3 measuring cylinder (272 mm height), and the cylinder was inverted end-over-end for 20 times. In order to evaluate the experimental results, the settling rate and turbidity values were determined. The settling rate (mm·min^{-1}) was calculated based on the changing slurry-supernatant interface height in time. After a settling time of 5 min, 15 cm^3 supernatants were drawn from a depth of 7.0 cm below the air-liquid interface for turbidity measurements. The turbidity of the supernatant was measured in Nephelo Turbidity Units (NTU) using an Orbeco-Hellige 966 turbidimeter. Additionally, the zeta potentials of the coal samples were measured at the experimental conditions of axial points, factorial points and centre point using a zeta potential analyzer (Malvern Instruments, Zetasizer Nano Z model).

Box-Wilson experimental design

The Box-Wilson statistical experimental design method includes three types of combinations, the axial (A), factorial (F), and center (C) points. The independent variables are at five specified levels depending on the number of variables in the experiment and their range. In order to maintain convenience, the following codes were used for the operating levels of the variables. For this purpose, a factor $k =$

range/2 is defined for each variable where k is approximately equal to $\sqrt{p}$ ($p =$ number of variables), and with three variables $k = 1.73$. The axial points included each variable at its extreme levels were coded as $-k$ and $+k$ with the others at their center point level. The factorial points, with two levels of each of the factors coded as -1 and $+1$, included all combinations of intermediate levels. A center point coded as 0 is a single test at the average level of each variable. The details of the method can be found elsewhere (Davies, 1956; Crozier, 1992).

Three operating parameters i.e., pH, salt concentration ($CaCl_2 \cdot 2H_2O$) and the amount of anionic flocculant (A-150) were chosen as the most important independent variables. The pH (X_1) was changed between 3 and 11, the salt concentration (X_2) between 0 and 0.001 M and A-150 amount (X_3) between 0 and 800 $g \cdot t^{-1}$. The experimental design consisted of six axial (A), eight factorial (F) and three centre (C) points. The center point was repeated three times for estimating experimental error. The experimental conditions as coded values and real values used for the Box-Wilson statistical design are presented in Table 1.

Table 1. Experimental conditions according to the Box-Wilson statistical design

No.	Coded Values			Real Values		
	X_1	X_2	X_3	pH	SC (M)	AF ($g \cdot t^{-1}$)
A1	1.73	0	0	11	0.000500	400
A2	−1.73	0	0	3	0.000500	400
A3	0	1.73	0	7	0.001000	400
A4	0	−1.73	0	7	0.000000	400
A5	0	0	1.73	7	0.000500	800
A6	0	0	−1.73	7	0.000500	0
F1	1	1	1	9.31	0.000789	631.21
F2	1	1	−1	9.31	0.000789	168.79
F3	1	−1	1	9.31	0.000211	631.21
F4	1	−1	−1	9.31	0.000211	168.79
F5	−1	1	1	4.69	0.000789	631.21
F6	−1	1	−1	4.69	0.000789	168.79
F7	−1	−1	1	4.69	0.000211	631.21
F8	−1	−1	−1	4.69	0.000211	168.79
C1	0	0	0	7	0.000500	400
C2	0	0	0	7	0.000500	400
C3	0	0	0	7	0.000500	400
C(Ave)	0	0	0	7	0.000500	400

SC: salt concentration; AF: amount of flocculant

The settling rate, turbidity and zeta potential (Y) were correlated with the other independent parameters (X_1, X_2, X_3) using Eq. (1). A Design Expert 8.0 program was

used for determination of the coefficients of Eq. (1) by regression analysis of the experimental data.

$$Y = b_0 + b_1 X_1 + b_2 X_2 + b_3 X_3 + b_{12} X_1 X_2 + b_{13} X_1 X_3$$
$$+ b_{23} X_2 X_3 + b_{11} X_1^2 + b_{22} X_2^2 + b_{33} X_3^2$$

(1)

where Y – the predicted response function (settling rate, turbidity or zeta potential)
b_0 – constant
b_1, b_2, b_3 – linear coefficients
b_{12}, b_{13}, b_{23} – cross product coefficients
b_{11}, b_{22}, b_{33} – quadratic coefficients.

Results and discussions

A comparison of the experimental and predicted values for the settling rates, turbidities and zeta potentials are summarized in Table 2. The observed settling rates varied between 1.050 and 500.740 mm·s⁻¹, turbidities varied between 9.2 and 195.8 NTU, while the observed zeta potentials varied between –35.80 and -7.25 mV.

Table 2. Observed and predicted settling rates, turbidities and zeta potentials

Experiment No.	Settling Rate (mm·min⁻¹)		Turbidity (NTU)		Zeta Potential (mV)	
	Observed	Predicted	Observed	Predicted	Observed	Predicted
A1	292.540	311.736	70.2	67.7	−35.80	−34.45
A2	1.050	−1.631	195.8	201.8	−7.25	−11.13
A3	183.426	208.403	71.0	78.0	−21.80	−23.33
A4	149.970	141.508	119.6	116.1	−24.90	−25.89
A5	434.226	377.279	9.2	50.9	−19.90	−20.30
A6	1.902	75.363	159.9	121.7	−18.10	−20.22
F1	500.740	463.554	19.2	14.7	−22.30	−23.11
F2	173.502	174.304	75.3	76.3	−29.00	−28.33
F3	226.305	298.200	118.6	89.6	−34.80	−35.11
F4	246.788	167.249	54.1	88.9	−30.30	−30.61
F5	132.444	199.460	140.8	103.4	−17.90	−15.70
F6	66.060	−18.619	159.4	186.0	−22.30	−20.12
F7	142.740	129.184	138.4	134.9	−17.60	−16.39
F8	44.508	69.404	153.2	155.1	−13.80	−11.08
C1	225.300	255.544	72.2	59.9	−20.90	−22.10
C2	281.106	255.544	36.4	59.9	−23.10	−22.10
C3	260.226	255.544	71.1	59.9	−22.30	−22.10

Experimental results were modeled using a Design Expert 8.0 Trial program to determine the coefficients of the response function (Eq. (3)). The calculated coefficients were used in calculating predicted values of flocculation recoveries and zeta potentials and are listed in Table 3. The determination coefficients (R^2 values) between the observed and predicted values were 0.8779, 0.8259 and 0.9426 for settling rate, turbidity and zeta potential, respectively, indicating a good agreement between the observed and predicted values.

Table 3. Coefficients of the response function

Coefficient	b_0	b_1	b_2	b_3	B_{12}	b_{13}
Settling Rate	−284.276696	95.973172	−96889.4670	−0.005819	35604.9375	0.033314
Turbidity	448.370069	−78.057864	20508.22816	−0.172501	−16275.0	0.009797
Zeta Potential	17.440958	−4.5828133	−31599.13	−0.0301012	4237.5	0.000375
Coefficient	b_{23}	b_{11}	b_{22}	b_{33}	R^2	
Settling Rate	592.261875	−6.280734	−322354952.38	−0.0001826421	0.8779	
Turbidity	−233.25	4.679167	148666666.67	0.0001651042	0.8259	
Zeta Potential	36.375	−0.042932	−10047619.05	0.0000114881	0.9426	

The effect of pH and A-150 amount

It is known that flocculation recovery or the extent of flocculation (floc size) depends on the surface properties of particles, suspension pH, and the nature of the flocculants (Somasundaran and Das, 1998; Foshee et al., 1982; Yu and Somasundaran, 1996; Rattanakawin and Hogg, 2001). The H^+ and OH^- ions are the potential determining ions for many mineral particles including coal, clay minerals, and quartz (Leja, 1982; Laskowski, 2001). Both the electrokinetic properties of the particles and charge characteristics and the conformation (structure) of polymer flocculant are subjected to change by the suspension pH, and thus may affect the flocculating power of the polymer (Foshee, 1982; Reuter and Hartan, 1986). Therefore, controlling the pH of the aqueous medium is important.

The flocculation strategy may depend on the process goals. For example, low turbidity would be critical for producing high water clarity while the high settling rate may be desired in other cases. In either case, the ideal flocculant should settle the largest amount of desired fine particles with the lowest flocculant concentration in the shortest time resulting in the highest clarity.

The variations of the settling rate, turbidity and zeta potential as functions of the pH and A-150 amount at a constant $CaCl_2 \cdot 2H_2O$ concentration of 0.0005 M are given in Fig. 1, Fig. 2 and Fig. 3, respectively.

Figure 1 shows that the settling rate increased with both rising pH and A-150 amount at a 0.0005 M $CaCl_2 \cdot 2H_2O$ concentration. Conversely, Fig. 2 indicates that the turbidity decreased by increasing pH value up to pH 9, and it increased partially
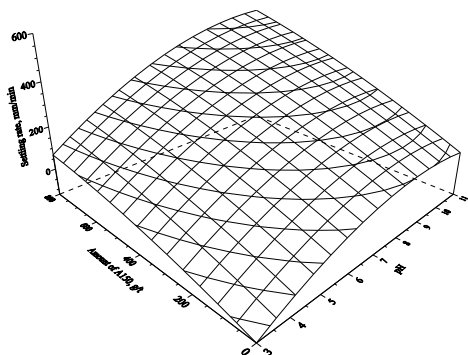
Fig. 1. Effect of pH and A-150 amount on settling rate (CaCl$_2$·2H$_2$O: 0.0005 M)
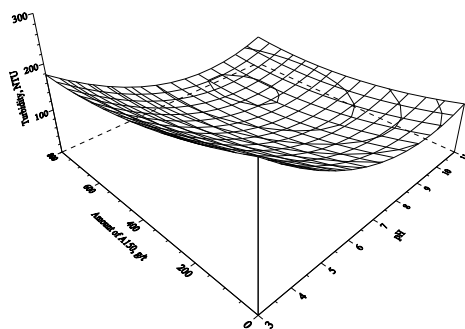
Fig. 2. Effect of pH and A-150 amount on turbidity (CaCl$_2$·2H$_2$O: 0.0005 M)
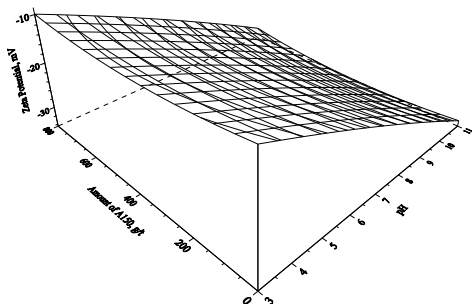
Fig. 3. Effect of pH and A-150 amount on zeta potential (CaCl$_2$·2H$_2$O: 0.0005 M)
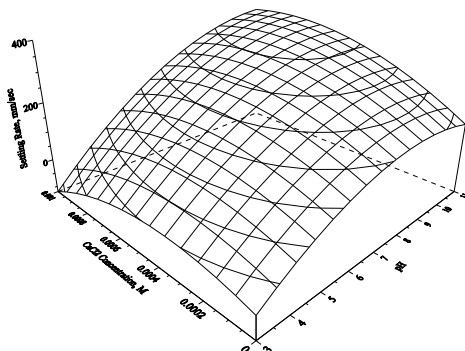
Fig. 4. Effect of pH and CaCl$_2$·2H$_2$O concentration on settling rate (A-150: 400 g·t^{-1})

afterward. Moreover, the turbidity partially decreased with increasing the A-150 amount. According to the effect of anionic flocculant dosage and pH values, Fig. 1 and Fig. 2 display a clear reverse relationship between the settling rate and the turbidity.

After dissociation of CaCl$_2$, Ca^{+2} ions may undergo association with hydroxyl ions yielding Ca(OH)$^+$ and Ca(OH)$_2$ species especially at alkaline pH values (Sillen and Martell, 1971). The positively charged Ca^{+2} ions alkaline salt products were specifically adsorbed onto the ash-forming mineral matter and coal particle surfaces (James and Healy, 1972a, 1972b, 1972c). As the specific adsorption of Ca^{+2} ions hydrolysis products increases, an attraction should take place between the anionic A-150 polymer chains and newly formed cationic surfaces, which facilitates polymer adsorption (Mpofu, 2005). Accordingly, we obtained a distinct increase in the settling rate at high pH values (maximum at pH 11), whereas the lowest settling rate was recorded at pH 3.

Low settling rates obtained at low pH values may be due to the weak electrostatic interaction of the negative particle surfaces. It can also be attributed to the covalent

bond and/or electrostatic bond formation between the (=C−O$^-$) groups of anionic polymers and metal cations on the external surface of mineral particles may be inhibited (Sabah and Cengiz, 2004). Furthermore, at low pH values (pH = 4 and below), except for electrostatic attraction forces, the low settling rate may indicate that the other forces such as hydrogen bonding would be more effective between the polar groups of flocculant and the particle surfaces (Sarioglu et al., 2002).

It is commonly known that high molecular weight polymers generate large size but less compact flocs (Hogg, 2000; Gregory, 1989; Tao et al., 2000). Similar to our observation, Sabah and Erkan (2005) reported that anionic flocculants with a high molecular weight produced large flocs sufficient for settling. At low flocculant amounts, low settling rates reflected an inadequate level of flocculant or insufficient flocculant bridging among the particles. In this case, the floc size was very small due to inadequate amount of polymer adsorption on particle surfaces. As the amount of adsorbed polymer increased, greater amounts of suspended particles were incorporated into the floc leading to enlargement of the floc size and increased settling rate.

As shown in Fig. 3, the zeta potential of the coal sample was negative at all pH values and without a zero point of charge. Moreover, the zeta potential decreased with increasing pH at all studied anionic flocculant amounts. This can be attributed to the increment of OH$^-$ and/or Cl$^-$ anions adsorption over the ash-forming mineral matter and coal particles. However, the zeta potential scarcely changed, depending on A-150 amount at all pH values. This situation may reflect the adsorbed A-150 amount on the particle surfaces.

The effect of pH and CaCl$_2$·2H$_2$O concentration

The settling rate, turbidity and zeta potential as a function of pH and CaCl$_2$·2H$_2$O concentration at a constant A-150 amount of 400 g/Mg are presented in Fig. 4, Fig. 5, and Fig. 6, respectively.
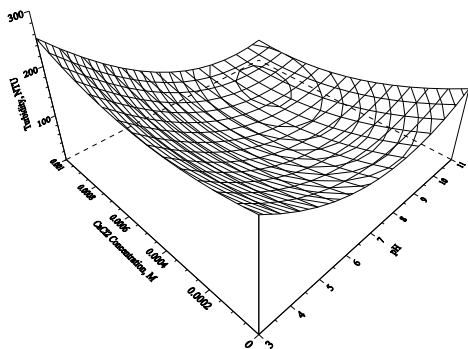
Fig. 5. Effect of pH and CaCl$_2$·2H$_2$O concentration on turbidity (A-150: 400 g/Mg)
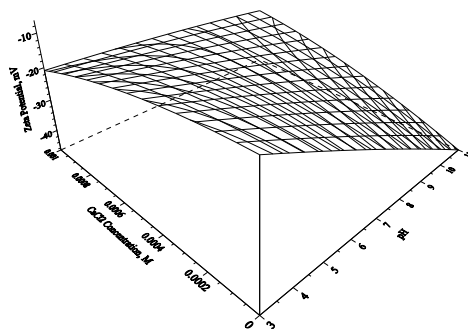
Fig. 6. Effect of pH and CaCl$_2$·2H$_2$O concentration on zeta potential (A-150: 400 g/Mg)

Because of the increment of A-150 adsorption after specific adsorption of Ca^{+2} ions hydrolysis products on particles surfaces, while the settling rate was increased, the turbidity was decreased with the increasing salt concentration up to 0.0007 M and it reversed partially afterward at all studied pH values. Furthermore, the settling rate was increased whereas the turbidity was decreased with increasing pH value, as can be seen in both Fig. 4 and Fig. 5, indicating a reverse relationship between settling rate and turbidity.

Figure 6 depicts the variation in the zeta potential as a function of pH and $CaCl_2 \cdot 2H_2O$ concentration at a constant A-150 amount of 400 g/Mg. The zeta potential was decreased slightly by increasing the $CaCl_2 \cdot 2H_2O$ concentration at low pH values while it was increased at high pH values. The increasing of the negative zeta potential value with boosting the $CaCl_2 \cdot 2H_2O$ concentration at low pH values can be attributed to the adsorption/precipitation of Cl^- anions onto the ash-forming mineral matter and coal particles surfaces. At high pH, the decreasing of the negative zeta potential value with increasing the $CaCl_2 \cdot 2H_2O$ concentration could be due to A-150 adsorption after specific adsorption of Ca^{+2} ions hydrolysis products on particles surfaces instead of OH^- and/or Cl^- anions adsorption.

The effect of $CaCl_2 \cdot 2H_2O$ concentration and A-150 amount

The variation of settling rate, turbidity and zeta potential with both A-150 amount and $CaCl_2 \cdot 2H_2O$ concentration at pH 7 are presented in Fig. 7, Fig. 8, and Fig. 9, respectively.

As seen from Fig. 7 and Fig. 8, there is a reverse relationship between settling rate and turbidity at pH 7. The settling rate increased with both A-150 amount and $CaCl_2 \cdot 2H_2O$ concentration at pH 7 (Fig. 7). The settling rate was greater at higher $CaCl_2 \cdot 2H_2O$ concentration, which can be attributed to the A-150 adsorption on particle surfaces. Correspondingly, the turbidity decreased as shown in Fig. 8 with increasing A-150 amounts at high $CaCl_2 \cdot 2H_2O$ concentration.
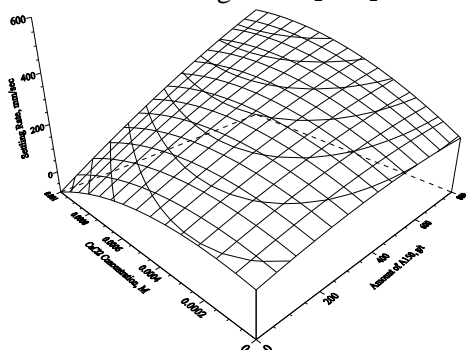
Fig. 7. Effect of A-150 amount and $CaCl_2 \cdot 2H_2O$ concentration on settling rate (pH 7)
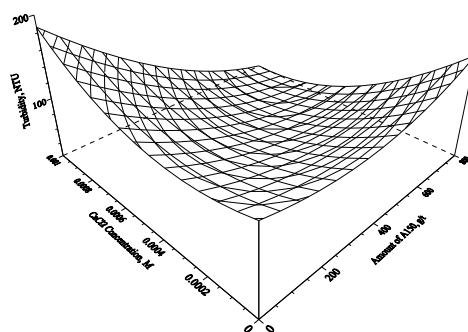
Fig. 8. Effect of A-150 amount and $CaCl_2 \cdot 2H_2O$ concentration on turbidity (pH 7)
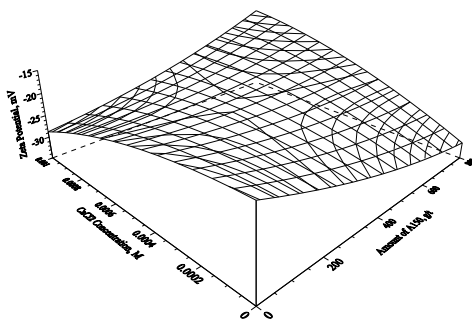
Fig. 9. Effect of A-150 amount and CaCl$_2$·2H$_2$O concentration
on zeta potential (pH 7)

Figure 9 indicates the variation in the zeta potential at pH 7 as a function of A-150 amount and CaCl$_2$·2H$_2$O concentration. As can be seen in Fig. 9, the negative zeta potential value boosted with increasing the CaCl$_2$·2H$_2$O concentration at low A-150 amounts, while it decreased at high A-150 amounts. This could indicate that the A-150 adsorption depends on both Ca^{+2} ions hydrolysis product amounts and pH value.

Conclusions

The Box-Wilson statistical experimental design procedure was found to be applicable to modeling the effects of important variables on the settling rate, turbidity and zeta potential in flocculation of coal. Response function predictions determined by regression analysis were in a good agreement with the experimental results. In general, there was a reverse relationship between settling rate and turbidity. The settling rate was increased with an increment in suspension pH, anionic flocculant (A-150) amount and salt (CaCl$_2$·2H$_2$O) concentration. The turbidity decreased with A-150 amount and CaCl$_2$·2H$_2$O concentration and increasing pH up to 9. The zeta potential value decreased with increasing pH values depending on both A-150 amount and CaCl$_2$·2H$_2$O concentration, contrary to the flocculation expectation.

Considering the minimum turbidity and maximum settling rate, flocculation of fine coal particles can be optimized at pH 9.8, salt (CaCl$_2$·2H$_2$O) concentration of 0.0009 M and anionic flocculant (A-150) amount of 791 g·Mg as predicted by the model.

References

AMERICAN CYANAMID COMPANY, 1989. *Mining Chemicals Handbook*. Revised Edition, Mineral Dressing Notes No: 26-1, USA.

ANGLE C.W., SMITH-PALMER T., WENTZELL B.R., 1997. *The effects of cationic polymers on flocculation of a coal thickener feed in washery water as a function of pH*, Journal of Applied Polymer Science, 64, 783–789.

ATESOK G., SOMASUNDARAN P., MORGAN L.J., 1988. *Adsorption properties of Ca^{2+} on Na-Kaolinite and its effect on flocculation using polyacrylamides,* Colloids and Surfaces A: Physicochemical and Engineering Aspects, 32(1,2), 127–138.

ATTIA Y.A., 1992. *Flocculation*, In: J.S. Laskowski and J. Ralston, Editors. Colloid Chemistry in Mineral Processing, Elsevier, Amsterdam, Chapter 9.

BESRA L., SENGUPTA D.K., ROY S.K., 2000. *Particle characteristics and their influence on dewatering of kaolin, calcite and quartz suspensions,* International Journal of Mineral Processing, 59(2), 89–112.

CEBECI C., SARIOGLU M., KAHRIMAN A., 2002. *Determination of various flocculants' performance in flocculation of lignite waste pulps,* Asian Journal of Chemistry, 14(1), 413–419.

CEBECI Y., SONMEZ I., 2006. *Application of the Box-Wilson experimental design method for the spherical oil agglomeration of coal,* Fuel, 85, 289–297.

CEBECI Y., 1996. *The investigation of effects of some parameters on the performance of selective agglomeration of lignites,* In: VI International Mineral Processing Symposium, Kusadasi, Turkey, 445–459.

CLARK A.Q., HERRINGTON T.M., PERTZOLD J.C., 1990. *The flocculation of kaolin suspensions with anionic polyacrylamides of varying molar mass and anionic character,* Colloids and Surfaces A: Physicochemical and Engineering Aspects, 44, 247–261.

CROZIER R.D., 1992. *Flotation,* Pergamon Press.

DAVIES O.L., 1956. *The design and analysis of industrial experiments,* Hafner Publishing Co., New York.

FOSHEE W.C., SWAN M.J., KLIMPEL R.R., 1982. *Improvement in coal preparation–water clarification through polymer flocculation,* Mineral Engineering, 34, 293–297.

GREGORY J., 1989. *Fundamental of flocculation,* Critical Reviews in Environmental Controls, 19, 185–230.

HAMZA H.A., MO A.W., FRENETTE R., 1988. *Chemical reagents for mechanical dewatering*, Industrial Practice of Fine Coal Processing, Colorado, USA, p. 231.

HOGG R., 1980. *Fine Particle Processing,* In P. Somasundaran (Ed.), Vol. 2, AIME, New York, 990–999.

HOGG R., 2000. *Flocculation and dewatering,* International Journal of Mineral Processing, 58, 223–236.

HOGG R., BRUNNAIL P., SUHARYONO H., 1993. *Chemical and physical variables in polymer-induced flocculation,* Minerals and Metallurgical Processing, 10, 81–5.

HULSTON J., DE KRETSER R.G., SCALES P.J., 2004. *Effect of temperature on the dewaterability of hematite suspensions,* International Journal of Mineral Processing, 73, 269–279.

JAMES R.O., HEALY T.W., 1972a. *Adsorption of hydrolysable metal ions at the oxide–water interface: I. Co(II) adsorption on SiO_2 and TiO_2 as model systems,* Journal of Colloid and Interface Science, 40, 42–52.

JAMES R.O., HEALY T.W., 1972b. *Adsorption of hydrolysable metal ions at the oxide–water interface: II. Charge reversal of SiO_2 and TiO_2 colloids by adsorbed Co(II), La(III), and Th(IV) as models systems,* Journal of Colloid and Interface Science, 40, 53–63.

JAMES R.O., HEALY T.W., 1972c. *Adsorption of hydrolysable metal ions at the oxide–water interface: III. A thermodynamic model of adsorption,* Journal of Colloid and Interface Science, 40, 65–81.

KIM S.S., MORSI B.I., ARAUJO G., CHIANG S.-H., BLACHERE J., SHARKEY A., 1991. *Effect of grinding conditions on the performance of a selective agglomeration process for physical coal cleaning,* Coal Preparation, 9(3–4), 141–153.

LASKOWSKI J.S., 2001. *Coal surface properties,* In: Fuerstenau, DW, editor. Coal flotation and fine coal utilization. Amsterdam: Elsevier Science BV.

LEJA J., 1982. *Surface Chemistry of Froth Flotation,* New York: Plenium Press.

MEHROTRA V.P., SASTRY K.V.S., MONEY B.W., 1983. *Review of oil agglomeration techniques for processing of fine coals,* International Journal of Mineral Processing, 11, 175–201.

MPOFU P., ADDAI-MENSAH J., RALSTON J., 2003. *Influence of hydrolyzable metal ions on the interfacial chemistry, particle interactions, and dewatering behavior of kaolinite dispersions,* Journal of Colloid and Interface Science, 261(2), 349–359.

MPOFU P., ADDAI-MENSAH J., RALSTON J., 2005. *Interfacial chemistry, particle interactions and improved dewatering behaviour of smectite clay dispersions,* International Journal of Mineral Processing, 75, 155–171.

PAWLAK W., TURAK A., IGNASIAK B., 1985. *Selective agglomeration of low rank bituminous and subbituminous cretaceous coals,* In: Proceedings 4th International Symposium on Agglomeration, Toronto, 907–915.

RATTANAKAWIN C., HOGG R., 2001. *Aggregate size distributions in flocculation,* Colloids and Surfaces A: Physicochemical and Engineering Aspects, 177, 87–98.

REUTER J.M., HARTAN H.G., 1986. *Structure and reaction kinetics of polyelectrolytes and their use in solid-liquid processing,* Aufbereitungs-Technik, 11, 598–606.

SABAH E., CENGIZ I., 2004. *An evaluation procedure for flocculation of coal preparation plant tailings,* Water Research, 38, 1542–1549.

SABAH E., ERKAN Z.E., 2005. *Interaction mechanism of flocculants with coal waste slurry,* Fuel, 85, 350–359.

SARIOGLU M., CEBECI Y., BEYAZIT N., 2002. *Investigation of the effects of some operating parameters by using anionic and cationic flocculants for removing solid material in the lignite wastewaters,* Asian Journal of Chemistry, 14, 388–394.

SILLEN L.G., MARTELL A.E., 1971. *Stability constant of metal-ion complexes,* Special Publications Nos. 17 and 25, The Chemical Society. London.

SOMASUNDARAN P., DAS K.K., 1998. *Flocculation and selective flocculation – An overview,* In: Atak, S., Önal, G., Çelik, M.S., (Editors), Proceedings of 7th International Mineral Processing Symposium (Innovation in mineral and coal processing), İstanbul, Turkey, Balkema, 81–91.

SOMASUNDARAN P., 1980. *Fine Particle Processing,* In P. Somasundaran (Ed.), Vol. 2, AIME, New York, 947–976.

SU F., RAO K.H., FORSSBERG K.S.E., SAMSKOG P.O., 1998. *Dephosphorization of magnetite fines – Part 2: Influence of chemical variables on flotation kinetics,* IMM Transactions of the Institution of Mining and Metallurgy, Section C: Mineral processing and Extractive Metallurgy, 107, C103–C110.

TAO D., GROPPO J.G., PAREKH B.K., 2000. *Enhanced ultrafine coal dewatering using flocculation filtration processes,* Minerals Engineering, 13, 163–171.

YU X., SOMASUNDARAN P., 1996. *Role of polymer conformation in interparticle-bridging dominated flocculation,* Journal of Colloid and Interface Science, 177, 283–287.

OPTIMIZATION OF FINE ILMENITE FLOTATION PERFORMED IN A CYCLONIC-STATIC MICRO-BUBBLE FLOTATION COLUMN

Guixia FAN[*,**], Jiongtian LIU[*,**], Yijun CAO[**], Tao HUO[*,**]

[*] School of Chemical Engineering and Technology, China University of Mining and Technology, Xuzhou 221116, Jiangsu, China

[**] National Engineering Research Center of Coal Preparation and Purification, Xuzhou 221116, Jiangsu, China, yijuncao@126.com

Abstract: A cyclonic-static micro-bubble flotation column was applied to upgrade fine ilmenite. The optimum parameters of flotation in the column were determined basing on the grade-recovery upgrading curve. A continuous pilot plant test was conducted using the optimum parameters during rougher-cleaner process. When compared with the optimized parameters of the industrial flotation machines, the cyclonic-static micro-bubble flotation column provides higher concentrate grade and recovery: 48.11% with a growth of 1.08 percentage points and 82.36% with an increment of 13.64 percentage points, respectively. Moreover, the flowsheet is simplified to two steps (rougher-cleaner) in the cyclonic-static micro-bubble flotation column from six steps (one rougher-two scavengers-three cleaners) in the flotation machines. Therefore, the cyclonic-static micro-bubble flotation column is an effective tool for fine ilmenite beneficiation.

Introduction

Titanium is an important raw material for space industry, nautical engineering and medicine (Omidvar et al., 2012; Parker and Stec, 2012). China, with the largest titanium reserves, accounts for about 48% of the world's reserves (Li et al., 2007a). The Panzhihua and Xichang region in Chinese Sichuan Province is a cornucopia of titanium, where there are more than 90% of titanium reserves of China (Li et al., 2006; Wu et al., 2011). About 98% of titanium is present as ilmenite ($FeTiO_3$). The theoretical grade of TiO_2 in ilmenite is 52.63%. This ilmenite ore is refractory to flotation processing (Fan and Rowson, 2000; Zhou et al., 2006). Flotation machines

are conventionally used for industrial flotation of ilmenite. However, the recovery is low and complicated flowsheets are used for the fine ilmenite fractions (Banisi and Finch, 2001; Rule and Anyimadu, 2007).

There is an interest in column flotation in mineral processing and industrial application (Honaker and Mohanty, 1996; Hulya and Ugur, 2012). In 1980, the first column was applied in Noranda's Mines Gaspe, which was shut down in 1983 (Dobby and Finch, 1991). The major disadvantages of flotation column were the mixing in the axis of the column, the blockage of spargers and problems posed by column height in installations. In recent decades, flotation column had directly driven some developments (e.g. in sparger systems), spawned derivatives (e.g. the packed column) and new concepts (e.g. the Jameson cell), for instance froth washing (Hasan and Hale, 2007). However, not all developments are accepted by the technology and market. One of the new approaches is the cyclonic-static micro-bubble flotation column (CSMC), commercially available as FCSMC, that is with additional F letter in the front of the acronym. It was invented by the China University of Mining and Technology. The characteristic innovation of the CSMC is multiple mineralization steps, including countercurrent mineralization, cyclone mineralization and pipe flow mineralization (Zhang et al., 2013; Gui et al., 2013). The CSMC has many advantages, such as higher concentration ratio and optimized flowsheet (Yianatos et al., 2005). Recently, the CSMC has been successfully used in flotation of metallic and non-metallic minerals. Cao et al. (2009) used the CSMC to separate copper-nickel sulfide. They obtained nickel concentrate with a grade of 8.21% and a recovery of 55.24%, compared to only 5.02% and 44.71%, respectively, when using flotation machines for the same ore.

In this work, a pilot plant test was carried out using the CSMC, to probe the optimum parameters of the fine ilmenite flotation in rougher and cleaner process. The 72 h continuous test was then performed under the optimum parameters. The feed, concentrate and tailings were sized to several fractions and each of them was assayed to calculate the by-size grade and recovery of concentrate in continuous pilot plant test.

Experimental

Materials

The ilmenite ore was supplied by the Pan Steel Mining Company of Sichuan in China. The valuable minerals in the ore were ilmenite and titanomagnetite while the gangue minerals were titanaugite, plagioclase, olivine, and kaersutite. The chemical analysis of the ore performed by the X-ray fluorescence (XRF) method is presented in Table 1. The ore liberation degree was determined by the mineral liberation analyzer (MLA). As shown in Fig. 1, most of the ilmenite was liberated.

The ilmenite ore was screened using the 154, 100 and 74 μm sieves and then the fine size fraction (–74 μm) was analyzed by a cyclosizer (cyclonic size analysis

instrument) having 38, 30 and 20 μm sieves. The obtained results are shown in Table 2. The grade of +74 μm size fraction is lower (12.37% TiO_2) than the ilmenite ore grade (20.26% TiO_2), which indicates that this fraction is hard to recovery. For the size from 30 to 74 μm, the yield is 51.45% and the TiO_2 distribution is 63.39%. The yield of –20 μm size fraction is only 3.70% due to pre-desliming. Therefore, the ilmenite ore is difficult to process because of non-uniform distribution in size. The TiO_2 grade and distribution at the size of –74+20 μm indicates that ilmenite is expected to be liberated from its associated gangues.

Table 1. Chemical composition of ilmenite ore by XRF

	Fe_T	FeO	TiO_2	Fe_2O_3	SiO_2	Al_2O_3	MgO	CaO	Others
Content (%)	7.61	22.95	20.52	6.40	22.68	5.98	7.34	5.28	1.24
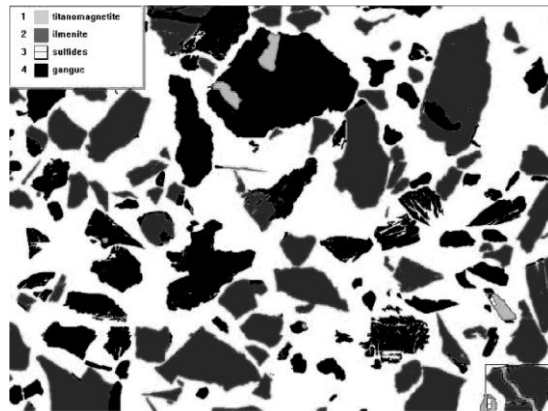
Fig. 1. Mineralogical and liberation analyses
of ilmenite ore by MLA technique

Table 2. Particle size distributions of the ilmenite ore

Particle size /μm	Yield (%)		Grade (TiO_2 %)		TiO_2 Distribution (%)	
	Individual	Accumulation	Individual	Accumulation	Individual	Accumulation
+154	9.53	9.53	4.73	4.73	2.22	2.22
–154+100	7.71	17.24	12.51	8.21	4.76	6.98
–100+74	18.86	36.10	16.17	12.37	15.05	22.03
–74+38	42.39	78.49	24.01	18.66	50.24	72.27
–38+30	9.06	87.55	29.41	19.77	13.15	85.42
–30+20	8.75	96.30	26.60	20.39	11.49	96.91
–20	3.70	100.00	16.90	20.26	3.09	100.00
Total	100.00		20.26		100.00	

Flotation reagents

H_2SO_4, MOH and diesel oil (D_O) were used as pH regulator, collector and auxiliary collector, respectively. H_2SO_4 (diluted to 25 wt%) was used for altering pH value of the pulp. MOH was dissolved in water to 3 wt% at 70 ^{o}C. MOH collector was invented by the Chinese Central South University (Zhu et al., 2007). It is a commercial collector, widely used in fine ilmenite upgrading. The detail composition of the MOH was neither provided by the company nor reported in literature. In order to get more information about MOH, a Fourier transform infrared spectrometer (FTIR) and atmospheric solids analysis probe (Model ASAP^{TM}, IonSense, USA)/time of flight-mass spectrometer (ASAP/TOF-MS) were applied.
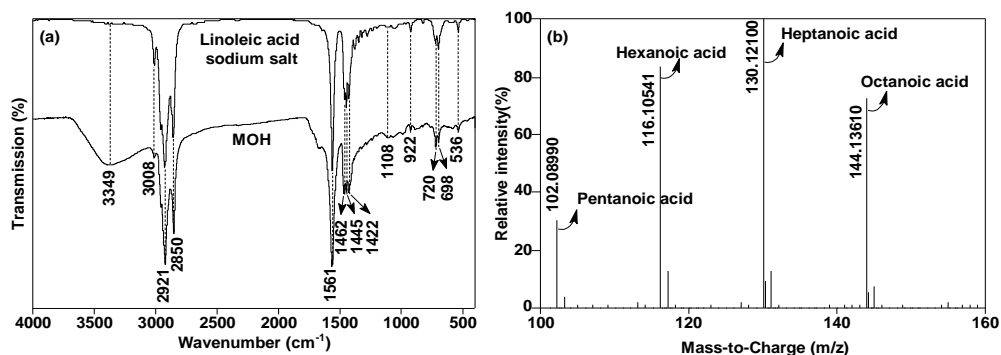
Fig. 2. FTIR (a) and ASAP/TOF-MS (b) analyses of the MOH

As Figure 2 shows, the spectrum of MOH is matched excellently with that of sodium salt of linoleic acid (peak at 3349 cm^{-1} was assigned to water). With ASAP/TOF-MS analysis, four compounds were identified in MOH, which probably were pentanoic acid, hexanoic acid, heptanoic acid and octanoic acid. Therefore, MOH seems to be a synthetic mixture of fatty acids or their salts. The auxiliary collector was industrial diesel oil (D_O), which has a synergistic effect with MOH. It can reduce the dosage of MOH and improves the flotation rate.

Flotation devices and tests

CSMC and its separation principles

As Figure 3 displays, the typical CSMC is composed of the column separation zone, cyclone separation zone and pipe flow mineralized zone. The sieve plates are packed in the column separation zone to improve the beneficiation efficiency, because the sieve plates provide the necessary low-turbulence environment, decrease the axial mixing, and increase the collision and adhesion effectively between bubbles and particles (Zhang et al., 2009; Kawatra and Eisele, 1995; Xia et al., 2006; Eisele and Kawatra, 2007). The CSMC has three input streams (feed, air and wash water) and two output streams (concentrate and tailings).

The separation principles of the CSMC was reported in literature (Zhang et al., 2013; Liu et al., 2013; Li et al., 2009; Yan et al., 2012; Deng et al., 2013). The circulation pressure (C_P) of circulating pump was measured by the pressure gaugue and adjusted by converter. The aeration quantity (A_Q) in pipe flow mineralized zone was modified by a flow meter.
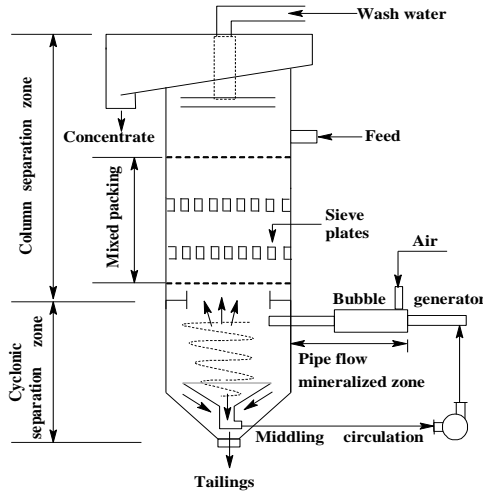
Fig. 3. Schematic representation of CSMC

Previous laboratory tests using the CSMC

The previous laboratory tests provide data for the pilot plant design of the best-suited circuit. According to previous laboratory tests (Table 3), the rougher-cleaner flotation flowsheet was chosen for the pilot plant test. The grade of the final cleaner concentrate is dependent on the grade of the rougher concentrate. In order to reach the optimum cleaner grade, it is necessary to keep the rougher grade at a predetermined value. As shown in Table 3, TiO_2 grade of rougher concentrate in pilot plant tests should reach

Table 3. Previous laboratory closed-circuit flotation tests. Rougher process was carried out in CSMC of diameter 100 mm and height 2000 mm while cleaner process in CSMC of diameter 50 mm and height 2000 mm

	Products	Yield (%)	Grade (TiO_2, %)	Recovery (TiO_2, %)
Rougher-cleaner process	Cleaner concentrate	35.40	47.98	83.91
	Rougher tailings	64.60	5.04	16.09
	Rougher concentrate		36.89	
	Cleaner tailings		19.56	
	Ilmenite ore	100.00	20.24	100.00

36–38% and rougher concentrate recovery should be as high as possible. Therefore, the quality of cleaner concentrate (the grade of TiO_2 is over 47.50%) was guaranteed.

Pilot plant tests using the CSMC

As described in Fig. 4, the pilot plant tests system consists of mixture section, separation and automatic control section. The flotation tests were optimum parameters exploration in rougher and cleaner process, and continuous pilot plant test.
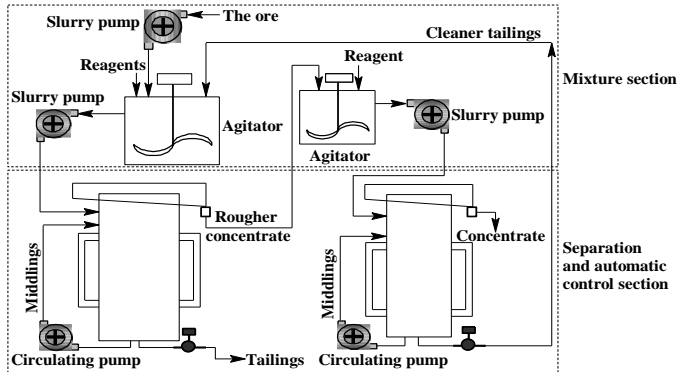
Fig. 4. Schematic diagram of pilot plant test. Rougher flotation was performed
in a CSMC of diameter 350 mm and height 4000 mm while cleaner flotation
in a CSMC of diameter 200 mm and height 4000 mm

In rougher process, the cleaner CSMC system was not operated. The optimum pH value, MOH dosage, ratio of solids to liquid phase (S/L ratio), D_O dosage, C_P and A_Q value were considered using one CSMC. The feed, concentrate and tailings were acquired after the system running steadily for 3 h. On each process variable, the experiment was repeated at least three times. The concentrate grade and recovery was analyzed with the grade-recovery curve (Neethling and Cilliers, 2008; Santana et al., 2008; Drzymala, 2007) and 95% confidence interval (*CI*) in both concentrate grade and recovery expressed as error bars in the y-direction and x-direction respectively. The *CI* can be calculated separately for each timed mean grade and recovery. The following formula is used for calculating *CI* (Napier-Munn, 2012):

$$CI = \pm \frac{t_\alpha}{\sqrt{n}} s \tag{1}$$

where t_α is the *t*-value for a 2-sided confidence level of $100(1-\alpha)$ % with $n-1$ degrees of freedom, the *t*-value can be obtained from a table of the *t*-distribution or from the Excel function = TINV (α, $n-1$); s is the standard deviation of the sample, and n is the number of replicates in the sample. In this paper, $1 - \alpha = 95\%$, $n = 3$, $t_\alpha = 4.30$, s is a variable.

The cleaner process was operated on the optimal rougher parameters. It's worth noting that the cleaner feed was the rougher concentrate, and the cleaner tailings was recycled (Fig. 4). The optimal pH, C_P and A_Q value were explored.

The 72 h continuous test was operated with two CSMCs, due to the optimized conditions in rougher-cleaner flowsheet. Flotation tests in industrial flotation machines proceeded with one rougher-two scavengers-three cleaners. The type of the flotation machines is GF-8/JJF-8, which consisted of GF-8 flotation machine (8 m^3 of effective volume, for adsorbing slurry) and JJF-8 flotation machine (8 m^3 of effective volume, for agitation). The GF-8/JJF-8 flotation machines are self-aerating and mechanical agitation flotation devices.

In the continuous test, the feed, concentrate and tailings were collected from the CSMC and GF-8/JJF-8 flotation machines at the same time to evaluate the beneficiation index. The particle size distributions of the feed, concentrate and tailings were analyzed to calculate the by-size grade and recovery of concentrate in CSMC and flotation machines by the following equation:

$$F(i) = \frac{\varepsilon\,\varepsilon(i)}{\gamma\,\gamma(i)} \qquad\qquad (2)$$

where $F(i)$ is the concentrate recovery of size i fraction (%), ε is the recovery of concentrate, $\varepsilon(i)$ is the metal distribution rate of size i fraction in concentrate, γ is the recovery of the ilmenite ore, $\gamma(i)$ is the metal distribution rate of size i fraction in the ilmenite ore.

Results and discussion

Optimum parameters in rougher process

Figure 5 plots the effect of the parameters on the mean grade-recovery in rougher process using one CSMC and 95% *CI* on the mean concentrate grade-recovery. The H$_2$SO$_4$ was chosen as the pH regulator to remove the hydration shell, deslime on the mineral surface and enhance the concentrate grade. Figure 5a shows pH value effect on concentrate grade and recovery when the other operating parameters were as follows: *S/L* ratio = 0.67, MOH = 2000 g/Mg, D_O = 500 g/Mg, C_P = 0.21 MPa, A_Q = 0.8 m^3/(m^2·min). With the pH decreases, the concentrate recovery decreases while the concentrate grade increases. The optimized pH value is 5.0, while the concentrate grade and recovery is 37.81% and 80.98%, respectively. MOH dosage is a vital flotation parameter in the flotation experiments. Suitable MOH dosage can enhance the stability of mineral particles and bubbles. In Fig. 5b (*S/L* ratio = 0.67, pH value = 5.0, D_O = 500 g/Mg, C_P = 0.21 MPa, A_Q = 0.8 m^3/(m^2·min)), as the MOH dosage increases, the concentrate grade declines and the recovery increases. Comprehensive consideration, 2800 g/Mg is selected as the optimal MOH dosage. The D_O was used to reinforce the flotation effect and strengthen the flotation rate. As exhibited in Fig. 5d (*S/L* ratio 0.67, pH value 5.0, MOH 2800 g/Mg, C_P 0.21 MPa and A_Q 0.8 (m^3/m^2·min)), 700 g/Mg is determined as the optimum dosage, and the concentrate grade is 36.73%, with a recovery of 84.34%. The effect of the *S/L* ratio on the flotation

is presented in Fig. 5c (pH value 5.0, MOH 2800 g/Mg, D_O 700 g/Mg, C_P 0.21 MPa and A_Q 0.8 (m³/m²·min)). Assay evidence indicated that the S/L ratio of 0.82 is established as the optimum condition.
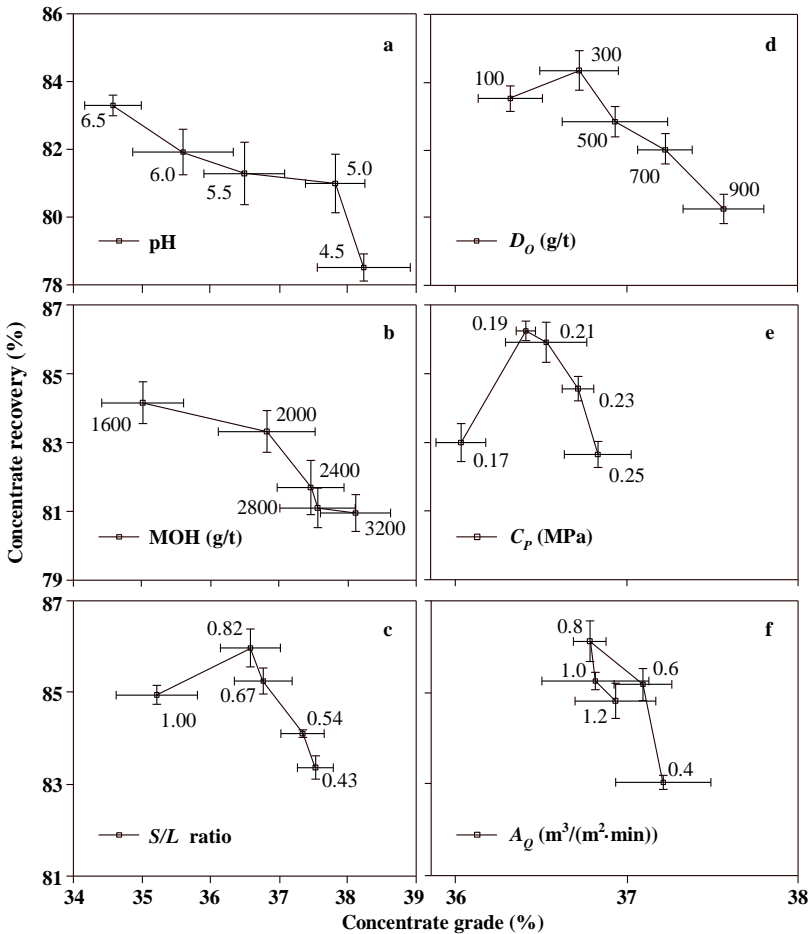
Fig. 5. Effect of the parameters on grade-recovery curves in rougher process using one CSMC, including 95% CI on the mean concentrate grade-recovery

The C_P has a critical influence on separation effect. In this section, other operating parameters were constant: S/L ratio 0.82, pH value 5.0, MOH 2800 g/Mg, D_O 700 g/Mg and A_Q 0.8 m³/(m²·min). As shown in Fig. 5e, when the C_P is 0.19 MPa, the concentrate recovery (86.24%) is higher than the others, and the concentrate grade is similar with the others. Herein, the optimum C_P is 0.19 MPa. The A_Q has an obvious influence on the particles-bubbles contact and bubbles quantities (Asplin et al., 1998). As exhibited in Fig. 5f (S/L ratio 0.82, pH value 5.0, MOH 2800 g/Mg, D_O 700 g/Mg and C_P 0.19 MPa), when the A_Q is 0.8 m³/(m²·min), the concentrate grade is 36.79%

and the recovery is 86.10%. Under this condition, the concentrate recovery is optimal even the concentrate grade has a slight decrease.

The 95% *CI* on the mean rougher concentrate grade-recovery (Fig. 5) indicates that there is a smaller uncertainty at each point, in both concentrate grade and recovery. This is a result of high stability of system and carefully control precision. The standard deviations for both concentrate grade (in the range < 1%) and recovery (in the range < 1%) are normal, so smaller *CI* can be achieved and good data repeatability obtained.

Optimum parameters in cleaner process

The principal role of cleaner process is to enhance the concentrate grade. This work investigates the influence of pH, C_P and A_Q value on the concentrate grade and recovery in cleaner. Results show that the optimal parameters of cleaner are follows: pH value 4.0, C_P 0.16 MPa and A_Q 0.5 $m^3/(m^2 \cdot min)$. Under these conditions, the cleaner concentrate grade is 48.18% with recovery of 82.25%.

Continuous pilot plant test using two CSMCs

The closed-circuit continuous pilot plant flotation test is to provide continuous operating data and compare equipment performance. Under the optimized parameters, the total reagent dosages in flotation machines are similar to that in CSMC. The detailed reagent dosages in flotation machines are: in one rougher, pH 5.0, MOH dosage 2300 g/Mg, D_O dosage 500 g/Mg; in one cleaner, pH 4.0; in one scavenger, MOH dosage 500 g/Mg, D_O dosage 180–200 g/Mg. No reagents were added in other steps.

Table 4. Comparison of separation system between FCSMC and FM for the ilmenite ore

Separation system	Grade (TiO$_2$, %)			Concentrate yield (%)	TiO$_2$ recovery in concentrate (%)
	Feed	Concentrate	Tailings		
FCSMC	20.16	48.11	5.43	34.51	82.36
FM	20.13	47.03	8.92	29.41	68.72

As Table 4 displays, the CSMC concentrate grade and recovery is 48.11% and 82.36%, respectively. Compared with the flotation machines, the CSMC concentrate grade and recovery increases 1.08 and 13.64 percentage points, respectively. Moreover, the flowsheet is simplified from six steps in flotation machines to two steps in the CSMC.

By-size grade and recovery of concentrate in continuous pilot plant test

Figure 6 shows the by-size grade and recovery of concentrate in the CSMC and flotation machines. As the particle size decreases, the by-size concentrate grade increases (+38 μm) then decreases (–38 μm), and the by-size concentrate recovery increases in both CSMC and flotation machines. However, the CSMC achieves significant concentrate grade and recovery for all size fractions expect for +74 μm size

fraction. In the −74+38 µm fraction, the CSMC concentrate recovery is 84.87%, while the CSMC concentrate grade is 49.33%. Nevertheless, the flotation machines concentrate grade and recovery is only 48.51% and 69.67%, respectively. In the size range −38+30 µm fraction, the CSMC concentrate grade increases by 2.32% and concentrate recovery increases by 14.33%, compared with flotation machines. In the size range −30+20 µm fraction, the CSMC obtained concentrate with a grade of 48.72% and a recovery of 92.71%, compared to only 44.40% and 80.09%, respectively, when using flotation machines for the same size fraction. For the fraction −20 µm, the CSMC concentrate recovery is the highest, however, the grade of this size fraction is lower relative to other size fractions, which may result from gangue entrainment.
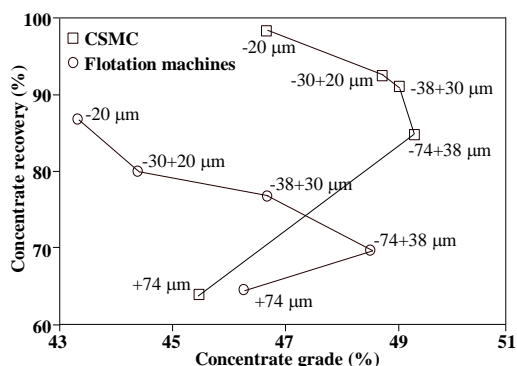
Fig. 6. By-size grade and recovery of concentrate curve
with CSMC and flotation machines

Therefore, the CSMC is a more effective device for fine ilmenite beneficiation, compared with flotation machines. The kinetic analysis of bubbles and particles in cyclone zone on the radial direction also gives the same conclusion (Li et al., 2012; Zhou and Liu, 2007).

Conclusion

This work exploits the CSMC to process fine ilmenite ore. The optimum parameters of the ilmenite flotation in rougher and cleaner process are obtained basing on the mean grade-recovery curve. A continuous pilot plant test is conducted in rougher-cleaner process using two CSMC's. The by-size grade and recovery of concentrate is analyzed. The conclusions drawn from this study are as follows.

- The optimal conditions in rougher are follows: S/L ratio 0.82, pH 5.0, MOH dosage 2800 g/Mg, D_o dosage 700 g/Mg, C_P 0.19 MPa, A_Q 0.8 m^3/(m^2·min). The optimal conditions in cleaner are follows: pH 4.0, C_P 0.16 MPa, and A_Q 0.5 m^3/(m^2·min).

▪ Compared with flotation machines, the cleaner concentrate grade of the CSMC is 48.11% with an improvement of 1.08 percentage points, while the concentrate recovery is 82.36% with 13.64 percentage points increment in continuous pilot plant test. The flowsheet is simplified from six steps (one rougher-two scavengers-three cleaners) in flotation machines to two steps (rougher-cleaner) in the CSMC. Results show the CSMC is an effective beneficiation device to recovery −74 μm size fraction.

Acknowledgments

References

ASPLIN R.A., SADR-KAZEMI N., CILLIERS J.J., 1998. *The effect of surfactant concentration on batch flotation mineral flux and froth structure*. Minerals Engineering, 11(3), 257–269.

BANISI S., FINCH J.A., 2001. *Technical note testing a flotation column at the Sarcheshmeh copper mine.* Minerals Engineering, 7, 785–789.

CAO Y.J., GUI X.H., MA Z.L., YU X.X., CHEN X.D., ZHANG X.P., 2009. *Process mineralogy of copper-nickel sulphide flotation by a cyclonic-static micro-bubble flotation column.* Mining Science and Technology, 19(6), 784–787.

DENG X.W., LIU J.T., WANG Y.T., CAO Y.J., 2013. *Velocity distribution of the flow field in the cyclonic zone of cyclone-static micro-bubble flotation column.* International Journal of Mining Science and Technology, 23(1), 89–94.

DOBBY G.S., FINCH J.A., 1991. *Column flotation: a selected revive, part II.* Minerals Engineering, 4, 911–923.

DRZYMALA J., 2007. *Atlas of upgrading curves used in separation and mineral science and technology, Part II.* Physicochemical Problems of Mineral Processing, 41, 27–35.

EISELE T.C., KAWATRA S.K., 2007. *Reverse column flotation of iron ore.* Minerals & metallurgical processing, 24(2), 61–66.

FAN X., ROWSON N.A., 2000. *The effect of $Pb(NO_3)_2$ on ilmenite flotation.* Minerals Engineering, 13(2), 205–215.

GUI X.H., WANG Y.T., ZHANG H.J., LI S.L., 2014. *Effect of two-stage stirred pulp-mixing on coal flotation.* Physicochemical Problems of Mineral Processing, 50(1), 299–310.

HASAN H., HALE, S., 2007. *Optimization of some parameters in column flotation and a comparison of conventional cell and column cell in terms of flotation performance.* Journal of the Chinese Institute of Chemical Engineers, 38(3–4), 287–293.

HONAKER R.Q., MOHANTY M.K., 1996. *Enhance column flotation performance for fine coal cleaning.* Minerals Engineering, 9(9), 931–945.

HULYA K., UGUR U., 2012. *Zinc recovery from lead-zinc-copper complex ores by using column flotation.* Mineral Processing and Extractive Metallurgy Review, 33(5), 327–338.

KAWATRA S.K., EISELE T.C., 1995. *Baffled-column flotation of a coal plant fine-waste stream.* Minerals and Metallurgical Processing, 12(3), 138–142.

LI C., LIANG B., GUO L.H., 2007. *Dissolution of mechanically activated Panzhihua ilmenites in dilute solutions of sulphuric acid.* Hydrometallurgy, 89(1–2), 1–10.

LI G.S., CAO Y.J., LIU J.T., WANG D.P., 2012. *Cyclonic flotation column of siliceous phosphate ore.* International Journal of Mineral Processing, 110–111(18), 6–11.

LIU J.T., LI X.B., WANG Y.T., CAO Y.J., LV F.K., 2008. *Experimental study on separating some molybdenum ore by using cyclonic-static micro-bubble flotation column.* Journal of Central South University: Science and Technology, 39(2), 300–309.

LIU J.T., XU H.X., LI X.B., 2013. *Cyclonic separation process intensification oil removal based on microbubble flotation.* International Journal of Mining Science and Technology, 23(3), 415–422.

NAPIER-MUNN T.J., 2012. *Statistical methods to compare batch flotation grade-recovery curves and rate constants.* Minerals Engineering, 34, 70–77.

NEETHLING S.J., CILLIERS J.J., 2008. *Predicting and correcting grade-recovery curves: Theoretical aspects.* International Journal of Mineral Processing, 89(1–5), 17–22.

OMIDVAR H., MIRZAEI F.K., RAHIMI M.H., SADEGHIAN Z., 2012. *A method for coating carbon nanotubes with titanium.* New Carbon Materials, 27(6), 401–408.

PARKER M., STEC B., 2012. *An alternative approach to plating of titanium and Ti alloys using carbon foam substrate.* Metal Finishing, 110(3), 19–22.

RULE C.M., ANYIMADU A. K., 2007. *Flotation cell technology and circuit design-an Anglo Platinum perspective.* Journal of the South African institute of mining and metallurgy, 107(10), 615–622.

SANTANA R.C., FARNESE A.C.C., FORTES M.C.B., ATAÍDE C.H., BARROZO M.A.S., 2008. *Influence of particle size and reagent dosage on the performance of apatite flotation.* Separation and Purification Technology, 64(1), 8–15.

WU F.X., LI X.H., WANG Z.X., WU L., GUO H.J., XIONG X.H., ZHANG X.P., WANG X.J., 2011. *Hydrogen peroxide leaching of hydrolyzed titania residue prepared from mechanically activated Panzhihua ilmenite leached by hydrochloric acid.* International Journal of Mineral Processing, 98(1–2), 106–112.

XIA Y.K., PENG F.F., WOLFE E., 2006. *CFD Simulation of alleviation of fluid back mixing by baffles in bubble column.* Minerals Engineering, 19(9), 925–937.

XIE, Z. J., WU, J. J., ZHANG, G. P., 2003. *Research and practice of technology for recovery of fine-grained.* Sichuan Nonferrous Metals, 1, 42–45. (in Chinese)

YAN X.K., LIU J.T., CAO Y.J., WANG L. J., 2012. *A single–phase turbulent flow numerical simulation of a cyclonic-static micro bubble flotation column.* International Journal of Mining Science and Technology, 22(1), 95–100.

YIANATOS J., BUCAREY R., LARENAS J., HENRIQUEZ F., TORRES L., 2005. *Collection zone kinetic model for industrial flotation columns.* Minerals Engineering, 18(15), 1373–1377.

ZHANG H. J., LIU J.T., WANG Y.T., CAO Y.J., MA Z.L., LI X.B., 2013. *Cyclonic-static micro-bubble flotation column.* Minerals Engineering, 45, 1–3.

ZHANG M., SHI C.S., LIU J.T., ZHAI A.F., 2009. *A honeycomb-tube packing medium and its application to column flotation.* Mining Science and Technology, 19, 775–778.

ZHOU X.H., LIU J.T., 2007. *Particle residence time in column flotation based on cyclonic separation.* Journal of China University of Mining & Technology, 17(3), 349–353.

ZHU J.G., CHEN S.M., YAO X.H., DENG Q.H., WANG, S. H., 2007. *Flotation of micro-fine ilmenite using new type collector-MOH.* Non-ferrous Metals, 6, 42–45 (in Chinese).

IN SEARCH OF AN EFFICIENT FROTHER FOR PRE-FLOTATION OF CARBONACEOUS SHALE FROM THE KUPFERSCHIEFER STRATIFORM COPPER ORE

Przemyslaw B. KOWALCZUK[*], Batuhan BULUC[**], Oktay SAHBAZ[**], Jan DRZYMALA[*]

[*] Wroclaw University of Technology, Wybrzeze Wyspianskiego 27, 50-370 Wroclaw, Poland
     przemyslaw.kowalczuk@pwr.edu.pl
[**] Department of Mining Engineering, Dumlupinar University, Kutahya, Turkey

Abstract: This papers shows that frothers such as aliphatic alcohols ($C_nH_{2n+1}OH$), poly(propylene glycols) ($HO(C_3H_6O)_mH$), poly(propylene glycol) alkyl ethers ($C_nH_{2n+1}O(C_3H_6O)_mH$) and poly(ethylene glycol) alkyl ethers ($C_nH_{2n+1}O(C_2H_4O)_mH$), can be used for collectorless flotation of a sample of carbonaceous copper shale manually separated from the Kupferschiefer stratiform copper ore. It was shown that flotation is influenced by the type and dose of frothers. The best flotation results were obtained with tri(propylene glycol) butyl ether C_4P_3, tri(propylene glycol) propyl ether C_3P_3 and tri(propylene glycol) P_3. For these frothers, the yield vs. frother dose relationship was in the form of convex curves indicating that carbonaceous copper shale can float at relatively low dosages of the frother. It means that these frothers can be used for pre-flotation of carbonaceous matter from the investigated copper ore. Other frothers formed concave yield–frother dose relationships and were less effective.

Keywords: *frother, pre-flotation, copper ore, shale*

Introduction

Frothers play a very important role in mineral processing. They reduce bubble size, prevent bubble coalescence and stabilize the froth (Cho and Laskowski, 2002). The influence of the type and dose of frothers on the flotation performance has been studied by many authors (Malysa et al., 1987; Laskowski, 2001; Pugh et al., 2007; Drzymala et al., 2007; Kowalczuk et al., 2014). Konieczny et al. (2013) showed that a mixture of frothers from the poly(ethylene glycol) alkyl ethers family, even applied without any collector, can be used to float carbonaceous shale from the Kupferschiefer stratiform copper ore located in Poland. Therefore, frothers alone can be applied for a

partial separation of organic carbon from the copper ore during the so-called pre-flotation (Konieczny et al., 2013). The pre-flotation stage is designed to reduce the amount of carbon in the final copper concentrate to make it suitable for a further pyrometallurgical processing. The removal of organic carbon from the copper concentrates is also very important because the presence of shale significantly decreases the copper content in the final concentrates (Foszcz and Drzymala, 2011). Konieczny et al. (2013) showed that pre-flotation of carbonaceous matter from the copper ore is possible, however they used only one industrial frother. In this work, we investigate the influence of the type and dose of eleven different frothers on flotation of carbonaceous copper shale originated from the Kupferschiefer stratiform copper deposit mined by KGHM Polska Miedz S.A.

Experimental

Flotation tests with carbonaceous copper shale were carried out in a Mekhanobr laboratory flotation machine. A sample of carbonaceous copper shale originated from the Kupferschiefer stratiform copper deposit (Fore-Sudetic Monocline copper ore) located in SW Poland. The advancing and receding contact angles for the investigated shale/water/air system was 42º and 24º, respectively (Bednarek, 2014). Seventy grams of the sample and distilled water were mixed together and agitated for two minutes in a 0.25 dm^3 flotation cell before adding any reagents. In each flotation tests the air flow rate was 20 dm^3/min and the stirring speed was 1200 rpm. The experiments were carried out under natural pH. The samples of carbonaceous copper shale were floated in the presence of different aliphatic alcohols ($C_nH_{2n+1}OH$), poly(propylene glycols) ($HO(C_3H_6O)_mH$), poly(propylene glycol) alkyl ethers ($C_nH_{2n+1}O(C_3H_6O)_mH$) and poly(ethylene glycol) alkyl ethers ($C_nH_{2n+1}O(C_2H_4O)_mH$) at three different concentrations of 0.044, 0.086, and 0.136 mmol/dm^3. The total time of flotation was 7 minutes in each test. The flotation products, that is concentrates and tailings, were dried and weighted to determine the concentrate yield.

The chemical reagents were obtained from Sigma-Aldrich (≥98% pure) and were used without further purification. The properties of the used chemical reagents, that is hydrophilic-lipophilic balance (HLB), molecular weight (MW), and critical coalescence concentration are given in Table 1. The value of the hydrophilic-lipophilic balance depends on hydrophilic and lipophilic (hydrophobic) groups in the considered molecule and can be estimated using formula HLB $= 7 + 1.3 \cdot (O) + 1.9 \cdot (OH) - 0.475 \cdot (C_xH_y)$ (Davies, 1957), where O and OH are numbers of hydrophilic oxygen and hydroxyl functional groups, respectively, and C_xH_y stands for the numbers of lipophilic (hydrophobic) –CH, –CH$_2$–, CH$_3$–, =CH– groups. The critical coalescence concentration (CCC$_{95}$), which characterizes reagent ability to prevent bubble coalescence, was calculated basing on the chemical structure of the frother, that is its molecular weight (MW) and hydrophilic-lipophilic balance (HLB), using a formula proposed by (Kowalczuk, 2013):

$$CCC_{95} = \frac{209.71 \cdot (HLB/MW)}{105.14 - 800(HLB/MW)}.$$ (1)

The CCC_{95} indicates the frother concentration at which there is a ninety five per cent reduction in the Sauter mean bubble diameter in comparison to the Sauter mean bubble diameter in water only (Zhang et al., 2012).

Table 1. Properties of chemical reagents used in flotation of carbonaceous copper shale
(n indicates number of carbon atoms in the alkyl groups while m stands for number of glycolic groups)

Type	n	m	HLB	MW g/mol	CCC_{95} mmol/dm^3
Aliphatic alcohols ($C_nH_{2n+1}OH$, C_n)					
1-Hexanol, $C_6H_{13}OH$	6	0	6.05	102	0.215
1-Nonanol, $C_9H_{19}OH$	9	0	4.63	144	0.085
1-Undecanol, $C_{11}H_{23}OH$	11	0	3.68	172	0.051
Poly(propylene glycols) ($HO(C_3H_6O)_mH$, P_m)					
Tri(propylene glycol), $HO(C_3H_6O)_3H$	0	3	9.13	192	0.149
Poly(propylene glycol) alkyl ethers ($C_nH_{2n+1}O(C_3H_6O)_mH$, C_nP_m)					
Tri(propylene glycol) methyl ether, $C_1H_3O(C_3H_6O)_3H$	1	3	7.98	206	0.110
Tri(propylene glycol) propyl ether, $C_3H_7O(C_3H_6O)_3H$	3	3	7.03	234	0.078
Tri(propylene glycol) butyl ether, $C_4H_9O(C_3H_6O)_3H$	4	3	6.55	248	0.066
Poly(ethylene glycol) alkyl ethers ($C_nH_{2n+1}O(C_2H_4O)_mH$, C_nE_m)					
Ethylene glycol monobutyl ether, $C_4H_9O(C_2H_4 O)_1H$	4	1	7.35	118	0.236
Di(ethylene glycol) monoethyl ether, $C_2H_5O(C_2H_4 O)_2H$	2	2	8.65	134	0.252
Di(ethylene glycol) monohexyl ether, $C_6H_{13}O(C_2H_4O)_2H$	6	2	6.75	190	0.097
Tri(ethylene glycol) monobutyl ether, $C_4H_9O(C_2H_4O)_3H$	4	3	8.05	206	0.111

Results and discussion

The influence of frother type and concentration on recovery of carbonaceous copper shale originated from the Kupferschiefer stratiform copper deposit was evaluated using eleven different frothers including aliphatic alcohols, poly(propylene glycols), poly(propylene glycol) alkyl ethers and poly(ethylene glycol) alkyl ethers. The flotation results are shown in the form of concentrate yield versus frother concentration expressed in three different forms, that is in mmol of frother per volume of solution (mmol/dm^3) (Fig. 1a), mass of frother per volume of solution (g/dm^3) as well as mass of frother per mass of shale (g/Mg) (Fig. 1b). In the case when the amount of solids and aqueous medium is the same, the g/dm^3 and g/Mg concentrations are the same. The flotation results were plotted in three different forms since it is not obvious what should be the concentration base for comparison of flotation results when different frothers are used. According to Malysa et al. (1987) the most promising base is a product of dynamic foamability index and frother concentration (DFI·c), however this approach is still awaiting for a wider verification.

Regardless of the way of expressing the frother concentration, two effects can be seen from Figures 1a and 1b. The first one indicates that for all reagents the concentrate yield increases with frother concentration, meaning that all of the considered in this work frothers can be used for carbonaceous shale flotation. The second observation is that the frothers can be divided into two families. The first group, with a convex shape of the yield vs. frother concentration curves is formed by the poly(propylene glycol) alkyl ethers C_nP_m and poly(propylene glycols) P_m. They float well carbonaceous copper shale at a relatively low dosage of the frother. The second group consists of poly(ethylene glycol) alkyl ethers C_nE_m and aliphatic alcohols C_n. For the second group the high recovery of carbonaceous copper shale is possible only at high frother concentrations.
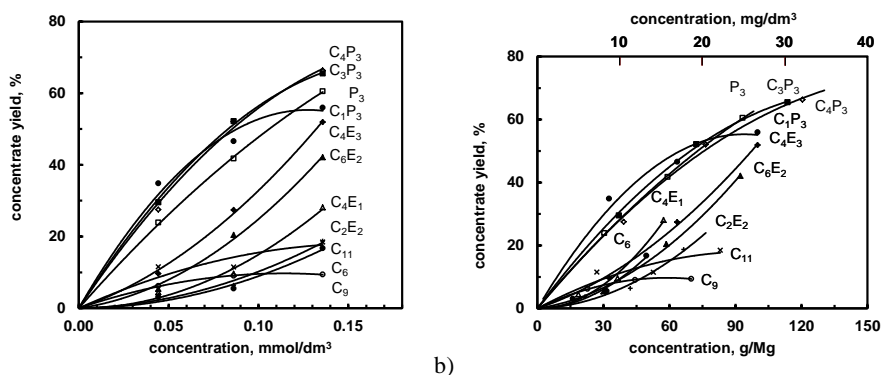
Fig. 1. Influence of frother concentration on shale concentrate yield, (a) concentration in mmol/dm^3, and (b) in g/Mg and in mg/dm^3

The chemical structure of frother plays a role in flotation (Malysa et al., 1987; Harris and Jia, 2000; Laskowski, 2001; Drzymala et al., 2007; Kowalczuk et al., 2014). One of essential parameters of a frother is its critical coalescence concentration (CCC). This parameter indicates the frother concentration at which the bubble coalescence is prevented (Cho and Laskowski, 2002). To show the influence of the critical coalescence concentration on the recovery of carbonaceous copper shale, the data from Fig. 1 were re-plotted to show concentrate yield versus normalized frother concentration (C/CCC_{95}), where frother concentration C and critical coalescence concentration CCC_{95} are expressed in the same units.

Figure 2 confirms the observation resulting from Figs. 1, that the investigated frothers can be used for flotation of hydrophobic shale particles and there are two, convex and concave patterns of the flotation yield-concentration curve.

Figures 1 and 2 clearly show that the lowest recovery of the carbonaceous copper shale is obtained with the aliphatic alcohols. Only for 1-hexanol the recovery exceeds 20%. The low efficiency of 1-nonanol and 1-undecanol is probably caused by their very low solubility in water. On the other hand, the best results were obtained for poly(propylene glycols) and poly(propylene glycol) alkyl ethers. The recovery of the

carbonaceous copper shale exceeds 60% only with tri(propylene glycol) butyl ether C_4P_3, tri(propylene glycol) propyl ether C_3P_3 and tri(propylene glycol) P_3.
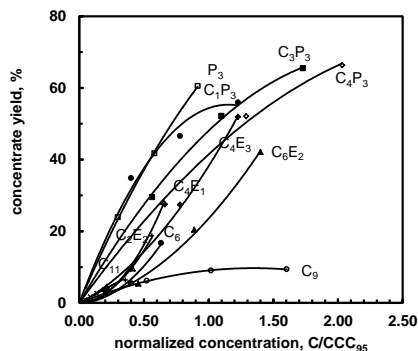
Fig. 2. Influence of normalized frother concentration C/CCC_{95} on concentrate yield

Among the investigated poly(ethylene glycol) alkyl ethers the best flotation occurs for the C_4E_3 and C_6E_2 frothers, while the yields for the remaining ethers, that is C_2E_2, C_4E_1, are very similar. However, it was shown elsewhere (Kowalczuk et al., 2014) that C_6E_2 and C_4E_1 exhibit an affinity towards quartz. Therefore, a low selectivity of copper ore flotation is expected in the presence of these frothers. Thus, poly(ethylene glycol) alkyl ethers with four carbon atoms in the alkyl (C_4) group and relatively high number (3) of ethylene groups provide high recovery of carbonaceous copper shale (Fig. 3a). Figures 1a and 1b also show that poly(propylene glycol) alkyl ethers C_nP_m form one, somehow scattered family of lines, exhibiting almost the same behaviour. However, the same results plotted as a 3D graph (Fig. 3b), indicate that from the C_nP_m family of frothers the most appropriate are those with four carbon atoms in the alkyl (C_4) group and having either three or four propylene (P_3 and P_4) groups.
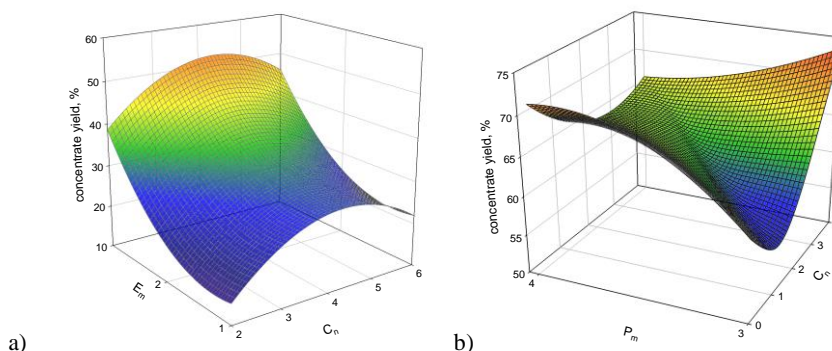
Fig. 3. Influence of number of carbon atoms in the alkyl (C_n) group, number of ethylene (E_m) (a) and propylene (P_m) (b) glycol groups in the chemical formula of frother on the concentrate yield for frother concentration equal to 0.136 mmol/dm^3

Conclusions

It appears from our investigations that all investigated frothers from the aliphatic alcohols, poly(propylene glycols), poly(propylene glycol) alkyl ethers and poly(ethylene glycol) alkyl ethers families can be used for pre-flotation of carbonaceous copper shale originated from the Kupferschiefer stratiform copper ore mined by KGHM Polska Miedz S.A. in the absence of any collector. The flotation performance depends on the frother type and dose. It was established that the yield versus frother concentration plots form two, convex and concave, patterns of the flotation curve. The best flotation results were obtained for C_4P_3, C_3P_3 and P_3. These frothers form the convex concentrate yield-frother dose relationship indicating that they float carbonaceous copper shale at a relatively low dosage of the frother.

Acknowledgements

References

CHO Y.S., LASKOWSKI J.S., 2002, *Effect of flotation frothers on bubble size and foam stability*, Int. J. Miner. Process., 64, 69–80.

BEDNAREK P., 2014, *Contact angle of carbonaceous copper shale for different chemical reagents*. BSc Thesis, Wroclaw University of Technology, in Polish.

DAVIES J.T., 1957, *A quantitative kinetic theory of emulsion type, I. Physical chemistry of the emulsifying agent, Gas/liquid and liquid/liquid interface*. Proceedings of the International Congress of Surface Activity, 426–438.

DRZYMALA J., MILCZARSKI E., MILCZARSKI J., 2007, *Adsorption and flotation of hydrophilic and hydrophobic materials in the presence of hydrocarbon polyethylene glycol ethers*, Colloids and Surfaces A: Physicochem. Eng. Aspects, 308(1–3), 111–117.

FOSZCZ D., DRZYMALA J., 2011, *Differentiation of organic carbon, copper and other metals contents by segregating flotation of final Polish industrial copper concentrates in the presence of dextrin*, Physicochem. Probl. Miner. Process., 47, 17–26.

HARRIS G.H., JIA R., 2000, *An improved class of flotation frothers*, Int. J. Miner. Process., 58(1–4), 35–43.

KONIECZNY A., PAWLOS W., KRZEMINSKA M., KALETA R., KURZYDLO P., 2013, *Evaluation of organic carbon separation from copper ore by pre-flotation*, Physicochem. Probl. Miner. Process., 49(1), 189–201.

KOWALCZUK P.B., 2013, *Determination of critical coalescence concentration and bubble size for surfactants used as flotation frothers*, Ind. Eng. Chem. Res., 52(33), 11752–11757.

KOWALCZUK P.B., ZALESKA E., DANCZAK O., 2014, *Flotation of a model carbonaceous copper shale-quartz mixture with poly(ethylene glycol) alkyl ethers*, submitted to Transactions of Nonferrous Metals Society of China.

LASKOWSKI J.S., 2001, *Coal flotation and fine coal utilization*, Vol. 14, in Developments in mineral processing, Elsevier Science Publishing, Amsterdam, The Netherlands.

MALYSA E., MALYSA K., CZARNECKI J., 1987, *A method of comparison of the frothing and collecting properties of frothers*, Colloids and Surfaces, 23, 29–39.

PUGH R.J., 2000, *Non-ionic polyethylene oxide frothers in graphite flotation*, Miner. Eng., 13(2), 161–162.

ZHANG W., NESSET J.E., RAO R., FINCH J.A., 2012, *Characterizing frothers through critical coalescence concentration (CCC)95-hydrophile-lipophile balance (HLB) relationship*, Minerals, 2, 208–227.

MODELING OF THE CARBON-IN-PULP (CIP) PROCESS IN GOLD CYANIDE LEACHING PLANTS USING PLANT DATA

Baris SAYINER

Koza Altin Isletmeleri A.S., Kaymaz Gold Mine, Eskisehir, Turkey

Abstract: An improved method to model CIP plants by plant data is presented. The Turkish gold cyanide leaching CIP plants, Bergama Ovacik, Gumushane Mastra and Eskisehir Kaymaz were modeled by using gold concentrations, solution, and solids samples from adsorption tanks without a need of laboratory work. Five carbon adsorption models were used namely k-n, Nicol-Fleming, Dixon, Film Diffusion with Langmuir isotherm and Film Diffusion with Freundlich isotherm (Johns model). Several monthly plant data were collected and modeled separately and model parameters as well as regression coefficient R^2 which values were found by a non-linear regression. By comparing R^2 values, the best fit model for the three CIP plants was determined as Film Diffusion with Langmuir Isotherm that R^2 values were above 0.95. Thus, by using the best fit model, the Kaymaz plant was optimized for existing 49 megagram per hour ore feed tonnage and plant parameters were predicted according to planned feed tonnage increase to 120 megagram per hour.

Introduction

Gold is predominantly produced from its ores by hydrometallurgical cyanide leaching process. The cyanide leaching process is applied by grinding the ore below 75 micrometers and dissolving the gold as $Au(CN)_2^-$ by mixing the ground ore with a dilute cyanide solution to obtain slurry above pH 10 and by supplying oxygen to leach tanks. Dissolution of gold-cyanide completes in about 24 hours. The hydrometallurgical reaction for extracting gold from its ores can be expressed as:

$$Au^0 + 2CN^- + \tfrac{1}{2} H_2O + \tfrac{1}{4} O_2 \rightarrow Au(CN)_2^- + OH^-. \qquad (1)$$

After dissolution of gold, the slurry passes through the carbon adsorption tanks. In the tanks, granulated activated coconut carbon is mixed into the slurry and the

disolved gold is adsorbed by carbon, leaving a barren solution. The adsorption phenomena can be defined by the reaction (Davidson and Sole, 2007; Pleysier et al., 2008):

$$2Au^0 + Ca^{+2} + 4CN^- + H_2O + \tfrac{1}{2}O_2 \rightarrow Ca[Au(CN)_2]_2 + 2OH^- . \tag{2}$$
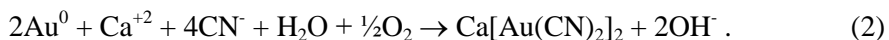
According to Eq. 2, the adsorption ocurrs by the formation of the $Ca[Au(CN)_2]_2$ complex. The $Ca[Au(CN)_2]_2$ complex is adsorbed by carbon. In this adsorption reaction Ca comes from added lime into the pulp to obtain the pH of 10 or above.

The slurry passes through from first adsorption tank to the last one, while the activated carbon follows the direction in reverse order from the last tank to the first one. By this counter current flow of the slurry and the carbon the $Au(CN)_2^-$ complex is loaded onto the carbon. From the first adsorption tank the most Au loaded final activated carbon is obtained and by column elution method obtained gold is stripped from carbon. To prevent the granulated carbon to move forward with the slurry, special sieves exist at the tanks discharge openings. Next, carbon is driven backward by special carbon pumps.

Adsorption of $Au(CN)_2^-$ by activated coconut carbon is a well proven process widely used to recover gold from slurry at cyanide leaching plants. In this research, modelling of adsorption of dissolved gold performed by using real CIP (carbon in pulp) plant data. For this aim, five kinetic models and the gold mass balance calculations were used together. After obtaining model parameters, optimization of the plant would be possible. By optimization of the plants according to these models, the optimum needed carbon amount in each tank, the residence time of the carbon for each tank, stripping amounts per week, adsorption tank amount and volumes and stripping column volume could be determined for certain plant feed ore tonnages.

In this research, the present CIP plants in Turkey, Bergama Ovacik, Gumushane Mastra and Eskisehir Kaymaz plants were modelled.

Gold mass balance

The counter current slurry and carbon flow with gold mass balance are presented in Fig.1. According to Fig. 1, the parameters are described as follows:

C_0 – solution Au concentration of the feed slurry, ppm
C_n – solution Au concentration of the slurry in tank n, ppm
Q_0 – Au concentration of pregnant carbon in tank 1, ppm
Q_n – Au concentration of loaded carbon in tank n, ppm
$ADS1–n$ – adsorption tanks
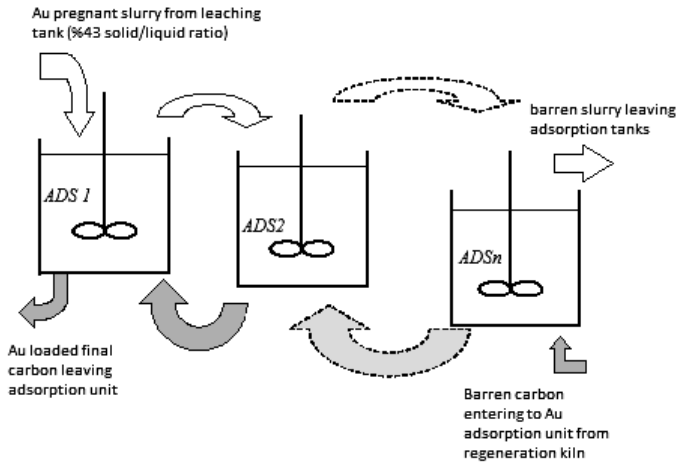
Fig. 1. Carbon adsorption unit of a carbon in pulp (CIP) Gold Ore Cyanide Leaching Plant

Mass balance can be defined by Eqs (3) and (4),

$$Vs(C_{n-1} - C_n) = Vc(Q_{n-1} - Q_n) \tag{3}$$

$$Vc = \frac{Mc}{tc}. \tag{4}$$

The parameters could be described as, Vs – solution flow rate in slurry Mg/hour; Vc – carbon flow rate Mg/hour, Mc – carbon amount in each adsorption tank, tc – carbon residence time in each tank as hours.

Gold adsorption kinetic models

Adsorption kinetics of gold (R) can be described in general as (Fleming and Nicol, 1984);

$$R = \frac{dQ}{dt}, \quad \text{or} \quad R = \frac{Q_{n-1} - Q_n}{tc} \tag{5}$$

and adsorption kinetics R can be defined by following five models (Le Roux et al., 1991; Fleming and Nicol, 1984; Fleming et al., 2011; Syna, and Valix, 2003; Ahmed et al., 1992; Jones and Linge, 1989; Rees and Van Deventer, 2001; Adams et al., 1987).

Fleming *k,n* model

The Fleming *k,n* model is the first carbon adsorption model defined by the equation:

$$\frac{\log(Q_{n-1} - Q_n)}{C} = \log k + n \log tc .$$ (6)

In this equation, k and n are model parameters, k is the rate constant, 1/hours, and n is a model parameter.

Nicol-Fleming model

This model includes an equilibrium constant as K as a difference from k,n model. The Nicol-Fleming model can be described as follows:

$$R = k(KC - Q) .$$ (7)

In Eq. 7 K is the equilibrium constant and k can be defined as rate constant.

Film Diffusion model with Freunlich isotherm (Johns model)

The Film Diffusion models define the adsorption process assuming that dissolved gold is adsorbed onto the carbon surface by passing film layer which separates the carbon surface and the solution phase. Thus, the equation can be shown as follows:

$$R = Ackf\left(C - \left(\frac{Q}{k} \right)^n \right) .$$ (8)

In Eq. 8 Ac is carbon film diffusion surface area, K, equilibrium constant, kf is film diffusion constant.

Film diffusion model with Langmuir isotherm

The Film Diffusion model with Langmuir isotherm can be defined as

$$R = Ackf\left(C - \left(\frac{bQ}{K - Q} \right) \right) .$$ (9)

In Eq. 9 Ac is carbon film diffusion surface area, K is the equilibrium constant, kf is film diffusion constant and b is a model constant.

Dixon model

The Dixon model can be defined as

$$R = k_1 C(K - Q) - k_2 Q .$$ (10)

In Eq. 10 k_1 is rate constant for gold adsorption and k_2 is defined as rate constant for gold desorption. Thus, this model takes into account existence of both adsorption and desorption phenomena at the same time. K is the equilibrium constant.

Material and method

In order to model the CIP plants, the samples that have been taken once a month were used. The samples include: solid (ore), solution, and carbons from each adsorption tank. While taking samples, the carbon amounts g/dm^3 slurry and solid concentration of slurry as %solid (w/w) for each tank were measured and noted.

Table 1. The average of separate 8 months sampling data from Mastra CIP plant

Adsorption tanks	Au conc. in ore, ppm	Au conc. in solution C, ppm	Au conc. in carbon Q, ppm	Solid concentration %40
Average of 8 months for Mastra CIP plant				Av. tonnage: 59 Mg/h
Feed slurry	2.63	6.45	-	gCarb/dm^{3}pulp
ADS1	0.86	0.81	4386	15.5
ADS2	0.79	0.74	3101	3.1
ADS3	0.72	0.47	2407	5.8
ADS4	0.67	0.27	1930	6.1
ADS5	0.62	0.20	1555	5.1
ADS6	0.58	0.14	1307	5.4
ADS7	0.58	0.09	1209	5.1
ADS8	0.53	0.10	993	13.4

Table 2. The average of separate 36 months sampling data from Ovacik CIP plant

Adsorption tanks	Au conc. in ore, ppm	Au conc. in solution C, ppm	Au conc. in carbon Q, ppm	Solid concentration %43
Average of 36 months for Ovacik CIP plant				Av. tonnage: 97 Mg/h
Feed slurry	1.21	3.64	-	gCarb/dm^{3}pulp
ADS1	0.75	1.39	5645	18.3
ADS2	0.55	0.71	3263	6.3
ADS3	0.47	0.53	2385	6.4
ADS4	0.39	0.30	1551	6.2
ADS5	0.35	0.17	1105	6.4
ADS6	0.34	0.09	820	6.6
ADS7	0.31	0.06	663	7.6
ADS8	0.31	0.03	544	9.5

Besides, ore throughput as megagram per hour (Mg/h) and tank volumes were taken into account. The average of monthly data for the Mastra, Ovacik and Kaymaz plants are shown in Tables 1-3.

Table 3. The average of separate 8 months sampling data from Kaymaz CIP plant

Average of 8 months for Kaymaz CIP plant				Av. tonnage: 49 Mg/h
Adsorption tanks	Au conc. in ore, ppm	Au conc. in solution C, ppm	Au conc. in carbon Q, ppm	Solid concentration %42
Feed slurry	1.58	3.91	-	gCarb/Lpulp
ADS1	0.99	0.85	3387	13.6
ADS2	0.87	0.43	1171	4.3
ADS3	0.78	0.17	754	6.1
ADS4	0.75	0.09	483	6.2
ADS5	0.74	0.04	301	4.4
ADS6	0.73	0.02	360	6.1
ADS7	0.73	0.03	286	1.5
ADS8	0.71	0.02	434	7.9

By using the mass balance (Eqs. 3 and 4) and data of Tables 1-3, tc_n for each adsorption tank, model parameters could be found by the calculation method as shown in Table 4.

Table 4. model parameters for different 5 models

Models	Model parameters
k, n model	k,n
Nicol-Fleming model	K,k
Johns model	$Ac.kf, n, K$
Film-diff. with Lang. isot.	$Ac.kf, b, K$
Dixon model	$k1, k2, K$

The model parameters presented in Table 4 were found by non-linear regression method. For each month, the model parameters and R^2 values were determined, thus it would be possible to determine the best fit model(s) for the CIP plants.

Furthermore, after model parameters were found, the plant tc and Mc values can be determined to obtain desired Q and C values by using model parameters. Besides, for different tonnage (Mg/h) of the ore feedings, the tc and Mc can be re-calculated to

obtain the same *Q* and *C*. Thus, optimization of the CIP plants would be possible after finding the model parameters by using real plant data.

Results and discussion

The model parameters and the regression coefficient (R^2) values for each models were calculated by nonlinear regression method and these R^2 values obtained by each models were compared to determine the nearest values to "1", thus, to find the best fit model for these three CIP plants. The R^2 values vs months were presented in Figs. 2-4.
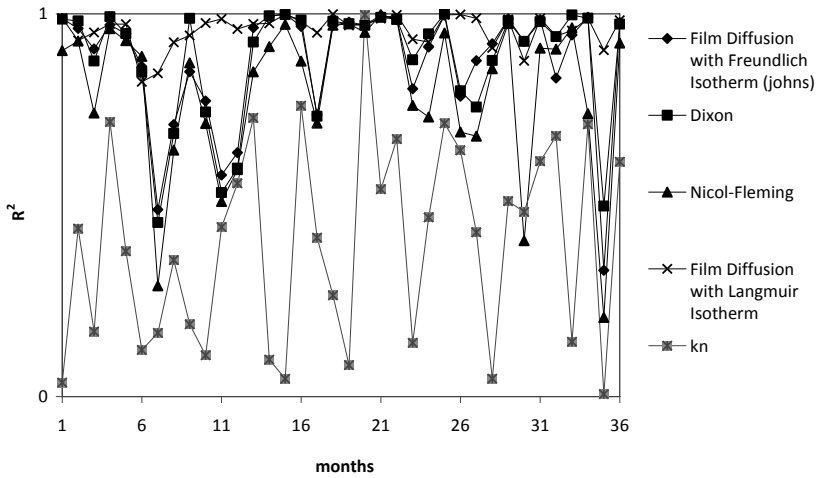
Fig. 2. Regression coefficient (R^2) values for different models for Ovacik CIP plant data

As shown in Fig. 2, the best fit model for Ovacik CIP plant is film diffusion model with Langmuir isotherm as its R^2 value is nearest to 1. For the Ovacik CIP plant using film diffusion model for optimization study, more reliable predictions would be performed such as carbon amount in each tank for the desired final carbon gold loading and final solution gold content for a different plant feed ore tonnage and thus for different slurry flow rates.

As presented in Fig. 3, the Film Diffusion and Dixon models are better (R^2 values are closed to 1) than the k,n and Nicol-Fleming models. Thus, for the Mastra plant the Film Diffusion models and Dixon model would supply most realistic predictions for the selected CIP model parameters as carbon amount in each tank and desired final carbon gold concentrations.
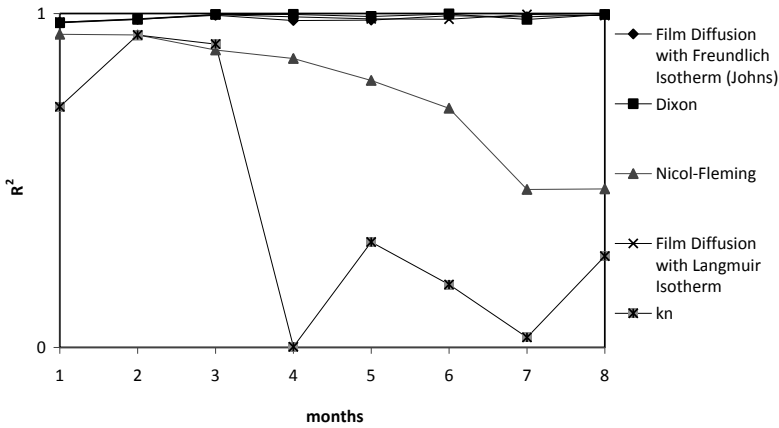
Fig. 3. Regression coefficient (R^2) values for different models for Mastra CIP plant data
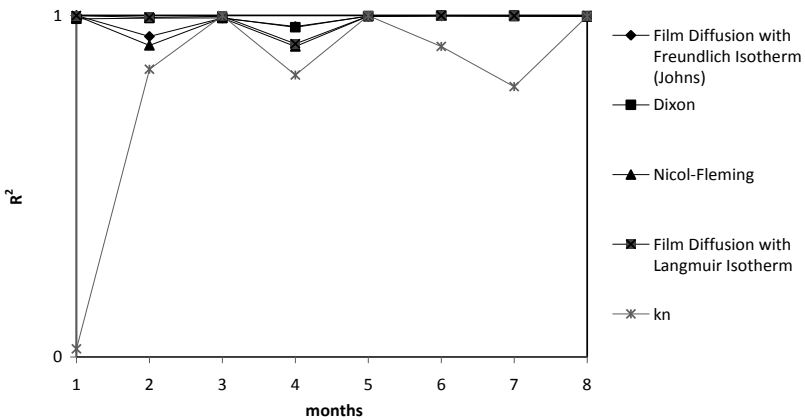
Fig. 4. Regression coefficient (R^2) values for different models
for Kaymaz CIP plant data

According to Fig. 4, the Film Diffusion and Dixon models are the best fit models to Kaymaz adsorption unit. Thus, the Film diffusion and Dixon models would be used for the most appropriate optimization results for the Kaymaz plant.

According to the Tables 1-3, in the Ovacik CIP tanks, solution gold ppm values C, continue to decrease through the last tank, indicating the adsorption continues regularly till last tank giving a reasonable final C value in the last tank. This phenomena shows that no optimization is required for Ovacik CIP plant. Besides, when the Kaymaz and Mastra plants are observed, the C values reduction finishes before the last tank, indicating that optimization would be beneficial for these two plants. This may be the reason that three models best fit for the Kaymaz and Mastra CIP plants. However, when the Ovacik plant was investigated, the models show

different fitting results. Thus, the Film Diffusion model with Langmuir isotherm is the best fit model for Ovacik and this model will be taken into account for the optimization processes of the plants since this model fits well all the three CIP plants.

Optimization of Kaymaz CIP Plant

The whole data (all *C* and *Q* values for each tanks of 8 months) were used to model the plant according to the Film Diffusion model with Langmuir equation. The model graph is shown in Fig. 5.
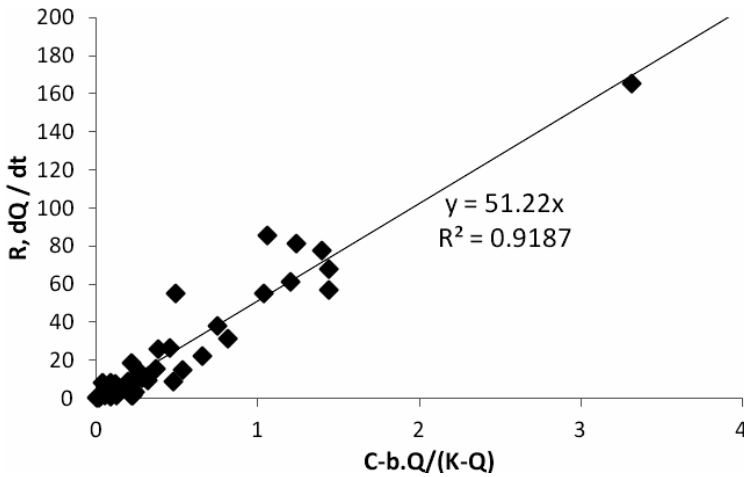
Fig. 5. Film Diffusion model with Langmuir isotherm graph
for Kaymaz CIP plant (8 months data)

By using a graphical form of equation (Fig. 5), the model parameters are determined by $Ac \cdot kf = 51.22$; $K = 13699$; $b = -1.789$ for the nonlinear regression method. Figure 5 gives a characteristic model graph for the Kaymaz ore with determined parameters, $Ac \cdot kf$, K and b. Thus, by using these parameters in conjunction with Eqs. 3-4 the optimization could be performed. Optimization processed for two different situations, that is first by acceptance of the same ore feed tonnage and second, estimating the increased ore tonnage up to 120 Mg/h. The optimization result are presented in Tables 5-7.

By using the best fit model, the Kaymaz CIP plant were optimized for the present ore tonnage and for the increased tonnage as 120 Mg per hour which is planned for the future. By the modeling process, required strip times/week for the 4 Mg capacity elution column; the residence time of carbon in each tank, tc, the carbon concentration in each tank gcarb/dm^3 pulp, solution and carbon gold concentrations in each tank were predicted.

Table 5. Kaymaz Cyanide leach plant CIP unit data without optimization

strip column capacity: 4Mg carb			Av. tonnage: 49 Mg/h		
Adsorption tanks	Au concentration in solution C, ppm	Au concentration in carbon Q, ppm	solid concentration 42%		
Feed slurry	3.91	-	Av. gCarb/dm^{3}pulp	tc, hours	strip times/week
ADS1	0.85	3387	6.3	11	
ADS2	0.43	1171	6.3	11	
ADS3	0.17	754	6.3	11	
ADS4	0.09	483	6.3	11	
ADS5	0.04	301	6.3	11	5
ADS6	0.02	360	6.3	11	
ADS7	0.03	286	6.3	11	
ADS8	0.02	434	6.3	11	

Table 6. Kaymaz Cyanide leach plant CIP unit data after optimization by the present ore feed tonnage

strip column capacity: 4 Mg carb			Av. tonnage: 49 Mg/h		
Adsorption tanks	Au concentration in solution C, ppm	Au concentration in carbon Q, ppm	solid concentration 42%		
Feed slurry	3.91	-	Av. gCarb/dm^{3}pulp	tc, hours	strip times/week
ADS1	1.93	5865	3.8	17.2	
ADS2	1.01	2985	3.8	17.2	
ADS3	0.54	1652	3.8	17.2	
ADS4	0.28	961	3.8	17.2	
ADS5	0.15	591	3.8	17.2	2
ADS6	0.07	390	3.8	17.2	
ADS7	0.03	281	3.8	17.2	
ADS8	0.01	221	3.8	17.2	

Table 7. Kaymaz Cyanide Leach plant CIP unit data after optimization
for 120 Mg per hour ore feed tonnage

strip column capacity: 4 Mg carb			Av. ton. 120 Mg/h		
Adsorption tanks	Au conc. in solution C, ppm	Au concentration in carbon Q, ppm	solid concentration 42%		
Feed slurry	3.91	–	Avr. gCarb/dm^{3}pulp	tc, hours	strip times/week
ADS1	1.93	5865	9.3	17.2	
ADS2	1.01	2985	9.3	17.2	
ADS3	0.54	1653	9.3	17.2	
ADS4	0.28	962	9.3	17.2	5
ADS5	0.15	593	9.3	17.2	
ADS6	0.07	392	9.3	17.2	
ADS7	0.03	283	9.3	17.2	
ADS8	0.01	223	9.3	17.2	

References

ADAMS M.D., MCDOUGALL G.J., HANCOCK R.D., REES K.L., VAN DEVENTER, J.S.J., DUNNE, R.C., 1987, *Models for the adsorption of aurocyanide onto activated carbon. Part II: Extraction of aurocyanide ion pairs by polymeric adsorbents,* Hydrometallurgy, 18, 139–154.

AHMED F.E., YOUNG B.D., BRYSON A.W., 1992, *Comparison and modelling of the adsorption kinetics of gold cyanide onto activated carbon and resin in a silica slurry*, Hydrometallurgy, 30, 257–275.

DAVIDSON R.J., SOLE M.J., 2007, *The major role played by calcium in gold plant circuits,* The Journal of The Southern African Institute of Mining and Metallurgy ,107, 463–468.

FLEMING C.A., NICOL M.J., 1984, *The adsorption of gold cyanide onto activated carbon. III. Factors Influencing the Rate of Loading and the Equilibrium Capacity,* J.S.Afr.Inst.Min.Metall., 84, 85–93.

FLEMING C.A., MEZEI A., BOURRICAUDY E., CANIZARES M., ASHBURY M., 2011, *Factors influencing the rate of gold cyanide leaching and adsorption on activated carbon, and their impact on the design of CIL and CIP circuits,* Minerals Engineering, 24, 484–494.

JONES W.G., LINGE H.G., 1989, *Effect of ore pulp on the adsorption rate of gold cyanide on activated carbon,* Hydrometallurgy, 22, 231–238.

LE ROUX J.O., BRYSON A.W., YOUNG B.O., 1991, *A comparison of several kinetic models for the adsorption of gold cyanide onto activated carbon,* J. S. Afr. Inst. Min. Metal., 91, 95–103.

PLEYSIER R., DAI X., WINGATE C.J., JEFFREY M.I., 2008, *Microtomography based identification of gold adsorption mechanisms, the measurement of activated carbon activity, and the effect of frothers on gold adsorption,* Minerals Engineering, 21, 453–462.

REES K.L, VAN DEVENTER J.S.J, 2001, *Gold process modelling. I. Batch modelling of the processes of leaching, preg-robbing and adsorption onto activated carbon,* Minerals Engineering, 14, 753-773.

SYNA N., VALIX M., 2003, *Modelling of gold (I) cyanide adsorption based on the properties of activated bagasse,* Minerals Engineering,16, 421–427.